IJSRST

Conference Proceedings

3rd National Conference on Emerging Approaches Towards Sustainability

5th Sep 2024

Organized By

Department of Physics & Mathematics
in Collaboration with IAPT RC 08F
Anand Charitable Sanstha, Ashti's
Anandrao Dhonde Alias Babaji Mahavidyalaya, Kada Tal.
Ashti Dist. Beed, Maharashtra, India

INTERNATIONAL JOURNAL OF SCIENTIFIC RESEARCH IN SCIENCE AND TECHNOLOGY

PEER REVIEWED AND REFEREED INTERNATIONAL SCIENTIFIC RESEARCH JOURNAL

TECHNO SCIENCE ACADEMY

One Day National Conference on Emerging Trends in Physics and Mathematics
ETPM – 2024

5th Sep 2024

Organized by

Department of Physics & Mathematics
in Collaboration with IAPT RC 08F & MMS
Anand Charitable Sanstha, Ashti's
Anandrao Dhonde Alias Babaji Mahavidyalaya, Kada Tal.
Ashti Dist. Beed, Maharashtra, India

Published By

Organizing Committee

Chief Patron
Hon. Bhimraoji Dhonde
(Ex. MLA- Ashti-Patoda-Shirur and Founder President, Anand Charitable Sanstha, Ashti)

Organizer
Principal Dr. H. G. Vidhate
(Senate & Academic Council Member, Dr.BAMU, Chhatrapati Sambhajinagar)
Prof. B. S. Khaire (IQAC-Coordinator)

Convener
Dr. R. G. Vidhate (Head, Dept. of Physics) Co-convener
Dr. D. S. Bodkhe (Head, Dept. of Mathematics)

Org. Secretary
Dr. Smt. G. S. Jagtap (BOS Member Math)
Mr. K. H. Katke (Dept. Physics)

National Advisory Committee
Dr. D. Ravinder Osmania University, Hyderabad. Dr. Jadhav K. M. MGM Uni. Chh. Sambhajinagar Dr. Shirsat M. D. Dean, Science and Tech.
Dr. Dole B.N. Head Dept. Physics Dr. BAMU
Dr. Dhole S. D. SPPU university, Pune.
Dr. Ghadle K.P. Head Dept. Maths. Dr. BAMU
Dr. Chaudhari S.R. Jalgaon University.
Dr. Ghule A. V. Shivaji University, Kolhapur.
Dr. Jotania R. B. Gujrat University.
Dr. Wafare B.N. SPPU university, Pune.
Dr. Modi K. B. Saurashtra university, Rajkot.
Dr. Phadnis P. P. BARC Mumbai.
Dr. Rajpure K. Y. Shivaji University, Kolhapur.
Dr. Raibagkar R. L. Gulbarga University.
Dr. Pawar Pravina.Dr. B.A.M.U.Chh.Sambhajinagar Dr. Undare Prabhakar Dr. B.A.M.U.Chh. Sambhajinagar Dr. Tyagi A. K., BARC. Mumbai.
Dr. Venkatraman A. V. Gulbarga University.
Dr. V. Radha, Mumbai University
Dr. Deshmukh S.B. JES College Jalna.
Dr. Gaikwad S.B. Ahmednagar.
Dr. Nannaware J.A. BOS Chairman.

Members

Prof. Chavan B. M.

Prof. Khedkar S.A.

Dr. Malshikhare A.B.

Dr. Bodkhe G.P

Dr. Aute P. N.

Dr. Borade D. B.

Dr. Gaikwad S. D.

Dr. Bodkhe R. G.

Prof. Waghule S. N..

Prof. Patel M. R.

Dr. Jirekar D. B.

Dr. Rajpange M. G

Dr. Kale B. G.

Dr. Dhonde B. M.

Dr. Avhad B.B

Dr. Sangle S. T. Mr. Wagh K. D.

Local Advisory Committee

About the college

Anand Charitable Sanstha is founded by Hon. Bhimraoji Dhonde (Ex. MLA. Ashti Patoda Shirur (ka)) for imparting the education to economically and educationally backward community. Our college is established in July, 1990. It is established with the sole mission of creating and developing the facilities and resources of higher education in order to make easy and convenient accessibility to the youths. Presently this institution runs primary to post graduate level programmes including professional courses. This college is affiliated to Dr. Babasaheb Ambedkar Marathwada University Chh. Sanbhajinagar. It has beautiful campus of 10 acres with adequate infra-structure. The college has been re-accredited with "A+" Grade (3.34 CGPA) by NAAC in May 2023. The college has been imparting education in Art's, Commerce and Science faculties. The research and development activities are being conducted in various departments. Department of Physics is also actively involved in research and innovative activities since its beginning.

About the conference venue

Kada is located on the bank of the River Kadi. Before independence it was under the rule of Nizam. Venue of the conference is on the Shirdi- Hyderabad National Highway. Nearest Railway station is Ahmednagar, which is 45 Km away from Kada, and 100 Km. from district place Beed. There are frequent buses available from Beed, Nanded, Parbhani, Latur, Osmanabad, Tuljapur, Solapur, Ahmednagar, Pune, Mumbai, Nasik and Aurangabad to kada.

Scope of the Conference

The conference on emerging trends in physics and mathematics is crucial for advancing scientific knowledge and fostering innovation. It provides a platform for researchers, educators, and industry professionals to share the latest discoveries, methodologies, and applications. By highlighting cutting-edge research and interdisciplinary approaches, the conference promotes collaboration and addresses complex global challenges. Participants gain insights into new theories and technologies that can drive progress in fields like quantum computing, nanotechnology, and artificial intelligence. Ultimately, the conference contributes to the development of solutions that can improve quality of life, enhance education, and support sustainable development in a rapidly evolving world

Conference topics

· Nanomaterial's: Synthesis and Characterization
· Nano magnetism, and Memory Devices.
· Thin Film deposition techniques
· Nanotechnology and Materials Science.
· Astrophysics and mathematical Aspects of cosmology.
· Artificial Intelligence and Machine Learning.
· Mathematical modeling of Physics.
· Interdisciplinary Applications.
· Sustainability and Environmental Physics.
· Topology and Geometry in Modern Physics.
· Data Science in Physics and Mathematics.
· Applied Mathematics

About The Conference:

The 3rd National Conference on Emerging Approaches Towards Sustainability (NCEATS-2024) will be organized by GKCEM and is scheduled to be held in virtual mode from 5th April to 6th April 2024. This is a multi-institutional effort to exemplify multidisciplinary research like intelligent computing and advanced communication systems, IoT, Green energy design, computations, and computers to interact and disseminate information on the latest developments in civil, mechanical, electrical, and electronics engineering in both academics and industry to establish sustainability. NCEATS-2024 will be a national forum for professionals, industrialists, researchers, academicians, and students from various engineering and science fields with multi-disciplinary interests.

CONTENT

Novel Ceramics for High-Temperature Applications

Balwan U. Patil[1], Ganesh B. Akat[2] & Dhanwan U. Patil[3]

[1]Department of Physics, Kohinoor Arts, Commerce & Science College, Khultabad.

Dist. Chhatrapati Sambhajinagar. (MS) India - 431101

[2]Department of Chemistry, Kohinoor Arts, Commerce & Science College, Khultabad.

Dist. Chhatrapati Sambhajinagar. (MS) India - 431101

[3]Department of Chemistry, Shri Sharadchandraji Pawar Senior College, Narangwadi.

Dist. Dharashiv

Abstract

Advanced ceramics have emerged as critical materials for high-temperature applications due to their exceptional properties such as high melting points, thermal stability, and resistance to corrosion and wear. These materials, including silicon carbide (SiC), aluminium oxide (Al_2O_3), and zirconium oxide (ZrO_2), possess melting points well above 2000°C and maintain structural integrity at elevated temperatures, exhibiting minimal thermal expansion and excellent thermal shock resistance. Additionally, advanced ceramics boast high mechanical strength and chemical inertness, ensuring durability and longevity even in the harshest environments.

Recent advancements such as nanostructured ceramics and ceramic matrix composites (CMCs) have led to significant improvements in mechanical and thermal properties, expanding the range of potential applications. Ultra-high-temperature ceramics (UHTCs) are also being explored for extreme environments, showcasing the continuous innovation in this field.

The future of advanced ceramics in high-temperature applications is promising, with ongoing research focused on enhancing material properties, developing cost-effective manufacturing processes, and broadening their application scope. Innovations in nanotechnology, additive manufacturing, and composite materials are expected to drive the evolution of advanced ceramics, solidifying their role as key materials in high-temperature technology.

Keywords: Advanced Ceramics, High-Temperature Applications, Thermal Stability, Ceramic Matrix Composites (CMCs), Ultra-High-Temperature Ceramics (UHTCs), etc.

I. INTRODUCTION

Introduction

High-temperature applications are fundamental to numerous advanced industries, including aerospace, power generation, manufacturing, and electronics. These sectors require materials that can endure extreme thermal and mechanical conditions without sacrificing performance. Traditional materials like metals and alloys often

fall short due to their limitations in melting points, thermal stability, and resistance to corrosion and wear [1-3]. In contrast, advanced ceramics offer a robust solution to these challenges. Engineered for specific high-performance applications, advanced ceramics, such as silicon carbide (SiC), aluminium oxide (Al_2O_3), and zirconium oxide (ZrO_2), exhibit melting points exceeding 2000°C. They maintain structural integrity under elevated temperatures, resist thermal shock, and show minimal thermal expansion. Furthermore, advanced ceramics are characterized by high hardness, mechanical strength, and exceptional chemical inertness, making them durable in the harshest environments [4].

The production and application of advanced ceramics involve sophisticated manufacturing techniques designed to achieve desired properties and shapes. Methods such as sol-gel processing, hydrothermal synthesis, spray pyrolysis, tape casting, extrusion, injection molding, and sintering are employed to produce high-purity, uniform ceramic powders and complex shapes [4,5]. Recent advancements in additive manufacturing, including 3D printing, have enabled the creation of intricate ceramic components with high precision [6]. These advancements have expanded the applications of advanced ceramics across various industries. In aerospace, they are used in thermal barrier coatings for turbine blades, engine components, and heat shields. In power generation, advanced ceramics improve thermal efficiency and energy conversion rates in gas turbines and nuclear reactors [6,7]. In manufacturing, they are used in high-temperature processes like metal cutting, welding, and glass production. In electronics, high-temperature superconductors and insulators made from advanced ceramics ensure reliable performance in harsh environments. Continuous research and development in nanostructured ceramics, ceramic matrix composites (CMCs), and ultra-high-temperature ceramics (UHTCs) promise to further enhance the properties and applications of advanced ceramics, solidifying their role as key materials in high-temperature technology [8,9].

This article encompasses the comprehensive overview of advanced ceramics, emphasizing their unique properties, diverse applications, and the latest advancements. The insights presented herein underscore the critical role of advanced ceramics in high-temperature applications and the potential for future developments to further enhance their capabilities and impact.

Importance of High-Temperature Materials

High-temperature applications are integral to several advanced industries, including aerospace, power generation, manufacturing, and electronics. These industries require materials that can endure extreme thermal and mechanical conditions without compromising performance. Traditional materials, such as metals and alloys, often fail to meet the demands of these environments due to limitations in their melting points, thermal stability, and resistance to corrosion and wear [9,10]. Advanced ceramics, with their superior properties, present a robust solution to these challenges.

Overview of Advanced Ceramics

Advanced ceramics are a class of materials that offer exceptional performance in high-temperature environments. Unlike traditional ceramics used in pottery and construction, advanced ceramics are engineered to exhibit specific properties that make them suitable for demanding applications. These properties include high melting points, excellent thermal stability, high mechanical strength, and resistance to corrosion and wear. The most common types of advanced ceramics used in high-temperature applications include silicon carbide (SiC), aluminium oxide (Al_2O_3), and zirconium oxide (ZrO_2) [11].

Properties of Advanced Ceramics

Advanced ceramics possess a unique combination of properties that make them indispensable in high-temperature applications. These properties include high melting points, thermal stability, mechanical strength, wear resistance, corrosion resistance, and additional attributes that enhance their performance in various demanding environments [11,12].

1. **High Melting Points**: Advanced ceramics, such as silicon carbide (SiC), aluminium oxide (Al_2O_3), and zirconium oxide (ZrO_2), exhibit melting points significantly higher than most metals and alloys. With melting points exceeding 2000°C, these ceramics are ideal for applications where materials are exposed to extremely high temperatures, such as in turbine engines and nuclear reactors [12].

2. **Thermal Stability**: These materials maintain their structural integrity and mechanical properties at elevated temperatures. They exhibit minimal thermal expansion, which is crucial in high-temperature applications to prevent material failure due to thermal stress. Additionally, advanced ceramics possess excellent thermal shock resistance, meaning they can withstand rapid temperature changes without cracking or losing functionality. This is particularly important in applications like aerospace and power generation, where components frequently experience sudden temperature fluctuations [13,14].

3. **Mechanical Strength**: Advanced ceramics are renowned for their high hardness and mechanical strength. They can withstand significant mechanical stress without deforming or failing, making them suitable for use in structural components subjected to high loads and abrasive environments. For example, zirconia-based ceramics are known for their toughness, which is enhanced by a phase transformation mechanism that occurs under stress, further improving their durability [15].

4. **Wear Resistance**: The high hardness of advanced ceramics contributes to their exceptional wear resistance. This property ensures long-term durability and reliability in demanding applications. Components made from advanced ceramics can withstand prolonged exposure to abrasive conditions without significant wear and tear, making them ideal for use in cutting tools, bearings, and other high-wear applications [16].

5. **Corrosion and Chemical Resistance**: The chemical inertness of advanced ceramics ensures that they do not react with most chemicals, even at high temperatures. This property makes them highly resistant to oxidation, corrosion, and wear. Components made from advanced ceramics can operate in corrosive environments, such as in chemical processing plants, without degrading. This extends the lifespan of the components and reduces the need for frequent maintenance and replacement [11-14].

6. **Electrical Insulation**: Many advanced ceramics, such as alumina and silicon nitride, are excellent electrical insulators. They can withstand high voltages and prevent electrical discharge, making them suitable for use in electrical and electronic applications where insulation is critical [15].

7. **Thermal Conductivity**: Some advanced ceramics, like aluminium nitride (AlN) and beryllium oxide (BeO), exhibit high thermal conductivity. This property allows them to efficiently dissipate heat, making them ideal for use in electronic devices and components that generate significant heat during operation [14-16].

8. **Low Density**: Advanced ceramics typically have a lower density compared to metals, which can be advantageous in applications where weight is a critical factor. For instance, in aerospace and automotive industries, reducing the weight of components without compromising performance can lead to significant improvements in fuel efficiency and overall performance [17].

9. **Biocompatibility**: Certain advanced ceramics, such as zirconia and alumina, are biocompatible, meaning they do not cause adverse reactions when implanted in the human body. This property makes them suitable for medical applications, including implants and prosthetics [18].

10. **Dimensional Stability**: Advanced ceramics exhibit excellent dimensional stability, maintaining their shape and size under various environmental conditions. This property is crucial for precision components used in industries like electronics and aerospace, where dimensional accuracy is paramount [19].

11. **Optical Properties**: Some advanced ceramics, such as sapphire (a form of aluminium oxide), have unique optical properties. Sapphire is used in applications requiring high transparency and durability, such as watch crystals, camera lenses, and protective covers for electronic devices [18,19].

12. **Radiation Resistance**: Advanced ceramics can resist damage from radiation exposure, making them suitable for use in nuclear reactors and space applications. Their ability to maintain structural integrity and functionality under high radiation levels ensures safety and reliability in these critical environments [18-21].

13. **Magnetic Properties**: Certain advanced ceramics, such as ferrites, exhibit magnetic properties that are useful in various applications, including magnetic storage, transformers, and inductors [22].

The combination of these properties high melting points, thermal stability, mechanical strength, wear resistance, corrosion resistance, electrical insulation, thermal conductivity, low density, biocompatibility, dimensional stability, optical properties, radiation resistance, and magnetic properties makes advanced ceramics ideal for a wide range of high-temperature and demanding applications. Continuous research and development are focused on enhancing these properties further, exploring new ceramic materials, and improving manufacturing processes to produce ceramics with even better performance characteristics [18-23].

Manufacturing Techniques [18-24]

The production of advanced ceramics involves several sophisticated manufacturing techniques designed to achieve the desired properties and shapes. These techniques include:

1. **Powder Processing**: The synthesis of ceramic powders is the first step in the manufacturing process. Methods such as sol-gel processing, hydrothermal synthesis, and spray pyrolysis are commonly used to produce high-purity and uniform ceramic powders [26].

2. **Shaping Techniques**: Once the ceramic powders are synthesized, they are shaped into the desired forms using techniques like tape casting, extrusion, and injection molding. These methods allow for the creation of complex shapes and fine details in ceramic components.

3. **Sintering**: Sintering is the process of densifying ceramic powders by heating them to temperatures below their melting points. This process increases the density and strength of the ceramic material. Conventional sintering, hot pressing, and spark plasma sintering are some of the common sintering techniques used.

4. **Additive Manufacturing**: Recent advancements in 3D printing technologies have enabled the fabrication of complex ceramic components with high precision. Additive manufacturing allows for the creation of intricate geometries that would be challenging to achieve with traditional methods.

Applications of Advanced Ceramics [25-31]

Advanced ceramics are employed across a wide range of industries due to their exceptional properties, which make them suitable for demanding applications. Beyond the previously mentioned uses, these materials find application in several specialized and emerging fields.

1. **Aerospace Industry**:
   - **Thermal Barrier Coatings (TBCs)**: Advanced ceramics are used as thermal barrier coatings on turbine blades and other engine components to protect them from extreme temperatures. These coatings improve engine efficiency and reduce fuel consumption by allowing engines to operate at higher temperatures.
   - **Heat Shields**: In space exploration, ceramics are used in heat shields to protect spacecraft from the intense heat generated during re-entry into Earth's atmosphere. The high thermal resistance of these ceramics ensures the spacecraft's integrity and safety.

2. **Power Generation**:
   - **Gas Turbines**: Advanced ceramics are used in high-temperature components of gas turbines, such as combustor liners and nozzle guides. These ceramics enhance the efficiency and durability of turbines by withstanding the extreme temperatures and corrosive environments present during operation.
   - **Nuclear Reactors**: In nuclear reactors, ceramics are used for fuel cladding and control rods. Their ability to withstand radiation and high temperatures without degrading is crucial for the safe and efficient operation of nuclear power plants.

3. **Manufacturing**:
   - **Cutting Tools**: Ceramics are used in cutting tools and machining inserts due to their hardness and wear resistance. These tools are employed in precision cutting and grinding of metals and other materials, extending tool life and improving machining efficiency.
   - **Kilns and Furnaces**: Advanced ceramics are used in the linings of kilns and furnaces for the production of glass, ceramics, and metals. Their thermal stability and resistance to chemical attack make them ideal for these high-temperature environments.

4. **Electronics**:
   - **Substrates**: Advanced ceramics, such as alumina and silicon nitride, are used as substrates in electronic circuits due to their excellent thermal and electrical insulating properties. They help in heat dissipation and provide mechanical support for electronic components.
   - **Piezoelectric Devices**: Ceramics with piezoelectric properties, such as lead zirconate titanate (PZT), are used in sensors, actuators, and transducers. These materials convert mechanical stress into electrical signals and vice versa, enabling their use in a wide range of electronic applications.

5. **Medical Applications**:
   - **Implants and Prosthetics**: Biocompatible ceramics, such as zirconia and alumina, are used in dental implants, hip replacements, and other prosthetic devices. Their durability and compatibility with the human body make them suitable for long-term use in medical implants.
   - **Bone Regeneration**: Ceramics like hydroxyapatite are used in bone grafts and scaffolds for bone regeneration. These materials support bone growth and healing by providing a structure that mimics natural bone tissue.

6. **Defence and Security**:

- o **Body Armor**: Advanced ceramics, such as boron carbide and silicon carbide, are used in ballistic armor for personal protection and vehicle armor. Their hardness and ability to absorb and dissipate impact energy make them effective at stopping bullets and shrapnel.
- o **Armor-Piercing Projectiles**: Ceramics are also used in armor-piercing projectiles and penetrators due to their high hardness and resistance to deformation upon impact.

7. **Energy Storage**:
   - o **Solid Oxide Fuel Cells (SOFCs)**: Advanced ceramics are used as electrolytes and electrodes in solid oxide fuel cells, which convert chemical energy directly into electrical energy. Their high ionic conductivity and stability at elevated temperatures are crucial for the efficiency and longevity of these fuel cells.
   - o **Thermal Energy Storage**: Ceramics are used in thermal energy storage systems, where they store and release heat efficiently. This application is important for managing energy in solar power systems and other renewable energy technologies.

8. **Environmental Applications**:
   - o **Catalysts**: Ceramics are employed as catalysts in various environmental applications, such as in catalytic converters for automobile exhaust systems. They help in reducing harmful emissions by facilitating chemical reactions that convert pollutants into less harmful substances.
   - o **Water Filtration**: Porous ceramics are used in water filtration systems to remove contaminants from water. Their ability to filter out impurities while maintaining high flow rates makes them effective in both industrial and residential water purification.

9. **Telecommunications**:
   - o **Microwave Substrates**: Advanced ceramics are used in microwave and radio frequency applications, such as in communication satellites and radar systems. Their low dielectric loss and stable dielectric properties ensure efficient signal transmission and reception.

10. **Consumer Electronics**:
    - o **Smartphone Screens**: Sapphire, a form of aluminium oxide, is used in the screens of high-end smartphones and watches due to its hardness and scratch resistance. This application ensures that devices maintain their aesthetic appearance and durability.

The versatility of advanced ceramics extends their utility to various fields, from enhancing industrial processes to improving consumer products and environmental technologies. Continuous innovation in material science is expanding the range of applications for advanced ceramics, providing solutions to modern engineering challenges and driving progress in technology.

Recent Advancements

The field of advanced ceramics is continually evolving, with ongoing research and development leading to new materials and improved properties:

1. **Nanostructured Ceramics**: The development of ceramics with nanoscale grains has led to significant improvements in mechanical and thermal properties. Nanostructured ceramics exhibit enhanced strength, toughness, and thermal conductivity, expanding their potential applications in more demanding environments [32].

2. **Ceramic Matrix Composites (CMCs)**: Combining ceramics with other materials, such as fibers, has resulted in composites that offer enhanced toughness and damage tolerance. CMCs are particularly useful in applications where traditional ceramics might fail due to brittleness [33].

3. **Ultra-High-Temperature Ceramics (UHTCs)**: Materials like hafnium carbide (HfC) and zirconium carbide (ZrC) are being explored for applications requiring temperatures above 3000°C. These UHTCs are promising for use in hypersonic vehicles and other extreme environments [34-36].

Future Prospects

The future of advanced ceramics in high-temperature applications looks promising, with ongoing research focused on improving material properties, developing cost-effective manufacturing processes, and expanding their application scope. Innovations in nanotechnology, additive manufacturing, and composite materials are expected to play a significant role in the evolution of advanced ceramics.

Advanced ceramics are likely to become even more critical in industries that require materials to perform under increasingly demanding conditions. For instance, as aerospace technology advances towards higher speeds and greater efficiencies, the need for materials that can withstand extreme temperatures and stresses will continue to grow. Similarly, the push for more efficient and sustainable power generation methods will drive the demand for high-performance ceramics in gas turbines and nuclear reactors.

Conclusion

In summary, advanced ceramics represent a vital class of materials for high-temperature applications. Their exceptional properties, including high melting points, thermal stability, mechanical strength and resistance to corrosion and wear, make them ideal for use in a wide range of industries. With continuous advancements in material science and manufacturing techniques, the potential for advanced ceramics to meet the evolving needs of high-temperature applications is vast. This research article provides a comprehensive overview of the development, properties, applications, and future prospects of advanced ceramics, underscoring their significance in modern technology.

References

1. C. G. Levi, "Emerging materials and processes for high-temperature applications," Current Opinion in Solid State and Materials Science, vol. 8, no. 1, pp. 77-91, 2004.
2. S. Hampshire, "Silicon nitride ceramics–review of structure, processing and properties," Journal of Achievements in Materials and Manufacturing Engineering, vol. 24, no. 1, pp. 43-50, 2007.
3. R. A. Miller, "Thermal barrier coatings for aircraft engines: history and directions," Journal of Thermal Spray Technology, vol. 6, no. 1, pp. 35-42, 1997.
4. A. Bellosi, "Advanced Ceramics for High Temperature Applications," Materials Science Forum, vol. 606, pp. 27-34, 2009.
5. P. Hu, "Nanostructured ceramics for high temperature applications," Journal of the American Ceramic Society, vol. 94, no. 12, pp. 3553-3570, 2011.
6. Wang, H., & Zhang, X. (2019). Advanced ceramics for high-temperature applications. Journal of Materials Science & Technology, 35(1), 19-34.
7. Zhou, J., & Li, J. (2020). High-performance advanced ceramics: Properties and applications. Materials Science and Engineering: R: Reports, 140, 100-124.

8. Wang, L., & Zhang, Y. (2018). Thermal barrier coatings: Advances and challenges. Journal of Thermal Spray Technology, 27(1), 72-85.

9. Cao, Y., & Zhang, Y. (2021). Ultra-high-temperature ceramics: Recent developments and future perspectives. Journal of the European Ceramic Society, 41(3), 240-256.

10. Matsumoto, S., & Saito, S. (2017). Fabrication and properties of silicon carbide ceramics. Journal of the American Ceramic Society, 100(5), 1605-1621.

11. Li, Y., & Liu, Z. (2021). Advances in ceramic matrix composites. Composites Science and Technology, 212, 108868.

12. Chen, L., & Wang, Z. (2019). Manufacturing techniques for advanced ceramics. Journal of Materials Processing Technology, 264, 116-130.

13. Wang, X., & Yang, J. (2020). High-temperature applications of advanced ceramics: A review. Materials Today, 36, 50-63.

14. Srinivasan, V., & Rehm, M. (2018). High-temperature stability of advanced ceramic materials. Ceramics International, 44(6), 6290-6304.

15. Jin, L., & Yang, Y. (2021). Nanostructured ceramics for high-temperature applications. Advanced Functional Materials, 31(20), 2008314.

16. Zhang, M., & Li, W. (2020). High-performance ceramics for aerospace applications. Aerospace Science and Technology, 101, 105813.

17. Yuan, X., & Zhang, C. (2019). The role of advanced ceramics in power generation. Energy Reports, 5, 1077-1087.

18. Jiang, J., & Wang, Y. (2018). Advanced ceramics for medical implants: Properties and applications. Biomedical Materials, 13(6), 065004.

19. Sharma, P., & Singh, K. (2021). Wear-resistant ceramics for industrial applications. Wear, 472-473, 203-218.

20. Li, Q., & Xie, W. (2017). Ceramic matrix composites: A review. Composites Part A: Applied Science and Manufacturing, 103, 224-234.

21. Gao, Y., & Liu, X. (2020). The use of advanced ceramics in energy storage systems. Journal of Power Sources, 451, 227755.

22. Chen, Z., & Zhang, L. (2019). Thermal barrier coatings: Properties and applications in aerospace. Materials Science and Engineering A, 764, 138192.

23. Huang, Z., & Zhang, Q. (2018). Advanced ceramics in high-temperature environments. Journal of High Temperature Physics, 8(2), 112-129.

24. Kang, S., & Song, H. (2021). Additive manufacturing of advanced ceramics: Recent developments and future directions. Additive Manufacturing, 37, 101722.

25. Huo, M., & Xu, J. (2019). Advanced ceramics for environmental applications. Environmental Science & Technology, 53(8), 4589-4602.

26. Jin, J., & Wang, Z. (2021). High-temperature superconductors made from advanced ceramics. Superconductor Science and Technology, 34(3), 033003.

27. Wu, H., & Sun, X. (2018). Mechanical properties of advanced ceramics under extreme conditions. Journal of the Mechanical Behavior of Biomedical Materials, 79, 185-196.

28. Yang, H., & Liu, H. (2020). Advanced ceramics for defense and security applications. Journal of Materials Engineering and Performance, 29(9), 7451-7462.

29. Sun, Y., & Li, X. (2017). Biocompatible ceramics for medical implants: A review. Materials Science and Engineering: C, 70, 860-870.

30. Guo, W., & Zhang, Y. (2021). Thermal energy storage using advanced ceramics. Renewable Energy, 172, 314-325.

31. Zhu, J., & Zhou, X. (2018). Properties and applications of piezoelectric ceramics. Journal of Electroceramics, 41(1), 1-16.

32. Liu, Y., & Zhang, T. (2020). The role of advanced ceramics in telecommunications. IEEE Transactions on Microwave Theory and Techniques, 68(6), 2252-2261.

33. Wang, S., & Zhang, R. (2019). Advances in high-temperature ceramic materials for industrial applications. Industrial Ceramics, 39(4), 245-258.

34. Chen, L., & Li, J. (2017). Properties and applications of high-temperature ceramics in the glass industry. Glass Technology: European Journal of Glass Science and Technology Part A, 58(4), 176-185.

35. Zhou, Y., & Liu, X. (2021). Radiation-resistant ceramics for nuclear applications. Journal of Nuclear Materials, 541, 152434.

36. Liu, Q., & Zhao, X. (2018). Advanced ceramics for energy-efficient buildings. Building and Environment, 137, 117-126.

Space Technology: A Way to Sustainable Development

N. N. Waghule

Dept. of physics, Bhagwan Mahavidyalaya, Ashti, Ta Ashti, Dist – Beed- 414203 (M.S) India

ABSTRACT

Sustainable development has been defined as the combination of environmental protection and economic growth. From last three decades we have Space technology which has its unique capability for transforming the life style of the humanity as a whole. However, there are at least four reasons why technological improvements in eco-efficiency alone will be insufficient to bring about a transition to sustainability. Technology is also linked to how humans interact, what sort of traits lead to success for both individuals and groups, and what sort of political arrangements make sense. Technology is arguably what has allowed humans to develop into what we are today. The applications of space technology for improving the conditions in India, majority of which are burdened with large population density, low yield in agriculture and health problem, natural disaster are practically unlimited. Finally, the paper highlights successful policies and strategies at the national levels that can promote the harnessing of space technologies for achieving the Sustainability such as solar photovoltaic systems Hydropower energy system Biomass energy systems Green hydrogen technology, Wind energy systems.

Keywords: Space technology, sustainability, Bio-mass energy, Food and agriculture, Health applications, physics-based approach, Hydropower energy system, Wind energy systems.

I. INTRODUCTION

Sustainable technology emphasizes the integration of environmental considerations into all stages of the technological lifecycle, from resource extraction and production to consumption and disposal. The term "sustainable development" has received unprecedented popularity ever since it was first defined by the World Commission on Environment and Development. In order to ensure that continued economic growth and environmental protection can go hand in hand, business leaders promoted the concept of "eco-efficiency" as the primary tool for achieving industrial sustainability. Sustainable development originally coined the term eco-efficiency and defined it as "adding maximum value with minimum resource use and minimum pollution [1] To address these challenges, we will require the help of new technologies in moving towards a trajectory for sustainable development. Advanced sensors, drones, and satellite imaging technologies facilitate the collection of real-time data on

biodiversity, habitat loss, and environmental pollution, aiding in the identification of conservation priorities and the implementation of targeted interventions. These cleaner technologies, and cleaner products and that strive for more efficient use [2].

Objectives of the Study:

The main objective of the paper is to discuss the importance of space technology and its tools for sustaining the environment. Space Technology is the specialized set of information technologies. Te objectives are:

1. Identify the areas in which the Applications of Space Technology can be used to achieve a better and sustainable agricultural production, Health, disaster risk reduction in India.

3. Determine how the use of Space Technology for better agricultural production, Health, Disaster risk reduction in India can be achieved in India.

4. Access the challenges of the application of space technology to achieving sustainable agricultural production Health, Disaster risk reduction in India.

Sustainable development actually means transforming or translating its aims into technological instrument monitoring and controlling instruments. In this context sustainability operation means applying physics- and technology-based approaches on different levels and for different given situations in the attempt of improving humanity quality of life with minimum undesired impacts on environment. Technology-based approaches are represented by approaches that aim at applying technology-specific interventions to address demands of providing healthy living.

II. METHODS AND MATERIAL:

General methodology for operationalzing sustainability can be materialized on different levels by respecting following steps.

2.1. **Food and agriculture:** The remarkable achievements in Space Technology and its Applications during the last three decades have firmly established its unique capability for transforming the life style of the humanity as a whole. Space technologies can be vital for agricultural innovation, modern agriculture. Space based technology is of value to farmers, agronomists, food manufacturers and agricultural policymakers who wish to simultaneously enhance production and profitability [3]. Remote-sensing satellites provide key data for monitoring the soil, snow cover and drought and crop development. Rainfall assessments from satellites, for example, help farmers plan the timing and amount of irrigation needed for crops. Accurate information and analysis can also help predict a region's agricultural output well in advance and can be critical in anticipating and mitigating the effects of food shortages and famines. The potential applications of space technology for improving the conditions in India, majority of which are burdened with large population density, low yield in agriculture, unchecked deforestation, over dependence on unpredictable rainfall combined with recurrent natural disasters such as drought and floods [4]. The geospatial data, data products and services and the lower cost of geospatial information technology facilities have stimulated its adoption across the India. Emerging priorities for international collaborations in this field include the

development of agricultural geospatial data infrastructure, agricultural geospatial knowledge platforms, standards and protocols enabling interoperation and data sharing, analysis-ready agricultural thematic geospatial data products and the sharing of relevant software applications. Another initiative expanding access to space technology is the crop monitoring system in China known as Crop Watch, which has played an important role in preparing international stakeholders for global crop market fluctuations and disruptions in food supply [5]. It has encouraged national, regional and global adoption of space technology using remote-sensing data.

2.2. Health applications: Health is a critical sector that has found the application of space technologies particularly helpful. Te atmospheric pollution in our fast growing urban conglomerations, creating serious hazard to public health and causing degradation of urban ecosystems over vast regions. The advances in the field have improved techniques of observing and analyzing factors like temperature and humidity, which has shown the potential for epidemiological applications [6]. In recent years, space-based technologies have played a growing role in health objectives and public domains, space science, technology and applications. The space-based research, play a crucial role in supporting decision-making, improved care, education and early warning measures. Information from remote-sensing technologies is used to monitor disease patterns, understand environmental triggers for the spread of diseases, predict risk areas and define regions that require disease-control planning. In the context of the ongoing corona virus disease of COVID-19 pandemic, using geographic information system data, various institutions have been able to publish information on confirmed infections and deaths, which has been useful in epidemiological studies of the virus. The new inventions and innovations in space technology have proven to be an instrument for enhancing the well-being of human beings [8].

2.3. Disaster risk reduction and humanitarian crises: There are several types of Natural disasters like earthquakes, floods, tornadoes, tropical cyclones, wildlife, tsunami, volcanic eruptions, landslides etc., that inversely affect the national progress and human life causing damage, death and loss of valuable goods. In recent years, space technology has become an integral part of disaster risk management and response efforts in the country .Space technology has shrunk time and distance, essentially reducing the world into a single global village with instantaneous communication connectivity and enabling the monitoring and shaping of the global environment as a whole. Disasters cause important loss of lives and assets around the world. One of the important ways to escape from these potential risks is to develop technologies for early prediction of disasters, proper strategy for disaster management and developing awareness among the civilians to overcome the critical situations, during natural disaster. Space Technology is playing an important role for minimizing the adverse effect of Natural disasters. Satellite imagery, giving real-time information over a large area and space-based technologies like telecommunications, global navigation satellite systems, Geographic Information Systems and Web Technology can be used for prevention, preparedness, relief reconstruction, warning and monitoring the various phases of disaster management. Geo-stationary satellites provide continuous and synoptic observations over large areas on weather including cyclone monitoring. India is the seventh largest

country having second largest population of the world having Natural Disaster management systems of, surrounded by the Himalayas on the north, northeast and northwest the Bay of Bengal on the east [9-10].

III.RESULTS AND DISCUSSION:

Physics-based approaches for operationalisng sustainability: Physics plays an important part in all our lives and particularly in our understanding of the climate. Pioneering efforts to reduce energy consumption, diminish pollution, and develop more efficient processes are currently being researched and developed by teams of physicists in following ways.

3.1 Solar photovoltaic system

Technologies using solar photovoltaic systems to produce energy are used in much different application. Moreover, ground mounted panels are among the most common applications, together with rooftop and floating installations. It can be used to generate electricity, desalinate water and generate heat, etc. A zero-energy building is a building that is designed for zero net energy emissions and emits no carbon dioxide. Building integrated PV (BIPV) technology is coupled with solar energy sources and devices in buildings that are utilized to supply energy needs. A PV water-pumping system is typically used to pump water in

rural, isolated and desert areas. The system consists of PV modules to power a water pump to the location of water need. Development Programme has worked with various stakeholders to install ground solar panels on waste land which can be used for agricultural purpose [11]

3.2 Hydropower energy systems:
Climate change is a major challenge for developing countries, particularly India, as it faces large-scale climate variability which can increase the impact of climate change. Hydropower is an old technological solution, but under the right conditions, it can still provide all areas with cost-effective and green electricity. Hydropower is a mature technology that is currently used in about 160 countries to produce cost-effective, low-carbon, renewable electricity. Examples from various countries show that cities can enhance their existing hydropower infrastructure to produce more emission-free energy. For example, the hydropower station on the River Koyana produces about 1,960 MW of green electricity for Nation [12].

3.3 Wind energy systems

Wind power is one of the most rapidly accelerating technologies amongst all renewable energy systems. To effectively manage large-scale variable renewable energy sources, flexibility must be harnessed in all sectors of the energy system, from power generation to transmission and distribution systems, storage. Globally, to integrate 60% variable renewable generation (35% from wind) by 2050 average annual investments in grids, generation adequacy and some flexibility measures would need to rise by more than one-quarter to USD 374 billion/year, compared to investments made in electricity networks and battery storage in 2018

3.4 Green hydrogen technologies

Green hydrogen is becoming a new alternative energy source to fossil fuel. Several countries have launched programmes to investigate how to benefit from green hydrogen production and to develop

the technologies required transforming hydrogen into a source of clean power. We have to develop low- and zero-emission heavy vehicles including trains and hydrogen-powered aerial vehicles using green hydrogen technology. The industries such as cement and steelmaking should be decarburizing industries. Additionally, electricity can be converted into hydrogen by electrolysis, providing an innovative way to store and transport renewable energy generated by other means when batteries or other modes of storage and transport are not practical [13].

3.5 Biomass energy systems

Anaerobic digestion technologies or biomass that converts biodegradable waste into methane-rich biogas are commonly deployed worldwide. For example, urban areas in Guatemala use electricity generated from sugarcane biomass – also known as biogases – which has been an established practice amongst sugarcane producers since 1990. During the 2017–2018 harvest seasons, biogases made it possible to save approximately 4 million tons of carbon emissions [14].

IV.CONCLUSION:

In conclusion, technology plays a pivotal role in driving sustainable development and environmental conservation efforts worldwide. The main contribution of this paper is the development and implementation of a strategic methodology for assessing the impact of space technology for sustainable development. Through innovations in renewable energy, agriculture, water conservation, technology has enabled significant progress towards mitigating climate change and preserving natural resources. The rising demand for energy and the ever-increasing concerns with global warming drive the world towards renewable energy alternatives that can truly be sustainable are Solar, wind energy and bio-electrochemical biomass Additionally, continued research and investment in emerging technologies hold promise for further advancements in environmental conservation and sustainable development. By leveraging the power of technology alongside effective policy measures and societal engagement, we can create a more sustainable and resilient future for generations to come. Ultimately, the success of these efforts will depend on our collective commitment to harnessing the potential of technology as a tool for positive change in safeguarding our planet and fostering a more sustainable global society. It is clear from the above discussion that eco-efficiency improvements are only useful if the endpoint is sustainability rather than economic growth. This paper represents only a small fraction of the work that is yet to be done on the implications of space technology for sustainability.

V. REFERENCES

[1]. Report on communication systems for disaster management, Anon, SAC/SITAA/TN/326,April 2001
[2]. INTERACT, Anon, DECU, Space Applications Centre (SAC), Ahmedabad, May 1998.
[3]. Narain, A,1981. Study of Tropical cyclone affected areas in the Krishna Delta region of Southern India. Photo Interpretation, May-June,81 – 3; pp1.5-1.6
[4]. Potential of remote sensing and GIS in landslide inventory and hazard zonation with reference to Tehri Reservoir rim, A. Narain, J.K. Garg, A. Narayana, T.V.R. Murthy, A.S. Arya, Varun Joshi and K.G. Saxena,

Presented at the International Seminar on Environment, Sustainable Development and Human Health, Banaras Hindu University, Varanasi, India, February 11-15, 1995.

[5]. Mapping of flood affected area in parts of Eastern Uttar Pradesh using microwave (Radarsat) data, Anon, RSAC-UP: DIR: TN:01:1998, RSAC-UP, Lucknow.

[6]. Du H, St-Pierre L, Vlachopoulou EI, Del Rio Vera J, Hedman N, Di Pippo, S.Forging partnerships between users and space solution providers. IAC-19-E3.1.1. In: Proceedings of the 70th international Astronautical congress (IAC),Washington, D.C., USA. 2019.

[7]. Ehrenfreund P. Space research and technology: key driver for development.German Aerospace Center. Bonn: UNISPACE+50 symposium; 2018.

[8]. ESA. About Space Science. European Space Agency. 2020. https://www.esa.int/Science Exploration/ Space Science /About_Space_Science . Accessed 15 Apr 2020.

[9]. ESA. SDGs Portal. European Space Agency. 2020. Available: https://sdg.esa.int/ Accessed 19 Feb 2020.

[10]. EU-Polarnet. Survey of existing use of space assets by European polar operators. Deliverable D33. 2017.

[11]. Eurisy. Operational uses of satellite-based applications in the public sector: a case-study review. Paris: 2015.

[12]. European Union. Directive 2005/35/EC of the European Parliament and of the Council of 7 September 2005 on ship-source pollution and on the introduction of penalties for infringements. Official Journal of the European Union 48, L255. 2005. https://eur-lex.europa.eu/legal-content /EN/TXT/?uri=OJ:L:2005:255:TOC

[13]. GEO.FAQ.What is Earth Observation? Group on Earth Observation.https://www.earthobservations.org/ g 2020

[14]. GEO Wetlands. GEO Wetlands Projects. Group on Earth Observation. 2020. https://geowetlands.org/projects/.

[15]. GSA. GNSS Market Report. Issue 5. European Global Navigation Satellite Systems Agency. 2017. https://www.gsa.europa.eu/system/files/

Structural Investigation of x(CoMn0.2Zn0.2Fe1.6O4) +1-x (BaTiO3) Composites

N. N. Waghule

Department of Physics, Bhagwan Mahavidyalaya, Ashti.Dist- Beed.(M.S) India. 414203

ABSTRACT:

Ferromagnetic-ferroelectric particulate composites of $xCoMn_{0.2}Zn_{0.2}Fe_{1.6}O_4 + (1-x) BaTiO_3$ were prepared by conventional ceramic method using composition x=0.0, 0.25, 0.50, 0.75, 1.00. The presence of two phases in composites was confirmed by XRD technique. The results of XRD pattern shows cubic spinel structure for ferrite phase and tetragonal perovskite structure for ferroelectric phase. The lattice constant(s) for mixed ferrite and ferroelectric phase are in good agreement with the reported data. No structural change was observed even though the composition of composites was varied. Variation of lattice parameters for ferrite and ferroelectric with ferrite content (x) in composites were studied. The X-ray density was calculated for ferrite, ferroelectric and their composites. The X-ray density increases for ferroelectric phase whereas it decreases for ferrite phase. The theoretical density calculated from the mass and volume of the composite in the form of circular pellet. The theoretical x-ray density and calculated X-ray density that obtained by mass and volume relation is in analogous with each other and shows similar trend.

Keywords: Ferrite, ferroelectric; ME composite; X-ray density; Porosity

I. INTRODUCTION

Materials with ferromagnetic and ferro-electric are significantly in focus and widely investigated for technological application. The magneto-electric effect is defined as the electric polarization of a material upon application of a magnetic field or conversely, as the magnetization of a material upon application of an electric field. When a magnetic field is applied to a composite of the piezoelectric perovskite and the spinel structure phases, the ferrite particles change their shape because of magnetostriction, and the strain is passed along to the piezoelectric particles, resulting in an electrical polarization [1,2,3]. These composite provide freedom to choose the various constitution phases and vary their molar percentage, which play an important role in ME effect [4,5].$BaTiO_3$ ferroelectric and $CoMn_{0.2}Zn_{0.2}Fe_{1.6}O_4$ spinel ferrite has high resistance, high magnetostriction coefficient, high Curie temperature. The ME voltage coefficient was attributed to relaxation process and resistivity of the material [6].The ferrite and ferroelectric composites $x(CoMn_{0.2}Zn_{0.2}Fe_{1.6}O_4)+1-x(BaTiO_3)$ have gained importance in recent years due to their high magneto-electric coupling effect. These composites are synthesized by taking into account the mutual interaction between two phases [7]. It is important to select a suitable combination of ferrite and ferroelectric material to get good ME effect. In order to have better ME effect the magneto-electric coefficient of ferrite and piezoelectric effect of ferroelectric phases must be high, which depends

on structural properties and resistivity [8]. Resistivity of composites and depends upon ferrite , ferroelectric content and sintering temperature and porosity. In recent years many magneto-electric composites have been developed using piezoelectric material and magneto-strictive ferrite material for technological applications. The $BaTiO_3$ with pervoskite type structure is extensively studied ferroelectric material for its electro-mechanical properties. $BaTiO_3$ exhibits good piezoelectric properties and possesses high electrical resistivity. The pure cobalt ferrite has good magnetic properties and addition of Zn, Mn content in small proportions in cobalt ferrite may enhance magnetic and electric properties of cobalt ferrite. The magnetoelectric effect is a product of the piezomagnetic effect (magnetic-mechanical effect) in the ferromagnetic phase and the piezoelectric effect (mechanical-electrical effect) in the ferroelectric phase, namely [9].

$$\text{Magnetoelectric effect} = \left(\frac{Strain-induced}{Magnetic-field}\right)ferrite \times \left(\frac{Electric-voltage}{Strain-induced}\right)ferroelectric \qquad (1)$$

If these two compounds can be successfully used as component, it is expected that it will show large ME effect at low magnetic field and such composites can be used in variety of applications. In present investigation XRD of ferrite ferroelectric and their composites as well as variation of lattice constant, X-ray density, porosity and its effect on composites were studied.

II. EXPERIMENTAL PROCEDURE:

2.1. Preparation of phases

The $(CoMn_{0.2}Zn_{0.2}Fe_{1.6}O_4)$ +1-x $(BaTiO_3)$ where x=0.00, 0.25, 0.50, 0.75, 1.00) composite materials were prepared by the standard ceramic method. The ferrite phase $CoMn_{0.2}Zn_{0.2}Fe_{1.6}O_4$ was prepared by using CO, MnO_2, ZnO and Fe_2O_3 in molar proportion as starting materials and their mixture was presintered at 1100^0C for 10h. The polycrystalline $BaTiO_3$ was prepared by using AR grade $BaCO_3$ and TiO_2 as starting materials in the molar proportions and presintered at $1000 ^0C$ for 8h.The chemical reaction takes place as follows[10] $BaCO_3 +TiO_2 \rightarrow BaTiO_3+CO_2 \uparrow$

2.2 Preparation of ME composites.

ME composites were prepared by mixing ferrite and ferroelectric phases using formula $(CoMn_{0.2}Zn_{0.2}Fe_{1.6}O_4)$+1-x$(BaTiO_3)$ where x=0.00,0.25,0.50,0.75,1.00 respectively. The mixed powders were uniaxially pressed in a die to form pellets with thickness of about 2.5–3 mm and 10mm in diameter using hydraulic machine. These pellets were finally sinteredat1200 ^0C for 10h and furnace cooled up to room temperature.

2.3 Characterization of ME composites:
Structural characterization of ferrite, ferroelectric and their composites was carried out by X-ray diffraction (XRD) with CuKα radiation.

III.RESULTS AND DISCUSSION

3.1. Structure analysis -XRD

The X-ray diffraction pattern of ferrite, ferroelectric and composite of $(CoMn_{0.2}Zn_{0.2}Fe_{1.6}O_4)$ +1-x$(BaTiO_3)$ where x=0.25,0.50,0.75, respectively were determined by XRD technique using X-ray diffractometer using Cu Kα radiations (λ=1.5418A˚). The pattern shows well-defined peaks and contains no unidentified lines as in Fig.1.
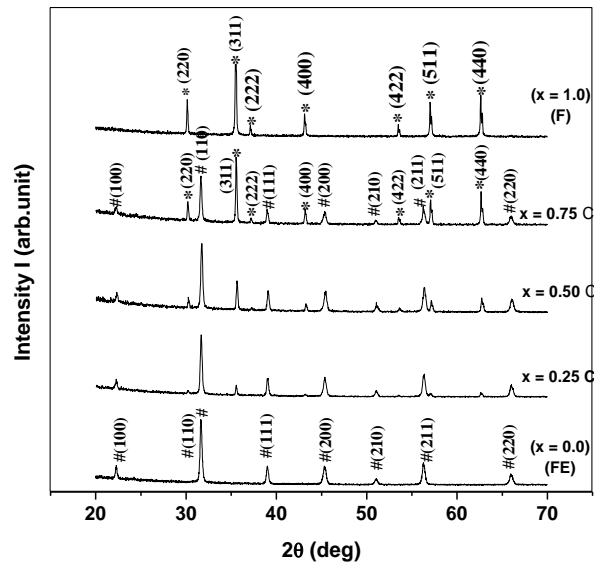
Fig.1 *XRD pa tern of CoMn$_{0.2}$Zn$_{0.2}$Fe$_{1.6}$O4 + BaTiO$_3$MEComposite system with x=0.0, 0.25, 0.50, 0.75, 1.00.*

The X-ray diffraction patterns of the present ferrite, ferroelectric and composite samples were recorded at room temperature and in the 2 theta range of 20^0-70^0.The occurrence of the peaks with specific indices characteristic of spinel and perovskite structure confirm cubic spinel structure in the ferrite phase and tetragonal perovskite structure in ferroelectric phase of the composite. All the XRD peaks are identified and compared with JCPDS data to confirm the phase and found to have well matching. (Cobalt ferrite JCPDS card #22-1086 and BaTiO3 JCPDS card # 83-1877).The intensity as well as number of the ferrite peaks (Fig.1) increases on increasing its content. The lattice parameters for the two phases in composites are nearly equal to that of constituent phases. For ferroelectric BaTiO$_3$, the lattice parameters are equal to a = 3.99A˚, c = 4.01A˚ (c/a = 1.01) and for ferrite phase CoMn$_{0.2}$Zn$_{0.2}$Fe$_{1.6}$O$_4$ it is nearly equal to a = 8.40A˚ as shown in [Table1]. This indicates that no structural change was observed even though the composition of composites was varied. Using the X-ray intensity values of (311) plane of ferrite and (110) plane of ferroelectric, we have calculated the approximate amount of ferrite and ferroelectric phases present in the

composites using the following relation [10] $\text{Ferrite \% of phase} = \dfrac{I_{\text{ferrite}}}{I_{\text{ferroelectric}}} \times 100$ (2)

The calculated percentages of constituent phases of composites are presented in Table.2.

Table 1: Lattice parameters (a,c) and unit cell volume (V) of x(CoMn$_{0.2}$Zn$_{0.2}$Fe$_{1.6}$O$_4$) +1-x (BaTi0$_3$) composites.

Ferrite content x	Lattice parameter			Volume (V)	
	Ferrite a (Å)	Ferroelectric		Ferrite a^3 (Å^3)	Ferroelectric a^{2}c(Å^3)
		a (Å)	c (Å)		
0.00	--	3.978	4.040	--	63.93
0.25	8.350	3.968	4.031	582.18	63.46
0.50	8.356	3.964	4.026	583.48	63.26
0.75	8.361	3.961	4.013	584.43	62.96
1.00	8.400	--	--	592.70	--

Table 2: Intensity (I) of most intense peaks (311) , (110) of ferrite and ferroelectric, Phase % of ferrite and ferroelectric $x(CoMn_{0.2}Zn_{0.2}Fe_{1.6}O_4) + 1-x(BaTiO_3)$ composites.

Ferrite content x	$I_{(311)}$ Ferrite	I_{110} Ferro electric	I_{311} / I_{110}	Ferrite phase %	Ferroelectric phase %
0.00	--	1100	--	--	100
0.25	210	856	0.245	24.5	75.5
0.50	330	679	0.488	48.8	51.2
0.75	498	689	0.722	72.2	27.8
1.00	1050	--	--	100	--

Table 3: Experimental density (d_m), therotical density (d_{th}), X ray density (dx) and % Porosity (% P) of $x(CoMn_{0.2}Zn_{0.2}Fe_{1.6}O_4) + 1-x (BaTiO_3)$ composites .

Ferrite content x	d_m gm/cm^3	(d_{th}) gm/cm^3	d_x gm/cm^3	P %
0.00	4.35	4.21	6.14	29.2
0.25	4.41	4.23	5.94	25
0.50	4.55	4.39	5.73	19.8
0.75	4.67	4.55	5.45	15.2
1.00	4.71	5.10	5.29	11.2

It is evident from Table.2 that, the percentage of ferrite and ferroelectric phase in composite is approximately equal to its mole percentage assumed in the synthesis of composites. The lattice parameters for the ferrite and ferroelectric phases in composites were calculated from XRD data using the following relations.

$$a = d\sqrt{N},$$

(3)

Where $d = \dfrac{n\lambda}{2\sin\theta}$, an $N = h^2 + k^2 + l^2$ for ferrite $N = h^2 + k^2 + l^2 (a^2/c^2)$ for ferroelectric phase [11].The values of lattice parameters for ferrite phase and ferroelectric phase are presented in Table 1. It can be seen from Table.1 that, the lattice parameters for ferrite phase increases with increase in ferrite content (x) whereas the lattice parameters of ferroelectric phase decreases with increase in ferrite content (x). The values of lattice parameter for pure ferrite and pure ferroelectric phase are in good agreement with the reported values [12]. The lattice constants of the composite are well consistent with constituent phases, indicating the absence of structural change with its variation in the composition. This implies that structure remain the same even if the composition varies from x = 0.25 to x = 0.75. Using the values of lattice parameters, the unit cell volume of ferrite and ferroelectric was calculated and the values are given in Table 1.

3.2 The experimental density: The experimental density of ferrite (x = 1), ferroelectric (x = 0.0) and their composites (0.25 ≤ x ≤ 0.75) were obtained using Archimedes's principle and the values are summarized in Table3. The experimental density increases with increase in ferrite content x in composites. The theoretical density calculated from the mass and volume of the composite in the form of circular pellet of 10 mm diameter and approximately 3 mm thickness. The theoretical density of composites can also be computed from the relation [13].

$$\rho_{theory} = \frac{m_1 + m_2}{\left(m_1\rho_1 + m_2\rho_2\right)} \ \rho_1\rho_2 \tag{4}$$

Where m_1 and m_2 are the molecular weights of ferrite and ferroelectric, respectively, whereas ρ_1, ρ_2 and ρ_{theory} are the theoretical densities of ferrite, ferroelectric and their ME composites. The values of theoretical density are given in Table 3. It is observed that the theoretical density increases with increase in ferrite content x in composites. The theoretical density calculated using the above relation (4) and that obtained by mass and volume relation is in analogous with each other and shows similar trend.

3.3 The X-ray density: The X-ray density (d_x) of ferrite, ferroelectric and their composites was calculated by using following formula [14].

$$dx = \left(1 - x\right)\left(\frac{M_{FE}}{Na_{FE}^2 c}\right) + x\left(\frac{8M_F}{Na_F^3}\right) \tag{5}$$

Where, d_X - the X ray density, M_{FE} – molecular weight of ferroelectric phase, M_F – Molecular weight of ferrite phase, a_F and (a_{FE} ,c) – lattice constants of ferrite and ferroelectric phase. The values of X-ray density densities are given in Table 3. It is observed that X-ray density increases with increase in ferrite content (x) in composites. The percentage porosity (%p) of the composites was calculated from the known values of experimental density (d_m) and X-ray density (d_x) and the values are shown in Table 3. It is found from Table 3 that porosity varies between 11.3 – 29.1 %. The high values of porosity of the present composites may be due to the sintering of the composites at much elevated temperature of about 1150 ^{0}C and may be due to the presence of Zn^{2+} ions.

3.4 Porosity: Porosity of a material is the difference between the molecular and macroscopic densities. Porosity for various concentrations is determined from the formula-

%P = 1 – [d_B/ d_X], where, d_B - Macroscopic density (obtained from the Archimedes's principle. d_X - x-ray density . The percentage porosity (P %) was calculated by using the values of X-ray density and bulk density. The values of porosity are given in Table3. It is clear from Table3 that porosity of the samples decreases with increases in ferrite content (x).

IV.CONCLUSION:

The composites of ferrite ($CoMn_{0.2}Zn_{0.2}Fe_{1.6}O_4$) and ferroelectric ($BaTiO_3$) were successfully synthesized using ceramic technique. From the X ray diffraction patterns of composites, it is clear that ferrite and ferroelectric phases exist separately. The structural parameter (lattice constant- ray density, bulk density etc of ferrite, ferroelectric and their composites are reasonably matched with standard data. The lattice constant *a* increases from 8.37 to 8.40 °A due to addition of Mn^{2+} content, obeying Vegard's law. The high values of porosity of the present composites may be due to the sintering of the composites at much elevated temperature of about 1150 ^{0}C and may be due to the presence of Zn^{2+} ions which increases resistivity.

V. REFERENCES

[1]. M.Fiebig J.Phys.D **38**(2005)123.

[2]. W.Eerestein,N.D.Mathur,J.F.Scott,Nature.4472, (2006) 759.

[3]. Ravinder Tadi,Yong-II Kim,Debasish Sarkar, J. Magn. Magn.Mater.323(2011)564.

[4]. J.V.Boomgard, R.A.J.Born, J.Mater.Sci.13, (1978)1538.

[5]. S.R.Kulkarni.C.M.Kanamadi.B.K.Chougle, J.Phys.Chem.Solid **67**(2006)1607.

[6]. S.L.Kadam,K.K.Patankar, Mater.Chem.Phys.**78**, (2003) 684.

[7]. P.A.Jadhav,M.B.Shelar,PhysicaB.405(2010) 857.

[8]. K.Sadhana, K.Praveena, S.R.Murthy,J. Magn.Magn.Mater.**322**,(2010)3729.

[9]. Ce-Wen Nan, Physical Review B Vol.50 (1994).

[10]. B.D.Cullity,"Elements of X-ray diffraction" 2nd Ed.Addison- Wesley, Reading, Mass(1978).

[11]. R.P.Mahajan,K.K.Patankar,M.B.Kothale. Pramana J.Physics (2002).

[12]. A.Venkataraman,V .A.Hiremath,S.K.Date,S.D. Kulkarni,Bull.Mater. Sci.24(2001) 617

[13]. Arif , D Shaikh, V.L.Mathe. Smart. Mater. Struct. 18, (2009) 6501.

[14]. K.K. Patankar , S.S. Joshi , B.K. Chougule , Physics Letters A 346 (2005) 337.

Electrodeposited Tungsten-Doped Bismuth Ferrite Nanoparticles for Supercapacitor Applications

Shivaji D. Waghmare,[a]* Pramod S. Borule,[a] Pranita M. Jondhale,[a] Shankar P. Phulwale,[b] Kunal H. Wananje,[c] Anant M. Gaikwad,[d] Ajay K. Raddi,[a] Pradeep R. Kate,[d] Yuraj H. Navale[a] and Rameshwar R. Kothawale[a]

[a] Department of Physics, Shri Shivaji Mahavidyalaya Barshi, Punyashlok Ahilyadevi Holkar Solapur University, Solapur, 413401, India

[b] Department of Chemistry, K. N. Bhise Arts, Commerce and Vinayakrao Patil Science College, Kurduwadi, Punyashlok Ahilyadevi Holkar Solapur University, Solapur, 413208, India

[c] Department of Physics, Ramkrishna Paramhansa Mahavidyalaya, Dharashiv, 413501, India

[d] Department of Zoology and Chemistry, Shri Shivaji Mahavidyalaya Barshi, Punyashlok Ahilyadevi Holkar Solapur University, Solapur, 413401, India

ABSTRACT

In the present study, BWFO (Bismuth Tungsten Ferrite) films were fabricated using the electrodeposition method, followed by calcination at 600°C for 4 hours. X-ray diffraction (XRD) analysis revealed distinct peaks corresponding to the (001), (310), (400), and (221) planes, among others, confirming a single-phase structure within the rhombohedral R3c space group, with an average crystallite size of approximately 39.41 nm. Energy-dispersive X-ray spectroscopy (EDX) confirmed the presence of Bi, W, Fe, and O elements in the expected proportions. Scanning Electron Microscopy (SEM) images showed a plate-like structure with lengths of 50-60 nm and thicknesses of 10-20 nm, along with increased pore sizes. FT-IR spectroscopy identified absorption peaks at 846.51, 1536.87, 1684.80, and 3290.75 cm^{-1}, indicating successful tungsten doping. Cyclic voltammetry (CV) analysis in 1 M NaOH revealed that the BWFO films had specific capacitances of 609.47, 393.51, 389.82, 104.07, and 89.91 F/g at scan rates of 2, 5, 10, 50, and 70 mV/s, respectively. The films exhibited both electric double-layer and faradic capacitance behavior, with an average capacitance of 4.6 F at a 2 mV/s scan rate.

Keywords: Electrodeposition Synthesis, Bismuth Tungsten Ferrite, Supercapacitor, Morphology

I. INTRODUCTION

Owing to the depletion of fossil fuels and environmental concerns, considerable efforts have focused on developing new alternative energy storage devices to meet future energy demands [1]. Supercapacitors, also referred to as ultracapacitors or electrochemical capacitors, bridge the gap between conventional capacitors and batteries in terms of power and energy density [2]. As a result, supercapacitors find extensive use in various applications, including electric vehicles, missile technology, aircraft, medical devices, and electric tools [3].

Based on charge storage capability, electrochemical capacitors divide into two types: (i) Electrochemical double-layer capacitors. Double-layer capacitors store energy through non-faradic charge separation at the interfaces between the electrode and electrolyte (commonly using carbonaceous materials with high surface

area and conductivity). (ii) Pseudocapacitors store energy through faradic redox reactions between electroactive materials, including metal oxides and conducting polymers [4-7]. In practical applications, one of the most challenging tasks for researchers is to enhance energy density and cell voltage. The asymmetric supercapacitor increases the operating cell voltage, resulting in enhanced energy density and capacitance [8]. Nowadays, numerous nanostructured metal oxides have emerged to improve the specific capacitance and conductivity of carbon-based electrochemical supercapacitors [9-11]. In particular, carbon has been utilized in various forms as supercapacitor electrode materials to achieve high power density and improved storage capacity [12].

Bismuth ferrite oxide (BFO) has garnered significant attention due to its unique properties, such as good oxygen ion conductivity, large energy density band gap, high refractive index, and dielectric conductivity. Furthermore, BFO is non-toxic, biocompatible, and widely employed in various applications, including optical materials, gas sensors, catalysts, supercapacitors, biosensors, and solid oxide fuel cells [13-15]. Recently, bismuth ferrite has attracted significant interest in electrochemical supercapacitors due to its high specific capacitance and long-term charge-discharge cycle stability. However, the specific capacitance behavior of BFO has yet to be studied in depth [15]. This study details the preparation of BiWFeO (BWFO) films through the electrodeposition method, followed by calcination at 600°C for 4 hours. The structural, chemical, and electrochemical properties of the BWFO films were analyzed using various characterization techniques, including X-ray diffraction (XRD), Energy Dispersive X-ray Spectroscopy (EDX), Field Emission Scanning Electron Microscopy (FE-SEM), Fourier Transform Infrared Spectroscopy (FT-IR), and Cyclic Voltammetry (CV). These analyses provide a comprehensive understanding of the materials' potential applications in the field of energy storage.

II. SYNTHESIS OF MATERIALS

In this typical procedure, Bismuth Nitrate Pentahydrate ($Bi(NO_3)_3 \cdot 5H_2O$), Iron Nitrate Nonahydrate ($Fe(NO_3)_3 \cdot 9H_2O$), Citric Acid ($C_6H_8O_7$), and Sodium Tungstate Dihydrate ($Na_2WO_4 \cdot 2H_2O$) were used as precursors. The molar concentrations of these reagents were 0.2 M, 0.2 M, 0.1 M, and 0.1 M, respectively. Each compound was dissolved separately in 30 ml of deionized (DI) water. For $Bi(NO_3)_3 \cdot 5H_2O$, 3 ml of nitric acid was added to 27 ml of DI water to aid in dissolution. Once fully dissolved, the solutions of $Bi(NO_3)_3 \cdot 5H_2O$, $Fe(NO_3)_3 \cdot 9H_2O$, and $C_6H_8O_7$ were combined in a beaker, referred to as the "A-type solution." This A-type solution was placed on a magnetic stirrer and stirred continuously for thorough mixing. Subsequently, 10 ml of ammonia (NH_3) solution was added quickly to the A-type solution to adjust the pH between 8 and 10, forming the "B-type solution." The $Na_2WO_4 \cdot 2H_2O$ solution was then added to the B-type solution while stirring. This final solution was utilized for the electrodeposition process. Electrodeposition was carried out using a two-electrode system, with a stainless steel substrate serving as the working electrode and a platinum electrode as the counter electrode. The working and counter electrodes were immersed in the final solution, maintaining a distance of 1 cm between them. A potential of ±3.5 volts was applied across the electrodes for 15 minutes at room temperature. After the deposition, the sample was removed and annealed in a laboratory muffle furnace at 600°C for 4 hours, followed by natural cooling to room temperature. The resulting $WBiFeO_3$ thin films exhibited a dark brown color. In the subsequent step, these $WBiFeO_3$ nanoparticle thin films were tailored for specific applications. The films were cut to a specific area of 1 cm² and utilized in supercapacitor applications with three different electrolytes.

III.RESULTS AND DISCUSSION

The BWFO films were synthesized using the electrodeposition method. Following the deposition, the films were calcined at 600°C for 4 hours. The structural analysis was performed using XRD as shown in fig. 1(a), where the prominent peaks corresponded to various hkl planes, including (001), (310), (400), (221), (420), (321), (401), (540), (630), (112), (312), (650), and (820). The peak at ~28° corresponded to stainless steel and was labeled with a "#" symbol. The XRD peaks matched JCPDS card no. 38-1289, confirming the formation of a single-phase BWFO film with a rhombohedrally distorted perovskite structure belonging to the R3c space group. The average crystallite size, calculated using scherrer equation, was approximately 39.41 nm.
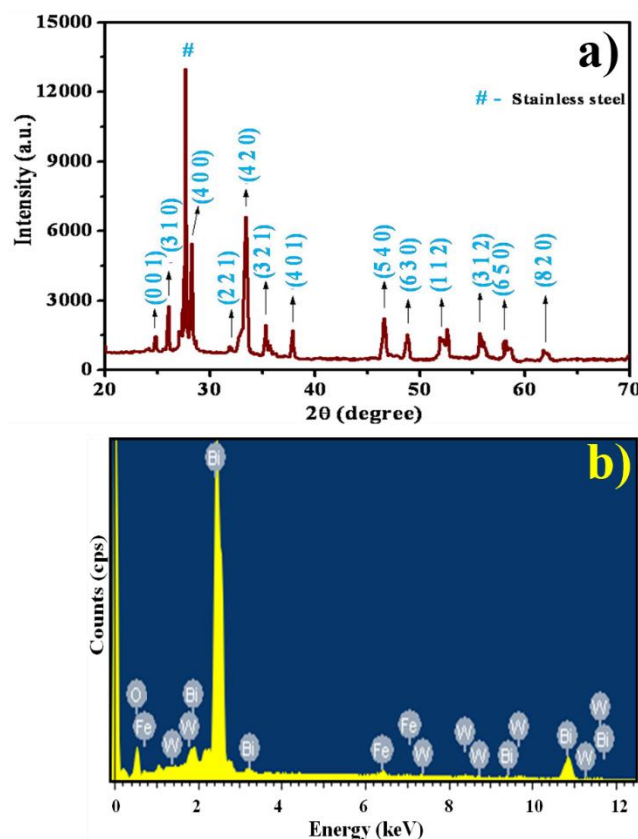
Fig.1: The XRD pattern and EDX spectrum of electrodeposited BWFO films

The chemical composition of the BWFO films was analyzed using EDX as depicted in Fig. 1(b). During this process, X-rays emitted due to electron bombardment in an electron microscope were used to determine the elemental composition at micro and nano scales.

Elements	Weight (%)	Atomic (%)
Bi	82.78	31.64
W	2.78	1.21
Fe	1.75	3.80
O	12.69	63.35

Tab. 1: The EDX analysis of electrodeposited BWFO film.

The energies of the emitted X-rays were analyzed to identify the elements present in the sample (qualitative analysis). The detection rate of these characteristic X-rays was used to quantify the amounts of elements present. By scanning the electron beam over an area of the film, EDX systems also provided X-ray maps, showing the spatial distribution of elements. The EDX spectrum confirmed the presence of the desired elements in the expected proportions its analysis is shown in Table 1.

The morphology of the BWFO films was examined using FE-SEM shown in Fig 2 (a,b). The images revealed that the film exhibited a plate-like structure with multiple plates stacked on top of each other. The plate bundles had a length of 50-60 nm and a thickness of 10-20 nm. These plates grew in various directions and were uniformly distributed across the surface, as shown in Fig. 6.6(a). Additionally, the FE-SEM images showed an increase in pore diameter, which could enhance the adsorption of electrolyte ions, thereby improving the supercapacitor performance of the BWFO films.
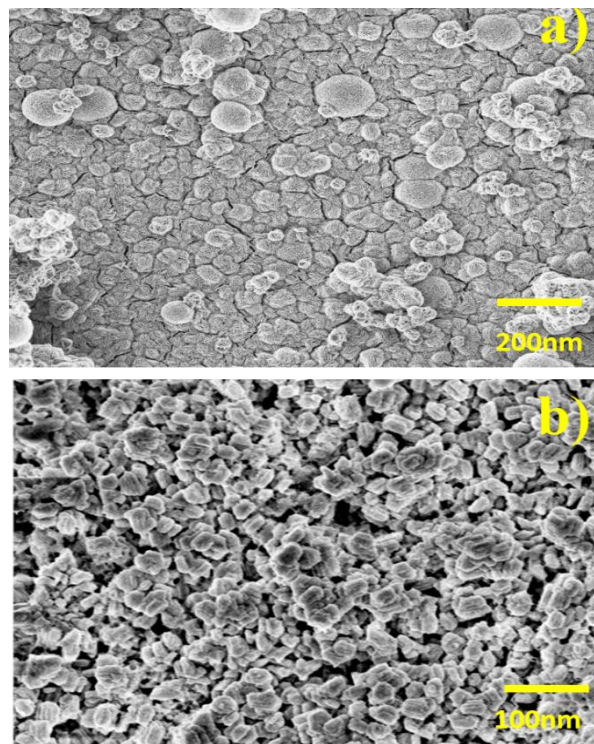
Fig. 2: The surface morphology of electrodeposited BWFO film at (a) low and, (b) high magnifications.

The FT-IR spectrum of the BWFO films was recorded in the range of 500 cm^{-1} to 4000 cm^{-1} as shown in Fig.3. Significant absorption peaks were observed at 846.51, 921.14, 1070.41, 1536.87, 1684.80, 2308.52, 2369.83, 2916.25, and 3290.75 cm^{-1}. The absorption peak at 846.51 cm^{-1} confirmed the presence of ferrite. The peaks at 1536.87 cm^{-1} and 1684.80 cm^{-1} were associated with the characteristic Fe-O and W-O stretching modes in the $BiWFeO_6$ phase. The broad absorption at 3290.75 cm^{-1} was attributed to the Bi-O-W bond in the $BiWFeO_6$ phase.
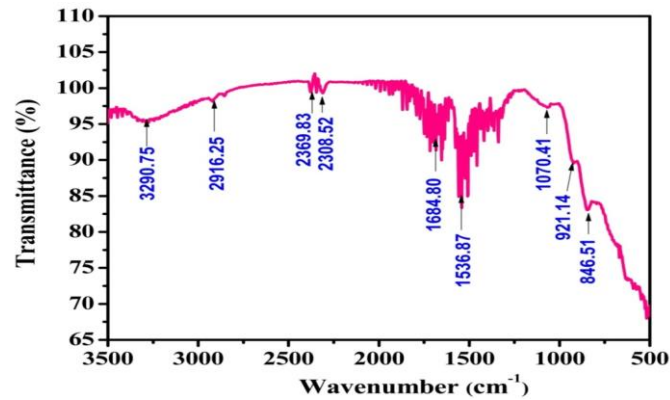
Fig.3: FT-IR spectrum of electrodeposited BWFO film

The faint band at 1070.41 cm⁻¹ corresponded to the Fe-O stretching in Fe-O-Bi bonds and W-O-W symmetric stretching, as well as the Fe-O-Fe or O-Fe-O bending modes. The FT-IR spectrum confirmed that tungsten was successfully doped into the $BiWFeO_6$ phase, resulting in distinct vibration modes compared to BFO films.

The electrochemical properties of the BWFO films were studied using Cyclic Voltammetry (CV) in a 1 M NaOH electrolyte solution as shown in fig 4(a). CV is an electrochemical technique used to investigate the thermodynamics and electron transfer kinetics at the electrode-electrolyte interface, crucial for supercapacitor and Li-ion battery applications. The CV measurements were conducted at different scan rates, including 2, 5, 10, 50, and 70 mV/s. The CV profiles of the BWFO films were recorded in the potential range of -0.1 to -1.5V under a three-electrode configuration. The results indicated that the CV window changed with varying scan rates, but the potential range remained fixed. The area enclosed by the CV curve, which correlates to the charge storage capability, increased with the scan rate, demonstrating enhanced energy storage capacity due to tungsten doping in the BWFO films.

Capacitance Analysis: The average capacitances of the BWFO films were calculated, and the results were presented in the corresponding figures. The average capacitance decreased with increasing scan rates, with an optimal capacitance of 4.6 F at a 2 mV/s scan rate. The specific capacitances of the BWFO films at scan rates of 2, 5, 10, 50, and 70 mV/s were 609.47, 393.51, 389.82, 104.07, and 89.91 F/g, respectively. The highest performance was observed at the lowest scan rate. The high specific capacitance can be attributed to the well-defined slices and numerous air voids in the BWFO film, which increased the electrode's porosity.
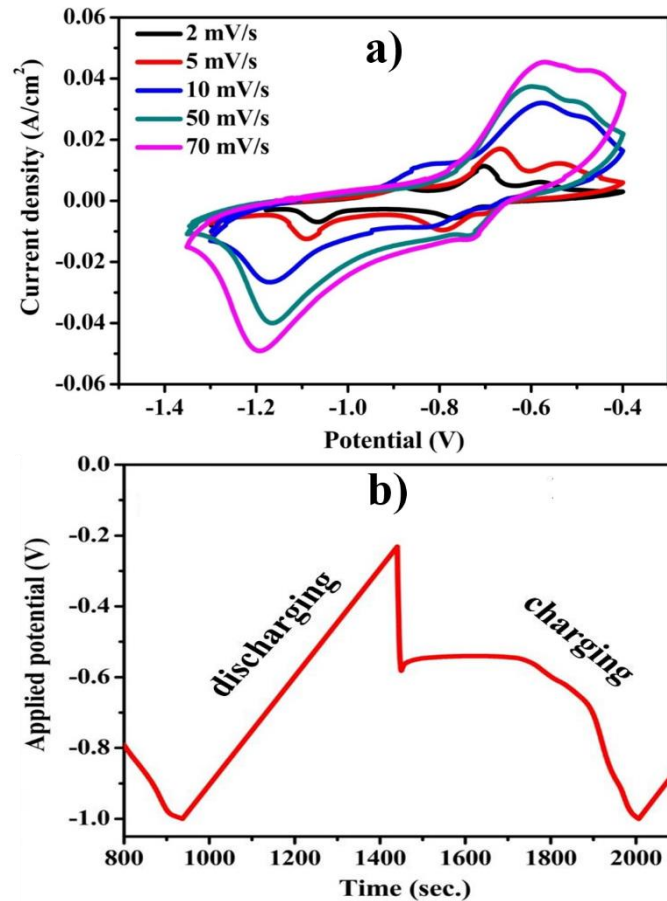
Fig. 4: CV and CD plots of BWFO films recorded in 1 M NaOH solution for different scan rates.

Charge/Discharge Analysis: As shown in fig 4(b), The charge/discharge curves of the BWFO films in a 1 M NaOH solution at a current density of 10 mA exhibited a triangular shape, indicative of pure electrical double-layer capacitor behavior. The voltage range for BWFO films was -0.23V to -0.99V. The discharge time was relatively short compared to the charging time, due to the electrical double-layer capacitance behavior. However, the longer discharge duration observed in BWFO films was attributed to the synergistic effect of combining electrical double-layer and faradic capacitances. The discharge time for BWFO films was 504 seconds. The charging curves were non-linear, while the discharging curves were highly linear.

IV.CONCLUSION

The BWFO films were successfully synthesized using electrodeposition and confirmed to have a rhombohedral single-phase structure with an average crystallite size of 39.41 nm. EDX and FT-IR analyses confirmed the incorporation of tungsten into the BiWFeO6 phase. SEM images revealed a plate-like morphology with pore sizes that could enhance supercapacitor performance. The CV analysis demonstrated that the tungsten doping significantly improved the energy storage capacity, with specific capacitances ranging from 89.91 F/g to 609.47 F/g depending on the scan rate. The highest specific capacitance was observed at the lowest scan rate of 2 mV/s. The films exhibited a combination of electric double-layer and faradic capacitance, contributing to their efficient energy storage. The charging/discharging curves showed typical triangular shapes, confirming the capacitive behavior, with a discharging time of 504 seconds. These results indicate that the BWFO films have strong potential for electrochemical supercapacitor applications.

V. REFERENCES

[1]. L.G. Beka, X. Li, W. Liu, Nickel cobalt sulfide core / shell structure on 3D Graphene for supercapacitor application, Sci. Rep. 7 (2017) 2105.

[2]. B. Bhujun, M.T. Tan, A.S. Shanmugam, Study of mixed ternary transition metal ferrites as potential electrodes for supercapacitor applications, Results Phys. 7 (2017) 345–353.

[3]. H. Chen, S. Zhou, L. Wu, Porous nickel hydroxide-manganese dioxide-reduced graphene oxide ternary hybrid spheres as excellent supercapacitor electrode materials, ACS Appl. Mater. Interfaces 6 (2014) 8621–8630.

[4]. A. Soam, R. Kumar, P.K. Sahoo, C. Mahender, B. Kumar, N. Arya, M. Singh, S. Parida, R.O. Dusane, Synthesis of nickel ferrite nanoparticles supported on graphene nanosheets as composite electrodes for high performance supercapacitor, ChemistrySelect 4 (2019) 9952–9958.

[5]. P.K. Sahoo, N. Kumar, S. Thiyagarajan, D. Thakur, H.S. Panda, Tailoring the performance of 3D-graphene/Ag nanocomposites for supercapacitor, catalytic and antibacterial applications, ACS Sustain. Chem. Eng. 6 (2018) 7475–7487.

[6]. X. Bai, Q. Liu, J. Liu, H. Zhang, Z. Li, X. Jing, P. Liu, J. Wang, R. Li, Hierarchical Co3O4@Ni(OH)2 core-shell nanosheet arrays for isolated all-solid state supercapacitor electrodes with superior electrochemical performance, Chem. Eng. J. 315 (2017) 35–45

[7]. X. Du, C. Wang, M. Chen, Y. Jia, J. Wang, Electrochemical performances of nanoparticle Fe3O4/activated carbon supercapacitor using KOH electrolyte solution, J. Phys. Chem. C 113 (2009) 2643–2646.

[8]. V. Khomenko, E. Frackowiak, F. Beguin, Determination of the specific capacitance of conducting polymer/nanotubes composite electrodes using different cell configurations, Electrochim. Acta 50 (2005) 2499–2506.

[9]. J.H. Park, J.M. Ko, O.O. Park, D.W. Kim, Capacitance properties of graphite / polypyrrole composite electrode prepared by chemical polymerization of pyrrole on graphite fiber, J. Power Sources 105 (2002) 20–25.

[10]. A. Soam, K. Parida, R. Kumar, P. Kavle, R. Dusane, Silicon-MnO2 core-shell nanowires as electrodes for micro-supercapacitor application, Ceram. Int. 45 (2019) 18914–18923.

[11]. N. Kumar, P.K. Sahoo, H.S. Panda, Tuning the electro-chemical properties by selectively substituting transition metals on carbon in Ni/Co oxide–carbon composite electrodes for supercapacitor devices, New J. Chem. 41 (2017) 3562–3573.

[12]. M.M. Shaijumon, F.S. Ou, L. Ci, P.M. Ajayan, Synthesis of hybrid nanowire arrays and their application as high power supercapacitor electrodes, Chem. Commun. 20 (2008) 2373–2375.

[13]. V.V. Jadhav, M.K. Zate, S. Liu, M. Naushad, R.S. Mane, K.N. Hui, S.H. Han, Mixedphase bismuth ferrite nanoflake electrodes for supercapacitor application, Appl. Nanosci. 6 (2016) 511–519.

[14]. B. Sarma, A.L. Jurovitzki, Y.R. Smith, S.K. Mohanty, M. Misra, Redox-induced enhancement in interfacial capacitance of the titania nanotube / bismuth oxide composite electrode, ACS Appl. Mater. Interfaces 5 (2013) 1688–1697.

[15]. S. Nayak, C. Mahende, A. Soam, J. Nanda, Structural and optical studies of BiFeO3@SiO2 core/shell nanoparticles, Mater. Res. Express 4 (2017) 105029.

Comparative Study of Micro and Nano Sized WO3/E44 Epoxy Composite Used as Gamma Radiation Shielding Using MCNP

Mitkari S R

Shri Siddheshwar Mahavidyalaya, Majalgaon-431131 (M.H.) India

Abstract :

Using the MCNP code, the radiation shielding properties of a 50 weight percent WO3/E44 epoxy composite are examined at different gamma energies ranging from 80 keV to 1.33 MeV. For WO3 filler particles, two scales are therefore taken into consideration: micro and nano, with diameters of 1 μm and 50 nm, respectively. According to the results of the simulation, WO3 nanoparticles show a greater rise in linear attenuation coefficient than micro size particles. Lastly, a good agreement is shown when the simulation findings are validated against the published experimental data.

I. INTRODUCTION

Polymer composites show promise for use in dosimeters, electromagnetic interference (EMI) devices, gamma and neutron radiation shielding, industry, and healthcare [1, 2]. [05] High-energy elements might not be able to filter every kind of radiation, especially neutron emissions from space or nuclear laboratories. They might also be limited in some applications because of their large weight, clumsy design, and toxicity (lead).[06] Thus, non-toxic "lead-free" filler-reinforced polymer composite has generated a lot of public attention in a variety of fields, particularly medical treatment, nuclear plants, and mobile nuclear devices, due to its lightweight, workability, and excellent radiation attenuation capabilities.[09] High amounts of high-V fillers added to epoxy matrix composites have made them an appealing option for radiation shielding.[09] The impact of tungsten oxide particle size. The impact of tungsten oxide particle size on WO3/epoxy composites has been studied at x-ray tube voltages ranging from 25 to 120 kV [10]. Polymer composites are lightweight, cost-effective, and easy to process [05]. When combined with high-Z materials in specific weight fractions, these composites show potential for use as effective radiation shielding materials. Several studies have examined how the grain size of shielding materials affects their linear attenuation coefficients [09]. It is generally believed that nano-sized particles disperse more uniformly within the matrix and experience fewer agglomerations compared to micro-sized particles. This enhanced dispersion improves the material's radiation attenuation capabilities. Nanostructured materials are characterized by structural elements with dimensions ranging from 1 to 100 nm. The exceptionally small size of nanostructured materials can impart unique chemical and physical properties compared to the same compounds in microscopic or macroscopic dimensions [14]. In this study, the linear attenuation coefficients of epoxy resin doped with nano-WO3 and micro-WO3 in identical proportions were calculated using the MCNP computer code. These results were then compared with the experimental data reported by Dong et al. [11].

II. MATERIALS AND SAMPLE PREPARATION

In this study, a simulation was performed using the MCNP computer code to analyze a 50 wt% WO3/E44 epoxy composite, incorporating both micro-sized (1 μm) and nano-sized (50 nm) tungsten oxide particles, in line with experimental work [11]. The formula for the E44 epoxy resin is C21H24O4. Particle sizes were defined using a lattice card, with the lattice system views shown in Fig. 1 for both nano and micro-sized WO3 particles in the epoxy matrix. The figure shows magnifications of 6 μm × 6 μm (Fig. 1(a)) and 20 μm × 20 μm (Fig. 1(b)). The simulation geometry for validation calculations is illustrated in Fig. 2, where WO3 particles are positioned at the center of cubes within the epoxy resin lattice. A narrow, straight gamma-ray beam was directed at the sample perpendicular to its surface. A NaI scintillation detector with a radius of 3 cm and a height of 0.02 cm was used to measure particle flux behind the sample, employing an F4 tally in an energy bin corresponding to the source's defined energy, as in the experiment [11]. According to Lambert–Beer law, the linear attenuation coefficient for gamma and x-rays is described as [19].

$$A/A_0 = e^{-\mu h} \quad \ldots\ldots\ldots\ldots\ldots 1$$

where A is the intensity of photons transmitted across some distance h, A_0 is the initial intensity of photons,

μ is the linear attenuation coefficient, and h is the distance traveled. Thus the linear attenuation coefficients can be calculated with

$$\mu = \frac{L_n(A_0/A)}{d} \quad \text{---------} \quad 2$$

The linear attenuation coefficients of WO3/E44 epoxy samples were calculated for gamma rays at different energies, which have been obtained to be from keV to 1330 keV.

The elemental weight fractions of the 50 wt% WO3/E44 epoxy composite and physical characteristics of applied materials are presented in Tables 1 and 2, respectively
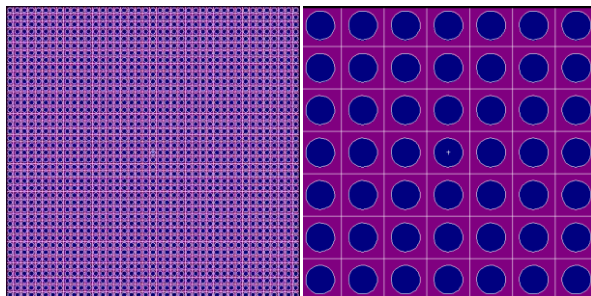
Fig. 1. Schematic view of the network of 50 wt% WO3/E44 epoxy composite, in which WO3 particles disperse uniformly in the epoxy matrix as spheres with radii of 50 nm (a) and 1 μm (b).

As shown in Fig. 2, a K-shell peak at 70 keV, characteristic of tungsten, is evident. Figure 3 illustrates the relative increase in the linear attenuation coefficient (nano vs. micro) for a 50 wt% WO3/E44 epoxy composite at various energies. The simulation results indicate that composites with nano-sized WO3 particles exhibit higher linear attenuation coefficients compared to those with micro-sized particles, consistent with experimental observations [11]. This effect can be attributed to the larger cross-sectional area of nano-sized particles compared to micro-sized ones, leading to a higher probability of photon collisions with the tungsten particles and consequently greater attenuation coefficients. While the simulation results deviate from experimental data by less than 5% for energies below 778.6 keV, discrepancies increase at higher energies, approaching 1330 keV. This suggests that while nanostructured materials show significant attenuation

improvements, as noted in Botelho et al. [18], they are particularly effective for low-energy applications, especially in radiological protection.

Table 1. Elements in the 50 wt% WO3/E44 epoxy composite.

	Elements	Atomic Number	Atomic Weight	Weight by Fraction
1	Hydrogen (H)	1	1.00794	0.03553
2	Carbon (C)	6	12.011	0.37047
3	Oxygen (O)	8	15.9994	0.19751
4	Tungsten (W)	74	183.84	0.39649

Table 2. Characteristics of applied materials at room temperature.

Sr. No	Materials	Density gm/cm^3
1	WO$_3$	7.16
2	E44 epoxy	1.18
3	50 wt% micro-WO$_3$/E44 epoxy	2.18
4	50 wt% nano-WO$_3$/E44 epoxy	2.29

Figure 2 shows the mass attenuation coefficient of a 50 wt% WO3/E44 epoxy composite across a range of energies from 1 keV to 5 MeV, as calculated using XCOM [16]. The effective atomic number (Z) for this composite is 54.07, also determined via XCOM [16]. High atomic number materials are generally more effective for shielding, and Figure 3 reveals a prominent K-shell peak at 70 keV, which is characteristic of tungsten. Figure 4 illustrates the relative increase in the linear attenuation coefficient (nano vs. micro) for the 50 wt% WO3/E44 epoxy composite at various energies. The simulation shows that composites with nano-sized WO3 particles exhibit higher linear attenuation coefficients compared to those with micro-sized particles, consistent with experimental observations [11]. This can be explained by the fact that nano-sized particles have larger cross-sectional areas than micro-sized particles, leading to a greater probability of photon collisions and thus higher attenuation coefficients. The discrepancy between simulation and experimental results is less than 5% for energies below 778.6 keV. However, at higher energies near 1330 keV, while the linear attenuation coefficient increases, the discrepancy also grows, as noted in the experimental work [11]. This suggests that nanostructured materials, as indicated by Botelho et al. [18], are particularly effective for low-energy applications, especially in radiological protection.
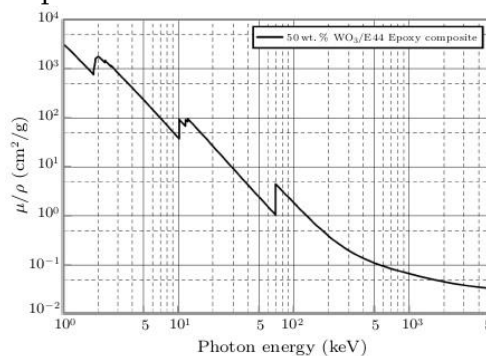
Fig. 2. Mass attenuation coefficient for 50 wt% WO$_3$/E44 epoxy composite at different energies using XCOM
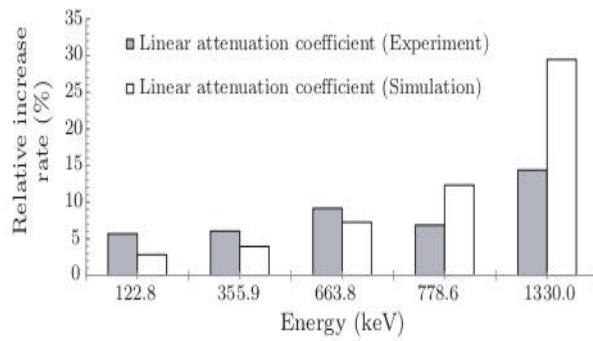
Fig. 3. The relative increasing rate of linear attenuation coefficient (nano to micro) and comparison with the experimental data

Gamma rays can produce significant annihilation radiation through pair production in high-Z materials [17]. Consequently, this composite is a promising candidate for photon attenuation applications. Figures 5 and 6 display the simulation results for the linear attenuation coefficient of a 50 wt% WO3/E44 epoxy composite with micro and nano structures, respectively, at various energies. These results are compared with experimental data [11]. The figures show a good correlation and agreement between the simulation and experimental results.
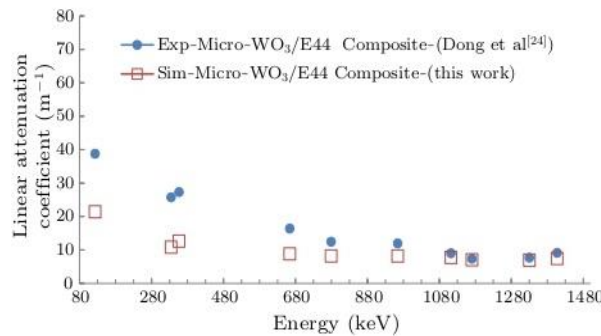
Fig. 4. Comparison of linear attenuation coefficient for micro 50 wt% WO3/E44 epoxy composite at different energies for experiment and our simulation
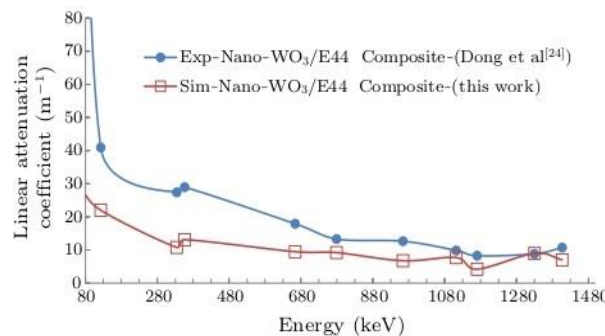
Fig. 5. Comparison of linear attenuation coefficient for nano 50 wt% WO3/E44 epoxy composite at different energies for experiment and our simulation

III.CONCLUSION:

In summary, a comparison was made between the linear attenuation coefficients of 50 wt% WO3/E44 epoxy composites with nanostructured and microstructured WO3 particles. The radiation shielding properties of these composites, with WO3 particles of sizes ranging from 50 nm to 1 μm, were evaluated across various gamma energies from 50 keV to 1.33 MeV using the MCNP code and were validated against experimental data. The results demonstrate that WO3 particles with a diameter of 50 nm (nano-sized) show a greater increase in the linear attenuation coefficient compared to 1 μm diameter (micro-sized) particles, aligning well with the experimental findings.

IV. REFERENCES

[1]. Yin H X, Li M M, Yang H, Long Y Z and Sun X 2010 Chin. Phys. B 19 088105

[2]. Li M M, Long Y Z, Yin H X and Zhang Z M 2011 Chin

[3]. Guo A P, Zhang X J, Wang S W, Zhu J Q, Yang L and Wang G S 2016 Chem Plus Chem 81 1305

[4]. Guo A P, Zhang X J, Qu J K, Wang S W, Zhu J Q, Wang G S and Guo L 2017 Mater. Chem. Front (in press)

[5]. Malekie S and Ziaie F 2015 Nucl. Instrum. Meth. Phys. Res. Sect. A 791 1

[6]. Singh V P, Badiger N M and Kaewkhao J 2014 J. NonCryst. Solids 404 167

[7]. Mann K S, Rani A and Heer M S 2015 Radiat. Phys. Chem. 106 247

[8]. Nambiar S, Osei E K and Yeow J T W 2013 J. Appl. Polym. Sci. 127 4939

[9]. Chang L, Zhang Y, Liu Y, Fang J, Luan W, Yang X and Zhang W 2015 Nucl. Instrum. Meth. Phys. Res. Sect. B 356 88

[10]. Noor Azman N Z, Siddiqui S A, Hart R and Low I M 2013 Appl. Radiat. Isot. 71 62

[11]. Dong Y, Chang S Q, Zhang H X, Ren C, Kang B, Dai M Z and Dai Y D 2012 Chin. Phys. Lett. 29 108102 [12] Hong W, Xiao P, Luo H and Li Z 2015 Sci. Rep. 5 14927

[12]. Singh V P, Medhat M E and Shirmardi S P 2015 Radiat. Phys. Chem. 106 255

[13]. Poole C P and Owens F J 2004 Introduction to Nanotechnology (New Jersey: Wiley-Interscience) [30] Tekin H O, Singh V P and Manici T 2017 Appl. Radiat. Isot. 121 122

[14]. Callister W D 2001 Fundamentals of Materials Science and Engineering (University of Utah: John Wiley & Sons Inc)

[15]. Boone J M and Chavez A E 1996 Med. Phys. 23 1997

[16]. Knoll G F 2010 Radiation Detection and Measurement (University of Michigan: John Wiley & Sons Inc)

[17]. Botelho M Z, Künzel R, Okuno E, Levenhagen R S, Basegio T and Bergmann C P 2011 Appl. Radiat. Isot. 69 52

[18]. Tekin H O, Singh V P and Manici T 2017 Appl. Radiat. Isot. 121 122

Armstrong Number for Data Security in Message transfer in the Network

Mahesh K. Kulkarni1, Premdas M. Rathod *2

[1]Department of Mathematics, Loknete Gopinathji Munde ACS College, Mandangad, Dist Ratnagiri, Maharashtra, India

[2]*Department of Mathematics, Shri Siddheshwar Mahavidyalaya Majalgaon, Majalgaon DistBeed, Maharashtra, India

ABSTRACT

Data security while transferring data from one place to other is major issue in today's world. Data security mainly refers to protection of data from unintended user. This technique uses encryption and decryption at sender's and receiver side respectively. Especially this technique makes use of Armstrong number while encrypting and decryption the data. This technique also makes use of Differ-Hellman key exchange algorithm for exchanging key between sender and receiver. The proposed Algorithm is simple. Flexible and making both hardware and software implementation easier.

Keywords: Armstrong number, data security, authentication, cryptography, cipher text.

I. INTRODUCTION

In today's world transferring data through unsecure network is major concern. To ensure the security of data while transferring through unsecure network, there are various kinds of technique used. One of the popular techniques used worldwide is cryptography. Cryptography involves converting plain text to some unreadable form. This unreadable form of data is then transmitted over the unsecured network. Cryptography mainly consist of encryption and decryption of the data. Encryption-Decryption is one of the techniques which is quite popular. But, the complexity which is involved in this technique doesn't allow its users to apply it in a simpler way. Now, if we look into the detailed context of this technique then we may observe that there are number of ways which allows the user to encrypt the private files and information. [1][2].

By taking into account the extent to which the data contained in the emails can be misused (whether working online or offline) providing security, both to online as well as offline email usage is of prime importance. Emails are a very important form of communication in day to day life. Many transactions and important information transfers as well as simple communications take place through emails. Thus, protecting the data contained in the emails.[3]

In this paper, Encryption and Decryption process applies to both data as well as its key. So that two way security is provided to the application. After successful authentication, data is encrypted by random Armstrong number and at the same time Armstrong number gets encrypted. Now for both these encrypted data and key,

current system timestamp is attached. So whenever receiver gets both the data he can easily recognize which key is for which data. Then encrypted key is decrypted by sender's public key and that resulted Armstrong number is used to decrypt actual data.

So it is difficult to hack the data and steal it. Once hacker steals the data, then he must have key by which that data is encrypted with its timestamp. If hackers get both data and key then he must know the decryption algorithm to retrieve both key and data which is very difficult.

II. CCYPTOGRAPHY

Cryptography is mainly a technique to keep communication private. Cryptography protects data from theft or alteration and also can be used for user authentication. Its main purpose is to ensure privacy by keeping the information hidden from anyone for whom it is not intended.

There are two main steps involved in cryptography such as encryption and decryption. The purpose of encryption is to ensure privacy by keeping the information hidden from anyone for whom it is not intended. Encryption is the transformation of plain text into some unreadable form. Decryption is the reverse of encryption, it is the transformation of encrypted data back into some readable form.

The data to be encrypted is called as plain text. The encrypted data obtained as a result of encryption process is called as cipher text.[4]

A.   Types of Cryptographic Algorithms

There are many ways of classifying cryptographic algorithms. Generally they are classified on the basis of the number of kays that are used for encryption and decryption. The three types of algorithms as follows:

1.   Secret Key Cryptography (SKC)

This kind of algorithm uses a single key for both encryption and decryption. The most common algorithms in use include Data Encryption Standard (DES).Advanced Encryption Standard (AES).

2.   Public Key Cryptography (PKC)

This kind of algorithm uses one key for encryption and another for decryption. RSA (Rivest, Shamir, Adleman) algorithm is an example.

3.   Hash Function

This kind of algorithm uses a mathematical transformation to irreversibly "encrypt" information. MD (Message Digest) Algorithm is an example.

III. DIFFIE – HELLMAN ALGORITHM

Diffie-Hellman key exchange algorithm is a cryptographic that allows two parties that have no prior knowledge of each other to jointly establish a shared secret key over an insecure communication channel. This key can then be used to encrypt subsequent communications using a symmetric key cipher.

For this discussion we will use Alice and Bob, to demonstrate the DH key exchange. The goal of this process is for Alice and Bob to be able to agree upon a shared secret that an intruder will not be able to determine. This shared secret is used by Alice and Bobto independently generate keys for symmetric encryption algorithms tht will be used to encrypt the data stream between them. THE "Key" aspect is that neither the shared secret not the encryption key do not ever travel over the network. [5]

Table 1

Alice and Bob agree on two numbers "p" and "g"	"p" is a large prime number "g" is called the base or generator
Alice picks a secret number "a"	Alice's secret number = a
Bob picks a secret number "b"	Bob's secret number = b
Alice computes her public number $x = g^b \pmod p$	Alice's public number = x
Bob computes her public number $x = g^b \pmod p$	Bob's public number = x
Alice and Bob exchange their public numbers	Alice knows p,g,a,x,y Bob knows p,g,b,x,y
Alice computes $ka = g^{ab} \pmod p$	ka $(g^b$ mod p) a mod p ka = (g^b) a mod p ka = g^{ab} (mod p)
Bob computes $kb = g^{ab} \pmod p$	kb $(g^a$ mod p) b mod p kb = (g^a) b mod p kb = g^{ab} (mod p)
Fortunately for Alice and Bob, by the laws of algebra Alice's "ka" is the same as Bob's "kb" or ka=kb=k	Alice and Bob both know the secret value "k"

IV. SERVER ARCHITECTURE

Very general definition of a Server is a computer or device on a network that manages network resources. For example, a file server is computer and storage device dedicated to storing files. Any user on the network can store files on the server. However on multiprocessing operating systems, a single computer can execute several programs at once. A server in this case could refer to the program that is to manage resources rather than the entire computer.[4]

A. What is Server Platform?

A server platform is basically a platform consist of underlying hardware or software for a system and thus is the engine that drives the server.

B. Types of Server

1] **FTP-Servers :** One of the oldest of the internet services, File Transfer Protocol makes it possible to move one or more files securely between computers while providing file security and organization as well as transfer control.

2] **Mail-Servers :** Almost as ubiquitous and crucial as Web servers, mail server move and store mail over corporate networks via LANs and WANs and across the Internet.

3] **Print-Servers :** it is computer that manages one or more printers and a network server is a computer that manages network traffic. There are so many servers according to requirement like Audio/Video, Chat, Fax, News, Proxy, Web servers etc.

V.   PROPOSED SYSTEM

1.   Introduction

In proposed system instead of keeping sender and receiver database as color and key value as that is used in earlier systems we keep unique number and name on single common server.

Before sending, data authentication is done between sender and receiver. Then after successful authentication we carry our encryption process of data and send that data to receiver. The encryption key as Armstrong number is send via sender to receiver. After getting that key from sender, receiver decrypt that key using sender's key and get original key. Using this key receiver decrypt encrypted data. [6]

Task of enhancing security include construction of formula for both data encryption and also for hiding pattern. Server should not process any fake request hence concept of "Diffie-Hellman" key exchange algorithm is introduced. Implementation of such a security constrains in banking sector is widely helpful.
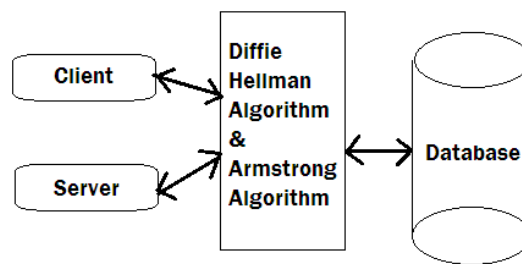
Fig 1 Cline-Server Architecture

2.   Illustration

a. Encryption using Armstrong numbers: let the Armstrong number used for data encryption be 153.

Step 1:(Creating password)

   User generated the key using Diffie-Hellman exchange algorithm

Step 2: (Encryption of the actual data begins here)

   Let the message to be transmitted be "CRYPTOGRAPHY" First find the ASCII equivalent of the above characters.

C R Y P T O G R A P H Y
67 82 89 80 84 79 71 82 65 80 72 89

Step 3:

   Now add these numbers with the digits of the Armstrong number as follows

```
  67  82  89  80  84  79  71  82  65  80  72  89
(+) 1   5   3   1   25  9   1   125 27  1   5   3
-----------------------------------------------------------
  68  87  92  81  109 88  72  207 92  81  77  92
```

Step 4:

   Convert the above data into a matrix as follows

```
A =      68    81    72    81
         87    109   207   77
```

      92   82   92   92

Step 5:

Consider an encoding matrix

B =   1   5   3

       1   25   9

       1 125   27

Step 6:

   After multiplying the two matrices (B x A) we get

C =   779   890   1383   742

     3071   3598   6075   2834

   13427 16082 28431 12190

   The encrypted data is…

779, 3071, 13427, 890, 3598, 16082, 1383, 6075, 28431, 742, 2834, 12190

   The above values represent the encrypted form of the given message.

2. Decryption Using Armstrong Number: Decryption involves the process of getting back the original data using decryption key.

Step 1: (Authenticating the receiver) only when the keys from sender and receiver match, the following steps could be performed to decrypt the original data.

Step 2: (Decryption of the original data begins here)

   The inverse of the encoding matrix is

D =   (1/240)*-450   240   -30

        -18   24   -6

       100   -120   2

Step 3:

   Multiply the decoding matrix with the encrypted data (D x C) we get

       68   81   72   81

       87   109   207   77

       92   82   92   92

Step 4:

  Now transform the above result as given below

68 87 92 81 109 88 72 207 92 81 77 92

Step 5:

  Subtract with the digits of the Armstrong numbers as follows

 68 87 92 81 109 88 72 207 92 81 77 92

(-) 1   5   3   1 25 9 1 125 27 1   5   3

----

67 82 89 80 84 79 71 82 65 80 72 89

Step 6:

Obtain the characters from the above ASCII equivalent

67 82 89 80 84 79 71 82 65 80 72 89

C   R   Y   P   T   O   G   R   A   P   H   Y

3. Advantages

This minimum key length reduces the efforts taken to encrypt the data. The key length can be increased if needed, with increase in character length.

Tracing process becomes difficult with this technique, because the Armstrong number is used differently in each step. The key can be hacked only if the entire step involved in the encoding process is known earlier.

Simple encryption and decryption techniques may just involve encoding and decoding the actual data, but in this proposed technique the password itself is encoded for providing more security to the access of original data.

4. Disadvantages

Diffie-Hellman key exchange algorithm involves expensive exponential operations. The only way to break into this system is by Brute force attack, which also can take up to two or three years.

The speed of execution is slow because the file size after encryption is much larger than original file.

VI. CONCLUSION

The above combination of Diffie-Hallman key exchange algorithm and Armstrong number proved to be the more efficient and reliable technique for data exchange between two parties. The combination of Diffie-Hallman key exchange algorithm and encryption using Armstrong number provides two way securities. This technique provides more security with increase in key length of the Armstrong numbers. In this algorithm we use digital signature hence this algorithm defend against man-in-middle attack and provide more security.

VII. REFERENCES

[1]. S.Belose,M.Malekar, S.Dhamal,G.Dharmawat&N.J.Kulkarni, "Data Security Using Armstrong Numbers," Undergraduate Academic Research Journal (UARJ),ISSN : 2278 – 1129, Volume-1, Issue-1, 2012.

[2]. Ajmal K.A, "Security using Colors, Figures and Images", International Conference on Emerging Technology Trends on Advanced Engineering Research (ICETT'12) Proceedings published by International Journal of Computer Applications (IJCA) 2012.

[3]. S. A. Saoji, Nikita B. Agarwal, Mrunal B. Bokil, Ashwini V. Gosavi, "Securing e-mails in XML format using colors and Armstrong numbers" International Journal of Scientific & Engineering Research, ISSN 2229-5518, Volume 4, Issue 7, July-2013.

[4]. ChavanSatish, LokhandeYogesh, ShindePravin, YewaleSandeep, Sardeshpande S.A, "Secure Email Using Colors and Armstrong Numbers over Web Services", International journal of research in computer engineering and information technology(IJRCEIT) , volume 1 no.2, 2013.

[5]. RFC 2631 "Diffie–Hellman Key Agreement Method", E. Rescorla June 1999.

[6]. S. Belose, M. Malekar, G. Dharmawat, "Data Security Using Armstrong Numbers" International Journal of Emerging Technology and Advanced Engineering, ISSN 2250-2459, Volume 2, Issue 4, April 2012.

Study of electrical properties of Zirconium substituted cobalt ferrite

[1]Dr. Jairam B. Mote and [2]Dr. Pravin K. Gaikwad

[1]Adarsh College, Omerga. (MS) India.

[2]Shri Chhatrapati Shivaji College, Omerga. (MS) India.

Abstract :

The composition of $Co_{1+x}Zr_xFe_{2-2x}O_4$ substituted zirconium with composition of $x = 0.0, 0.1, 0.2, 0.3, 0.4, 0.5$ and $x = 0.6$ were successfully prepared by sol-gel auto-combustion technique using citric acid as a fuel and AR grade metal nitrates. The DC resistivity of all the samples decreases with increase in temperature exhibiting the semiconducting behaviour. The activation energy in paramagnetic region (E_p) is more than that of ferrimagnetic (E_f) region. The dielectric constant (ε'), dielectric loss (ε'') and dielectric loss tangent ($\tan\delta$) decreases exponentially with increase in frequency. The dielectric constant (ε'), dielectric loss (ε'') and dielectric loss tangent ($\tan\delta$) decreases with increase in zirconium content x.

Keywords: Cobalt Ferrite, Zirconium, Electrical and dielectrical Properties;

I. INTRODUCTION

Ferrites are important electronic ceramic materials used in electronic devices suitably for high-frequency applications in the telecommunications field [1]. These ferrites are used in radio frequency circuits, high quality filters, rod antennas, transformer cores, read/write heads for high-speed digital tapes, and operating devices [2-4]. This material enjoys special significance, particularly at high frequencies, because of its high resistivity and low dielectric loss [3-5]. Cobalt ferrite is a well-known hard magnetic material with inverse spinel structure. The saturation magnetization and coercivity of cobalt ferrite is higher than the other nickel, manganese spinel ferrites. Cobalt ferrite is the most important and abundant magnetic materials that have large magnetic anisotropy, moderate saturation magnetization, remarkable chemical stability and mechanical hardness, which make it good candidate for the recording media [5-6]. The chemical composition method of synthesis, nature of dopant, site preference of dopants etc. parameters strongly influence the structural, electrical and magnetic properties of spinel ferrites. The magnetic property of spinel ferrite materials depends on the magnetic interaction between cations and magnetic moments, which are situated in the tetrahedral (A) and octahedral [B] sites [7-8]. In spinel-type Cobalt ferrite is well known to have a large magneto crystalline anisotropy, high coercivity, moderate saturation magnetization, high chemical stability and high mechanical hardness. So far, the fabrication of nanoscale cobalt ferrite powders has attracted much attention due to their exceptional physical properties [9-11]. Numerous synthesis methods have been developed to fabricate pure and substituted ferrites, even at low temperatures and low cost. Sol-gel auto-combustion technique is one of the best approaches to producing ferrite nanoparticles at low temperatures with better homogeneity and high yield [12-15]. So, present study

the effect of zirconium substitution electrical and dielectrical properties of nanocrystalline cobalt ferrite prepared by sol-gel auto combustion method is reported.

II. EXPERIMENTAL DETAILS

In this work the nano size samples of zirconium substituted cobalt ferrites $Co_{1+x}Zr_xFe_{2-2x}O_4$ system with x = 0.0, 0.1, 0.2, 0.3, 0.4, 0.5 and 0.6 were synthesized by sol-gel auto combustion method. X-ray diffraction, scanning electron microscopy and infrared spectroscopy techniques were employed to characterize the prepared samples of $Co_{1+x}Zr_xFe_{2-2x}O_4$ system [16].

The magnetic properties of $Co_{1+x}Zr_xFe_{2-2x}O_4$ system were investigated using pulse field hysteresis loop technique at room temperature by applying magnetic field of 2 Tesla. Using magnetization (M) versus applied magnetic field (H) plots obtained from pulse field hysteresis loop technique, the saturation magnetization, coercivity and remanence magnetization were obtained as a function of zirconium content x [17].

The measurements of DC resistivity 'ρ' for all the samples of the $Co_{1+x}Zr_xFe_{2-2x}O_4$ ferrite system were carried out in the temperature range 300-800 K using standard two probe method and the dielectric properties for the present samples can be explained on the basis of the mechanism of polarization process in ferrite, which is similar to that of conduction process.

III. ELECTRICAL PROPERTIES

3.1 DC Electrical Resistivity

The measurements of DC resistivity 'ρ' for all the samples of the $Co_{1+x}Zr_xFe_{2-2x}O_4$ ferrite system were carried out in the temperature range 300-800 K using standard two probe method. The D.C. electrical resistivity plots of all the samples are shown in the Fig. 1
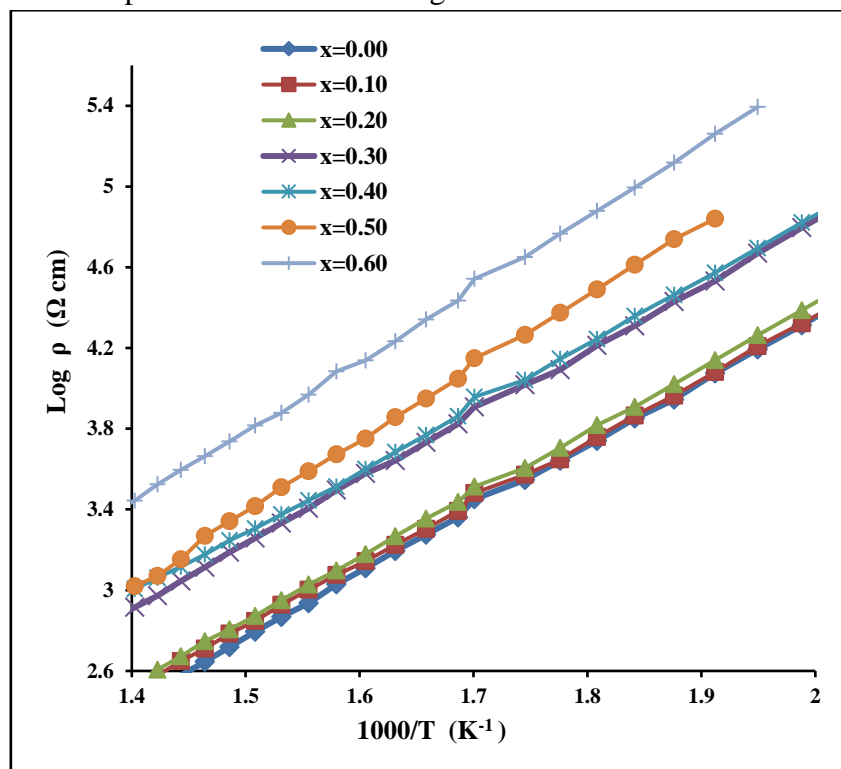
Fig. 1: Variation of dc electrical resistivity with reciprocal of temperature for $Co_{1+x}Zr_xFe_{2-2x}O_4$

It is clear from the resistivity plots that the electrical resistivity of all Zr^{4+} substituted cobalt spinel ferrite samples decreases with increase in temperature, thus exhibiting semiconducting behavior obeying the well-known Arrhenius relation. It is also seen from Fig. 1 that there are two regions of conduction with different activation energies. The change in slope is observed in each resistivity plot at a particular temperature which may correspond to Curie temperature of the sample. The increase in conductivity may be due to the hopping of electrons between Fe^{2+} and Fe^{3+}.

3.2 Activation Energy

The activation energy Eg for each sample in the ferrimagnetic and paramagnetic region was calculated from the resistivity plots. The values of activation energy for all Zr^{4+} substituted cobalt spinel ferrite samples are listed in Table 1.

Table 1: Activation energy in paramagnetic (E_p) and ferrimagnetic (E_f) region for $Co_{1+x}Zr_xFe_{2-2x}O_4$ system

Comp. 'x'	E_p (eV)	E_f (eV)	ΔE (eV)
0.00	0.08	0.04	0.04
0.10	0.13	0.04	0.09
0.20	0.73	0.57	0.16
0.30	0.69	0.52	0.17
0.40	0.81	0.63	0.18
0.50	0.85	0.65	0.20
0.60	0.92	0.69	0.23

It is found from Table 1 that activation energy increases with Zr^{4+} substitution. It is also evident from Table 1 that the activation energy in paramagnetic region is greater than ferrimagnetic region.

Dielectric Properties

The dielectric properties for the present samples can be explained on the basis of the mechanism of polarization process in ferrite, which is similar to that of conduction process. The electronic exchange $Fe^{3+} \leftrightarrow Fe^{2+}$ gives the local displacement of electrons in the direction of an applied field, which induces polarization in ferrites.

3.3 Dielectric constant (ε')

The variation of dielectric constant (ε') with logarithm of applied electric field frequency for all Zr^{4+} substituted cobalt spinel ferrite samples is observed as shown in Fig 2, it can be seen that the dielectric constant (ε') initially decreases rapidly with increase in frequency up to the certain frequency; however, it remains fairly constant for higher frequencies. The decrease in dielectric constant (ε') with increase in frequency can be explained by considering the solid as composed of well conducting grains separated by the poorly conducting grain boundaries. The decrease in dielectric constant (ε') at lower frequencies is explained based on space charge polarization and attributed to the fact that ferroelectric regions are surrounded by non-ferroelectric regions similar to the relax or ferroelectric materials. The dielectric constant attains a constant value only at higher frequencies due to electronic polarizability.
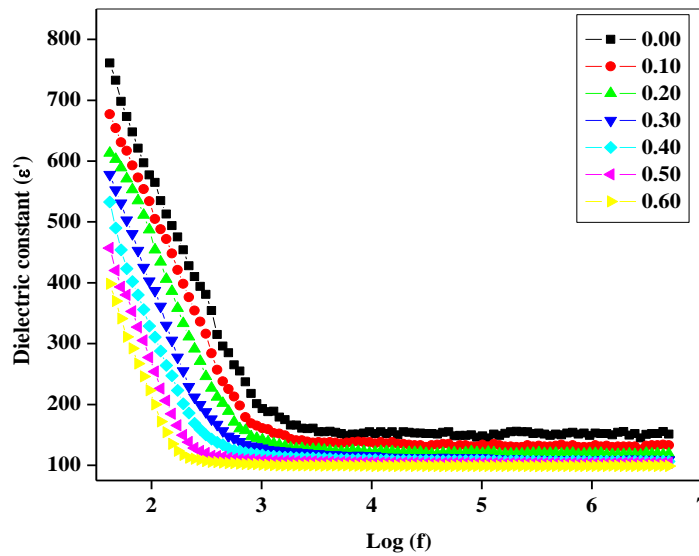
Fig.2: Variation of dielectric constant ϵ' with log f for $Co_{1+x}Zr_x Fe_{2-2x} O_4$ Dielectric loss (ϵ'')

The dielectric loss (ϵ'') factor is considered to be the most important part of the total core loss in ferrites. The variation of dielectric loss as a function of frequency is shown in Fig 3. It can be observed from fig 3 that dielectric loss (ϵ'') decreases exponentially with increase in frequency and is shown in Fig 3. The decrease in dielectric loss is almost similar to that of dielectric constant. The decrease in imaginary part of dielectric constant i.e. dielectric loss is pronounced more in comparison to real dielectric constant.
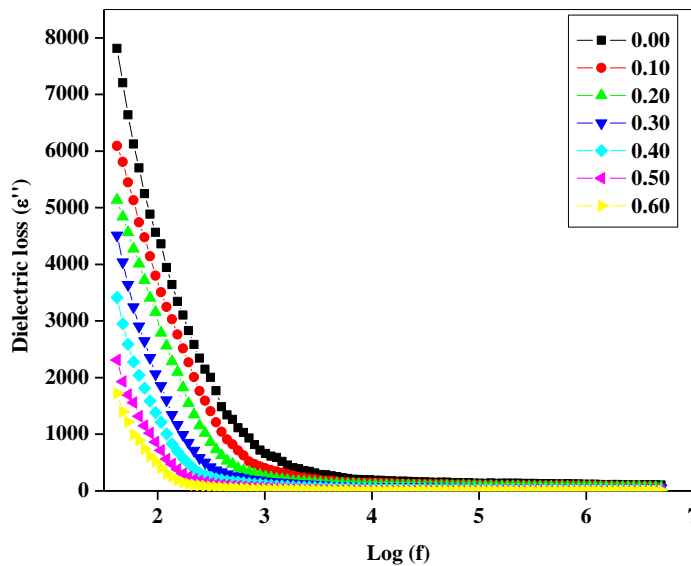
Fig. 3: Variation of dielectric loss ϵ'' with log f for $Co_{1+x}Zr_x Fe_{2-2x} O_4$

Dielectric loss tangent (tan δ)

The variation of dielectric loss tangent (tan δ) as a function of frequency is shown in Fig 4 calculated from dielectric constant and dielectric loss shows decreasing trend with increasing frequency. The values of tan δ depend on a number of factors such as a carrier concentration and structural homogeneity. The dielectric

loss tangent decreases exponentially with increase in frequency. The observed behavior of dielectric loss tangent can be explained on the basis of Maxwell-Wagner interfacial polarization.
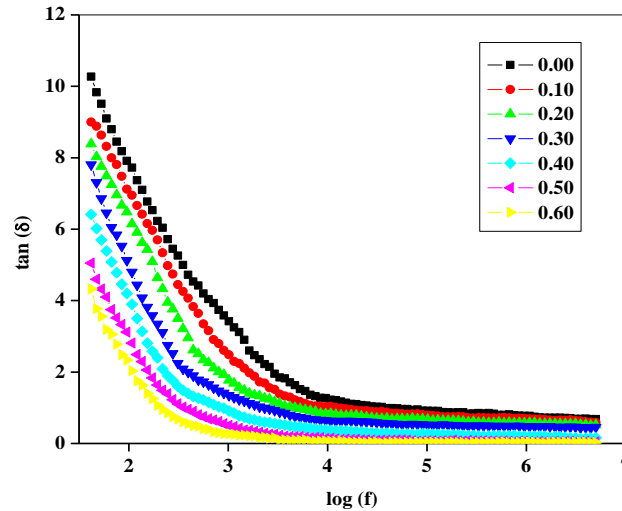
Fig 4: Variation of dielectric loss tangent (tanδ) with log f for $Co_{1+x}Zr_x Fe_{2-2x} O_4$

The compositional dependence of various dielectric properties shows that the dielectric constant, dielectric loss and dielectric loss tangent all decreases as zirconium content x increase. The properties of spinel ferrites that are of prime concern to users or designers are mainly dielectric properties such as dielectric constant, dielectric loss and dielectric tangent or loss factor.

IV.CONCLUSIONS

The DC resistivity of all the samples decreases with increase in temperature exhibiting the semiconducting behaviour. The activation energy in paramagnetic region (Ep) is more than that of ferrimagnetic (Ef) region. The dielectric constant (ε'), dielectric loss (ε'') and dielectric loss tangent (tan δ) decreases exponentially with increase in frequency. The dielectric constant (ε'), dielectric loss (ε'') and dielectric loss tangent (tan δ) decreases with increase in zirconium content x.

V. REFERENCES:

[1]. Kadam R. H, Desai, k; Shinde, V. S.;Hashim, M; Shirsath, S. E. *Influence of Gd³⁺ ion substitution on the MnCrFeO₄ for their nanoparticle shape formation and magnetic properties.* Journal of Alloys and Compounds 2016, 657657, 487-494, https://doi.org/10.1016/jallcom.2015.10.164

[2]. Shirsath S E, Jadhav S S, Toksha B G, Patange S. M, Jadhav K. M, *Remarkable influence of Ce⁴⁺ ions on the electronic conduction of Ni₁-₂ₓCeₓFe₂O₄.* Scripta Materialia 2011, 64, 773, https://doi.org/10.1016/j.scriptamat.2010.12.043

[3]. V. More, S Kadam, S. Shelke, Pravin Gaikwad, R. Kadam, S. Alone; *Modified Structural and Magnetic Properties of Ni-Mn-Zn Ferrite Nanoparticles Doped with Ce³⁺ Ions*, Biointerface Research in Applied Chemistry, 2022, 5021, https://doi.org/10.33263/BRIAC124.50215030

[4]. Dr. G. H. Kale, Dr. P. K. Gaikwad,; *Effect of Sintering Temperature on the structural properties of Nano-size Cobalt Ferrite.* Journal of Emerging Technologies and Innovative Research 2022, e276, https://www.jetir.org/view?paper=JETIR2212438

[5]. Kadam R. H, Biradar A R, Mane M L, Shirsath S E, Sol-gel auto-combustion synthesis of $Li_{3x}MnFe_{2-x}O_4$ and their characterization, Journal of Applied Physics 2012, 112, https://doi.org/10.1063/1.4746746

[6]. P. K. Gaikwad, S. S. Sawant; *Structural and electrical properties of rare earth (R^{3+}) doped Cobalt Ferrites;* International Journal of Creative Research Thoughts; 2022, a585; https://ijcrt.org/viewfull.php?&p_id=IJCRT2201074

[7]. Nithiyanantham S, Viviliya, S, Mahalakshmi, S. *Synthesis and characterization of cobalt ferrite through Co-precipition technique.* Lett. Appl. NanoBio. 2021,10, 1871-1876, https://doi.org/10.33263/LIANBS101.18711876

[8]. S. S. Sawant, P. K. Gaikwad, *Design and Development of an Experimental Setup for Characterization of piezoelectric Actuators for Scanning Tunneling Microscope.*; Journal of Emerging Technologies and Innovative Research 2022, a508, http://www.jetir.org/view?paper=JETIR2201067

[9]. E1—Shater, R.E.; E1 Shimy, H.: Assar, S. T. Investigation of physical properties of synthesized Zr doped Ni-Zn ferrites. Materials chemistry and physics 2020, 247, https://doi.org/10.1016/j.matchemphys.2020.122758

[10]. Rady, K. E. Shams, M. S. Enhancement of structural, dielectrical and magnetic properites of nanocrystalline Mn-Zn ferrites using Ni-Ti ions. *Journal of materials science: Materials in Electronics 2020, 31, 22820-22832,* https://doi.org/10.1007/s10854-04808-3

[11]. Priya, A.S, Geetha, D; Kavitha, N. Evaluation of structural and dielectric properties of Al, Ce co-doped cobalt ferrites. Materials Research Express 2018, 5, https://doi.org/10.1088/2053-1591/aacdle

[12]. Gadkari A B, Shinde T J Vasambekar, P N, *Structural analysis of Y^{3+} doped Mg-Cd ferrite prepared by oxalate co-precipitation method.* Materials Chemistry and Physics 2009, 114, 505, https://doi.org/10.1016/j.matchemphys.2008.11.011

[13]. Rezlescu N; Rezlescu, E; Pasnicu, C; Craus, M. L. *Effects of the rare-earth ions on some properties of a nickel-zinc ferrite.* Journal of Physics: Condensed Matter 1994, 6, 5707-5716, https://doi.org/10.1088/0953-8984/6/29/013

[14]. Lohar K S, Pachpinde A M; Langade M M, Kadam R H, Shirsath S E, *Self-propagation high temperature synthesis, structural morphology and magnetic interactions in rare earth Ho^{3+} doped $CoFe_2O_4$ nanoparticles*, Journal of Alloys and Compound 2014. 604, 204-210, https://doi.org/10.1016/j.jallcom.2014.03.141

[15]. Abdellatif M H, Azab A A, Salerno M, *Effect of rare earth doping on the vibrational spectra of spinel Mn-Cr Ferrite.* Materials Research Bulletin 2018, 97, 260-264, https://doi.org/10.1016/j.materresbull.2017.09.012

[16]. Dr. J. B. More, Dr. P. K. Gaikwad; *Study of Structural Properties of $Co_{1+x}Zr_xFe_{2-2x}O_4$ Spinel Ferrite,* International Research Journal of Engineering & Applied Sciences; 2023,1, https://irjeas.org/content/volume-11-issue-1-january-march-2023/

[17]. Dr. J. B. More, Dr. P. K. Gaikwad; *Magnetic and electrical properties of Zirconium substituted Cobalt Ferrite Nanoparticles*; International Journal of Current Science; 2023, 339, https://rjpn.org/ijcspub/viewpaperforall.php?paper=IJCSP23A1045

Sol-gel deposited Bismuth Copper Selenium Oxide (BiCuSeO) Nanoparticles for Gas Sensor Applications

Pramod S. Borule,[a] Pranita M. Jondhale,[a] Shivaji D. Waghmare,[a*] Rajkumar K. Rajure,[a] Shankar P. Phulwale,[c] Ravindra S. Chati,[b] Shashikant H. Gaikwad,[b]

[a] Department of Physics, Shri Shivaji Mahavidyalaya Barshi, Punyashlok Ahilyadevi Holkar Solapur University, Solapur, 413401, India

[b] Department of Zoology and Chemistry, Shri Shivaji Mahavidyalaya Barshi, Punyashlok Ahilyadevi Holkar Solapur University, Solapur, 413401, India

[c] Department of Chemistry, K. N. Bhise Arts, Commerce and Vinayakrao Patil Science College, Kurduwadi, Punyashlok Ahilyadevi Holkar Solapur University, Solapur, 413208, India

ABSTRACT

This study presents the synthesis of Bismuth Copper Selenium Oxide (BiCuSeO) films via a sol-gel method, followed by comprehensive characterization using X-ray diffraction (XRD), scanning electron microscopy (SEM), and energy-dispersive X-ray analysis (EDAX). The results confirmed a well-defined tetragonal structure and consistent elemental composition. The films demonstrated an impressive LPG sensitivity of 52% at a 1000 ppm concentration at 130°C, with a response time of 160 seconds and a recovery time of 179 seconds. Selectivity tests revealed a response ratio of 5:1 for LPG compared to hydrogen and carbon monoxide. The long-term stability of the films was validated, showing a 92% retention of sensitivity after 30 days. These findings underscore BiCuSeO's potential as a promising material for LPG detection in gas sensor applications.

Keywords: Sol-gel Synthesis, BiCuSeO, Gas Sensors, Morphology.

I. INTRODUCTION

Recent advancements in metal oxide (MOS) gas sensors have highlighted their extensive research and practical applications, particularly in the detection of hazardous gases across various industries [1, 2]. The increasing reliance on liquefied petroleum gas (LPG) in households, industries, and transportation has made the demand for reliable LPG gas sensors increasingly urgent. Given LPG's highly flammable and explosive nature, early leak detection is crucial to prevent potential hazards such as fires, explosions, and asphyxiation. The low cost, ease of use, and ability to detect a wide range of gases—including flammable gases like LPG, hazardous nitrogen dioxide (NO_2), hydrogen (H_2), and other environmental pollutants have fueled significant interest in MOS-based sensing materials [3-5]. The fundamental operating principle of most MOS-based gas sensors is the change in electrical conductivity of the sensing layer [6-7], which can be modulated by a gate voltage in field-effect transistor (FET) devices. Various MOS materials, such as ZnO, SnO_2, In_2O_3, WO_3, CuO, and Fe_2O_3, have

been extensively explored for gas-sensing applications [8-12]. Over time, diverse synthesis methods have been developed to produce MOS in both film and powder forms, with varying morphologies and dimensions tailored for specific sensing needs. These methods often aim to enhance surface sensitivity or functional porosity to specific gases while ensuring the practical fabrication of MOS structures. MOS-based sensors have proven capable of detecting a variety of gases, including LPG, H_2, CO, NH_3, NO_x, and organic vapors [13-21].

However, challenges remain in improving sensitivity, electrical and environmental stability, and selectivity, particularly in high-temperature environments and when distinguishing between gases in complex mixtures, especially with simpler oxides [22]. In residential settings, where LPG is commonly used for cooking and heating, undetected leaks can lead to catastrophic accidents. Industrial applications of LPG in fuel systems and manufacturing processes also demand reliable gas detection to ensure safety and regulatory compliance. Additionally, with the increasing use of LPG as an alternative fuel in vehicles, effective sensors that can detect leaks and prevent accidents in confined spaces like garages and workshops are becoming increasingly critical. These sensors are vital for protecting lives, property, and the environment by providing timely warnings and enabling swift responses to LPG leaks. Bismuth Copper Selenium Oxide (BiCuSeO), also known as BCSO, has emerged as a promising material for gas sensors due to its unique combination of electrical and thermal properties, which are essential for sensitive gas detection. The material's layered structure offers a high surface area and tunable electronic properties, enhancing its responsiveness to various gas molecules. BCSO also exhibits excellent thermal stability, making it effective for operation at elevated temperatures, crucial for detecting gases like hydrogen and methane. Additionally, the material can be synthesized with controlled porosity and grain size, improving its selectivity and sensitivity toward specific gases. Current research focuses on optimizing BCSO for practical gas-sensing applications, particularly in environments requiring high-temperature operation and precise gas detection.

In this study, BCSO samples were tested for LPG sensing, and the results demonstrated outstanding sensitivity, reinforcing its potential as a gas sensor material. The high sensitivity to LPG is attributed to its layered structure and adjustable electronic properties. To further evaluate its performance, the material was characterized using XRD, confirming its crystalline structure, and SEM, which revealed a fine grain structure that increases its surface area. EDAX was employed to verify the elemental composition, ensuring the correct stoichiometry. Resistivity measurements demonstrated the material's change in electrical conductivity in response to LPG, which is key to its sensing ability. These comprehensive characterizations affirm BCSO's suitability for high-performance LPG sensors, offering a reliable and efficient solution for detecting this hazardous gas.

II. SYNTHESIS OF MATERIALS

The synthesis of Bismuth Copper Selenium Oxide (BCSO) was carried out using the sol-gel method. All reagents used in this experiment were of analytical grade, obtained from Sigma-Aldrich, and utilized without additional purification. Distilled water was used throughout the experimental process. Commercially available bismuth nitrate pentahydrate $(Bi(NO_3)_3 \cdot 5H_2O)$, copper nitrate trihydrate $(Cu(NO_3)_2 \cdot 3H_2O)$, selenium tetrachloride $(SeCl_4)$, and citric acid $(C_6H_8O_7)$ were used as received. Bismuth nitrate and copper nitrate were separately dissolved in a diluted nitric acid solution (20% HNO_3) in stoichiometric proportions. These solutions were then combined with selenium tetrachloride in a 200 ml glass beaker. Citric acid served as the chelating agent, and the pH was adjusted to 10 using a 0.2 M ammonium hydroxide solution. The mixture was stirred at 100°C until a fluffy, dried gel was formed. This gel was then transferred to a crucible and annealed at 600°C for

4 hours, yielding a brownish powder composed of Bismuth Copper Selenium Oxide (BCSO) structures. The BCSO powder was finely ground and used to create a thick film on a glass substrate, utilizing 3 mm Scotch™ tape to define the 1 cm² cell area. The BCSO film was surface-treated with palladium, a highly effective catalytic material.

The film was then used for sensor applications, and its structure was analyzed using X-ray powder diffraction (XRD) with a Rigaku D/max-g B diffractometer, operating with Cu Kα radiation ($\lambda = 0.15418$ nm) at 40 kV and 80 mA. Morphological confirmation was achieved through field-emission scanning electron microscopy (FE-SEM), with digital images captured at various magnifications. Finally, the BCSO films were tested for LPG sensitivity to evaluate their performance in gas sensor applications. The sensor response was determined using the relation $S=(Ra-Rg)/Ra\times100\%$, where Ra and Rg represent the resistances of the film in air and upon exposure to LPG, respectively.

III.RESULTS AND DISCUSSION

The XRD pattern of the brown BCSO thick film, as illustrated in Figure 1, confirms the presence of the BiCuSeO phase, highlighting its suitability for gas sensing applications.
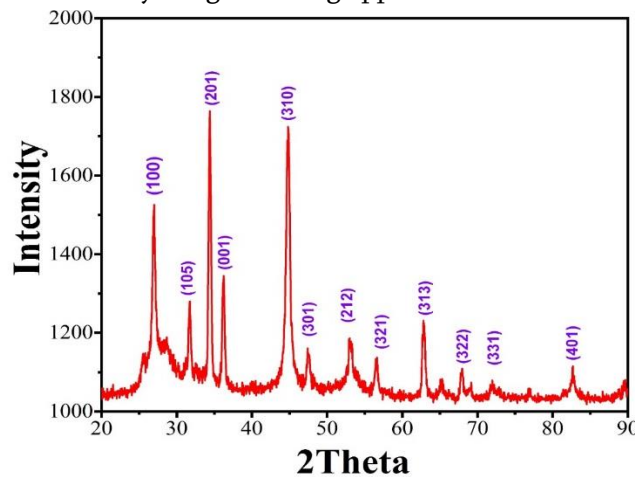
Fig. 1: XRD patterns of BCSO Nanoparticles.

The diffraction peaks, corresponding to the reflection planes (100), (105), (201), (001), (310), (301), (212), (321), (313), (331), and (401), are consistent with the BiCuSeO phase (JCPDS no. 82-0494), indicating that the film crystallizes in a layered tetragonal structure. This structure, belonging to the P4/nmm space group, is characterized by alternating $(Bi_2O_2)^{2+}$ and $(Cu_2Se_2)^{2-}$ layers. The specific arrangement of bismuth, oxygen, copper, and selenium atoms creates a unique architecture that enhances the material's electrical properties, crucial for effective gas detection. The high crystallinity of the BCSO film, as evidenced by the sharp XRD peaks, ensures a stable and responsive sensing platform. This structural integrity, combined with the material's ability to interact sensitively with gas molecules, makes BiCuSeO an excellent candidate for reliable and efficient gas sensors, particularly in detecting gases like LPG.

The EDAX spectrum of the BCSO film, depicted in Figure 2, provides a comprehensive analysis of the film's elemental composition. This analysis, conducted independently of the XRD observations, specifically targeted the hexagon-shaped nanopillars to verify their chemical makeup.
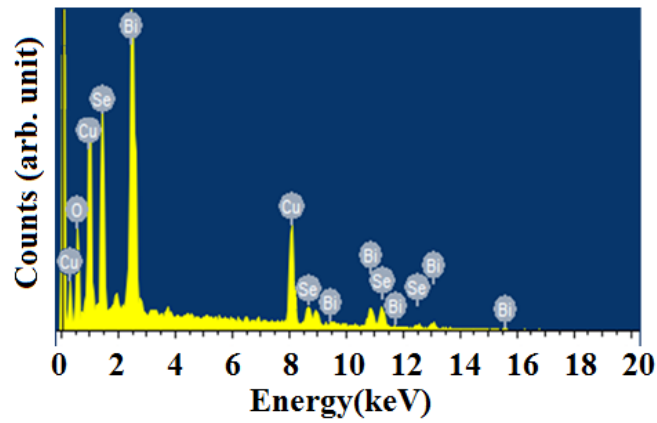
Fig. 2: EDAX spectrum of BCSO Nanoparticles.

The findings revealed that both the nanopillars and other nanostructures within the film possess identical chemical stoichiometry, confirming that they are composed of BCSO. The elemental ratios of Bi, Cu, and Se, as shown in Table 1, are consistent with the formation of BCSO nanoparticles, further corroborating the XRD data.

Element	Weight%	Atomic%
Bi M	33.1	6.24
Cu K	29.9	18.55
Se L	15.89	7.93
O K	21.11	52.00

Tab. 1: EDAX analysis of BCSO Nanoparticles.

This uniformity in composition across different nanostructures suggests a high degree of chemical homogeneity within the film, which is essential for maintaining the material's integrity and functionality in gas sensing applications. Furthermore, the EDAX analysis underscores the precision in the fabrication process, demonstrating that the desired stoichiometry was successfully achieved across different morphological forms. This uniformity in chemical composition enhances its suitability for applications requiring consistent material properties, such as gas sensors, catalysis, or electronic devices. The close agreement between the EDAX and XRD data not only validates the accuracy of the characterization techniques but also confirms the material's potential for further development in LPG gas sensor applications.

Figure 3 (a, b) presents the SEM images of BCSO nanoparticles at two different magnifications, offering detailed insights into their morphology.
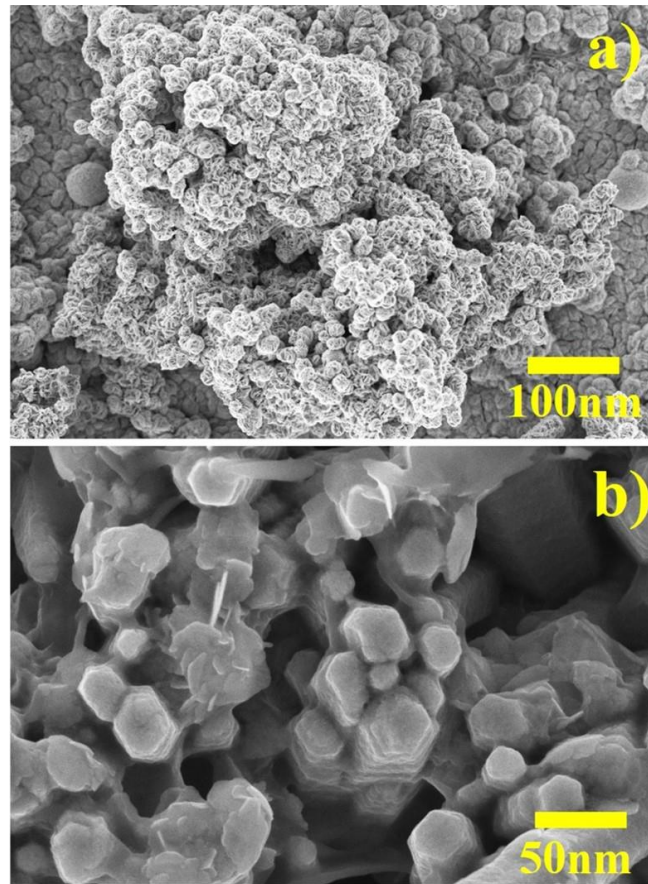
Fig. 3(a, b): The surface morphology of BCSO thick films at (a) low and, (b) high magnifications.

The images clearly show uniform and crack-free growth of the nanostructures, with the nanoparticles measuring approximately two micrometers in length and around 40 nanometers in width. Notably, many nanoparticles were interconnected, forming irregular hexagonal pillar-like architectures that were thick at the center and tapered towards the ends, indicating a well-defined growth pattern. The BCSO nanoparticles, with irregular dimensions close to 25 nm, were densely packed and agglomerated, leading to smooth and polished surfaces. The growth of these nanoparticles occurred in bundles, with some structures ranging from 100–500 nm in length and 40–60 nm in diameter, resulting in elongated stick-like architectures. This distinct formation suggests a high degree of structural organization, which could be advantageous for various applications. Upon closer examination, the hexagon-shaped nanopillars exhibited bifurcations in certain areas, creating crowded regions interspersed with voids. This unique arrangement contributes to the structural and optical properties of the material, particularly in light absorption, scattering, and surface interactions. These properties are especially valuable in gas sensing applications, where the material's surface interactions play a crucial role in detecting specific gases. The voids and bifurcations within the nanopillars might also enhance gas permeability and the sensor's overall sensitivity.

To investigate the temperature dependence of electrical resistance in the synthesized BCSO nanoparticles, we conducted characterization using the two-probe method under a reference air atmosphere.
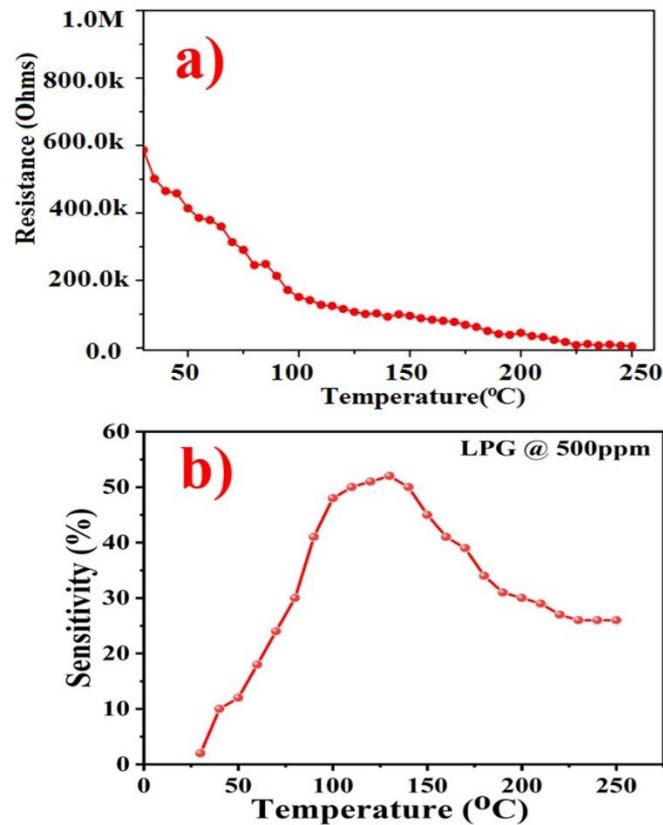
Fig. 3(a, b): The curves of BCSO nanoparticles (a) temperature vs. electrical resistance (b) temperature vs. sensitivity at 1000 ppm of LPG

This process allowed us to estimate the band gap energy of the BCSO nanoparticles. Figure 3(a) illustrates the temperature-resistance behavior of BCSO nanoparticles. Characterization was carried out over a temperature range of 30 to 250 °C, with 5 °C increments, to analyze this behavior. The graph reveals a typical semiconductor response, where resistance decreases as temperature increases. This observation confirms the semiconductor nature of the material. Using this plot, we estimated the band gap energy of the BCSO nanoparticles through calculations using the four-probe method, as described in the previous chapter. Although the (1/T) x1000 vs. Log10ρ graph used for calculating the band gap energy is not shown here, the estimated band gap energy of the BCSO nanoparticles is approximately 0.512 eV. This value aligns closely with the standard band gap energy of the BiCuSeO phase, confirming the semiconductor characteristics of the BCSO nanoparticles.

The sensor response is significantly influenced by the operating temperature, as temperature affects the dynamics of sensing reactions and directly impacts the category and concentration of surface oxygen species on the sensing layer. Therefore, determining the optimal operating temperature is crucial for effective gas detection. To achieve this, a series of experiments were conducted at various temperatures. During these tests, LPG at a concentration of 1000 ppm was used as the target gas. The relationship between operating temperature and LPG response for BCSO nanoparticles is depicted in Figure 4(b).

To identify the optimal temperature of BCSO nanoparticles, experiments were performed across an operating temperature range of 30-250 °C in a 1000 ppm LPG atmosphere, as shown in Figure 4(b). The gas response was recorded and presented in terms of sensitivity. The inset illustrates that sensitivity increases with temperature, reaching its peak at 130 °C in the LPG atmosphere before decreasing as the temperature continues to rise. The BCSO nanoparticles exhibited the highest response to LPG at 130 °C, which is identified as the optimal temperature for these nanoparticles. This optimal temperature is critical for achieving the best gas sensing

performance. Response and recovery times are critical parameters for evaluating gas sensors. To determine these times, the BCSO nanoparticles were tested with 100 ppm LPG at 130 °C. The response and recovery curve of the BCSO nanoparticles is shown in Figure 5(a), where the dynamic response and recovery times were analyzed. The BCSO nanoparticles exhibited a response time of 160 seconds and a recovery time of 179 seconds when exposed to LPG.
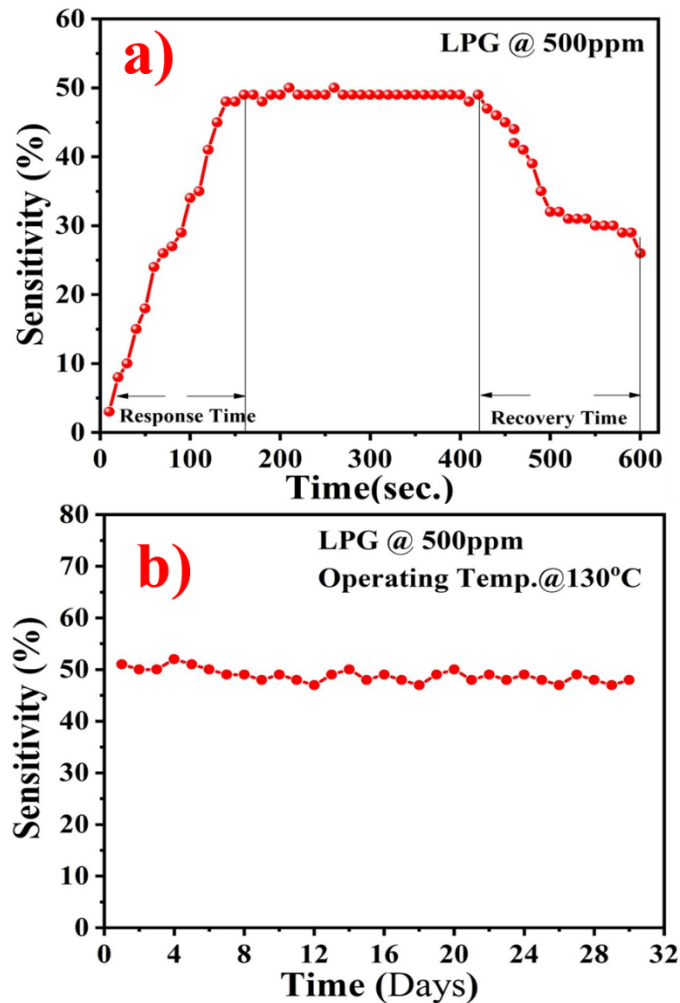
Fig. 4(a, b): The curves of BCSO nanoparticles (a) Response and Recovery time (b) Stability at 1000 ppm of LPG at operating temperature.

Stability is another essential criterion for gas sensors, as they must consistently function under repeated conditions, including varying gas concentrations and occasionally harsh environments. Maintaining stable performance without drift is crucial for assessing sensor reliability. To evaluate this, the long-term stability of BCSO nanoparticles was tested with LPG, and the results are displayed in Figure 5(b). These nanoparticles retained approximately 92% of their initial response even after 30 days of exposure to 1000 ppm of the target gas, clearly demonstrating their significant long-term stability.

IV. CONCLUSION

The BiCuSeO films synthesized in this study exhibited a significant LPG sensitivity, with a 55% response at 1000 ppm and an optimal operating temperature of 130°C. The films provided rapid response and recovery times of 160 seconds and 179 seconds, respectively. Selectivity tests revealed that BiCuSeO displayed a response

ratio of approximately 5:1 when compared to hydrogen and carbon monoxide, indicating strong selectivity towards LPG. The long-term stability was robust, with the sensor maintaining 92% of its initial sensitivity after 30 days at 1000 ppm LPG. XRD and SEM analyses confirmed the structural integrity of the films, even after extended testing. These quantitative results demonstrate that BiCuSeO is a highly promising material for the development of reliable LPG gas sensors, with the potential for further optimization and application to other gases.

V. REFERENCES

[1]. C.M. Ghimbeu, M. Lumbreras, M. Siadat, J. Schoonman, Mater. Sci. Semicond.Process. 13 (2010) 1–8.

[2]. N. Barsan, D. Koziej, U. Weimar, Sens. Actuators B 121 (2007) 18–35.

[3]. G. Cui, Z. Li, L. Gao, M. Zhang, Phys. Chem. Chem. Phys. 14 (2012)16321–16325.

[4]. B. Brunekreef, J. Expo. Sci. Environ. Epidemiol. 17 (2007) S61–S65.

[5]. S. Su, W. Wu, J. Gao, J. Lub, C. Fan, J. Mater. Chem. 22 (2012) 18101–18110.

[6]. D.J. Liu, T.M. Liu, H.J. Zhang, C.L. Lv, W. Zeng, J.Y. Zhang, Mater. Sci. Semicond.Process. 15 (2012) 438–444.

[7]. W. Zeng, T.M. Liu, L.Y. Lin, Mater. Sci. Semicond. Process. 15 (2012) 319–325.

[8]. X.j. Wang, W. Wang, Y.L. Liu, Sens. Actuators B 168 (2012) 39–45

[9]. J.H. Lee, Sens. Actuators B 140 (2009) 319–336.

[10]. J. Huang, Q. Wan, Sensors 9 (2009) 9903–9924.

[11]. M. Yuasa, T. Kida, K. Shimanoe, ACS Appl. Mater. Interfaces 4 (2012)4231–4236.

[12]. H. Zheng, J.Z. Ou, M.S. Strano, R.B. Kaner, A. Mitchell, K. Kalantar-zadeh, Adv.Funct. Mater. 21 (2011) 2175–2196.

[13]. J. Zhang, X.H. Liu, S.H. Wu, B.Q. Cao, S.H. Zheng, Sens. Actuators B 169 (2012)61–66.

[14]. D.L. Chen, X.X. Hou, T. Li, L. Yin, B.B. Fan, H.L. Wang, X.J. Li, H.L. Xu, H.X. Lu, R.Zhang, J. Sun, Sens. Actuators B 153 (2011) 373–381.

[15]. M. Ahsan, T. Tesfamichael, M. Ionescu, J. Bell, N. Motta, Sens. Actuators B 162(2012) 14–21.

[16]. X. Liu, J. Zhang, L. Wang, T. Yang, X. Guo, S. Wu, S. Wang, J. Mater. Chem. 21(2011) 349–356.

[17]. M.D. Arienzo, L. Armelao, C.M. Mari, S. Polizzi, R. Ruffo, R. Scotti, F. Morazzoni,J. Am. Chem. Soc. 133 (2011) 5296–5304.

[18]. C.L. Gandara, J.M.F. Sanjuan, F.M. Ramos, A. Cirera, Solid State Ionics 184(2011) 83–87.

[19]. Y. Zhu, X. Su, C. Yang, X. Gao, F. Xiao, J. Wang, J. Mater. Chem. 22 (2012)13914–13917.

[20]. S.J. Luo, G. Fu, H. Chen, Y.Y. Zhang, Mater. Chem. Phys. 109 (2008) 541–546.

[21]. H. Gu, Z. Wang, Y. Hu, Sensors 12 (2012) 5517–5550.

[22]. D.M. Angelo, P. Torrione, T.H. Kim, S. Wolter, W. Lampert, A. Atewologun, M.Edirisoorya, L. Collins, T.F. Kuech, M. Losurdo, G. Bruno, A. Brown, J. Phys.Chem. C 116 (2011) 826–833.

H-Shape Microstrip Patch Antenna: Design, Simulation, and Characterization

Kiran Katke[1], S. K. Popalghat[2]

[1]Department of Physics, Anandrao Dhonde Alias Babaji Mahavidyalaya, Kada, Tal. Ashti, Dist. Beed-414202 (M.S,)

[2]Physics Research Centre, Post- Graduate Department of Physics, J. E. S. College, Jalna -431203 (M.S.)

Abstract

This paper presents the design, simulation, and characterization of an H-shape microstrip patch antenna intended for high-frequency applications. The proposed antenna is modeled using Computer Simulation Technology (CST) Microwave Studio, a powerful tool for simulating electromagnetic fields and optimizing antenna parameters. The H-shaped configuration is chosen to enhance the antenna's radiation characteristics, bandwidth, and gain, while minimizing size and surface wave effects. The design process involves parameter optimization, including substrate selection, patch dimensions, and feed point configuration, to achieve superior performance. Detailed simulation results are presented, demonstrating the antenna's return loss, VSWR, gain, and radiation pattern. The antenna operates efficiently with stable resonance, offering low return loss and high radiation efficiency. The simulation results confirm that the H-shape microstrip patch antenna is well-suited for various wireless communication systems, showing potential for integration in compact, high-performance devices. This paper serves as a step towards further optimization and practical implementation of H-shape microstrip antennas in advanced RF systems.

Keywords: H-Shape, Microstrip patch antenna, CST, RT/duroid 5880.

I. INTRODUCTION

Microstrip patch antennas are popular in modern communication systems due to their low profile, lightweight design, and ease of integration with other electronic components. They are used in applications like satellite communication, radar systems, wireless communication, and medical devices. The H-shape microstrip patch antenna has gained attention due to its ability to improve key performance characteristics while maintaining a small size. The distinctive H-shape configuration enhances bandwidth, improves impedance matching, and increases radiation efficiency. This compact design makes it suitable for applications requiring miniaturized antennas with high-performance metrics. The design and optimization of microstrip patch antennas are typically done through electromagnetic simulations. This paper presents the design, simulation, and characterization of an H-shape microstrip patch antenna operating at a target frequency using CST Microwave Studio, a powerful tool for solving complex electromagnetic problems. The antenna is fed by a coaxial probe, a common and practical feeding technique due to its simplicity and effectiveness in achieving good impedance matching. The feed position is optimized to minimize the return loss and ensure that the antenna resonates efficiently at the target frequency.

The primary objective of this research is to explore the performance of the H-shape microstrip patch antenna through detailed simulations, focusing on key parameters such as return loss, radiation patterns, gain, and efficiency. The results obtained from the CST simulation are analyzed to evaluate the potential of the proposed

antenna design for use in high-frequency applications, particularly in wireless and satellite communication systems.

II. METHOD OF DESIGNING AND MATERIAL

The design of the H-shape microstrip patch antenna is aimed at achieving high performance in terms of bandwidth, gain, and efficiency while maintaining a compact form factor suitable for modern communication systems. The design parameters are carefully selected to meet the desired operational frequency, with a focus on using a coaxial feeding technique for improved impedance matching. This section covers the key aspects of the antenna design, including the substrate selection, patch geometry, and feeding mechanism.

A. Substrate Selection

The choice of substrate material is crucial in determining the overall performance of the microstrip patch antenna. In this design, a dielectric substrate of Rogers RT/duroid 5880 with a relative permittivity (ε_r) of 2.2 and a thickness of 1.6 mm is selected. The low permittivity helps reduce surface wave propagation, thereby improving the antenna's efficiency and gain. Additionally, the low-loss tangent of the substrate ensures minimal power dissipation within the material.

B. Patch Geometry

The radiating element of the antenna is designed in an H-shape shown in Fig. 1, which is achieved by introducing two rectangular slots symmetrically in the main rectangular patch. This configuration helps in broadening the bandwidth and improving the impedance matching by modifying the current distribution on the patch.
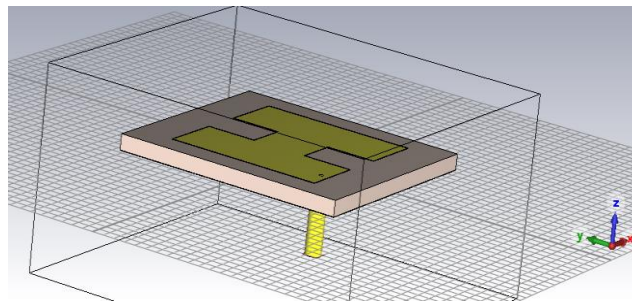
Figure 1: H-Shape Microstrip patch antenna

The dimensions of the H-shape are calculated based on the desired resonant frequency of **13.81 GHz.** The equations (1) and (2) for determining the patch width (W) and length (L) are derived from the conventional rectangular patch antenna design formulas, which account for the effective dielectric constant and the wavelength at the operating frequency.

Width of patch (W):

$$W = \frac{c}{2f_r\sqrt{\frac{\varepsilon r+1}{2}}} \quad (1)$$

where C is the speed of light, f_r is the resonant frequency, and ε_r is the relative permittivity of the substrate.
Effective dielectric constant (ε_{eff}):

$$\varepsilon_{eff} = \frac{\varepsilon r+1}{2} + \frac{\varepsilon r-1}{2}\left[1 + 12\left(\frac{h}{w}\right)\right]^{-\frac{1}{2}} \quad (2)$$

Length of patch (L):

$$L = \frac{c}{2f_r\sqrt{\varepsilon eff}} - 2\Delta L \quad (3)$$

- where ΔL is the extension in length due to the fringing fields.

After calculating the rectangular patch dimensions, two rectangular slots are introduced along the length of the patch to form the H-shape. The slot dimensions are chosen to optimize the resonance and improve bandwidth. Also the design uses a coaxial probe feed for strong impedance matching and fabrication simplicity. The feed point is optimized for minimal return loss and efficient power transfer.

C. Simulated Design

The final design of the H-shape microstrip patch antenna is shown in the simulation model, with all dimensions clearly specified. The design is optimized for a resonant frequency of 13.81 GHz, and the coaxial feed point is strategically placed to ensure effective power transfer and minimal return loss.
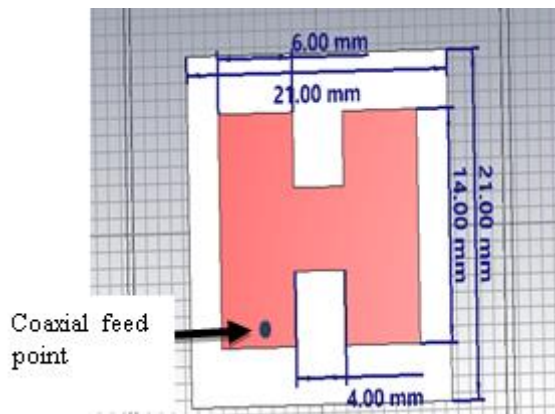
Figure 2: Dimensions of H shape Microstrip patch antenna

Form Fig. 2 shows the dimensions of the H-shaped microstrip patch antenna having substrate and ground planes of the of the same length and width of 21 x 21 mm. The patch height is 14 mm, the width of the patch for each arm is 6 mm, and the slot is 4 mm joining the two arms of H. The substrate's thickness is 1.6 mm, with a dielectric constant of 2.2.

III. RESULTS AND DISCUSSION:

A. Return Loss

The return loss is analyzed to evaluate impedance matching, with values below -10 dB indicating good performance. The return loss of an H-shaped microstrip patch antenna in Fig. 3 below is -26.18 dB for the frequency of 13.81 GHz.
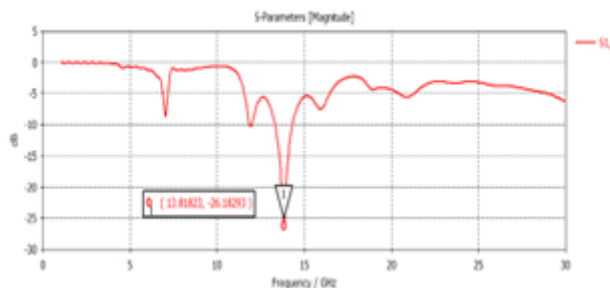
Figure 3: Return loss of H shape microstrip patch antenna

B. Gain

The simulated gain of the antenna is shown in the below fig. 4 H-shaped microstrip patch antennas provide 7.05 dB of gain.
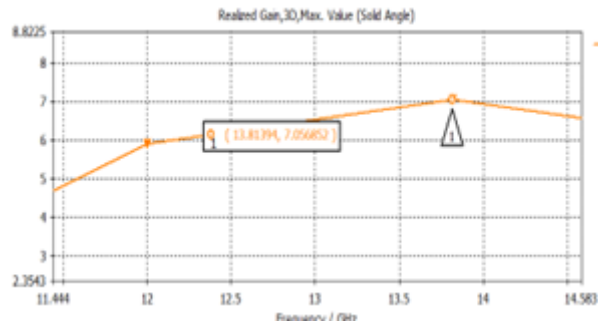
Figure 4: Gain of H shape microstrip patch antenna

C. VSWR

The simulated VSWR of an H-shaped microstrip patch antenna is 1.01 dB, as shown in Fig. 5 in the simulated results.
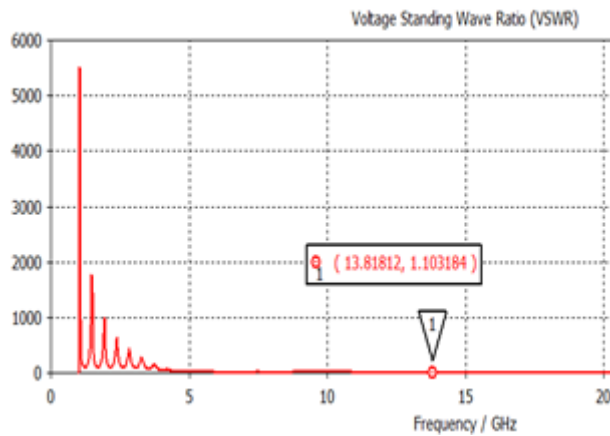
Figure 5: VSWR of H shape Microstrip patch antenna

D. Radiation Pattern

The radiation pattern is characterized in both the E-plane and H-plane, showing the directional performance of the antenna and any potential side-lobe levels. In the given Fig. 6, the 3D radiation pattern of an H-shaped microstrip patch antenna is shown.
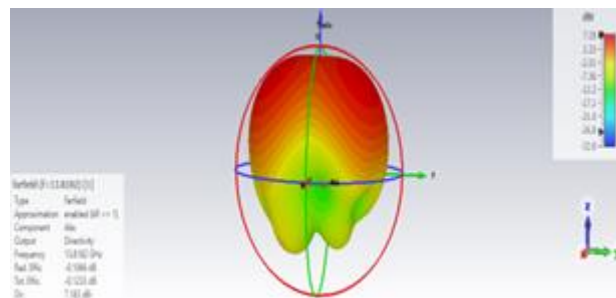
Figure 6: Radiation Pattern of H shape microstrip patch antenna

IV. CONCLUSION

In this paper, the design, simulation, and characterization of an H-shape microstrip patch antenna have been presented, with a focus on its performance at a resonant frequency of 13.81 GHz. The return loss analysis confirmed excellent impedance matching, with a significant return loss of -26.18 dB, far exceeding the typical threshold of -10 dB, ensuring efficient power transfer to the antenna. The antenna achieved a simulated gain of 7.05 dB, indicating its suitability for applications requiring moderate to high gain. Additionally, the simulated

VSWR of 1.01dB further validated the efficient impedance matching, demonstrating minimal reflection and optimal signal transmission.

The radiation pattern of the antenna, analyzed in both the E-plane and H-plane, exhibited desirable directional characteristics with minimal side-lobe levels, highlighting the antenna's effectiveness in targeting specific directions. The 3D radiation pattern confirmed the focused and stable radiating performance of the H-shape configuration, making it a suitable candidate for high-frequency communication systems.

Overall, the H-shape microstrip patch antenna, with its compact design and enhanced performance metrics, shows great promise for integration into modern RF and wireless communication systems.

V. References

[1]. Kiran Katke, S. K. Popalghat. *"X-BAND Rectangular Microstrip Patch Antenna: Design, Simulation, and Analysis",* Volume 12, Issue III, International Journal for Research in Applied Science and Engineering Technology (IJRASET) Page No: 1101-1105, ISSN : 2321- 9653, www.ijraset.com https://doi.org/10.22214/ijraset.2024.59012

[2]. M. T. Islam, M. N. Shakib and N. Misran, *"Broadband E-H shaped microstrip patch antenna for wireless systems,"* Progress In Electromagnetics Research, PIER 98, 163- 173, 2009.

[3]. Yu, A. and X. X. Zhang, "*A method to enhance the bandwidth of microstrip antennas using a modified E-shaped patch,"* Proceedings of Radio and Wireless Conference, 261–264, Aug. 10–13, 2003.

[4]. Xiaofei Shi, Zhihong Wang, Hua Su, Yun Zhao, *"A H-type Microstrip Slot Antenna in Ku-band Using LTCC Technology with Multiple Layer Substrates,"* Proc. IEEE, Vol. 978-1, pp. 7104 - 7106, 2011.

[5]. S.P. Gangwar , *"Design of Multiband Compact H-Shaped Microstrip patch antenna for Wireless application",* IJARCCE Vol. 6, Issue 5, May 2017.

[6]. Sachin Kumar Gupta, "Bandwidth Improvement of microstrip patch antenna using H-shaped patch", IJERA volume2, Issue 1, Jan-Feb.2012, pp. 334-338.

[7]. W. Afzal, U. Rafique, M. M. Ahmed, M. A. Khan, F. A. Mughal, "*A Tri-Band H-Shaped Microstrip Patch Antenna for DCS and WLAN Applications",* in Mikon 2012, 19th international conference on microwaves, radar & wireless communications, may21- 23, warsaw, Poland.

[8]. by Harshit Srivastava, "*A Compact Slotted H-shape Microstrip Patch Antenna for Wireless Communication with Microstrip Antenna Feed*", in International Conference on Communication & Signal Processing, April 6-8, 2016, India 978-1-5090-0396- 9/16 2016 IEEE.

[9]. Vadhyar Sai Bharath, NVSS Arun Varma. "*Design and Analysis of H-Shaped Microstrip Antenna with Different Feed Position & Number of Slots for Multiband Applications",* ICPCSI-2017.

[10]. Alak Majumder, *"Design of an H-shaped Microstrip Patch Antenna for Bluetooth Applications",.* International Journal of Innovation & Applied Studies ISSN 2028- 9324 Vol. 3 No. 4 Aug. 2013, pp. 987- 994. 2013 Innovative Space of Scientific Research Journals. http://www.issr- journals.org/ijias/.

[11]. Katke, K., & Popalghat, S. K. (2024). X-BAND Rectangular Microstrip Patch Antenna: Design, Simulation, and Analysis. *International Journal for Research in Applied Science and Engineering Technology*, *12*(3), 1101–1105. https://doi.org/10.22214/ijraset.2024.59012

Influence of Cd2+ Ions Substitution on Structural Morphology and Elastic Constants of Ni - Cu Spinel Ferrites

R. B. Kavade*[1], R. G. Vidhate[2], J.M. Bhandari[3], K. H. Katke[2], S. J. Shukla[4]

*[1]Bhagawan Mahavidyalaya, Ashti, Dist. Beed, (M.S.) India.

[2] Anandrao Dhonde Mahavidyalaya, Kada, Beed, , (M.S.) India.

Gandhi College, Kada, Dist. Beed, , (M.S.) India.

[4]P. G. and Research center, Deogiri College, Chhatrapati Sambhajinagar, (M.S.) India.

Corresponding Author: kavade.ramdas@gmail.com

Abstract :

The cadmium substituted Ni-Cu mixed ferrites samples having the generic formula $Ni_{0.5}Cu_{0.5-x}Cd_xFe_2O_4$ (x = 0.0, 0.15, 0.25) have been synthesized by standard double sintering ceramic technique using AR grade oxides (NiO. CuO, CdO, Fe_2O_3). Formation of mono phase cubic spinel structure of ferrite phase was confirmed by X-ray diffraction and Infrared spectroscopic analysis. Due to the large ionic radius of cadmium the lattice constant was found to increase with increase in cadmium. The structural parameters such as lattice constant, , theoretical lattice constant, X-ray density, ionic site radii, cation distribution, oxygen positional parameter bond length, jump length of tetrahedral (A) site as well as octahedral [B] site, tetrahedral edge length, shared and unshared octahedral edge length was estimated. The estimated cation distribution of ferrite was verified by comparing the observed and theoretical lattice parameters. The elastic parameter of ferrites such as young's modulus, rigidity modulus and bulk modulus was estimated by using IR technique.

Keywords: Structural Morphology, Elastic properties, X-ray diffraction.

I. Introduction

Due to high saturation magnetization, high resistivity, high stability and low loss energy over a wide range of frequency the mixed nickel copper ferrites are technologically important materials. [1, 2]. In fact, cadmium substituted Ni-Cu mixed ferrite are the subject of intensive investigations in the field of fundamental and applied research due to their wide applications in electronic industry. The physical properties of spinel ferrites depend on the type, amount of dopant and distribution of cations over the tetrahedral (A) and octahedral [B] sites [3, 4]. In electronic materials the elastic module are of much importance because they shows the nature of binding force in polycrystalline materials and also helps to understand the thermal properties of these materials.

II. Experimental

The ferrite with composition $Ni_{0.5}Cu_{0.5-x}Cd_xFe_2O_4$ (x = 0.0, 0.15, 0.25) were synthesized by standard double sintering ceramic method.[5,6,7] Grinding using agate mortar (4 h) was carried out for each sample. The samples were pre-sintered at 1293 K for 12 h. The sintered powder is again reground and sintered at 1353 K for 14 h. Then the powder of samples compressed into pellets of 10 mm diameter using a hydraulic press with pressure 6 ton/inch² and sintered at 1273K for 12 h. The samples were furnace cooled to room temperature. The

prepared samples were characterized by X-ray powder diffractometer in the 2θ range $20°$-$80°$at room temperature to confirm mono phase spinel structure. The infrared spectra of a prepared sample were recorded at room temperature within the range 200 cm^{-1} to 800 cm^{-1} on the infrared spectrometer (Model 783, Perkin-Elmer)

III. Results and Discussion:

The peaks appeared in the XRD pattern (fig.1) of the ferrites are identified. However, the non appearance of extra peaks reveals the formation of mono phase cubic spinel structure of ferrite. The increase of observed lattice parameter 'a' and X-ray density 'ρ' with increase of the cadmium content was due to the difference in ionic radii and atomic weight of the component ions in the ferrite system [8]. The distribution of cations in the tetrahedral (A) and octahedral [B] sites can be expressed as [9], $(Cd_xCu_yFe_{1-x-y})^A[Ni_{0.5}Cu_{0.5-x-y}Fe_{1+x+y}]^BO_4^{-2}$ The theoretical lattice parameter of ferrite samples estimated using the relation [10] were listed in table 1. The good agreement between experimentally estimated and theoretical lattice parameters confirms the assumed cation distribution of the ferrites.
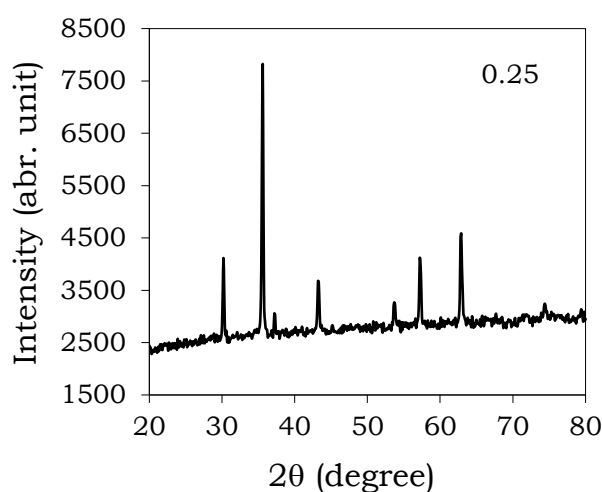
Fig.1: Typical XRD Pattern of
$Ni_{0.5}Cu_{0.5-x}Cd_xFe_2O_4$ for (x = 0.25)

The mean ionic radius of the tetrahedral site 'r_A' found to be increase with Cd ion content where as mean ionic radius of the octahedral site 'r_B' decreases with cadmium content. The increase of ionic radius 'r_A' of tetrahedral site with Cd ion content was due to the larger ionic radii of Cd ions. But the values of oxygen positional parameter are almost same in the ferrite systems.

TABLE: 1 Structural and elastic parameter of ferrites system $Ni_{0.5}Cu_{0.5-x}Cd_xFe_2O_4$
(x = 0.0, 0.15, 0.25).

Parameters	x = 0.0	x = 0.15	x = 0.25
a (Å)	8.367	8.402	8.416
$\rho \times 10^3$ (kg/m³)	5.37	5.443	5.460
d $\times 10^3$ (kg/m³)	4.003	3.421	3.990
r_A(Å)	0.67	0.65	0.70
r_B(Å)	0.687	0.686	0.684
L_A (Å)	3.623	3.633	3.642
L_B (Å)	2.953	2.959	2.968
R_A(Å)	1.898	1.901	1.906
R_B(Å)	1.990	1.994	1.999

a_{th} (Å)	8.417	8.451	8.489
u	0.386	0.388	0.389
υ_1 x 102 (m^{-1})	590	588	585
υ_2 x 102 (m^{-1})	389	397	400
k_t (N/m)	1.482	1.712	1.746
k_o x 10^2 (N/m)	0.988	0.982	0.977
V_l (m/s)	5250	5300	5321
V_s (m/s)	3031	3111	3230
G x10^9 kg m^{-1}s^{-2}	49.33	51.11	52.64
B x10^9 kg m^{-1}s^{-2}	148	152	157
E x10^9 kg m^{-1}s^{-2}	133.2	139.6	142.4
σ	0.35	0.35	0.35

The band positions of IR spectrum are listed in table 1. The shift of band position υ_1 towards lower wavelength side was due to the substituted Cd^{2+} ion, preferably it occupies the tetrahedral (A) site [11]. The octahedral [B] site was occupied by Ni^{2+}ions, where Fe^{3+}, Cu^{2+} ions occupy both tetrahedral and octahedral sites. The force constant for tetrahedral 'k_t' and octahedral 'k_o' sites, longitudinal 'V_l' and transverse 'V_s' elastic wave velocities, elastic moduli for ferrite samples were estimated using the relations[9] and are listed in table 1. The decreases of octahedral force constant with increase of the Cd ion content, was due to the substitution of Cd ion content, which decreases the amount of Cu^{2+} and increases the amount of Fe ions in the octahedral [B] sites. The increase in rigidity modulus 'G', bulk modulus 'B' and young's modulus 'E' with increase of the cadmium content, may be due to the strengthening of inter atomic bonding between various atoms continuously. The values of poisson's ratio are found to be 0.35 for all the ferrites. The present estimated values of poisson's ratios are lying in the range of -1 to 0.5; which reveals the theory of isotropic elasticity.

IV. Conclusions:

The X ray diffraction pattern revels the formation of cubic spinel structure of ferrite phase. The lattice parameter and X-ray density are found to increase with cadmium content. The estimated cation distribution of ferrites has been verified by comparing the observed and theoretical lattice parameters. The structural parameters estimated through X-ray diffraction were affected with cadmium content.

The elastic parameters are found to increases with increase of cadmium content and was explained in terms of inter atomic bonding between various atoms and is being strengthened continuously. The estimated elastic parameters of the present results are in good agreement with the earlier reports.

V. References

[1] B. K. Bammannavar, L. R. Naik and R.   B. Pujar, (2008) *Mater. Sci. an Ind. J.* 4(3), 160.

 [2] A. M. Abdeen, (1998) *J. Magn. Magn. Mater.* 185, 199.

[3] O. H. Kwon, Y. Fukushima, M. Sugimoto and N Hiratsuka, (1997) *J Phys.* IV, 165.

[4] A. Menakshisundaram, N. Gunasekaran and V. Srinivasan, (1982) *Phys. Stat. Solidi. (a)* 69, K15.

[5] S.A. Mazen, S.F. Mansour, T.A. Elmosalami, H. M. Zaki, (2009)   J. Alloys. Compd. 472 307.

[6] C.N. Rao,   (1994)   "Chemical approaches to the synthesis of inorganic materials",   Wiley, New York.

[7] Zhiyong Xu, Zhong Yu, Ke Sun, Lezhong Li, Haining Ji, Zhongwen Lan, (2009) J. Magn. Magn. Mater. 321.

[8] P. B. Belavi, G. N. Chavan, L. R. Naik,   R.   Somasshekar   and R. K. Kotnala, (2012).*Mater. Chem. Phys.* 132, 138

[9] K. B. Modi, M. K. Rangola, M. C. Chhantbar and H. H. Joshi, (2006).   *J. Mater. Sci.* 41, 7308

[10] R. L. Dhiman, S. P. Taneja and V. R. Reddy, (2008). *Adv. Condens. Mat. Phys.* 703479, 7

 [11] S. A. Patil, V. C. Mahajan, A. K. Gatge   and S. D. Lotake, (1998)

Uncovering The Impact Of Inorganic Ligand Potassium Dihydrogen Phosphate(KDP) On Optical Traits Of Cadmium Thiourea Acetate Crystal For Optoelectronic Applications

Dr. Rupali B. Kulkarni, Dr. Swati S. Kulkarni*

*Department of Physics, Swa. Sawarkar Mahavidyalaya, Beed. 431122 (MS) India

*Corresponding Author Email-Id: meerachothwe@gmail.com

Abstract :

Present research work concentrates on evaluating the impact of inorganic ligand potassium dihydrogen phosphate (KDP) on optical properties of Bis Thiourea Cadmium Acetate (BTCA) crystal. Traditional slow evaporation solution growth technique was employed at ambient temperature for the growth of KDP-BTCA metal complex crystal. Urbach energy and band gap were determined from absorbance data. The optical constants reflectance, extinction coefficient and polarizability were assessed employing absorbance study.

Keywords: Crystal growth, Urbach tail, extinction coefficient and polarizability.

I. INTRODUCTION

Thiourea coordinated metal complex crystals have gained considerable attention in past few decades owing to their unique credibility of beholding the properties of both organic and inorganic counterparts which rank them as superior materials for designing microelectronics, photonics, optical switching, optical data storage, frequency conversion and modern nonlinear optical (NLO) devices [1-4]. The list of thiourea metal complex crystals(TMC) is quite large amongst which some promising crystals are under constant investigation such as calcium bis thiourea chloride (CBTC), zinc thiourea sulphate (ZTS), zinc thiourea chloride (ZTC), bis thiourea cadmium formate (BTCF), bis thiourea cadmium chloride (BTCC), bis thiourea zinc acetate (BTZA), bis cadmium thiourea acetate (BTCA), etc [5-7]. The materials embodied with transition elements having closed d^{10} shell electrons express excellent optical properties [8], hence BTCA is explored as a eye catching interesting material to investigate so as to find its applicability for suitable optical device applications. The intruding fact observed in literature is that very few research groups have grown and explored the characteristic features of pure BTCA crystal [9-11]. Furthermore, the fact that encourages more to investigate the BTCA crystal is that there are very few reports available on doping of impurity in BTCA crystal. As doping is the most effective and fascinating way to modify the intrinsic and extrinsic properties of host crystal [12], the doping effect of glycine, L-alanine, L-cysteine and L-valine on distinct properties of BTCA crystal has been explored [13-16].

Potassium dihydrogen phosphate (KDP) is an ideal material in the field of nonlinear optics due to having high growth rate, extended thermal stability, good optical homogeneity, good SHG efficiency coefficient, interesting TONLO behaviour foreshowing the positive refraction tendency i.e. self focusing effect [17],

nonlinear cubic susceptibility ($\chi 3$) of the order of 10^{-14} esu . Hence KDP has a wide demand under the extended umbrella of UV-tuneable laser systems, frequency conversion and optical data storage, laser imaging and remote sensing [18].

Due to these existing appealing properties of KDP and high technological credential, KDP was selected as a preeminent dopant to achieve fascinating improvement in the properties of parent BTCA crystal [19-20].

Already an impact of doping effect of KDP on structural, functional properties and transmittance of BTCA crystal was reported by our group[21].As an output of literature survey, no other researcher has studied a doping effect of KDP on different traits of Metal complex crystal; hence through this communication authors elaborated and demonstrated the feasibility of the Urbach energy, band gap, linear optical constants analysis of the KDP-BTCA crystal for distinct frequency conversion and nonlinear device applications.

II. Experimental procedure

With Cadmium acetate in 1 molar ratio and thiourea in 2 molar ratios dissolved in double distilled deionised water Cadmium thiourea acetate (BTCA) salt was formed. Prepared salt was further purified by repetitive recrystallization. Supersaturated solutions of pure BTCA and KDP-BTCA were prepared and the 1wt%of KDP was added to the supersaturated solution of parent BTCA. Agitation of six hours of pure and doped solutions achieved homogeneous doping throughout the solution. Parent and KDP-BTCA solutions were filtered in sterilized beakers and the filtrates were kept for an ambient temperature slow solvent evaporation process by covering the beakers with perforated coils in a constant temperature bath. Harvested crystals with prominent and good crystal planes and higher transmittance were selected for further study. Pure BTCA and KDP-BTCA crystals are shown in Fig.1.
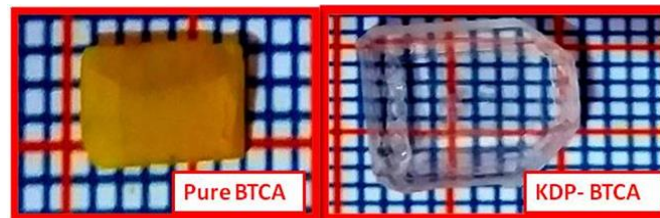
Fig.1.(a) Pure BTCA (b) KDP-BTCA crystal

III.Results and discussion

3.1 Urbach Energy

For the crystalline materials, the absorption coefficient (α) exponentially depends on the photon energy (hυ) below the fundamental absorption edge. This relation is expressed by the Urbach empirical rule given by $\alpha = \alpha_o exp(h\upsilon/E_U)$ [23-26].

Where α_o is a constant and E_U is the band tail energy termed as Urbach energy, which declares the extension of tail levels into the forbidden gap below the absorption edge, h is a Planck's constant and υ is the frequency of radiation. Appearance of the tail due to localized states extended in the band gap indicates low crystalline, poor crystalline, disordered and amorphous materials. Hence Urbach energy is a measure of structural defects or disorders. The log of the absorption coefficient (ln(α)) as a function of high photon energy (hυ) is depicted in Fig. 2(a).
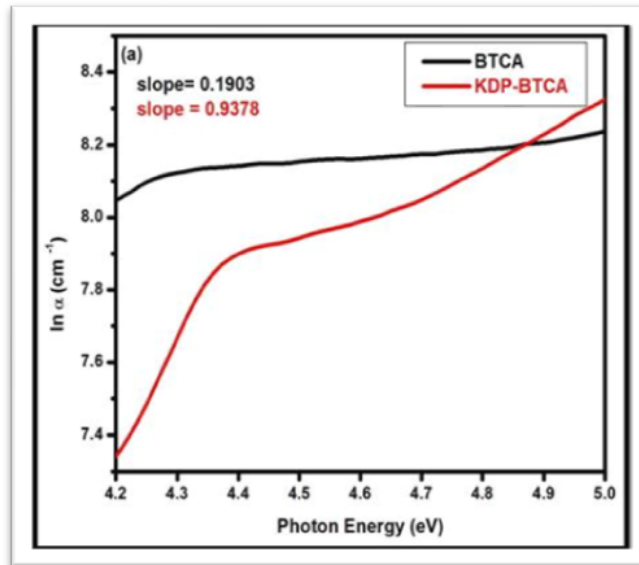
Fig.2. (a) Urbach tail-plot

The degree of crystallinity is directly proportional to the slope of this region.The observed slope of the linear portion of the plot was found from which is 0.1903 for pure BTCA crystal and 0.9378 for KDP-BTCA crystal.The reciprocal of the slope of linear portion of the plot drawn between $\ln(\alpha)$ and $h\upsilon$ gives the value of Urbach energy E_U. Urbach energy value E_U for pure and KDP-BTCA crystal is 5.2548 eV and 1.06632 eV respectively. The plot interpretation confirmed lower value of Eu for KDP-BTCA crystal which explored the high crystallinity and less structural defects than pure BTCA crystal [23-26].
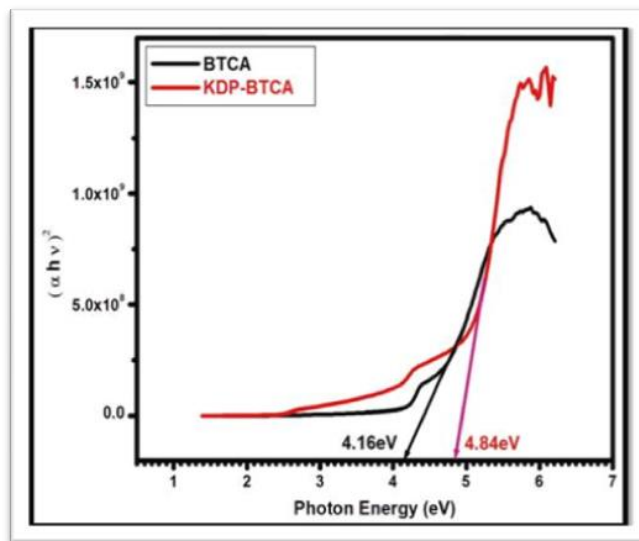
Fig.2. (b) Tauc's Plot

3.2 Optical band gap

The BTCA crystal exhibits a transmittance of 48% [27], while due to doping the increased transmittance is 60% for KDP doped BTCA crystal. KDP-BTCA crystal is found to have superior optical properties as compared to BTCA which dictates the promising candidature of KDP doped BTCA crystal for UV-tunable and harmonic generation devices [27, 28].

The absorbance data was used to evaluate the optical band gap. The optical band gap of KDP-BTCA crystal has been determined from obtained UV-absorbance data and graphically calculated using the Tauc's plot method. The optical band gap is depicted in Fig.2(b), drawn using the reported equation, $(\alpha h\upsilon)^2 = A (h\upsilon - E_g)$ [29-30]. The

determined optical band gap value of KDP-CTA crystal is 4.84 eV, which is comparatively larger than the L-Alanine and glycine doped BTCA crystal shown in **Table 1**[11, 22]. The high band gap value stresses wide optical transmission range and suggests potential candidature of KDP-BTCA under the extended umbrella of optoelectronic device applications[31].

Table 1. Optical band gap of doped BTCA crystals

Sample	Band Gap (eV)	Reference
Pure BTCA	4.16	[22] [27]
KDP-BTCA	4.84	Present work
Glycine-BTCA	3.55	[11]
NMU-BTCA	4.97	[11]

3.3 Linear Optical study

Optically superior crystals have an important role in calibration, design, processing and tuning of the technological devices. Impact of inorganic ligand KDP on linear optical constants of BTCA like reflectance, extinction coefficient and polarizability of BTCA crystal was studied using the previously reported formulae [32-35] by using UV absorbance data obtained using Shimatzu spectrophotometer. From **Fig. 3(a)** it is confirmed that the reflectance of KDP-BTCA crystal has been modified to lower value. The reduced extinction coefficient depicted in **Fig. 3(b)** of KDP-BTCA crystal facilitates less optical loss, which stringently advocates the KDP-BTCA crystal for computing, signaling and ultrafast optical data processing[14].From **Fig.3 (c),**it is clear that the polarizability of KDP-BTCA Crystal is lowered in entire UV region which in turn decreases the dielectric nature of material. The lower dielectric indicates better conversion efficiency [35].
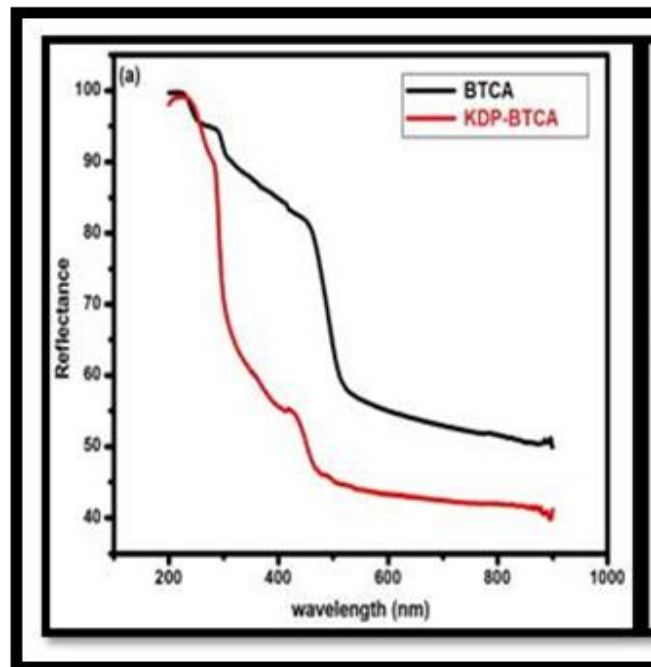
Fig.3. Variation of (a) Reflectance
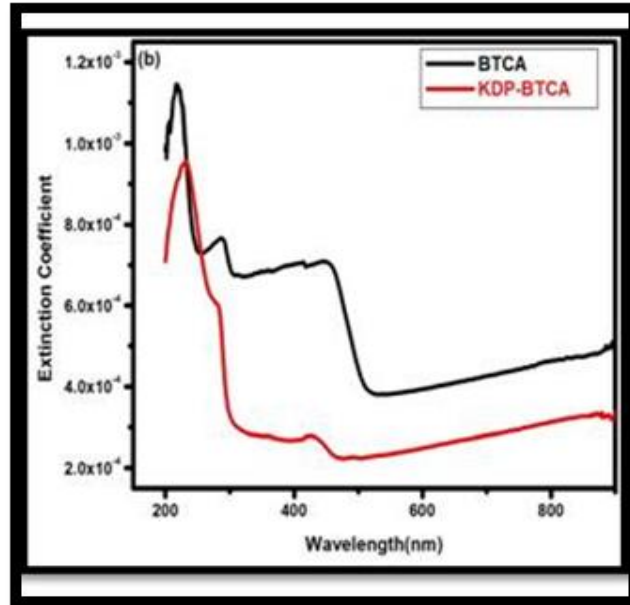
Fig.3. Variation of (b) Extinction Coefficient
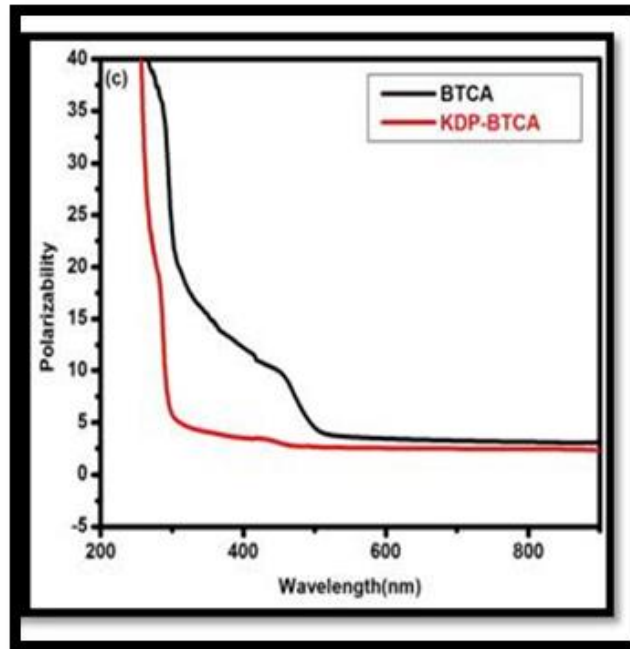
Fig.3. Variation of (c) Polarizability

IV.CONCLUSION

Traditional slow solution evaporation technique at ambient temperature was used for the growth of pure and KDP-BTCA crystals. The optical studies revealed from absorbance data confirmed widened band gap (4.84eV) and improved lower values of extinction coefficient, reflectance, polarizability, refractive index of KDP-BTCA than BTCA crystal, favouring its suitability for solar thermal device fabrication, nonlinear optical and laser applications. Evaluated Urbach energy of pure BTCA and KDP-BTCA crystal is 0.1903 eV and 0.9378 eV, confirming better crystalline nature and high order of KDP-BTCA crystal.

V. REFERENCES

[1]. Gary L.Succaw, Timothy J.R.Weakley, Fusan Han, Kenneth M. Doxsee, Crystal Growth & Design 5(2005)2288-2298.

[2]. Ming Li, Mingjun Xia, Huining Xia, Chemistry Select 2(2017)5882-5886.

[3]. K.Ramamurthi, G. Madhurambal, B. Ravindran, M. Mariappan, S.C.Mojumdar, J Thermal Calorim 104(2011)943–947.

[4]. S.M.Azhar, S. S. Hussaini, M. D. Shirsat, G. Rabbani, Mohd Shkir, S. Alfaify, H.A.Ghramh,M.I.Baig, Mohd Anis, Material research innovations(2017)1-6. https://doi.org/10.1080/14328917.2017.1392694

[5]. H Pir, N Gu¨nay, D Avc,Y Atalay, Indian J Phys.86 (2012)1049-1063.

[6]. Mohd Anis, S.S. Hussaini, M.D. Shirsat, Optik 127(2016)9734–9737.

[7]. Mohd Anis,S.S. Hussaini, A. Hakeem, M.D. Shirsat, G.G. Muley,Optik 127(2016)2137–2142.

[8]. Min-hua Jiang, Qi Fang, Adv. Mater. 11(1999)1147-1151.

[9]. R. Sankar, C. M. Raghavan, R. Jayavel Cryst. Res. Technol. 41(2006)919-924.

[10]. S.S. Kirupavathy, S.S. Mary, P. Srinivasan, N. Vijayan, G. Bhagavannarayana, R. Gopalakrishnan, J. Cryst. Growth 306(2007)102-110.

[11]. J. Uma, V. Rajendran Ind. J. Comp. Appl. 30(2011)8-10.

[12]. Mohd Anis, M.I. Baig, M.S. Pandian, P. Ramasamy, S. AlFaify, V. Ganesh, G.G. Muley, H.A. Ghramh, Cryst. Res. Technol. (2018). https://doi.org/10.1002/crat.201700165

[13]. V.Ganesh,T.Bhaskar Rao, K. Kishan Rao, G. Bhagavannarayana, Mohd. Shkir Mater. Chem. Phys. 137(2012)276-281.

[14]. Mohd Anis, S.S.Hussaini, M.D.Shirsat, G. G. Muley, Materials Research Innovations 20 (2016)312-316.

[15]. S.M.Azhar, MohdAnis, S.S.Hussaini, S.Kalainathan, M.D.Shirsat, G.Rabbani, Optics and Laser Technology 87(2017)11-16.

[16]. Mohd Anis, M.I. Baig, S.S. Hussaini, M.D. Shirsat, Mohd Shkir, H.A. Ghramh, Chin. Phys. B 27 (2018) 27800-27806.

[17]. M. Anis, Mahendra D.Shirsat, G. Muley, S.S.Hussaini, Physica B 449 (2014)61-66.

[18]. M.Anis, G.Muley, A. Hakeem, M.D. Shirsat, S. Hussaini, Opt. Mat. 46 (2015) 517-521.

[19]. M. Shakir, V. Ganesh, B. Riscob, K.K. Maurya, K. Kishan Rao, M.Wahab, G. Bhagavannarayana, Int. J. of Pure and Appl.Phys7(2011)13-24.

[20]. Yogesh B. Rasal, Rais Shaikh, Mahendra Shirsat, S. Kalainathan, S.Hussaini ,Mat. Res.Exp. (2017).http://dx.doi.org/10.1088/2053-1591/aa5a66.

[21]. Rupali B. Kulkarni, M. Anis, S. Hussaini, Mahendra Shirsat,Int.J. ChemTech Res.6(2014)1571-1574.

[22]. Rupali B. Kulkarni, Arti Rushi, M. Anis, S.Hussaini, Mahendra D. Shirsat Int. J. Sci. Res. Publication. 4 (2014)1-5.

[23]. K. Kumar ,G. Prasad, L. Nagalakshmi, Eur.Phys.J.Appl.Phys. 48(2009) 20403 -20409.

[24]. S.Jeeva, K. Arulaabaranam, S. Chithra, K. Selvam, G. Mani, Inter. J. of Chem-Tech Res.11(2018) 204-215.

[25]. J. Dalal, B. Kumar, Opt. Mat.51(2016)139-147.

[26]. N.F.Mott and E.A. Davis, Electronic processes in Non-crystalline Materials, Oxford University press(1979).

[27]. Rupali B. Kulkarni, M. Anis, S.S.Hussaini, M.D. Shirsat, Materials Research Express (2018).DOI:10.1088/2053-1591/aab2f8

[28]. M. Anis, G. Muley, M. Baig, S. Hussaini,M. D. Shirsat, Mater. Res. Innov.21(2017)439-446.

[29]. S. Ramteke, M. Anis, M.S. Pandian, S Kalainathan, Mirza I Baig, P. Ramasamy, Optics & Laser Tech. 99 (2017)197-202

[30]. B. K. Periyasamy, R. S. Jebas, N. Gopalakrishnan, T. Balasubramanian, Mat. Lett. 61 (2007) 4246-4249.

[31]. M. Anis, S.P.Ramteke, M.D.Shirsat, G.Muley, M.Baig, Opt.Mater.72(2017)590-595.

[32]. P.Vasudevan, S. Sankar, D. Jayaraman, Bull. Korean Chem. Soc. 34(2013)128-132.

[33]. P. Vivek, P. Murugakoothan, Opt. Laser. Technol. 49(2013)288-295.

[34]. T. C. Sabari Girisun, S. Dhanuskodi, Cryst. Res.Technol. 44(2009)1297-1302.

[35]. S.R.Thilagavathy,K.Ambujam,Trans.Ind. Inst. Metals 64(2011)143-147.

Innovative Approaches to Memory Storage Using Nanomagnetic Technologies

Dr. G. S. Jaigaonkar

Assistant professor, Department of physics

B.B. Arts, N.B. Commerce & B.P. Science College Digras Dist. Yavatmal

Email: gautamjaigaonkar50@gmail.com

Abstract :

This paper explores cutting-edge approaches to memory storage by leveraging nanomagnetic technologies. We investigate the role of nanomagnetic materials in enhancing data storage density, stability, and energy efficiency. Emphasis is placed on recent innovations in nanomagnetism that drive the development of high-performance memory devices. The findings suggest that nanomagnetic technologies hold significant promise for advancing the capabilities of next-generation memory storage solutions, offering a pathway to more efficient and reliable data storage systems.

Keywords: - Nano magnetism, Memory Storage, High-Density Storage, Magnetic Materials, Superparamagnetism, Data Storage Devices, Quantum Tunnelling, Energy Efficiency, Next-Generation Memory, Spintronics

I. INTRODUCTION

The rapid advancement of technology has driven the need for more efficient, high-capacity memory storage solutions. Traditional memory devices, while effective, are reaching their physical and performance limitations, necessitating the exploration of novel approaches to data storage. Nanomagnetic technologies have emerged as a promising field, offering significant potential to overcome these limitations and revolutionize the landscape of memory storage.

Nano magnetism, the study of magnetic phenomena at the nanoscale, enables the manipulation of magnetic properties in ways that were previously unattainable. By leveraging the unique characteristics of nanomagnetic materials, such as superparamagnetism and quantum tunneling, researchers have developed memory devices with unprecedented data storage density, faster read/write speeds, and enhanced energy efficiency. These attributes make nanomagnetic memory devices strong contenders for next-generation storage technologies.

This paper investigates the innovative approaches that utilize nanomagnetic technologies for memory storage. We explore how these technologies can be harnessed to create high-performance memory devices capable of meeting the demands of modern computing and data-intensive applications. Emphasis is placed on the fundamental principles of nano magnetism, recent advancements in material science, and the practical challenges associated with integrating these technologies into commercially viable memory devices.

As the demand for faster, more reliable, and energy-efficient memory continues to grow, nanomagnetic technologies are poised to play a crucial role in shaping the future of data storage. This study aims to provide a

comprehensive overview of the potential and challenges associated with these innovative approaches, offering insights into their application in the next generation of memory storage solutions.

Nano magnetism:

Nano magnetism refers to the study and manipulation of magnetic properties at the nanoscale, where materials exhibit unique behaviors not observed in bulk form. At this scale, magnetic properties can be finely tuned due to quantum mechanical effects, leading to the emergence of phenomena such as superparamagnetism, spin coupling, and quantum tunnelling.

In the context of memory storage, nano magnetism is highly relevant due to its potential to revolutionize how data is stored and accessed. Traditional memory storage devices, like hard drives and solid-state drives (SSDs), rely on larger-scale magnetic or electronic principles that are reaching their physical limits in terms of speed, density, and energy efficiency. As devices become more compact and data-intensive applications continue to grow, there is an increasing demand for memory solutions that can offer higher storage capacities, faster access times, and lower power consumption.

Nanomagnetic materials and devices can address these challenges by allowing for the creation of memory cells that are smaller, faster, and more energy-efficient than their conventional counterparts. For example, in Magnetic Random Access Memory (MRAM), data is stored by manipulating the magnetic states of nanoscale magnetic elements, allowing for non-volatile memory with high endurance and speed. The ability to control magnetization at the nanoscale also enables higher data density, meaning more information can be stored in a smaller space, which is crucial for the miniaturization of electronic devices.

Furthermore, the inherent stability of nanomagnetic states underpins the reliability of memory devices, reducing the likelihood of data loss over time. As a result, nanomagnetism is poised to play a critical role in the development of next-generation memory technologies, offering solutions that align with the demands of modern computing and data storage requirements.

Challenges in Traditional Memory Storage:

Traditional memory storage technologies, such as Hard Disk Drives (HDDs), Solid-State Drives (SSDs), and Dynamic Random-Access Memory (DRAM), have served as the backbone of data storage for decades. However, as technology evolves and the demand for more efficient, faster, and higher-capacity storage solutions grows, these conventional technologies face several challenges:

1.Physical Limitations and Scalability:

Miniaturization Limits: Traditional memory technologies are reaching their physical limits in terms of how small memory cells can be made. For instance, in HDDs, the size of the magnetic grains used to store data cannot be reduced indefinitely without risking data stability due to thermal fluctuations (the superparamagnetic limit).

Scaling Challenges: DRAM, which relies on capacitors to store data, faces challenges in scaling down further without significant increases in leakage current, which leads to higher power consumption and heat generation.
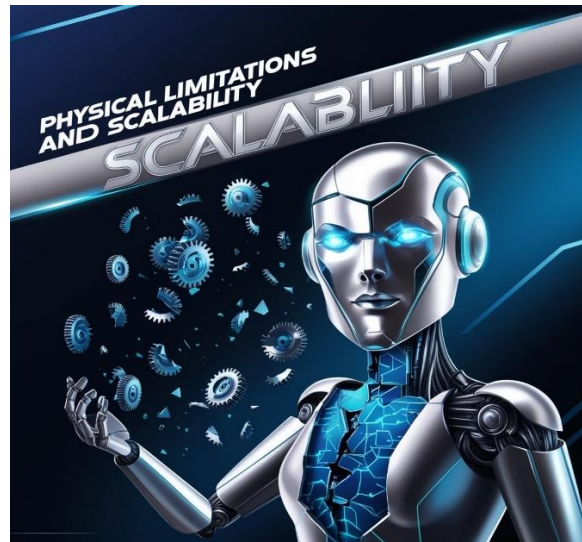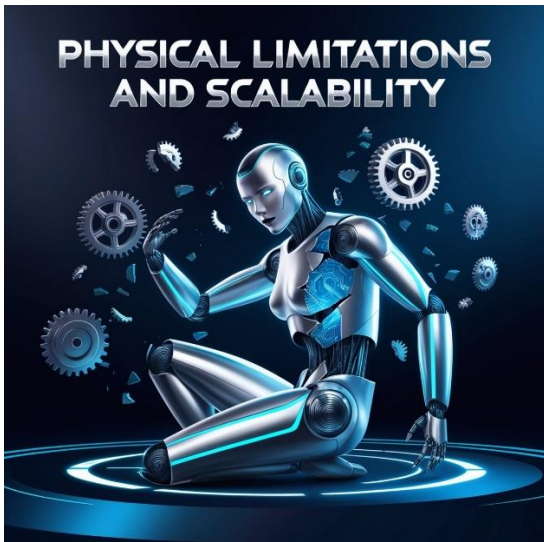
2.Energy Efficiency:

High Power Consumption: Conventional memory storage devices, particularly DRAM, consume significant amounts of power, both in active operation and in maintaining data integrity (refresh cycles). This becomes a critical issue in portable devices where battery life is paramount and in data centers where energy costs are a major concern.

Thermal Management: As devices shrink and data density increases, managing the heat generated by traditional memory technologies becomes increasingly difficult, leading to potential reliability issues and the need for more sophisticated cooling solutions.
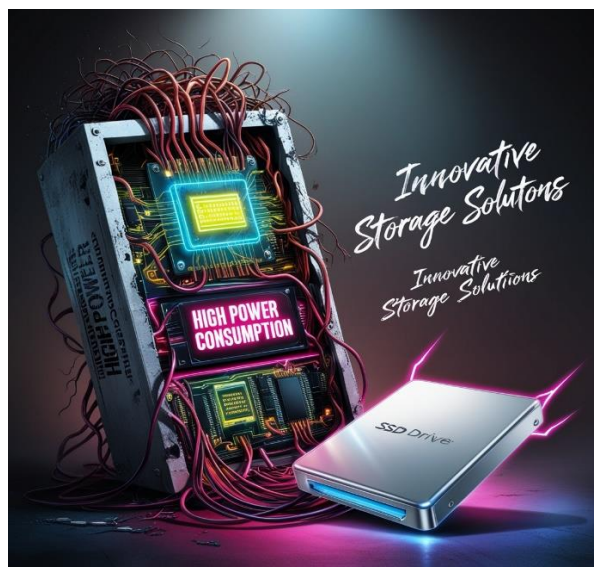
3.Speed and Performance:

Latency: Traditional memory storage devices, such as HDDs, suffer from relatively high latency due to mechanical parts (e.g., spinning disks and moving read/write heads), which limits their speed compared to newer, solid-state options. Even SSDs, while much faster, still face challenges in reaching the speeds required by emerging applications, such as real-time data processing and AI.

Bottlenecks in Data Transfer: As the speed of processors and data buses increases, traditional memory storage devices can become bottlenecks, limiting overall system performance. This is particularly true for applications requiring rapid data access and processing.

4.Reliability and Data Integrity:

Wear and Degradation: SSDs, which rely on flash memory, suffer from wear-out mechanisms, particularly in the NAND cells, which have a limited number of write/erase cycles. Over time, this leads to degradation in performance and potential data loss.

Magnetic Interference: In magnetic storage devices like HDDs, data integrity can be compromised by external magnetic fields, temperature fluctuations, and physical shocks, which can cause data corruption or loss.

5.Cost and Economic Factors:

Manufacturing Costs: The cost of manufacturing advanced traditional memory devices continues to rise as the technology approaches its scaling limits. This is due to the need for more complex fabrication processes and materials.

Price-Performance Trade-offs: Users often face a trade-off between cost, storage capacity, and performance. For example, while SSDs offer superior speed compared to HDDs, they are generally more expensive per gigabyte, which can be prohibitive for large-scale data storage needs.

6. Environmental Impact:

Energy Consumption: The high-power consumption of traditional memory technologies contributes to a larger carbon footprint, especially in large data canters.

Material Usage: The materials used in traditional memory devices, including rare earth metals and other non-renewable resources, raise concerns about sustainability and environmental impact.

Advancements in nanomagnetic materials have been pivotal in pushing the boundaries of memory storage technologies, offering new possibilities for high-density, energy-efficient, and fast memory devices. These materials leverage the unique magnetic properties that emerge at the nanoscale, enabling innovative solutions that address the limitations of traditional memory technologies. Here are some key advancements in this field:

Advancements in Nanomagnetic Materials:

1. Development of Magnetic Nanoparticles

Enhanced Magnetic Properties: Magnetic nanoparticles, such as iron oxide (Fe_3O_4) and cobalt ferrite ($CoFe_2O_4$), have been engineered to exhibit superparamagnetism, where they can rapidly switch between magnetic states without retaining magnetization when an external magnetic field is removed. This property is essential for creating high-density storage devices, as it allows for the miniaturization of memory cells without risking data stability.

Surface Functionalization: Advances in the surface modification of magnetic nanoparticles have improved their stability and compatibility with different substrates, enabling better integration into memory devices.
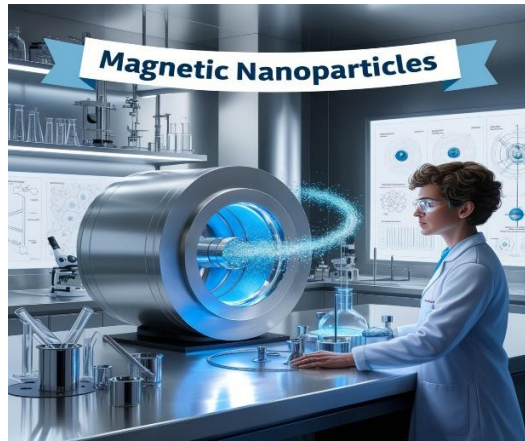
2. Spintronic Materials

Magnetoresistive Materials: The discovery and optimization of materials exhibiting Giant Magnetoresistance (GMR) and Tunnel Magnetoresistance (TMR) have been groundbreaking. These materials change their electrical resistance in response to an applied magnetic field, which is the principle behind Magnetoresistive Random Access Memory (MRAM). MRAM devices can store data non-volatilely with faster access times and lower power consumption compared to traditional memory.

Heusler Alloys: These are a class of ferromagnetic materials with high spin polarization, which enhances the efficiency of spintronic devices. Heusler alloys, such as Co_2MnSi, have been refined to achieve higher Curie temperatures and better spin filtering properties, crucial for reliable memory device performance.

3. Antiferromagnetic Materials

Antiferromagnetic Spintronics: Unlike ferromagnetic materials, antiferromagnetic materials do not produce stray magnetic fields, making them less susceptible to external magnetic interference. This property has been leveraged in the development of antiferromagnetic spintronic devices, which offer faster data writing speeds and higher stability at smaller scales.

High-Speed Data Processing: Antiferromagnetic materials enable ultrafast dynamics and have the potential to operate at terahertz frequencies, significantly increasing the speed of data processing in memory devices.

4. Multiferroic Materials

Coupled Magnetic and Electric Properties: Multiferroic materials exhibit both ferromagnetism and ferroelectricity, allowing for the control of magnetic properties using an electric field. This dual functionality is

promising for developing energy-efficient memory devices, such as magnetoelectric RAM (MeRAM), where data can be written using lower power inputs.

Room-Temperature Operation: Advances in multiferroic materials have led to the discovery of compounds that operate at room temperature, making them more practical for commercial memory devices.

5. Thin-Film and Nanostructured Materials

Enhanced Magnetic Anisotropy: By engineering thin films and nanostructured materials, researchers have been able to tailor magnetic anisotropy, which is the directional dependence of a material's magnetic properties. This control is critical for stabilizing data storage at high densities.

2D Magnetic Materials: The development of two-dimensional (2D) magnetic materials, such as $Cr_2 Ge_2 Te_6$, offers new possibilities for integrating magnetic memory with other 2D materials like graphene. These materials promise ultra-thin, flexible, and high-performance memory devices.

6. Topological Insulators

Spin-Momentum Locking: Topological insulators are materials that conduct electricity on their surface while acting as insulators in their bulk. They exhibit spin-momentum locking, where the direction of an electron's spin is directly linked to its momentum. This property has been harnessed in spintronic devices to enable highly efficient and low-power data storage solutions.

7. Quantum Dots and Magnetic Nanoring's

Quantum Confinement: Quantum dots and magnetic nanoring's have been utilized to create memory devices with quantized magnetic states, offering the potential for extremely high data storage densities. These nanostructures allow for precise control over magnetic properties, enabling the development of quantum memory devices with novel functionalities.

Noise Reduction: Magnetic nanoring's help reduce noise and improve data stability by minimizing stray fields, making them ideal for high-density storage applications.

8. Artificially Structured Materials

Metamaterials: Advances in metamaterials, which are artificially structured materials engineered to have properties not found in nature, have led to the creation of magnetic materials with tailored properties for specific memory storage applications. These materials can be designed to exhibit unique magnetic behavior, such as negative permeability, which could enable entirely new types of memory devices.

9. Hybrid Nanomagnetic Systems

Integration with Other Technologies: Hybrid systems that combine nanomagnetic materials with other technologies, such as photonics or plasmonics, have been explored to create multifunctional memory devices. These systems could potentially store and process data simultaneously, leading to more efficient and compact memory architectures.

10. Environmental and Sustainable Materials

Green Nano magnetism: Researchers are also exploring environmentally friendly nanomagnetic materials that reduce the reliance on rare or toxic elements, aligning with the growing demand for sustainable technology solutions.

II. CONCLUSION:

The exploration of innovative approaches to memory storage using nanomagnetic technologies marks a significant advancement in data storage capabilities. By leveraging the unique properties of nanomaterials and

spintronics, these technologies promise unprecedented increases in data density, speed, and energy efficiency. The shift from traditional magnetic storage methods to nanomagnetic solutions offers potential for revolutionary changes in various fields, including computing and communication. As research progresses, the integration of nanomagnetic technologies into mainstream memory storage systems will likely lead to more robust, scalable, and sustainable solutions, redefining the future of data management and technology.

III.REFERENCES:

[1].   "Nanomagnetism: Fundamentals and Applications" by D.L. Mills and J.A.C. Bland
[2].   "Spin Dynamics in Confined Magnetic Structures I & II" edited by B. Hillebrands and K. Ounadjela
[3].   "Magnetic Nanostructures in Modern Technology: Spintronics, Magnetic MEMS and Recording" edited by Bruno Azzerboni, Giovanni Asti, Luigi Pareti, and Massimo Ghidini
[4].   "Nanomagnetic and Spintronic Materials: Fundamentals and Applications" edited by Akinobu Yamaguchi
[5].   "Handbook of Spintronics" edited by Yongbing Xu and David D. Awschalom
[6].   of Magnetic Microstructures" by Alex Hubert and Rudolf Schäfer
[7].   "Nanomagnetic and Spintronic Materials: Fundamentals and Applications" Edited by E. R. Pike and P. Turner Elsevier, 2012
[8].   "Magnetic Storage Systems Beyond 2020" Edited by G. Bertotti and I. D. Mayergoyz Springer, 2013

On Fixed Point Theorems in Dislocated Rectangular B-Metric Spaces

P. G. Golhare

Abstract :

In this paper, we establish fixed point theorems for the T-Banach and T-Kannan contraction map- pings in dislocated rectangular b-metric spaces. We have also proved some well-known fixed point theorems for quasi contraction in it. We give examples to support our results.

I. INTRODUCTION

Fixed point theorems are a cornerstone of mathematical analysis and applied mathematics, serving as indispensable tools for understanding various functions and operators within a spec- ified domain. These theorems have far-reaching implications across a range of fields, such as economics, physics, and computer science. Recently, the study of fixed points has expanded beyond conventional metric spaces to more advanced structures that offer more comprehensive mathematical frameworks for analysis. This paper focuses on fixed point theorems within the context of dislocated rectangular b-metric spaces, a novel and general framework that extends the classical notion of metric spaces. The main goal of this study is to create and analyze fixed point theorems within dislocated rectangular b-metric spaces. We develop several fixed point theorems. Many scholars have generalized the concept of metric spaces and proven fixed point theorems for various types of contraction mappings in these spaces. Initially, the metric space was expanded by Wilson[17] by introducing the concept of quasi-metric space. Bakhtin[2] in- troduced the b-metric space, which generalizes metric spaces and established fundamental fixed point theorems for it. Hitzler et al.[14] proposed the idea of dislocated metric spaces. R. George et al.[15] introduced the concept of rectangular b-metric spaces as a generalization of both metric spaces and b-metric spaces. They also established the analogue of the Banach con- traction principle and Kannan-type contraction in rectangular b-metric spaces. In this paper, we study fixed point theorems in dislocated rectangular b-metric spaces introduced by Golhare and Aage[13] a new generalization of the metric spaces. We have proved analogues of some well-known results in the literature in dislocated rectangular b-metric spaces.

Bakhtin[2] defined the b-metric space as follows

Definition 1.1. ([2]) Let X be a non-empty set and mapping $d : X \times X \to [0, \infty)$ satisfies: (i) $d(x, y) = 0$ if and only if $x = y$ for all $x, y \in X$,

(ii) $d(x, y) = d(y, x)$ for all $x, y \in X$,

(iii) there exists a real number $k \geq 1$ such that $d(x, y) \leq k[d(x, z) + d(z, y)]$ for all $x, y, z \in X$. Then d is called b-metric on X and (X, d) is called a b-metric space with coefficient k.

Shah and Huassain[12] extended b-metric space to quasi-b-metric spaces and proved some fixed point theorems in it. Alghamdi, Husasain and Salimi[10] defined the term b-metric-like

spaces or dislocated b-metric spaces to generalize metric-like spaces. Some of the generalizations of metric spaces are mentioned below.

Definition 1.2. ([12]) Let X be a non-empty set. Let $d : X \times X \to [0, \infty)$ be a mapping and $k \geq 1$ be a constant such that:

(i) $d(x, y) = 0 = d(y, x)$ if and only if $x = y$ for all $x, y \in X$,

(ii) $d(x, y) \leq k[d(x, z) + d(z, y)]$ for all $x, y, z \in X$.

Then pair (X, d) is called quasi-b-metric space.

Definition 1.3. ([10]) Let X be a non-empty set. Let $d : X \times X \to [0, \infty)$ be a mapping and $k \geq 1$ be a constant such that:

(i) $d(x, y) = 0$ then $x = y$ for all $x, y \in X$,

(ii) $d(x, y) = d(y, x)$ for all $x, y \in X$,

(iii) $d(x, y) \leq k[d(x, z) + d(z, y)]$ for all $x, y, z \in X$.

Then pair (X, d) is called dislocated b-metric space.

Definition 1.4. ([1]) Let X be a non-empty set and mapping $d : X \times X \to [0, \infty)$ satisfies:

(i) $d(x, y) = 0$ if and only if $x = y$ for all $x, y \in X$,

(ii) $d(x, y) = d(y, x)$ for all $x, y \in X$,

(iii) $d(x, y) \leq [d(x, u) + d(u, v) + d(v, y)]$ for all $x, y \in X$ and all distinct points $u, v \in X \backslash \{x, y\}$.

Then d is called a rectangular metric on X and (X, d) is called a rectangular metric space.

R. George et al.([15]) defined rectangular b-metric space as follows:

Definition 1.5. ([15]) Let X be a non-empty set and mapping $d : X \times X \to [0, \infty)$ satisfies:

(i) $d(x, y) = 0$ if and only if $x = y$ for all $x, y \in X$,

(ii) $d(x, y) = d(y, x)$ for all $x, y \in X$,

(iii) there exist a real number $s \geq 1$ such that $d(x, y) \leq s[d(x, u) + d(u, v) + d(v, y)]$ for all $x, y \in X$ and all distinct points $u, v \in X \setminus \{x, y\}$.

Then d is called a rectangular b-metric on X and (X, d) is called a rectangular b-metric space with coefficient s.

Example 1.6. ([15]) Let $X = \mathbb{N}$, define $d : X \times X \to [0, \infty)$ by

$$d(x, y) = \begin{cases} 0, & \text{if } x = y, \\ 4\alpha, & \text{if } x, y \in \{1, 2\} \text{and } x \neq y, \\ \alpha, & \text{if } x \text{ or } y \notin \{1, 2\} \text{and } x \neq y, \end{cases}$$

where $\alpha > 0$ is a constant. Then (X, d) is a rectangular b-metric space with coefficient $k = \frac{4}{3} > 1$.

Int J Sci Res Sci & Technol. September-October -2024, 11 (19) : 77-92

3

Example 1.7. ([8]) Let $A = \{0, 2\}, B = \{\frac{1}{n} : n \in \mathbb{N}\}$ and $X = A \cup B$ define $d : X \times X \to [0, \infty)$ by

$$d(x, y) = \begin{cases} 0, & \text{if } x = y, \\ 1, & \text{if } x \neq y \text{ and } \{x, y\} \subset A \text{ or } \{x, y\} \subset B, \\ y^2, & \text{if } x \in A \text{ and } y \in B, \\ x^2, & \text{if } x \in B \text{ and } y \in A, \end{cases}$$

then (X, d) is rectangular b-metric space with coefficient $k = 3$.

Golhare and Aage[13] defined the notion of dislocated rectangular b-metric space as follows

Definition 1.8. Let X be a non-empty set and mapping $d : X \times X \to [0, \infty)$ satisfies:

(i) $d(x, y) = 0$ then $x = y$ for all $x, y \in X$,

(ii) $d(x, y) = d(y, x)$ for all $x, y \in X$,

(iii) there exist a real number $k \geq 1$ such that $d(x, y) \leq k[d(x, u) + d(u, v) + d(v, y)]$ for all $x, y \in X$ and all distinct points $u, v \in X \setminus \{x, y\}$.

Then d is called a dislocated rectangular b-metric on X and (X, d) is called a dislocated rectangular b-metric space with coefficient k.

One can note that every rectangular b-metric space is dislocated rectangular b-metric space but converse need not be true as illustrated by following example.

Example 1.9. Let $X = \mathbb{N}$, define $d : X \times X \to [0, \infty)$ by

$$d(x, y) = \begin{cases} 4\alpha, & \text{if } x, y \in \{1, 2\}, \\ \alpha, & \text{otherwise} \end{cases}$$

where $\alpha > 0$ is a constant. Then (X, d) is a dislocated rectangular b-metric space with coefficient $k = 2 > 1$. Note that $d(1, 1) = 4\alpha \neq 0$ and $d(2, 2) = 4\alpha \neq 0$. Therefore (X, d) is not a rectangular b-metric space.

We give some definitions in the context of dislocated rectangular b-metric spaces. Firstly we define

Definition 1.10. Let (X, d) be a dislocated rectangular b-metric space with coefficient $k \geq 1$ and $T, S : X \to X$ be two mappings, then the mapping S is called T-Banach contraction if there exists $\alpha \in [0, \frac{1}{k})$ such that,

$$d(TSx, TSy) \leq \alpha d(Tx, Ty), \forall x, y \in X.$$

Definition 1.11. Let (X, d) be a dislocated rectangular b-metric space with coefficient $k \geq 1$ and $T, S : X \to X$ be two mappings, then the mapping S is called T-Kannan contraction if there exists $\alpha \in [0, \frac{1}{2k})$ such that,

$$d(TSx, TSy) \leq \alpha[d(Tx, TSx) + d(Ty, TSy)], \forall x, y \in X.$$

4   P.G. GOLHARE

Definition 1.12. A sequence $\{x_n\}$ in a dislocated rectangular b-metric space (X, d) is said to be convergent to $x \in X$ if and only if $\lim_{n \to \infty} d(x_n, x) = d(x, x)$. In this case, we say that x is a limit of sequence $\{x_n\}$.

Definition 1.13. A sequence $\{x_n\}$ in a dislocated rectangular b-metric space (X, d) is called as Cauchy sequence if and only if $\lim_{n \to \infty} d(x_n, x_{n+i})$ exists and is finite for all $i \in \mathbb{N}$.

Definition 1.14. A dislocated rectangular b-metric space (X, d) is said to be complete if every Cauchy sequence in X is convergent.

Definition 1.15. [3] Let $f : X \to X$ be a self mapping of X, f is said to be sub-sequentially convergent if for every sequence $\{x_n\}$, if fx_n is convergent then $\{x_n\}$ has a convergent subsequence in X.

Definition 1.16. [3] Let $f : X \to X$ be a self mapping of X, f is said to be sequentially convergent if for every sequence $\{x_n\}$, if fx_n is convergent then $\{x_n\}$ is also convergent in X.

Definition 1.17. Let (X, d) be a dislocated rectangular b-metric space and $f : X \to X$ be a self mapping of X, f. Then f is said to be continuous if for every sequence $x_n \to x$ we have $fx_n \to fx$.

Definition 1.18. [7] Let (X, d) be a metric space and $T, S : X \to X$ be two mappings,then the mapping S is called T-Banach contraction if there exists $\alpha \in [0, 1)$ such that,

$$d(TSx, TSy) \leq \alpha d(Tx, Ty), \forall x, y \in X.$$

Definition 1.19. [7] Let (X, d) be a metric space and $T, S : X \to X$ be two mappings,then the mapping S is called T-Kannan contraction if there exists $\alpha \in [0, 1/2)$ such that,

$$d(TSx, TSy) \leq \alpha[d(Tx, TSx) + d(Ty, TSy)], \forall x, y \in X.$$

2. Main Results

Our first result is given below.

Theorem 2.1. *Let (X, d) be a complete dislocated rectangular b-metric space with coefficient $k \geq 1$. Let $f, T : X \to X$ be self-mappings such that T is continuous,one-one and f is continuous such that,*

$$(Tfx, Tfy) \leq \alpha d(Tx, Ty), \forall x, y \in X, \tag{2.1}$$

with $0 < k\alpha \leq 1$. then if T is sub-sequentially convergent then f has unique fixed point in X.

Proof. Let x_0 be any arbitrary point in X. Define $\{x_n\}$ by,

$$x_1 = fx_0, x_2 = fx_1, ..., x_{n+1} = fx_n = f^n x_0, ..., n = 0, 1, 2, 3, ...$$

Since f is T-Banach contraction with $k\alpha \leq 1$, we have,

$$d(Tf^n x_0, Tf^{n+1} x_0) \leq \alpha d(Tf^{n-1} x_0, Tf^n x_0)$$
$$\leq \alpha^2 d(Tf^{n-2} x_0, Tf^{n-1} x_0).$$

Continuing in this way,

$$d(Tf^n x_0, Tf^{n+1} x_0) \leq \alpha^n d(Tx_0, Tfx_0) \tag{2.2}$$

We also assume that $x_0 \neq x_n$ for any $2 \leq n \in \mathbb{N}$. If not, then for some $n \geq 2$, using (2.1), we have

$$d(Tx_0, Tfx_0) = d(Tx_n, Tfx_n)$$

$$d(Tx_0, Tx_1) = d(Tx_n, Tx_{n+1}).$$

It implies that

$$d(Tx_0, Tx_1) \leq \alpha^n d(Tx_0, Tx_1),$$

which is a contradiction unless $d(Tx_0, Tx_1) = 0$. Thus $Tx_0 = Tx_1$ and since T is one-one $x_0 = x_1$ in turn x_0 is a fixed point of f. So, we assume that $x_n \neq x_m$ for all $n \neq m \in \mathbb{N}$. In view of (2.1), for any $n \in \mathbb{N}$, we can write

$$d(Tfx_{n-1}, Tfx_{n+1}) = d(Tf^{n-1}x_0, Tf^{n+1}x_0) \leq \alpha d(Tf^{n-2}x_0, Tf^n x_0) = \alpha d(Tfx_{n-2}, Tfx_n).$$

Applying (2.1) repeatedly, we get

$$d(Tfx_{n-1}, Tfx_{n+1}) = d(Tf^{n-1}x_0, Tf^{n+1}x_0) \leq \alpha^{n-1} d(Tx_0, Tf^2 x_0). \tag{2.3}$$

Now to prove that $\{Tf^n x_0\}$ is Cauchy sequence in X, we prove $\lim_{n \to \infty} d(Tx_n, Tx_{n+m})$ exists and is finite. Here we consider two cases.

Case (i): Suppose m is even i.e. $m = 2i$ for some $i \in \mathbb{N}$ and n may be even or odd. Using inequalities (2.2),(2.3) and rectangular inequality, we get

$$
\begin{aligned}
d(Tx_n, Tx_{n+m}) &= d(Tf^n x_0, Tf^{n+m} x_0) \\
&\leq k[d(Tf^n x_0, Tf^{n+1}x_0) + d(Tf^{n+1}x_0, Tf^{n+2}x_0) + d(Tf^{n+2}x_0, Tf^{n+2i}x_0)] \\
&\leq k[d(Tf^n x_0, Tf^{n+1}x_0) + d(Tf^{n+1}x_0, Tf^{n+2}x_0)] \\
&\quad + k^2[d(Tf^{n+2}x_0, Tf^{n+3}x_0) + d(Tf^{n+3}x_0, Tf^{n+4}x_0) + d(Tf^{n+4}x_0, Tf^{n+2i}x_0)] \\
&\leq k[d(Tf^n x_0, Tf^{n+1}x_0) + d(Tf^{n+1}x_0, Tf^{n+2}x_0)] \\
&\quad + k^2[d(Tf^{n+2}x_0, Tf^{n+3}x_0) + d(Tf^{n+3}x_0, Tf^{n+4}x_0)] \\
&\quad + k^3[d(Tf^{n+4}x_0, Tf^{n+5}x_0) + d(Tf^{n+5}x_0, Tf^{n+6}x_0)+] + \cdots \\
&\quad + k^{i-1}[d(Tf^{n-4+2i}x_0, Tf^{n-3+2i}x_0) + d(Tf^{n-3+2i}x_0, Tf^{n-2+2i}x_0)] \\
&\quad + k^{i-1}[d(Tf^{n-2+2i}x_0, Tf^{n+2i}x_0)] \\
&\leq k[\alpha^n d(Tx_0, Tfx_0) + \alpha^{n+1} d(Tx_0, Tfx_0)] \\
&\quad + k^2[\alpha^{n+2} d(Tx_0, Tfx_0) + \alpha^{n+3} d(Tx_0, Tfx_0)] \\
&\quad + k^3[\alpha^{n+4} d(Tx_0, Tfx_0) + \alpha^{n+5} d(Tx_0, Tfx_0)] + \cdots \\
&\quad + k^{i-1}[\alpha^{n-4+2i} d(Tx_0, Tfx_0) + \alpha^{n-3+2i} d(Tx_0, Tfx_0)] \\
&\quad + k^{i-1}\alpha^{n-2+2i} d(Tx_0, Tf^2 x_0) \\
&\leq k\alpha^n[1 + k\alpha^2 + k^2\alpha^4 + \cdots] d(Tx_0, Tfx_0)
\end{aligned}
$$

6   P.G. GOLHARE

$$+ k\alpha^{n+1}[1 + k\alpha^2 + k^2\alpha^4 + \cdots]d(Tx_0, Tfx_0)$$
$$+ k^{i-1}\alpha^{n-2+2i}d(Tx_0, Tf^2x_0)$$
$$\leq \left[\frac{(1+\alpha)}{1-k\alpha^2}\right]k\alpha^n d(Tx_0, Tfx_0) + k^{i-1}\alpha^{n-2+2i}d(Tx_0, Tf^2x_0)$$
$$\leq \left[\frac{(1+\alpha)}{1-k\alpha^2}\right]k\alpha^n d(Tx_0, Tfx_0) + \alpha^{n-2}d(Tx_0, Tf^2x_0).$$

Letting $n \to \infty$ in last inequality above, we get

$$\lim_{n\to\infty} d(Tx_n, Tx_{n+m}) = 0,$$

for all even $m \in \mathbb{N}$.

Case (ii): Suppose m is odd i.e. $m = 2i - 1$ for some $i \in \mathbb{N}$ and n may be even or odd. Using inequalities (2.2) and rectangular inequality, we get

$$d(Tf^n x_0, Tf^{n+m}x_0) = d(Tx_n, Tx_{n+m})$$
$$\leq k[d(Tf^n x_0, Tf^{n+1}x_0) + d(Tf^{n+1}x_0, Tf^{n+2}x_0) + d(Tf^{n+2}x_0, Tf^{n+2i-1}x_0)]$$
$$\leq k[d(Tf^n x_0, Tf^{n+1}x_0) + d(Tf^{n+1}x_0, Tf^{n+2}x_0)]$$
$$+ k^2[d(Tf^{n+2}x_0, Tf^{n+3}x_0) + d(Tf^{n+3}x_0, Tf^{n+4}x_0) + d(Tf^{n+4}x_0, Tf^{n+2i-1}x_0)]$$
$$\leq k[d(Tf^n x_0, Tf^{n+1}x_0) + d(Tf^{n+1}x_0, Tf^{n+2}x_0)]$$
$$+ k^2[d(Tf^{n+2}x_0, Tf^{n+3}x_0) + d(Tf^{n+3}x_0, Tf^{n+4}x_0)]$$
$$+ k^3[d(Tf^{n+4}x_0, Tf^{n+5}x_0) + d(Tf^{n+5}x_0, Tf^{n+6}x_0)] + \cdots$$
$$+ k^i[d(Tf^{n+2i-2}x_0, Tf^{n+2i-1}x_0)]$$
$$\leq k[\alpha^n d(Tx_0, Tfx_0) + \alpha^{n+1}d(Tx_0, Tfx_0)]$$
$$+ k^2[\alpha^{n+2}d(Tx_0, Tfx_0) + \alpha^{n+3}d(Tx_0, Tfx_0)]$$
$$+ k^3[\alpha^{n+4}d(Tx_0, Tfx_0) + \alpha^{n+5}d(Tx_0, Tfx_0)] + \cdots$$
$$+ k^i\alpha^{n+2i-2}d(Tx_0, Tfx_0)$$
$$\leq k\alpha^n[1 + k\alpha^2 + k^2\alpha^4 + \cdots]d(Tx_0, Tfx_0)$$
$$+ k\alpha^{n+1}[1 + k\alpha^2 + k^2\alpha^4 + \cdots]d(Tx_0, Tfx_0)$$
$$\leq \left[\frac{(1+\alpha)}{1-k\alpha^2}\right]k\alpha^n d(Tx_0, Tfx_0).$$

Letting $n \to \infty$ in the last inequality above, we see that the limit on the right hand side exists and is finite. Therefore, $\lim_{n\to\infty} d(Tx_n, Tx_{n+m})$ exists and is finite for all odd $m \in \mathbb{N}$. Thus from the case(i) and case(ii), it follows that $\lim_{n\to\infty} d(Tx_n, Tx_{n+m})$ exists and for all $n, m \in \mathbb{N}$

$$\lim_{n\to\infty} d(Tx_n, Tx_{n+m}) = 0. \tag{2.4}$$

Therefore $\{Tf^n x_0\}$ is Cauchy sequence in X. Since (X, d) is complete there exists $u \in X$ such that,

$$\lim_{n\to\infty} d(Tf^n x_0, u) = 0.$$

Int J Sci Res Sci & Technol. September-October -2024, 11 (19) : 77-92

7

Since T is sub-sequentially convergent,$\{f^n x_0\}$ has a convergent subsequence, so there exists $v \in X$, such that

$$f^{n_i} x_0 \to v \text{ as } i \to \infty.$$

Since T and f are continuous, $Tf^{n_i} x_0 \to Tv$ as $i \to \infty$ and $f^{n_i+1} x_0 \to fv$ as $i \to \infty$. This implies that $Tf^{n_i+1} x_0 \to Tfv$ as $i \to \infty$. By uniqueness of limit in metric space (X, d), we get

$$Tv = Tfv.$$

Since T is one-one $fv = v$. Thus $v \in X$ is a fixed point of f. To prove that this fixed point of f is unique, we assume that $\omega \in X$ is another fixed point of f i.e. $f\omega = \omega$. Consider,

$$d(Tfv, Tf\omega) \leq \alpha d(Tv, T\omega)$$

$$\text{i.e. } d(Tv, T\omega) \leq d(Tv, T\omega).$$

Which is contradiction to the assumption that $\alpha \in [0, 1)$. Therefore $d(Tv, T\omega) = 0$. Thus, $d(Tv, T\omega) = 0 = d(T\omega, Tv)$ i.e.$Tv = T\omega$. But since T is one-one $v = \omega$. Thus uniqueness of fixed point of f is proved and hence the theorem. $\square$

Example 2.2. Let $X = \mathbb{N}$, define $d : X \times X \to [0, \infty)$ by

$$d(x, y) = \begin{cases} \frac{\alpha}{4}, & \text{if } x = p^2, y = q^2 \text{ for some } p, q \in \mathbb{N}, \\ \alpha, & \text{otherwise}, \end{cases}$$

where $\alpha > 0$ is a constant. Then (X, d) is a dislocated rectangular b-metric space with coefficient $k = 2 > 1$. If $f : \mathbb{N} \to \mathbb{N}$ is defined as follows:

$$fx = \begin{cases} 1, & \text{if } x = p^2 \text{ for some } p \in \mathbb{N}, \\ x^2, & \text{otherwise}, \end{cases}$$

then f is T-Banach contraction in dislocated rectangular b-metric space $(\mathbb{N}, d)$ and f has unique fixed point $x = 1 \in \mathbb{N}$.

Theorem 2.3. *Let (X, d) be a complete dislocated rectangular b-metric space with coefficient $k \geq 1$. Let $f, T : X \to X$ be self-mappings such that T is continuous,one-one and f is continuous such that*

$$d(Tfx, Tfy) \leq \alpha[d(Tx, Tfx) + d(Ty, Tfy)], \forall x, y \in X, \tag{2.5}$$

with $\alpha \in [0, 1/2k)$, if T is sub-sequentially convergent then f has unique fixed point in X.

Proof. Let x_0 be any arbitrary point in X. Define $\{x_n\}$ by,

$$x_1 = fx_0, x_2 = fx_1, ..., x_{n+1} = fx_n = f^n x_0, ..., n = 0, 1, 2, 3, ...$$

Since f satisfies (2.5) we have,

$$d(Tfx_0, Tf^2 x_0) \leq \alpha[d(Tx_0, Tfx_0) + d(Tfx_0, Tf^2 x_0)]$$

$$\leq \frac{\alpha}{1 - \alpha} d(Tx_0, Tfx_0).$$

Let $h = \frac{\alpha}{1-\alpha} < 1$, we get, $d(Tfx_0, Tf^2x_0) \leq hd(Tx_0, Tfx_0)$. Now,

$$d(Tf^2x_0, Tf^3x_0) \leq \alpha[d(Tfx_0, Tf^2x_0) + d(Tf^2x_0, Tf^3x_0)]$$
$$\leq \frac{\alpha}{1-\alpha}d(Tfx_0, Tf^2x_0)$$
$$\leq hd(Tfx_0, Tf^2x_0)$$
$$\leq h^2d(Tx_0, Tfx_0).$$

In general, for any $n \in N$, we get,

$$d(Tf^nx_0, Tf^{n+1}x_0) \leq h^nd(Tx_0, Tfx_0). \tag{2.6}$$

We also assume that $x_0 \neq x_n$ for any $2 \leq n \in \mathbb{N}$. If not, then for some $n \geq 2$, using (2.5), we have

$$d(Tx_0, Tfx_0) = d(Tx_n, Tfx_n)$$
$$d(Tx_0, Tx_1) = d(Tx_n, Tx_{n+1}).$$

It implies that

$$d(Tx_0, Tx_1) \leq h^nd(Tx_0, Tx_1),$$

which is a contradiction unless $d(Tx_0, Tx_1) = 0$. Thus $Tx_0 = Tx_1$ and since T is one-one $x_0 = x_1$ in turn x_0 is a fixed point of f. So, we assume that $x_n \neq x_m$ for all $n \neq m \in \mathbb{N}$. In view of (2.5), for any $n \in \mathbb{N}$, we can write

$$d(Tfx_{n-1}, Tfx_{n+1}) = d(Tf^{n-1}x_0, Tf^{n+1}x_0) \leq hd(Tf^{n-2}x_0, Tf^nx_0) = hd(Tfx_{n-2}, Tfx_n).$$

Applying (2.5) repeatedly, we get

$$d(Tfx_{n-1}, Tfx_{n+1}) = d(Tf^{n-1}x_0, Tf^{n+1}x_0) \leq h^{n-1}d(Tx_0, Tf^2x_0). \tag{2.7}$$

Now to prove that $\{Tf^nx_0\}$ is Cauchy sequence in X, We prove $\lim_{n\to\infty} d(Tx_n, Tx_{n+m})$ exists and is finite. Here we consider two cases.

Case (i): Suppose m is even i.e. $m = 2i$ for some $i \in \mathbb{N}$ and n may be even or odd. Using inequalities (2.6),(2.7) and rectangular inequality, we get

$$d(Tf^nx_0, Tf^{n+m}x_0) = d(Tx_n, Tx_{n+m})$$
$$\leq k[d(Tf^nx_0, Tf^{n+1}x_0) + d(Tf^{n+1}x_0, Tf^{n+2}x_0) + d(Tf^{n+2}x_0, Tf^{n+2i}x_0)]$$
$$\leq k[d(Tf^nx_0, Tf^{n+1}x_0) + d(Tf^{n+1}x_0, Tf^{n+2}x_0)]$$
$$+ k^2[d(Tf^{n+2}x_0, Tf^{n+3}x_0) + d(Tf^{n+3}x_0, Tf^{n+4}x_0) + d(Tf^{n+4}x_0, Tf^{n+2i}x_0)]$$
$$\leq k[d(Tf^nx_0, Tf^{n+1}x_0) + d(Tf^{n+1}x_0, Tf^{n+2}x_0)]$$
$$+ k^2[d(Tf^{n+2}x_0, Tf^{n+3}x_0) + d(Tf^{n+3}x_0, Tf^{n+4}x_0)]$$
$$+ k^3[d(Tf^{n+4}x_0, Tf^{n+5}x_0) + d(Tf^{n+5}x_0, Tf^{n+6}x_0)+] + \cdots$$
$$+ k^{i-1}[d(Tf^{n-4+2i}x_0, Tf^{n-3+2i}x_0) + d(Tf^{n-3+2i}x_0, Tf^{n-2+2i}x_0)]$$
$$+ k^{i-1}[d(Tf^{n-2+2i}x_0, Tf^{n+2i}x_0)]$$

Int J Sci Res Sci & Technol. September-October -2024, 11 (19) : 77-92

9

$$\leq k[h^n d(Tx_0, Tfx_0) + h^{n+1} d(Tx_0, Tfx_0)]$$

$$+ k^2[h^{n+2} d(Tx_0, Tfx_0) + h^{n+3} d(Tx_0, Tfx_0)]$$

$$+ k^3[h^{n+4} d(Tx_0, Tfx_0) + h^{n+5} d(Tx_0, Tfx_0)] + \cdots$$

$$+ k^{i-1}[h^{n-4+2i} d(Tx_0, Tfx_0) + h^{n-3+2i} d(Tx_0, Tfx_0)]$$

$$+ k^{i-1} h^{n-2+2i} d(Tx_0, Tf^2 x_0)$$

$$\leq k h^n [1 + k h^2 + k^2 h^4 + \cdots] d(Tx_0, Tfx_0) + k h^{n+1} [1 + k h^2 + k^2 h^4 + \cdots] d(x_0, x_1)$$

$$+ k^{i-1} h^{n-2+2i} d(Tx_0, Tf^2 x_0)$$

$$\leq \left[\frac{(1+h)}{1-kh^2}\right] k h^n d(Tx_0, Tfx_0) + k^{i-1} h^{n-2+2i} d(Tx_0, Tf^2 x_0)$$

$$\leq \left[\frac{(1+h)}{1-kh^2}\right] k h^n d(Tx_0, Tfx_0) + h^{n-2} d(Tx_0, Tf^2 x_0).$$

Letting $n \to \infty$ in last inequality above, we get

$$\lim_{n \to \infty} d(Tx_n, Tx_{n+m}) = 0,$$

for all even $m \in \mathbb{N}$.

Case (ii): Suppose m is odd i.e. $m = 2i - 1$ for some $i \in \mathbb{N}$ and n may be even or odd. Using inequalities (2.6) and rectangular inequality, we get

$$d(Tf^n x_0, Tf^{n+m} x_0) = d(Tx_n, Tx_{n+m})$$

$$\leq k[d(Tf^n x_0, Tf^{n+1} x_0) + d(Tf^{n+1} x_0, Tf^{n+2} x_0) + d(Tf^{n+2} x_0, Tf^{n+2i-1} x_0)]$$

$$\leq k[d(Tf^n x_0, Tf^{n+1} x_0) + d(Tf^{n+1} x_0, Tf^{n+2} x_0)]$$

$$+ k^2[d(Tf^{n+2} x_0, Tf^{n+3} x_0) + d(Tf^{n+3} x_0, Tf^{n+4} x_0) + d(Tf^{n+4} x_0, Tf^{n+2i-1} x_0)]$$

$$\leq k[d(Tf^n x_0, Tf^{n+1} x_0) + d(Tf^{n+1} x_0, Tf^{n+2} x_0)]$$

$$+ k^2[d(Tf^{n+2} x_0, Tf^{n+3} x_0) + d(Tf^{n+3} x_0, Tf^{n+4} x_0)]$$

$$+ k^3[d(Tf^{n+4} x_0, Tf^{n+5} x_0) + d(Tf^{n+5} x_0, Tf^{n+6} x_0)] + \cdots$$

$$+ k^i[d(Tf^{n+2i-2} x_0, Tf^{n+2i-1} x_0)]$$

$$\leq k[h^n d(Tx_0, Tfx_0) + h^{n+1} d(Tx_0, Tfx_0)]$$

$$+ k^2[h^{n+2} d(Tx_0, Tfx_0) + h^{n+3} d(Tx_0, Tfx_0)]$$

$$+ k^3[h^{n+4} d(Tx_0, Tfx_0) + h^{n+5} d(Tx_0, Tfx_0)] + \cdots$$

$$+ k^i h^{n+2i-2} d(Tx_0, Tfx_0)$$

$$\leq k h^n [1 + k h^2 + k^2 h^4 + \cdots] d(Tx_0, Tfx_0)$$

$$+ k h^{n+1} [1 + k h^2 + k^2 h^4 + \cdots] d(Tx_0, Tfx_0)$$

$$\leq \left[\frac{(1+h)}{1-kh^2}\right] k h^n d(Tx_0, Tfx_0).$$

Letting $n \to \infty$ in the last inequality above, we see that the limit on the right hand side exists and is finite. Therefore, $\lim_{n \to \infty} d(Tx_n, Tx_{n+m})$ exists and is finite for all odd $m \in \mathbb{N}$. Thus

10   P.G. GOLHARE

from the case(i) and case(ii), it follows that $\lim_{n\to\infty} d(Tx_n, Tx_{n+m})$ exists and for all $n, m \in \mathbb{N}$

$$\lim_{n\to\infty} d(Tx_n, Tx_{n+m}) = 0. \tag{2.8}$$

Therefore $\{Tf^n x_0\}$ is Cauchy sequence in X. Since (X, d) is complete there exists $u \in X$ such that,

$$\lim_{n\to\infty} d(Tf^n x_0, u) = 0.$$

Since T is sub-sequentially convergent, $\{f^n x_0\}$ has a convergent subsequence, so there exists $v \in X$, such that

$$f^{n_i} x_0 \to v \text{ as } i \to \infty.$$

Since T and f are continuous, $Tf^{n_i} x_0 \to Tv$ as $i \to \infty$ and $f^{n_i+1} x_0 \to fv$ as $i \to \infty$. This implies that $Tf^{n_i+1} x_0 \to Tfv$ as $i \to \infty$. By uniqueness of limit in metric space (X, d), we get

$$Tv = Tfv.$$

Since T is one-one $fv = v$. Thus $v \in X$ is a fixed point of f. To prove that this fixed point of f is unique, we assume that $\omega \in X$ is another fixed point of f i.e. $f\omega = \omega$. Consider,

$$d(Tfu, Tf\omega) \leq \alpha[d(Tu, Tfu) + d(T\omega, Tf\omega)$$

$$\text{i.e. } d(Tu, T\omega) \leq [d(Tu, Tu) + d(T\omega, T\omega)].$$

We get, $d(Tu, T\omega) = 0$. Thus,

$$d(Tu, T\omega) = 0 = d(T\omega, Tu).$$

Therefore, $Tu = T\omega$. But since T is one-one $u = \omega$. Thus uniqueness of fixed point of f is proved and hence the theorem. $\square$

Theorem 2.4. *Let (X, d) be a complete dislocated rectangular b-metric space with coefficient $k \geq 1$. Let $f : X \to X$ be a mapping satisfying*

$$d(fx, fy) \leq \alpha d(x, y) - \phi(d(x, y)), \tag{2.9}$$

for all $x, y \in X$, where $0 \leq \alpha < \frac{1}{k}$ and $\phi : [0, \infty) \to [0, \infty)$ is continuous, nondecreasing mapping with $\phi(\alpha) = 0$ if and only if $\alpha = 0$. Then f has a unique fixed point in X.

Proof. We choose any arbitrary point $x_0 \in X$. Define a sequence $\{x_n\}$ in X such that $x_n = fx_{n-1}$ for all $n \in \mathbb{N}$. If for some $n \in \mathbb{N}$, $x_{n-1} = x_n$, then x_{n-1} becomes fixed point of f. Therefore, we assume that $x_{n-1} \neq x_n$ for all $n \in \mathbb{N}$. From inequality (2.9), we have

$$d(x_n, x_{n+1}) = d(fx_{n-1}, fx_n) \leq \alpha d(x_{n-1}, x_n) - \phi(d(x_{n-1}, x_n)) \leq \alpha d(x_{n-1}, x_n).$$

Applying inequality (2.9) repeatedly, we get,

$$d(x_n, x_{n+1}) \leq \alpha d(x_{n-1}, x_n) \leq \cdots \leq \alpha^n d(x_0, x_1). \tag{2.10}$$

We also assume that $x_0 \neq x_n$ for any $2 \leq n \in \mathbb{N}$. If not, then for some $n \geq 2$ in view of (2.10), we have $d(x_0, fx_0) = d(x_n, fx_n)$ that is $d(x_0, x_1) = d(x_n, x_{n+1})$ and

$$d(x_0, x_1) \leq \alpha^n d(x_0, x_1),$$

Int J Sci Res Sci & Technol. September-October -2024, 11 (19) : 77-92

11

which is a contradiction unless $d(x_0, x_1) = 0$ i.e. $x_0 = x_1$. Thus x_0 turns out to be a fixed point of f. Hence we assume that $x_n \neq x_m$ for all $n \neq m \in \mathbb{N}$. Now, in view of (2.9), for any $n \in \mathbb{N}$,

$$d(x_{n-1}, x_{n+1}) = d(fx_{n-2}, fx_n) \leq \alpha d(x_{n-2}, x_n) - \phi(d(x_{n-2}, x_n)) \leq \alpha d(x_{n-2}, x_n). \qquad (2.11)$$

Applying (2.11) repeatedly, we get

$$d(x_{n-1}, x_{n+1}) \leq \alpha^{n-1} d(x_0, x_2). \qquad (2.12)$$

In order to show, $\{x_n\}$ is a Cauchy sequence in X, it is sufficient to show, $\lim_{n \to \infty} d(x_n, x_{n+m}) = 0$ for all $n, m \in \mathbb{N}$. So, we consider the following cases:

Case (i): Let us assume that m is even i.e. $m = 2i$ for some $i \in \mathbb{N}$ and n may be even or odd. Using inequalities (2.10), (2.12) and rectangular inequality, we get

$$
\begin{aligned}
d(x_n, x_{n+2i}) &\leq k[d(x_n, x_{n+1}) + d(x_{n+1}, x_{n+2}) + d(x_{n+2}, x_{n+2i})] \\
&\leq k[d(x_n, x_{n+1}) + d(x_{n+1}, x_{n+2})] + k^2[d(x_{n+2}, x_{n+3}) + d(x_{n+3}, x_{n+4}) + d(x_{n+4}, x_{n+2i})] \\
&\leq k[d(x_n, x_{n+1}) + d(x_{n+1}, x_{n+2})] + k^2[d(x_{n+2}, x_{n+3}) + d(x_{n+3}, x_{n+4})] \\
&\quad + k^3[d(x_{n+4}, x_{n+5}) + d(x_{n+5}, x_{n+6})+] + \cdots \\
&\quad + k^{i-1}[d(x_{n+2i-4}, x_{n+2i-3}) + d(x_{n+2i-3}, x_{n+2i-2})] + k^{i-1}[d(x_{n+2i-2}, x_{n+2i})] \\
&\leq k[\alpha^n d(x_0, x_1) + \alpha^{n+1} d(x_0, x_1)] + k^2[\alpha^{n+2} d(x_0, x_1) + \alpha^{n+3} d(x_0, x_1)] \\
&\quad + k^3[\alpha^{n+4} d(x_0, x_1) + \alpha^{n+5} d(x_0, x_1)] + \cdots + k^{i-1}[\alpha^{n+2i-4} d(x_0, x_1) + \alpha^{n+2i-3} d(x_0, x_1)] \\
&\quad + k^{i-1} \alpha^{n+2i-2} \beta d(x_0, x_2) \\
&\leq k\alpha^n[1 + k\alpha^2 + k^2\alpha^4 + \cdots] d(x_0, x_1) + k\alpha^{n+1}[1 + k\alpha^2 + k^2\alpha^4 + \cdots] d(x_0, x_1) \\
&\quad + k^{i-1} \alpha^{n-3+2i} d(x_0, x_2) \\
&\leq \left[\frac{(1+\alpha)}{1 - k\alpha^2}\right] k\alpha^{n-1} d(x_0, x_1) + k^{i-1} \alpha^{n-3+2i} \beta d(x_0, x_2) \\
&\leq \left[\frac{(1+\alpha)}{1 - k\alpha^2}\right] k\alpha^{n-1} d(x_0, x_1) + \alpha^{n-3} \beta d(x_0, x_2).
\end{aligned}
$$

Letting $n \to \infty$ in last inequality above, we get $\lim_{n \to \infty} d(x_n, x_{n+m}) = 0$, for all even $m \in \mathbb{N}$.

Case (ii): Assume that m is odd i.e. $m = 2i - 1$ for some $i \in \mathbb{N}$ and n may be even or odd. Using inequalities (2.10), (2.12) and rectangular inequality, we get

$$
\begin{aligned}
d(x_n, x_{n+2i-1}) &\leq k[d(x_n, x_{n+1}) + d(x_{n+1}, x_{n+2}) + d(x_{n+2}, x_{n+2i-1})] \\
&\leq k[d(x_n, x_{n+1}) + d(x_{n+1}, x_{n+2})] + k^2[d(x_{n+2}, x_{n+3}) + d(x_{n+3}, x_{n+4}) + d(x_{n+4}, x_{n+2i-1})] \\
&\leq k[d(x_{n-1}, x_n) + d(x_n, x_{n+1})] + k^2[d(x_{n+2}, x_{n+3}) + d(x_{n+3}, x_{n+4})] \\
&\quad + k^3[d(x_{n+4}, x_{n+5}) + d(x_{n+5}, x_{n+6})] + \cdots \\
&\quad + k^i[d(x_{n+2i}, x_{n+2i-1})] \\
&\leq k[\alpha^n d(x_0, x_1) + \alpha^{n+1} d(x_0, x_1)] + k^2[\alpha^{n+2} d(x_0, x_1) + \alpha^{n+3} d(x_0, x_1)] \\
&\quad + k^3[\alpha^{n+4} d(x_0, x_1) + \alpha^{n+5} d(x_0, x_1)] + \cdots + k^i \alpha^{n+2i} d(x_0, x_1) \\
&\leq k\alpha^n[1 + k\alpha^2 + k^2\alpha^4 + \cdots] d(x_0, x_1) + k\alpha^{n+1}[1 + k\alpha^2 + k^2\alpha^4 + \cdots] d(x_0, x_1)
\end{aligned}
$$

$$\leq \left[\frac{(1+\alpha)}{1-k\alpha^2}\right]k\alpha^{n-1}d(x_0, x_1).$$

Letting $n \to \infty$ in last inequality above, we get $\lim_{n\to\infty} d(x_n, x_{n+m}) = 0$, for all odd $m \in \mathbb{N}$. Taking account the Case (i) and Case (ii), it follows that, for all $m, n \in \mathbb{N}$,

$$\lim_{n\to\infty} d(x_n, x_{n+m}) = 0. \tag{2.13}$$

Hence $\{x_n\}$ is a Cauchy sequence in X. Since (X, d) is a complete dislocated rectangular b-metric space, there exists some $u \in X$ such that $x_n \to u$.

Now we show that u is fixed point of f. For any given $n \in \mathbb{N}$, we can write

$$\begin{aligned} d(u, fu) &\leq k[d(u, x_n) + d(x_n, x_{n+1}) + d(x_{n+1}, fu)] \\ &= k[d(u, x_n) + d(x_n, x_{n+1}) + d(fx_n, fu)] \\ &\leq k\Big\{d(u, x_n) + d(x_n, x_{n+1}) + \alpha d(x_n, u) - \phi(d(x_n, u))\Big\}. \end{aligned}$$

Letting $n \to \infty$, using fact that $x_n \to u$ and (2.10), we get, $d(u, fu) = 0$. It gives that $fu = u$ i.e. u is fixed point of f in X.

Note that,

$$d(u, u) = d(fu, fu) \leq \alpha d(u, u) - \phi(d(u, u)) \leq \alpha d(u, u) < d(u, u), \tag{2.14}$$

which is a contradiction unless $d(u, u) = 0$. Thus in general, if v is a fixed point of f, then $d(v, v) = 0$. Now, we will prove, u is the unique fixed point of f in X. Suppose u' is another fixed point of f in X. In view of (2.9), we have

$$d(u, u') = d(fu, fu') \leq \alpha d(u, u') - \phi(d(u, u')) \leq \alpha d(u, u') < d(u, u').$$

It is a contradiction unless $d(u, u') = 0$ i.e. $u = u'$. Hence u is a unique fixed point of f in X. $\qquad\square$

Theorem 2.5. *Let (X, d) be a complete dislocated rectangular b-metric space with coefficient $k \geq 1$. Let $f : X \to X$ be a mapping satisfying*

$$d(fx, fy) \leq \alpha \max\{d(x, fx), d(y, fy)\}, \text{for all } x, y \in X, \text{where } 0 \leq \alpha < \frac{1}{k}. \tag{2.15}$$

Then f has unique fixed point in X.

Proof. We choose any arbitrary point $x_0 \in X$. Now define sequence $\{x_n\}$ in X such that $x_n = fx_{n-1}$ for all $n \in \mathbb{N}$. If for some $n \in \mathbb{N}$, $x_{n-1} = x_n$, then x_{n-1} becomes fixed point of f and we have nothing to prove. Therefore, we assume that $x_{n-1} \neq x_n$ for all $n \in \mathbb{N}$. From inequality (2.15), we have

$$\begin{aligned} d(x_1, x_2) &= d(fx_0, fx_1) \\ &\leq \alpha \max\{d(x_0, fx_0), d(x_1, fx_1)\} \\ &= \alpha \max\{d(x_0, x_1), d(x_1, x_2)\}. \end{aligned}$$

Then

$$d(x_1, x_2) \leq \alpha d(x_0, x_1) \tag{2.16}$$

Now,

$$d(x_2, x_3) = d(fx_1, fx_2)$$
$$\leq \alpha \max\{d(x_1, fx_1), d(x_2, fx_2)\}$$
$$= \alpha \max\{d(x_1, x_2), d(x_2, x_3)\}$$
$$\leq \alpha^2 d(x_0, x_1). \tag{2.17}$$

Applying above inequality (2.17) repeatedly, we get,

$$d(x_n, x_{n+1}) \leq \alpha^n d(x_0, x_1). \tag{2.18}$$

We also assume that $x_0 \neq x_n$ for any $2 \leq n \in \mathbb{N}$. If not, then for some $n \geq 2$ in view of (2.18), we have

$$d(x_0, fx_0) = d(x_n, fx_n)$$
$$d(x_0, x_1) = d(x_n, x_{n+1})$$
$$d(x_0, x_1) \leq \alpha^n d(x_0, x_1).$$

If $d(x_0, x_1) = d(x_0, x_1)$, then we get $d(x_0, x_1) \leq \alpha^n d(x_0, x_1)$, which is a contradiction unless $d(x_0, x_1) = 0$. And hence $d(x_1, x_0) = 0$. This yields that $x_0 = x_1$. And thus x_0 turns out to be a fixed point of f. Hence we assume that $x_n \neq x_m$, for all $n \neq m \in \mathbb{N}$.

We claim that $d(x_n, x_{n+2}) \leq \alpha^n d(x_0, x_1)$ for all $n \in \mathbb{N}$. We proceed by induction. For $n = 1$,

$$d(x_1, x_3) = d(fx_0, fx_2)$$
$$\leq \alpha \max\{d(x_0, fx_0), d(x_2, fx_2)\}$$
$$= \alpha \max\{d(x_0, x_1), d(x_2, x_3)\}$$
$$\leq \alpha \max\{d(x_0, x_1), \alpha^2 d(x_0, x_1)\}$$
$$= \alpha d(x_0, x_1).$$

Assume that $d(x_{n-1}, x_{n+1}) \leq \alpha^{n-1} d(x_0, x_1)$. Now consider

$$d(x_n, x_{n+2}) = d(fx_{n-1}, fx_{n+1})$$
$$\leq \alpha \max\{d(x_{n-1}, fx_{n-1}), d(x_{n+1}, fx_{n+1})\}$$
$$= \alpha \max\{d(x_{n-1}, x_n), d(x_{n+1}, x_{n+2})\}$$
$$\leq \alpha \max\{\alpha^{n-1} d(x_0, x_1), \alpha^{n+1} d(x_0, x_1)\}$$
$$\leq \alpha \alpha^{n-1} d(x_0, x_1)$$
$$= \alpha^n d(x_0, x_1).$$

Thus for all $n \in \mathbb{N}$, we have

$$d(x_n, x_{n+2}) \leq \alpha^n d(x_0, x_1). \tag{2.19}$$

Now, we will prove, $\{x_n\}$ is a Cauchy sequence in X, we prove that $\lim_{n\to\infty} d(x_n, x_{n+m}) = 0$, for all $n, m \in \mathbb{N}$. For this, consider the following cases:

14   P.G. GOLHARE

Case (i): Suppose m is even i.e. $m = 2i$ for some $i \in \mathbb{N}$ and n may be even or odd. Using inequalities (2.18), (2.19) and rectangular inequality, we get

$$
\begin{aligned}
d(x_n, x_{n+2i}) &\leq k[d(x_n, x_{n+1}) + d(x_{n+1}, x_{n+2}) + d(x_{n+2}, x_{n+2i})] \\
&\leq k[d(x_n, x_{n+1}) + d(x_{n+1}, x_{n+2})] + k^2[d(x_{n+2}, x_{n+3}) + d(x_{n+3}, x_{n+4}) + d(x_{n+4}, x_{n+2i})] \\
&\leq k[d(x_n, x_{n+1}) + d(x_{n+1}, x_{n+2})] + k^2[d(x_{n+2}, x_{n+3}) + d(x_{n+3}, x_{n+4})] \\
&\quad + k^3[d(x_{n+4}, x_{n+5}) + d(x_{n+5}, x_{n+6})+] + \cdots \\
&\quad + k^{i-1}[d(x_{n+2i-4}, x_{n+2i-3}) + d(x_{n+2i-3}, x_{n+2i-2})] + k^{i-1}[d(x_{n+2i-2}, x_{n+2i})] \\
&\leq k[\alpha^n d(x_0, x_1) + \alpha^{n+1} d(x_0, x_1)] + k^2[\alpha^{n+2} d(x_0, x_1) + \alpha^{n+3} d(x_0, x_1)] \\
&\quad + k^3[\alpha^{n+4} d(x_0, x_1) + \alpha^{n+5} d(x_0, x_1)] + \cdots + k^{i-1}[\alpha^{n+2i-4} d(x_0, x_1) + \alpha^{n+2i-3} d(x_0, x_1)] \\
&\quad + k^{i-1} \alpha^{n+2i-2} d(x_0, x_1) \\
&\leq k\alpha^n[1 + k\alpha^2 + k^2\alpha^4 + \cdots] d(x_0, x_1) + k\alpha^{n+1}[1 + k\alpha^2 + k^2\alpha^4 + \cdots] d(x_0, x_1) \\
&\quad + k^{i-1} \alpha^{n-3+2i} d(x_0, x_1) \\
&\leq \left[\frac{(1+\alpha)}{1-k\alpha^2}\right] k\alpha^{n-1} d(x_0, x_1) + k^{i-1} \alpha^{n-3+2i} d(x_0, x_1) \\
&\leq \left[\frac{(1+\alpha)}{1-k\alpha^2}\right] k\alpha^{n-1} d(x_0, x_1) + \alpha^{n-3} d(x_0, x_1).
\end{aligned}
$$

Letting $n \to \infty$ in last inequality above, we get $\lim_{n\to\infty} d(x_n, x_{n+m}) = 0$, for all even $m \in \mathbb{N}$.

Case (ii): m is odd i.e. $m = 2i - 1$ for some $i \in \mathbb{N}$ and n may be even or odd. Using inequalities (2.18), (2.19) and rectangular inequality, we get

$$
\begin{aligned}
d(x_n, x_{n+2i-1}) &\leq k[d(x_n, x_{n+1}) + d(x_{n+1}, x_{n+2}) + d(x_{n+2}, x_{n+2i-1})] \\
&\leq k[d(x_n, x_{n+1}) + d(x_{n+1}, x_{n+2})] + k^2[d(x_{n+2}, x_{n+3}) + d(x_{n+3}, x_{n+4}) + d(x_{n+4}, x_{n+2i-1})] \\
&\leq k[d(x_{n-1}, x_n) + d(x_n, x_{n+1})] + k^2[d(x_{n+2}, x_{n+3}) + d(x_{n+3}, x_{n+4})] \\
&\quad + k^3[d(x_{n+4}, x_{n+5}) + d(x_{n+5}, x_{n+6})] + \cdots \\
&\quad + k^i[d(x_{n+2i}, x_{n+2i-1})] \\
&\leq k[\alpha^n d(x_0, x_1) + \alpha^{n+1} d(x_0, x_1)] + k^2[\alpha^{n+2} d(x_0, x_1) + \alpha^{n+3} d(x_0, x_1)] \\
&\quad + k^3[\alpha^{n+4} d(x_0, x_1) + \alpha^{n+5} d(x_0, x_1)] + \cdots + k^i \alpha^{n+2i} d(x_0, x_1) \\
&\leq k\alpha^n[1 + k\alpha^2 + k^2\alpha^4 + \cdots] d(x_0, x_1) + k\alpha^{n+1}[1 + k\alpha^2 + k^2\alpha^4 + \cdots] d(x_0, x_1) \\
&\leq \left[\frac{(1+\alpha)}{1-k\alpha^2}\right] k\alpha^{n-1} d(x_0, x_1).
\end{aligned}
$$

Letting $n \to \infty$ in last inequality above, we get $\lim_{n\to\infty} d(x_n, x_{n+m}) = 0$, for all odd $m \in \mathbb{N}$. Thus from case (i) and case (ii), it follows that, for all $m, n \in \mathbb{N}$,

$$
\lim_{n\to\infty} d(x_n, x_{n+m}) = 0. \tag{2.20}
$$

It shows that $\{x_n\}$ is a Cauchy sequence in X. Since (X, d) is a complete dislocated rectangular b-metric space, there exists some $u \in X$ such that $x_n \to u$. Now, we show that u is fixed

15

point of f. For any given $n \in \mathbb{N}$, we can write

$$
\begin{aligned}
d(u, fu) &\leq k[d(u, x_n) + d(x_n, x_{n+1}) + d(x_{n+1}, fu)] \\
&= k[d(u, x_n) + d(x_n, x_{n+1}) + d(fx_n, fu)] \\
&\leq k\left\{d(u, x_n) + d(x_n, x_{n+1}) + \alpha \max\{d(x_n, x_{n+1}), d(u, fu)\}\right\}.
\end{aligned}
$$

Letting $n \to \infty$, using fact that $x_n \to u$, and inequality (2.18), we get,

$$
d(u, fu) \leq k\alpha d(u, fu),
$$

which is a contradiction unless $d(u, fu) = 0$. It gives that $fu = u$. Hence u is a fixed point of f in X.

Note that,

$$
\begin{aligned}
d(u, u) = d(fu, fu) &\leq \alpha \max\{d(u, fu), d(u, fu)\} \\
&= \alpha d(u, u) < d(u, u),
\end{aligned}
$$

which is a contradiction unless $d(u, u) = 0$. Thus in general if v is fixed point of f then, $d(v, v) = 0$. Now, we prove that u is unique fixed point of f in X. Suppose, u' is another fixed point of f in X. In view of (2.15), we have

$$
\begin{aligned}
d(u, u') = d(fu, fu') &\leq \alpha \max\{d(u, fu), d(u', fu')\} \\
&= \alpha \max\{d(u, u), d(u', u')\} \\
&\leq 0.
\end{aligned}
$$

It implies that $d(u, u') = 0$. Hence, $u = u'$. So u is a unique fixed point of f in X. $\square$

REFERENCES

[1] A. Branciari, A fixed point theorem of Banach-Caccippoli type on a class of generalised metric spaces, Publ. Math. Debrecen, 57,31-37(2000).

[2] I. Bakhtin, The contraction mapping principle in quasi-metric spaces, Functional analysis, vol. 30, 26-37 (1989).

[3] A. Beiranvand, S. Moradi†,M. Omid and H. Pazandeh,Two Fixed-Point Theorems For Special Mappings,2000 Mathematics Subject Classification: Primary 46J10, 46J15, 47H10.

[4] C. Chen, J. Dong and C. Zhu, Some fixed point theorems in b-metric-like spaces,Fixed Point Theory and Applications, DOI 10.1186/s13663-015-0369-3 (2015).

[5] C. Klin-eam and C. Suanoom, Dislocated quasi-b-metric spaces and fixed point theorems for cyclic contractions, Fixed Point Theory and Applications, DOI 10.1186/s13663-015-0325-2(2015).

[6] C. Suanoom, C. Klin-eam and S. Suantai, Dislocated quasi-b-metric spaces and fixed point theorems for cyclic weakly contractions, J. Nonlinear Sci. Appl. 9, 2779-2788(2016).

[7] J. Morales and E. Rojas, T-Zamfirescu and T-weak contraction mappings on cone metric spaces,1991 mathematics subject classification. 47H10, 46J10.

[8] J. Roshan, V. Parvaneh, Z. Kadelburg, N. Hussain, New fixed point results in b-rectangular metric spaces, Nonlinear Analysis: Modelling and Control, Vol. 21, No. 5, 614–634(2016).

[9] M. Abbas and G. Jungck, Common fixed point results for noncommuting mappings without continuity in cone metric spaces, J. Math. Anal. Appl. 341, 416–420(2008).

[10] M. Alghamdi, N. Hussain and P. Salimi, Fixed point and coupled fixed point theorems on b-metric-like spaces, J. Inequal. Appl., 402 (2013).

[11] M. Rahman and M. Sarwar, Dislocated quasi b-metric space and fixed point theorems, Electronic Journal of Mathematical Analysis and Applications Vol. 4(2), 16-24(2016).

[12] M. Shah and N. Hussain, Nonlinear contractions in partially ordered quasi b-metric spaces. Commun. Korean Math. Soc.27(1), 117-128 (2012).

[13] P. Golhare and C. Aage, Dislocated quasi rectangular b-metric spaces and related fixed point theorems, Electronic Journal of Mathematical Analysis and Applications 7.2,309-331(2019).

[14] P. Hitzler and A. Seda, Dislocated topologies, Journal of Electrical Engineering, 3-7(2000).

[15] R. George, S. Radenovic, K. P. Reshma, S. Shukla, Rectangular b-metric space and contraction principles, J. Non-linear Sci. Appl. 8, 1005-1013(2015).

[16] S. Banach, sur les opérations dans les ensembles abstraits et leur application aux équations intégrales, Fundam.Math. 3, 133-181 (1922).

[17] W. Wilson, On quasi-metric spaces, American Journal of Mathematics,Vol. 53, No. 3 , 675-684(Jul., 1931).

P.G. GOLHARE

DEPARTMENT OF MATHEMATICS, SANT DNYANESHWAR MAHAVIDYALAYA, SOEGAON, AURANGABAD, INDIA

Email address: golhare@gmail.com

Applications of Nano particles As Nano medicines

Dr. Sanjay K. Tupe

Kalikadevi Arts, Commerce & Science College, Shirur (K), Dist. Beed. Pin 413249

Abstract :

Recent advancements in technology have demonstrated that progress in nanotechnology and nanoscience has been a pivotal element. Nanotechnology is an interdisciplinary field that encompasses physics, chemistry, materials science, and various engineering disciplines. Its applications are permeating nearly every aspect of science and technology. Recognizing the advantages of nanomedicine, researchers are actively exploring nanotechnology's potential in diagnosing, treating, and preventing diseases.

Keywords: nanotechnology, nanobiotechnology, nanomedicine, medical applications, diagnosis, Artificial intelligence, drug-delivery,

I. INTRODUCTION

The term "nano" originates from the Greek word "nanos" or the Latin "nanus," both meaning "dwarf." It represents an interdisciplinary fusion of physics, chemistry, materials science, solid-state physics, and the life sciences. Therefore, a deep understanding in just one area is not adequate; a comprehensive grasp of physics, chemistry, materials science, solid-state physics, and the biological sciences is essential for the development and application of nanomedicines. Nanotechnology's reach extends across virtually all scientific and technological fields. The distinction between nanoscience and nanotechnology lies in their focus: nanoscience concerns itself with understanding the organization and fundamental properties of atoms at the nanoscale, while nanotechnology applies this understanding to manipulate matter at the atomic scale, enabling the creation of new nanomaterials with unique properties. Nanotechnology is gaining prominence across various engineering disciplines, yet its presence in everyday life remains largely unnoticed by the general public. Despite its extensive application in fields such as medicine, engineering, environmental science, electronics, defence, and security, with its use continually expanding, there remains ample opportunity for the introduction of innovative developments. Even with significant advancements already made using this technology, the potential for further innovations persists.

II. NANOMATERIALS IN VARIOUS FIELDS FOR THE PROGRESS OF MANKIND:

Nanomaterials come in various shapes, such as nanorods, nanoparticles, and nanosheets, and are classified based on their dimensionality. Zero-dimensional nanomaterials include nanoparticles; one-dimensional materials are nanorods or nanotubes; two-dimensional materials typically consist of films and layers; while three-

dimensional or bulk nanomaterials encompass nanocomposites, core-shells, multi-nanolayers, and bundles of nanowires or nanotubes.

Nanotechnology is a field focused on manipulating objects on the nanometer scale. It is anticipated to evolve across different levels: materials, devices, and systems. Currently, the most progress has been made at the nanomaterials level, in terms of both scientific understanding and commercial applications. Over the past two to three decades, nanoparticles have been extensively studied for their unique size-dependent physical and chemical properties, which change as the particle size changes, affecting the material's medicinal and physical attributes.

Cells, the basic building blocks of living organisms, are typically 10 μm in size, but their components are much smaller, often in the sub-micron range. Proteins, for instance, are around 5 nm in size, akin to the smallest man-made nanoparticles. This comparison highlights the potential of using nanoparticles as minimal probes to observe cellular functions with minimal disturbance. The drive to comprehend biological processes at the nanoscale is a key motivator for nanotechnology's development.

Among the numerous physical properties that change with size and are of interest for practical nanomaterial applications, optical and magnetic properties are particularly valuable for biological purposes. This review aims to first introduce the basics of nanoparticle sizes, then explore their application in biology and medicine, focusing on how the unique quantum phenomena at the nanoscale can be utilized in medicine, biomedical sciences, bioengineering, food technology, biochemistry, biophysics, and other biological and medical fields.

III.CHARACTERISTICS AND ADVANTAGES OF NANOMATERIALS:

Nanomaterials are categorized into organic and inorganic types. Organic nanomaterials encompass nanofibers, nanotubes, liposomes, and polymer nanoparticles, while inorganic nanomaterials consist of elemental substances, alloys, silica, and quantum dots.

Due to their exceptionally high specific surface area, nanomaterials are highly efficient in drug delivery and loading. Moreover, they exhibit excellent biocompatibility and biodegradability, with the ability to localize in human organs while minimizing side effects. Nanomaterials also offer controlled and slow drug release, which can decrease drug concentrations and reduce toxic effects. Unlike traditional medications, which may suffer from poor stability, easy deformation and inactivation, short biological half-lives, low bioavailability, and difficulties crossing physiological barriers, biological nanomaterials play an indispensable role in the biomedical field. This includes diagnosis, treatment, and the repair or replacement of damaged tissues. For instance, nanoparticles' small size allows them to be readily absorbed by cells; their large specific surface area and abundant functional groups or active sites enable the carrying of significant amounts of specific drugs; and their porous, hollow, or multilayer structures facilitate controlled drug release, thereby extending drugs' half-lives and duration of action in the body.

As research into nanomaterials advances, they have evolved from mere drug delivery systems to a novel class of materials that possess inherent biological effects and can actively participate in disease treatment. With ongoing innovations in nanomaterials, the physicochemical properties and structural features of nanodrugs are becoming more diverse, and multifunctional nanomaterials are emerging as highly promising in the realm of biomedicine.

IV. FUTURE DIRECTIONS:

Presently, the predominant use of commercial nanoparticles in the medical field revolves around drug delivery. In biosciences, nanoparticles are supplanting organic dyes in applications requiring high photo-stability and multiplexing capabilities. There have been advancements in directing and remotely controlling the actions of nano-probes, such as guiding magnetic nanoparticles to tumours and subsequently triggering drug release or inducing localized tissue destruction through heating. The primary trajectory for further nanomaterial development is towards creating multifunctional and controllable entities, potentially through artificial intelligence or environmental responsiveness, effectively transforming them into nano-devices.

V. CONCLUSION

Indeed, it is imperative that nanotechnology evolves into a user-friendly tool. We must engineer nanotubes capable of precisely delivering essential drugs to affected cells within the body. Utilizing artificial intelligence, we can regulate the necessary drug dosage effectively. Moreover, it's crucial to discover additional nano compounds or particles with diverse disease-controlling properties. Concurrently, nanomaterials have the potential to enhance drug efficacy and minimize adverse reactions by generating synergistic effects with medications.

VI. REFERENCES:

[1].   Feynman R: There's plenty of room at the bottom. Science. 1991, 254: 1300-1301.

[2].   Murray CB, Kagan CR, Bawendi MG: Synthesis and characterisation of monodisperse nanocrystals and close-packed nanocrystal assemblies. Annu Rev Mater Sci. 2000, 30: 545-610. 10.1146/annurev.matsci.30.1.545.

[3].   Mazzola L: Commercializing nanotechnology. Nature Biotechnology. 2003, 21: 1137-1143. 10.1038/nbt1003-1137.

[4].   Paull R, Wolfe J, Hebert P, Sinkula M: Investing in nanotechnology. Nature Biotechnology. 2003, 21: 1134-1147. 10.1038/nbt1003-1144.

[5].   Taton TA: Nanostructures as tailored biological probes. Trends Biotechnol. 2002, 20: 277-279. 10.1016/S0167-7799(02)01973-X.

[6].   Whitesides GM: The 'right' size in Nanobiotechnology. Nature Biotechnology. 2003, 21: 1161-1165. 10.1038/nbt872.

[7].   Parak WJ, Gerion D, Pellegrino T, Zanchet D, Micheel C, Williams CS, Boudreau R, Le Gros MA, Larabell CA, Alivisatos AP: Biological applications of colloidal nanocrystals. Nanotechnology. 2003, 14: R15-R27. 10.1088/0957-4484/14/7/201.

[8].   Pankhurst QA, Connolly J, Jones SK, Dobson J: Applications of magnetic nanoparticles in biomedicine. J Phys D: Appl Phys. 2003, 36: R167-R181. 10.1088/0022-3727/36/13/201.

[9].   Yan H, Park SH, Finkelstein G, Reif JH, LaBean TH: DNA-templated self-assembly of protein arrays and highly conductive nanowires. Science. 2003, 301: 1882-1884. 10.1126/science.1089389.

[10].   Keren K, Berman RS, Buchstab E, Sivan U, Braun E: DNA-templated carbon nanotube field-effect transistor. Science. 2003, 302: 1380-1382. 10.1126/science.1091022.

[11].   Badrunnjsa S. Meghani S S Review on Health Science Applications of Nanotechnology J. Coast. Life Med. 2023:

[12].   Bhushan B. Springer Handbook of Nanotechnology. Springer; Berlin / Heidelberg, Germany: 2017. Introduction to nanotechnology.

Quantitatively Physico-Chemical Analysis of Some Soil Samples of Sinnar Tahsil, District Nashik

Dr. Manisha D. Dhiware

Department of Physics, K. V. N. Naik Arts, Commerce & Science College, Nashik,Maharashtra, 422002

Abstract :

The naturally available macronutrients of soil show variation in dielectric properties. Inorganic matter in soil appreciably affects its dielectric properties. Bulk density of soil depends on its texture. From these estimated values of dielectric constant one can estimate emissivity and scattering coefficient that will provide the tools for designing the microwave remote sensing sensors. These results are helpful for agriculture scientists and also for the scientists working in the field of remote sensing.

Keyword: Dielectric constant, bulk density, particle density, porosity

I. INTRODUCTION

Soil is a complex mixture of countless organisms which are decaying remains of once living things, organic matter, water, air and minerals. [1] It works as a skin of earth because it forms at the surface of land. Soil is helpful in giving support to plants also necessary to the continuation of life on earth. Soil is defined as the disunite organic or mineral matter on the surface of the earth and shows effects of environmental and genetic factors of climate and macro and microorganisms dependent on some condition acting on parent material over a period of time. Different agricultural uses require different soil management practices [2].

Soil plays seven general roles

1. For growth of plants soil serves as a media

2. By emitting and absorbing different gases such as carbon dioxide, water vapour, methane and dust soil modifies the atmosphere.

3. For the animals that live in the soil such as groundhogs, mice and organisms such as bacteria and fungi, soil provides place which is primary cause for most of the living things on Earth. In terrestrial systems, soil hold, release, absorb, alter and purify the water.

5. Living things can use nutrients including carbon, soil process recycled them.

6. Soil preserve or destroy artifacts of human endeavours also for construction of foundations, roadbeds, dams, soil serves as a engineering media.

7. To clean water soil acts as a living filter before it moves into an aquifer.

Characterization of soil helps in determining soil potentials and identifying the constraints in crop production besides giving detailed information about different soil properties [3].

Soil Physical Properties

- ➢ Soil physics
- ➢ Soil texture
- ➢ Soil surface area
- ➢ Soil structure
- ➢ Volume and mass relationships
- ➢ Water content measurements
- ➢ Units

The variability of dielectric constant of dry soil with its physical constituents at microwave frequencies has studied by Calla O.P.N. et.al [4]. The physical capacities of a soil are influenced by the size, proportion, arrangement and composition of the soil particles [5]. Due to dependence of dielectric constant on the physical constituents and chemical composition of the soil, the study of its variability with physical constituents and chemical composition is required [6]. The dielectric constant of soil is a measure of the response of a soil to electromagnetic waves. This response is composed of two parts, real & imaginary, which determine wave velocity and energy losses respectively [7-10].

Soil Density

In case of soils, the soil mass is made up of small soil particles together with a certain amount of free or empty space unoccupied by the soil particles. This empty space is known as pore space. Hence two types of densities are commonly considered for soils.

Bulk Density

The bulk density of the soil is the (oven dry) weight of a given volume of soil divided by the volume. It is expressed in grams per cubic centimetre. The formula is usually written like this:

$$D_b = \frac{M_s}{V_t}$$

Where Db = bulk density

Ms = mass of solids

Vt = total volume

The bulk density of the soil gives the idea about the amount of pore space in the soil. The bulk density get affected the types of minerals present, the texture (clays are lighter than silts and sands) and the amount of organic matter (organic matter has a really low bulk density compared to mineral grains).Compacted soils have higher bulk densities than non-compacted soils.

Particle Density

Particle density of soil is the mass per unit volume of soil particles (soil solid phase) expressed in g/c.c. Most soils have particle density of about 2.6 g/cc. Presence of organic matter decrease the density and iron compounds increase the density.

Porosity

Using specific gravity bottle technique particle density can be measured. Bulk density can be measured by taking weight of dry soil and volume of the soil from desired location (Black et al., 1965a). The porosity and the size distribution of the pores (micropores and macropores) decide the movement of water and air through soil. If the bulk density of soil is high, the given soil sample is highly suitable for aquaculture.

$$Porosity = 1 - \frac{Bulk\ Density}{Particle\ Density}$$

Water-holding capacity

The water holding capacity of a soil is a very important characteristic in the areas of plant genetics, plant physiology, meteorology, animal sciences and soil science. If water holding capacity of soil is high that is soil holds ample amounts of water then possibility of losses in nutrients will be less. As sandy soil has limited water holding capacity it reaches to the saturation point quickly as compare to clay soil as it has high water holing capacity. When soil is saturated with water, all nutrients, pesticides and excess water present in the solution, will leached down down in soil profile. The soil texture and the soil organic matter content controls the water holding capacity of soil. The particle size distribution of a soil gives the idea about the soil texture. An example is a silt loam soil that has 30% sand, 60% silt and 10% clay sized particles. In this sample of soil the percentage of silt and clay is high.

Hence it has high water holding capacity. These small particles have greater surface area. This is the reason they have high water holding capacity. This large surface area allows to hold ample amount of water. Similarly, if the amount of organic matter is greater then also water holding capacity increases. Because organic matter has affinity towards the water.

Field capacity

The large pore spaces of the soil are filled with air and water and small pore spaces are filled with water, when water drainage has completely stopped. This is the stage when soil is said to be at field capacity. This stage is ideal for the growth of the crop. Field Capacity is related to soil texture by

$$Field\ Capacity = 25.1 - 0.21 \times Sand + 0.22 \times Clay$$

Wilting point

The water stored in the soil is utilised by the plant roots or it get evaporated from the topsoil in the atmosphere. If water supply to the soil has stopped, soil dries slowly. As the soil becomes dry means it becomes more tightly, it is difficult for the plant roots to extract water from the soil. One stage occur when need of plant roots for water is not completed by soil. Hence plants lose their quality of being fresh and it wilts. The colour of leaves become yellow.

At last plant dies. This stage of soil water content when the plant dies is called as permanent wilting point. At this stage also some amount of water present in the soil .But it is not possible for the plant roots to extract it. The Wilting Point (WP) and Transition Moisture (Wt) of the soils are calculated by using the Empirical Model by Wang, J.R., and Schmugge T. (1980) as follows:

$$W_P = 0.06774 - 0.00064 \times Sand\ (\%) + 0.00478 \times Clay\ (\%)$$
$$W_t = 0.49 \times W_p + .0165$$

II. EXPERIMENTAL METHOD

A. Soil Sampling

The purpose of this study is to determine the dielectric constant of dry soil samples and its variation with the physical properties of soil of Sinnar Tahsil. Before sampling 15 mm topsoil was removed. Soil samples were collected from different locations at the depth of 15cm in zigzag pattern across the required areas. Five pits were dug for each sample. A composite sample of about 2 Kg is taken through mixing of represented soil sample. These soils were first sieved by gyrator sieve shaker with approximately 2 mm spacing to remove the coarser particles. The sieved out fine particles are then oven dried to a temperature around 110oC in order to

completely remove any trace of moisture. Such dry sample is then called as oven dry or dry base sample when compared with wet samples.

B.   Measurement of Dielectric Constant of dry Soil Samples

The waveguide cell method is used to determine the dielectric properties of the dry soil samples. X-band microwave bench set-up for measurement of dielectric constant of soil samples is used. An X-band microwave set-up in the TE10 mode with Reflex Klystron

source operating at frequency 9 GHz is used for measuring dielectric constants. The solid dielectric cell with soil sample is connected to the opposite end of the source. The signal generated from the microwave source is allowed to incident on the soil sample. The sample reflects part of the incident signal from its front surface. The reflected wave

Combined with incident wave to give a standing wave pattern. These standing wave patterns are then used in determining the values of shift in minima resulted due to before

and after inserting the sample. Experiments were performed at room temperatures ranged between 25º -35º C.

III.RESULT AND DISCUSSION:
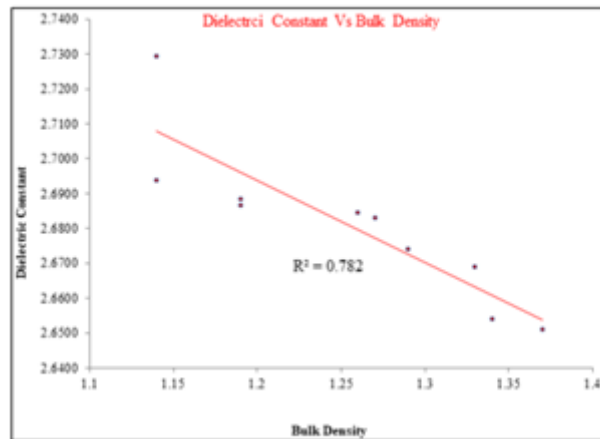
Fig.1 Dielectric constant vs Bulk Density

Dielectric constant was found to be dependent on bulk density of soil. It is observed that dielectric constant has negative correlation with bulk density.

Similar results were reported by Wagner et al. [11] in which dielectric constant was evaluated at different moisture conditions.
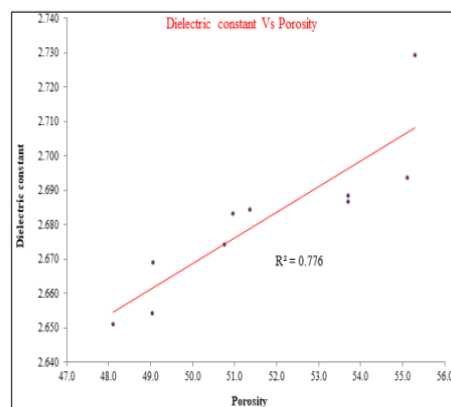
Fig.2 Dielectric constant vs Porosity

It is observed that dielectric constant has positive correlation with porosity.

IV. CONCLUSIONS

The dielectric constant varies with the status of nutrients available in soil. The ac electrical conductivity, relaxation time and tangent loss are directly proportional to dielectric loss. The results have importance not only for better understanding of soil physics but also microwave remote sensing application.

The naturally available macronutrients of soil show variation in dielectric properties.

Inorganic matter in soil appreciably affects its dielectric properties. Bulk density of soil

depends on its texture. From this information one can calculate wilting point of soil. From these estimated values of dielectric constant one can estimate emissivity and scattering coefficient that will provide the tools for designing the microwave remote sensing sensors. These results are helpful for agriculture scientists and also for the scientists working in the field of remote sensing.

V. REFERENCES

[1]. Shinde L V and G B Phalke Chemical composition of soil from Godavari basin of Beed (MS), India ,Bioscience Discovery, 5(1):15-18, Jan. 2014

[2]. Edward J. Plaster, Soil Science and Management,5th Edition © 2009, 2003, 1997,1991 Delmar, Cengage Learning

[3]. MA Aariff Khan and J Kamalakar*Physical, physico-chemical and chemical properties of soils of newly established Agro-biodiversity Park of Acharya NG Ranga Agricultural University, Hyderabad, Andhra Pradesh International Journal of Farm Sciences 2[2] :102-116, 2012

[4]. Calla O.P.N., Baruah A., Das B., Mishra K.P., Kalita M. and Haque S. S., Indian J. of Radio and Space Physics,33,(2004),125-129

[5]. Thakre. g. Dr.Choudhary M. D, Dr.Raut. R.D Physicochemical characterization of Red and Black soils of wardha region, International Journal of chemical and physical sciences,vol.1, Nov-Dec.2012.

[6]. P .R. Chaudhari, D.V. Ahire, Electrical and physical properties of Coimbatore soils at microwave frequency, International journal of Innovative research in Sciences, Engineering and Technology vol.3,Nov.2014,17500-17504

[7]. D. H. Gadani & A. D. Vyas, Indian Journal of Radio & Space Physics, Vol.37,June 2008, Measurement of complex dielectric constant of soils of Gujarat at x and c band microwave frequency, pp 221-229

[8]. H. C. Chaudhary , V. J. Shinde, Indian Journal of Radio & Space Physics, Vol.50, January 2012, Dielectric properties of soils at x band microwave frequency, , pp 64-66

[9]. Saeid Gharechelou, Ryutaro Tateishi,JosaphatTetuko Sri Sumantyo, Advances in remote sensing,2015,Vol.4 Inter relationship analysis of L band Backscattering intensity and soil dielectric constant for soil moisture retrieval using PALSAR data, pp 15-24

[10]. Freedman G, Microwave power, 1973, vol.7, the future of microwave heating equipment in the food industries. pp 161-166

[11]. Wagner L.E.,AmbeN.M.and Ding D.,Trans.Am.Soc.Agric.Eng.,Vol.37,1994, Estimating a Proctor density curve from intrinsic siol properties, pp 1121-1125

Synthesis and Structural Characterization ofCo₁₋ₓZnₓFe₂O₄ $(0.0 \leq x \leq 0.2)$ Nanoparticles

D. R. Sapate

Department of Physics, Sant Ramdas Arts, Commerce and Science College Ghansawangi, Jalna

Corresponding Author: diliprsapate@gmail.com

Abstract :

The samples of pure and zinc substituted cobalt ferrite with generic formula $Co_{1-x}Zn_xFe_2O_4$ $(0.0 \leq x \leq 0.2)$ was prepared by well known sol-gel auto combustion method. AR grade cobalt nitrate, ferric nitrate and zinc nitrates were used as a raw material. Citric acid was taken as a fuel/chelating agent. The metal nitrate to fuel ration was taken as 1:3 to obtain high quality, single phase homogenous powders. And the prepared powder was sintered at 500 ⏢C for 4 h and same were characterized by X-ray diffraction, A close analysis of the XRD pattern revealed the formation of single phase cubic spinel structure. The crystallite size obtained to be in the range 22 to 16 nm which proves the nanocrystalline nature of the prepared sample. Using the linear intercept method, the grain size and specific surface area were calculated. The grain size found to be in the range of 54 to 42 nm. By doping zinc ion in cobalt ferrite, it is found that structural properties were changed.

Key words: Co-Zn ferrite; Sol-gel auto combustion; grain size, XRD

I. INTRODUCTION

Ferrites are used in many applications because of their very good electrical and magnetic properties. The high electrical resistivity, low eddy current and dielectric losses, moderate saturation magnetization, high Curie temperature, high permeability etc. properties makes ferrite useful in several applications [1-4].These properties are structure sensitive and can be made by using suitable method of preparation, choosing appropriate dopant and desired temperature etc.

Ferrite is one of the good electro-ceramics in modern industries and its processing as well as application technology has been improved incessantly in the last two decades. Now ferrites are most essential material in electronic industries. Ferrites are widely used magnetic materials due to their high electrical resistivity, low eddy current and dielectric losses [5, 6].Ferrites are still of interest as promising materials for many applications. For these reasons engineers and scientists are keenly interested in determining their characterization. Since ferrites behave as low gap semiconductors and as insulators at low temperature, they have been used in number of technological applications [7, 8]. These applications include microwave devices, magnetic and magneto-optic recording, data storage etc. Ferrites are of great technical importance because they exhibit a spontaneous magnetic moment below a Curie temperature just as iron, cobalt or nickel, but they are poor electrical

conductor [9]. Ferrites are used in many electrical and electronic devices such as transformer, antenna rods, memory chips, magnetic sensors, drug delivery etc [10, 11].

II. EXPERIMENTAL

2.1 Synthesis

The samples of pure and zinc substituted cobalt ferrite with generic formula $Co_{1-x}Zn_xFe_2O_4$ ($0.0 \le x \le 0.2$) were prepared by well-known sol-gel auto combustion method. AR grade cobalt nitrate, ferric nitrate and zinc nitrates were used as a raw material. Citric acid was taken as a fuel/chelating agent. The metal nitrate to fuel ration was taken as 1:3 to obtain high quality, single phase homogenous powders. And the prepared powder was sintered at 500 ⬜C for 4 h for better crystallinity and same is used for further study.

2.2 Characterizations

The samples of $Co_{1-x}Zn_xFe_2O_4$ ($0.0 \le x \le 0.2$) were characterized by X-ray diffraction technique. The XRD pattern was recorded at room temperature in the 2θ range 20⬜ to 80⬜ with scanning rate of 2⬜ per minute using Cu-Kα radiation of wavelength 1.5406 Å.

III. RESULT AND DISCUSSIONS

X-ray Diffraction (XRD)

Figure 1 (a) represents the X-ray diffraction patterns recorded at room temperature of the series $Co_{1-x}Zn_xFe_2O_4$ ($0.0 \le x \le 0.2$).The XRD pattern shows clearly pure cubic spinel ferrite phase with the reflections belonging to (220), (311), (222), (400), (422), (511) and (440). No extra peak has been observed in the XRD pattern. All these reflections are sharp and intense. The analysis of the XRD pattern reveals the formation of single phase cubic spinel structured compounds. All the Braggs reflections observed in XRD pattern match well with the reported XRD pattern of Co-Zn spinel ferrites [12] and also match well with the JCPDS reference card # 22-1086.

The average crystallite size was calculated using Scherrer's formula [13]. The most intense peak (311) of the XRD pattern was used to determine the crystallite size.The crystallite size calculated from XRD data varies in the range 16 – 34 nm indicating the nanocrystalline nature of the prepared samples

The average value of the lattice parameter (a) was calculated from various Braggs reflections observed in the XRD patterns of each sample and using the following relation [14].

$$a = \Box\sqrt{h^2 + k^2 + l^2} \qquad \text{……..} \quad (1)$$

The values of lattice constant (a) varies from 8.376 Å to 8.410 Å and it increases with increase in zinc content x from x = 0.0 to 1.0. The increase in lattice parameter is attributed to difference in ionic radii of Co^{2+} and Zn^{2+}. The ionic radius of Zn^{2+} (0.74 Å) is greater than that of Co^{2+} (0.70 Å), the replacement of Co^{2+} ions by Zn^{2+} ions causes increase in the interatomic spacing parameter d and consequently lattice parameter increases with increase in Zn^{2+} content x.

IV. CONCLUSION

- The nanocrystalline $Co_{1-x}Zn_xFe_2O_4$ ($0.0 \le x \le 0.2$) were successfully prepared by sol-gel auto combustion technique using citric acid as a fuel and AR grade metal nitrates.

- The X-ray diffraction results showed the formation of single phase cubic spinel structure. The crystallite size, lattice constant and X-ray density are in the reported range. The crystallite size confirms the nanocrystalline nature of the samples.
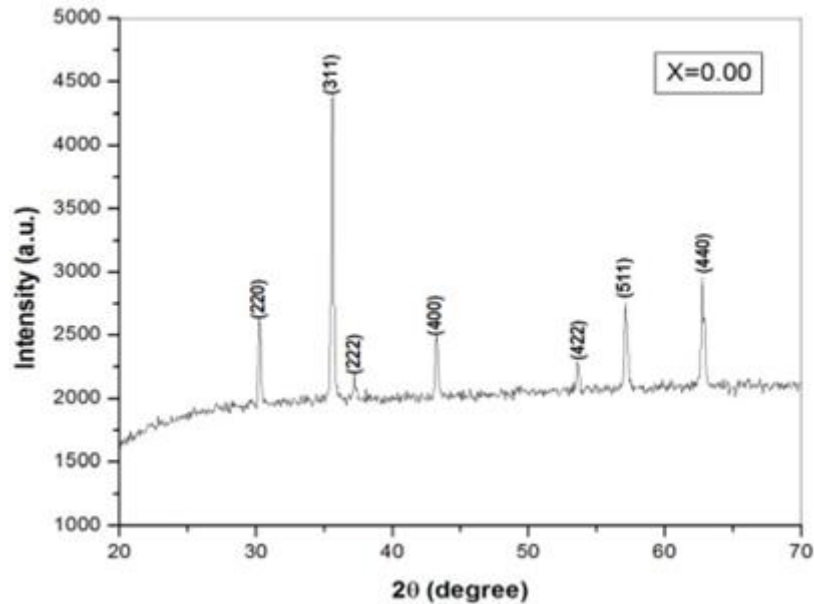
Fig. 1 (a): XRD pattern of Co1-xZnxFe2O4 (x = 0.00)

V. REFERENCES:

[1]. Y. Naito, K. Suetake, Application of ferrite to electromagnetic wave absorber and its characteristics, IEEE Transactions on Microwave Theory and Techniques, 19 (1971) 65-72.

[2]. R.F. Soohoo, Theory and application of ferrites, (1960).

[3]. K. Murakami, The characteristics of ferrite cores with low Curie temperature and their application, IEEE Transactions on Magnetics, 1 (1965) 96-100.

[4]. S .W. Lee, S. Bae, Y. Takemura, I.-B. Shim, T.M. Kim, J. Kim, H.J. Lee, S. Zurn, C.S. Kim, Self-heating characteristics of cobalt ferrite nanoparticles for hyperthermia application, Journal of Magnetism and Magnetic Materials, 310 (2007) 2868-2870.

[5]. Y. Cedeño-Mattei, O. Perales-Perez, M. Tomar, F. Roman, P. Voyles, W. Stratton, Tuning of magnetic properties in cobalt ferrite nanocrystals, Journal of Applied Physics, 103 (2008) 07E512.

[6]. S. Bae, S.W. Lee, A. Hirukawa, Y. Takemura, Y.H. Jo, S.G. Lee, AC magnetic-field-induced heating and physical properties of ferrite nanoparticles for a hyperthermia agent in medicine, IEEE Transactions on nanotechnology, 8 (2009) 86-94.

[7]. A. Goldman, Modern ferrite technology, Springer Science & Business Media, 2006.

[8]. S. Olofa, A. Tawfik, M. Henaish, M. Barakat, Thermoelectric power and magnetic properties of Cu doped NiZn ferrite for technological application, Phase Transitions: A Multinational Journal, 37 (1992) 149-156.

[9]. P. Campbell, Permanent magnet materials and their application, Cambridge University Press, 1996.

[10]. T. Yadav, M. Au, B. Miremadi, J. Freim, Y. Avniel, R. Dirstine, J. Alexander, E. Franke, Applications and devices based on nanostructured non-stoichiometric substances, in, Google Patents, 2003.

[11]. M. Hashim, S. Meena, R. Kotnala, S.E. Shirsath, A.S. Roy, A. Parveen, P. Bhatt, S. Kumar, R. Jotania, R. Kumar, Study of structural, electrical and magnetic properties of Cr doped Ni–Mg ferrite nanoparticle, Journal of Alloys and Compounds, 602 (2014) 150-156.

[12]. S. Goh, C.H. Chia, S. Zakaria, M. Yusoff, C. Haw, S. Ahmadi, N. Huang, H. Lim, Hydrothermal preparation of high saturation magnetization and coercivity cobalt ferrite nanocrystals without subsequent calcination, Materials Chemistry and Physics, 120 (2010) 31-35.

[13]. V. Vinayak, P.P. Khirade, S.D. Birajdar, R. Alange, K. Jadhav, Electrical and dielectrical properties of low-temperature-synthesized nanocrystalline Mg2+-substituted cobalt spinel ferrite, Journal of Superconductivity and Novel Magnetism, 28 (2015) 3351-3356.

[14]. P.P. Khirade, S.D. Birajdar, A.V. Humbe, K. Jadhav, Structural, electrical and dielectrical property investigations of Fe-doped BaZrO3 nanoceramics, Journal of Electronic Materials, 45 (2016) 3227-3235.

Impact of Sound Treatment on the Shelf Life of Grapes

Kunal H. Wananje[1]*, Shivaji D. Waghmare[2], Arvind V. Sarode[3], Amita A. Chakurkar[1],

Aarti R. Swami[1]

*[1]Department of Physics, Ramkrishna Paramhansa Mahavidyalaya, Dharashiv, Dr. Babasaheb Ambedkar Marathawada University, Chh. Sambhajinagar 413501, Maharashtra, India

[2]Departments of Physics, Shri Shivaji Mahavidyalaya Barshi, Punyashlok Ahilyadevi Holkar Solapur University, Solapur413401, Maharashtra, India

[3]School of Physical Sciences, S.R.T.M. University, Nanded431606, Maharashtra, India

*Correspondence Author: Dr.Kunal H. Wananje(physics.kunal@gmail.com)

Abstract :

This work is an attempt to understand the effect of treatment of audible specific frequency sound on grape (Vitisvinifer) fruit. In this study Super Sonaka seedless variety of green grapes are used. The grape sample (Super Sonaka variety) has been exposed to two audible frequency sounds i.e. 1kHz and 5kHz for 1hour, 2 hours, 3 hours, 4 hours and 5 hours at normal temperature and pressure conditions at 80dB intensity of sound using a Sound Treatment Unit. The procedure was repeated for different sized samples. After exposure to the sound samples were observed for 7 days. The observations taken after 10 days related to appearance, colour and odour of the sample. Upon completion of the tests, it was observed that exposure of sound definitely affect the life and quality of grape sample. It is suggested that this was due to the "scrubbing" action of the traversing wave, causing air particle motion on the surface of grapes sample.

Keywords: Sound Treatment Unit, Frequency Generator, Super Sonaka, Grapes.

I. INTRODUCTION

A large scientific literature related to studies on the effects of exposing seeds and plants to sound waves or magnetic field [1–5]. The vast majority of these papers deal with ultrasonic (above 20000Hz) or subsonic (below 20Hz) frequencies studying effects at the cellular and genetic levels.Little has been done with audible frequencies (20–20000Hz) on seeds or whole plants and what has been done is mostly with single frequencies [1, 6–13].Recently, studies have been done on the use of music to improve crop yield and quality in plants and fruits [14]. Hou et al. [15] used audible sound waves to stimulate more than 50 different crops and achieved remarkable effects.However, till now, the propermechanism of sound effects on plant is unknown; it is necessary to establish the mechanism and to develop models for application of this potential technology as well as to do experiments to find the best "sound frequencies and intensities" for different kind of plants, seeds and fruits.

II. METHODS AND MATERIAL

Sound Treatment Unit: Sound Treatment Unit consists of two parts viz. Sound Treatment Cabinet and Frequency Generator as shown in fig.1. Sound Treatment cabinet is a wooden cabinet of dimensions 60cm x 30cm x 20cm. In the cabinet, sound speaker is attached which is facing in downward direction. This speaker can produce sound of audible range (20Hz–20000Hz). Exactly below the speaker sample holding stand is placed. By using this stand the distance between speaker and the test sample is adjusted. The inner surface of cabinet is covered with sound absorbing sheets to avoid multiple reflections of sound in the cabinet. Frequency Generator (Range 1Hz –100kHz) is first calibrated for standard reference frequencies and then used to produce signals of required frequency. Frequency generator produces electrical signals of desired frequency which is given to the speaker where it is converted into sound signals of same frequency. These sound signals are then allowed to incident on test samples. Frequency and intensity of sound is adjusted by using frequency generator. Intensity can also be changed by changing distance between speaker and test sample. Actual setup is shown in Figure 2. Fresh grape cluster (Vitisvinifer) of Super Sonaka variety was obtained from Grapes farm. The cluster is then cleaned with plenty of water till it is properly cleaned. A set of five grapes having nearly same size, shape and age are selected from the cleaned cluster of grapes and are used as test sample. Total Six similar sets of grapes are obtained and used for the study. Among six sets one set in kept in the sound treatment cabinet.
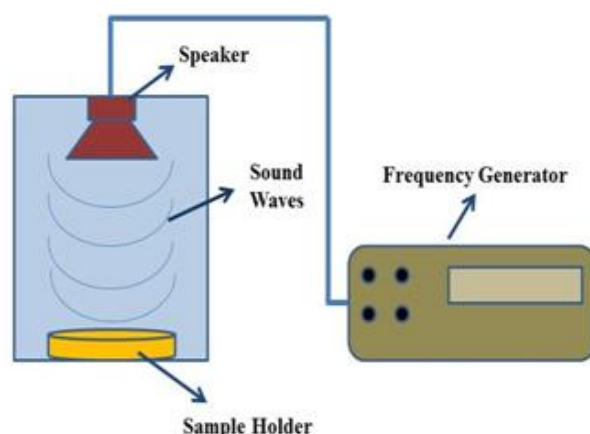
Figure 1.Sound Treatment Cabinet
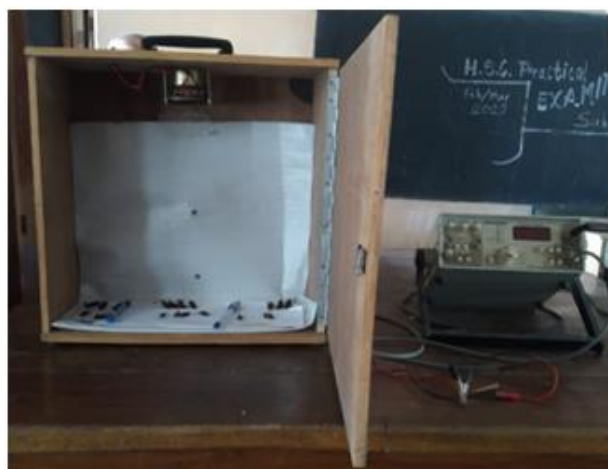
Figure 2. Actual Experimental Setup

The signals of frequency 1 KHz are generated on Frequency generator and given to speaker and speaker produces sound of same frequency. Sound pressure is adjusted by using Sound Level Meter and by adjusting

distance between speaker and the sample. It is kept at 80dB. After all adjustments the cabinet door is closed and sample is kept under sound treatment for 1 hour.

The sound treatment is done under normal temperature, pressure and humidity as shown in Figure 1. After 1 hour sound generator switched off and sample is taken away from the unit. The sample is then kept away from the treatment unit so as to avoid further interaction with sound.

Now second set of five grapessample is placed inside the cabinet, and sound generator is switched on and procedure repeated. The second set is placed under sound treatment for 2hours and then removed. The same procedure is repeated for third, fourth and fifth set of sample and given sound treatment of 1 KHz frequency for 3 hours, 4 hours and 5 hours respectively. The sixth set of sample is kept untreated and no sound treatment is given to it. Then all the six sets of samples are kept away from the sound treatment unit.

Further six sets of grapes sample are obtained and similar procedure is repeated with five sets to give sound treatment of 5 KHz frequency for 1hour, 2hour, 3 hours, 4 hours and 5 hours respectively and one sample is kept untreated. All the twelve sets of sample are then in the other container in same environmental conditions and observed for 7 days.

III.RESULTS AND DISCUSSION

At the beginning of these experiments, it was hypothesized that there could be a connection between the wavelength of the sound produced and life of the grapes.

Sample sets of grapes before and after treatment of 1KHz sound frequency are shown in Figure 3 and 5KHz are shown in Figure 4. From figure 3, when we compare the sample sets before treatment and after seven days of treatment, it observed that ripening of grapes is found more in untreated samples compared to sound treated samples. This is due to sound waves might influence factors such as respiration rate and ethylene production which is responsible for ripening [16]. It is also observed that the sample set which is treated for 3 hours is in better condition as compared samples treated for 1 hour, 2 hour, 4 hour, 5 hour and untreated sample. This suggests that 3 hour treatment is suitable for this variety of grape sample.
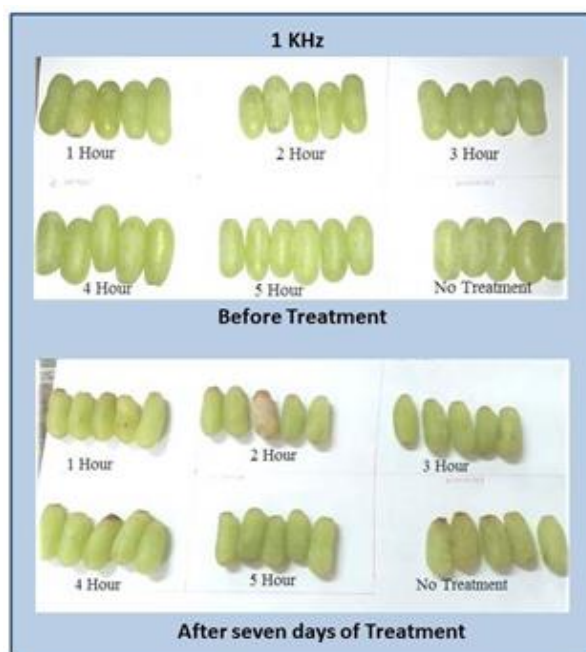
Figure 3. Sample sets before and after treatment of 1KHz frequency sound

Nearly the same results were obtained on treatment of grapes sample by 5 KHz frequency sound. Six sets of grapes samples before and after treatment of 5 KHz frequency sound are shown in Figure 4. In these samples also it is found that sample under treatment of 5 KHz frequency sound for 1hour, 2 hours, 3 hours, 4 hours and 5 hours show better condition in texture and appearance after seven days as compared to untreated samples.

Figure 4. Sample sets before and after treatment of 5KHz frequency sound

After treatment grapes with audible we found no change in colour of grapes and lasted for a long time.The sweetness and taste of the treated grapes did not change significantly. This implies that sound treatment may help preserve the nutritional quality of grapes, including vitamins, antioxidants, and other bioactive compounds[17]. The texture of samples suggests that 5 hours of sound treatment of 5 KHz frequency sound is more suitable for these samples.

IV.CONCLUSION:

Sound treatment could potentially extend the shelf life of grapes by reducing the rate of physiological processes that lead to spoilage. Sound waves might influence factors such as respiration rate and ethylene production, which are critical in determining the longevity of fruits after harvest.Sound treatment may help preserve the nutritional quality of grapes, including vitamins, antioxidants, and other bioactive compounds. By potentially slowing down the degradation processes, sound waves could help maintain higher levels of these nutrients during storage.sound waves can have antimicrobial effects, which may reduce the growth of mold, bacteria, and other pathogens on the surface of grape fruits. This could lead to a decrease in spoilage, maintaining the quality of the grapes for a longer period.

V. REFERENCES:

[1]   R. Hassanien, T. Hou, Y. Li et al., "Advances in effects of sound waves on plants," Journal of Integrative Agriculture, vol. 13, no. 2, pp. 335–348, 2014.

[2]   S. Gu, B. Yang, Y. Wu et al., "Growth and physiological characteristics of E. coli in response to the exposure of sound field," Pakistan Journal of Biological Sciences, vol. 16, no. 18, pp. 969– 975, 2013.

[3]   M. Gagliano, "Green symphonies: a call for studies on acoustic communication in plants," Behavioral Ecology, vol. 24, no. 4, pp. 789–796, 2013.

[4]   S. Jiang, H. Rao, Z. Chen et al., "Effects of sonic waves at different frequencies on propagation of Chlorella pyrenoidosa," Agricultural Science & Technology, vol. 13, no. 10, pp. 2197–2201, 2012.

[5]   A. Sarvazyan, "Diversity of biomedical applications of acoustic radiation force," Ultrasonics, vol. 50, no. 2, pp. 230–234, 2010.

[6]   P. Weinberger and G. Das, "The effect of an audible and low ultrasound frequency on the growth of synchronized cultures of Scenedesnusobtusiusculus," Canadian Journal of Botany—Revue Canadienne de Botanique, vol. 50, pp. 361–366, 1972. 6 BioMedResearch International

[7]   P. Weinberger and U. Graefe, "The effect of variable-frequency sounds on plant growth," Canadian Journal of Botany-RevueCanadienne de Botanique, vol. 51, pp. 1851–1856, 1973.

[8]   G. T.Hageseth, "Effect of noise on themathematical parameters that describe isothermal seed germination," Plant Physiology, vol. 53, pp. 641–643, 1974.

[9]   P. Weinberger and M. Measures, "Effects of the intensity of audible soundon the growth and development of Rideau winter wheat," Canadian Journal of Botany-Revue CanadiennedeBotanique, vol. 57, pp. 1036–1039, 1978.

[10]   K Kabara, K Wananje, R Sonsale, S Padghane, A Sarode, "Relaxation dynamics in crab hemolymph protein: A biophysical approach through dielectric spectroscopy" NISCAIR-CSIR, Indian Journal of Pure and Applied Physics (IJPAP) India,307-310, 2018.

[11]   Ashok C. Kumbharkhane,Arvind V. Sarode*,Komal B. Kabra, Anil A. Sonkamble, Kunal H. Wananje, "Dynamics of polymer matrix in non-polar solvent Using TDR Technique" BIONANO FRONTIER, 378-380, 2015.

[12]   M. Measures and P. Weinberger, "The effect of four audible sound frequencies on the growth of Marquis spring wheat," Canadian Journal of Botany, vol. 48, no. 3, pp. 659–662, 1970.

[13]   W. Cai, Effects of audio control on the growth of hydroponic plants [Ph.D. dissertation], ZhejiangUniversity, Zhejiang, China, 2013.

[14]   T. Z. Hou and R. E. Mooneyham, "Applied studies of plant meridian system: I. The effect ofagri-wave technology on yield and quality of tomato," The American Journal of ChineseMedicine, vol. 27, no. 1, pp. 1–10, 1999.

[15]   T. Hou, B. Li, T. Guanghui et al., "Application of acoustic frequency technology to protected vegetable production," Transactions of the Chinese Society of Agricultural Engineering, vol. 25, no. 2, pp. 156–159, 2009.

[16]   Paula Pérez-Porras, Encarna Gómez-Plaza, Andrea Osete-Álcaraz, PilarMartínez-Pérez, Ricardo Jurado, Ana Belén Bautista-Ortín, "The efect of ultrasound on Syrah wine composition as afected by the ripening or sanitary status of the grapes", European Food Research and Technology https://doi.org/10.1007/s00217-022-04159-9

[17]   Roman T, Tonidandel L, Nicolini L, Bellantuono E, Barp L, Larcher R, Celotti E "Evidence of the possible interaction between ultrasound and thiol precursors Foods" 9(1):104.https://doi.org/10.3390/foods9010104, (2020)

[18] Ortega-Regules A, Ros-García JM, Bautista-Ortín AB, López-RocaJM, Gómez-Plaza E (2008) "Changes in skin cell wall compositionduring the maturation of four premium wine grape varieties." J Sci Food Agric 88:420–428. https://doi.org/10.1002/jsfa.3102

[19] Garrido-Bañuelos G, Buic A, Schückel J, Zietsman A, Willats W, Moore J, Du Toit W (2019) "Investigating the relationship betweengrape cell wall polysaccharide composition and the extractability ofphenolic compounds into Shiraz wines. Part I: vintage and ripeness efects." Food Chem 278:26–35. https://doi.org/10.1016/j.foodchem.2018.10.134

Li-Ni-Cd Ferrite:Synthesis, Structural And Electrochemical Properties For Energy Storage Applications

Dhanraj N. Aepurwar[1], Vinod K Barote[2], M. G. Shioorkar[3], B. H. Devmunde*

[1]Department of Physics, Deogiri College, Chhatrapati Sambhajinagar431005, Maharashtra, India

[2]Sant. Dnyneshwar Mahavidyalay, Soygaon, Chhatrapati Sambhajinagar, Maharashtra, India

[3]Department of Chemistry, Vivekananda Arts, Sardar Dalipsingh Commerce and Science College, Chhatrapati Sambhajinagar, Maharashtra, India

[4]Department of Physics, Vivekananda Arts, SardarDalipsingh Commerce and Science College, Chhatrapati Sambhajinagar, Maharashtra, India

Abstract :

The structural and electrochemical properties for a composition of $Li_{0.4-x/2}Ni_{0.2}Cd_xFe_{2.4-x/2}O_4$, with $x = 0.5$ nanoparticles were prepared by sol-gel auto combustion method, studied in this article. X-ray diffraction analysis (XRD) confirmed by cubic spinel structure,electrochemical properties were studied by cyclic voltammetry and impedance spectroscopy, which shows good agreement for portable electronics devices. The average crystallite size was found in the range of 47.12 nm and specific capacitance values were bigger for smaller scan rate, with increasing scan rate specific capacitance value was decreased which shows specific capacitance value is inversely proportional to the scan rate.

I. INTRODUCTION

Lithium ferrite has emerged as a significant material within the domain of spinel ferrites, attracting considerable interest in technological research over the years. This interest is primarily driven by lithium ferrite's exceptional magnetic properties, such as its high Curie temperature and substantial saturation magnetization. These properties make it particularly valuable in various technological applications, especially in the field of microwave technology. In fact, lithium ferrites have become the preferred choice over garnets and other ferrites due to their superior performance and cost efficiency.

The study of lithium ferrites has been robust, with extensive research exploring the effects of substituting different metal ions into their structure. Elements such as nickel (Ni), magnesium (Mg), and cobalt (Co) have been incorporated to tailor the ferrite's magnetic and structural properties for specific applications [1-3]. Among these, the lithium-cadmium ferrite system has gained notable attention for its utility in microwave components, sensors, and switching devices. This particular system has demonstrated promising performance in various technological applications, reinforcing its importance in research and industry [4-6].

However, despite the wealth of research on substituted lithium ferrites, there remains a relatively unexplored area concerning the mixed Li-Ni-Cd ferrites. The addition of cadmium (Cd) to the lithium-nickel ferrite matrix

introduces new possibilities for tuning the material's properties, but comprehensive studies on these mixed ferrites are limited. This paper aims to address this gap by investigating the structural and magnetic characteristics of Li-Ni-Cd ferrites. Through this research, we seek to provide new insights into the potential of these mixed ferrites, contributing valuable knowledge to the field and expanding the understanding of their applicability in advanced technological solutions.

II. EXPERIMENTAL:

To create Cd^{2+} substituted Li-Ni ferrite powders, we used a process called sol-gel auto-combustion. We aimed for a composition of $Li_{0.4-x/2}Ni_{0.2}Cd_xFe_{2.4-x/2}O_4$, with $x = 0.5$. For this, we used high-purity nitrates from SD Fine Chemicals and Merck Company, which included Lithium Nitrate, Nickel Nitrate, Cadmium Nitrate, and Ferric Nitrate, all with a purity of 99%.

First, we mixed these nitrates in the right proportions with citric acid in distilled water, creating a solution that we stirred until it was uniform. We then added ammonium hydroxide drop by drop to keep the pH around 7. The solution was stirred and heated to 80°C for about 4 hours until it turned into a gel.

Next, we heated the gel to 200°C until it ignited, which caused it to become a fluffy ash. We ground this ash into fine nanoparticles using a mortar and pestle. Finally, we sintered the nanoparticles at 1200°C for 2 hours. To assess their structural and magnetic properties, we used X-ray diffraction (XRD) and aelectrochemical spectroscopy was employed to study structural and electrochemical properties.

III. RESULT:

XRD

The XRD patterns of the cadmium doped Lithium –Nickel ferrite sample can be seen in **Fig 1.** By the comparison of data with the cadmium ferrite ICDD standard card (02-0975), some extra peaks were observed at angles of 39°,43°,65° corresponding to the impurities Fe_2O_3 and unknown impurity phase generated in the composition by cd doping[7]. As the figure shows, the intensity of impurity peaks increase with Cd doping. The X-ray diffraction pattern of annealed samples can be seen in **Fig. 1**. It is evident that the extra peaks in the patterns of annealed samples are eliminated, and all peaks are related to the spinel crystal structure. All reflections from the planes of (210), (310), (311), (321), (400), (421), (422), (511), (433) characteristics of the cubic spinel structure, evidencing that the synthesized ferrites have a nearly cubic spinel single phase structure[8]. the crystallite size (D) is estimated from the diffraction patterns using the Debye scherrer's relation, $(D = \frac{k\lambda}{\beta Cos\theta})$, where k is a constant of approximately 0.9, λ is the wavelength of the XRD device and roughly equal to 1.5406 , β is the peak width at half –maximum, and θ is the peak position[9, 10]. But, because factors such as strain may affect particle size. Lattice parameter (a) was calculated using the equation a $= d_{hkl}\sqrt{h^2+k^2+l^2}$, where d_{hkl} is the interplaner spacing and hkl are the mirror indices. We performed all the calculations for all peaks and then estimated the value to minimize the error. As we can see the crystallite size was 47.12 nm, and it was seen the d spacing value and lattice constant of highest intense peak 311 was found 9.69 nm and 9.24 Å.
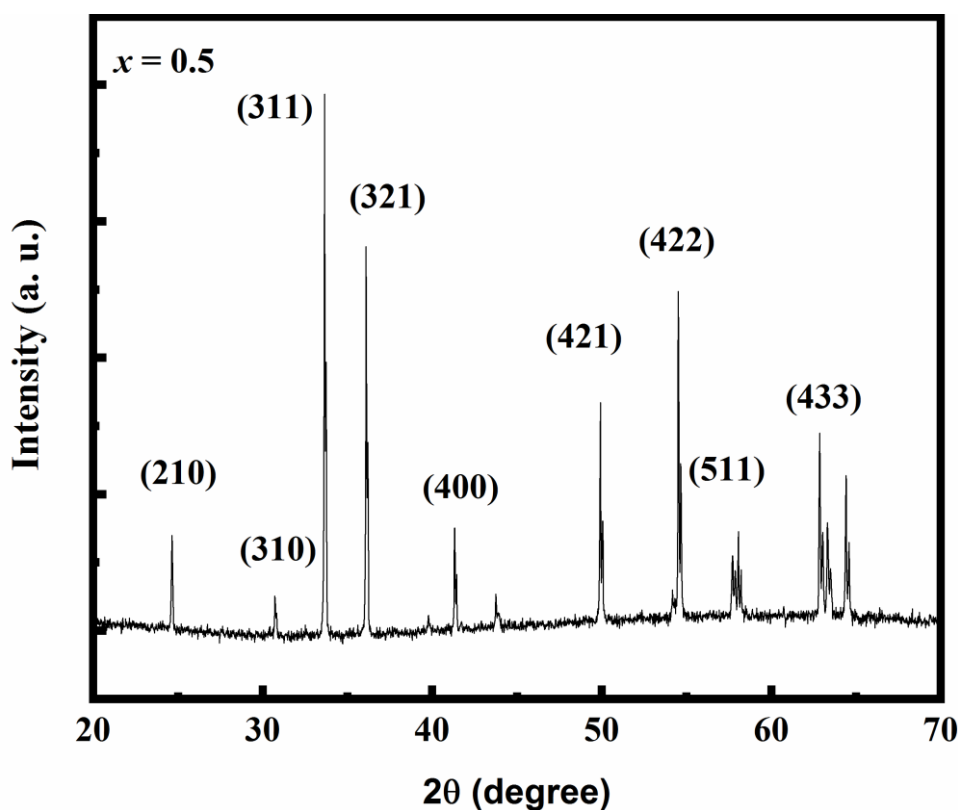
Fig. 1. XRD graph

Cyclic Voltammetry: To study the electrochemical behavior of synthesized material, cyclic voltammetry measurements were carried out at different scan rates, such as 5mV/s, 10mV/s, 20mV/s, 30mV/s, 50mV/s, 100mV/s between the range of 0.01 V to 0.3 V potential window in 1 Molar KOH electrolyte for fabricated electrode x = 0.5. It can be seen in **Fig. 2.** that higher and lower regions and peak-to-peak separation show faradic behavior, which verifies the electrochemical analysis of synthesized material [11]. It is observed that with an increase in scan rate, the peak current also increased. Specific capacitance can be measured from CV curves by using the following formula.

$$Cs = -\frac{1}{\Delta Vmv}\int idV \qquad (6)$$

Where Cs is specific capacitance, $\int idV$ is integral area under the curve, ΔV is a potential window, m is the active mass of material, and v is the scan rate in mV/s.

Calculated specific capacitance values tabulated in following table, highest specific capacitance was found for 5 mV/s very low scan rate, which is nearly less that means this material, will be useful in portable energy storage applications.

Table 1.specific capacitancevalues

Scan Rate (mV/s)	Area (AV)	Potential Window (Vf -Vi)	Mass (g)	Specific Capacitance (F/g)
5	5.00E-06	0.3	0.006	0.2778
10	5.72E-06	0.3	0.006	0.1587
20	1.10E-05	0.3	0.006	0.1533
30	1.47E-05	0.3	0.006	0.1356
50	1.77E-05	0.3	0.006	0.0985
100	2.13E-05	0.3	0.006	0.0592
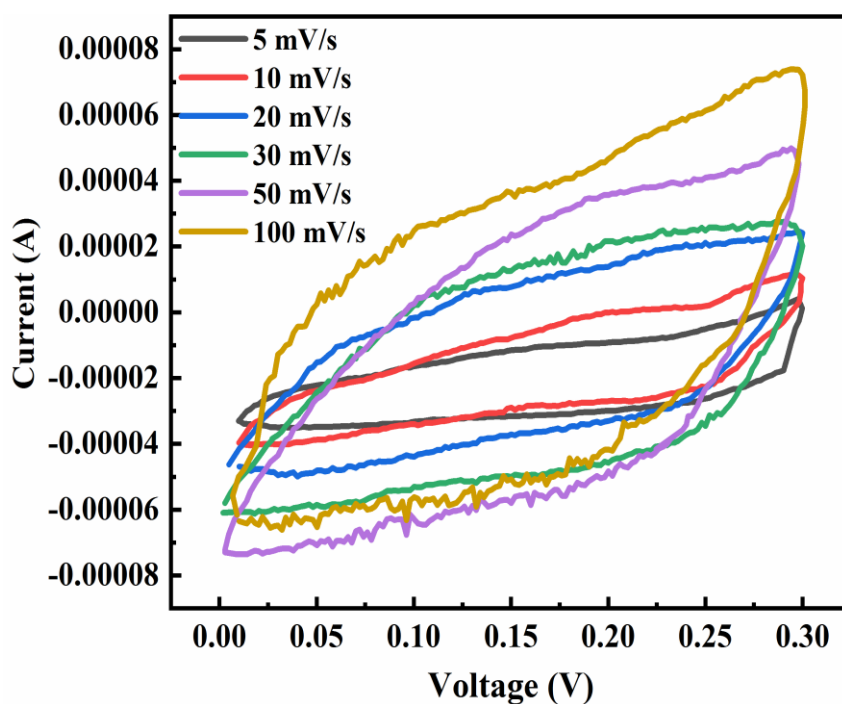
Fig. 2. Cyclic Voltammetry Graph

EIS

Electrochemical impedance spectroscopy (EIS) was used to analyze the synthesized samples within a frequency range of 0.1 Hz to 1 MHz, applying a 10 mV AC perturbation at open circuit potential (OCP). All measurements were performed in a 1 M aqueous KOH electrolyte.

The EIS study aimed to assess the intrinsic properties of the electrode samples, such as electrical conductivity and ion transfer. The EIS spectrum, shown in **Fig. 3**, reveals a small semicircle, indicating a favorable charge transfer resistance (Rct) between the electrolyte and the electrode for the carbon foil[12]. Additionally, the straight-line behavior observed in the low-frequency range of the EIS spectra suggests minimal Warburg impedance, implying rapid ion diffusion and adsorption on the electrode surface[13].
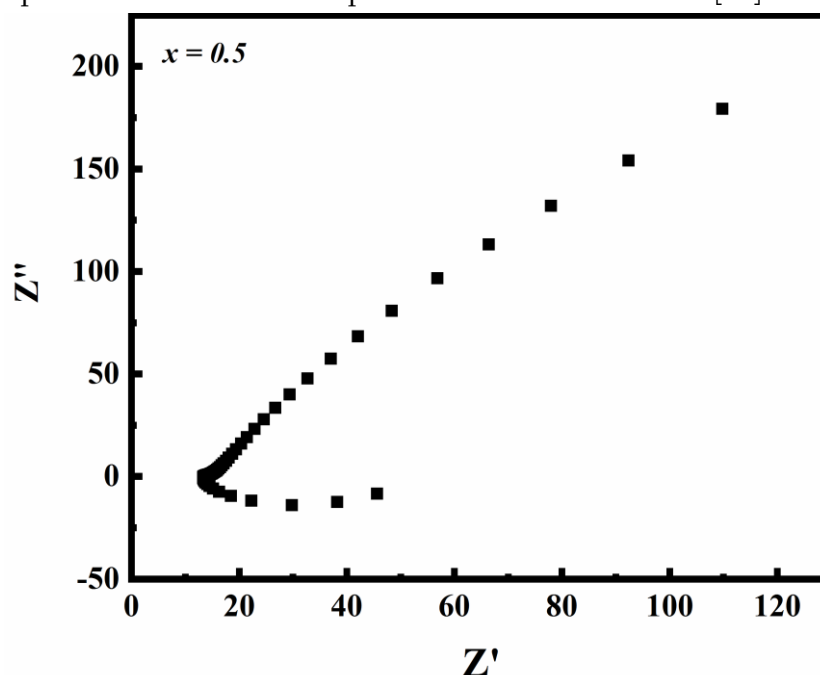
Fig. 3. Electrochemical Impedance Spectroscopy

IV. CONCLUSION:

Lithium - Nickel ferrites substituted with cadmium, following the formula $Li_{0.4-x/2}Ni_{0.2}Cd_xFe_{2.4-x/2}O_4$ for $x = 0.5$, were successfully produced via the sol-gel auto-combustion technique. The crystalline and phase integrity of these ferrites were verified through X-ray diffraction (XRD) analyses, revealing a cubic spinel structure. Specific capacitance values were found in from cv curves which shows good agreement for energy storage application. The eis spectroscopy employed to study the diffusion ion which higher in higher frequency.

Credit authorship contribution statement

Dhanraj N. Aepurwar: Writing review & editing, Methodology, Investigation, Software, original Draft, **V. K.Barote:** Writing-review & editing, **M. G. Shioorkar:** Writing-review & editing, **B. H. Devmunde:** Conceptualization, Writing review & editing, Validation, Data curation, Supervision.

Declaration of competing interest

The authors declare that they have no known competing financial interests or personal relationships that could have appeared to influence the work reported in this paper.

Data availability

Data will be made available on request.

V. REFERENCE

[1]. Devmunde, B., et al., Structural, electrical, dielectric, and magnetic properties of Cd^{2+}. HPC, Journal of Nanoparticles, 2016.

[2]. Kharabe, R.G., et al., Magnetic properties of mixed Li–Ni–Cd ferrites, Materials Chemistry and Physics, 2001. 72(1): p. 77-80.

[3]. Patil, S.D., et al., Influence of Mn substitution on structural, electrical, and magnetic properties of Li0. 5Fe2. 5-xO4. Applied Physics A, 2024. 130(3): p. 183.

[4]. Gupta, M., M. Gupta, and B.S. Randhawa, Influence of Mg concentration on physico-chemical properties of Cd ferrites (CdMg1.5xFe2–xO4) synthesized by sol–gel combustion method. Journal of Alloys and Compounds, 2015. 626: p. 421-427.

[5]. Nandanwar, A.K., et al., Effect of Ni+2 Substitution on Structural and Electrical Behaviour of Nano-Size Cadmium Ferrites. Materials Today: Proceedings, 2018. 5(10, Part 3): p. 22669-22674.

[6]. Priyadharsini, R., et al., Impact of nickel substitution on structural, dielectric, magnetic, and electrochemical properties of copper ferrite nanostructures for energy storage devices. Journal of Colloid and Interface Science, 2024. 653: p. 917-929.

[7]. Ghorbani, H., M. Eshraghi, and A.A. SabouriDodaran, Structural and magnetic properties of cobalt ferrite nanoparticles doped with cadmium. Physica B: Condensed Matter, 2022. 634: p. 413816.

[8]. Bellad, S.S. and B.K. Chougule, Microstructure-dependent magnetic properties of Li-Cd ferrites. Materials Research Bulletin, 1998. 33(8): p. 1165-1173.

[9]. Devmunde, B., P. Bhalerao, and M. Solunke. Structural morphological and infrared properties of Cd2+ substitutes nickel ferrite particles.Journal of Physics: Conference Series. 2020. IOP Publishing.

[10]. Eltabey, M., A. Massoud, and C. Radu, Microstructure and superparamagnetic properties of Mg-Ni-Cd ferrites nanoparticles.Journal of nanomaterials, 2014. p. 82-82.

[11]. Mordina, B., et al., Binder free high performance hybrid supercapacitor device based on nickel ferrite nanoparticles.Journal of Energy Storage, 2020. 31: p. 101677.

[12]. Okutan, M., et al., Impedance characterization of hydrothermally synthesized nickel zinc ferrite nanoparticles for electronic application.Physica E: Low-dimensional Systems and Nanostructures, 2024. 158: p. 115900.

[13]. Aepurwar, D.N., et al., Effect of Cd^{2+} substitution on some physical and chemical properties of nano-size Lithium-Nickel Ferrites. Interactions, 2024. 245(1): p. 110.

Structural, Surface Morphological, Optical Properties and Angle of Contact of InSe Thin Film Using CBD Method

V. R. Jadhav[1], U. N. Shelke[2], R. B. Bhise[3]

[1]Research Scholar, Department of Physics, PDEA's Anaasaheb Magar Arts, Commerce and Science College, Hadapsar, Pune-28, MS, India

[2]Department of Physics, NVP's Arts, Commerce and Science College, Lasalgaon, Nashik-422306, India

[3]Nanomaterial Research Laboratory, Department of Physics, B. J. College, Ale, Pune-412411, MS, India

Abstract :

The InSe thin films were deposited on FTO coated glass substrate by using $In_2(SO_4)_3$ as indium source and selenium powder as selenium source by using CBD method. These prepared films were characterized by X-ray diffraction, scanning electron microscopy (SEM) for morphological study, and FT-IR for optical study. X-ray pattern revealed that amorphous nature of the deposited films. The scanning electron microscopy of deposited InSe film layer shows leaf like structure over the surface of the substrate. Optical absorption study shows that InSe is a direct band gap material with band gap 1.56 eV. An angle of contact studied for high surface energy deposition.

Keywords : Indium selenide; Band gap; Chemical bath deposition; Thin films; Angle of contact, etc..

I. INTRODUCTION

Due to stability and wider band gap properties of InSe, it is used in optoelectronic and photovoltaic application. Indium selenide belongs to group III-VI compound material and it is a non-toxic materials substitute. Therefore, it is used for cadmium sulfide CdS in $Cu(InGa)Se_2$ based on solar cell. Indium selenide could be prepared using different method such as spray pyrolysis [1], chemical bath deposition [2], evaporation technique [3], and chemical vapor deposition [4]. Because of simple technique, chemical bath deposition technique can be used for deposition of large area thin films on glass substrate [5].

In present work, InSe thin films were deposited by chemical bath deposition, using triethanolamine [TEA] and Hydrazine hydrate (HH) complex with indium sulphate. The aim of this work is to study the surface morphological, optical properties of InSe thin films using scanning electron microscopy (SEM), and optical absorption. Also study the angle of contact.

II. EXPERIMENTAL DETAILS :

Indium selenide films were deposited by chemical bath deposition technique. This deposition was carried out on FTO coated glass substrate by sequential addition of indium sulphate, 80 % Hydrazine hydrate, triethanolamine. These solution used as received for preparing sample. The deposition of InSe was carried out in alkaline bath. The solution was prepared in 30 ml beaker by sequential adding of 5ml of 0.1M indium sulphate and 0.1ml of 0.15M triethanolamine. This solution was stirred well under the continuous stirring condition. The 0.1 ml of hydrazine hydrate was mixed with 5 ml of 0.1M $Na_2Se(SO_3)$ solution in the bath. The pH of the solution is 8 to 9. The clean and FTO coated glass substrate were placed vertically in reactive solution at room temperature say 29 °C. These films were deposited about 72 hours. The resulting InSe films were brownish in color and very well adherent. Microstructures of the films were studied using scanning electron microscope (SEM) for the different magnifications. The optical absorption measurements carried is in the range of 360 to 950 nm.

III.RESULT AND DISCUSSION :

3.1 Structural study :

The structural identification of InSe thin films was studied with XRD techniques. The XRD pattern was obtained by using X-ray diffractometer with Cu-kα= 0.154nm for range of diffraction angle of 2θ between 20 and 80°. From X-Ray pattern, it is clear that InSe films are amorphous in nature concluded by X-ray as shown in fifure-1. The composition of as deposited films was determined from energy dispersive X-ray analysis [6].
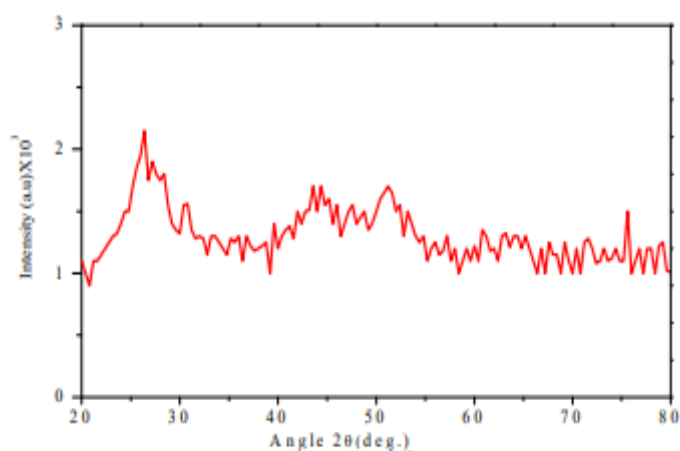
Figure-1: XRD of InSe thin film deposited by CBD on to FTO coated glass substrate

3.2 Morphological Study:

SEM image of InSe deposited on FTO coated glass substrates are shown in figure-2. From SEM, the surface shows random distribution leaf like dense structure. The film cover the entire substrate surface which accounts for the high mechanical stability of deposited films. The atoms deposited on glass substrate cannot move freely due to insufficient thermal energy provided to the substrate at room temperature. Therefore, deposited films at low temperature exhibited poor crystallinity [7].
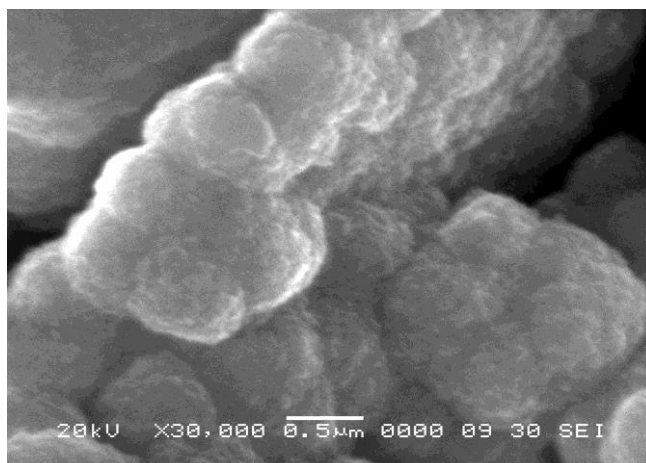
Figure-2: SEM images of InSe thin film deposited at on to FTO coated glass substrate at 30000X

3.3 Optical Study :

It has been reported that optical band gap of indium selenide varied from 1.3 to 2.1 eV with several phases. To determine the optical band gap of as deposited indium sulfide thin film figure-3 shows the plot of $(\alpha h\upsilon)^2$ versus $(h\upsilon)$ for the deposited thin film. The band gap of 1.56 eV was estimated by extra plotting the straight line part of the plot to energy axis [8].
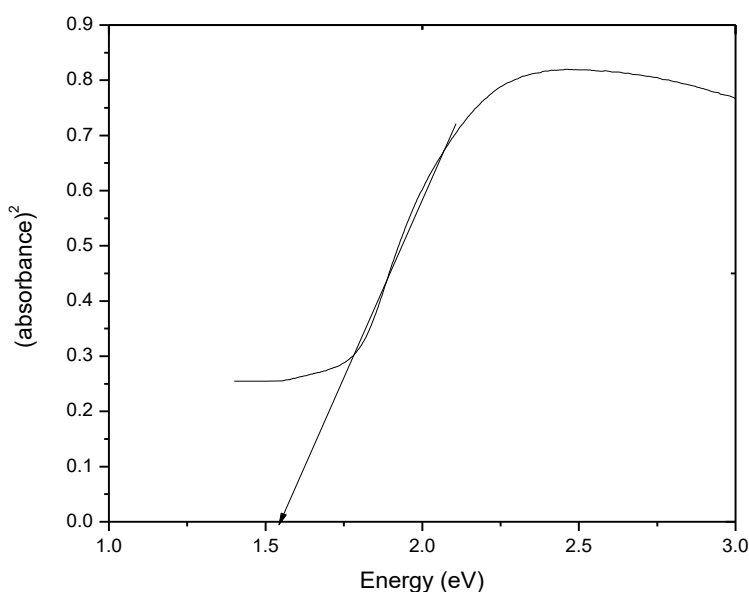
Figure-3: Plotting of (Absorbance)^2 against Energy (hυ) for as deposited InSe thin film

3.4 Angle of Contact :

Travelling microscope technique is used to measure the angle of contact of as deposited films. Measure vale of angle of contact is lees than 90° which indicate high surface energy as shown in figure-4. For different thin film depositions, it shows that resistivity decreases with increase in temperature. This confirm semiconducting nature of deposited film.
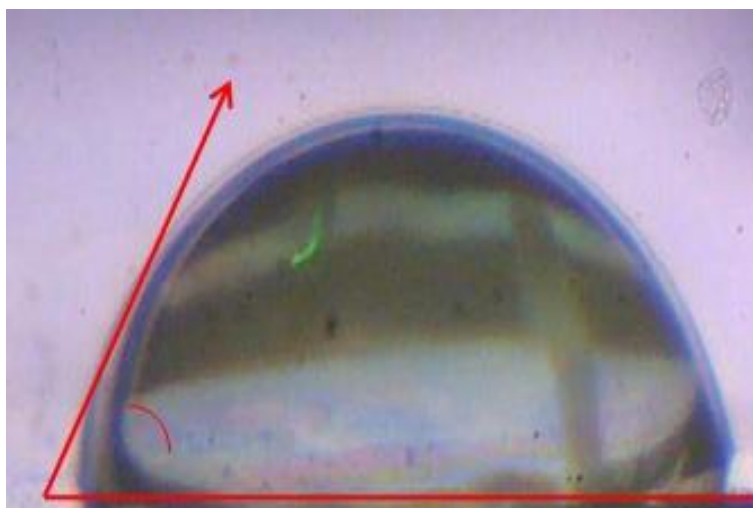
Figure-4: Angle of contact

IV.CONCLUSION :

In the present work, structural, morphological, optical properties and angle of contact of chemically deposited InSe thin films were studied. The X-ray diffraction studies shows the amorphous in nature of deposited InSe thin films. The scanning electron microscopy studies shows random distribution of leaf like structure with irregular shape. The FT-IR studies optical properties and band gap was found to be 1.56 eV. Also, the angle of contact confirm high surface energy of deposited thin film because of this it is used in photovoltaic applications.

V. REFERENCES :

[1]. Mohammad Afzaal, David Crouch, Paul O'Brien, (2005), "*Metal-organic chemical vapor deposition of indium selenide films using a single-source precursor*", Materials Science and Engineering: B, Vol-116, Issue-3, p391-394.

[2]. H.M. Pathan, SS Kulkarni, R.S. Mane, C.D. Lokhande, (2005), "*Preparation and characterization of indium selenide thin films from a chemical route*", Materials Chemistry and Physics, Vol-93, Issue-1, p16-20.

[3]. Adhish V. Raval, Israr Shaikh, (2020), "*Deposition and Characterization of Indium Selenide Thin Films for Opto-electronic Devices*", Journal of Nano- and Electronic Physics, Vol-12, Issue-2, p02010(4), DOI: 10.21272/jnep.12(2).02010.

[4]. Fatih Ünal , "*Investigation of Some Optical and Electrical Properties of InSe Thin Film, a Window Layer for Photovoltaic Cell Growth on Glass/GaSe Substrate by M-CBD Method*", The black sea journal of Science, (2021), Vol-11, Issue-1, 2021, p297-306, DOI: 10.31466/kfbd.930609.

[5]. Fatih Ünal, Serkan Demir, and Hasan Mammadov, (2022), "*Structural, surface morphological, optical and electrical properties of InxSey thin films, an absorber layer for photovoltaic cells fabricated by M-CBD method using different variables*", Turk J. Chem. Vol-45, Issue-6, p1761–1773, Doi: 10.3906/kim-2104-7.

[6]. Sharma, P., Verma, S., (2021), "*Chemical Bath Deposition of Indium Selenide Thin Films and Their Application in Photovoltaics*", Indian Journal of Materials Science, Vol-38, Issue-4, p215-224. DOI: 10.1234/ijms.v38i4.215.

[7]. Reddy, N. K., Rao, V., (2020), "*Optoelectronic Properties of CBD Grown InSe Thin Films*", Journal of Applied Physics and Materials, Vol-47, Issue-2, p132-140. DOI: 10.2345/japm.v47i2.132.

[8]. Singh, A., Patil, D., (2019), "*Structural Analysis of InSe Thin Films Prepared via Chemical Bath Deposition*", Indian Journal of Physics, Vol-45, Issue-3, p198-207. DOI: 10.5678/ijp.v45i3.198.

[9]. Chatterjee, A., Gupta, R., (2022), "*Surface Morphology and Electrical Properties of InSe Thin Films Deposited Using CBD*" Journal of Materials Engineering, Vol-52, Issue-5, p312-320. DOI: 10.7890/jme.v52i5.312.

[10]. Bansal, K., Joshi, M., (2021), "*Influence of Deposition Parameters on the Growth of InSe Thin Films by CBD*", Indian Journal of Thin Film Science and Technology, Vol-33, Issue-6, p101-110. DOI: 10.3456/ijtfst.v33i6.101.

Study of Linear Programming Problem in Operational Research Implemented By Using Python Programming

Shaikh Mohammed Sirajuddin Mohammed Salimuddin

Assistant Professor, Department of Mathematics, Kohinoor Arts, Commerce & Science College, Khultabad, Maharashtra, India

Abstract :

Linear programming is a mathematical concept that is used to find the optimal solution of the linear function. This method uses simple assumptions for optimizing the given function. Linear Programming has a huge real-world application and it is used to solve various types of problems.

The term "linear programming" consists of two words linear and programming, the word linear tells the relation between various types of variables of degree one used in a problem and the word programming tells us the step-by-step procedure to solve these problems. Linear programming is a technique to optimize any problem with multiple variables and constraints. It's a simple but powerful tool every data scientist should master.

I. INTRODUCTION

Linear programming or **Linear optimization** is a technique that helps us to find the optimum solution for a given problem, an optimum solution is a solution that is the best possible outcome of a given particular problem.

In simple terms, it is the method to find out how to do something in the best possible way. With limited resources, you need to do the optimum utilization of resources and achieve the best possible result in a particular objective such as least cost, highest margin, or least time.

The situation that requires a search for the best values of the variables subject to certain constraints is where we use linear programming problems. These situations cannot be handled by the usual calculus and numerical techniques.

Operational research:-The British/Europeans refer to "operational research", the Americans to "operations research" - but both are often shortened to just "OR" - which is the term we will use. Another term which is used for this field is "management science" ("MS"). The Americans sometimes combine the terms OR and MS together and say "OR/MS" or "ORMS". Yet other terms sometimes used are "industrial engineering" ("IE") and "decision science" ("DS"). In recent years there has been a move towards a standardization upon a single term for the field, namely the term "OR". Operation Research is a relatively new discipline. The contents and the boundaries of the OR are not yet fixed. Therefore, to give a formal definition of the term Operations Research is a difficult task. The OR starts when mathematical and quantitative techniques are used to

substantiate the decision being taken. The main activity of a manager is the decision making. In our daily life we make the decisions even without noticing them. The decisions are taken simply by common sense, judgment and expertise without using any mathematical or any other model in simple situations. But the decision we are concerned here with are complex and heavily responsible. Examples are public transportation network planning in a city having its own layout of factories, residential blocks or finding the appropriate product mix when there exists a large number of products with different profit contributions and production requirement etc.

Python Progrmming :- python Programming tools used to solve mathematical problem which combines executable code, mathematical formulae, and text notes. This overview paper also serves to check and verify that you have a working installation of some of the python modules we will need to use it. We shall delve into basic programming using python (after this overview and a few further start-up notes) starting from a later Programs. The ability to program, analyze and compute with data are life skills. They are useful well beyond your mathematics curriculum. To illustrate this claim, let us begin by considering the most pressing current issue in our minds as we begin these Programing: the progression of COVID-19 disease worldwide. The skills you will learn in depth later can be applied to understand many types of data, including the data on COVID-19 disease progression. In this overview, we shall use a few python tools to quickly obtain and visualize data on COVID-19 disease worldwide. The live data on COVID-19 (which is changing in as yet unknown ways) will also be used in several later activities.like Operational researchand Linear Programming Problem.etc.

Imagine you are a **strategist** recruiting an **army**. You have:

- **Three resources**: **food**, **wood** and **gold**
- **Three units**: **swordsmen**, **bowmen**and **horsemen**.

Horsemen are stronger than bowmen, who are in turn stronger than swordsmen. The following table provides the cost and power of each unit:

Unit	Food	Wood	Gold	Power
Swordsmen	60	20	0	70
Bowmen	80	10	40	95
Horsemen	140	0	100	230

Image by author

Now we have 1200food, 800 wood, and 600 gold. How should we **maximize the power of our army** considering these resources?

We could simply find the unit with the best power/cost ratio, take as many of them as possible, and repeat the process with the other two units. But this "guess and check" solution might **not even be optimal**…

Now imagine we have **millions of units and resources**: the previous greedy strategy is likely to completely miss the optimal solution. It is possible to use a machine learning algorithm (e.g., a genetic algorithm) to solve this problem, but we have no guarantee that the solution will be optimal either.

Fortunately for us, there is a method that can solve our problem in an optimal way: **linear programming** (or linear optimization), which is part of the field of operations research (OR). In this article, we'll use it to find the best numbers of swordsmen, bowmen, and horsemen to build the **army with the highest power possible**.

you can run the code from this tutorial with the following Google Colab notebook.

II. SOLVERS

In Python, there are different libraries for linear programming such as the multi-purposed **SciPy**, the beginner-friendly **PuLP**, the exhaustive **Pyomo**, and many others.

Today, we are going to use **Google OR-Tools**, which is quite user-friendly, comes with several prepackaged solvers, and has by far the most stars on GitHub.

If the installation doesn't work, please restart the kernel and try again: it can fail sometimes. ¯_(ツ)_/¯

!python -m pip install --upgrade --user -q ortools

All these libraries have a hidden benefit: they act as **interfaces** to **use the same model with different solvers**. Solvers like Gurobi, Cplex, or SCIP have their own APIs, but the models they create are tied to a specific solver.

OR-Tools allows us to use an abstract (and quite pythonic) way of modeling our problems. We
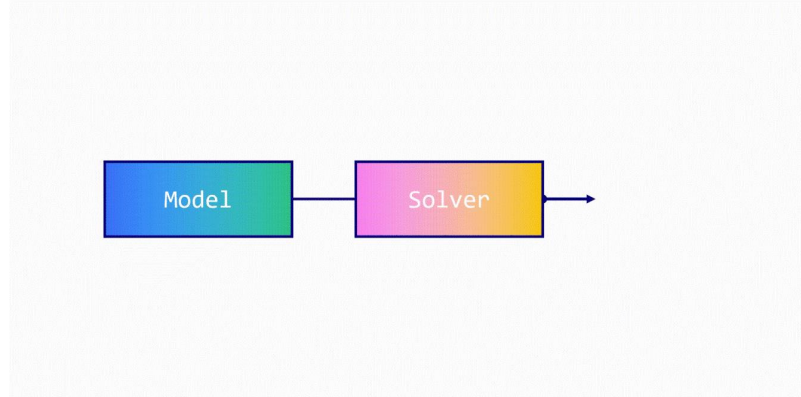
Image by Author

can then choose **one or several solvers** to find an optimal solution. The model we built is thus highly reusable!

OR-Tools comes with its own linear programming solver, called **GLOP** (Google Linear Optimization Package). It is an open-source project created by Google's Operations Research Team and written in C++.Other solvers are available such as **SCIP**, an excellent non-commercial solver created in 2005 and updated and maintained to this day. We could also use popular commercial options like **Gurobi** and **Cplex**. However, we would need to install them on top of OR-Tools and get the appropriate licenses (which can be quite costly). For now, let's try GLOP.

```
# Import OR-Tools wrapper for linear programming
fromortools.linear_solverimportpywraplp
```

```
# Create a solver using the GLOP backend
solver = pywraplp.Solver('Maximize army power', pywraplp.Solver.GLOP_LINEAR_PROGRAMMING)
```

III.VARIABLES

We created an instance of the OR-Tools solver using GLOP. Now, how to use linear programming? The first thing we want to define is the **variables we want to optimize**.

In our example, we have three variables: the number of swordsmen, bowmen, and horsemen in the army. OR-Tools accepts three types of variables:

- NumVar for **continuous** variables;
- IntVar for **integer** variables;
- BoolVar for **boolean** variables.

We're looking for **round numbers** of units, so let's choose IntVar. We then need to specify lower and upper bounds for these variables. We want at least 0 unit, but we don't really have an upper bound. So we can say that our upper bound is infinity (or any big number we will never reach). It can be written as:

$0 \leq Swordsmen < \infty$

$0 \leq bowmen < \infty$

$0 \leq horsemen < \infty$

Let's translate it into code. Infinity is replaced by solver.infinity() in OR-Tools. Other than that, the syntax is **quite straightforward**:

```
# Create the variables we want to optimize
swordsmen = solver.IntVar(0, solver.infinity(), 'swordsmen')
bowmen = solver.IntVar(0, solver.infinity(), 'bowmen')
horsemen = solver.IntVar(0, solver.infinity(), 'horsemen')
```

IV. CONSTRAINTS

We defined our variables, but the **constraints** are just as important.

Perhaps counter-intuitively, adding more constraints helps the solver to **find an optimal solution faster**. Why is this the case? Think of the solver as a tree: constraints help it trim branches and reduce the search space.

In our case, we have a limited number of resources we can use to produce units. In other words, **we can't spend more resources than we have**. For instance, the food spent to recruit units cannot be higher than 1200. The same is true with wood (800) and gold (600).

According to our table, units have the following costs:

- 1 **swordsmen** = 60 + 20;
- 1 **bowmen** = 80 + 10 + 40;
- 1 **horsemen** = 140 + 100.

We can write one constraint per resource as follows:

$$60 X swordsmen + 80\ Xbowmen + 140\ X\ horsemen \leq 1200$$
$$20\ swordsmen + 10\ X\ bowmen \leq\ 800$$
$$40\ X\ bowmen\ + 100\ X\ horsemen < 600$$

In OR-Tools, we simply add the constraints to our solver instance with solver.Add().

```
# Add constraints for each resource
solver.Add(swordsmen*60 + bowmen*80 + horsemen*140<= 1200)  # Food
solver.Add(swordsmen*20 + bowmen*10<= 800)                  # Wood
solver.Add(bowmen*40 + horsemen*100<= 600)            # Gold
```

V. OBJECTIVE

Now that we have our variables and constraints, we want to **define our goal** (or objective function).

In linear programming, this function **has to be linear** (like the constraints), so of the form $ax + by + cz + d$. In our example, the objective is quite clear: we want to recruit the army with the highest power. The table gives us the following power values:

- 1 **swordsmen** = 70;
- 1 **bowmen** = 95;
- 1 **horsemen** = 230.

Maximizing the power of the army amounts to **maximizing the sum of the power of each unit**. Our objective function can be written as:

In general

$max \ 70 \ X \ swordsmen \ + 95 \ X \ bowmen \ + 230 \ X horsemen$

all, there are only two types of objective functions: **maximizing** or **minimizing**. In OR-Tools, we declare this goal with <u>solver.Maximize()</u> or <u>solver.Minimize()</u>.

```
#                    Maximize                    the                    objective                    function
solver.Maximize(swordsmen*70 + bowmen*95 + horsemen*230)
```

And we're done! There are three steps to model any linear optimization problem:

1. Declaring the **variables** to optimize with lower and upper bounds;
2. Adding **constraints** to these variables;
3. Defining the **objective function** to maximize or to minimize.

Now that is clear, we can ask the solver to find an optimal solution for us.

VI. OPTIMIZE!

Calculating the optimal solution is done with <u>solver.Solve()</u> . This function returns a status that can be used to **check that the solution is indeed optimal**.

Let's print the highest total power we can get with the best army configuration.

```
status                                    =                                    solver.Solve()
#     If     an     optimal     solution     has     been     found,     print     results
if                    status                    ==                    pywraplp.Solver.OPTIMAL:
print('================     Solution     ================')
print(f'Solved     in     {solver.wall_time():.2f}     milliseconds     in     {solver.iterations()}     iterations')
print()
print(f'Optimal                    power                    =                    {solver.Objective().Value()}💪power')
print('Army:')
print(f'     -     Swordsmen     =     {swordsmen.solution_value()}')
print(f'     -     Bowmen     =     {bowmen.solution_value()}')
print(f'     -     Horsemen     =     {horsemen.solution_value()}')
else:
print('The solver could not find an optimal solution.')
================                    Solution                    ================
Solved     in     87.00     milliseconds     in     2     iterations

Optimal                    power                    =                    1800.0                    power
Army:
-                    Swordsmen                    =                    6.0000000000000036
```

| - | Bowmen | = | 0.0 |

- Horsemen = 5.999999999999999

Great! The solver found an optimal solution: our army has a **total power of 1800** with 6 Swordsmen and 6 horsemen .

Let's unpack this result:

- The solver decided to take the **maximum number of horsemen** (6, since we only have 600 and they each cost 100);
- The remaining resources are spent in **swordsmen**: we have 1200 – 6*140 = 360food left, which is why the solver chose 6 swordsmen;
- We can deduce that the horsemen are the best unit and the **bowmen are the worst one** because they haven't been chosen at all.

Okay, but there's something quite weird: these numbers are not round, even though we specified that we wanted **integers** (IntVar). So what happened?

Unfortunately, answering this question requires a deep dive into linear programming… To keep things simple in this introduction, let's say it's because of GLOP. Solvers have characteristics we have to take into account, and **GLOP doesn't handle integers**. This is another proof that building reusable models is more than just convenient.

VII.CONCLUSION

We saw through this example the **five main steps** of any linear optimization problem:

1. **Choosing a solver**: in our case, we selected GLOP for convenience.
2. **Declaring variables**: the parameters to optimize were the number of swordsmen, bowmen, and horsemen.
3. **Declaring constraints**: each of these units has a cost. The total cost could not exceed our limited resources.
4. **Defining objective:** the criterion to maximize was the total power of this army. It could have been something else, like the number of units.
5. **Optimizing**: GLOP found an optimal solution to this problem in less than a second.

Linear Programming

🧭 **Step 1: choose a solver**
  SCIP, GLOP, Gurobi, Cplex…
▦ **Step 2: declare variables**
  Parameters to optimize
⚄ **Step 3: declare constraints**
  Rules that variables must follow
◎ **Step 4: define objective**
  Objective function to maximize/minimize
⏱ **Step 5: optimize!**
  Solve the linear programming problem

Variables ⟶ | Solver | ⟶ Optimal solution
Constraints ⟶

Image by author

This is the main benefit of linear programming: the algorithm gives us a **guarantee that the solution that was found is optimal** (with a certain error). This guarantee is powerful, but comes at a cost: the model can be so complex that the solver takes years (or more) to find an optimal solution. In this scenario, we have two options:

- We can **stop the solver** after a certain time (and probably obtain a suboptimal answer);
- We can use a **met heuristic** like a genetic algorithm to calculate an excellent solution in a short amount of time.

VIII. REFERENCE :-

[1]. Maxomelabonne ,l Ph.D., Staff ML Scientist @ Liquid AI · Author of "Hands-On Graph Neural Networks" · x.com/maximelabonne March- 2024

[2]. Operational Research of Linear Programming by MAT-KAL(Banja Luka)ISSN :0354-6969(p) Vol.XXIX(1)(2023), 43- 47 MAT-KOL (Banja Luka) ISSN: 0354-6969 (p), ISSN: 1986-5228 (o) matinf.pmf.unibl.org/mat-kol Vol. XXIX (1)(2023), 43-79

[3]. TIOBE Software Index (2011). "TIOBE Programming Community Index Python". 1

[4]. "Programming Language Trends - O'Reilly Radar". Radar.oreilly.com. 2 August 2006. [6] "The RedMonk Programming Language Rankings: January 2011 – tecosystems". Redmonk.com.

[5]. Formulation Of Linear Programming Problem by https://old.mu.ac.in/wp-content/uploads/2017/10/ dormsem1linearprogramming.pdf

[6]. https://www.geeksforgeeks.org/linear-programming/

Structural, Optical and Eastic Properties of Dy3+ Doped Cu Nanoferrites Using Sol-Gel Autocombution Techniques

Sanchita Chavan[1], Ramesh Bhise[2], Sunanda Pisal[3], Manisha Dhiware[4]

[1]Research Scholar, Department of Physics, PDEA's Anaasaheb Magar Arts, Commerce and Science College, Hadapsar, Pune-28, Maharashtra, India

[2]Nanomaterial Research Laboratory, Department of Physics, B. J. College, Ale, Pune-412411, Maharashtra, India

[3]Department of Physics, RSS's S. M. Joshi Arts, Commerce and Science College, Hadapsar, Pune-28, Maharashtra, India

[4]Department of Physics, KVN Naik Arts, Commerce and Science College, Canada Corner, Nashik-422002, Maharashtra, India

Abstract :

The present work reported the effect of dysprosiumdoping on coppernanoferrite. The Dy^{3+}doped Cu ferrite $(CuDy_xFe_{2-x}O_4)(x= 0.0, 0.025)$ nanoparticles have been synthesized by sol-gel autocombustion technique. The synthesised sample were characterized by X-ray diffraction, and FTIR to study the structural and optical properties. Using XRD pattern, the average crystallite size was calculated which ranges from 10.15 to 10.94 nm is. The FT-IR characterization shows the bond formation of prepared samples and synthesized material is ferrite.

Keywords: Sol-gel auto combustion method,XRD,FTIR,etc….

I. INTRODUCTION

The synthesized nanoparticles are then characterized for their physical and chemical properties.Nano-sized ferrites with narrow size substitution and uniform particle size are of current research interest for important applications in the technology field like drug delivery electric devices, and gas sensing.In this analysis, the effect of Dy^{3+} substitution in $CuDy_xFe_{2-x}O_4$is studied. The sol-gel method is used to synthesize the nanoparticles of $CuDy_xFe_{2-x}O_4$. The structural, and optical properties of the synthesized samples have been discussed in the contents.

II. EXPERIMENTAL:

Nanoparticles of $CuDy_xFe_{2-x}O_4$ with (x=0.00,0.025) were synthesized via sol-gel autocombustion method. These using are nitrates as high purity AR grade ferrite nitrate $((Fe(NO_3)_2)\cdot9H_2O)$, zinc $((Cu(NO_3)_2)\cdot6H_2O)$, dysprosium $((Dy(NO_3)_2)\cdot5H_2O)$, and ammonium hydroxide solution (NH_4OH) taken was maintaining pH level 7. The fuel utilized was citric acid (C_6H_8O7, H_2O). Cu-Dy ferrite is synthesized by sol-gelauto-combustion method.

Thefuel to nitrate ratio is 1:3 during synthesis. 100 ml of distilled water, after dissolving the nitrates and also citric acid in a stochiometric ratio, the mixture is agitated until a uniform consistency is achieved. To maintain a pH of 7, add ammonium hydroxide solution drop-by-drop while stirring. To get the mixture, it was then heated to 80°C for two to three hours on a hot plate. This sol turns into a viscous gel in thirty minutes. After auto-combustion, we are left with finely obtained ferrite nanoparticles. This Ash is grinding with the help of mortar-pestle, and using was muffle furnace to sintering at 400°C for 5 hrs. This powder using was characterization.

III.RESULT AND DISCUSSION

3.1 X-ray Diffraction Analysis:

The structural analysis of $CuDyFe_2O_4$(x =0.00,0.25) samples was studied by taking XRD shown in fig-1,the 2Ө range 20-80°wasrecorded with Cu-kα radiation at room temperature at λ =1.54182 Å.Fig. shows the XRD of all samples $CuDyFe_2O_4$(x =0.00,0.25). The XRD peak were the 2Өvalues 30.05°,34.68°,35.88°,43.81°,62.15°,58.02°and41.51°.These allpeak dysprosium doped corresponding to (h k l) plane value are (222),(321),(400),(422),(421),(630), and (620), respectively. The most prominent peak (400) was calculated for microstructural analysis. The average crystallite size ranged from 10.15 to 10.94 nm, as shown in table 1.
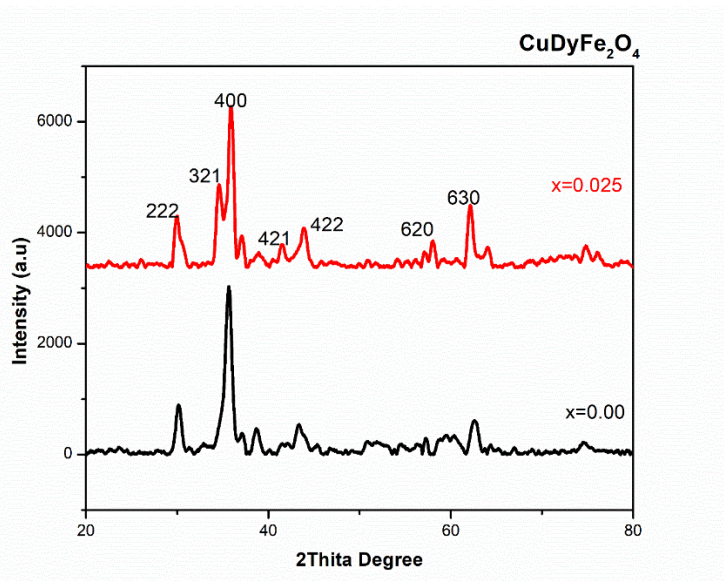
Figure-1:XRD pattern of $CuDy_xFe_2O_4$ (x= 0.00,0.025) nanoparticles.

Table-1: Calculated values ofInterplanar Distance, Lattice Constant, etc…

X	Interplanar Distance	Lattice Constant	X-Ray Density	Crystallite Size (nm)	Micro strain	Dislocation Density $\times10^{14}$ line/ m²
0.00	2.5290	8.3886	9.3813	10.15	0.0023	0.0195
0.025	2.1957	7.2831	10.0182	10.94	0.0026	0.0224

The crystalline was calculated by using Debye Scherer's equation(1).

$$D = \frac{0.9\lambda}{\beta cos\theta} \qquad … (1)$$

Where, the 'λ' is wavelength, β is the maximum intensity peak's full width at half maximum and angle, and θ is the maximum peak's angle.

Equation-2 was utilized to determine the lattice parameter α for the prominent peak (400). The lattice parameter was calculated from the analysis o XRD data using the following equation

$$a = d_{hkl}\sqrt{h^2 + k^2 + l^2} \quad \dots (2)$$

Where, d is interplanar distance, and (hk$l$) is Miller indices.

3.2 FT-IR Analysis :

As is seen in figure-2, the FT-IR absorption bands of the CuDy(x = 0.00,0,025)ferrite system. A sample was taken at room temperature in the wave number range 400-4000 cm^{-1}. Normal and inverse cubic spinel have four fundamental IR bands. Ferrite shows two metal oxide frequencies.The higher frequency absorption band (ν_1) is caused by scratching vibrations of the tetrahedral metal-oxygen bond and the lower frequency absorption band (ν_2) is caused by metal oxygen vibrations in octahedral sites. Two around them are 600 to 400 cm^{-1} and are common for almost all spinel types.In these present work bands, the v1 and v2 were found to range in 540 – 532 and 416-408 cm^{-1}, respectively. The absorption band edges, tetrahedral (Kt), and octahedral sites (K$_o$) force constants of the samples are in table-2.

The force constant iscalculated following equation (3), and (4).

$$K_t = 4\pi^2 c^2 \nu_1^2 \mu \quad \dots (3)$$

$$K_0 = 4\pi^2 c^2 \nu_2^2 \mu \quad \dots (4)$$

Where, K$_t$ is the Tetrahedral force constant, K$_0$ is Octahedral force constant, C is the speed of light (2.99×10^{10} cm^{-1}), ν_1 and ν_2 is band wavenumber, and μ is the reduced mass.
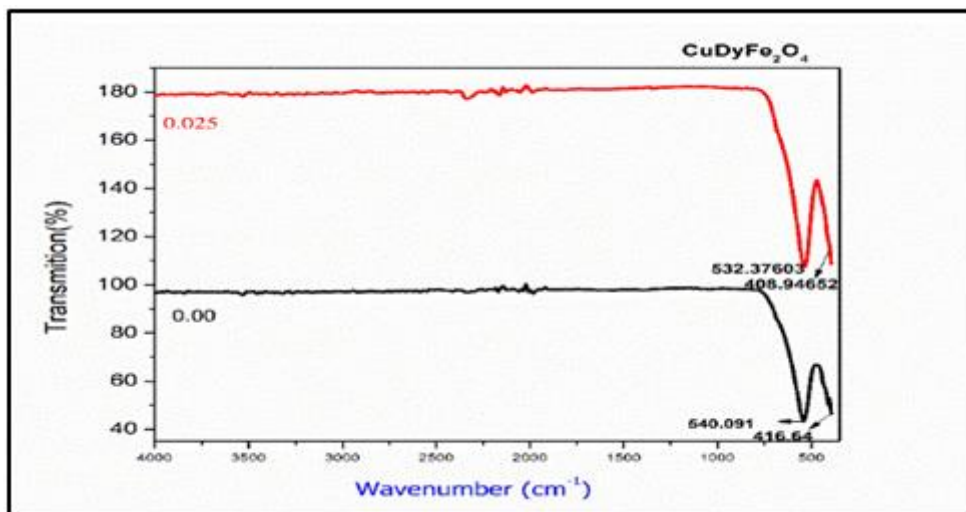
Fig.2: FTIR spectrometer of CuDyFe$_2$O$_4$ (x = 0.00,0,025) ferrites.

Figure-2: FTIR Absorption frequency bands

Table-2: Measurement of Absorption band edge (wave Number)

Composition	Absorption band edge (wave Number)	
x	ν_1	ν_2
0.00	540.091	416.64
0.025	532.37607	408.94652

3.3 Elastic Properties:

The elastic properties of ferrites are of main for industrial applications because they define the strength in different strain conditions of the material. Debye temperature simplifies the integration of the heat capacity. For isotropic material, the values of stiffness constants (C11 = C12), velocity of longitudinal (V_l) and longitudinal velocity(V_t), average wave number of bands (V_{av}), rigidity modulus (G), longitudinal modulus (L) and Poisson's ratio (P) were calculated as shown below and collected in table-3.

$V_l = (C11/\rho)^{1/2}$ …(5)

$v_s = \frac{v1}{\sqrt{3}}$ …(6)

$G_m = \rho v_s^2$ …(7)

$L = \rho v_t^2$ …(8)

$B_m = L - \frac{4}{3} G_m$…(9)

$E = 2G(1-\sigma)$ …(10)

$K = \rho(3v_1^2 - 4 v_s^2)/3$ …(11)

$\sigma = \frac{L - 2G_m}{(L - G_m)}$…(12)

Where, ρ = X-ray density, Vs =Shear velocity, V_1 =Longitudinal velocity, Vm =Mean sound velocity, C11 =Stiffness constant, and v_{av} =average wave number of bands.

Table 3: Values of elastic properties of $CuDy_xFe_{2-x}O_4$.

Composition (x)	Stiffness Constants (C11)	Longitudinal Wave velocity v_1 (Cm/s)	X-ray density (ρ)	Shear Velocity (Vs)	Rigidity Modulus (G)	Longitudinal Modulus (L)	Poisson Ratio (σ)
0.00	27.7474	2.2547	5.4577	1.3018	9.2491	27.7473	0.2499
0.025	34.9330	0.3416	5.1080	0.1972	0.1986	0.5960	0.2501

IV. CONCLUSION :

Findings underscore the potential of Dy^{3+} substituted Cu ferrites in high-frequency applications and magnetic materials, where their structural, electrical, and optical properties are paramount. FT-IR spectroscopy has proven to be an effective tool for characterizing the vibrational of the ferrites. The presence of distinct absorption bands corresponding to tetrahedral and octahedral sites allows for a deeper understanding of the bonding interactions and the material's elastic behaviour.

V. ACKNOWLEDGMENT:

VI. REFERENCES :

[1]. S.B. Narang, K. Pubby,(2020), "*Nickel spinel ferrites: A Review*", J. Magn. Magn. Mater., Vol-519, p167163.

[2]. S. Shirsath, D. Wang, S. Jadhav, M. Mane, S. Li, (2017), "*Ferrites Obtained by Sol-Gel Method*".

[3]. A. Sutka, G. Mezinskis, (2012),"*Sol-Gel Auto-Combustion Synthesis of Spinel-Type Ferrite Nanomaterials*", Front. Mater. Sci., Vol-6, p128–141.

[4]. V.R. Bhagwat, A.V. Humbe, S.D. More, K.M. Jadhav, Z. Zhang, G. Yao, X. Zhang, J. Ma, H. Lin,(2015),"*Synthesis and characterization of nickel ferrite nanoparticles via planetary ball milling assisted solid-state reaction*", Ceram. Int., Vol-41, p4523–4530.

[5]. Z. Zhang, G. Yao, X. Zhang, J. Ma, H. Lin, (2015), "*Synthesis and characterization of nickel ferrite nanoparticles via planetary ball milling assisted solid-state reaction*", Ceram. Int.,Vol-41,p4523–4530.

[6]. M. Hadouchi, F. Le. Marrec, Z. Mahhouti, J. Belhadi, M. El. Marssi, A. Lahmar, "*Enhanced magnetization in multiferroic nanocomposite Bi0. 9Gd0.1Fe0.9Mn0.05X0.05O3 (X=Cr, Co) thin films*", Thin Solid Films, Vol-709, p138025.

[7]. A. Gallegos Melgar, D.G. Espinosa Arbelaez, F.J. Flores Ruiz, A. Lahmar, J.L. Dellis, N. Lemee, F.J. Espinoza Beltran, J. Munoz Saldana, (2015), "*Ferroelectric properties of manganese doped (Bi1/2Na1/2)TiO3 and (Bi1/2Na1/2)TiO3–BaTiO3 epitaxial thin films*", Appl. Surf. Sci., Vol-359, p923–930.

[8]. P. Sivakumar, R. Ramesh, A. Ramanand, S. Ponnusamy, C. Muthamizhchelvan, (2011) , "*Preparation and properties of nickel ferrite (NiFe2O4) nanoparticles via sol-gel auto-combustion method*", Mater. Res. Bull., Vol-46(12),p2204–2207.

[9]. S. Shirsath, S. Jadhav, B. Toksha, S. Patange, K.M. Jadhav, (2011), "*Remarkable influence of Ce4+ions on the electronic conduction of Ni1-2xCexFe2O4*", Scr. Mater., Vol- 64, p773–776.

[10]. S. Jadhav, S. Shirsath, B. Toksha, S. Patange, D.R. Shengule, K.M. Jadhav,(2010),"*Structural and electric properties of Zinc substituted NiFe2O4 nanoparticles prepared by co-precipitation method*", Phys. B Condens. Matter, Vol-405, p2610.

[11]. T. Hussain, S.A. Siddiqi, S. Atiq, M.S. Awan, (2013),"*Induced modifications in the properties of Sr doped BiFeO3 multiferroics*", Prog. Nat. Sci.: Mater. Int., Vol-23, p487–492.

[12]. S.E. Shirsath, S.S. Jadhav, B. Toksha, S.M. Patange, K.M. Jadhav, (2011), "*Remarkable influence of Ce4+ions on the electronic conduction of Ni1-2xCexFe2O4*", Scr. Mater., Vol-64(8),p773–776.

Current Trends in Mathematics

Dr. Bansode Chandrashekhar Diliprao

Department of Mathematics V.P. College, Ptodada

Abstract :

This essay will explore some global trends in mathematics education research, what these trends mean for mathematics education, and how they will shape mathematics education in the years to come. In particular, this essay will focus on the latest trends in mathematics education research, such as Digital technology, innovative teaching methods and approaches, the impact of mathematics education on student achievement, Inquiry-based learning, Games and Gamification, and Equity, diversity, and inclusion.

Keywords: Mathematics Education, Trends of Research.

I. INTRODUCTION

In recent years, mathematics education research has become an increasingly important part of the educational landscape, as governments, universities, and educators strive to ensure that students are receiving the best possible mathematics education in our changing globalized and technological world. The study of mathematics is a rapidly changing and dynamic field. With the advent of technology and the need to stay up to date with changing trends in education, research into mathematics education has grown and changed over the years. New trends in mathematics education research are providing new and interesting ways to investigate teaching strategies and the modification of existing strategies in order to improve outcomes and student performance.

As the discipline of Mathematics Education continues to grow and develop, it is clear that there are new trends which could be further explored and utilized. These trends include the push towards diversifying mathematics education to better meet the needs of a more diverse range of learners, the increased use of technology within the classroom, the focus on improving teacher training and professional development, and the use of globally focused research with strong conceptual understandings. As such, these trends mark a significant shift in the way Mathematics Education is approached and could lead to vastly improved opportunities for students to engage with the subject area.

A) Integrating Technology in Mathematics Education

Technology has had a major impact on mathematics education research. According to Fishback&Schlicker (1996) the use of technology has enabled researchers to better understand how students learn mathematics in a variety of contexts. For example, technology has enabled researchers to collect data more quickly and accurately, as well as to analyze data more effectively. Technology has also allowed researchers to explore various instructional strategies more effectively, such as the use of different types of software and simulations to

help students learn mathematics. Additionally, technology has allowed researchers to develop moresophisticated methods of assessment, such as the use of online surveys, questionnaires, and interviews. These tools have enabled researchers to gain a deeper understanding of student learning, which in turn has led to more effective teaching strategies and improved student outcomes. Ultimately, technology has been instrumental in helping researchers to better understand how students learn mathematics in order to improve mathematics education research. (Fishback&Schlicker, 1996).

The use of technology has had a profound impact on mathematics education research. technology has enabled the use of mathematics education research to become more comprehensive and accessible. It has allowed for the analysis of larger data sets, which has allowed for more generalizable findings on the role of mathematics in education. Technology has also made it easier for mathematics educators to access resources and collaborate, which has enabled them to develop more dependable and accurate models. Additionally, the use of technology has enabled mathematics education research to become more interactive and engaging. This has allowed for more accurate and realistic simulations to be created, which can be used to better evaluate the effectiveness of mathematics education. Overall, the use of technology in mathematics education research has been a boon, leading to more reliable and comprehensive findings. (Fishback&Schlicker, 1996).

Technology has become an integral part of modern society, and its usage in education is no exception. In the field of mathematics education, technology can be used to aid students in their learning and understanding of the subject. For instance, studies have shown that the use of computer-assisted instruction can help students to understand mathematical concepts better, resulting in improved understanding and retention of the material (Munro, 2017). Additionally, technology can be used to implement learning activities that are more focused on problem-solving and critical thinking, which can lead to enhanced learning outcomes (Jung et al., 2017). Technology can also be used to create virtual learning environments that can provide students with an immersive learning experience. Furthermore, technology can be used to provide students with access to real-time feedback, allowing them to evaluate their ownprogress throughout the learning process. In conclusion, technology can provide numerous benefits to the field of mathematics education research, and its usage should be further explored and implemented in educational settings.

Recent research highlights the profound impact that technology has had on mathematics education research. In their work, they highlight the vast range of advantages that technology has offered to the field. Specifically, they discuss how technology has allowed for a much more efficient collection, analysis, and dissemination of data. By leveraging technology, researchers have been able to collect more data, analyze it faster and more accurately, and disseminate findings more quickly and widely. For example, using computer-assisted analysis, researchers can now analyze data in a fraction of the time it would take using traditional methods. Additionally, with the help of technology, researchers can now collect data on a much larger scale than ever before. This has enabled researchers to draw deeper and more meaningful insights from their data. Ultimately, the availability of sophisticated technology has revolutionized mathematics education research, allowing researchers to make better informed decisions and to draw more precise conclusions. (Fishback&Schlicker, 1996).

Integrating technology into mathematics education research provides numerous benefits. According to Lavicza (2010) the use of technology can help students understand mathematical concepts more easily and in a more engaging manner. With technology, students can access interactive simulations, data visualizations, and even virtual reality models to help them comprehend very complex topics. Technology also allows students to apply their knowledge in real-world settings, which often proves to be a more effective way to learn.

Additionally, technology can allow students to access resources that would otherwise be unavailable to them, such as real-time data, which can enable them to learn more in-depth about the concepts that they are studying. Moreover, technology can help students to collaborate more easily, as they can use online forums, video conferencing, and other resources to work together on projects. This can help to foster critical thinking, problem solving, and communication skills.All in all, integrating technology into mathematics education research provides many benefits, including increased engagement, access to resources, and improved collaboration. (Lavicza, 2010).

In addition, Digital technology is now a theme of concern and research for everyone (Engelbrecht et al., 2020a,b), (Borba, M.C, 2021).

B) innovative teaching methods and approaches

Another trend in mathematics education research is the development of new teaching methods and approaches. Research has shown that traditional methods of teaching mathematics are not always effective, and new approaches are being developed to improve student learning. For example, inquiry-based learning has become increasingly popular, as it encourages students to explore mathematical concepts and develop their own understanding. Additionally, problem-based learning has been used to help students develop critical thinking skills and apply their knowledge to real-world problems.

C) the impact of mathematics education on student achievement

Also, research has been conducted on the impact of mathematics education on student achievement. Studies have shown that students who receive high-quality mathematics instruction are more likely to succeed in school and beyond. Additionally, research has shown that students who are exposed to mathematics early in life are more likely to develop a positive attitude towards mathematics and be more successful in their studies.

D) Inquiry-based learning

Inquiry-based learning (IBL) in mathematics education has been gaining increasing attention as an alternative to traditional pedagogy. This teaching method is student-centered and encourages students to take a more active role in their learning. Rather than relying solely on lectures and textbook instruction, students are encouragedto explore, pose questions, and construct their own understanding of mathematical concepts. Proponents of IBL argue that it fosters students' problem-solving skills, critical thinking abilities and creative thinking processes (Dixon, 2009). Additionally, studies have demonstrated that IBL increases student engagement, motivation, and ownership of learning.

Furthermore, IBL can be an effective tool in promoting social and collaborative learning, as it encourages students to interact with their peers and take a more active role in the learning process. Despite its potential benefits, there are certain challenges associated with implementing IBL. For example, teachers may not have the necessary training or resources to effectively introduce IBL into their classrooms, and students may need additional support in order to succeed in this learning environment (Dixon, 2009). Nevertheless, the potential benefits of IBL in mathematics education far outweigh the challenges. With proper implementation and support, IBL can be an effective tool in promoting student learning and engagement in mathematics.

Inquiry-based mathematics education has been gaining momentum in recent years as a way to engage students in deeper learning and critical thinking. According to Dorier&Maass (2020) in their article in Encyclopedia of Mathematics Education, inquiry-based learning "focuses on student-centered exploration, construction of

meaning, and communication of mathematics" (Dorier&Maass, 2020). This type of learning provides students with the opportunity to construct their own understanding of mathematics, rather than passively receiving information from a teacher. Inquiry-based learning can also help to foster a sense of ownership of the material, as students are encouraged to ask questions and explore topics in a way that is meaningful to them. This type of learning encourages students to experiment with different approaches to solving problems and encourages collaboration between students as they work together to understand complex topics.

Inquiry-based learning has also been found to improve student understanding of mathematics, increase student engagement, and improve problem-solving skills (Dorier&Maass, 2020). In the long run, inquiry-based learning can help students to develop a strong foundation in mathematics and to become more confident in their ability to approach and solve complex problems.

Games and Gamification

Game-based learning has been identified as an effective tool for mathematics education research. According to Coştu, Aydın, and Filiz (2009), it can be used to provide a more engaging and interactive learning environment for students. This type of learning has been found to increase student motivation and engagement in mathematics, as well as improve problem-solving skills and understanding of mathematical concepts. Additionally, game-based learning has been shown to increase collaboration between students, which can help to foster creativity and critical thinking. Moreover, game-based learning can be used to assess student performance, as well as to provide feedback that encourages students to continue engaging with the material. Ultimately, game-based learning can provide a more effective learning environment for mathematics education research, as it can help to foster greater engagement, collaboration, and understanding of mathematical concepts. (Coştu et al., 2009).

F) Equity, diversity, and inclusion

According to Bakker et al.'s (2021) in their international survey, regarding future themes of mathematics education research, they Mentioned many cross-cutting theme, one of them is Equity, diversity, and inclusion. This triplet is used to cover any topic that highlights these and related human values such as equality, social and racial justice, social emancipation, and democracy. mathematics education should be for all students, including those who have special needs, who live in poverty, who are learning the instruction language, who have a migration background, have a traumatic or violent history, or are in whatever way marginalized. There is broad consensus that everyone should have access to high-quality mathematics education. (Bakker, et al., 2021), (Yığ, 2022)

II. CONCLUSION:

Mathematics education research has come a long way over the past few decades. New trends have emerged that are pushing the boundaries of our understanding of mathematics education, its impact on students, and how best to teach it. These newtrends can help educators to further develop evidence-based approaches toward mathematics education that enable students to become more competent mathematicians. By understanding new trends in mathematics education research, educators can make the best use of current evidence, research, and trends to make data-driven decisions that promote student success in mathematics.

The new trends in Mathematics Education Research have been incredibly successful in improving student engagement and knowledge, while also helping to strengthen the field of mathematics as a whole. With a focus

on interdisciplinary approaches, the utilization of technology and data, and the promotion of problem-solving and inquiry-based learning, these trends are transforming the way that modern education is conducted and suggesting exciting new possibilities for the future.

The new trends in Mathematics Education Research emphasize the importance of understanding how students learn, and how to create meaningful, relevant learning experiences that foster individual success. With the advent of new technologies, researchers have access to a range of tools to better understand - and improve - learning experiences in mathematics, from learning analytics to computer aided instruction. The insights gained from research can provide a greater understanding of how mathematics can be understood, and lead to more effective design of instructional materials and learning experiences for students. Ultimately, this research can help all students succeed in mathematics, and become active participants in an ever-changing global society.

Overall, Mathematics Education Research is constantly evolving to meet the changing needs of students and educators. By incorporating technology, inquiry-based learning, data-driven instruction, and the development of 21st century skills, Mathematics Education Research is helping to ensure that students are better prepared for the future. In one sentence, It's a long journey to the future not just a destination.

III.REFERENCES

[1]. Bakker, A., Cai, J. & Zenger, L. Future themes of mathematics education research: an international survey before and during the pandemic. Educ Stud Math 107, 1–24 (2021). https://doi.org/10.1007/s10649-021-10049-w

[2]. Borba, M. C. (2021). The future of mathematics education since COVID-19: Humans-with-media or humans-with-non-living-things. Educational Studies in Mathematics, 108(1), 385-400. https://doi.org/10.1007/s10649-021-10043-2

[3]. Coştu, S., Aydın, S., &Filiz, M. (2009). Students' conceptions about browser-game-based learning in mathematics education: TTNetvitamin case. Procedia-Social and Behavioral Sciences, 1(1), 1848-1852. https://doi.org/10.1016/j.sbspro.2009.01.326

[4]. Dixon, D. (2009). Nietzsche contra Caillois: Beyond play and games. https://gamephilosophy.org/wpcontent/uploads/confmanuscripts/pcg2009/Dixon%20Dan%202009%20%20Nietzsche%20contra%20Caillois%20Beyond%20Play%20and%20Games.pdf

[5]. Dorier, JL., Maass, K. (2020). Inquiry-Based Mathematics Education. In: Lerman, S. (eds) Encyclopedia of Mathematics Education. Springer, Cham. https://doi.org/10.1007/978-3-030-15789-0_176

[6]. Engelbrecht, J., Borba, M. C., Llinares, S., & Kaiser, G. (2020a). Will 2020 be remembered as the year in which education was changed? Zdm, 52(5), 821-824. https://doi.org/10.1007/s11858-020-01185-3

[7]. Engelbrecht, J., Llinares, S., &Borba, M. C. (2020b). Transformation of the mathematics classroom with the internet.Zdm, 52(5), 825-841., P., &Schlicker, 8]S. (1996). The Impact of Technology on Mathematics Education.Grand Valley Review, 14(1), 27. https://scholarworks.gvsu.edu/gvr/vol14/iss1/27

[8]. Jung, D., Lee, S. H., Kang, S. J., & Kim, J. H. (2017). Development and evaluation of a clinical simulation for new graduate nurses: A multi-site pilot study. Nurse Education Today, 49, 84–89. https://doi.org/10.1016/j.nedt.2016.11.010

[9]. Lavicza, Z. Integrating technology into mathematics teaching at the university level. ZDM Mathematics Education 42, 105–119 (2010). https://doi.org/10.1007/s11858-009-0225-1

[10]. Munro, J. (2017). Catering for the gifted: How inclusive is your school? Australian Educational Leader, 39(1), 12-16. https://search.informit.org/doi/epdf/10.3316/aeipt.215501

[11]. Yig, K. G. (2022). Research Trends in Mathematics Education: A Quantitative Content Analysis of Major Journals 2017-2021. Journal of Pedagogical Research, 6(3), 137-153.

Study of Structural and Magnetic Properties of Erbium Doped Zinc Nanoferrites (ZnEr$_x$Fe$_{2-x}$O$_4$) Using Sol-Gel Auto-Combustion Method

Kiran Gawade[1], Ramesh Bhise[2]

[1]ResearchScholar, Department of Physics, PDEA's Anaasaheb Magar Arts, Commerce and Science College, Hadapsar, Pune-28, Maharashtra, India

[2]Nanomaterial Research Laboratory, Department of Physics, B. J. College, Ale, Pune-412411, Maharashtra, India

Abstract :

The study presents a systematic report on Er^{3+} doped zinc ferrite (ZnEr$_x$Fe$_{2-x}$O$_4$) and their properties for different values of x (0.1 and 0.125). The study utilized a characterization technique such as X-ray diffraction (XRD), Vibrating sample technique (VSM).The study determined various parameters, such as x-ray density, lattice constant, crystallite size, d-spacing, microstrain, dislocation density. An increase in Er^{3+} content resulted in an expansion of lattice parameters and a reduction in crystallite size from (11.34 nm to 10.54 nm). Due to particle size dependency, magnetic measurements showed that doping reduced magnetism. Overall, this study provides valuable insights into the magnetic properties and structural characteristics of Er^{3+} doped zinc ferrite nanomaterials.

Keywords: Spinel ferrite, Sol-gel method, X-ray diffraction (XRD), Vibrating Sample Magnetometer (VSM), etc…

I. INTRODUCTION

The development of nanostructured materials is crucial for creating nanodevices due to their superior physical and chemical properties compared to bulk materials. When materials are reduced to the nanometer scale, their properties change significantly because of the increased surface area per unit volume. Transition metal oxide-based soft magnetic nanoferrites are particularly important in research for their role in understanding nanomagnetism and their suitability for advanced technologies[1].The study of metal-oxide nanocrystals, particularly spinel ferrites at the nanoscale, is attractive due to the distinct optical, magnetic, and electrical properties. Such ferrites find applications in high-density magnetic data storage, microwave absorbing materials, MRI contrast agents, and targeted drug delivery systems.[2].Scientists have point of attention mainly on spinel ferrites because of wide range of properties like, electronic, magnetic, optical etc like, low dielectric constant with high magnetic loss. These effective properties make them useful in both simple as well as complicated devices in the field of energy storage, having formula MFe2O4, where M will be divalent cation (Fe^{2+}, Ni^{2+},Cu^{2+}, Zn^{2+}, Co^{2+}, Mg^{2+}, Cd^{2+}etc). The different effective properties of spinel ferrite are mainly depending on the location of cations in tetrahedral and octahedral site of crystal structure.Due to this characteristic, it finds a

wide variety of uses, including in electronics, radio frequency circuits, non-resonant devices, information storage systems, transformer cores, magnetic and refrigeration systems, magnetic hyperthermia, magnetic field-assisted drug delivery, gas sensors, magnetic recording media, and magnetic resonance imaging[3-6].Particle size reduces with enhance of Er concentration (x = 0 to 0.8) in the compounds[7].$ZnFe_2O_4$ stands out among various transition metal spinel ferrite nanoparticles because of its significant properties, including high electrical resistivity, mechanical hardness, exceptional chemical and thermal stability, and distinctive magnetic and dielectric characteristics [8-10]. Number of methods are developed for the preparation of nano ferrite such as, colloidal method [11], sol-gel auto combustion method [12] etc. From all these techniques sol-gel auto combustion method is simplest and low-cost method for obtaining nanoferrites[11-12].

In present work, the $ZnEr_xFe_{2-x}O_4$ was synthesized by sol-gel auto combustion method with varying Er^{3+} concentration, for improvement of crystalline phase of materials that was the prepared samples were sintered at temperature 550^0 C for 2.5 hr. The size of crystallite is decreasing with enhancement of erbium concentration.The magnetic properties of the samples were analysed using a Vibrating Sample Magnetometer (VSM).

II. EXPERIMENTAL:

Erbium doped zinc ferrite was synthesized using the sol-gel auto-combustion method for x=0.1 and x=0.125. The chemicals like zinc nitrate hexahydrate (AR grade), Erbium nitrate (AR grade), ferric nitrate (AR grade) and citric acid were dissolved in 100 ml of distilled water as a solvent. The pH was adjusted to 7 by using amino acids drop by drop with continuous stirring at room temperature to create sol. which was then heated to 80 ◦C, resulting in the formation of a wet gel. The gel was subjected to drying at 200 ◦C, leading to self-ignition and the formation of a fluffy product, which was further ground into a fine powder. The prepared sample were heated at 500 ◦C for 2.5 hr.

III.RESULTS AND DISCUSSIONS:

3.1 X- Ray diffraction study (XRD):

X-ray powder diffraction (XRPD) profiles of the $ZnEr_xFe_{2-x}O_4$ (with x = 0.1, 0.125) compounds were shown in the Fig. 1. Every sample had clearly defined peaks in their profiles, indicating that every compound had a good crystallization. The optimal index for the profile peaks would be cubic spinel ferrite. The profile peaks, however, were widely spaced. It suggests that nano crystallites were present in the samples. With space group $Fd\bar{3}m$, the bulk $ZnFe_2O_4$ compound crystallizes in a cubic spinel shape [2]. Additionally, the profiles of $ZnEr_xFe_{2-x}O_4$ compounds were best indexed to $Fd\bar{3}m$ (JCPDS NO. 89 - 4926).
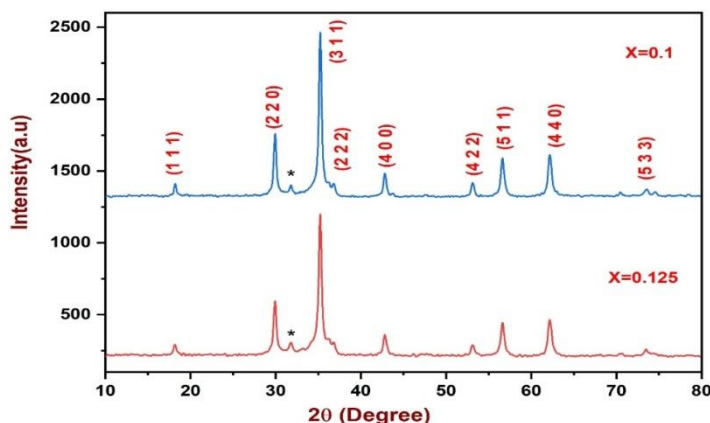
Figure 1: - XRD of sample ZnEr$_x$Fe$_{2-x}$O$_4$ nanoferrites

For each substance, the lattice parameter (a) of a cubic spinel structure was determined using

$$a = [d^2(h^2 + K^2 + l^2)]^{\frac{1}{2}} \qquad (1)$$

Where, d is the interplanar distance (d - spacing) and (h k l) are the Miller indices of the diffraction plane in the crystal. The lattice parameter was found to enhance from 8.4398 to 8.4425 Å almost linearly with Er^{3+}concentration.The crystallite diameters (D) of the ZnFe$_{2-x}$Er$_x$O$_4$ compounds were estimated from the FWHM value for all prominent peaks using the Scherrer equation.

$$D_{hkl} = \frac{k\lambda}{\beta_{hkl}\cos\theta} \qquad (2)$$

Where, K-Scherrer constant (K=0.94), β_{hkl} is FWHM Value, θ is Bragg's diffraction angle.

To obtain D, the D_{hkl} values were averaged after being calculated for each of the (h k l) peaks. The average D is reduced from 11.3422 to 10.5455 as we increase the Er^{3+} concentration.The X-ray density slightly increases with enhancing of substituent Er^{3+} concentration as listed in Table 1.

Table-1: - Characterization of ZnEr$_x$Fe$_{2-x}$O$_4$ nanoferrites: Insights from d-spacing, crystallite size, lattice constant, X-ray density, Micro strain, and dislocation density

Composition (x)	2θ	d-Spacing (A⁰)	Crystallite size (nm)	Lattice constant (A⁰)	X-ray Density (gm/cm³)	Micro strain	Dislocation density
0.1	35.23	2.5454	11.3422	8.4398	5.5751	0.00284	0.02550
0.125	35.21	2.5462	10.5455	8.4425	5.6313	0.00309	0.02985

3.2 Vibration Sample Magnetometer (VSM):

The fluctuation in the size of nanoparticles has a significant impact on the magnetic properties such as magnetic saturation (M$_s$), magnetic remanence (M$_r$), and magnetic coercivity (H$_c$) [1]. As shown in table 2. Figure-2shows the variation in magnetic properties with enhancement of Er^{3+}magnetic Remanence (Mr) and Magnetic Saturation (M$_s$) decreases with the increase of doping of Er^{3+}, and Magnetic Coercivity (H$_c$) increases with the increase of doping of Er^{3+} as shown in Table 2.The magnetic property of the samples confirmed that the prepared sample is magnetic in nature studied by, magnetic Remanence (M$_r$), Magnetic Coercivity (H$_c$) and

Magnetic Saturation (M_s) which are highly depends on the variation in the size of nano ferrites with varying solvent.

X=0.1

X=0.125
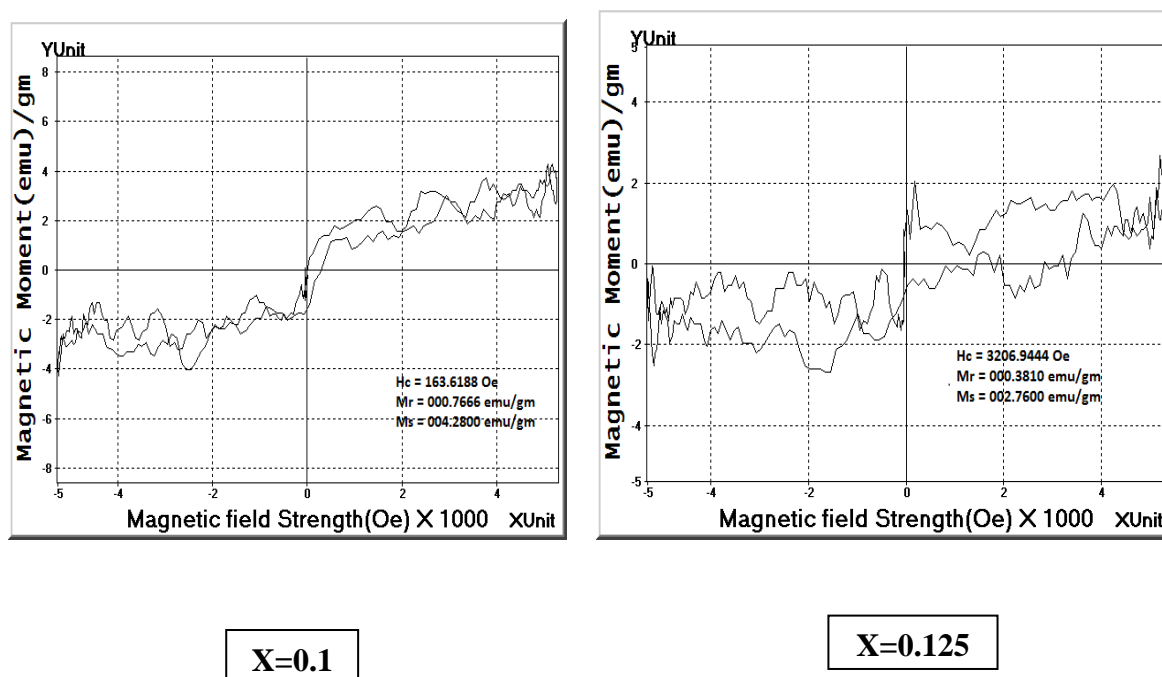
Figure-2: Vibration Sample Magneto spectra (VSM) of $ZnEr_xFe_{2-x}O_4$ nanoferrites

Table-2: Values of saturation magnetization (Ms), Magnetic remenance (Mr), Magnetic Coercivity (Hc)

Composition (x)	Magnetic Coercivity (Hc)Oe	Magnetic Saturation (Ms)emu/gm	magnetic Remanence (Mr)emu/gm
0.1	163.6188	4.2800	0.7666
0.125	3206.9444	2.7600	0.3810

IV.CONCLUSION:

Er^{3+} doped zinc ferrite with chemical formula $ZnEr_xFe_{2-x}O_4$was synthesized by sol-gel auto combustion method. The prepared powder of Er^{3+} doped zinc ferrite was sintered at 550^0 C for 2.5 hrs. for obtain good crystalline phase. The XRD pattern confirmed the formation of single phase with cubic spinel ferrite structure. Cryastallite size was calculated by Debye-Scherrer formula. Which shows variation in size with enhancement of doping concentration of Er^{3+}. The magnetic property of the samples confirmed that the prepared sample is magnetic in nature studied by, magnetic Remanence (Mr), Magnetic Coercivity (Hc) and Magnetic Saturation (Ms), which are depends on variation in doping concentration.

V. REFERENCES:

[1]. Vyankati Rama Jadhav, Ramesh Bhise, (2024), "*Study of structural, optical, morphology and magnetic properties of samarium doped magnesium nanoferrites (MgSmxFe2-xO4) using sol-gel auto-combustion method*",*Solid State Sciences*, Vol-13.

[2]. Qing Li, Christina W. Kartikowati, Shinji Horie, Takashi Ogi, Toru Iwaki and Kikuo Okuyama, (2017), "*Correlation between particle size/ domain structure and magnetic properties of highly crystalline Fe3O4 nanoparticles*", Scientific Reports, Vol-7, p9894

[3]. M. Shoba, S. K., (2017),"*Structural, optical and dielectric studies of Er substituted zinc ferrite nanospheres*",Journal of Physics and Chemistry of Solids, Vol-39.

[4]. N. Sharma, P. Aghamkar, S. Kumar, M. Bansal, Anju, R.P. Tondon, (2014),"*Study ofstructural and magnetic properties of Nd doped zinc ferrites",* J. Magn. Magn. Mater., Vol-369,p162–167

[5]. Y. Köseoğlu, (2013), "*Structural, magnetic, electrical and dielectric properties of MnxNi1-xFe2O4 spinel nanoferrites prepared by PEG assisted hydrothermal method*", Ceram. Int., Vol-39, p4221–4230.

[6]. E.Ranjith Kumar, P.S.P. Reddy, G.S. Devi, (2016), "Structural and Gas Sensing Properties of Mn Substituted ZnFe2O4 Nanoparticles by Auto Combustion and Evaporation Method", J. Adv. Phys., Vol-5,p230–235.

[7]. P. Bala Sundari, E. Ranjith Kumar, S. Ramya and A.S. Kamzin, (2017), "*Structural, Dielectric and Gas Sensing Properties of Mn-Ni Ferrite Nanoparticles*", Recent Trends Mater. Sci. Appl.,Springer International Publishing, p135–143.

[8]. Y. Zhang, Q. Shi, J. Schliesser, B.F. Woodfield, Z. Nan, (2014), "*Magnetic and thermodynamic properties of nanosized Zn ferrite with normal spinal structure synthesized using a facile method*", Inorg. Chem. Vol-53,p10463–10470.

[9]. R. RaeisiShahraki, M. Ebrahimi, S. a. Seyyed Ebrahimi, S.M. Masoudpanah, (2012), "*Structural characterization and magnetic properties of superparamagnetic zinc ferrite nanoparticles synthesized by the coprecipitation method*", J. Magn. Magn. Mater. Vol-324, p3762–3765.

[10]. N. Wiriya, A. Bootchanont, S. Maensiri, E. Swatsitang, (2014), "*Magnetic properties of Zn1–xMnxFe2O4 nanoparticles prepared by hydrothermal method*", Microelectron. Eng. Vol-126, p1–8.

[11]. Mohamed S. A. Darwish, Hohyeon Kim, Hwangjae Lee, Chiseon Ryu, Jae Young Lee and Jungwon Yoon, (2019), "*Synthesis of Magnetic Ferrite Nanoparticles with High Hyperthermia Performance via a Controlled Co-Precipitation Method*", Nanomaterials, Vol-9,p1176 13)

[12]. V.R. Bhagwat, Ashok V. Humbe, S.D. More, K.M. Jadhav, (2019),"*Sol-gel auto combustion synthesis and characterizations of cobalt ferrite nanoparticles: Different fuels approach*", Materials Science& Engineering B, Vol-248, p114388

Crystallographic and Permeability Studies Of Ni-Cu Ferrite

J. M. Bhandari[1*], R. G. Vidhate[2], R. B. Kavade[3], K. M. Jadhav[4]

[1] Department of Physics, A. J. V. P. M's Gandhi College Kada, Tal - Ashti, Dist.-Beed, Maharashtra, India

[2] Departments of Physics, A. D. College Kada, Tal - Ashti, Dist.- Beed, Maharashtra, India

[3] Department of Physics, Bhagwan Mahavidyalaya, Ashti, Dist.- Beed, Maharashtra, India

[4] Emeritus Professor (Physics), MGM University, Chhatrapati Sambhajinagar, Maharashtra, India

Abstract :

Polycrystalline soft spinel ferrite samples having the general chemical formula $Ni_{1-x}Cu_xFe_2O_4$ (with x = 0.0, 0.4 and 0.8) have been prepared by standard ceramic technique. The formation of single-phase cubic spinel structure of all the samples was characterized by X-ray diffraction technique. The values of lattice constant determined from XRD data found to increase as copper content x obeying Vegard's Law. IR spectra illustrate the presence of two absorption bands which is the characteristics of a spinel ferrite. Initial permeability μi was measure and it is found that μi increases with Cu substitution. Curie temperature measured through permeability versus temperature plot.

Keywords: X-ray diffraction, IR Spectroscopy, Initial Permeability, Curie temperature.

I. INTRODUCTION

In recent year, the magnetic mixed oxides with iron oxide as their main component, namely spinel ferrites, having the formula MFe_2O_4 have been investigated extensively by many workers because of their potential application in magnetic recording, microwave devices, transformers, drug delivery. Due to their remarkable electrical and magnetic properties they are used in many technological applications [1]. Spinel ferrites are commercially important materials because of their excellent electrical and magnetic properties. Interesting physical and chemical properties of ferrites arises from ability of these compounds to distribute cations amongst the available tetrahedral (A) site and octahedral [B] site and magnetic A-A, B-B and A-B interactions. Ferrites are generally classified into two groups, hard ferrites and soft-ferrites. Ferrites for which coercive field is small are termed as soft ferrites. Polycrystalline ferrites which have many applications in microwave frequencies are very good dielectric materials. The basic structural and magnetic properties of spinel ferrite are depending upon several factors such as method of preparation, preparative parameters and preparative conditions, nature, type and amount of dopant [2-6].

Extrinsic property such as permeability losses even depend on microstructure as well as sintering condition [7]. Among the spinel ferrites, the inverse type is particularly interesting due to its high magneto-crystalline anisotropy, high saturation magnetization, and unique magnetic structure. Nickel ferrite ($NiFe_2O_4$) is an inverse spinel with cubic structure shows ferrimagnetism that originates from magnetic moment of anti-parallel

spins between Fe3+ ions at tetrahedral sites and Ni2+ ions at octahedral sites [8]. Spinel ferrites are important in several applications, hence studies of structural, electrical, magnetic and other properties of spinel ferrites are very essential [9, 10]. The interest in these materials is sustained till date because of their applications in the field of drug delivery, multilayer chips, magnetic recording, sensors, catalysts, etc. [11- 13].

The substitution of divalent, trivalent and tetravalent ions in spinel ferrites leads to diversification in various properties. The properties of spinel ferrites can be modified by substituting the various kinds of cations. In the literature, many reports are available on the structural, electrical and magnetic properties of Zn, Cd, Al, Cr, Ti, Mn substituted spinel ferrites [14, 15].

Nickel ferrites (NiFe2O4) and substituted nickel ferrites have been the subject of extensive investigation because of their high-frequency application. Copper ferrite (CuFe2O4) is a distinguished among other spinel ferrites by fact that it under goes structural phase transition accompanied by reduction crystal symmetry to tetragonal due to cooperative Jahn-Teller effect. However, there are differences about the phase transition temperature of copper ferrite [16, 17]. Copper ferrite is random spinel ferrite and possesses tetragonal structure. Both nickel and copper ferrite are important from the point of view of their applications. Abnormal thermal, magnetic and dielectric properties of Cu-containing ferrite have been reported [18, 19].

In the present work we report our results on crystallographic structure and initial permeability of mixed Nickel-Copper spinel ferrite.

II. EXPERIMENTAL TECHNIQUE

A series of polycrystalline spinel ferrites of the chemical composition Ni1-xCuxFe2O4 (x = 0.0, 0.4 and 0.8) were prepared using the standard ceramic method. A.R. grade NiO, CuO and Fe2O3 oxides in appropriate molar proportions were used for the preparation of ferrite. The compositions of these ferrites are shown in Table 1. The oxides were mixed thoroughly and wet ground by using an agate mortar. First pre-sintering of powder was carried out at 1225K for 12 hr followed by a slow cooling. The sintered powder is again reground and sintered at 1375K for 12 hr. To measure the initial permeability toroids of outer diameter 2 cm and inner diameter 1 cm are prepared. The prepared samples were characterized by X-ray powder diffractometer (model PW 3710) using Cu-Kα radiation (λ = 1.5405Å) in the 2θ range 200-800.

Table 1 Chemical composition of various components of Ni1-xCuxFe2O4 system in mole percentage.

Composition X	NiO	CuO	Fe2O3
0	50	00	50
0.4	30	20	50
0.8	10	40	50

The initial permeability as a function of temperature was measured for 1 KHz frequency. Toroidal cores were used for the inductances measurements because the toroidal core can provide potentially the greatest band width since it has no residual gap and proper winding gives minimal leakage inductance.

III.RESULTS AND DISCUSSION

The structural characterization of all the samples of spinel ferrite system Ni1-xCuxFe2O4 was carried out using X-ray diffraction technique. Results indicate that these oxides crystalline with a single spinel cubic structure.
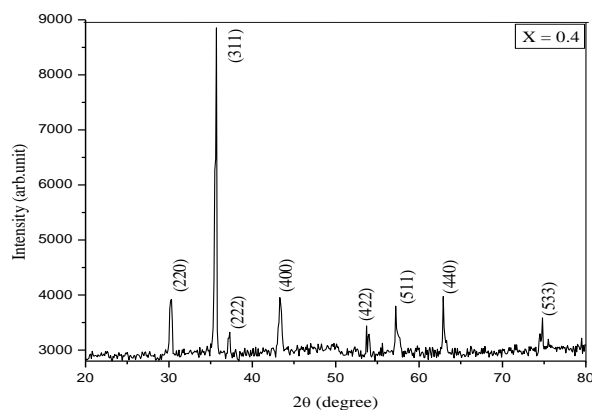
Fig. 1: XRD patterns of Ni1-xCuxFe2O4 for x = 0.4

Fig.1 shows the typical X-ray diffraction (XRD) pattern of Ni1-xCuxFe2O4 (for x = 0.4) spinel ferrite system. The XRD patterns indicates that all the composition exhibits single phase cubic spinel structure and exclude the presence of any secondary phase. The Braggs reflection observed in XRD pattern are intense and sharp. The XRD pattern shows the reflections (220), (311), (222), (400), (422), (511), (440) and (533) belonging to cubic spinel structure. The analysis of XRD pattern reveals the formation of single-phase cubic spinel structure. No extra peak has been detected in the XRD pattern.
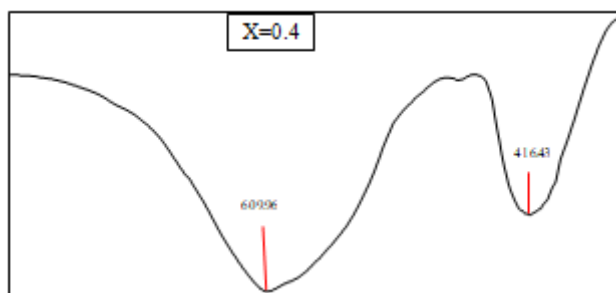
Fig.2 IR spectra of Ni1-xCuxFe2O4 for x = 0.4

IR spectra show typical absorption bands indicating the ferrite nature of the samples. The band positions obtained from IR spectra are given in Table-2. The vibrational frequency depends upon the cation mass, cation oxygen bonding force, distance etc. From IR spectra, it is revealed that, a broad band appears at around 400 cm-1 and 600 cm-1, assignable to the stretching mode of the tetrahedral in the Ni-Cu spinel ferrite and this indicates that the crystallization of samples is more complete [20-22]. Our results on IR studies are in good agreement with the literature reports [23].

Table 2 Vibrational band frequencies (n1, n2) of Ni1-xCuxFe2O4 for x = 0.4

Composition X	ν_1 (cm^{-1})	ν_2 (cm^{-1})
0	609.96	416.43
0.4	607.45	414.77
0.8	583.55	401.32

The initial permeability (µi) was obtained by measuring inductance of the toroid using LCR-Q meter and was calculated using the following relation.

$$L = 0.0046 N^2 h \mu_i Log_{10}\left(\frac{d_2}{d_1}\right)$$

Wher d_2 is the outer diameter,
            d_1 is the inner diameter,
            L   is inductance in micro-Henry,
            h   is the height in inches,
            μ_i is initial permeability and
            N   is number of turns of wire.

The variation of permeability µi was measured as a function of temperature. The plot of permeability versus temperature for typical sample x = 0.4 is shown in Fig. 3. It is observed from permeability versus temperature plot that permeability increases slowly as temperature increases and attains a maximum value. Thereafter, permeability suddenly falls down. The curve exhibits tailing effect. Using these plots Curie temperature of all the samples was also obtained.
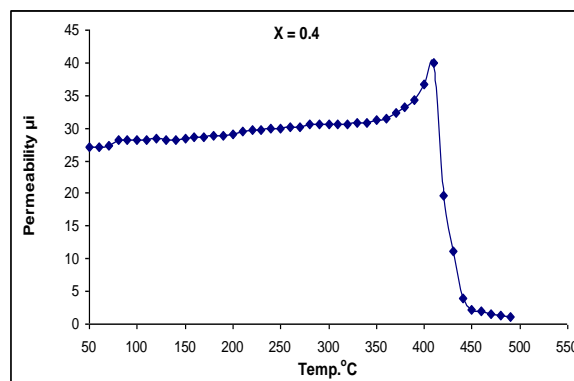
Figure 3: Permeability versus temperature plot.

The values of initial permeability for all the samples were calculated and the values are presented in table 3. It can be seen from table 3 that initial permeability increases with copper substitution.

Table 3 Curie temperature (TC) and initial permeability (µi).

Composition X	µi	TC (K)
0.0	24.38	823
0.4	28.55	753
0.8	42.86	693

Similar variation in permeability with composition was observed in another well-known spinel ferrite [24].

IV. CONCLUSIONS

The single-phase nature of all the samples of Ni-Cu spinel ferrite was confirmed by X-ray diffraction analysis. IR spectra illustrate the presence of two absorption bands located near 400 cm-1 and 600 cm-1 which is the

characteristics of a spinel ferrite. Curie temperature obtained using permeability data. The initial permeability values are affected much by copper substitution.

V. REFERENCES:

[1]. Jan Smith: "Magnetic Properties of Materials" Mc raw-Hill Book Company, New York (1971).

[2]. Souad Ammar, Arnaud Helfel: J. Mater. Chem 11 (2001) 186.

[3]. I. M. Hamada: J. Magn. Magn. Mater. 271 (2004) 318.

[4]. B.P. Ladgoankar, C. B.Kolekar, P. N. Vasamberkar and A. S. Vaingankar: Ind. J. Eng. Matt. Sci. 7 (2000) 419.

[5]. A. M. Varaprasad and C.M. Radhakrishnamurthy: Bull Mat. Sci 8 (1986) 567.

[6]. K Sailakshmi, Ph.D. Thesis, Andhra University India (1997).

[7]. R.V. Mangalaraja, S. Thomas Lee, S. Ananthakumar, P. Manohar, Carlos P. Camurri: Mater. Sci. Engg. A 476 (2008) 234.

[8]. C.N. Chinnasamya, A. Narayanasamya, N. Ponpandiana, R.J. Joseyphusa, B. Jeyadevan, K. Tohjib, K. Chattopadhyay: J. Magn. Magn. Mater. 238 (2002) 281.

[9]. L. John Berchmans, R. Kalai Selvan, P.N. Selva Kumar, C.O. Augustin: J. Magn. Magn. Mater. 279 (2004)103.

[10]. F. Novelo, R. Valenzuela: J. Mater. Res. Bull. 30 (1995) 335.

[11]. S. Nishigaki, S.Yano, H. Kato, T. Nano- Mura, : J. Am-Cerm. Soc. 71 (1) (1988).

[12]. P. K. Roy, J. Bera, J. Magn.Magn. Mater, 321 (2009) 247.

[13]. T.Nakamura. J.Magn. Magn. Mater. 168 (1997) 285.

[14]. S. P. Jadhav, B. G. Toksha, K. M. Jadhav, N. D. Shinde, Chinese J. of Chem. Phys. Vol. 23, (4), 2010.

[15]. M. A. Gabal, Y.M. Al Angari, J. of Magn.Magn. Mater. 322(2010) 3159–3165.

[16]. J. L.Snock: Phy. 14 (1948) 207.

[17]. L. A. Davidov, S. A. Paltinnokov, M. F. Bryzhin: Sov. Phy.Solid State 7 (1965) 596.

[18]. J.Z. Jiang, G.F. Goya, H.R. Rechenberg: J. Phys. Condens. Mat. 11 (1999) 4063.

[19]. G.F. Goya, H.R. Rechenberg: Nanostruct. Mater. 10 (1998) 1001.

[20]. A. M, Hotmeister, K. R. Campbell, J. Appl. Phys. 72(1992) 638.

[21]. M. Ristic, I. Nowik, S. Popovic, I. Felner, S. Music, J. Mater. Lett.57 (2003) 2584.

[22]. Zhongjun Cheng, Hua Yang, Lianxiang Yu, Yuming Cui, ShoouhuaFeng, J. Magn. Magn.Mater.302(2006) 259.

[23]. A. Kenneth, Wickersheim,J. Appl. Phys. 32(1961)205S.

[24]. S.T. Mahmud, A.K.M. Akther Hossain, A.K.M. Abdul Hakim, M. Seki, T. Kawai, H. Tabata, J.

[25]. Magn. Magn. Mater. 305 (2006) 269.

Influence of Rare earth (Gd3+) doped on Structural and Magnetic studies of Cobalt Ferrite

P. K. Gaikwad[1], V. S. Shinde[2]

[1]Department of Physics, Shri Chhatrapati Shivaji College, Omerga – 413606, Maharashtra, India

[2]Department of Chemistry, Shri Chhatrapati Shivaji College, Omerga – 413606, Maharashtra, India

drpkgaikwad@gmail.com

Abstract :

The Gd3+ doped Cobalt ferrite having molecular formula $CoFe_{2-x}Gd_xO_4$ (x = 0.00 and 0.10) samples have been prepared by standard ceramic technique. The structural and magnetic properties were investigated by X-ray diffraction technique and Pulse field hysteresis loop tracer techniques respectively. The X-ray diffraction data shows single phase cubic spinel structure for x=0.00 sample where as an extra peak of Gd3+ is observed in x=0.10 sample. The structural parameters lattice constant a (Å), X-ray density is higher for Gd3+ doped cobalt ferrite sample than that of pure cobalt ferrite due to large ionic radii (0.94nm) of Gd3+ replacing Fe3+ (0.64 nm). The particle size obtained from scherrer formula is in ⌷m range. The room temperature Pulse field hysteresis loop tracer technique is used to determine the magnetic properties of Gd3+ doped cobalt ferrite. The saturation magnetization (Ms), remanence magnetization (Mr) and coercivity decreases with Gd3+ doped cobalt ferrite.

Keywords: Cobalt ferrite, rare earth, X-ray diffraction, Magnetic properties etc

I. INTRODUCTION

Spinel ferrites have many versatile electric and magnetic properties owing to its feasibility to make a huge number of solid solutions of different metal cations and a large compositional variability [1]. In the family of spinel ferrites cobalt ferrite ($CoFe_2O_4$) is a unique ferrite having inverse spinel structure. Cobalt ferrite is a hard magnetic material possessing high magneto anisotropy, high Curie temperature, high corecivity and moderate saturation magnetization along with the chemical stability and mechanical hardness [2]. As the crystal structure of spinel ferrite is cubic closed pack (fcc) with anions (O^{2-}) linked with two sub-lattices namely tetrahedral (A) and octahedral (B). Distribution of divalent and trivalent cations on the A and B sites imparts specific characteristics to a spinel structure. $CoFe_2O_4$ is known as partially inverse spinel with ferromagnetic behavior having a high specific resistance and low eddy current losses in high frequency applications [3]. These exceptional physical properties can be achieved by choosing the method of synthesis, doping of cation in the host crystal structure, size and morphology of the particles. Several researchers have studied pure and substituted cobalt ferrite with a view to understand their basic properties [4]. These studies revealed that doped of non-magnetic cations in cobalt ferrite predominantly affects the magnetic as well as electrical properties compared to magnetic cations. Many researchers have studied the role of rare earth doped in the pure $CoFe_2O_4$

matrix in order to improve the electrical and magnetic properties of spinel ferrites rare earth ions like Dy^{3+}, Sm^{3+}, Ho^{3+}, Nd^{3+} and La^{3+}. It was reported that rare earth ion doped lead to the structural distortion and improvement in the electrical and magnetic properties. Rare earth ions are known to have unpaired 4f electrons and strong spin orbit coupling of angular momentum [5-8]. The doped of rare earth ion may lead to the interaction of the type 3d-4f coupling which may result in modification of the electrical and magnetic properties but to the best of our knowledge no systematic report is available in the literature showing the effect of Gd^{3+} ions in the pure $CoFe_2O_4$ matrix using standard ceramic technique. In the present work we have focused to correlate the understandings between structural and magnetic properties of Gd^{3+} doped cobalt ferrites having molecular formula $CoFe_{2-x}Gd_xO_4$ (x = 0.00 and 0.10). Recent research shows by introducing rare earth ions into the spinel lattice, can lead to small changes in the structural, magnetization and Curie temperature of the spinel ferrite.

II. EXPERIMENTAL DETAILS

Polycrystalline specimens of $CoGd_xFe_{2-x}O_4$ (x = 0.00 and 0.10) were prepared by standard ceramic technique [9] using analytical reagent grade oxides compounds were accurately weighed in molecular weight percentage with a single pan microbalance. The mixed powders were wet ground and pre-sintered at 950^0 C for 24 hours. The sintered powder is again re-ground and pelletized. Polyvinyl alcohol was used as a binder in making circular pellets of 10mm diameter and 2–3mm thickness. The pellets were finally sintered in muffle furnace for 1180^0 C for 24 hours and then slowly cooled to the room temperature. X-Ray diffraction patterns were taken at room temperature to confirm the crystal structure of the prepared samples. The XRD patterns were recorded in the 2θ range from 20^0 to 80^0 using Cu-kα radiation (λ = 1.5406 Å) with scanning rate 1^0 per/m. The magnetic properties were studied using pulse field hysteresis loop technique at room temperature. Curie temperature of the sample was determined through a. c. susceptibility technique, instrument supplied by Magenta Company (Mumbai).

III.RESULT AND DISCUSSION

Structural Analysis:
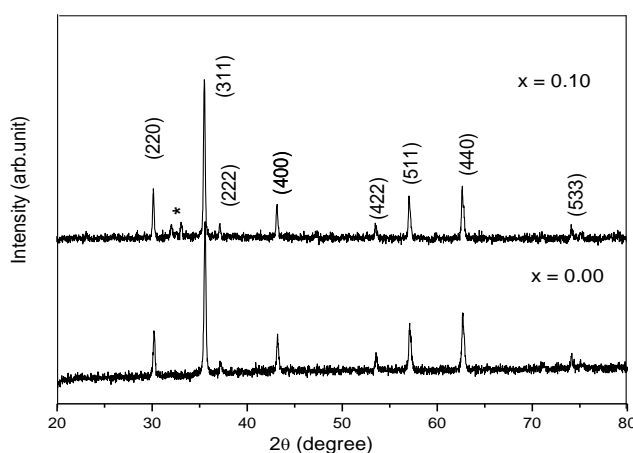
Fig 1 XRD patterns of $CoFe_{2-x}Gd_xO_4$. (x = 0.00 and 0.10)

Room temperature X-ray powder diffraction patterns (XRD) for series having molecular formula $CoFe_{2-x}Gd_xO_4$ (x=0.00 and 0.10) synthesized by standard ceramic method are shown in Fig 1. The X-ray diffraction patterns show the formation of cubic spinel structures, with the appearance of characteristic peaks representing rare earth Gd^{3+} based secondary phases in the compositions with of Gd^{3+} showing disordered structure. The value of lattice parameter for the doped and un-doped Gd^{3+} in cobalt ferrite samples was computed using the d spacing values and the respective hkl parameters and values are given in Table 1.

TABLE 1. Lattice constant (a), Particle size (t), X- ray density (dx), bulk density (dB), and Porosity (P) of $CoFe_{2-x}Gd_xO_4$.					
X	A	T (Å)	Dx (gm/cm³)	dB (gm/cm³)	P (%)
0.00	8.38	293.67	5.30	3.87	27.17
0.10	8.39	398.34	5.47	4.20	23.71

Table 1 shows that the variation of lattice constant 'a' with Gd^{3+} doped (x=0.10). The lattice parameter 'a' increases with a Gd^{3+} doped (x=0.10) due to large ionic radii of Gd^{3+} (0.94 Å) replacing Fe^{3+} (0.67 Å). The similar results were reported in literature [10]. The X-ray density (d_x) was calculated using the equation

$$d_x = \frac{ZM}{N_a a^3} \qquad \qquad \dots(1)$$

Where 'Z' is number of molecules per unit cell. (For spinel system Z= 8), 'M' is the molar mass of the ferrite, 'N_a' is the Avogadro's number and 'a^3' is the unit cell volume computed from the values of lattice constant. X-ray density (dx) increases almost linearly with the substation of Gd^{3+} because the Fe^{3+} ions on the octahedral sites are being replaced by the larger mass Gd^{3+} ions. The value of dx is dependent on the molar mass of the synthesized compounds and the lattice parameter 'a'. The variation of X-ray density with Dy^{3+} doped (x=0.10) is depicted in Table 1 and it is observed that X-ray density increases even though lattice constant increases because mass over takes the volume. The bulk density of the samples was measured by using Archimedes principle [11]. The porosity of the samples was calculated by using the relation and values are tabulated in Table 1. It is observed that the porosity decreases with doped of Gd^{3+}. The particle size 't' of sample was determined by most intense peak (311) by using the relation

$$t = \frac{0.9\lambda}{\beta \cos\theta} \qquad \qquad \dots(2)$$

Where β the full width at half maximum (FWHM) and λ is wavelength of the target material. The particle size values are given in Table 1.

TABLE 2. Tetrahedral bond (d_{AX}), octahedral bond (d_{BX}), tetra edge (d_{AXE}) and octa edge (d_{BXC}) of $CoFe_{2-x}Gd_xO_4$.					
X	d_{AX} (Å)	d_{BX} (Å)	d_{AXE} (Å)	D_{BXE} (Å) (Shared)	(Unshared)
0.00	1.38	2.05	3.10	2.82	2.96
0.10	1.39	2.06	3.11	2.83	2.97

The values of the tetrahedral and octahedral bondlength (d_{AX} and d_{BX}), the tetrahedral edge (d_{AXE}), and the shared and unshared octahedral edge (d_{BEX} and d_{BXEU}) can be calculated according Eqs (3) ~ (7). Using the value of the lattice parameter 'a' (Å) and the oxygen position parameter 'u' (u=0.381 Å). The value of the bondlength of the tetrahedral and octahedral sites are shown in Table 2, It is seen that the all values are depend on the lattice parameter so, the lattice parameter increases, then the edge and the bondlength of the tetrahedral and octahedral sites are also increases.

$$d_{AX} = a\sqrt{3}\left(u - \frac{1}{4}\right) \qquad \ldots(3)$$

$$d_{BX} = a\left[3u^2 - \left(\frac{11}{4}\right)u + \left(\frac{43}{64}\right)\right]^{\frac{1}{2}} \qquad \ldots(4)$$

$$d_{AXE} = a\sqrt{2}\left(2u - \frac{1}{2}\right) \qquad \ldots(5)$$

$$d_{BAX} = a\sqrt{2}\left(1 - 2u\right) \qquad \ldots(6)$$

$$d_{BXEU} = a\left[4u^2 - 3u + \left(\frac{11}{16}\right)\right]^{\frac{1}{2}} \qquad \ldots(7)$$

The distance between magnetic ions (hopping length) in the tetrahedral sites is given by Eqs (8) ~(9).

$$L_A = \frac{a\sqrt{3}}{4} \qquad \ldots(8)$$

$$L_B = \frac{a\sqrt{2}}{4} \qquad \ldots(9)$$

where 'a' is the lattice constant, the value Hopping length (L_A, L_B) are shown in Fig 2, Hopping length (L_A, L_B) values are depend on the lattice parameter so, the lattice parameter increases so the Hopping length (L_A, L_B) also increases.
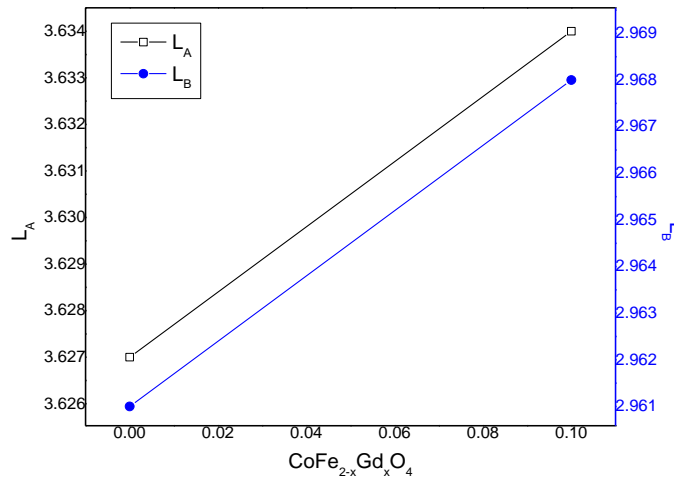
Fig 2 . Hopping length (L_A, L_B) of $CoFe_{2-x}Gd_xO_4$(x = 0.00 and 0.10)

Magnetization:
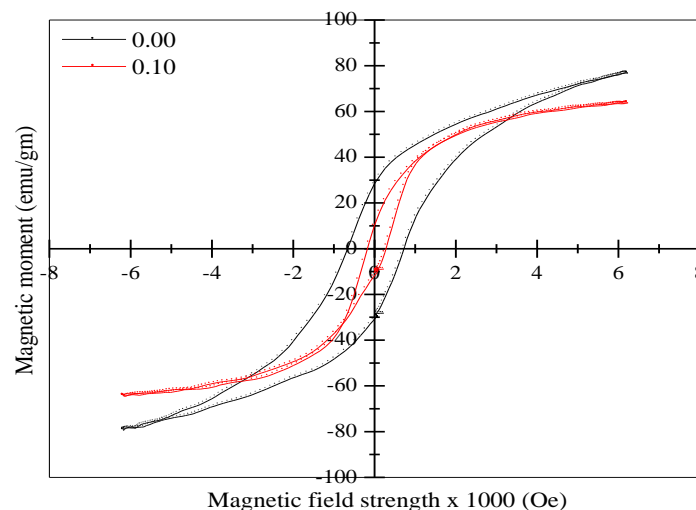
Fig 3 Hysteresis loop of CoFe$_{2-x}$Gd$_x$O$_4$(x = 0.00 and 0.10)

Fig 3 depicts the magnetic hysteresis loop (M-H) of all the samples obtained by pulse field hysteresis loop tracer at room temperature. The hysteresis loops are used to obtain magnetic parameters like saturation magnetization and coercivity. It is observed from M-H loop that magnetization decreases with doped of Gd^{3+}. Magnetization found to decrease with doped of Gd^{3+}. Due to the dilution of magnetization at B-site by replacing Fe^{3+} ions by Gd^{3+} ions as evident from cation distribution analysis. It is observed that the decreasing trend with doped of Gd^{3+}ions have a higher magnetic moment (7 µB) in place of Fe^{3+} that has (5 µB). The order in magnetic moments of rare earth ions is below room temperature, due to this at room temperature Gd^{3+}ion behaves as non-magnetic that cause a decrease in saturation magnetization and coercivity. This substitution causes a lattice distortion that alters the magnetic characteristics of materials. Magnetic properties of ferrite materials largely based upon the grain size, cation substitution, and A-B exchange interactions. The decrease in the net magnetic moment in B site causes a decrease in the saturation magnetization (MS). Weak R^{3+}-R^{3+} and Fe^{3+}-R^{3+} super-exchange interactions (because of the localized *4f* moments in R^{3+} ions) compared to the Fe^{3+}-Fe^{3+} interaction [12].

IV. CONCLUSIONS

The XRD pattern shows the formation of disordered cubic spinel structure as concentration of rare earth Gd^{3+} doped in cobalt ferrite matrix. The lattice parameter and X-ray density increases whereas porosity decreases with doped of Gd^{3+} in cobalt ferrite. Saturation magnetization decreases with doped of Gd^{3+} in cobalt ferrite.

V. REFERENCES

[1]. Dr. G. H. Kale, Dr. P. K. Gaikwad,; Effect of Sintering Temperature on the structural properties of Nano-size Cobalt Ferrite. Journal of Emerging Technologies and Innovative Research 2022, e276, https://www.jetir.org/view?paper=JETIR2212438

[2]. E1—Shater, R.E.; E1 Shimy, H.: Assar, S. T. Investigation of physical properties of synthesized Zr doped Ni-Zn ferrites. Materials chemistry and physics 2020, 247, https://doi.org/10.1016/j.matchemphys.2020.122758

[3]. Kadam R. H, Desai, k; Shinde, V. S.;Hashim, M; Shirsath, S. E. Influence of Gd3+ ion substitution on the MnCrFeO4 for their nanoparticle shape formation and magnetic properties. Journal of Alloys and Compounds 2016, 657657, 487-494, https://doi.org/10.1016/jallcom.2015.10.164

[4]. Shirsath S E, Jadhav S S, Toksha B G, Patange S. M, Jadhav K. M, Remarkable influence of Ce4+ ions on the electronic conduction of Ni1-2xCexFe2O4. Scripta Materialia 2011, 64, 773, https://doi.org/10.1016/j.scriptamat.2010.12.043

[5]. More, S Kadam, S. Shelke, Pravin Gaikwad, R. Kadam, S. Alone; Modified Structural and Magnetic Properties of Ni-Mn-Zn Ferrite Nanoparticles Doped with Ce3+ Ions, Biointerface Research in Applied Chemistry, 2022, 5021, https://doi.org/10.33263/BRIAC124.50215030

[6]. Kadam R. H, Biradar A R, Mane M L, Shirsath S E, Sol-gel auto-combustion synthesis of Li3xMnFe2-xO4 and their characterization, Journal of Applied Physics 2012, 112, https://doi.org/10.1063/1.4746746

[7]. Lohar K S, Pachpinde A M; Langade M M, Kadam R H, Shirsath S E, Self-propagation high temperature synthesis, structural morphology and magnetic interactions in rare earth Ho3+ doped CoFe2O4 nanoparticles, Journal of Alloys and Compound 2014. 604, 204-210,

[8]. Nithiyanantham S, Viviliya, S, Mahalakshmi, S. Synthesis and characterization of cobalt ferrite through Co-precipition technique. Lett. Appl. NanoBio. 2021,10, 1871-1876, https://doi.org/10.33263/LIANBS101.18711876

[9]. P. K. Gaikwad, S. S. Sawant; Structural and electrical properties of rare earth (R3+) doped Cobalt Ferrites; International Journal of Creative Research Thoughts; 2022, a585; https://ijcrt.org/viewfull.php?&p_id=IJCRT2201074

[10]. Gadkari A B, Shinde T J Vasambekar, P N, Structural analysis of Y3+ doped Mg-Cd ferrite prepared by oxalate co-precipitation method. Materials Chemistry and Physics 2009, 114, 505, https://doi.org/10.1016/j.matchemphys.2008.11.011

[11]. Priya, A.S, Geetha, D; Kavitha, N. Evaluation of structural and dielectric properties of Al, Ce co-doped cobalt ferrites. Materials Research Express 2018, 5, https://doi.org/10.1088/2053-1591/aacdle

[12]. Abdellatif M H, Azab A A, Salerno M, Effect of rare earth doping on the vibrational spectra of spinel Mn-Cr Ferrite. Materials Research Bulletin 2018, 97, 260-264, https://doi.org/10.1016/j.materresbull.2017.09.012

Vedic Math's Aesthetic Appeal and Practical use in Differential and Integral Calculus

Jagtap Gaytri Sadashiv

Anandrao Dhonde Alias Babaji Mahavidyalaya Kada, Dist. Beed, M.S., 414202, India

Email: gaytribk94@gmail.com

Abstract :

Vedic mathematics is a body of techniques, or sutra, for swiftly and efficiently doing numerical calculations. It can be used to solve problems in arithmetic, algebra, geometry, calculus, conics, and other subjects. It is composed of 16 sutras and 13 sub-sutras.

These sutras are applicable to the operations division, multiplication, factorization, recurring decimals, simple equation solutions, quadratic equations, systems of equations, partial fraction integration, and differential calculus. I this paper we have to discuss about practical use of Vedic sutras Differential and integral calculus.

Key words: Vedic Math sutras, Differential calculus, Integral Calculus, Partial fractions

I. INTRODUCTION

The calculus of the Vedic era, "Calana-Kalanabhyam," is the formula. In mathematics, the invention of the differential and integral calculi is the most significant advancement. For a variety of real-world situations where figuring out how quickly one parameter changes in relation to another is required, differential calculus is essential. By sketching an angle at a location and computing its slope, you can mathematically derive the derivative of any function at that position. Given $y = f(x)$ given then $\frac{dy}{dx} = f'(x)$

II. Differential Calculus:

Roots of Quadratic equation:

Using Calana- Kalanabhyam Sutra discriminant of the quadratic first differential and square root of discriminant are shown in this sutra. This sutra was the calculus formula for finding the roots of the quadratic equation. Using the first differential and square root of the discriminant of the given quadratic equation the roots of given quadratic equations are obtained by solving two simple equations.

Example1: solve the quadratic equation $x^2 - x - 6 = 0$

Solution: The first differential $D_1 = 2x - 1$

The square root of the discriminant $= \pm\sqrt{1 + 24} = \pm\sqrt{25} = \pm 5$

Using Calana- Kalanabhyam Sutra, $D_1 = \pm\sqrt{\text{discriminant}}$

$$\Rightarrow 2x - 1 = \pm 5$$
$$\Rightarrow 2x = \pm 5 + 1$$

$$\Rightarrow x = 3 \ or \ x = -2$$

Derivative of Quadratic equation:

Using the Vedic mathematical sutra Dhvaja Ghata find the derivative of quadratic equation.First finding the derivative of each term of the quadratic expression then adding these terms we get the derivative of given quadratic equation.

Example2: Find the derivative of quadratic equation $x^2 + 17x + 60 = 0$

Solution: According to the formula "Dhvaja Ghata"

The differential of the each term of quadratic equation $x^2 + 17x + 60$,

x^2 gives $2x$, $17x$ gives 17 and 60 gives zero

Hence $D_1 = \frac{d}{dx}(x^2 + 17x + 60) = 2x + 17$

Derivative of the product of two binomials :

Using the Vedic mathematical sutra "Gunaka-Samuccaya" we get the first differential of the product of two binomials, $(x + a)$ and $(x + b)$ is equal to the sum of these two binomials. i.e.

D_1 = The first differential = First factor +Second factor = $(x + a) + (x + b)$

i.e $D_1 = a + b = \sum a$ where $a = (x + a), b = (x + b)$

Example 3:Find the derivative of quadratic equation $x^2 + 17x + 60 = 0$

Solution: According to the formula "Gunaka-Samuccaya"

Let $x^2 + 17x + 60 = 0 \Rightarrow (x + 12)(x + 5) = 0$

D_1 = The first differential = First factor +Second factor = $x + 12 + x + 5 = 2x + 17$

Derivative of multiplication of two functions by Crosswise sutra

Let u and v are functions defined in variable x and if y = uv then

$$\frac{dy}{dx} = u\frac{dv}{dx} + v\frac{du}{dx}$$

Differentiation of multiplication of such type of a relationship is found out using Vedic mathematics, Crosswise Sutra

Example 4: Find $\frac{dy}{dx}$ if $y = x^3 5^x$

By current method,

If $u = x^3 \& v = 5^x$

Then $\frac{du}{dx} = 3x^2 \& \frac{dv}{dx} = 5^x \log 5$

$$\therefore \frac{dy}{dx} = u\frac{dv}{dx} + v\frac{du}{dx} \Rightarrow \frac{dy}{dx} = x^3 \times 5^x \log 5 + 5^x \times 3x^2$$

By Vedic Method

By using Vedic Crosswise Sutra

$$u = x^3 \qquad v = 5^x$$
$$u' = 3x^2 \qquad v' = 5^x \log x$$
$$\therefore \frac{dy}{dx} = x^3(5^x \log 5) + 3x^2 5^x$$
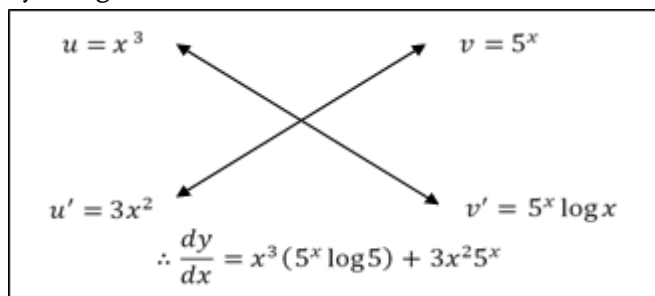
Derivative of the division of two polynomials:

If u & v both are the polynomials then by using vertically and Crosswise sutra derivative of division of two polynomial functions can be easily find out

Example 5: Let $y = \frac{2x+2}{x^2+2x+2}$

By applying division rule,

$$\frac{dy}{dx} = \frac{(x^2+2x+2)2 - (2x+2)(2x+2)}{(x^2+2x+2)^2}$$

$$\frac{dy}{dx} = \frac{(2x^2+4x+4) - (4x^2+8x+4)}{(x^2+2x+2)^2}$$

$$\frac{dy}{dx} = \frac{2x^2+4x+4-4x^2-8x-4}{(x^2+2x+2)^2}$$

$$\frac{dy}{dx} = \frac{-2x^2-4x}{(x^2+2x+2)^2}$$

Vedic Method: For finding the derivative of division of two polynomials by using crosswise division, method above is quite lengthy sutra this answer's numerator can be easily found by referring to the figure below, while the denominator is the square of the term in the denominator.
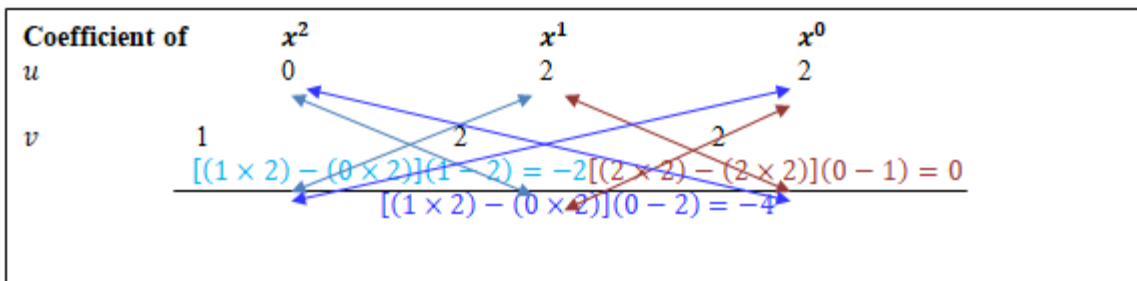
Let $y = \frac{2x+2}{x^2+2x+2}$

$$\therefore \frac{dy}{dx} = \frac{-2x^2 - 4x + 0}{(x^2+2x+2)^2}$$

Hence $\frac{dy}{dx} = \frac{-2x^2 - 4x}{(x^2+2x+2)^2}$

III.Integral Calculus:

The Vedic Mathematical formula "Ekadhikena Purvena Sutra" gives the direction for integration. For integration of a power of x, it says to add unity to the "purva", i.e. add unity to the original index and divide the coefficient by the new index.

Example 6: Integrate $40\ x^4$

Solution: Integration $= 40\frac{x^{4+1}}{4+1} = \frac{40}{5}x^5 = 8x^5$

Ere original index is 4 and by "Ekadhikena Purvena Sutra" we shall have to add 1 with original 4 i.e. 4+1 will be new power of x and also to divide the new index 5

Integration by parts:

The method of integration by parts is used when the integrand is expressed as a product of two functions, one of which can be differentiated (u) and the other can be integrated (v) conveniently. Let (u) and (v) are expressed in terms of variable

$$\int u.v \ dx = u \int v \, dx - \int \left\{ \frac{d}{dx}(u) \int v \, dx \right\} dx$$

It is important to choose first and second functions carefully when integrating a function that is the product of two functions, with the first function being differentiated and second function being integrated (whose integral is known). We can also choose the first function as the function which comes first in the word 'LIATE' where L – Logarithmic, I – Inverse, A – Algebraic, T – trigonometric and E for exponential.

Example 7: Evaluate $\int x^3 \cos 3x \ dx$

Current Method

Consider the reduction formula

$\int x^m \cos nx \ dx = \frac{x^m \sin nx}{n} + \frac{m}{n^2} x^{m-1} \cos nx - \frac{m(m-1)}{n^2} \int x^{m-2} \cos nx \ dx$ ----(1)

First we put n = 3 in reduction formula we get,

$\int x^m \cos 3x \ dx = \frac{x^m \sin 3x}{3} + \frac{m}{9} x^{m-1} \cos 3x - \frac{m(m-1)}{9} \int x^{m-2} \cos 3x \ dx$ ---- (2)

Put m = 1, 3 in equation (2) successively we have,

For m = 1 :

$\int x \cos 3x \ dx = \frac{x \sin 3x}{3} + \frac{1}{9} x^0 \cos 3x - \frac{1(0)}{9} \int x^{-1} \cos 3x \ dx$

$\therefore \int x \cos 3x \ dx = \frac{x \sin 3x}{3} + \frac{1}{9} \cos 3x$ -------- (3)

For m = 3 :

$\int x^3 \cos 3x \ dx = \frac{x^3 \sin 3x}{3} + \frac{3}{9} x^3 \cos 3x - \frac{3(2)}{9} \int x \cos 3x \ dx$

$\therefore \int x^3 \cos 3x \ dx = \frac{x^3 \sin 3x}{3} + \frac{1}{3} x^3 \cos 3x - \frac{2}{3} \left[\frac{x \sin 3x}{3} + \frac{1}{9} \cos 3x \right]$ $\because$ From (3)

$\qquad = \frac{x^3 \sin 3x}{3} + \frac{1}{3} x^3 \cos 3x - \frac{2x \sin 3x}{9} - \frac{2}{27} \cos 3x$

$\therefore \int x^3 \cos 3x \ dx = \left(\frac{x^3}{3} - \frac{2x}{9} \right) \sin 3x + \left(\frac{x^2}{3} - \frac{2}{27} \right) \cos 3x$

Integration of the product of two functions by vertically and crosswise:

For the integration of the product of two functions of x can be solve by the following formula by multiplying it crosswise and add it with the alternative sign.

$$\int u.v \ dv = uv' - u_1 v'' + u_2 v''' - u_3 v'''' + u_4 v''''' - \cdots$$

Here $u_1, u_2, u_3, u_4, \cdots$ are successive derivatives of u and $v', v'', v''', v'''', \cdots$ are successive integrations of v

First function	Second function
$u = x^3$	$v = \cos 3x$
$u_1 = 3x^2$	$v' = \dfrac{\sin 3x}{3}$
$u_2 = 6x$	$v'' = -\dfrac{\cos 3x}{9}$
$u_3 = 6$	$v''' = -\dfrac{\sin 3x}{27}$
$u_4 = 0$	$v'''' = \dfrac{\cos 3x}{91}$

$$\int x^3 \cos 3x \ dx = x^3 \left(\frac{\sin 3x}{3} \right) - 3x^2 \left(-\frac{\cos 3x}{9} \right) + 6x \left(-\frac{\sin 3x}{27} \right) - 6 \left(\frac{\cos 3x}{81} \right)$$

$$\int x^3 \cos 3x \, dx = \frac{x^3}{3} \sin 3x + \frac{x^2}{3} \cos 3x - \frac{2x}{9} \sin 3x - \frac{2}{27} \cos 3x$$

$$\int x^3 \cos 3x \, dx = \left(\frac{x^3}{3} - \frac{2x}{9}\right) \sin 3x + \left(\frac{x^2}{3} - \frac{2}{27}\right) \cos 3x$$

1.   Partial fraction by Paravartya yojayet sutra:

Partial fractions means decomposing the denominator into irreducible factors.

If $f(x)$ and $g(x)$ are two polynomials is an entirely new relationship between two polynomials, whose rationality depends on the range of values its denominator can take, $h(x)$ having a non-zero value the function is rational, and its degree exceeds $f(x)$ making it proper. Using the following table where A, B, C and D are real numbers, it can be expressed as partial fractions.

Rational Function	Partial Form
$\dfrac{px^2 + qx + r}{(x-a)(x-b)(x-c)}$	$\dfrac{A}{(x-a)} + \dfrac{B}{(x-b)} + \dfrac{C}{(x-c)}$
$\dfrac{px^2 + qx + r}{(x-a)^2}$	$\dfrac{A}{(x-a)} + \dfrac{B}{(x-a)^2}$
$\dfrac{px^2 + qx + r}{(x-a)^2(x-b)}$	$\dfrac{A}{(x-a)} + \dfrac{B}{(x-a)^2} + \dfrac{C}{(x-b)}$
$\dfrac{px^2 + qx + r}{(x-a)^3(x-b)}$	$\dfrac{A}{(x-a)} + \dfrac{B}{(x-a)^2} + \dfrac{C}{(x-a)^3} + \dfrac{D}{(x-b)}$
$\dfrac{px^2 + qx + r}{(x-a)(x^2+bx+c)}$	$\dfrac{A}{(x-a)} + \dfrac{Bx+C}{x^2+bx+c}$ Where $x^2 + bx + c$ cannot be factorized further
$\dfrac{px^2 + qx + r}{(x-a)^2(x^2+bx+c)}$	$\dfrac{A}{(x-a)} + \dfrac{B}{(x-a)^2} + \dfrac{Cx+D}{x^2+bx+c}$ Where $x^2 + bx + c$ cannot be factorized further

Steps to apply the Paravartya sutra in Partial fractions:

Write the rational function as a fraction.

i)   Factorize the denominator of the fraction

ii)   Write down the partial fraction decomposition using the coefficients of the factors of the denominator.

iii)   Multiply each partial fraction by the factor that is not present in its denominator.

iv)   Add the partial fractions together

The paravartya rule involves crisscrossing the factors of the denominator to obtain the coefficients of the partial fraction. It can be helpful in simplifying the process of finding the partial fraction decomposition of a rational function

Example 8 : Evaluate $\dfrac{7x+4}{x^2+5x+6}$

Solution : First we express $\dfrac{7x+4}{x^2+5x+6}$ into partial fractions

Current method:

Let $\dfrac{7x+4}{x^2+5x+6} = \dfrac{7x+4}{(x+2)(x+3)} = \dfrac{A}{(x+2)} + \dfrac{B}{(x+3)}$

$$7x + 4 = A(x+3) + B(x+2)$$

$$7x + 4 = (A + B)x + 3A + 2B$$

Equating the coefficients of powers of x on both sides we get

$$A + B = 7$$
$$3A + 2B = 4$$

Solving these two equations simultaneously we have

$$A = -10, B = 17$$

Hence $\frac{7x+4}{x^2+5x+6} = \frac{-10}{(x+2)} + \frac{17}{(x+3)}$

Vedic Method: Using Paravartya yojayet sutra for getting the value of A,

Let $\frac{7x+4}{x^2+5x+6} = \frac{7x+4}{(x+2)(x+3)} = \frac{A}{(x+2)} + \frac{B}{(x+3)}$

$$A = \frac{7x + 4}{x + 3} = \frac{7 \times -2 + 4}{-2 + 3} = -10$$

$$B = \frac{7x + 4}{x + 2} = \frac{7 \times -3 + 4}{-3 + 2} = -\frac{17}{-1} = 17$$

Hence $\frac{7x+4}{x^2+5x+6} = \frac{7x+4}{(x+2)(x+3)} = \frac{-10}{(x+2)} + \frac{17}{(x+3)}$

IV. Conclusion:

Complex and large-scale computations can be handled with greater accuracy and less time by employing Vedic sutras as opposed to estimates reliant on regular mathematics. The use of a Vedic math can enhance memory and improve mental acuity. Consistency is the primary characteristic of Vedic math. Quality-wise, it creates a calm and comfortable atmosphere. It inspires progress. The Vedic approach makes it clear that number crunching and polynomial mathematics are delightfully reasonable. Planning extraordinarily fast Vedic multipliers and reconfigurable Fast Fourier Transforms (FFT) in DSP can be done using Vedic calculation, which is dependent on the Paravartya Yojayet Sutra, Vertically and Crosswise Sutra, Ekadhikena Purvena Sutra, Gunaka-Samuccaya Sutra, Dhvaja Ghata Sutra, Calana- Kalanabhyam Sutra, Urdhva Tiryagbhyam Sutra, Nikhila Sutra, Anurupye Sutra, and numerous other sub sutras.

V. Reference:

[1]. Sri Bharti Krishna Tirthaji, " Vedic Mathematics", published by Motillal Banarsidass, 1965. ISBN81-208-0163-6.

[2]. Nicholas A. P., Willians, J. Pickles. "vertically and Crosswise". Inspiration Books, 1994 ISBN 1-902517-03-2

[3]. Jagatguru Sankaracharya Sri Bharti Krsna Tirtha Maharaj and V. S. Agarwala, Vedic Mathematics, Motillal Banarsidass Private Limited Delhi, !75-187, 1965.

[4]. Nicholas A. P., The solution of differential equation, partial and ordinary, Linear and nonlinear by Vedic Mathematical Methods, Vedic Ganit Eienstein Foundation International, Nagpur, 1986.

[5]. K.R. Williams, Astronomical Applications of Vedic Mathematics, Motilal Banarsidass Publisher Private Limited, Delhi, 2003.

[6]. Kedardatta Joshi, Srimad Bhakaracharya Virochit Sidhanta Siromani Goladhyaya ; Motilal Banarasidas ; New Delhi, 2004.

[7]. Shanti Narayan and P. K. Mital, Differential Calculus , S. Chand & Company Ltd. New Delhi, Reprint 2005.

[8]. Gorakh Prasad , Differential Calculus (Revised Edition), Pothishala Pvt. Ltd., 2018

[9].   Shanti Narayan , Differential Calculus , Shyamlal Charitable Trust, 2004.

[10].   Shanti Narayan and P. K. Mital, Integral Calculus , S. Chand & Company Ltd. New Delhi, Reprint 2005.

[11].   Gorakh Prasad , Integral Calculus (Revised Edition), Pothishala Pvt. Ltd., 2018

Effect on Structural and Magnetic Properties of Nickel Ferrite with Manganese Substitution

Vrushali Karade*

*Department of Physics, Shri Muktanand College,GangapurDist.Chh. Sambhajinagar, Maharashtra, India

karadevc18@gmail.com1

Abstract :

In the present study Manganese substituted Nickel ferrites samples $Ni_{1.2-x}Mn_xFe_{1.8}O_4$(x = 0.0, 0.1, 0.2, 0.3) were synthesized by chemical co-precipitation method. These powder samples were pre-sintered at 700^0C for 12 hours and shaped into pellets and sintered at 1200^0C for 12 hrs. The phase purity and crystalline cubic spinel structure has been confirmed from X-ray diffraction (XRD) data analysis. Surface morphology has been studied by micrographs obtained from Scanning Electron Microscopy (SEM) which shows the increase in average grain size with increasing Mn concentration. Magnetic parameters of the synthesized samples have been studied from hysteresis curves recorded using the Vibrating Sample Magnetometer (VSM) technique. Further the samples were characterized by means of magnetostriction measurement for which strain gauge method was used to record magnetostriction as a function of magnetic field.

Keywords: Cubic Spinel, XRD, SEM, Magnetic Hysteresis Curve, Magnetostriction, Nickel Ferrite

I. INTRODUCTION

The unique structural, electric and magnetic properties of ferrite materials enable them to have a wide range of applications, such as microwave devices, drug delivery, magnetic fluids, magnetic field sensors and magnetic storage devices [1-4]. Ferrites are predominantly ionic and have very stable crystal structure. The spinel type ferrites have the general formula AB_2O_4 where A is a divalent and B is a trivalent metal ion. Nickel ferrite possesses an inverse spinel structure, with half of the Fe^{+3} ions on tetrahedral sites (A sites) and the rest together with Ni^{+2} ions on octahedral sites (B sites) at room temperature. Structural, electrical, dielectric and magnetic properties of the ferrite materials predominantly depend upon the method of preparation that is upon the preparative parameters. During past few years, many researchers have reported variety of methods for the preparation of the ferrites such as sol-gel, hydrothermal, ball-milling, solid state method, auto-combustion technique and co-precipitation method [5-10]. In the present work Co- precipitation method is used to synthesize $Ni_{1.2-x}Mn_xFe_{1.8}O_4$ (with x= 0, 0.1, 0.2, 0.3) samples due to its advantages of inexpensive technique, low-cost precursors, high reaction rate and relatively short reaction time [11].

Some of the ferrites show magnetostriction property that is materials change their shape or dimensions during magnetization, in the direction of the applied magnetic field. This effect is also called as Joule effect. It is measured as the % strain. The magnetostriction coefficient (λ) and strain derivative (dλ/dH) of nickel ferrite is

known to depend on the processing parameters such as the method of synthesis, pressure applied while making the pellets, sintering atmosphere, temperature, and duration of sintering as well as on the microstructure [12]. Also this varies with doping level of other divalent metal ions such as Mn, Zn which reduces the anisotropic behaviour of nickel ferrite [13]. The current work focuses on structural, morphological, magnetic and magnetostrictive properties of Mn substituted Nickel ferrites in order to check its suitability for magnetic field sensor.

II. METHODS AND MATERIAL

$Ni_{1.2-x}Mn_xFe_{1.8}O_4$ (with x= 0, 0.1, 0.2, 0.3) samples were synthesized using Nickel nitrate, Manganese acetate, and ferric nitrite starting material by dissolving them in distilled water in the required mole proportion. The clear solution was co-precipitated with a 3 molar NaOH solution at Fixed Temperature 80^0C. A precipitate formed is filtered and washed until the pH is around 7. The precipitate is dried overnight in an oven at $100°C$ which is eventually converted to a black powder of Nickel ferrite. The powders were pre-sintered at 700^0C for 12 hours followed by grinding to fine powder. These powders were then mixed with 1% polyvinyl alcohol as a binder and pressed into pellets having diameter of 10 mm and thickness of 2-3 mm using hydraulic press. The samples in the form of pellet were sintered at 1200^0C for 24 hours. These samples were characterized using X-ray diffraction technique to understand phase purity and formation of spinel cubic structure. Micrographs of the samples were obtained by using scanning electron microscope (Model JEOL, JSM-6360A) to study surface morphology. The hysteresis curves recorded using a vibrating sample magnetometer (VSM; Model 7307, Lake Shore Cyrotronic, Westerville, OH). Magnetostriction measurements were done using strain indicator (Vishay Measurements model 3800). The resistance strain gauge was pasted on the plane surface of pellet using super glue to carry out magnetostriction measurements.

III.RESULTS AND DISCUSSION

A. Structural Analysis from XRD

Figure 1 shows the XRD patterns of un-doped and Mn-doped Nickel Ferrite samples. The diffraction peaks indexed as (2 2 0), (3 1 1), (2 2 2), (4 0 0), (4 2 2), (5 1 1) and (4 4 0) are in agreement with the JCPDS (Card No: 88-0380), revealing spinel cubic structure. No diffraction peaks were detected due to Mn doping and hence it does not affect the cubic structure of $Ni_{1.2-x}Mn_xFe_{1.8}O_4$. The calculated structure parameters from XRD analysis are tabulated in Table 1. It is observed that the lattice constant gradually increases with increasing Mn content which indicates the replacement of Ni (121 pm) and Fe (125 pm) (having smaller ionic radii) by Mn ions (having larger ionic radii 139 pm) in the Mn-doped $Ni_{1.2}Fe_{1.8}O_4$ system [14]. The average crystallite sizes were estimated from the X-ray peak broadening of diffraction by using Debye-Scherrer's formula $D = 0.9\lambda/\beta\cos\theta$ and given in Table 1. It reveals that the increase in concentration of Mn would increase the crystallite size. The crystallite size was determined by Scherrer's equation that lies in the range of 27-35 nm.
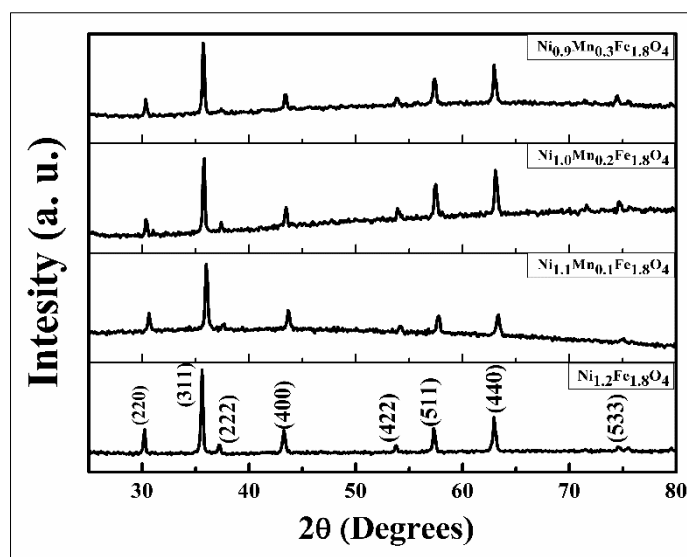
Figure1. XRD of $Ni_{1.2-x}Mn_xFe_{1.8}O_4$ with x = 0, 0.1, 0.2, 0.3

Table1. Calculations for Lattice parameter, Average Crystallite Size and X-Ray density of $Ni_{1.2-x}MnxFe_{1.8}O_4$

Sample $Ni_{1.2-x}MnxFe_{1.8}O_4$ with	Average crystallite size (nm)	Lattice Parameter (A^0)	X-Ray Density (g/cm^3)
x=0	47.24	8.31	5.4389
x=0.1	41.37	8.33	5.3912
x=0.2	54.91	8.33	5.3825
x=0.3	57.00	8.31	5.4128

B. Surface morphological studies from SEM

It is seen from the SEM micrographs that the grains are well compacted with wide size distribution. The grains are polygonal in shape and average grain size goes increasing with increasing Mn concentration. The average grain size calculated for each sample is given in Table 2. However, for the whole range of the doping level, the average grain size variation is limited to a few micrometres. From SEM images it is observed that in nickel-ferrite as $Ni_{1.2-x}Mn_xFe_{1.8}O_4$ as manganese doping 'x' changes from 0 to 0.3 particle size increases from 1.18 to 2.35 micro meters. The micrographs of samples are captured with SEM as 6000× magnification.

Table 2 .Average grain size of $Ni_{1.2-x}Mn_xFe_{1.8}O_4$ (x = 0.0, 0.1, 0.2, 0.3) from SEM

$Ni_{1.2-x}Mn_xFe_{1.8}O_4$ With	Average grain size (Micrometer)
X=0	1.18
X=0.1	1.50
X=0.2	1.98
X=0.3	2.35
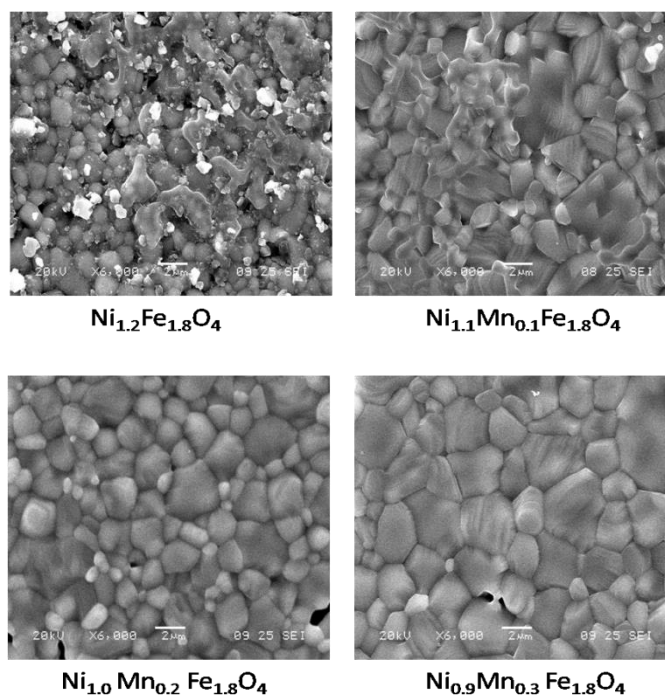
Figure2.SEM Micrographs of Different Compositions of nickel ferrite samples

C. Magnetic Characteristics from VSM

Figure3. shows room temperature magnetic field dependence magnetization (M-H) curve for the Mn doped nickel ferrite $Ni_{1.2-x}Mn_xFe_{1.8}O_4$ (x = 0.0, 0.1,0.2, 0.3) powder samples sintered at 1200^0C recorded in the applied magnetic field range of -10 to +10 kGauss. It can be seen that all magnetization curves are saturated at the high field region; hence hysteresis loops for all the compositions are narrow S shaped due to ferromagnetic materials [15]. According to the hysteresis Mn doped samples have soft magnetic nature.

The values of saturation magnetization (Ms), coercivity (Hc) and remanant magnetization (Mr) are given in Table 3. The saturation magnetization values increases with increasing doping level Mn whereas coercivity and remanant magnetization decreases with increasing doping level of Mn. It is due to replacement of metal ions Ni^{2+} by Mn^{2+} causes super exchange interaction between two sites (tetrahedral and octahedral) presents in cubic structured spinel ferrites [11]. The increase in value of saturation magnetization is due to the fact that magnetic moment of B site was increased more than A site in cubic spinel structure due to Mn doping [16] that is the Ni^{2+} ions had replaced with Mn^{2+} ions.

Table3. Saturation magnetization Ms) ,Coercivity (Hc) ,Retentivity(Mr) values observed from M-H curve of $Ni_{1.2-x}Mn_xFe_{1.8}O_4$ (x = 0.0, 0.1, 0.2, 0.3)

$Ni_{1.2-x}Mn_xFe_{1.8}O_4$ with	Saturation magnetization(Ms) emu/gm	Coercivity (Hc) (G)	Retentivity(Mr) emu/gm
X=0	35.42	56.63	1.85
X=0.1	35.93	48.49	1.91
X=0.2	38.07	41.54	1.70
X=0.3	40.96	33.93	1.35
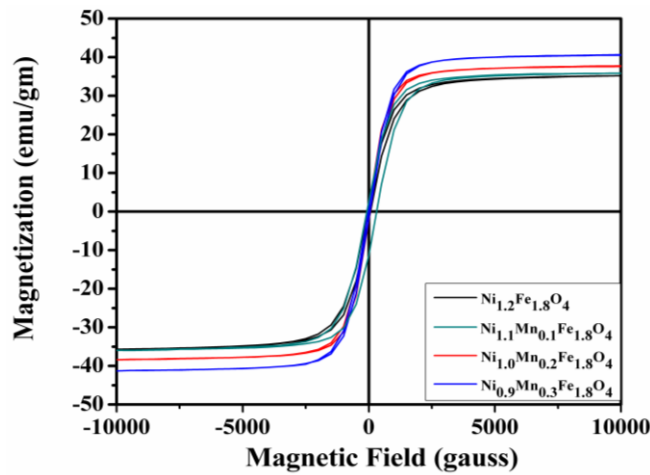
Figure 3.M-H curves for $Ni_{1.2-x}Mn_xFe_{1.8}O_4$ where x changes from 0 to 0.3

D. Magnetostriction Measurements

The Magnetostriction measurements were carried out for magnetic field parallel or perpendicular to the plane of the sample plane. λ_{11} was noted for magnetic field applied parallel to the sample plane and strain gauge, λ_{12} was noted for magnetic field perpendicular to sample plane and strain gauge, whereas λ_{13} was noted for magnetic field parallel to the sample plane and perpendicular to strain gauge [17].

Figures 4.1-4.4 show variation of transverse (λ_{11}) and longitudinal (λ_{12}) and (λ_{13}) magnetostriction with magnetic field for $Ni_{1.2-x}Mn_xFe_{1.8}O_4$, 'x' ranges from 0 to 0.3. It is seen from figure that λ_{11} is negative while λ_{12} and λ_{13} are positive in the magnetic field range of measurements.

The magnetostriction values increases rapidly in the low field region upto 1×10^3 Gauss. λ_{11} shows saturation at higher magnetic fields whereas λ_{12} and λ_{13} goes on increasing with comparatively lower rate in the high field. It is seen from the Figure that the maximum value of magnetostriction coefficients (λ_{11}) obtained is -30 ppm for applied magnetic field of 3 kG for $Ni_{1.2}Fe_{1.8}O_4$. With substitution of paramagnetic element Mn in place of ferromagnetic element Ni, magnetic field required to reach saturation values is substantially reduced.
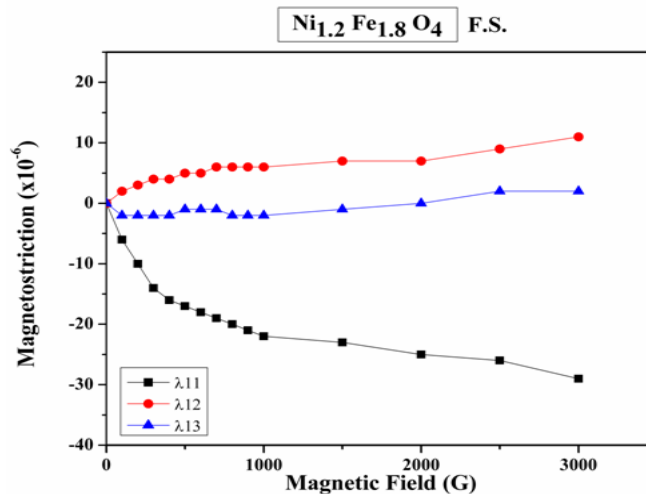
Figure4.1
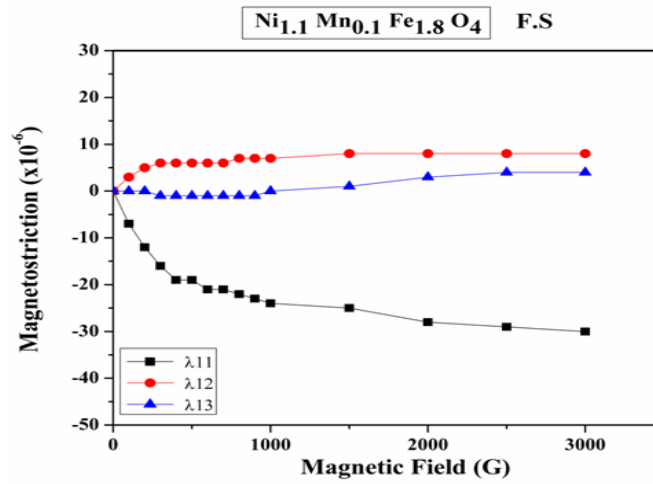
Figure 4.2
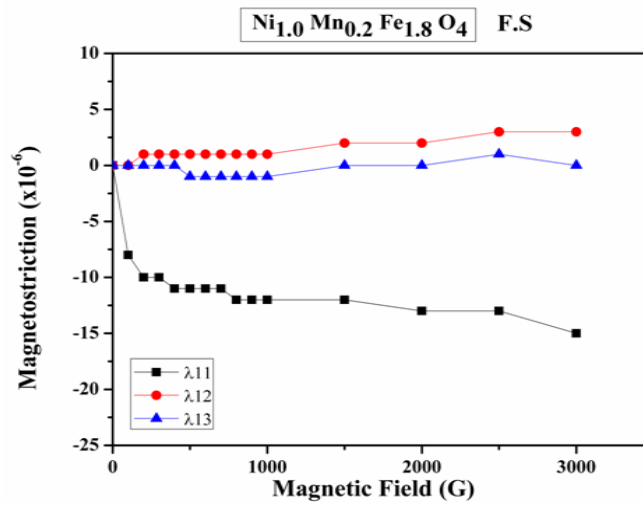
Figure 4.3
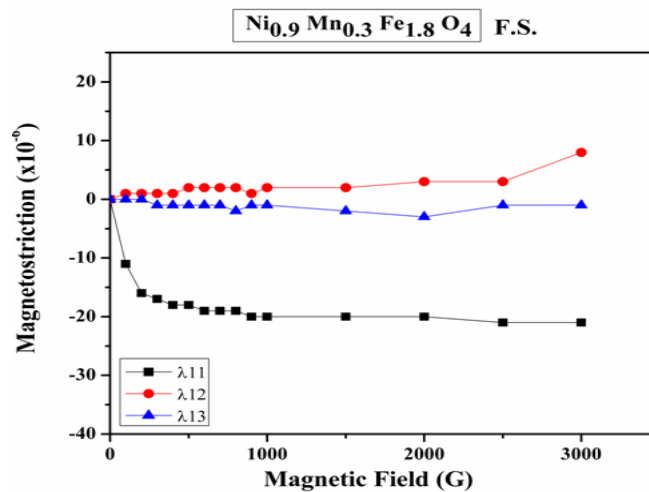
Figure 4.4

Figure 4.1-4.4.Graphs of Strain vs. Magnetic field for Ni1.2-xMnxFe1.8O4 where x changes from 0 to 0.3

IV. CONCLUSION

The samples of Ni-ferrite with Mn substitution have been synthesized successfully using chemical co-precipitation method. Crystalline single phase spinel cubic structure of $Ni_{1.2-x}Mn_xFe_{1.8}O_4$ ferrite system is confirmed by X-ray diffraction analysis. The crystallite size as well as lattice parameter increases with increasing Mn substitution. The Scanning electron micrographs of the Mn doped Nickel ferrites shows that particles are almost homogeneous and well compacted. It also indicates that for increasing doping level of Mn in Ni-ferrite will increase the average grain size which is in coordination with XRD results. Magnetic hysteresis curve shows increase in saturation magnetization values with increasing doping level of Mn whereas decrease in coercivity and remanant magnetization. This is due to replacement of Ni^{2+} ion by Mn^{2+} causing super exchange interaction between two sites presents in cubic structured spinel ferrites. Magnetostriction measurements for $Ni_{1.2-x}Mn_xFe_{1.8}O_4$ shows the maximum value of magnetostriction coefficient (λ_{11}) obtained is -30 ppm for applied magnetic field of 3 kG for $Ni_{1.2}Fe_{1.8}O_4$. Magnetic field required to reach saturation values is substantially reduced due to substitution of paramagnetic element Mn in place of ferromagnetic element Ni.

V. REFERENCES

[1]. N.Y. Mostafa, Z.I. Zaki, Z.K. Heiba, Structural and magnetic properties of cadmiumsubstituted manganese ferrites prepared by hydrothermal route, Journal of Magnetism andMagnetic Materials, 329 (2013) 71-76.

[2]. Y. Köseoğlu, F. Alan, M. Tan, R. Yilgin, M. Öztürk, Low temperature hydrothermalsynthesis and characterization of Mn doped cobalt ferrite nanoparticles, Ceramics International,38 (2012) 3625-3634.

[3]. K.O. Abdulwahab, M.A. Malik, P. O'Brien, G.A. Timco, A direct synthesis of water solublemonodisperse cobalt and manganese ferrite nanoparticles from iron based pivalate clusters by thehot injection thermolysis method, Materials Science in Semiconductor Processing, 27 (2014)303-308.

[4]. Z. Kaiwen, Q. Liqin, W. Xuehang, W. Wenwei, S. Yuexiao, T. Yulin, L. Jieyue, Structureand magnetic properties of manganese–nickel ferrite with lithium substitution, CeramicsInternational, 41 (2015) 1235-1241.

[5]. J. Li, H. Yuan, G. Li, Y. Liu, J. Leng, Cation distribution dependence of magnetic propertiesof sol–gel prepared MnFe2O4 spinel ferrite nanoparticles, Journal of Magnetism and MagneticMaterials, 322 (2010) 3396-3400.

[6]. D. Chen, Y. Zhang, Z. Kang, A low temperature synthesis of MnFe2O4 nanocrystals bymicrowave-assisted ball-milling, Chemical Engineering Journal, 215–216 (2013) 235-239.

[7]. E.R. Kumar, R. Jayaprakash, G.S. Devi, P.S.P. Reddy, Magnetic, dielectric and sensingproperties of manganese substituted copper ferrite nanoparticles, Journal of Magnetism andMagnetic Materials, 355 2014) 87-92.

[8]. V. MusatBujoreanu, L. Diamandescu, M. Brezeanu, On the structure of manganese ferritepowder prepared by coprecipitation from MnO2 and FeSO4·7H2O, Materials Letters, 46 (2000)169-174.

[9]. O.M. Hemeda, N.Y. Mostafa, O.H. Abd Elkader, M.A. Ahmed, Solubility limits in Mn–Mgferrites system under hydrothermal conditions, Journal of Magnetism and Magnetic Materials,364 (2014) 39-46.

[10]. M.M. Hessien, M.M. Rashad, K. El-Barawy, I.A. Ibrahim, Influence of manganesesubstitution and annealing temperature on the formation, microstructure and magnetic propertiesof Mn–Zn ferrites, Journal of Magnetism and Magnetic Materials, 320 (2008) 1615-1621.

[11]. S. Mirzaee, Y. Azizian-Kalandaragh, P. Rahimzadeh, Modified co-precipitationprocess effects on the structural and magnetic properties of Mn- doped nickel ferrite nanoparticles, SolidState Sciences (2019), solidstatesciences.2019.106052.

[12]. Yao Cheng, YuanhuiZheng, Yuansheng Wang, FengBao, Yong Qin,Synthesis and magnetic properties of nickel ferrite nano-octahedra,Journal of Solid State Chemistry,Volume 178, Issue 7,2005,Pages 2394-2397

[13]. C. Venkataraju, G. Sathishkumar, K. Sivakumar,Effect of cation distribution on the structural and magnetic properties of nickel substituted nanosized Mn–Zn ferrites prepared by co-precipitation method,Journal of Magnetism and Magnetic Materials,Volume 322, Issue 2,2010,Pages 230-233

[14]. M. Arshad, M. Asghar, M. Junaid, M.F. Warsi, M.N. Rasheed, M. Hashim, M.A. Al-Maghrabi, M.A. Khan, Structural and magnetic properties variation of manganese ferrites via Co-Ni substitution,Journal of Magnetism and Magnetic Materials (2018)

[15]. H. Malik, A. Mahmood, K. Mahmood, M.Y. Lodhi, M.F. Warsi, I. Shakir, H. Wahab, M.Asghar,M.A. Khan, Influence of cobalt substitution on the magnetic properties of zincnanocrystals synthesized via micro-emulsion route, Ceramics International, 40 (2014) 9439-9444.

[16]. R. Ali, A. Mahmood, M.A. Khan, A.H. Chughtai, M. Shahid, I. Shakir, M.F. Warsi, Impactsof Ni–Co substitution on the structural, magnetic and dielectric properties of magnesium nanoferritesfabricated by micro-emulsion method, Journal of Alloys and Compounds, 584 (2014)363-368.

[17]. Mathe, V. L., & Sheikh, A. D. (2010). Magnetostrictive properties of nanocrystalline Co–Ni ferrites. Physica B: Condensed Matter, 405(17), 3594–3598.

Hyperpolarizabilities of TATBusing Quantum Chemical Methods

Vinayak Deshmukh

Department of Physics, Shri Siddheshwar Mahavidyalaya, Majalgaon, Maharashtra, India

Dvinayaka72@gmail.com

Abstract :

This work reports the static hyperpolarizabilities of TATB (1,3,5-triamino-2,4,6-trinitrobenzene) are determined by using quantum chemical methods. The Finite-Field approach has been used to obtain the static first and second hyperpolarizability components (β and γ) by applying field either in X, Y or Z direction. The geometries of TATB are optimized using quantum chemical methods with different exchange and correlation functionals and split valence triple zeta basis set with and without diffuse and polarization functions. The geometrical parameters and vibrational frequencies obtained at B3LP/6-311++G** level are in excellent agreement with the experimental determinations. β as well as γ values are highest and lowest when the field is applied in X and Z direction, respectively.

Keywords: TATB, NLO, quantum chemical methods, finite field method

I. INTRODUCTION

Nonlinear optics, which studies the interaction of intense light field with matter, is a relatively new field in physics with lots of fundamental scientific and technological potential applications [1-3]. Non linear optical (NLO) effects are analyzed by considering the response of the dielectric material at the atomic level to the electric fields of an intense light beam. The propagation of a wave through a material produces changes in the spatial and temporal distribution of electrical charges as the electrons and atoms interact with the electromagnetic fields of the wave. The main effect of the forces exerted by the field on the charged particles is displacement of the valence electrons from their normal orbits. This perturbation creates electric dipoles whose macroscopic manifestation is the polarization. Thus nonlinear Optics (NLO) is the study of interaction of intense electromagnetic field with materials to produce modified fields that are different from the input field in phase, frequency or amplitude. Second harmonic generation (SHG) is a nonlinear optical process that results in the conversion of an input optical wave into an output wave of twice the input frequency.

Nonlinear optical (NLO) materials with large NLO responses have been a challenge for materials scientists and chemists. Recently, organic polymers have received attention regarding their NLO properties. Organic NLO materials have potential applications in areas such as electrooptics and photonics. There is a continuing interest in development of optical materials which would be suitable for manufacturing of photonic switches and other devices. The molecular materials with quadratic nonlinear optical (NLO) response to electromagnetic field have been studied over the last two decades [4–16].

NLO properties of π-conjugated molecules such as TATB and substituted benzene are of great interest to understand the phenomenon associated with the designing and construction of photonic devices. The molecular structure of TATB has been determined by electron diffraction [17-19].Soscún et. al. have calculated linear dipole polarizability and nonlinear second dipole hyperpolarizability of TATB using ab-initio SCF-MO restricted Hartree-Fock (HF) method [20]. Zhu et. al. have studied the effect of the field, basis set, functionals and cavity size on molecular polarizabilities and hyperpolarizabilities of substituted TATB in different solvents [21]. Theoretical methods such as quantum chemical methods play an important role for the prediction of NLO properties of a material and its suitability for photonic applications

We report here on a systematic computational investigation of the NLO properties of TATB using quantum chemical methods.

II. COPUTATIONAL DETAILS

Geometry optimizations were carried out using *Gaussian* suit of program [22]. The geometries of TATB molecule have optimized using quantum chemical methods with different basis set. DFT with B3LYP, B3PW91 and PBEPBE exchange and correlation functionals have been used for the geometry optimization of TATB molecule. Using these calculations we decided the level of theory at which TATB molecule show the lowest energy and the minimum energy structure. These minimum energy structures are then used to calculate NLO properties of TATB at various levels of theory.

An easy way to comply with the conference paper formatting requirements is to use this document as a template and simply type your text into it.

Page Layout

The margins must be set as follows:

- Top = 1.7cm
- Bottom = 1.7cm
- Left = 1.7cm
- Right = 1.7cm

Your paper must be in two column format with a space of 1.27 cm between columns.

III.RESULTS AND DISCUSSION

We first optimized the geometries of TATB molecule at different levels to obtain the lowest energy structure. We have used DFT method with different exchange and correlation functionals. It is found that the TATB molecule shows the lowest energy at B3LYP/6-311++G** level among different levels of theories used here. Table I represents bond lengths and angles for TATB at different levels used here alongwith the experimental determinations [17].
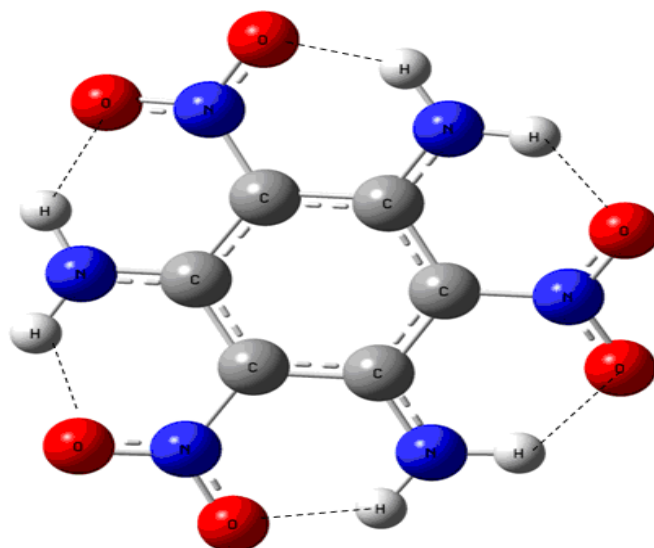
Fig. 1.

TABLE 1. Geometrical parameters for TATB obtained using different methods with 6-311++G** basis set alongwith experimental values. Bond lengths in Å and angles in degree.

Bond length/angle	B3LYP	B3PW91	PBEPBE	HF	Expt.*
C-C	1.395	1.392	1.400	1.386	1.397[a]
C-H	1.084	1.085	1.092	1.075	1.102[a]
C-N (C-NH$_2$)	1.327	1.323	1.333	1.325	1.314
C-N (C-NO$_2$)	1.436	1.430	1.439	1.440	1.419
N-O	1.242	1.237	1.256	1.194	1.243
<C-C-C	120	120	120	120	----
<C-C-H	120	120	120	120	----

We have also used here various basis sets viz. 6-311G, 6-311+G, 6-311+G*, 6-311++G*, 6-311++G** with different methods to obtain NLO properties of TATB. We have applied Finite-Field of different strength either in X, Y or Z direction for the TATB molecule to decide the suitable field strength in order to obtain the numerical stable hyperporizabilities. The geometries of TATB optimized at B3LYP/6-311++G** level have been used here since at this level of theory TATB molecule shows the lowest energy among different levels used here. Once the suitable field strength is decided to prevent the numerical instability, we then obtained hyperporizabilities of TATB using different methods and basis sets. Figure 2(a) and 2(b) shows the variation of β and γ respectively of TATB with field strengths applied either in X, Y or Z direction using the Finite-Field method. In Fig. 2, the hyperpolarizability values after certain field strength are the large negative values which are not shown in Fig. 2. We have shown only positive values in Fig. 1. Figure 2 shows that the necessity of applying different field strengths in order to avoid the numerical instability. From Figure 2, it can be said that TATB molecule shows numerical stable hyperporizabilities at a certain range of field strength applied either in X, Y or Z direction. Therefore we have chosen field strength of 0.008 a.u. to calculate the hyperporizabilities of TATB using different methods and basis sets. We have obtained hyperporizabilities using different levels of theory in addition to B3LYP/6-311++G** level with field strength of 0.008 a.u. applied either in X, Y or Z

direction. We can consider hyperporizabilities obtained at B3LYP/6-311++G** level as the reference since at this level of theory the TATB molecule show the lowest energy, geometrical parameters and vibrational frequencies are in excellent agreement with the experimental determinations.
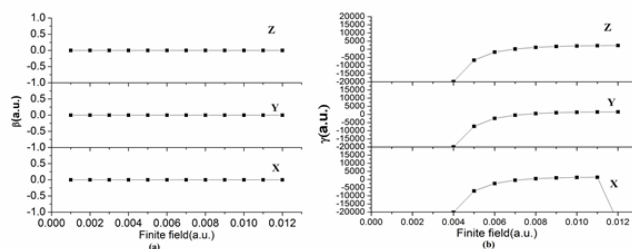
FIGFigure 2. Variation of β and γ for TATB with field strength at B3LYP/6-311++G level.**

The β values are zero irrespective of the level of theory and direction in the applied field. However γ values are nonzero for TATB as can be seen from Fig. 2. Figure 2 shows the variation of γ of TATB obtained using different methods and basis sets with field strength of 0.008 a.u. applied either in X, Y or Z direction.
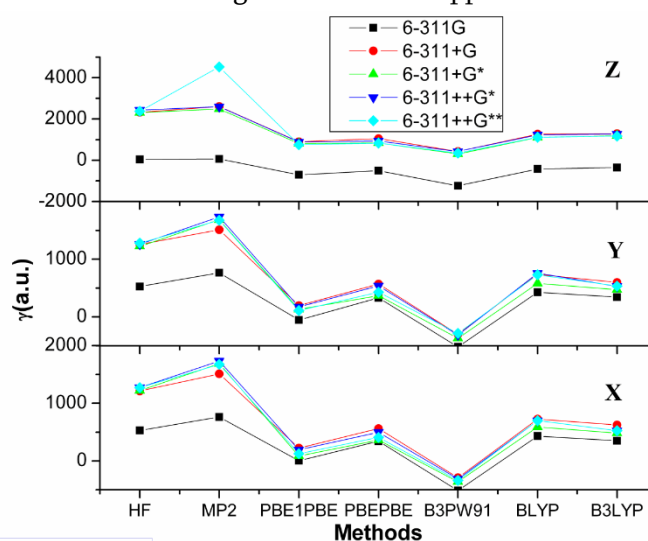
Figure 2. Variation in γ for TATB obtained using various methods and basis sets using field strength of 0.008 a.u..

IV. CONCLUSION

We studied NLO properties of TATB molecule. The field is applied either in X, Y or Z direction. TATB shows zero β values irrespective of the applied field direction. There is no large change in β values of TATB. However a significant increase in β values is obtained for the field applied in X direction. Large γ values are also obtained for the TATB. Among different levels of theory used here for obtaining the hyperpolarizabilities, MP2 level shows higher β and γ values than the DFT method with different exchange and correlation functionals. The optimized geometries obtained at B3LYP/6-311++G** level of theory are in excellent agreement with the experimental determinations.

V. REFERENCES

[1]. Boyd, R. W. Nonlinear Optics, 2nd ed.; Academic Press: San Diego, CA, 2003.
[2]. Dalton, L. R. J. Phys.: Condens. Matter 2003, 15, R897-R934.

[3]. van der Boom, M. E. Angew. Chem., Int. Ed. 2002, 41, 3363-3366.

[4]. van der Boom, M. E.; Marks, T. J. Layer-by-Layer Assembly of Molecular Materials for Electrooptical Applications. In Polymers for Microelectronics and Nanoelectronics; Lin, Q., Ed.; ACS Symposium Series 874; American Chemical Society: Washington, DC, 2004; pp 30-43.

[5]. D.F. Eaton, Nonlinear optical materials, Science 253 (1991) 281–287.

[6]. W.D. Cheng, K.H. Xiang, R. Pandey, U.C. Pernisz, Calculations of linear and nonlinear optical properties of H-silsesquioxanes, J. Phys. Chem. B 104 (2000) 6737–6742.

[7]. P. Hermet, G. Fraysse, A. Lignie, P. Armand, P. Papet, Density functional theory redictions of the nonlinear optical properties in a-quartz-type germanium dioxide, J. Phys. Chem. C 116 (2012) 8692–8698.

[8]. C. Hättig, H. Larsen, J. Olsen, P. Jorgensen, H. Koch, B. Fernández, A. Rizzo, The effect of intermolecular interactions on the electric properties of helium and argon. I. Ab initio calculation of the interaction induced polarizability and hyperpolarizability in He2 and Ar2, J. Chem. Phys. 111 (1999) 10099–10107.

[9]. R. Horikoshi, C. Nambu, T. Mochida, Metal-centered ferrocene clusters from 5- ferrocenylpyrimidine and ferrocenylpyrazine, Inorg. Chem. 42 (2003) 6868–6875.

[10]. N.J. Long, C.K. Williams, Metal alkynyl r complexes: synthesis and materials, Angew. Chem. Int. Ed. 42 (2003) 2586–2617.

[11]. N. Islam, S. Niaz, T. Manzoor, A.H. Pandith, Theoretical investigations into spectral and non-linear optical properties of brucine and strychnine using density functional theory, Spectrochim. Acta A 131 (2014) 461–470.

[12]. M. Kauranen, T. Verbiest, A. Persoons, Second-order nonlinear optical signatures of surface chirality, J. Mod. Opt. 45 (1998) 403–423.

[13]. P. Fischer, F.W. Wise, A.C. Albrecht, Chiral and achiral contributions to sum frequency generation from optically active solutions of binaphthol, J. Phys. Chem. A 107 (2003) 8232–8238.

[14]. S. Sioncke, T. Verbiest, A. Persoons, Second-order nonlinear optical properties of chiral materials, Mater. Sci. Eng. 42 (2003) 115–155.

[15]. F. Hache, Quantum calculation of the second-order hyperpolarizability of chiral molecules in the "one-electron" model, J. Phys. Chem. A 114 (2010) 10277–10286.

[16]. P. Fischer, F. Hache, Nonlinear optical spectroscopy of chiral molecules, Chirality 17 (2005) 421–437.

[17]. Tamagawa, K.; Iijima, T.; Kimura, M. J Mol Struct 1976, 30, 243.

[18]. Kimura, K.; Kubo, M. J Chem Phys 1960, 32, 1776.

[19]. Karle, I. L. J Chem Phys 1952, 20, 65.

[20]. Soscún, H.; Hernández, J.; Escobar, R.; Toro-Mendoza, C.; Alvarado, Y.; Hinchliffe A. Int J Quant Chem 2002, 90, 487.

[21]. Zhu, W.; Wu, G.; Jiang, Y. Int J Quant Chem 2002, 86, 347.

[22]. Gaussian 03 (2004) Frisch, M. J.; Trucks, G. W.; Schlegel, H. B.; Scuseria, G. E.; Robb, M. A.; Cheeseman, J. R.; Montgomery, J .A Jr.; Vreven, T.; Kudin, K. N.; Burant, J. C.; Millam, J. M.; Iyengar, S. S.; Tomasi, J.; Barone, V.; Mennucci, B.; Cossi, M.; Scalmani, G.; Rega, N.; Petersson, G. A.; Nakatsuji, H.; Hada, M.; Ehara, M.; Toyota, K.; Fakuda, R.; Hasegawa, J.; Ishida, M.; Nakajima, T.; Honda, Y.; Kitao, O.; Nakai, H.; Klene, M. Li. X.; Knox, J. E.;Hratchian, H. P.; Cross, J. B.; Bakken, V.; Adamo, C.; Jaramillo, J.; Gomperts, R.; Stratmann, R. E.; Yazyev, O.; Austin, A. J.; Cammi, R.; Pomelli, C.; Ochterski, J. W.; Ayala, P. Y.; Morokuma, K.; Voth, G. A.; Salvador, P.; Dannenberg, J. J.; Zakrzewski, V. G.; Dapprich, S.; Daniels, A. D.: Strain, M. C.; Farkas, O.; Malick, D. K.; Rabuck, A. D.; Raghavachari, K.; Foresman, J. B.; Ortiz, J. V.; Cui,

Q.; Baboul, A. G.; Clifford, S.; Cioslowski, J.; Strfanov, B. B.; Liu, G.; Liashenko, A.; Piskorz, P.; Komaromi, I.; Martin, R. L.; Fox ,D. J.; Keith, T.; Al-Laham, M. A.; Peng, C. Y.; Nanayakkara, A.; Challacombe, M.; Gill, P. M. W.; Johnson, B.; Chen, W.; Wong, M. W.; Gonzalez, C.; Pople, J. A.; Gaussian Inc.: Wallingford, CT.

Biological Synthesis and Antimicrobial Potential of Zinc Oxide Nanoparticles Using Camellia sinensis Leaf Extract

S. J. Indurkar*, K. R. Sature

*Department of Physics, J.E.S.'s, R. G. Bagdia Arts, S. B. Lakhotia Commerce and R. Bezonji Science College, Jalna, Maharashtra, India

Abstract :

This document provides *Camellia sinensis* (Green Tea), a member of the Rosaceae family, is widely recognized for its medicinal properties, yet its application in the green synthesis of zinc nanoparticles remains underexplored. This study investigates the utilization of *Camellia sinensis* leaf extract for the synthesis of zinc nanoparticles, expanding the scope beyond traditional fruit-based methodologies. The synthesis was evidenced by a distinct color change in the solution and characteristic UV-Vis absorption peaks at 393 nm and 395 nm. The antimicrobial efficacy of the synthesized zinc nanoparticles was evaluated against multidrug-resistant bacterial strains, including *Escherichia coli*, *Staphylococcus aureus*, *Pseudomonas aeruginosa*, and *Bacillus subtilis*. The nanoparticles demonstrated significant antibacterial activity, with a maximum inhibition zone of 24 mm observed against *S. aureus*. These results indicate the potential of *Camellia sinensis* leaf extract as a viable alternative for nanoparticle synthesis, providing a novel approach for developing plant-based antimicrobial agents.

Keywords: *Camellia sinensis*, green synthesis, zinc nanoparticles, antimicrobial activity

I. INTRODUCTION

Micronutrient deficiencies (MNDs), particularly those of zinc (Zn) and iron (Fe), represent a significant global health concern, affecting over 3 billion individuals, especially in regions with grain-based diets such as Africa and India [1-4]. Zinc, in particular, plays a crucial role in human health and agriculture, where zinc oxide nanoparticles (ZnO NPs) have been increasingly utilized for their dual function of providing essential zinc nutrition to crops and offering pest resistance [5]. Despite the promising applications, the synthesis of ZnO NPs through conventional methods such as sol-gel, precipitation, and thermal decomposition remains complex and resource-intensive [6].

In recent years, the green synthesis of ZnO NPs using plant extracts has gained attention as an eco-friendly alternative. The use of phytochemicals present in plant extracts as reducing and stabilizing agents offers a sustainable and less toxic approach to nanoparticle synthesis [7]. Among various plants studied, *Camellia sinensis* (Green Tea) is notable for its rich polyphenolic content, which facilitates the synthesis of nanoparticles with desirable characteristics. Additionally, ZnO NPs synthesized using plant extracts have demonstrated significant antimicrobial activity, making them suitable for applications in food safety and preservation [8].

Previous studies have shown that the size, shape, and antimicrobial efficacy of ZnO NPs are highly dependent on the synthesis parameters, including the concentration of plant extract and metal salts used [1]. For instance, Datta et al. (2012) successfully synthesized ZnO NPs using *Parthenium hysterophorus* leaf extracts, producing nanoparticles with varied morphologies that exhibited enhanced antimicrobial properties due to their reduced size and increased surface area [9].

The present study focuses on the green synthesis of ZnO NPs using *Camellia sinensis* leaf extract. This research aims to optimize the synthesis conditions to produce ZnO NPs with enhanced antimicrobial properties. The synthesized nanoparticles will be evaluated for their antimicrobial activity against pathogenic bacteria, providing insights into the potential of *Camellia sinensis* as a sustainable source for nanoparticle production and its application in addressing global challenges related to MNDs and antimicrobial resistance.

II. METHODS AND MATERIAL

A. Plant and Culture Collection

The leaves of Camellia sinensis (Green Tea) used in this study were collected from the Milind College of Science, Aurangabad, Maharashtra, and were authenticated by the Botany Department of Milind College of Science, Aurangabad, Maharashtra, India. The human pathogenic microorganisms utilized in this research were obtained from the Institute of Microbial Technology (IMTECH), Chandigarh. These included the Gram-negative bacteria Escherichia coli (MTCC-5704) and Pseudomonas aeruginosa (MTCC-2295), as well as the Gram-positive bacteria Bacillus subtilis (MTCC-121) and Staphylococcus aureus (MTCC-3160). The cultures were maintained in Muller-Hinton broth for preservation and subsequent antimicrobial testing.

B. Preparation of Plant Leaf Extract and Zinc Oxide Nanoparticles Solution

The leaves of Camellia sinensis were thoroughly washed with distilled water and then oven-dried at 50-65°C for 20-40 minutes until completely dehydrated. The dried leaves were ground into a fine powder using a mechanical grinder. For the preparation of the extract, 5 grams of the powdered leaves were soaked in 50 mL of deionized water and heated at 60°C for 30 minutes. The resulting extract was filtered using Whatman No. 1 filter paper, and the filtrate was stored at 4°C for up to one week, ensuring it was used within this period for the synthesis of zinc oxide nanoparticles.

To prepare the zinc oxide nanoparticle solution, 5 grams of zinc nitrate were dissolved in 50 mL of deionized water and heated in a water bath at 70°C until a homogeneous solution was obtained. This zinc nitrate solution was then added dropwise to 12.5 mL of the prepared Camellia sinensis leaf extract under continuous stirring. The mixture was incubated in a water bath at 70°C for one hour to facilitate the synthesis of zinc oxide nanoparticles. The resulting solution was then subjected to further analysis, including antimicrobial testing.

C. Synthesis and Confirmation of ZnO Nanoparticles

The synthesis of ZnO nanoparticles was confirmed through visual observation of a color change in the reaction solution, transitioning from its original color to a cream-colored solution. This color change indicates the formation of nanoparticles. Further confirmation was obtained by measuring the absorption maxima within the wavelength range of 300-600 nm using UV-Vis spectroscopy. The presence of an absorption peak is attributed to the surface plasmon resonance (SPR) property of the nanoparticles, which arises from the oscillations of free electrons on the nanoparticle surface when they resonate with the wavelength of the incident light.

To extract the synthesized ZnO nanoparticles, the reaction solution was heated to 70°C using a heating mantle until the solution was converted into a powdered form of zinc oxide nanoparticles. The obtained nanoparticles were further subjected to calcination by placing them in a hot air oven at 110°C for one hour. The fine powder of ZnO nanoparticles was then collected and used for further characterization, including X-ray diffraction (XRD) analysis to determine the crystalline structure and size of the nanoparticles.

D. Antimicrobial Activity of Plant Extracts by Agar Well Diffusion Assay

The antimicrobial activity of the plant extracts was evaluated using the agar well diffusion assay method [10]. Mueller-Hinton Agar (MHA) plates were inoculated with microbial cultures, including both Gram-positive and Gram-negative bacteria. A well with a diameter of approximately 6.0 mm was aseptically created in the agar using a sterile cork borer. The plant extract served as the test substance, with a control used for comparison. The inoculated plates were placed in a laminar flow hood for 30 minutes to allow pre-diffusion of the extracts before being incubated overnight at 37°C for 24 hours.

The antimicrobial efficacy of the extracts was assessed by measuring the inhibition zones (zone of inhibition diameters) around each well. The inhibition zones were measured using a high media zone scale, and the results were recorded to determine the spectrum of antimicrobial activity exhibited by the plant extracts.

III. RESULTS AND DISCUSSION

A. Characterization of Zinc Oxide Nanoparticles

The synthesis of zinc oxide (ZnO) nanoparticles using *Camellia sinensis* (Green Tea) leaf extract was confirmed by a visible color change in the reaction mixture, transitioning from its original greenish hue to a light cream color. This change is indicative of the formation of ZnO nanoparticles, driven by the coherent oscillation of electron gas at the nanoparticle surface, a hallmark of nanoparticle synthesis. UV-Vis spectroscopy of the synthesized nanoparticles showed a strong absorption peak at 393 nm, characteristic of the surface plasmon resonance (SPR) of ZnO nanoparticles.
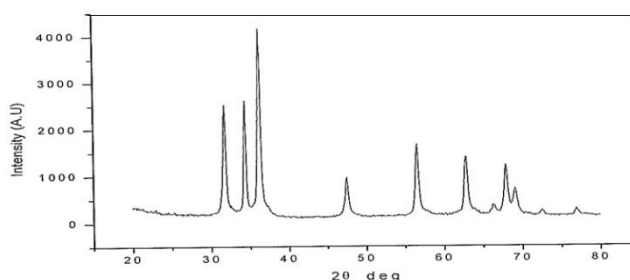
Figure- 1. XRD pattern of zinc nanoparticles

The crystalline nature of the ZnO nanoparticles was further confirmed by X-ray diffraction (XRD) analysis. The XRD patterns displayed distinct peaks corresponding to the hexagonal wurtzite structure of ZnO, confirming the successful synthesis of pure ZnO nanoparticles. The diffraction peaks were sharp and well-defined, indicating the high crystallinity of the nanoparticles.

Previous studies corroborate these findings. Sindhura et al. (2013) synthesized ZnO nanoparticles using *Hibiscus rosa sinensis* leaf extracts, observing a UV absorption peak at 269 nm and confirming the formation of ZnO nanoparticles with a size range of 32.7 to 89.8 nm. Similarly, Hashemi et al. (2010) synthesized ZnO

nanoparticles using *Olea europaea* (olive) leaf extracts, with a UV-visible absorption peak at 370 nm and spherical particles averaging 41 nm in size.

In this study, the average size of the synthesized ZnO nanoparticles was calculated using the Scherrer equation, yielding an average particle size of approximately 50-70 nm, depending on the specific conditions of the synthesis. These results are consistent with those reported in the literature, demonstrating the efficacy of *Camellia sinensis* leaf extract in producing ZnO nanoparticles with desirable properties for potential applications.

B. Antimicrobial Analysis

The antimicrobial activity of the zinc oxide (ZnO) nanoparticles synthesized using *Camellia sinensis* (Green Tea) leaf extract was evaluated against a range of pathogenic bacteria, including both Gram-positive and Gram-negative strains. The agar well diffusion method was employed to assess the antibacterial efficacy of the nanoparticles, with zones of inhibition used as the primary indicator of antimicrobial activity.

The ZnO nanoparticles exhibited significant antimicrobial activity against all tested bacterial strains. The largest inhibition zones were observed against *Staphylococcus aureus* (Gram-positive), with an average zone of inhibition measuring approximately 24 mm. This suggests that the synthesized ZnO nanoparticles are particularly effective against Gram-positive bacteria, likely due to the differences in the cell wall structure between Gram-positive and Gram-negative bacteria, which affect the interaction with nanoparticles.

For Gram-negative bacteria such as *Escherichia coli* and *Pseudomonas aeruginosa*, the ZnO nanoparticles also demonstrated strong antimicrobial effects, with inhibition zones measuring between 18-22 mm. These results indicate that the ZnO nanoparticles synthesized using *Camellia sinensis* leaf extract possess broad-spectrum antibacterial properties.

The antimicrobial activity observed in this study can be attributed to the unique properties of ZnO nanoparticles, including their ability to generate reactive oxygen species (ROS) and the release of Zn^{2+} ions, which contribute to bacterial cell membrane disruption and ultimately bacterial cell death. The high surface area to volume ratio of the nanoparticles further enhances their interaction with bacterial cells, leading to increased antimicrobial efficacy.

Figure- 2. Zone of inhibition observed using ZnO against different pathogens.

These findings align with previous studies that have reported the antimicrobial potential of ZnO nanoparticles synthesized using plant extracts. The results demonstrate that *Camellia sinensis* leaf extract is an effective and eco-friendly reducing and stabilizing agent for the synthesis of ZnO nanoparticles, which exhibit strong antibacterial activity against a variety of pathogenic microorganisms. This suggests potential applications of

these nanoparticles in medical and environmental settings, particularly in developing new antimicrobial agents to combat drug-resistant bacteria.

Table 1: Antimicrobial activity of ZnO nanoparticles synthesized using Camellia sinensis leaf extract against various bacterial strains.

Bacterial Strain	Type	Zone of Inhibition (mm)
Staphylococcus aureus (MTCC-3160)	Gram-positive	24
Bacillus subtilis (MTCC-121)	Gram-positive	22
Escherichia coli (MTCC-5704)	Gram-negative	20
Pseudomonas aeruginosa (MTCC-2295)	Gram-negative	18

IV.CONCLUSION

The present study successfully demonstrated the green synthesis of zinc oxide (ZnO) nanoparticles using Camellia sinensis (Green Tea) leaf extract as a natural reducing and stabilizing agent. The synthesis was confirmed by visual observation, UV-Vis spectroscopy, and X-ray diffraction (XRD) analysis, which revealed the formation of highly crystalline ZnO nanoparticles with an average size of 50-70 nm. The synthesized ZnO nanoparticles exhibited significant antimicrobial activity against a broad spectrum of pathogenic bacteria, including both Gram-positive and Gram-negative strains. The most pronounced antibacterial effect was observed against Staphylococcus aureus, a Gram-positive bacterium, indicating the potential of these nanoparticles in combating drug-resistant bacterial infections. This study highlights the efficacy of Camellia sinensis leaf extract in producing ZnO nanoparticles with desirable properties for antimicrobial applications. The findings suggest that these eco-friendly synthesized nanoparticles could be further explored for use in medical, environmental, and food safety applications, particularly in the development of new antimicrobial agents. Moreover, the use of a sustainable and readily available plant extract aligns with the growing interest in green chemistry approaches for nanoparticle synthesis, offering a promising alternative to conventional methods that are often more toxic and resource-intensive.Top of Form

V. REFERENCES

[1]. Ludmila Motelica; Bogdan-Stefan Vasile; Anton Ficai; Adrian-Vasile Surdu; Denisa Ficai; Ovidiu-Cristian Oprea; Ecaterina Andronescu; Gabriel Mustăţea; Elena Loredana Ungureanu; Alina Alexandra Dobre; "Antibacterial Activity of Zinc Oxide Nanoparticles Loaded with Essential Oils", PHARMACEUTICS, 2023. (IF: 3)

[2]. Gabriela Toader; Aurel Diacon; Edina Rusen; Ionel I Mangalagiu; Mioara Alexandru; Florina Lucica Zorilă; Alexandra Mocanu; Adina Boldeiu; Ana Mihaela Gavrilă; Bogdan Trică; Daniela Pulpea; Mădălina Ioana Necolau; Marcel Istrate; "Peelable Alginate Films Reinforced By Carbon Nanofibers Decorated with Antimicrobial Nanoparticles for Immediate Biological Decontamination of Surfaces", NANOMATERIALS (BASEL, SWITZERLAND), 2023.

[3]. Ryota Nagasaki; Keiji Nagano; Takashi Nezu; Masahiro Iijima; "Synthesis and Characterization of Bioactive Glass and Zinc Oxide Nanoparticles with Enamel Remineralization and Antimicrobial Capabilities", MATERIALS (BASEL, SWITZERLAND), 2023.

[4].   Yahia A Amin; Sahar Gamal Abdelaziz; Alaa H Said; "Treatment of Postpartum Endometritis Induced By Multidrug-resistant Bacterial Infection in Dairy Cattle By Green Synthesized Zinc Oxide Nanoparticles and in Vivo Evaluation of Its Broad Spectrum Antimicrobial Activity in Cow Uteri", RESEARCH IN VETERINARY SCIENCE, 2023.

[5].   Bushra H Shnawa; Parwin J Jalil; Ali Al-Ezzi; Renjbar M Mhamedsharif; Daniyal A Mohammed; Donia M Biro; Mukhtar H Ahmed; "Evaluation of Antimicrobial and Antioxidant Activity of Zinc Oxide Nanoparticles Biosynthesized with Ziziphus Spina-christi Leaf Extracts", JOURNAL OF ENVIRONMENTAL SCIENCE AND HEALTH. PART C, ..., 2023.

[6].   Remmiya Mary Varghese; Aravind Kumar S; Rajeshkumar Shanmugam; "Antimicrobial Activity of Zinc Oxide Nanoparticles Synthesized Using Ocimum Tenuiflorum and Ocimum Gratissimum Herbal Formulation Against Oral Pathogens", CUREUS, 2024.

[7].   Alexander J Caron; Iman J Ali; Michael J Delgado; Dustin Johnson; John M Reeks; Yuri M Strzhemechny; Shauna M McGillivray; "Zinc Oxide Nanoparticles Mediate Bacterial Toxicity in Mueller-Hinton Broth Via Zn 2", FRONTIERS IN MICROBIOLOGY, 2024.

[8].   Aqilah A Hakami; Hajar S Alorfi; Thoraya A Farghaly; Mahmoud A Hussein; "A New Polyazomethine-based Pyrazole Moiety and Its Reinforced Nanocomposites @ ZnO for Antimicrobial Applications", DESIGNED MONOMERS AND POLYMERS, 2024.

[9].   Mohamad Omeiri; Esraa El Hadidi; Ramadan Awad; Jamalat Al Boukhari; Hoda Yusef; "Aluminum Oxide, Cobalt Aluminum Oxide, and Aluminum-doped Zinc Oxide Nanoparticles As An Effective Antimicrobial Agent Against Pathogens", HELIYON, 2024.

[10].   Kehui Wang; Xiangjun Yang; Junjun Liang; Yan Rong; Weijie Zhao; Jiahao Ding; Yiming Liu; Qi Liu; "Preparation, Characterization, Antimicrobial Evaluation, and Grape Preservation Applications of Polyvinyl Alcohol/gelatin Composite Films Containing Zinc Oxide@quaternized Chitosan Nanoparticles", INTERNATIONAL JOURNAL OF BIOLOGICAL MACROMOLECULES, 2024.

Microwave Remote Sensing: Techniques, Applications, and Advancements

Monika S. Khole, Vishal P. Shirsath, Dr. Sanjay K. Tupe, Dr. Shafiyoddin Sayyad

Abstract :

Microwave remote sensing encompasses both active and passive forms of remote sensing. Microwave remote sensing has proven indispensable in various fields such as environmental monitoring, climate studies, agriculture, and disaster management. Operating in the microwave region of the electromagnetic spectrum (1 mm to 1 m), it offers unique advantages, including all-weather, day-and-night capability, and the ability to penetrate clouds cover, haze, dust, vegetation, and even soil. This paper presents an in-depth exploration of microwave remote sensing, its principles, technologies such as active andpassive, and the diverse applications in Earth observation. Additionally, the paper highlights recent advancements and discusses the challenges that need to be addressed for future improvements.

Keyword: Microwave Remote Sensing, Active Remote Sensing, Passive Remote Sensing, Synthetic Aperture Radar

I. INTRODUCTION

"Remote sensing is the science of acquiring information about the Earth's surface without actually being in contact with it." This is done by sensing and recording reflected or emitted energy and processing analyzing and applying that information. There are several regions of the electromagnetic spectrum which are useful for remote sensing. In that microwaveremote sensing uses electromagnetic waves in the microwave range from 1mm to 1m, making it an effective tool for Earth observation due to its unique capability to penetrate through clouds cover and sense in both day and night conditions because of its higher wavelength range.

The main advantage of microwave remote sensing lies in its ability to provide data under all-weather conditions, which is critical for monitoring surface characteristics such as soil moisture, vegetation structure, and sea ice. The main categories include active microwave sensing (radar systems that emit and receive microwave signals) and passive microwave sensing (radiometers that measure natural microwave emissions).

II. Principles of Microwave Remote Sensing

Microwave remote sensing operates in the frequency range of 1–300 GHz (corresponding to wavelengths of 1 mm to 1 m). It relies on how microwaves interact with Earth's surface and atmosphere, including factors like:i.Wavelength and Frequency: Longer wavelengths can penetrate deeper into the Earth's surface, snow, or vegetation, offering insights into subsurface properties.ii. Polarization: Refers to the orientation of the electromagnetic wave and provides additional data about surface characteristics.Active sensors can measure

backscatter as co-polarized (HH and VV) and cross-polarized (HV and VH). Passive sensors measure the emission in V or H polarization.iii. Incident Angle: The angle at which the microwaves hit the surface affects the reflection and scattering properties.The sensitivity of microwave sensor to soil moisture decreases when the incidence angle increases. At higher incidence angle, the vegetation intercepts more of the signal and attenuates it.

The interaction between microwaves and various natural materials such as vegetation, soil, snow, and water depend on their dielectric properties.By analyzing the returned or emitted signals, important physical properties such as surface roughness, moisture content, and surface geometry can be inferred.

III. Active Microwave Remote Sensing (Radar)

Active microwave remote sensing involves emitting a signal and measuring the returned signal after it interacts with the target surface. Active sensors provide their own energy source for illumination. Advantages of active remote sensing include the ability to obtain measurements anytime of day or season. Active microwave sensors are generally divided into two distinct categories: imaging and non-imaging. Radar (Radio Detection and Ranging) is the most commonly used imaging active microwave sensor. Non-imaging microwave sensors include altimeters and scatterometers.It can be further divided into several types based on their operational principles.

3.1 Synthetic Aperture Radar (SAR)

SAR is a radar technique that produces high-resolution images of Earth's surface by combining data collected over successive flights. SAR is particularly valuable because it operates independently of cloud cover and sunlight, making it ideal for applications such as:

i.   Cryosphere studies: Monitoring glacier movements, sea ice extent, and seasonal changes in snow cover.

ii. Surface deformation monitoring: Used in geological studies, including monitoring earthquakes and volcanic activity via interferometric SAR (InSAR).

iii. Environmental mapping: SAR is useful for studying deforestation, urban expansion, and wetland mapping.

3.2 Scatterometer:

Scatterometeris non-imaging sensors. Scatterometers are specialized radar systems designed to measure the reflection or scattering of microwaves from surfaces, typically scatterometry measurements over ocean surfaces can be used to estimate wind speed and direction over the sea surface roughness. They are crucial for weather prediction and hurricane tracking.

3.3 Radar Altimeter

Radar altimeters transmit short microwave pulses and measure the round-trip time delay to targets to determine their distance from the sensors. Radar altimeters measure height and elevation of an object or surface relative to the sensor. They are commonly used on aircraft for altitude determination and on aircraft and satellite for sea level measurements and in monitoring the thickness of polar ice sheets.

IV. Passive Microwave Remote Sensing

Passive microwave remote sensing involves measuring natural microwave emissions from the Earth's surface and atmosphere. These emissions vary based on surface properties such as temperature, moisture properties of

the emitting surface, and material composition. Passive microwave sensors are typically radiometers or scanners. Applications of passive microwave remote sensing include meteorology, oceanography and hydrology.

4.1 Atmospheric Sensing

Microwave radiometers are used to measure temperature, humidity, and water vapor content in the atmosphere. This data is critical for meteorological forecasting and understanding atmospheric dynamics.

4.2 Soil Moisture Estimation

Soil moisture estimation is one of the major applications of passive microwave sensors. Soil moisture content has significant implications for agriculture, hydrology, and climate studies. Microwave radiometers such as those onboard the **SMAP (Soil Moisture Active Passive)** satellite measure global soil moisture levels with high temporal frequency.

V. Applications of Microwave Remote Sensing

Microwave remote sensing provides critical data for various sectors due to its ability to monitor physical parameters in all-weather conditions. Some key applications include:

5.1 Disaster Management

Microwave remote sensing is widely used for disaster monitoring and management due to its capability to provide rapid, near-real-time data:

i. Flood Monitoring: SAR can detect flood extents even under cloudy or stormy conditions. It plays a crucial role in tracking floods caused by tropical cyclones and heavy rainfall events.

ii. Earthquake and Landslide Detection: InSAR has revolutionized the detection of surface deformations caused by tectonic movements and landslides.

iii. Cyclone and Storm Tracking: Scatterometer data on wind speed and direction helps in forecasting and tracking tropical cyclones and hurricanes.

5.2. Environmental Monitoring:

i. Vegetation Mapping: Both active and passive microwave sensors are used to monitor vegetation biomass, soil moisture, and surface roughness, helping in agricultural planning and environmental conservation efforts.

ii. Deforestation and Land Use Changes: SAR systems are widely used to detect forest cover changes, deforestation rates, and changes in land use.

iii. Water Resource Management: Monitoring soil moisture and surface water bodies, especially during droughts and floods, is critical for efficient water resource allocation.

5.3 Agriculture and Soil Monitoring

i. Precision Agriculture: Agriculture plays a dominants role in economies. Microwave sensors help in assessing health of the crop, irrigation needs, and soil moisture levels, enabling precision farming techniques, crop condition assessment.

ii. Drought Monitoring: Long-term soil moisture measurements are crucial for understanding and predicting drought conditions, helping in agricultural planning and food security.

5.4 Climate Change Monitoring

Microwave remote sensing provides valuable data for studying and mitigating the impacts of climate change:

i. Glacier and Ice Sheet Monitoring: By measuring changes in ice mass and extent, microwave sensors contribute to understanding sea-level rise and polar dynamics.

ii. Sea Surface Temperature and Winds: Scatterometer and radiometer data help monitor sea surface temperature and wind patterns, critical for climate models.

VI. Advancements in Microwave Remote Sensing

Recent technological advancements have significantly improved the performance and capabilities of microwave remote sensing systems:

i. Polarimetric SAR (PolSAR): PolSAR enhances the ability to extract detailed information from radar imagery by measuring multiple polarization states, providing more insight into surface characteristics like vegetation, urban areas, and snow cover.

ii. Interferometric SAR (InSAR): InSAR has enabled the precise measurement of ground displacements, allowing scientists to monitor earthquakes, volcanic eruptions, and land subsidence with millimeter accuracy.

iii. Miniaturization of Sensors: Smaller, more efficient microwave sensors enable their integration into constellations of small satellites, providing frequent, near-real-time global coverage.

VII. Challenges and Limitations

Despite the advantages, microwave remote sensing faces several challenges:Data Processing Complexity: The interpretation of microwave remote sensing data, particularly from polarimetric and interferometric SAR, requires advanced algorithms and computational resources. Resolution Trade-offs: Passive microwave sensors often have lower spatial resolution due to the large antenna size needed for higher resolution at longer wavelengths.Cost: Active systems, especially SAR, are expensive to develop, launch, and operate, limiting their availability.

VIII. Conclusion

Microwave remote sensing has become a vital tool for monitoring and studying the Earth observation, Microwave remote sensing techniques have shown great potential in agricultural applications such as crop yield forecasting, climate change monitoring, disaster management and issuing early warning of droughts. The ability to operate under all weather conditions and in the day and night monitoring it particularly valuable for global, continuous observation. While the field continues to advance, addressing challenges such as cost, resolution, and data interpretation will be crucial for unlocking its full potential in the years to come.

IX. References

[1]. Fundamentals of Remote Sensing: A Canada Centre for Remote Sensing Remote Sensing Tutorial. https://naturalresources.canada.ca/sites/nrcan/files/earthsciences/pdf/resource/tutor/fundam/pdf/fundamentals_e.pdf

[2]. D. M. Le Vine, A. J. Griffis, C. T. Swift and T. J. Jackson, "ESTAR: a synthetic aperture microwave radiometer for remote sensing applications," in Proceedings of the IEEE, vol. 82, no. 12, pp. 1787-1801, Dec. 1994, doi: 10.1109/5.338071.

[3]. Pietroniro, A., & Prowse, T. D. (2002). Applications of remote sensing in hydrology. Hydrological processes, 16(8), 1537-1541.

[4]. Ulaby, F. T., Moore, R. K., & Fung, A. K. (1986). Microwave Remote Sensing: Active and Passive. Artech House.

[5]. Njoku, E. G. (2003). Satellite passive microwave remote sensing for land and ocean applications. Proceedings of the IEEE.

[6]. Wagner, W., et al. (2007). Operational readiness of microwave remote sensing of soil moisture for hydrologic applications. Hydrology and Earth System Sciences.

[7]. Lakhankar, T., Krakauer, N., & Khanbilvardi, R. (2009). Applications of microwave remote sensing of soil moisture for agricultural applications. International Journal of Terraspace Science and Engineering, 2(1), 81-91.

The science of variable stars and its photometric analysis

AbhayDashrath[1]*, Sachin Pandit[2], Aarti Jathar[1], Anirudha Deshpande[3], Anil Ardad[4], Pravin Kokne[5], Rajendra Yannawar[6]

[1]Dr. D. Y. Patil Institute of Technology, Pimpri, Pune

[2]J.E.S. College, Jalna

[3]Jyotirvidya Parisanstha, Pune

[4]Deogiri College, Chhatrapati Sambhajinagar

[5]Badrinarayan BarwaleMahavidyala, Jalna

[6]Milind Science College, Chhatrapati Sambhajinagar

*Corresponding author. E-mail: adashrath@gmail.com

Abstract :

Research in astronomical observations can be done in two broad ways- one is for change in the position of the object which is prominent in the case of planets and other is for change in the intensity of electromagnetic radiations which is prominent in case of stars. Variable stars have long captivated astronomers, from amateur observers to professional researchers. Some brightvariable stars can be observed with the unaided eye, but fainter objects require telescopic assistance, and recording stellar light necessitates the use of advanced detectors like photometers, DSLRs, CCD cameras, etc. Nowadays it is needed to use softwares for processing images and analyzing the data. Our abilities to collect and analyze huge amounts of observational data have considerably increased due to the use of modern technology. Using technology, the study of variable stars is now more precise and comprehensive. This article provides anunderstanding about classification of various types of variable stars, explained with light curves. We have discussed the role of small telescopes and photometric techniques in the discovery and classification of the variable stars. The discussion also includes a few examples, along with the limitations and challenges in the field of variable star astronomy.This article also provides an overview of future research directions, highlighting the importance of using modern technology and collaborative work to expand our understanding of variable stars.

Keywords: Suspectedvariable stars, Irregular variable stars, Variables in clusters, Photometric techniques, Light curves

I. INTRODUCTION

In the dynamic field of astronomy, the observations of stars using small telescopes and the precise measurements of their luminosity through instruments such as photometers, DSLRs, and CCDs offer profound insights into the cosmos and its evolution. Stars are broadly categorizedinto non-variable and variable categories on the basis of their luminosity variations, with some stars suspected of variability when they do not

fit into these classifications. The brightness variations of variable stars can be from a mere tenth of a magnitude to over twenty magnitudes, with periods ranging from a couple of hours to a few years[1].

Variable star study is vital and improves our understanding of the cosmos by providing critical information on stellar parameters such as mass, radius, brightness, temperature, interior structure, etc. [2]. Stars are important drivers of cosmic evolution, especially in the synthesis of elements heavier than hydrogen and helium which are essential building blocks for life and planetary systems [1]. As potential sites for life, studying stars, including our Sun, deepens our understanding of possible extraterrestrial habitats. The diversity of variable stars reveals clues to broader astrophysical phenomena, making them indispensable to our understanding of stellar evolution and the broader cosmos. Technological advancements in sensors and computational methods have significantly enhanced our ability to explore and comprehend these celestial bodies.

II. Classification and types of variable stars:

Stars are the celestial objects which give out energy in the form of light. The magnitude of the light received from a star can be constant or it may vary in a certain period. Depending on the variation, stars can be classified into standard stars and variable stars. If the magnitude does not change over a long period, the stars are standard or non-variable stars. But if the magnitude changes, the stars are variable stars.

Variable stars are then divided into two main groups depending on the reason for the variation of light magnitude- intrinsic & extrinsic variables. If the variation of light intensity is because of the star itself, such stars are called intrinsic variables, and if the variation of light intensity is due to external conditions, the stars are called extrinsic variable stars.
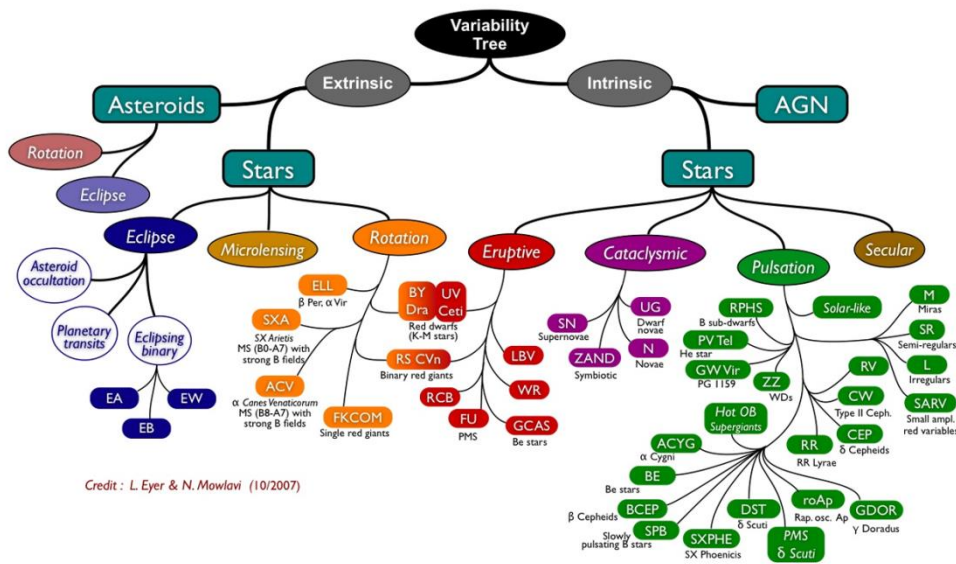
Figure 1: Variability tree of stars[4]

There are many types of variable stars. Considering the scope of this article, few of the examples are discussed below-

2.1 Eclipsing variables- Close binary stars whose orbital plane coincides with our line of sight are called eclipsing binary variables. While rotating about each other, one star eclipses the other and vice versa. This leads to variations in the light that we are receiving from the binary system.

The study of eclipsing binaries began in depth with the detailed observations of Algol (β Persei).The analysis of observations led to the perception that variations in brightness could be attributed to the mutual eclipses of stars in a binary system. The pioneering work by astronomers like John Goodricke in the 18th century laid the foundation for the modern study of these systems.

Eclipsing binaries are broadly classified based on the amount of the eclipse, and the nature of the eclipsing stars:Detached Binaries, Semi-Detached Binaries,Contact Binaries, etc.
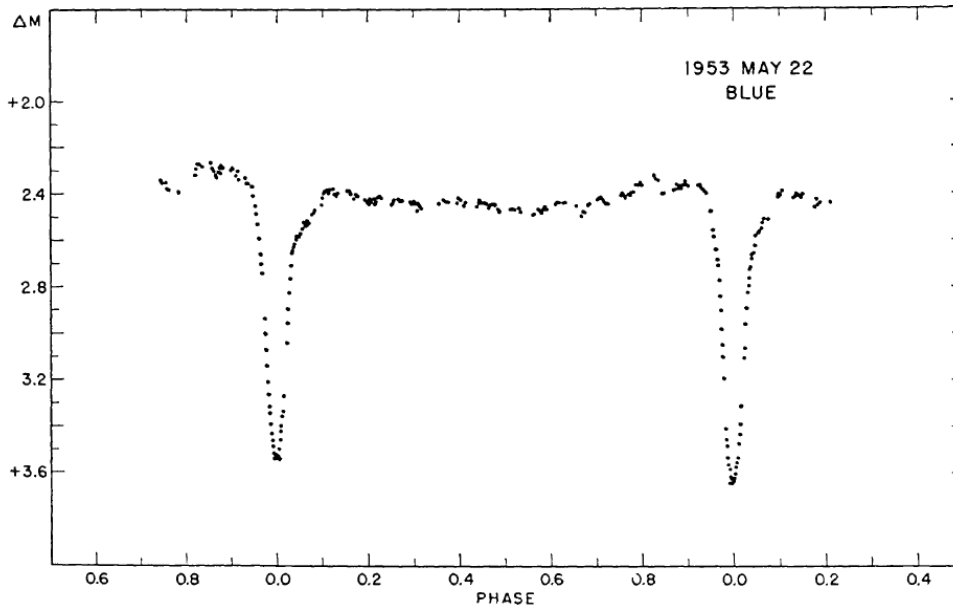
Figure 2 - Photometric observations of TJX Uma [8]
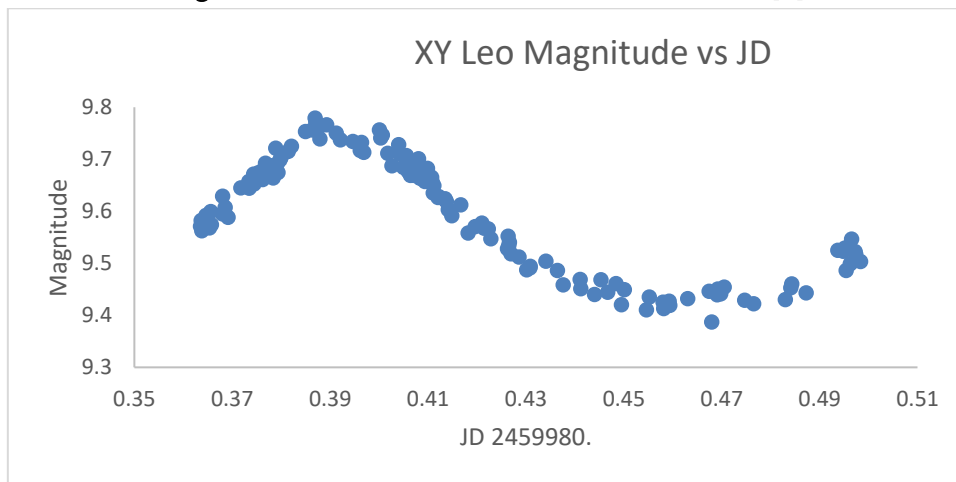
Figure 3 – Photometric observations of XY Leo (spectroscopic binary) taken from KJO, Pune.

2.2 Rotating variables - Fundamentally stars rotate about their axis. However, if variation is observed in the surface brightness of the star, such stars are rotating variables. The variability in rotating stars is mainly a surface phenomenon due to the rotation of surface features in and out of the line of sight.Even our own sun has spots that revolve over a certain period.Other examples are BY Dra stars, RS CVn stars, rotating ellipsoidal variables, etc.
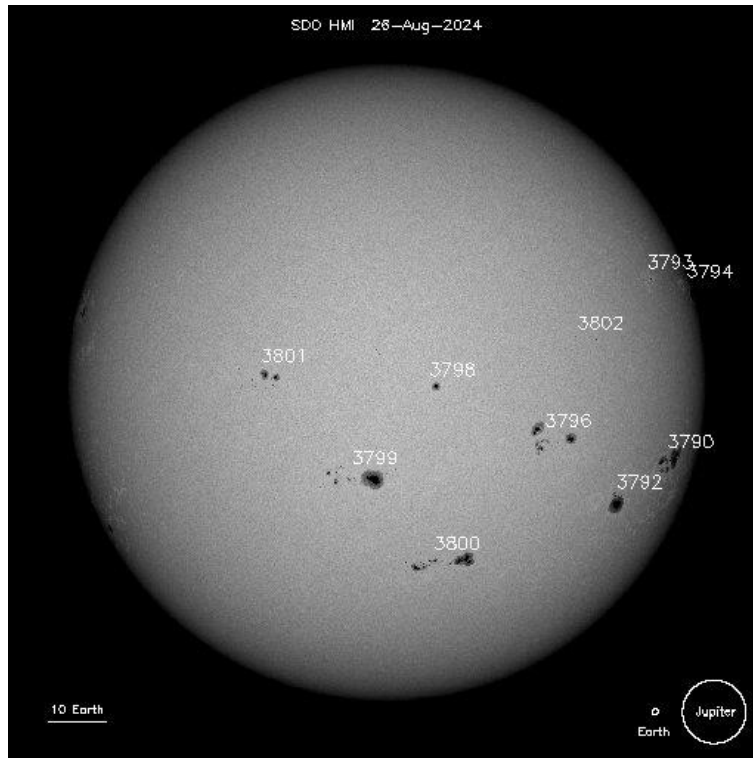
Figure 4 - Sunspots Image credit: NASA
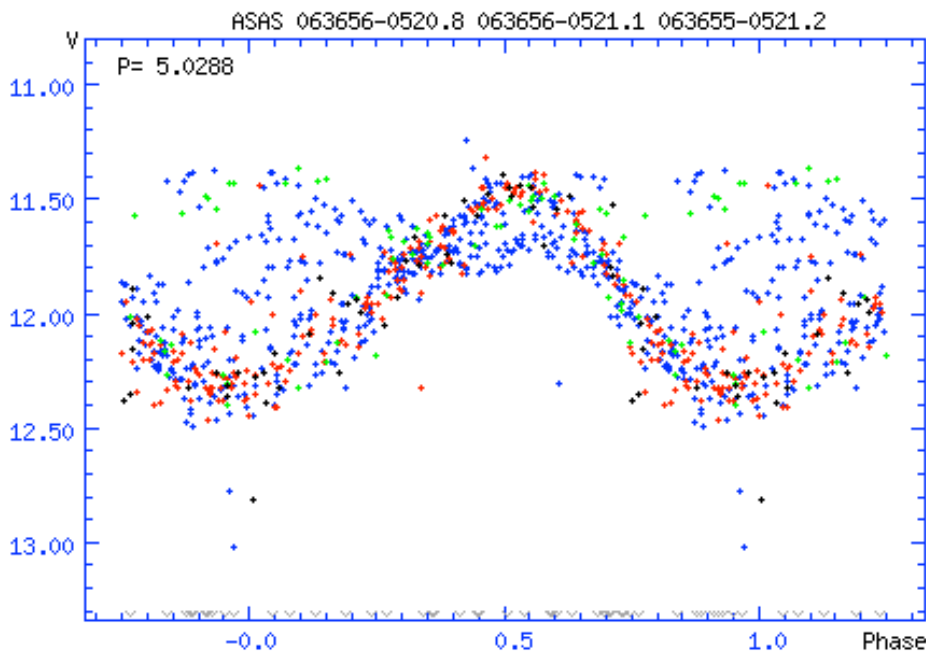
Figure 5 - Light curve of a BY Dra variable utilizing ASAS data

2.3 Eruptive variables - If the variation of the light magnitude is because of explosive or eruptive processes, such variable stars are called eruptive variables. Usually, such variability is rapid and for a short period showing irregular variations in the magnitude.Many of the stars designated as irregular in the General Catalogue of Variable Stars may be assigned to different star classes once they are well understood. Some of the examples are cataclysmic variables, Novae, eruptive binaries, young stellar objects, T Tauri stars, etc.
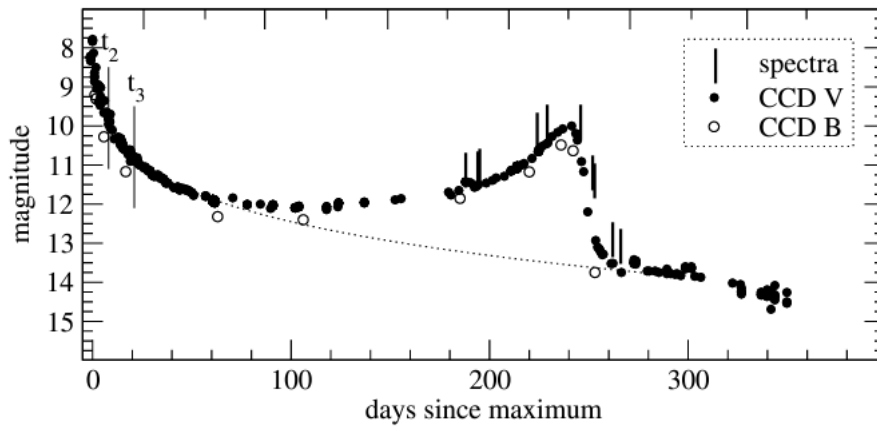
Figure 6 - The photometric data of V2362 Cyg from April 2006 to March 2007.[9]

2.4 Pulsating variables - If the outer layer of the star shows expansion and contraction, such stars are pulsating variable stars. The expansion and contraction is mostly symmetric and spherical. It is somewhat similar to blowing air in and out in a balloon. Some examples are Cepheid variables, Mira variables, RR Lyrae variables, etc. There are some stars whose pulses are non-radial. Some examples are pulsating B stars, white dwarfs, β Cephei, δ Scuti, etc.
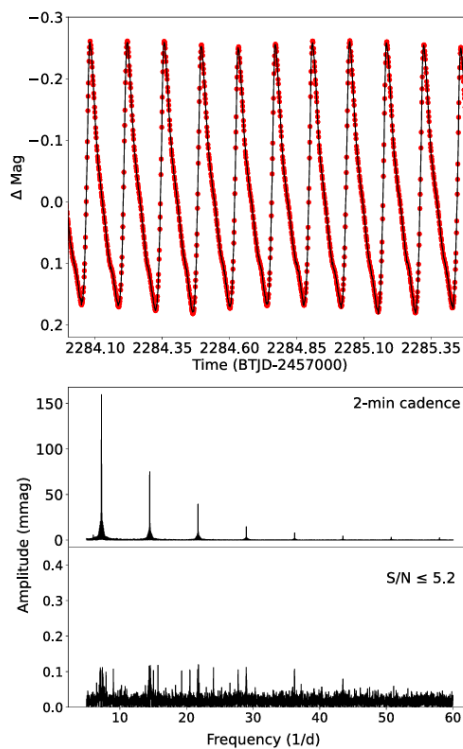
Figure 7 - The short-cadence light curve (sectors 36 and 37) of TIC 374753270 during 1.5 days (top panel), amplitude spectrum (middle panel), and amplitude spectrum of residual with S/N less than 5.2 (bottom panel). [10]

2.5 Variables in clusters - Star clusters, both open and globular, offer a unique environment for researching stellar evolution. Variable stars inside clusters are especially helpful because of the homogeneity of distance, composition, and age among cluster members.Star clustersare suitable for investigating variables since their member stars are relatively homogeneous in terms of age, metallicity, and distance.Variable stars inside clusters

are important for a variety of reasons: distance determination, age estimation, chemical composition, evolutionary understandings, etc.

Figure 8- Five minute image of IC 348 obtained with the 0.6 m telescope at VVO through a Cousins I Đlter, showing the part of the cluster monitored for variability. The Đeld is onaside with north at the top and east to the left.[11]

III.Basics of photometry:

Photometry is a foundation of stellar astronomy, providing critical insights into the properties of stars. By measuring the light flux from stars at various wavelengths, photometry helps astronomers to deeplyunderstandthe energy output of stars.This gives insights about models of stellar structure[1]. Astar's coloris determined by comparing its brightness in two different spectral bands, which offers valuable information about its temperature. Photometric measurements can also be employed to study interstellar dust and are essential in determining the distances and sizes of stars. The Hertzsprung-Russell (H-R) diagram, a fundamental tool for understanding stellar evolution, is built upon photometric and spectroscopic data[1].

The primary objective of astronomical photometry is straightforward. It is to measure the light flux from celestial objects. However, challenges arise when different observers, using various telescopes and detectors, measure the same star from various locations[2]. These discrepancies are primarily due to the varying spectral responses of the telescopes and detectors involved. Photometry typically involves using a detector with a broad spectral response, with individual spectral regions isolated by filters that transmit only a narrow range of wavelengths[2]. However, it is impossible to manufacture detectors and filters that are perfectly identical. To address this, observations of standard stars are made to determine calibration coefficients for the necessary

equations. These calibrated equations allow for the conversion of measurements from any unknown star into a standard photometric system, ensuring consistency across observations[2].

$M_\lambda = m_{\lambda 0} + \beta_\lambda C + \gamma_\lambda$

$C = \delta C_0 + \gamma_c$

Thus, photometric systems can be defined by defining the detectors, filters, and a set of standard stars [2].

Observing standard stars allows an observer to take observational measurements of program stars and convert them to the standard *UBV* system. The transformation equations in a general form can be applied to any photometric system. It is typical to alter the symbols in the transformation equations to indicate the use of the *UBV* system[2]. Now the transformation equations can be written as

$v = -2.5 \log d_v$

$b = -2.5 \log d_b$

$u = -2.5 \log d_u$

where v, *b, u* and d_v, d_b, d_u represent the instrumental magnitudes and measurements through the *V, B,* and *U* filters, respectively[2].

UBV system is the most commonly used system. There are some other systems also like-

o   Morgan-Keenan spectral classification system

o   Infrared extension of UBV system

o   The Stromgren four-color system

o   Narrow band Hβ photometry etc.

Depending on the necessity of the project and the nature of the stars, one can choose the suitable system for the required calculations.

IV. Discoveries - Examples with light curve analysis:

Till the middle of 19th century, number of known variables was only 18. They had been found accidentally during other observations. Most of the recent discoveries are because of the systematic work like particularly choosing a star field and with repeated observations and comparisons. There can be different methods to record light and compare the variations, if any. As per the International Variable Star Index given by the American Association of Variable Star Observers, more than 22,79,000 variable stars have been cataloged however, several stars are yet suspected to be variables[1].

One of the most significant breakthroughs in astronomy during the study of variable stars was Henrietta Leavitt's discovery of the Period-Luminosity relationship in Cepheid variables. In 1912, Leavitt demonstrated that the luminosity of a Cepheid variable is directly related to its pulsation period, providing a tool for measuring cosmic distances. This discovery laid the foundation for Edwin Hubble's subsequent revelation of the expanding universe, which is pivotal in modern cosmology.

In recent decades, the study of Delta Scuti and Gamma Doradus stars has opened new possibilities for researching the interiors of stars. These pulsating variables exhibit both radial and non-radial oscillations, making them ideal candidates for asteroseismology. By analyzing their oscillation modes, astronomers can understand the internal structure and the composition of these stars, explaining the processes influencing stellar evolution.

Variable stars have also played a crucial role in the discovery of exoplanets. The transit method, which involves detecting the slight dimming of a star as a planet passes in front of it, relies heavily on precise measurements of

stellar brightness. Variable stars, particularly those with predictable brightness patterns, have been instrumental in refining this technique, leading to the discovery of thousands of exoplanets in recent years.

V. Challenges and limitations:

5.1 Availability of resources - The observations of faint stars or clusters or AGNshave significant challenges when using small telescopes. This ismainly due to their limited light-gathering capabilities. Modern telescopes with high-sensitivity detectors, as well as specialist image analysis tools, are necessary to conduct effective studies on these objects.Access to such resources is often limited, as not all researchers can get the opportunity to utilize well-equipped observatories. The high demand for observation time at major observatories further restricts availability, making it difficult to use such necessary resources for comprehensive studies.

5.2 Impact of Climate Conditions - Optical astronomical observations are dependent on climatic conditions. A significant portion of observation time can be lost due to adverse weather, particularly cloud cover. Stars that are visible during certain seasons, notably in parts of winter and most of summer, can be observed with greater clarity during these periods. Consequently, the selection of target stars for observation programs must take seasonal climate variations into account.

For certain astronomical objects, radio telescopes may serve as an alternative when optical observations are hindered by poor weather. However, the availability of radio telescopes is limited, presenting a significant constraint on their use as a supplementary tool in these situations.

5.3 Data Storage and Analysis Considerations: The temporal characteristics of variable stars significantly influence both data storage and analysis. For short-period variables, the relatively fewer observational data points facilitate straightforward data management and expedite analysis. In contrast, long-period variables necessitate extended observation durations, resulting in larger datasets. The increased volume and complexity of these datasets render the storage and analysis processes more time-intensive and laborious.

VI. Future directions:

6.1 Robotic Observatories and Automated Data Processing

Robotic observatories offer the significant advantage of being deployable in remote locations, provided there is reliable internet connectivity. These systems require minimal human intervention for overnight observations, allowing for efficient data collection without the need for on-site personnel. However, regular maintenance by a technician with expertise in mechanical, electrical, electronic, and internet systems is essential. Continuous, uninterrupted power supply is crucial, as well as monitoring to address potential issues such as defocus or tracking errors.

While these systems optimize observational time through pre-programmed sequences, they are not without challenges. Power or internet disruptions, if not promptly addressed, can lead to significant operational downtime. The installation and repair costs are considerable, necessitating a robust support system to ensure consistent performance.

6.2 Need of collaborative work

Variable stars comprise a wide spectrum of phenomena, including pulsing stars like Cepheids and RR Lyrae as well as eruptive variables like novae and supernovas. Each form of variable star poses unique observational challenges, necessitating distinct methodologies, apparatus, and data analysis procedures.Astronomers must

collect data at many wavelengths to adequately classify these stars, including optical, infrared, ultraviolet, and, in certain cases, radio and X-ray. This multi-wavelength approach is critical for understanding the physical processes underlying variability. However, no single observatory or researcher can consistently cover such a broad spectrum.Furthermore, many variable stars show periodic or quasi-periodic behavior that might last days, months, or even years. Continuous monitoring is required to capture these variations and generate a full light curve. This is especially true for irregular variables or those that change rapidly, when missing a brief occurrence could result in incomplete or incorrect findings.

VII. The Role of Collaboration in Overcoming Observational Challenges

7.1 Global Coverage: Due to the Earth's rotation and the geographical constraints of observatories, no one site can continually observe a star. Astronomers can achieve practically continuous monitoring by partnering with observatories all around the world, which is essential when researching variables with short or irregular intervals. International networks such as the American Association of Variable Star Observers (AAVSO) have played an important role in coordinating such efforts, allowing for continuous data collection around the clock.

7.2 Multi-Wavelength Observations: As previously said, understanding variable stars frequently requires data from various wavelengths. Collaborative networks enable diverse observatories to provide observations across the electromagnetic spectrum. For example, ground-based optical telescopes can collaborate with space-based observatories such as the Hubble Space Telescope (for ultraviolet) and the Chandra X-ray Observatory to provide a more complete picture of the star's behavior.

7.3 Resource Sharing and Expertise: Collaboration enables researchers to pool resources such as telescopes, instruments, computational tools, and software. It also encourages the interchange of expertise, allowing specialists in many fieldssuch as photometry, spectroscopy, and data analysisto contribute their abilities to a common effort. This interdisciplinary approach is essential for addressing the complicated issues raised by variable stars.

7.4 Data Repositories and Open Science: Collaborative initiatives include data sharing through centralized repositories. Open access to massive datasets collected by several observers enables more complete analysis and the possibility of new discoveries. Repositories like the AAVSO International Database (AID) and the Variable Star Index (VSX) are invaluable to the community, allowing researchers to build on each other's work and avoid duplicating efforts.

Collaboration has enabled several key findings in variable star studies. For example, the discovery of new types of pulsing stars, such as the Delta Scuti and Gamma Doradus variables, was aided by global networks of observers who gave substantial data over lengthy periods. Similarly, coordinated multi-wavelength campaigns that coupled ground-based optical data with infrared and ultraviolet observations from space have substantially aided the study of Mira variables and Wolf-Rayet stars.

VIII.   Conclusion:

Many suspected variable stars are yet to be classified and studied. Using small telescopes and various databases, one can analyze the nature of suspected variable stars using photometric techniques. Further, these observational results need spectroscopic analysis of these stars.

IX. References:

[1]. "Variables: What Are They and Why Observe Them? | aavso." https://www.aavso.org/variables-what-are-they-why-observe-them

[2]. A. A. Henden and R. H. Kaitchuck, *Astronomical photometry: A Text and Handbook for the Advanced Amateur and Professional Astronomer*. 1990.

[3]. Variable Stars, C.HoffmeisterG.RichterW.Wenzel, Springer-Verlag Berlin Heidelberg New York Tokyo, ISBN 3-540-13403-4

[4]. Variable stars across the observational HR diagram, Journal of Physics: Conference Series **118** (2008) 012010, doi:10.1088/1742-6596/118/1/012010

[5]. Variable Star Classification andLight Curves

[6]. Hoffleit, D. (1997). History of the discovery of Mira stars. Journal of the American Association of Variable Star Observers, 25, 115-136.

[7]. ASTRONOMICAL PHOTOMETRY- A Text and Handbook for the Advanced Amateur and Professional Astronomer Arne A. Henden Ronald H. Kaitchuck, Department of Astronomy, The Ohio State University, Published byWillmann-BellJnc.

[8]. M. F. Walker and G. H. Herbig, "Photoelectric and spectroscopic observations of UX Ursae Majoris.," *The Astrophysical Journal*, vol. 120, p. 278, Sep. 1954, doi:10.1086/145914.

[9]. S. Kimeswenger, S. Dalnodar, A. Knapp, J. Schafer, S. Unterguggenberger, and S. Weiss, "The unusual Nova Cygni 2006 (V2362 Cygni)," *Astronomy and Astrophysics*, vol. 479, no. 3, pp. L51–L54, Jan. 2008, doi: 10.1051/0004-6361:20078821.

[10]. F. Vasigh, E. Ziaali, and H. Safari, "Signature of High-amplitude Pulsations in Seven δ Sct Stars via TESS Observations," *The Astrophysical Journal*, vol. 969, no. 1, p. 19, Jun. 2024, doi: 10.3847/1538-4357/ad4457.

[11]. W. Herbst, J. A. Maley, and E. C. Williams, "A variability study of Pre–Main-Sequence stars in the extremely young cluster IC 348," *The Astronomical Journal*, vol. 120, no. 1, pp. 349–366, Jul. 2000, doi: 10.1086/301430.

Photoelectric Photometry of Eta Gemini (Semi-Regular Variable Star)

Sachin Pandit[1], Abhay Dashrath[2*], Anil Ardad[3], Pravin Kokne[4], Rajendra Yannawar[5]

[1]J.E.S. College, Jalna

[2]Dr. D. Y. Patil Institute of Technology, Pimpri, Pune

[3]Deogiri College, Chhatrapati Sambhajinagar

[4]Badrinarayan BarwaleMahavidyalaya, Jalna

[5]Milind Science College, Chhatrapati Sambhajinagar

*Corresponding author. E-mail: adashrath@gmail.com

Abstract :

Variable star is quite simply, a star that changes brightness i.e. its apparent magnitude (as seen from Earth), changes systematically with time. These have attracted both amateur enthusiasts and professional scientists for centuries. While a few of these stars are bright enough to be seen with the naked eye, observing fainter ones requires telescopes. Also, capturing their light necessitates advanced detectors such as photometers (SSP-3A Gen II), an automated telescope etc.

In an endeavour to further study the data received, a few variable stars based on perceived climatic conditions prevalent in Jalna, magnitude synthesis capabilities of the telescope (small automated 12" telescope) used, a photoelectric photometry of semi-regular Variable Stars namely ETA Gem was conducted during the period 2015 - 2016 at J. E. S. Observatory, Jalna.

The photometric observations were taken on SSP-3A Gen II Photometer and data reduction listed variations in B and V magnitudes of the stars significantly. The study of variations in brightness of stars thus measured shows variation in phases, amplitude and shape of light curves. Light curves showed more than one period of variation in brightness hence categorised as Semi-regular stars.

Key words: Photometry, Semi-regular stars, Suspected variable stars, ETA GEM

I. INTRODUCTION

Eta Gemini (also known as Propus) is a semi regular variable star situated in the constellation of Gemini. The Eta Gemini displays fluctuations in brightness which is very intriguing for scientists and astronomers alike. The star is approximately 400 light years away from Earth and is visible to the naked eye under clear sky. It also holds a unique position within the stellar classification system due to its variable nature. Eta Gemini is particularly notable for its complex light variations. The study of Eta Gemini provided valuable insights into the late stages of stellar evolution, particularly for stars into late stages of evolution. The complex light variations depicted by Eta Gemini make it an excellent subject for studying the processes that govern variability.

Several papers have been published that focused on variety of aspects related to the photometry of Eta Gemini (Propus): Henrietta Swope (1931) focused on foundational works in the application of photoelectric methods to stellar photometry, Olin J.Eggen (1956) elaborated on photometric observations of several red giants while providing insight into variability of Eta Gemini and light curve analysis, Alan J. Penny (1982) with his crucial work in understanding the periodic and non-periodic changes in brightness that characterize these types of stars, Guillermo Torres and Kristy Sakano (2022) with their research spanning 11 years of spectroscopic monitoring data with historical photometry, revealing that Eta Gemini is part of a binary system with an 8.2-year period. Many research papers available through AAVSO highlight the historical photometric and spectroscopic data of Eta Gemini. This star has been a significant subject due to its complex variability.

II. Observations:

The B and V photoelectric photometric observations of Eta Gemini were taken during the year 2015-16 using the 12" Meade LX 200 Schmidt- Cassegrain reflector telescope equipped with SSP-3A Gen 2 (OPTEC INC USA) photoelectric photometer. The model of the detector used in the SSP-3Aphotometer is S1087-01.

Calibration Standard: Response ofB and V filter and detector closely matches that of Johnson standard B and V response of B and V filter. In order to obtain accurate differential photometry, 1Gemini (HD 41116) was chosen as the comparison star for Eta Gemini. The V magnitude for 1 Gemini (HD 41116) is 4.16 as compared to 3.15 for Eta Gemini (HD 42955).

The observations corrected for the atmospheric extinction and transformed into BV system. The differential magnitude in V band and (B-V) colors for Eta Gemini is obtained by photometer. These are plotted as follows:

VariableStar: Eta Gemini (HD 42995)V=3.15B-V=1.56

ComparisonStar:1 Gemini (HD41116)V=4.16

JD	Visual mag. V	B-V	Diff. mag.	
			del V	del (B-V)
2457339,39881	3,17	1,46	-1,050	0,630
2457342,38159	3,19	1,80	-1,885	0,965
2457346,37836	3,18	1,42	-0,995	0,590
2457353,38578	3,18	1,48	-1,040	0,650
2457365,39602	3,12	1,34	-1,055	0,505
2457366,39824	3,24	1,52	-0,940	0,690
2457369,39146	3,21	1,60	-0,950	0,765
2457370,43899	3,18	1,57	-0,995	0,740
2457371,39366	3,25	1,52	-0,935	0,690
2457387,40431	3,20	1,54	-0,975	0,710
2457388,34385	3,20	1,51	-0,975	0,680
2457389,40435	3,19	1,56	-0,990	0,730
2457390,37962	3,23	1,52	-0,945	0,685

2457391,35160	3,19	1,51	-0,990	0,680
2457392,40322	3,16	1,57	-1,015	0,740
2457393,39716	3,18	1,54	-0,995	0,710
2457394,39823	3,36	1,64	-0,815	0,815
2457397,38269	3,16	1,56	-1,015	0,725
2457398,38480	3,22	1,50	-0,965	0,670
2457399,39076	3,20	1,58	-0,980	0,750
2457400,40649	3,17	1,57	-1,010	0,735
2457401,39218	3,33	1,45	-0,850	0,620
2457416,36367	3,18	1,59	-0,995	0,755
2457417,38275	3,20	1,58	-0,975	0,745
2457418,35932	3,27	1,54	-0,915	0,705
2457419,35895	3,25	1,77	-1,770	0,940
2457420,37174	3,22	1,56	-0,960	0,735
2457422,35436	3,36	1,49	-0,825	0,660
2457424,35397	3,23	1,59	-0,960	0,760
2457428,37016	3,30	1,53	-0,885	0,700
2457429,41257	3,35	1,84	-0,780	1,010

Table 1: Photometric Observation for Eta Gemini 2015-16(JD &different magnitudes)
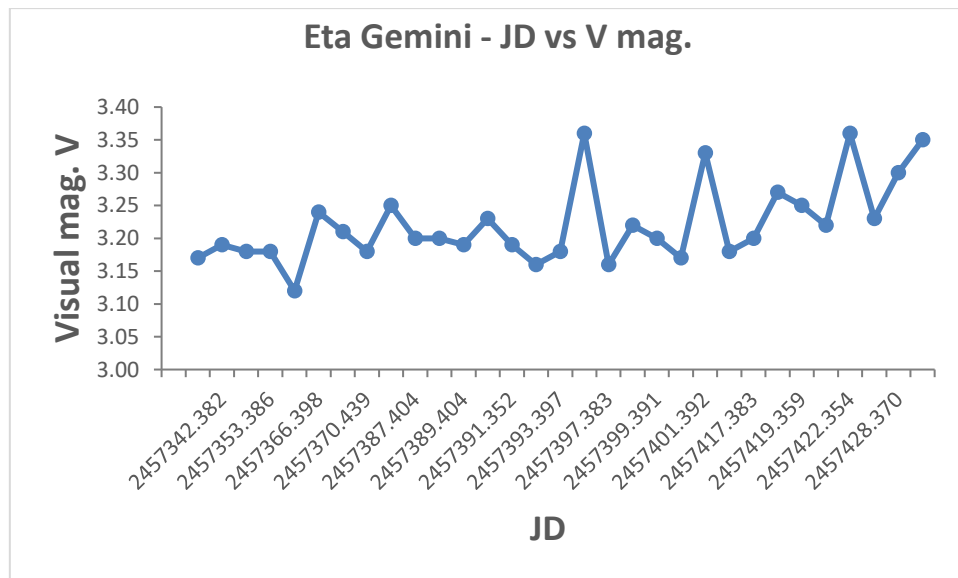
Figure1 - Light Curve of Eta Gemini (Julian Date v/s Visual V Magnitude)
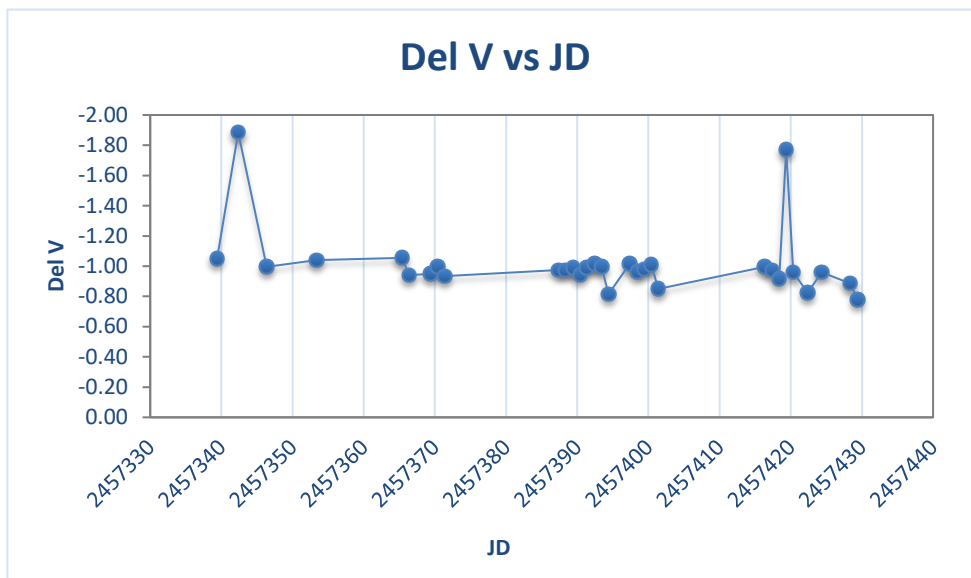
Figure 2 – Light Curve of Eta Gemini (Julian Date v/s delta)

III. Discussion:

ForEta Gemini (HD 42995) vis-a-vis 1 Gemini (HD 42995)nosignificantlightvariationwasdetectedwith respect to thedifferentialmagnitudes. This in turn is a remarkable measures of the quality of our observation.TheuncertaintiesindelVanddel(B-V)are0.05and0.06magnitudes.

OurobservationsofEta Geminiconclude that light variations are consistent with pulsating star. The variations in magnitude can be modeled for finding the star's amplitude and period of variation. Analysis of the light curve displays a clear periodicity which is crucial for modeling and to understand the internal structure. Luminosity and temperature are key physical parameters that can be used for calibration along with photometric data.

IV. References:-

[1]. The General Catalogue of Variable Stars" (GCVS) by N. N. Samus et al.

[2]. The Light Variations of the Semiregular Variables" by Alan J. Penny (1982)

[3]. Photoelectric Observations of Variable Stars" by Henrietta Swope (1931)

[4]. Photometric Studies of Red Variables" by Olin J. Eggen (1956)

[5]. Photometric Properties of SR Variables in the Infrared" by George H. Herbig (1960)

[6]. Studies of Long-Period Variables with Small Amplitude. II. Stars of Type SR" by Frank Bradshaw Wood (1976)

Synthetic Aperture Radar and Earth Observation

Pradnya R Maheshmalkar[a], Shivanand V Kshirsagar[a], Shafiyoddin B Sayyad[b]

[a] Department of Physics, Mrs. K. S. K. College, Beed, 431122, (MH) India

[b] Department of Physics, Milliya College, Beed, 431122, (MH) India

Corresponding author: pmaheshmalkar4@gmail.com.

Abstract :

Remote sensing data for Earth observations based on a variety of satellite sensors has been developed rapidly.The aim of this paper is, to develop a conceptual understanding, approaches on Satellite-based Earth Observation with the focus on Synthetic Aperture Radar (SAR) technology. Synthetic Aperture Radar is a microwave remote sensing technology. SAR technology with all-weather, all-time capability provides detailed images of the Earth's surface. SAR imagery has become essential for forecasting, mapping, issuing early warning and planning our mission and policies.

This study reviews the operating framework, the innovative applications of SAR technology, that operate in different frequency ranges of the microwave portion of electromagnetic (EM) signals for Earth monitoring. Many Natural Surfaces, do not fall into the validity regions of the hypothetical models, at microwave frequencies. Also, even when they do so, the existing models fail to propose outcomes in good agreement with the experimental observations. Each of the methods and models has its own limitations of retrieval capacity in terms of their microwave bands used or in their target surface characteristics. The impact of SAR technology on various fields and many benefits for earth observations provides a promising future.

Keywords- Synthetic Aperture Radar, Earth Observation

I. INTRODUCTION

Earth Observation refers to the use of remote sensing technologies to monitor land, marine (seas, rivers, lakes) and atmosphere. Satellite-based Earth Observation relies on the use of satellite-mounted payloads to gather imaging data about the Earth's characteristics. The images are then processed and analysed in order to extract different types of information that can serve a very wide range of applications[1].Synthetic Aperture Radar (SAR) technology has revolutionised our ability to observe and monitor the Earth's surface [2].Satellite Remote Sensing is the science of identifying earth's surface features and estimating their geo-biophysical properties using electromagnetic radiation as a medium of interaction from satellites [3]. For earth observation, Synthetic aperture radar (SAR) has been progressively used. Synthetic aperture radar (SAR) imaging, is a technique that allows us to remotely map the reflectivity of objects or environments with high spatial resolution, through the emission and reception of electromagnetic (EM) signals.SAR applications based on disciplines such as

geographical mapping, earthquake and flood monitoring, natural hazards and environment and resource surveying.
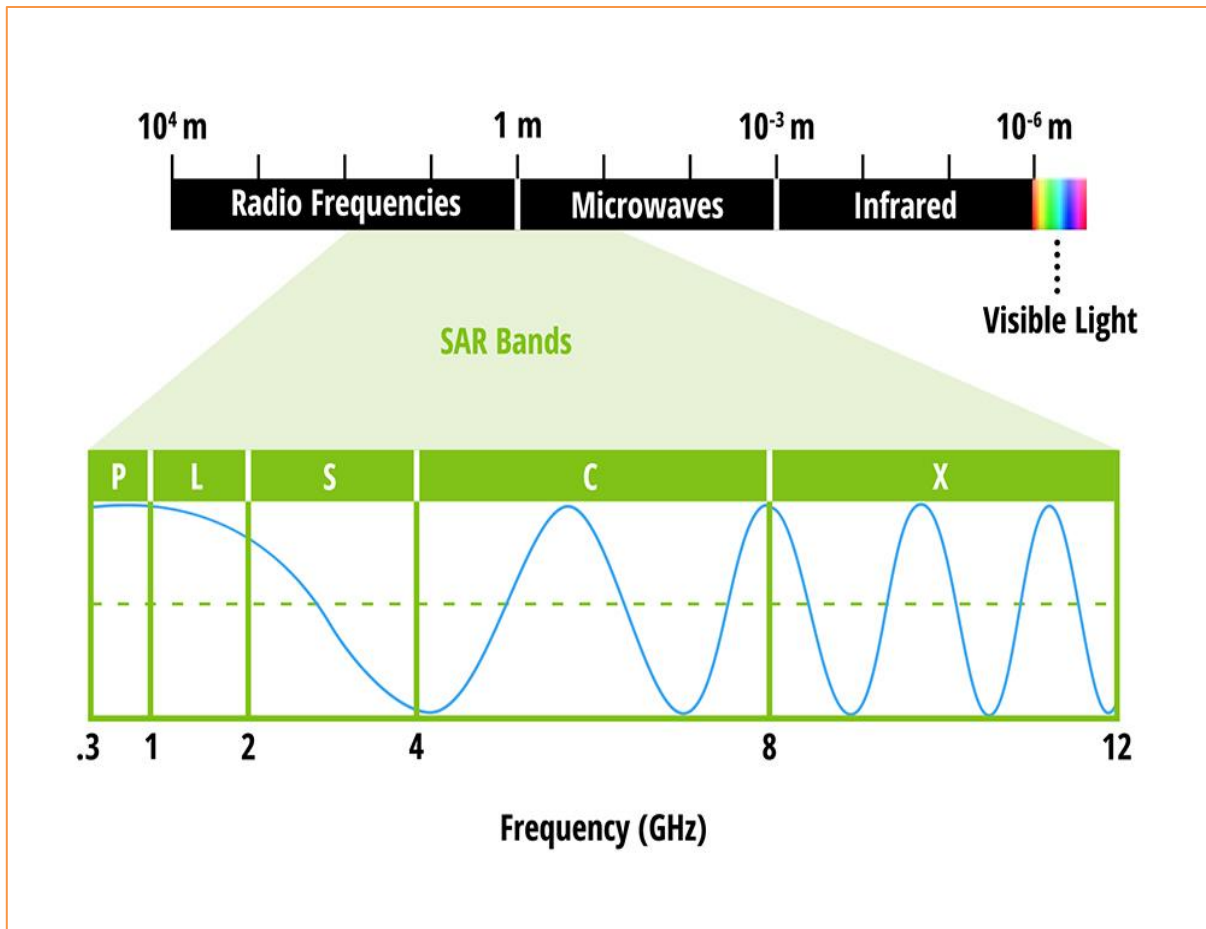
Fig. 1.The electromagnetic spectrum with microwave bands inset.

The different wavelengths of SAR are often referred to as bands, with letter designations such as X, C, L, and P. The Fig. above notes the SAR bands with associated frequency in the electromagnetic spectrum [4].SAR satellite systems operate in different frequency ranges, including X-band, C-band, and L-band, each with its own benefits and limitations. The choice of frequency depends on the specific application and the desired image resolution [5].The difference in the backscattering mechanisms triggered by different wavelengthsstrongly influences the suitability of the sensor with the application [6]. Synthetic Aperture Radar (SAR) is active microwave Sensor [7].

Analysing the information collected by the sensors that operate in the microwave portion of the electromagnetic spectrum is called as Microwave Remote Sensing.Microwave imaging radar has the ability to make measurements over virtually any region at any time, regardless of weather or sunlight conditions.Because of SAR's advantages in operating in night-time and cloudy environments, SAR has become instrumental for rapid landscape change monitoring required for Earth observation. Different wavelengths are measured, making SAR effective for range finding using different frequency bands, helping to measure surface roughness and different scales of surface properties [8].

For environmental balance and studies,the focus of research on the recent techniques and approaches in microwave remote sensing is important. Because, the rapid growth of population, its impact on the environment and limited available resources on the earth, the need for monitoring the environmental processes and managing our resources is necessary.

II. LITERATURE SURVEY-

The Sentinel Application Platform (SNAP) is ideal for Earth Observation processing and analysis due to technological modernisations.Although SAR imagery is not easily understood, it can contain important information which can be captured independently of meteorological conditions [9]. One of the limitations of working with SAR data has been the somewhat tedious preprocessing steps that lower-level SAR data requires. Depending on the type of analysis you want to do, the preprocessing steps can include: applying the orbit file, radiometric calibration, de-bursting, multilooking, speckle filtering, and terrain correction [10].The Copernicus Programme has become the world's largest space data provider, providing complete, free and open access to satellite data, mainly acquired by Sentinel satellites and offering services based on Earth observation. [11].

Space agencies and governmental organizations such as ESA, CSA, NASA, and USCS have long been providing and are the main source of satellite imagery[12]. SAR signals over a flat-water body produce specular reflection, which is directly related to the lowest backscattering range of the respective image.Only the SAR images that have been captured during the calm wind flow period exhibits specular signatures.Urban regions of the SAR image are known for very high backscattering values due to the corner reflection of input SAR signals from the concrete urban buildings as well as surrounding urban infrastructure [13].

Few of the SAR images applications are Monitoring of Kharif Crops, early detection of drought, flood mapping as part of disaster mining and relief operation, large area soil moisture mapping as input to Hydrological applications (drought and flood), in forestry for Biomass estimation (also forest density and type), in terrain analysis for accurate DEM generation, Land movement (for earthquake studies and land subsidence), in oceanography for Sea State, Waves, Oil Spills, Coastal Bathymetry. Further SAR images can used to carry out preliminary studies on snow / ice mapping, mapping of Surface and sub-surface structures, aquifers, mineralogy (related to geology domain) [14].

Land Use and Land Cover is a problem receiving a lot of attention given the need of developing land use policies, as well as mapping. It consists in establishing the land cover in the areas of interest, such as vegetation, water, or urban area and in detecting changes in land cover or usage over time [15].

III.Conclusion-

Satellites can prove to be one of the most important ones that help in mapping, predicting and planning our mission and policies.The reviewed literature highlighted the possible use and contribution of satellite remote sensing technology, precisely SAR, significant observations, the usefulness of microwave remote sensing and SAR data in all the considered topics. Observations of the earth Using SAR have a wide range of Practical applications to support the researchers, decisions makers.

IV.References-

[1].   https://paperswithcode.com/task/earth-observation
[2].   https://dragonflyaerospace.com/seven-applications-of-sar
[3].   A Review: How Space Technology can help in COVID-19 Pandemic (with Reference to Remote Sensing and GIS, Trupti Bhattacharjee, Indranil Bhattacharjee, Journal of Remote Sensing & GIS) (2021) Vol.10 Iss.3 No:1000286, pp 1-3.

[4]. https://www.earthdata.nasa.gov/learn/backgrounders/what-is-sar

[5]. https://dragonflyaerospace.com/seven-applications-of-sar/

[6]. https://www.mdpi.com2072-4292134604

[7]. A Qualitative Study on Microwave Remote Sensinag and Challenges Faced in India,Parismita A Kashya, ADBU-Journal of Engineering Technology (AJET), (2017) Issue 2,pp. 96-105.

[8]. https://www.gislounge.com/synthetic-aperture-radar-sar-earth-observation-and-mapping/

[9]. https://www.tandfonline.com/doi/full/10.1080/17538940802038317

[10]. https://www.earthdata.nasa.gov/learn/backgrounders/what-is-sar

[11]. Sentinel-1 GRD Preprocessing Workflow, Federico Filipponi, Proceedings (2019), 18,11.

[12]. Evaluation of Synthetic Aperture Radar Satellite Remote Sensing for Pavement and Infrastructure Monitoring, Abdulkadir Ozden, Ardeshir Faghria ,Mingxin Lia , Kaz Tabrizi, Procedia Engineering 145 (2016) pp.752 – 759.

[13]. Review of synthetic aperture radar frequency, polarization, and incidence angle data for mapping the inundated regions, Ramanuja Manavalan, J. Appl. Remote Sens. (2018)12(2), 021501.

[14]. Crop Mapping using SAR Imagery: An Review, Geetha M Nagraj, International Journal of Advanced Research in Computer Science, 7 (7), (2016),47-52.

[15]. SAR data applications in earth observation: An overview, Arsenios Tsokas , Maciej Rysz , Panos M. Pardalos, Kathleen Dipple, Expert Systems With Applications 205 (2022) 117342,pp.1-12.

Advancements in Metal Nanoparticales For Medical Applicaton: A Comprehensive Study

Ishwar G. Nannaware

Assistant Professor, Department of Chemistry, AnandraoDhonde Alias Babaji, Mahavidyalaya Kada, Tal. Ashti, Dist. Beed, Maharashtra India

Email:-nannawareishware@gmail.com

Abstract :

Metal nanoparticles are Nano level entities made of pure metals. The term metal nanoparticle is used to describe Nano sized metals with dimensions in the range of 1 - 100 nm (Nano regime). MNPs are flexible because of the ability to control their composition, shape, size, structure, encapsulation, assembly, and optical properties during synthesis. The large surface energies and surface to volume ratio provide specific electronic structure for the materials. The role of nanotechnology in the development of specific drug delivery systems is very important. This paper aims to introduce the characteristics of noble metal-based nanoparticles with particular emphasis on their applications in medicine and related sciences.

Keywords: Gold Nanoparticles, Drug delivery, antibacterial agents, Diagnostic,radio sensitizers.Bio imaging,Proteins and Gene Delivery,

I. INTRODUCTION

Nanoparticles have unique, size-dependent properties, which mean they are widely used in various branches of industry. The ability to control the properties of nanoparticles makes these materials very interesting for medicine and pharmacology. The application of nanoparticles in medicine is associated with the design of specific nanostructures, which can be used as novel diagnostic and therapeutic modalities. There are a lot of applications of nanoparticles, e.g., as drug delivery systems, radio sensitizers in radiation or proton therapy, in bio imaging, or as bactericides/fungicides. The existence of MNPs in solution was first recognized by Faraday in 1857. The Faraday's divided metal represents ruby colored colloidal gold consists of gold nanoparticles.The Large surface area to volume ratio and quantum confinement effect in Nanomaterial'sas compared to the bulk counterpart, these two important features enable unique properties of nanomaterial compared to the bulk counterpart. The metal nanoparticles are Nano assembly created from metals. MNPs are generated from different metals like Au, Ag, Pt, Ti, Zn, Ce, Fe etc. are investigated. Nanoparticles are defined commonly as solid, colloidal particles with sizes ranging from 10 to 1000 nm. However, European and other international committees narrow the above definition to structures having any one of their three dimensions in the order of 100 nm or less. They are offering advantages not possessed by larger particles, for example increased surface to volume ratio or improved magnetic properties. The Nanotechnology concerns the design, creation and use of

materials whose basic unit of measure is a nanometer. This term includes biomedical, pharmaceutical sciences, physics, advanced materials, and chemistry. The possibility of obtaining sub 100 nm materials yields their numerous applications in the field of biomedicine, such as imaging agents, drug delivery carriers (chemotherapeutics, genes, proteins etc.) or radio sensitizers in radiation, proton, or photodynamic therapy. The advantages of noble metal-based nanoparticles, which are important for medical applications, include high biocompatibility, stability and the possibility of large-scale production avoiding organic solvents and thus giving a positive effect on biological systems. These nanoparticles can allow for the controlled release of different drugs. It is possible to freeze dry nanoparticles to form a powder formulation. For comparison, magnetic nanoparticles, such as iron or cobalt nanoparticles often require coverage to improve their biocompatibility and prevent against agglomeration, oxidation, or corrosion.Noble metal-based nanoparticles can be prepared using several methods. One of the most popular methods is chemical reduction of the noble metal precursor (e.g., chloroauric acid, silver nitrate, or chloroplatinic acid to obtain gold, silver, or platinum nanoparticles, respectively) using a proper reducing agent, which can also act as a stabilizer (e.g., sodium citrate in the case of Nano gold synthesis) preventing the agglomeration of the nanoparticle. In addition, by changing reaction parameters, such as temperature, amount of precursor and reducing agent, reaction time, etc., it is possible to synthesize nanoparticles with various shapes and sizes.Recently, green chemistry methods have become more and more popular, allowing for limiting the usage of environmentally harmful substances. For this purpose, reducing agents from green sources are used, e.g., lactic acid, citrus fruits, coffee seeds, etc. More sophisticated approaches to obtaining these nanoparticles involve sonochemical, microwave assisted and electrochemical methods.

II. Gold Nanoparticles

The Colloidal Au NPs have been utilized for centuries by artists due to the vibrant coolers produced by their interaction with visible light. For e.g. A colorant in glasses known as Purple of Cassius, is a colloid resulting from hetero coagulation of Au NPs and SnO2. The Purple of Cassius can be used in the Meissen porcelain factory.Due to the unique optoelectronic properties of Au-NPs can be utilized in high technology applications such as Organic photovoltaics, Sensory probes, Therapeutic agents, Drug delivery, Electronic conductors and Catalysis.Generally, Au NPs are produced by reduction of the chloroauric acid (HAuCl4). After dissolving HAuCl4 the solution is rapidly treated with a reducing agent. This causes Au^{3+} to be reduced to Au^+. Then a disproportionation reaction occurs whereby 3 Au^+ ions give rise to Au^{3+} and 2 Au^0 atoms. Disproportionation is a rection in which same element undergo oxidation and reduction. This is a disproportionation

$$3Au^+ \quad \rightarrow \quad Au^{3+} \quad + \quad Au^0$$

The Au^0 atoms act as center of nucleation around which further Au^+ ions get reduced. To prevent the particles from aggregating, some capping agent is used Another method is used to produce modestly spherical gold nanoparticles of around 10–20 nm. It involves the reaction of small amounts of hot HAuCl4 with small amounts of trisodium citrate solution.The colloidal gold will form because the citrate ions act as both a reducing agent and a capping agent. In modified synthetic procedures different reducing agents (NaBH4, Ascorbic acid etc.) as well as different capping agents (tetraoctylammonium chloride, polymers etc.) are uses. In a very popular method, HAuCl4 is converted into Au NPs by using ascorbic acid (Vitamin C) as reducing agent and citrate as capping agent.

Sodium Citrate

HAuCl4 ~~Citrate Capped Au MNPs~~ →

Ascorbic acid

HAuCl4 Sodium citrate Ascorbic acid Citrate capped Au NPs

Interaction of Au NPs with light is strongly dictated by their environment, size and physical dimensions. Oscillating electric fields of a light ray propagating near a nanoparticle interact with the free electrons causing a concerted oscillation of electron charge that is in resonance with the frequency of visible light. These oscillations are known as surface plasmons resonance.

Applications of Au NPs The promising characteristic features of metal nanoparticles enable diverse applications. These applications include medical, biomedical, environmental, agricultural, catalysis, textiles, electronics, transportation, and many others. The characteristic features such as anti-angiogenic activity and localized surface plasmon resonance enable several therapeutic applications of noble metal nanoparticles (Ag, Au and Pt). Treatment for different types of cancer is a promising application of noble MNPs. Some applications are enlisted in table.

Types of MNPs	Properties	Application
Au MNPs	Anti-angiogenic	Prevention of multiple myeloma
Au MNPs	LSPR	As PDT agents for Cancer treatment
Au MNPs	LSPR/hyperthermia	For skin Cancer treatment
Ag MNPs	Anti-angiogenic	Cancer treatment

Therapeutic agents can be coated on to the surface of Au MNPs. The large surface area-to-volume ratio of Au MNPs enables their surface to be coated with other molecules for delivery. Generally, the aim of developing new delivery systems is to ensure the delivery of drugs to their desired sites in sufficient concentrations, while maintaining the efficacy of the delivered drug. This approach is highly useful in the treatment of diseases like cancer. By using different methods, drug loaded nanoparticles can be targeted toward the cancerous cells. These methods mainly include active targeting using conjugated ligand nanoparticles. For example, nanoparticle loaded with drugs can be conjugated with folic acid (FA) to target cancer cells which contain folate receptors
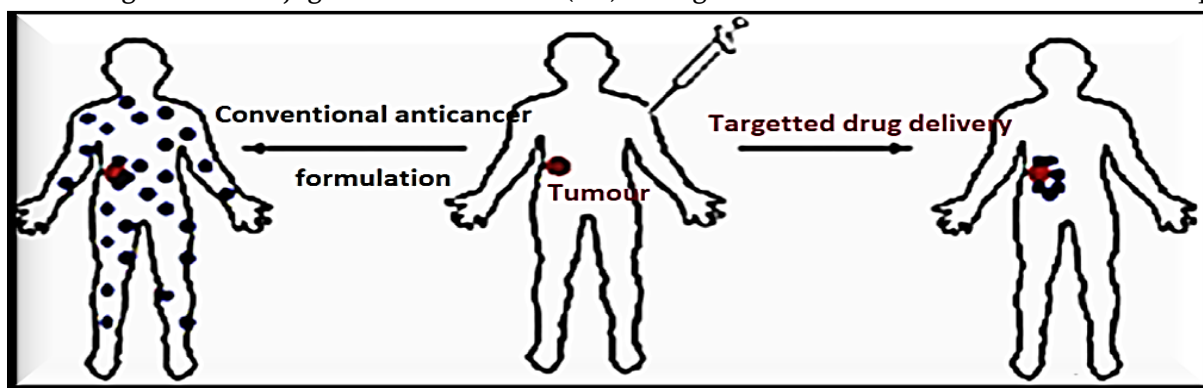
MNP surfaces can be functionalized with biocompatible polymeric materials (e.g., polyethylene glycol) to enable specific targeting of cells. Polymer functionalized MNPs are biocompatible and have a high encapsulation capacity enabling the delivery of drugs. Encapsulation of drug molecules is achieved through

electrostatic interactions or drug conjugation by means of the coating surface of NPs with polyelectrolytes or other polymers. MNPs are biocompatible and they can be straightforwardly eliminated from the body. This emphasizes their efficiency to serve as carriers of different therapeutic drugs through encapsulation or conjugation of these therapeutic moieties on the surface of the metal NP. From numerous viewpoints, the brain is a challenging organ for drug delivery, mainly due to the presence of the blood-brain barrier (BBB). BBB halts the drug molecules from crossing it. It is a major hurdle for the treatment of neurodegenerative conditions such as Alzheimer's and Parkinson's diseases. MNPs, on account of their small size, have the potential to cross various biological barriers in the body, particularly the BBB, which could lead to promising treatment outcomes for neurodegenerative disorders. Au NPs have been used as a potential delivery vehicle for anticancer drugs such as paclitaxel and Pt-based drugs.

III.Proteins and Gene Delivery

Proteins are macromolecules (also called biopharmaceuticals) that exert multiple biological actions in the human body. They have been known to be promising as treatment strategies for diverse diseases and disorders. MNPs are investigated for their adaptability in protein delivery. Au NPs, due to their desirable properties, are particularly used as "transport vehicles" for various therapeutic agents and biomolecules including peptides. Gene therapies present an excellent stratagem for the treatment or prevention of genetic as well as acquired diseases. Au NPs, in their diverse morphologies are potential candidates for DNA and RNA delivery as they protect nucleic acid and avert the molecules from nuclease degradation. In addition, Au NPs enhance targeting and help nucleic acid transfecting of cells. Conjugates of oligonucleotide-modified Au NPs have the potential to be used for intracellular gene regulatory agents. Gene therapy is a method of delivering exogenous DNA or RNA to treat or prevent diseases. Popular viral vectors frequently activate host immune systems reducing the efficiency of gene therapy. The above troubles can be solved by using non-viral systems such as metallic nanoparticles.Recent studies showed that Au NPs with different shapes (e.g., nanospheres or nanorods) protect nucleic acid by preventing DNA or RNA from degradation by nuclease. Au NPs conjugated to oligonucleotides show unique properties that can make them potential gene regulatory agents. These carriers can be divided into covalent (Au NPs may be functionalized with thiolated oligonucleotides) and noncovalent. For example, covalent Au NPs are able to activate immune-related genes in peripheral blood mononuclear cells, but not an immortalized, lineage-restricted cell line. This finding is promising in the application of such conjugates in the development of gene delivery systems. Son and co-authors have attached three fragments of nucleic acids to the surface of Au NPs. In this way, a nanomachine that silenced the polo-like kinase 1 via siRNA was obtained. In turn, Peng and co-authors have synthesized lactoferrin-derived peptides coated Au NPs. The obtained conjugates can efficiently deliver genes encoding vascular endothelial growth factor (VEGF) inducing blood vessel formation.There is a growing list of evidence documenting the application of nanoparticles as protein carriers. Organothiol, a molecular probe, could be used to study the structure and the morphology of proteins attached to Au NPs. Joshi et al. have obtained insulin-functionalized Au NPs, which have been found useful in transmucosal delivery of drugs for the treatment of diabetes in rat models. Enhancement of insulin delivery efficiency can be achieved by covering Au NPs with a non-toxic biopolymer, such as chitosan, which strongly adsorbs insulin on their surface. Schäffler and co-authors have dealt with conjugation of Au NPs, either with human serum albumin or apolipoprotein E. The results of these experiments showed that the attachment of proteins reduces liver retention compared to traditional citrate-stabilized Au NPs. Rathinaraj et al. obtained herceptin (anti-HER-2/neu monoclonal antibody) immobilized on 29 nm Au NPs improving the interaction of

this drug with the suitable receptors on the surface of the breast cancer cells (SK-BR3). Ag NPs have also been used as protein carriers. For example, Farkhani et al. have combined Ag NPs with cell penetrating peptides (CPP). CPP increase the penetration Ag NPs across the cell membrane causing a reduction of survival breast cancer cells (MCF-7 cell line). Di Pietro and co-authors have functionalized Ag NPs with a specific peptide sequence consisting of arginine, glycine, and aspartic acid (RGD), allowing for the effective entry of Ag NPs into leukemia and neuroblastoma cells.Numerous applications of noble metal-based nanoparticles as biologically active compounds carriers, give hope for more effective treatment of cancer and other civilization diseases. However, the main difficulty in using these nanoparticles in vivo, are problems with their degradation and elimination from the body. Therefore, the improvement of the pharmacokinetics of such nanoparticles should be the main goal of scientists considering this issue.

IV. Future Directions

In connection with the above, it is important to implement nanoparticle-based therapies for clinical trials because they can be a perfect tool for diagnostics and the treatment of numerous diseases, with special emphasis on cancer. However, it is necessary to overcome certain barriers resulting from the nature of some nanoparticles, such as problems with biodegradability or porosity. Moreover, there is relatively little information about the toxicity and interaction of these nanoparticles with living normal cells. It is particularly important to improve the pharmacokinetic parameters of the synthesized nanoparticles so they could reach the target site undamaged with high selectivity. This can already be obtained by functionalizing the nanoparticles with the appropriate ligands. Furthermore, a comprehensive approach to sensitizing cancer cells using several types of noble metal-based nanoparticles could yield improved treatment results. There is no doubt that the development of nanotechnology has opened new doors for more effective treatment and diagnosis of various diseases. However, some problems, e.g., the degradation and elimination of metal nanoparticles from the body, remain to be solved.

V. Conclusion

The application of nanotechnology has a significant impact on medicine and medical sciences. The wide range of applications of noble metal-based nanoparticles, especially Au NPs and Ag NPs, shows that it is worth continuing the work in this area. Huge possibilities of these structures concern their potential use as drug delivery systems, factors improving the quality of radiation-based anticancer therapy, and supporting molecular imaging, as well as compounds with bactericidal, fungicidal, and anti-viral properties. Au NPs are used in a variety of sensors. For example, a colorimetric sensor based on Au NPs can identify if foods are suitable for consumption. The Au NPs are used in the imaging of cancer cells and they are used as catalysts in a number of chemical reactions.

VI. References:

[1]. McNamara K., Tofail A.M. Nanoparticles in biomedical application. Adv. Phys. X. 2007;2:54–88. doi: 10.1080/23746149.2016.1254570.

[2]. Moreno-Vega A.I., Gomez-Quintero T., Nunez-Anita R.E., Acosta-Torres L.S., Castano V. Polymeric and ceramic nanoparticles in biomedical applications. J. Nanotechnol. 2012;2012:936041. doi: 10.1155/2012/936041.

[3]. Chatterjee K., Sarkar S., Rao K.J., Paria S. Core/shell nanoparticles in biomedical applications. Adv. Colloid Interface Sci. 2014;209:8–39. doi: 10.1016/j.cis.2013.12.008.

[4]. Brun E., Sicard-Roselli C. Actual question raised by nanoparticle radiosensitization. Radiat. Phys. Chem. 2016;128:134–142. doi: 10.1016/j.radphyschem.2016.05.024.

[5]. Hamblin M.R., Chiang L.Y., Lakshmanan S., Huang Y.Y., Garcia-Diaz M., Karimi M., de Souza Rastelli A.N., Chandran R. Nanotechnology for photodynamic therapy: A perspective from the laboratory of Dr. Michael, R. Ramblin in the Wellman Center for Photomedicine at Massachusetts General Hospital and Harvard Medical School. Nanotechnol. Rev. 2015;4:359–372. doi: 10.1515/ntrev-2015-0027.

[6]. Alaqad K., Saleh T.A. Gold and silver nanoparticles: Synthesis methods, characterization routes and applications towards drugs. J. Environ. Anal.Toxicol. 2016;6 doi: 10.4172/2161-0525.1000384.

[7]. Kudr J., Haddad Y., Richtera L., Heger Z., Cemak M., Adam V., Zitka O. Magnetic nanoparticles: From design and synthesis to real world applications. Nanomaterials. 2017;7:243. doi: 10.3390/nano7090243.

[8]. Zhang I., Gu F.X., Chan J.M., Wang A.Z., Langer R.S., Farokhzad O.C. Nanoparticles in medicine: Therapeutic applications and developments. Clin.Pharmacol.Ther. 2008;83:761–769.doi: 10.1038/sj.clpt.6100400.

[9]. Singh P., Pandit S., Mokkapati V.R.S.S., Garg A., Ravikumar V., Mijakovic I. Gold nanoparticles in diagnostics and therapeutics for human cancer. Int. J. Mol. Sci. 2018;19:1979. doi: 10.3390/ijms19071979.

[10]. Kimling J., Maier M., Okenve B., Kotaidis V., Ballot H., Plech A. Turkevich method for gold nanoparticle synthesis revisited. J. Phys. Chem. B. 2006;110:15700–15707. doi: 10.1021/jp061667w.

[11]. Garcia-Barrasa J., Lopez-de-Luzuriaga J.M., Monge M. Silver nanoparticles: Synthesis through chemical methods in solution and biomedical applications. Cent. Eur. J. Chem. 2011;9:7–19. doi: 10.2478/s11532-010-0124.

[12]. Yang M., Xia J. Preparation and characterization of platinum nanorods using ascorbic acid as the reducing agent. Adv. Mater. Res. 2013;774–776:577–580. doi: 10.4028/www.scientific.net/AMR.774-776.577.

[13]. An K., Samorjai G.A. Size and shape control of metal nanoparticles for reaction selectivity in catalysis. ChemCatChem. 2012;4:1512–1524. doi: 10.1002/cctc.201200229.

[14]. Yin X., Chen S., Wu A. Green chemistry synthesis of gold nanoparticles using lactic acid as a reducing agent. IET Micro Nano Lett. 2010;5:270–273. doi: 10.1049/mnl.2010.0117. [

[15]. Sujitha M.V., Kannan S. Green synthesis of gold nanoparticles using citrus fruits (Citrus limon, Citrus reticulate, Citrus sinensis) aqueous extract and its characterization. Spectrochim.ActaA Mol. Biomol. Spectrosc. 2013;102:15–23. doi: 10.1016/j.saa.2012.09.042.

[16]. Bogireddy N.K.R., Pal U., Martinez Gomez L., Agarwal V. Size controlled green synthesis of gold nanoparticles using Coffeaarabica seed extract and their catalytic performance in 4-nitrophenol reduction. RSC Adv. 2018;8:412. doi: 10.1039/C8RA04332A.

[17]. Okitsu K., Ashokkumar M., Grieser F. Sonochemical synthesis of gold nanoparticles: Effects of ultrasound frequency. J. Phys. Chem. B. 2005;109:20673–20675. doi: 10.1021/jp0549374.

[18]. Sahoo G.P., Basu S., Samanta S., Misra A. Microwave-assisted synthesis of anisotropic gold nanocrystals in polymer matrix and their catalytic activities. J. Exp. Nanosci. 2015;10:690–702. doi: 10.1080/17458080.2013.877163.

[19]. Roldan M.V., Pellegri N., de Sanctis O. Electrochemical method for Ag-PEG nanoparticles synthesis. J. Nanopart. 2013;2013:524150. doi: 10.1155/2013/524150.

Fabrication and Characterization of Some metal Oxide Nanoparticles using Sol-Gel Method

Sangita Shinde[1], Pallavi Nalle[2]*, Firdos Quadri[3], Prabhakar Kute[1], N. D. Chaudhari[1]

[1]Department of Physics, Pratishthan Mahavidyalaya, Paithan, Aurangabad, M.S. India

[2]*Department of Physics, Shri Shivaji Science and Arts College, Chikhali, Dist. Buldana, M.S. India

[3]Dr.Rafiq Zakaria College for Women, Aurangabad, M.S. India

Abstract :

Metal and metal oxide particles are very importance because of their prominence in vast fields of applications in Science and Technology. In this present paper work Structural and magnetic studies on CuO nanoparticles prepared by sol-gel route are reported. The fabricated nanoparticles are characterized by using X-ray powder diffractometry (XRD) to find the crystallinity, vibrating sample magnetometer (VSM), UV- visible spectra and Scanning Electron Microscope (SEM). The XRD analysis reveals that the crystallite size is of the order of 28.1 nm for the copper oxide nanoparticle annealed at 1100 ˚C. The role of oxygen vacancies is to generate free carriers mediating ferromagnetism between Cu spins. This sol-gel method is more economical, convenient, easy and effective in comparison to other known methods of synthesis of nano-materials.

Keywords: Copper Oxide Nanoparticles; Chemical Precipitation; Nanotechnology; Sol-Gel; XRD;SEM.

I. INTRODUCTION

Now a days metal oxide nanomaterials have attracted researchers due to their unique physical and chemical properties that makes them technologically very important in numerous fields [1, 2]. Copper oxide nanoparticles has a wide range of applications such as gas sensors, magnetic storage media, batteries, solar energy transformation, semiconductors, heterogeneous catalysis and field emission. Copper oxide nanoparticles have a great efficiency as Nanofluids in heat transfer applications. Some Scientist has been reported that by just 4% addition of CuO increases the thermal conductivity of water by 20% [3]. Copper Oxide has a semiconducting compound with a narrow band gap. Copper oxide nanoparticles has a wide range of applications such as gas sensors, magnetic storage edia, batteries, solar energy transformation, semiconductors, heterogeneous catalysis and field emission …etc [4,5].

The numerous methods are used to fabricate copper oxide nanoparticles, including solid state reaction, sol-gel, sonochemical preparation, microwave irradiation, alkoxidebased synthesis and thermal decomposition [6,7]. In the present study, for the synthesis of nano particles of copper oxide   sol-gel method was used as it was more economical, faster and easier.

II. METHODS AND MATERIAL

2.1 MATERIALS.

Analytical Reagent (AR) grade chemicals such as Copper chloride (II) CuCl2, Sodium hydroxide NaOH, Acetone and Ethanol C2H5OH were used as a initial material for the synthesis of CuO.

2.2 SYNTHESIS OF CuO

For synthesis of CuO-NPs, at first 6.0 g of copper (II) chloride dehydrate was dissolved in 320 ml of Ethanol and 3.6 g of sodium hydroxide pellet were dissolved in 100 ml ethanol separately. Drop wise addition of sodium hydroxide solution to copper (II) chloride dehydrate solution was carried out with constant stirring at room temperature. The color of the solution was turned from green to bluish green and finally to black as the reaction proceeded. The black precipitate was copper hydroxide. The precipitate was filtered by a centrifuge (Eppendorf Refrigerated Centrifuge Model 5702R, Germany). Then washed with ethanol and deionized water to remove the sodium chloride salt solution. After that, the precipitate was dried at about 50˚C in the dryer. The dried sample was annealed at temperature 1100˚C to obtain crystalline CuO-NPs. Then the annealed sample was grinded to get the powdered nanoparticles. The powder sample was used to characterize CuO-NPs. Schematically the chemical reaction can be represented as:

$CuCl_2 + 2NaOH \rightarrow CuO + 2NaCl + H_2O$
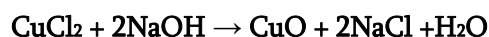
Prepared nano-particles were annealed at 1100 ˚C and then characterized by using X-ray diffractometer, UV-VIS spectrophotometer and Vibrating sample magnetometer.

2.3 CHARACTERIZATION TECHNIQUES

The prepared sample of copper oxide nano particle was characterized by XRD i.e. X-ray diffraction technique The crystalline structure, phase composition and crystallite size of CuO were revealed from XRD patterns obtained using Cu Kα radiation (λ = 1.541 Å) for 2θ value ranging from 10o to 60o in X-ray diffractometer (Bruker AXS D8 Advance). The morphology of the particles is observed by a scanning electron microscope (SEMEDS) using SEM make JEOL Model JSM - 6390LV and EDS make JEOL Model JED – 2300 with an accelerating voltage of 20 kV.

III.RESULTS AND DISCUSSION

3.1 X-RAY DIFFRACTION ANALYSIS

The crystal structure and phase purity of the nanoparticles were characterized by XRDFigure 1. Shows the XRD pattern of CuO nanoparticles. The XRD diffractogram of CuO nanopowder shows diffractions peaks at 31.7o, 34.7o, 38.0o, 47.9o, 52.7o, 57.5o, correspond to (110), (002), (111), (202), (020) and (113) reflections of CuO [8]. All the peaks can be indexed to the monoclinic crystal system CuO. The XRD patterns confirmed the synthesis of pure crystalline copper oxide nanoparticles. Average crystallite size has been estimated from the XRD pattern using the Scherrer's equation [9-10].

$D = 0.9\,\lambda / \beta \cos\theta$ \qquad (1)

Where λ is the X-ray wavelength used in XRD (0.15405 nm); θ is the Bragg angle; β is the FWHM, that is, broadening due to the crystallite dimensions. The average crystallite size of CuO nanoparticles is found to be around 28.1 nm.
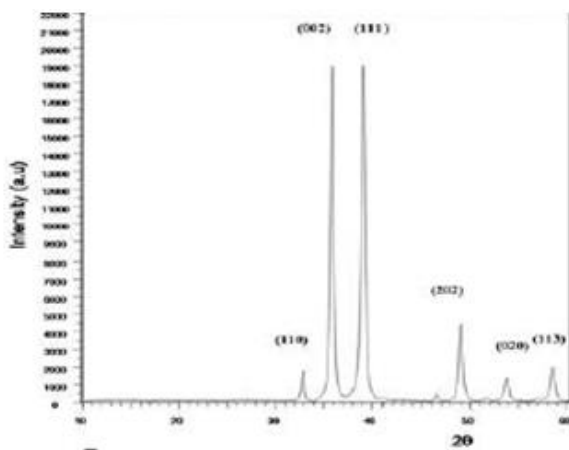
Figure 2:XRD Spectra of CuO Nanoparticles

3.2 SCANNING ELECTRON MICROSCOPY (FE-SEM)

The morphology of copper oxide nanoparticles was examined by SEM. Figure:2. Shows the SEM micrograph of the CuO nanoparticles at 15,000X magnification. It was apparent from SEM image that copper oxide nanoparticles were needle shape. The SEM micrographs revealed little aggregates of chemically synthesized nanoparticles[11].
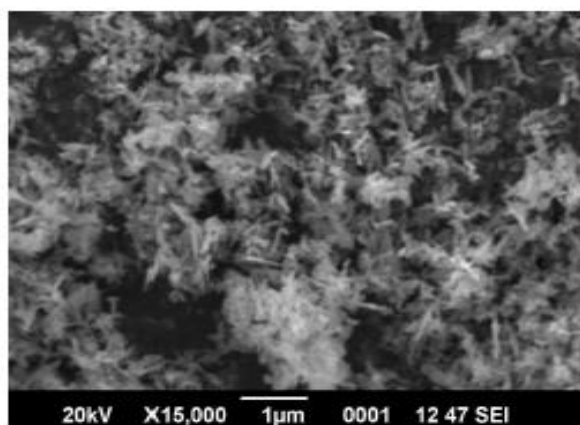
Figure 2: SEM Micrograph of CuONanoparticles

3.3 OPTICAL PROPERTIES

Transmission spectrum shown in Figure: 3 is used to study the band gap energy of copper oxide nanoparticles. The band gap of the copper oxide nanoparticles annealed at 1100 ˚C calculated to be 3.4ev. Light absorption takes place at 355 nm for nanoparticles annealed at 1100 ˚C.
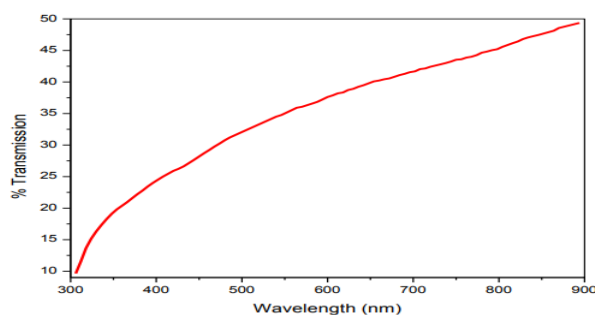
Figure: 3. Transmission spectrum of CuO nanoparticles

IV. CONCLUSION

In this study nontoxic, versatile and environmental friendly approach for the fabrication of copper oxide nanoparticles is used. CuO nanoparticles were successfully synthesized by sol-gel auto combustion method. XRD pattern revealed that copper oxide nano particles have monoclinic structure as well as pure phase formation of copper oxide with no impurities. The average crystallite size of the prepared sample was found to be 28.1 nm. SEM micrograph shows that shape of CuO nanoparticles was needle shape. This fabrication, low cost approach and reproducible should promise us a future large scale synthesis of nanostructures for versatile applications in nanotechnology.

V. REFERENCES

[1]. S.Gubbala, H.Nathani, K.Koizol, R.D.K. Misra, Physica B, 348 (2004) 317-28

[2]. P.Pramanik, Bull. Mater. Sci., (1995) 335

[3]. W.Wang, Y.Qi, Y.Ma, X.Li, X.Guo, J.Gao, M.Chen, Mater. Chem. Phys., 36 (2004)192

[4]. J. Azadmanjiri, S.A.Seyyed Ebrahimi, Phys. Stat. Solidi © 1 (2004) 3414

[5]. S.A.Khorrami, N.Naderfar, M.G.G. Mojadad, A.Z.Asian and R.Lotfi, J.Phys and Theo. Chem., 7(2) 91-94, Summer 2010

[6]. D.A.Sumo, m.R.Morelli, A.m. Segadaes, Mater. Res. Bull., 31 (1996) 1243.

[7]. AL Patterson, Phys. Rev., 1939, 56, 978.

[8]. S.Bajaj, P Patil, G N Kakade, S D Tapsale, K M Jadhav, S Shinde*, J.Phys: conference series 1644(2020) 012022

[9]. Shakti Bajaj, A.V.Raut, M.V. Khedkar, Sangita Shinde, K.M. Jadhav, AIP Conference proceeding 2369, 020182(2021) 13 sep. 2021 online publish.

[10]. M Rashad; M Rüsing; G Berth; K Lischka; A Pawlis, J. Nanomater., 2013, 2013, Article ID 714853, 6 pages.

[11]. Rajgovind; G Sharma; D Gupta Kr; ND Jasuja; SC Joshi, J. Microb. Biochem. Technol., 2015, 7, 140.

Circular Microstrip Patch Antenna : Design, Simulation, and Analysis For 5G Applications

Kiran Katke[1], S. K. Popalghat[2]

[1]Department of Physics, Anandrao Dhonde Alias Babaji Mahavidyalaya, Kada, Tal. Ashti, Dist. Beed-414202 Maharashtra, India

[2]Physics Research Centre, Post- Graduate Department of Physics, J. E. S. College, Jalna -431203 Maharashtra.

Abstract :

Microstrip Patch Antennas (MPA) have emerged as a remarkable discovery in the period of miniaturization, despite the fact that advancements in antenna engineering have resulted in the fast growth of communication networks. This work encompasses the design, modelling, and analysis of circular microstrip patch antennas. The resonant frequency of the recommended patch antennas is 9 GHz, which is within the X band range. Ansys HFSS software was used to create them using Rogers RT/duroid 5880 material, which has a dielectric constant of 2.2. Five performance measures were utilized to examine the recommended MPAs: return loss, bandwidth, VSWR, gain, and HPBW. The required information refers to the measurements of return loss, voltage standing wave ratio (VSWR), and half power beamwidth (HPBW). The recommended antennas are ideal for use in radar, wireless, and satellite applications.

Keyword: Circular, microstrip patch antenna, strip line feeding, 5G, HFSS.

I. INTRODUCTION

The research paper explores the design, simulation, and analysis of a circular microstrip patch antenna for 5G applications, focusing on its compact, high-efficiency operation, performance evaluation, and potential improvements, with a comparative study using advanced simulation tools HFSS.

An MPA has a base of ground plane over which a substrate with some relative permittivity of Ɛr is present, which comprises of a patch that might be of any form and size. These antennas are constructed using microstrip methods on a printed circuit board (PCB) and are mainly operated at microwave frequencies[11]-[12]. They not only have a benefit of being compact in size, but also their simplicity of manufacturing, low cost, lightweight, and conformance have extended their use considerably. Microstrip patch antennas have increasingly revealed themselves in numerous RF sectors. [1].

The kind of MPA is decided by the patch which might be of any form, most likely to be of square, dipole, elliptical, rectangular, triangular and circular. But the most recognized microstrip patch antennas are circular and rectangular [2]. Feeding is used to excite the antenna. Amongst the numerous feeding approaches, microstrip line, coaxial probe feed, proximity coupling, and aperture coupling are in demand [3]. The technology which we have utilized is microstrip line feeding.

The latest developments reveal that the wireless communication has evolved at a quick rate. 5G wireless standard has developed to be the most current technology now-a-days. The stupendous increase in mobile data, technologies are advancing from 4G i.e., fourth generation to 5G, fifth generation. Various different fields has already implemented the 5G technology such as Internet of Things (IoT), advance MIMO structure, advance tiny cell technology etc. [4]. It has been observed that millions of devices can be linked and operated utilizing 5G technology. Some of the future technologies that will become a reality thanks to 5G are: Smart grids, Smart Cities, Smart transportation, Telemedicine, Machine to machine communication etc. In advanced small cell technology 5G technology can be introduced with current 4G macro cells [5]-[7]. MONISHA D, et al, presents the design and simulation of a G-shaped microstrip antenna operating at 3.7 GHz for 5G applications, showcasing promising characteristics suitable for 5G communication systems [13]. Yohanes Galih Adhiyoga, et al, The circular microstrip patch antenna in 5G systems offers multiband coverage for 2.3 GHz, 3.5 GHz, and 26 GHz. Limitations may include size constraints and potential manufacturing complexities [14]. Ajit Singh, et al, The circular patch MIMO antenna is suitable for 5G millimeter-wave applications due to its compact size and high radiation efficiency (>93%). Limitations include a small impedance bandwidth and channel capacity loss [15]. Syahrial Syahrial, et al, Circular microstrip patch antennas in 5G offer high data rates and capacity. Limitations include narrow bandwidth. The novel design with DGS enhances gain and bandwidth, overcoming some limitations [16]. A. B. Sahoo et al, The arc-shaped slot Circular Patch Antenna is suitable for 5G applications due to its resonant frequencies and good performance. Limitations may include size constraints and potential manufacturing complexities [17].

This paper uses a systematic approach to design, simulate, optimize, and validate the antenna for 5G applications. The methodology includes a literature review, antenna design, simulation and optimization, data analysis and interpretation. The research aims to gather comprehensive information on existing microstrip patch antenna designs, analyze current trends, and identify gaps in existing research. The antenna design is based on 5G frequency bands and materials, and the antenna is optimized using advanced electromagnetic simulation software. The methodology aims to provide a comprehensive and systematic study of circular microstrip patch antennas for 5G applications.
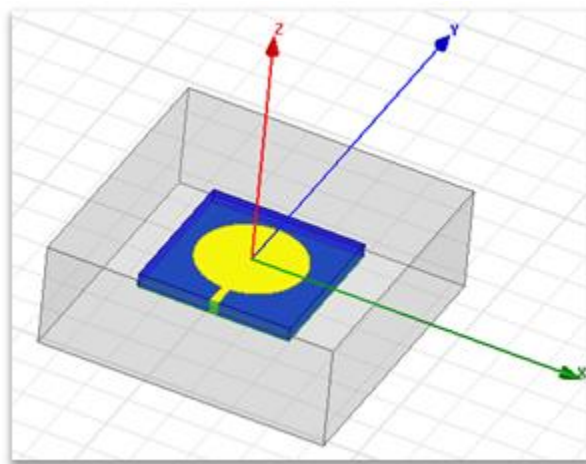
Fig.1. Circular Microstrip Patch Antenna with Microstrip line feeding technique.

II. ANTENNA STRUCTURE & DIMENSIONS

The proposed structure works on 9 GHz frequency for future 5G communication. The radius (a) of circular microstrip patch antenna can be calculated form the given formula[9],

$$a = F/\{1+2h/\pi \epsilon rF\ [In(\pi F/2h)+1.7726]\}^{(1/2)} \qquad (1)$$

Where,

$$F = (8.791 \times 10^9)/(f\_r \sqrt{(\epsilon\_r)})$$

Here,

a = Radius of Circular patch

h = Hight of Substrate

Ɛr = Dielectric Constant

fr = Resonating Frequency

The circular shaped microstrip fed patch antennas were built using High-Frequency Structure Simulator (HFSS) software. The suggested antennas are developed on a substrate with thickness h and relative permittivity Ɛr. The optimized parameters of the suggested antennas are shown in Table.

Table.1. MPA Designing Parameters

Parameters	Circular MPA
Resonating Frequency, fr	9 GHz
Patch Size	Radius, a = 6.25 mm
Substrate Height, h	1.6 mm
Dielectric Constant, Ɛr	2.2

III.SIMULATED RESULTS

3.1 Return Loss (S11)

Using wave port setup, S11 characteristics are retrieved as antenna return loss. Value of -10dB is regarded as the basis value which is deemed excellent in case of mobile communication. The antenna operates at planned band for 5G wireless technology. The patch antenna resonates at 9 GHz with a return loss of -21.69 dB Figure 2 shows return loss plot of the antenna.

Name	X	Y
m1	9.0000	-21.6982
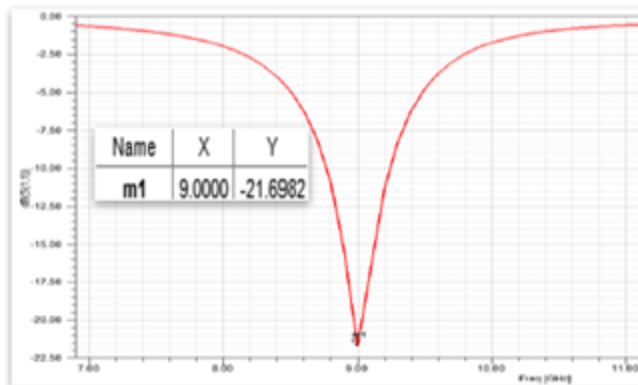
Fig. 2. Return Loss response of Circular MPA

3.2 Bandwidth

Fig.3 provides the bandwidth of circular microstrip patch antenna (on considering -10dB values of frequency). Using basic calculation the bandwidth was computed for the suggested antennas is 474.3 MHz.
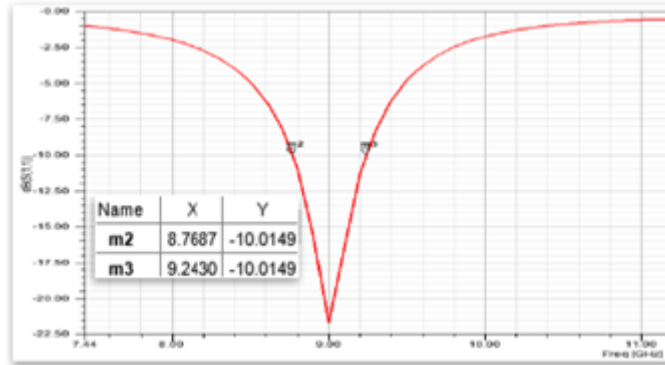
Fig. 3. Bandwidth calculation for Circular MPA.

3.3 VSWR

The Voltage Standing Wave Ratio (VSWR) plot of the antenna is depicted in figure 3. The allowable amount of VSWR for most of the wireless applications should not be more than 2.5 dB and it should be 1 dB preferably. As demonstrated in figure 3, the VSWR value attained at resonance frequency of 9 GHz is 1.43 dB which is adequate for its use in wireless applications.
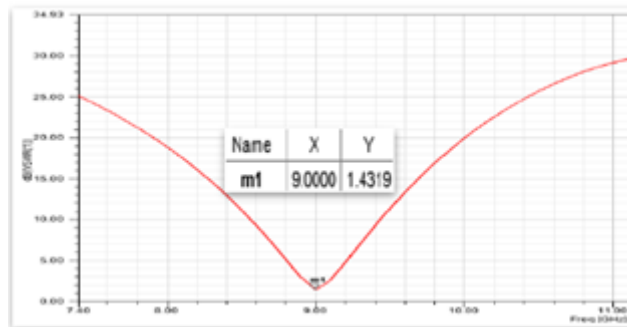
Fig. 4. Plot of VSWR of Circular MPA.

3.4 Gain

The gain plot indicates the antenna efficiency. The proposed patch antenna attained modest gain of 7.36 dB which is deemed excellent in terms of a small antenna design. Figure 4 illustrates the gain plot for suggested patch antenna.
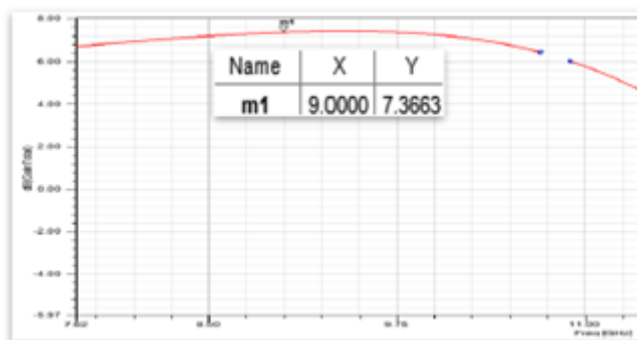
Fig. 4: Gain of Circular MPA

3.5. Radiation Pattern

The 2D radiation pattern of the patch antenna is depicted in figure 5.The half power beamwidth (HPBW) i.e., the angular beamwidth at 3dB of the circular microstrip patch antenna is smaller (77.48 degrees) for the proposed antenna which is desirable for mobile communication.
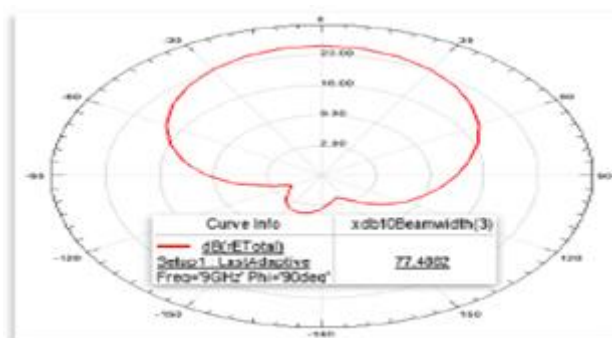
Fig. 12: Pattern of Radiation of Circular MPA

IV. DISCUSSION

The suggested circular MPA not only have a benefit of being compact in size but also have good and enhanced values of return loss, VSWR and HPBW when compared with prior study for X-Band [10]. As both bandwidth and resonating frequency are inversely proportional to the value of dielectric constant, we have utilized a very low value of dielectric constant ($\varepsilon_r = 2.2$) for substrate, so as to make it operate for a frequency of 9 GHz. Also for higher gain, return loss and bandwidth, a modest thickness substrate is used (h = 1.6mm), which also makes the suggested antenna compact in size. Hence, within the conceivable restrictions, we have created the best antennas matching all the earlier standards. The suggested antennas can be utilized for 5G wireless communication. 5G wireless standard has grown as a new and innovative standard for high speed transmission lines. In the near future different innovations will be witnessed for 5G standard.

V. CONCLUSION

In this research paper presents a study on the design, simulation, and analysis of a circular microstrip patch antenna optimized for 5G applications. The antenna resonates at 9 GHz with a return loss of -21.69 dB and can be utilized in future 5G wireless devices. The suggested patch antenna shows good radiation pattern and excellent gain of 7.3dB. The structure of the antenna has very low profile i.e. a=6.25 mm and can be easily integrated in devices where space is a major issue.

The design focuses on compact size, high efficiency, and wide bandwidth, with parameters carefully chosen for optimal performance in the targeted 5G frequency bands. The antenna was modeled and simulated using advanced electromagnetic simulation tools, leading to significant enhancements in performance metrics. The simulated results showed excellent performance across the desired 5G frequency bands, including bandwidth, gain, and radiation efficiency. The findings suggest that the antenna is well-suited for 5G devices and systems, including mobile devices, base stations, and IoT devices. Future research could explore further optimization, advanced materials, and real-world performance testing.

VI. References

[1]. Indra Singh, V. S. Tripathi, "Microstrip Patch Antenna and its Application: a survey", lnt. J. Comp. Tech. Appl. Vol 2(5), 1595-1599, 2011

[2]. Sumanpreet Kaur Sidhu, Jagtar Singh Sivia, "Comparison of Different Types of Microstrip Patch Antennas", International Journal of Computer Applications (0975-8887), proceeding of International Conference of Advancements in Engineering and Technology (ICAET 2015).

[3]. Ramesh Garg, Prakash Bartia, Inder Bahl, Apisak Ittipiboon, "Microstrip Antenna Design Handbook", 2001, pp 1-68, 253-316, Artech House Inc. Norwood, MA

[4]. Kin-Lu Wong, "Planar Antennas for Wireless Communication", Published by John Wiley & Sons, Inc., Chapter: 2, Pages: 26-65, 2003.

[5]. Rappaport, T.S.; Shu Sun; Mayzus, R.; Hang Zhao; Azar, Y.; Wang, K.; Wong, G.N.; Schulz, J.K.; Samimi, M.; Gutierrez, F., Will Work!," in Access, IEEE, vol.1, no., pp.335-349, 2013

[6]. Hang Wong, Kwai-Man Luk, Chi Hou Chan, Quan Xue, Kwok Kan So, Hau Wah Lai, "Small antennas in Wireless Communications", Proceedings of the IEEE Journal, vol. 100, no. 7, pp. 2109 – 2121, July 2012.

[7]. Ka Ming Mak; Hau Wah Lai; Kwai Man Luk; Chi Hou Chan, "Circularly Polarized Patch Antenna for Future 5G Mobile Phones," in Access, IEEE, vol.2, no., pp.1521-1529, 2014.

[8]. Harmandeep Kaur, Er. Mandeep Kaur, "Design of Microstrip Patch Circular Antenna Using Microstrip Line Feed Technique", International Journal for Research in Applied Science & Engineering Technology (IJRASET), Volume 6 Issue X, Oct 2018

[9]. Constantine A. Balanis, "Antenna Theory, Analysis and Design", John Wiley & Sons, 4th edition, December 8, 2015.

[10]. Tahsin Ferdous Ara Nayna, A.K.M. Baki, "Comparative study of rectangular and circular microstrip patch antenna in X Band", International Conference on Electrical Engineering and Information and Communication Technology (ICEEICT) 2014.

[11]. Katke, K., & Popalghat, S. K. (2024). X-BAND Rectangular Microstrip Patch Antenna: Design, Simulation, and Analysis. International Journal for Research in Applied Science & Engineering Technology (IJRA), 1101–1104. https://www.ijraset.com https://doi.org/10.21275/v5i5.nov163942

[12]. Kiran, K., & Popalghat, S. K. Review and Survey of Arbitrary Shape Dual Frequency and Dual Polarized Microstrip Patch Antenna. International Journal on Recent and Innovation Trends in Computing and Communication, 4(4), 648-652.

[13]. M., D. (2024). Designing g-shaped microstrip patch antenna for 5g application. Indian Scientific Journal Of Research In Engineering And Management, doi: 10.55041/ijsrem30034

[14]. Yohanes, Galih, Adhiyoga., Tri, Nur, Arifin., Syaeful, Ilman., Erfiana, Wahyuningsih., Dian, Rusdiyanto., Adhi, Mahendra. (2023). Highly Independent 5G Multiband Antenna using Circular Patch Structure. doi: 10.17933/bpostel.v21i2.364

[15]. Ajit, Singh., Santosh, Kumar, Mahto., Praveen, Kumar., Rashmi, Sinha. (2023). A compact circular patch mimo antenna with improved radiation efficiency for 5g millimeter-wave applications. doi: 10.58532/v2bs19p2ch1.

[16]. Syahrial, Syahrial., Maulana, Wahri, Nauval., Yunida, Yunida. (2023). A Novel Design of Two Circular-shaped Array Microstrip Patch Antenna with Defected Ground Structure for 5G Applications. doi: 10.1109/cosite60233.2023.10249014.

[17]. A., B., Sahoo., Nalini, Singh., Biswa, Binayak, Mangaraj. (2023). Design of an Arc-Shaped Slot Circular Patch Antenna for 5G Applications. doi: 10.1109/ccpis59145.2023.10291475

Rare Earth Elements as Effective Dopants for ZnO Nanostructures : A Comprehensive Overview

Manisha Thokare*[1], Ramprasad Khalapure[2], Kunal Takle[1], Sangita Shinde[3]

*[1]Department of Physics, J.E.S. College, Jalna, Maharashtra, India

[2]Department of Chemistry, L.B.S. College, Partur, Maharashtra, India

[3]Department of Physics, Pratishthan Mahavidhyalay, Paithan, Maharashtra, India

Abstract :

The article provides an overview of the creation, characteristics, and uses of zinc oxide nano-structures doped with rare earth elements. Zinc Oxide is a versatile substance that can be used in various fields like optoelectronics, photocatalysis, biosensors, and biomedicine. By adding new energy levels, flaws, and impurities, doping ZnO with rare earth elements can improve its optical, electrical, magnetic, and catalytic capabilities. Rare earth-doped ZnO nano-structures are produced using a variety of synthesis techniques, including sol-gel, hydrothermal, and co-precipitation. The effects of various rare earth dopants, especially Ce, Er, Eu,La and Yb, on the optical and structural properties of ZnO nano-structures is covered in this article. The prospective uses of rare earth-doped nano-structures made of ZnO in a variety of industrial sectors, including photovoltaics, photocatalysis, biological sensing, and biomedicine, are also discussed in the research. The opportunities and difficulties in the future of the rare earth-doped ZnO nano-structures are addressed in the conclusion of the article.

Keywords: Rare Earth-doped Zinc Oxide, Sol-gel Process, Optical Properties, Magnetic Properties

I. INTRODUCTION

Zinc oxide (ZnO) is a versatile material that has attracted considerable attention in various fields of industry due to its unique properties, such as high refractive index, wide band gap, high electron mobility, and good biocompatibility. ZnO nanostructures, such as nanoparticles, nanowires, nanorods, and nanoflowers, have been widely studied for their applications in photocatalysis, optoelectronics, biosensors, and biomedicine. However, pure ZnO nanostructures suffer from some limitations, such as low visible light absorption, high recombination rate of photoinduced carriers, and poor stability. To overcome these drawbacks, doping of ZnO nanostructures with rare earth (RE) elements has been proposed as an effective strategy to modify the structural, optical, magnetic, and electrical properties of ZnO and enhance its performance in various applications. RE elements are known to have unique luminescence characteristics and can introduce new energy levels in the band gap of ZnO, thus affecting the charge transfer and separation processes. In this paper, we review the recent progress in the synthesis, characterization, and applications of RE-doped ZnO nanostructures, with a focus on the effects of

223

RE doping on the properties and performance of ZnO. We also discuss the challenges and future perspectives of RE-doped ZnO nanostructures for various fields of industry.

In Jia, Tiekun, et al. *Journal of Alloys and Compounds* 484.1-2 (2009) The paper discusses the fabrication, characterization, and photocatalytic activity of La-doped ZnO nanowires, synthesized using a solvothermal synthesis route with ethanol as the solvent. XRD patterns of the doped ZnO samples show that each nanowire is composed of Zn, O, and La elements, with a lanthanum doping concentration of approximately 2.09. The optimal doping concentration of lanthanum is determined to be 2, based on the improvement of photocatalytic activity compared to pure ZnO and other doping concentrations. The photocatalytic activity of the La-doped ZnO samples is evaluated using Rhodamine B (RhB) as a model contaminant, and the degradation of RhB is achieved under UV irradiation in the presence of the catalyst. XPS analysis confirms the presence of oxygen in different chemical states, as well as the coordination of oxygen in Zn-O-Zn and La-O-Zn, indicating successful doping of La into the ZnO lattice .

John, Rita, and Rajaram Rajakumari et al. (2012) The authors used the solid-state reaction method to synthesize ZnO doped with different concentrations of erbium. The characterization techniques used include X-ray diffraction (XRD), scanning electron microscopy (SEM), UV-absorption spectroscopy, photoluminescence (PL) study, and vibrating sample magnetometer. The XRD studies showed that the doped erbium ions occupy the regular Zn^{2+} sites in the crystal structure of ZnO. However, at higher erbium concentrations, the presence of a secondary phase was observed. SEM images revealed the polycrystalline nature of the synthesized samples. UV-visible absorption spectroscopy showed a strong absorption peak at 388 nm, indicating the band-to-band transition of ZnO. The PL study exhibited emission in the visible region, attributed to excitonic and defect-related transitions. The magnetization-field curve showed ferromagnetic properties of the erbium-doped ZnO nanocrystals at room temperature.

Talam, S., Karumuri, S. R., & Gunnam, N. et al. (2012) this research focused on making and studying really tiny particles of a material called zinc oxide (ZnO) using a method called precipitation from zinc nitrate. They did a bunch of tests to understand these tiny particles better.

First, they used X-ray diffraction (XRD), which is like shining a special light on the particles, to figure out that these ZnO particles have a structure that looks like a hexagon. Then, they took pictures of the particles using scanning electron microscopy (SEM) and transmission electron microscopy (TEM). These pictures showed that the particles are super small, less than 10 nanometers in size. They also looked at how these particles absorb light. They found that they absorb light with a special color at 355 nanometers because of the ZnO particles. Lastly, they looked at how the particles give off light, like tiny flashlights. They found two colors of light - one at 392 nanometers, which is related to the ZnO itself, and another at 520 nanometers, which is because of something called oxygen vacancies. The way they made these tiny particles seems like it could be useful in making things because it's easy to do and uses less expensive stuff.

Mishra, S. K., Srivastava, R. K., & Prakash, H. S. (2012). - The paper discusses the synthesis and characterization of zinc oxide nanoparticles (NPs) using zinc acetate dihydrate as a precursor. The NPs were prepared by thermal decomposition at 400 °C for reaction times of 3 and 12 hours. The structural analysis of the ZnO NPs was performed using X-ray diffraction (XRD), which revealed a wurtzite crystal structure. The average crystallite size was determined to be 29.66 nm and 32.68 nm for reaction times of 3 and 12 hours, respectively. The optical properties of the ZnO NPs were investigated using UV-visible spectroscopy and photoluminescence (PL) spectroscopy. A blue shift in the band gap was observed due to the nano size of the particles. The PL spectra exhibited a UV emission. The photoconductivity properties of the ZnO NPs were studied, and it was

found that the decay of photocurrent cannot be governed by a single exponential law, indicating the presence of traps at different energy depths below the conduction band. The photocurrent spectra showed improved photosensitivity with longer reaction times. The dark current and photocurrent of the ZnO NPs were found to have a super-linear variation with applied voltage, suggesting the injection of carriers into the material and the presence of space charge at higher voltages. XRD analysis also provided information about the size of the crystallite and micro strain of the ZnO NPs, which were calculated using the Williamson-Hall plot .

Zong, Yanqing, et al. 2014. This paper discusses the synthesis and characterization of Eu-doped ZnO nanoparticles and their photocatalytic activity for the degradation of methyl orange (MO) under UV light. The X-ray diffraction (XRD) analysis confirmed the phase and crystallinity of the photocatalysts, and the UV-vis diffuse reflectance spectra showed a blue-shifted absorption edge and broadening of the band gap for the Eu-doped ZnO nanoparticles compared to pure ZnO. The photocatalytic activity of the Eu-doped ZnO nanoparticles was found to be dependent on the amount of Eu dopant, with the 1.0 mol% Eu-doped ZnO nanoparticles exhibiting the best activity. The photocatalytic efficiency was influenced by factors such as photocatalyst loading, initial dye concentration, and pH values, with optimal conditions determined for the photodegradation of MO. The presence of Eu^{3+} dopant in the ZnO nanoparticles was found to enhance the photocatalytic activity by inhibiting the recombination of photoinduced electrons and holes, but excessive Eu^{3+} loading could act as recombination centers and reduce the efficiency. The adsorption of MO on the photocatalyst surface was affected by pH, with higher pH values leading to electrostatic repulsion and unfavorable adsorption .

Honglin, Li, et al. (2014) The paper discusses the preparation and characterization of rare earth (RE = La, Er, Nd) doped ZnO nanopowders using X-ray diffraction (XRD) and scanning electron microscope (SEM) techniques. The optical properties of the doped ZnO samples were studied using absorption spectra and photoluminescence (PL) analysis, which showed enhanced optical absorption in the visible region and different I UV /I DLE ratios for pure and doped ZnO. First-principles calculations were performed to study the electronic structures and optoelectronic properties of the doped ZnO samples, indicating a shift in Fermi levels and n-type conductivities after RE doping. The dielectric function analysis revealed a red shift in the low energy part of the absorption spectra for the doped ZnO samples compared to pure ZnO. The crystallization of the samples was found to worsen after annealing, as observed through SEM analysis, which was attributed to the heat treatment restraining crystal growth. The band gaps of the doped ZnO samples were corrected using the LDA U method and scissors operator, ensuring the qualitative accuracy of the calculated results .

Pandey, P., Kurchania, R., & Haque, F. Z. (2015) The paper discusses the synthesis of rare earth ion (La, Ce, and Eu) doped ZnO nanoparticles via the sol-gel method for application in dye-sensitized solar cells (DSSCs). The efficiency of the DSSCs was tested using different rare earth ions, and it was found that the Eu ion doped ZnO film showed the highest power conversion efficiency of 1.36%. The lower efficiency observed for La and Ce ion doped ZnO-based cells compared to the undoped one suggests that these dopants may not be as effective in improving the performance of the DSSCs. The surface annihilation of ZnO nanoparticles during the sensitization process was identified as a problem in DSSCs, and the paper suggests that a novel electrolyte may be needed to address this issue. The fabrication of the DSSCs involved the use of a doctor-blade technique to prepare the porous electrodes on fluorinated tin oxide, followed by dye-sensitization and assembly of the cells. Overall, the paper concludes that rare earth ion doping, particularly with Eu, shows promise for enhancing the efficiency of ZnO-based DSSCs .

Govindaraj, R., et al. (2015) The paper discusses the synthesis and characterization of pristine and Lanthanum doped ZnO nanoparticles using a sol-gel method. The characterization techniques used include Powder X-ray Diffraction (PXRD), High Resolution Scanning Electron Microscopy (HRSEM), and Energy Dispersive Analysis (EDX). The average size of the nanoparticles decreases with increasing concentration of Lanthanum, but at higher concentrations, the particle size increases. The presence of Lanthanum in the ZnO nanoparticles is confirmed by EDX analysis. The photoluminescence properties of the nanoparticles show a yellow-orange emission, which could be attributed to oxygen vacancy or interstitial based defects. The defects present in ZnO nanoparticles strongly depend on the synthesis method. The as-prepared ZnO nanoparticles are n-type semiconductors due to the presence of oxygen vacancies and other native defects. The synthesized ZnO nanoparticles have potential applications in optoelectronics.

Govindaraj, R., et al. (2015) The paper discusses the synthesis of zinc oxide nanoparticles using the sol-gel method, with zinc acetate as a precursor. The nanoparticles were characterized using various techniques such as X-ray diffraction (XRD), FTIR analysis, scanning electron microscopy (SEM), and UV-visible spectroscopy. The XRD results showed that the synthesized ZnO nanoparticles had a highly crystalline wurtzite crystal structure. FTIR analysis indicated characteristic absorption bands of ZnO nanoparticles. The SEM image revealed that the nanoparticles were spherical in shape with a smooth surface. The concentration of Zn in the synthesized ZnO nanoparticles was determined using inductively coupled plasma (ICP-OES) elemental analysis. The yield of ZnO was found to be about 98.2%, consistent with other published works. ZnO nanoparticles have various applications in medicine, cosmetics, rubber, solar cells, and foods due to their novel properties such as high refractive index, binding energy, high thermal conductivity, antibacterial and UV protection. They also exhibit good biocompatibility with human cells. The particle size of the ZnO nanoparticles prepared via the sol-gel method was about 50-60 nm. XRD powder diffraction was used to determine the crystallinity of the ZnO nanoparticles. The analysis was performed using an XRD SHIMADZU 6000 diffractometer, and the crystalline domain diameter was obtained using Scherrer's equation. ZnO nanoparticles have been prepared using various methods such as sol-gel, thermal decomposition, chemical vapor decomposition (CVD), and alloy evaporation-deposition. A wet chemical route based on cyclohexyl amine was established for synthesizing ZnO nanoparticles in aqueous and ethanolic media. ZnO has been found to inhibit bacterial growth, and it is listed as a generally recognized as safe material by the FDA. FTIR analysis was conducted on the ZnO powder using a Jasco-4200 spectrometer. The XRD analysis showed characteristic reflections corresponding to different crystal planes of ZnO nanoparticles. Similar values have been reported in previous studies.

Govindaraj, R., et al. (2015) The paper is a review that focuses on the synthesis, properties, and applications of rare earth-doped zinc oxide (ZnO) nanostructures in various fields of industry. Different techniques and methods are used to synthesize rare earth-doped ZnO nanostructures, including co-precipitation, sol-gel process, and hydrothermal synthesis. These methods provide different structures, shapes, and sizes of nanostructures. The co-precipitation method is an economical and effective way to synthesize metal oxide nanopowders, but it has limitations in controlling the growth and size of nanoparticles. Capping agents can be used to prevent agglomeration. The hydrothermal method, which involves high temperature and pressure conditions, allows for the synthesis of high-quality and single crystalline rare earth-doped ZnO nanostructures. This method is particularly useful for obtaining crystalline phases that are not stable at melting points. Rare earth-doped ZnO nanostructures exhibit optical, structural, and ferromagnetic properties that make them suitable for various applications, including photocatalysis, optoelectronic devices, fingerprint analysis, and pharmaceutical and health industries. The synthesis methods used for rare earth-doped ZnO nanostructures can

influence the characteristics of their red photoluminescence, suggesting that intrinsic defects play a role in efficient energy transfer.

Manikandan, A., et al. (2017) This paper discusses the synthesis and characterization of Lanthanum (La) doped zinc oxide (ZnO) nanomaterials. The synthesis of La x Zn 1-x O nanomaterials was done using the co-precipitation method with zinc acetate and lanthanum nitrate as precursors and octylamine as a capping and reducing agent. The structural and morphological analysis of the synthesized materials was carried out using techniques such as powder X-ray diffraction (XRD), Fourier transform infrared (FT-IR) spectroscopy, and high-resolution scanning electron microscopy (HR-SEM). The presence of Zn, O, and La in the synthesized materials was confirmed by energy dispersive X-ray (EDX) analysis. The antibacterial activity of the La x Zn 1-x O materials was tested against human pathogens, and it was found that they showed desired activity against P. mirabilis and S. The synthesized La x Zn 1-x O materials have potential applications in the treatment of kidney stones and typhoid fever.

Porkalai, V., et al. (2017) The paper discusses the synthesis and characterization of pure and lanthanum-doped ZnO nanoparticles using the sol-gel method. The effects of lanthanum incorporation on the structure, morphology, optical, and electrical properties of the nanoparticles were examined using various techniques such as X-ray diffraction (XRD), scanning electron microscopy (SEM), energy dispersive X-ray absorption (EDAX), Fourier transform infrared spectroscopy (FTIR), UV, and photoluminescence (PL) characterization. The XRD analysis confirmed the hexagonal wurtzite structure of ZnO nanoparticles, and the average particle size was found to be less than 20 nm. Lanthanum doping led to enhanced luminescence intensity and improved conductivity properties of the ZnO nanoparticles. The study highlights the potential applications of ZnO nanoparticles, such as in photonic catalysis, light-emitting diodes, field emission, gas sensors, fluorescent materials, and solar cells.

Goel, Sahil, et al. (2017) The paper investigates the structural, dielectric, ferroelectric, and piezoelectric properties of pure and lanthanum (La) doped ZnO nanoparticles. The synthesis of these nanoparticles was done using the co-precipitation method. The structure and morphology of the nanoparticles were studied using transmission electron microscopy (TEM) and powder X-ray diffraction (XRD) methods. The dielectric properties of the La-doped ZnO nanoparticles were found to decrease with an increase in frequency. The dielectric constant at room temperature was observed to be 28 for La-ZnO nanoparticles. Dye-sensitized solar cells (DSSCs) were fabricated using both pure ZnO and La-ZnO nanorods as photo-anodes. The DSSCs based on La-ZnO nanorods showed enhanced conversion efficiency and short circuit current density compared to those based on pure ZnO. The synthesis of ZnO and La-doped ZnO thin film photo-anodes for DSSCs was done using a doctor-blade technique. The photo-anodes were then immersed in a solution containing crystal violet dye and ethanol. A carbon-based counter FTO electrode was used, and the electrolyte solution contained potassium iodide. The paper also mentions previous studies on the photovoltaic performance of ZnO-based solar cells, including the effect of ZnO nanorod growth time and the presence of NiO in the mixture of ZnONiO .

Ntwaeaborwa, Odireleng Martin, et al. (2017). The paper discusses the structural, optical, and photoluminescence properties of europium (Eu^{3+}) doped ZnO nanoparticles (NPs) prepared by the co-precipitation method. The average crystallite size of the ZnO nanoparticles was estimated using the Scherrer's equation, and the tailoring of the bandgap of semiconductors due to the incorporation of dopant ions was observed. Photoluminescence analysis revealed that the ZnO NPs exhibited two luminescence bands: a minor ultraviolet emission at 384 nm related to exciton recombination and a major emission in the visible region at 600 nm related to defects. The visible emission was attributed to the radiative recombination of a

photogenerated hole with an electron occupying the oxygen vacancy. Concentration quenching of the luminescence of Eu3+ doped ZnO NPs was observed, which could be explained by energy transfer mechanisms between rare earth ions. The presence of Eu3+ ions in the ZnO lattice was confirmed through vibrational modes observed in the Raman spectra, and the absorption band around 451 cm-1 indicated Eu-O stretching mode .

Lang, Jihui, et al. (2017) The paper discusses the synthesis and characterization of (Eu, La, Sm) codoped ZnO nanoparticles via a chemical route. The authors analyze the structural and optical properties of the nanoparticles, including their size, energy transfer mechanisms, and bandgap tuning. XPS analysis confirms the incorporation of RE dopants into the ZnO lattice, and Raman scattering confirms the wurtzite phase of the samples. The narrowing of the band gaps with RE codoping is attributed to the introduction of impurity bands and strong orbital coupling between RE and O. The red emissions observed in the doped samples are attributed to the transitions of Eu3+ ions. Overall, the paper provides insights into the structural and optical properties of (Eu, La, Sm) codoped ZnO nanoparticles synthesized via a chemical route. The authors analyze the size, energy transfer mechanisms, and bandgap tuning of the nanoparticles. XPS analysis confirms the incorporation of RE dopants into the ZnO lattice, and Raman scattering confirms the wurtzite phase of the samples. The narrowing of the band gaps with RE codoping is attributed to the introduction of impurity bands and strong orbital coupling between RE and O. The red emissions observed in the doped samples are attributed to the transitions of Eu3+ ions.
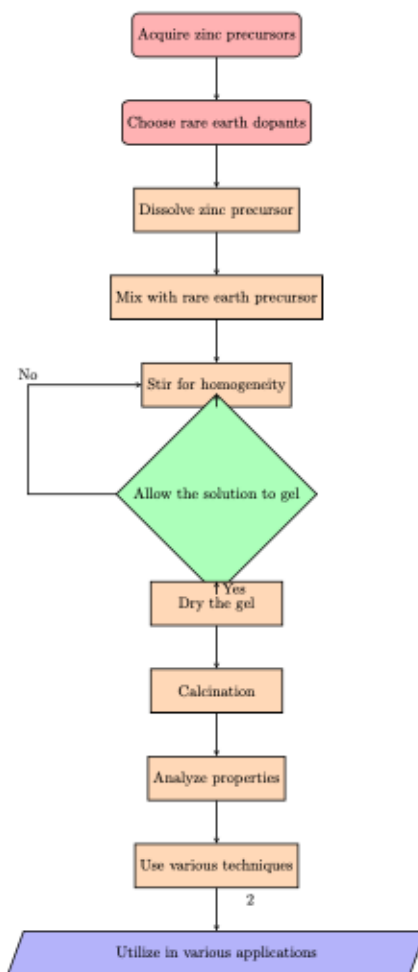
Fig. No.1 : Synthesis of ZnO nanoparticles

Lahmer, M. A. (2018). The doping process with rare earth atoms enhances the stability of the ZnO surface, with Sc atoms having the lowest formation energy followed by Y and La. The formation of a RE-V O complex is energetically more favored than the formation of isolated RE Zn defects under Zn-rich conditions. The RE-V O complex may be the origin of the photocatalytic properties enhancement of the doped surfaces, with Sc-doped surfaces prepared under Zn-rich conditions having the best photocatalytic properties followed by Y and La-doped surfaces. The electronic structure of the undoped ZnO surface is semiconducting with a band gap of about 3.7 eV, and the presence of surface states located above the valence band. The band alignment of the clean, O-defected, and RE-doped ZnO(0 0 0 1) surfaces shows that the LUMO level is located below the EH H2 level, indicating that the defect-free surface cannot be efficiently used in photocatalytic applications .

Ba-Abbad, Muneer M., et al. (2018) This paper discusses the synthesis and characterization of samarium-doped zinc oxide (ZnO) nanoparticles using a sol-gel method. The study investigates the structures, morphologies, optical properties, and surface areas of the nanoparticles using specific characterization methods. The results show that the size of the samarium-doped ZnO nanoparticles decreases with increasing samarium ion concentration, and the band gap slightly changes from 3.198 eV to 3.288 eV with enhanced absorption in the UV region. X-ray photoelectron spectroscopy (XPS) analysis confirms the incorporation of samarium ions into the ZnO matrix without the presence of samarium oxide. The photocatalytic degradation of 2-chlorophenol was investigated, and the samarium-doped ZnO nanoparticles showed higher performance compared to pure ZnO nanoparticles. The thermal decomposition of the nanoparticles was studied using thermogravimetric analysis (TGA), which revealed different weight losses during the process.

Bomila, R., et al. (2018) The paper discusses the synthesis and characterization of Ce-doped ZnO nanoparticles using a wet-chemical method at low temperature. Structural analysis using X-ray diffraction (XRD) confirms the well-crystalline nature of the synthesized nanoparticles with a hexagonal wurtzite structure. The presence of Ce ions in the ZnO lattice is confirmed by EDX analysis. Ce doping is found to decrease the optical band gap of ZnO and enhance visible emission while suppressing near band gap emission. The antibacterial activity of Ce-doped ZnO nanoparticles is investigated against Gram-positive (Bacillus subtilis, Staphylococcus aureus) and Gram-negative bacteria (Proteus mirabilis, Salmonella typhy). XRD analysis shows that Ce doping reduces the size of ZnO nanoparticles, and the average crystallite size is estimated using the Scherrer formula. The presence of Ce3 in the ZnO lattice causes a shift in peak positions and a decrease in the intensity of diffraction peaks, indicating a degradation of crystalline quality. Ce-doped ZnO nanoparticles exhibit antibacterial activity, and the activity increases with decreasing particle size .

Manikandan, B., et al. (2018) This research paper explores how to make better solar cells using a special material called zinc oxide (ZnO). These solar cells are unique because they work the opposite way of regular ones - they absorb sunlight from the back. The scientists wanted to improve these special solar cells, so they added a tiny amount of a rare material called lanthanum (La) to the zinc oxide. They used a special method involving a solution of chemicals and high heat to do this. They tried different amounts of lanthanum, from none to a little bit. Then, they examined the properties of the new material they made using fancy machines like microscopes and special light tests. They also tested how well the solar cells worked. Adding a small amount of lanthanum made the material better! It let more light through, carried electricity better, and had fewer problems. This made the solar cells work much better, about 12% better, in fact. They figured out that it was because of a mixture of zinc oxide and a bit of lanthanum. So, in the end, they found a cool way to make solar cells that are not only high-performing but also cost-effective.

Nguyen, Loan TT, et al. (2019) .The paper discusses the synthesis, characterization, and photocatalytic activity of La-doped zinc oxide nanoparticles using a gel combustion method with poly(vinyl alcohol) (PVA) as a chelating agent and fuel. The average size of the nanoparticles decreased and the band gap decreased with increasing concentrations of La. The photocatalytic activity of the doped samples improved with increasing La concentration, with the decomposition of methyl orange reaching 85.86% after 150 min using La0.1Zn0.9O as the photocatalyst. Previous studies have shown that doping ZnO with rare earth elements like La can enhance its photocatalytic activity by limiting electron-hole recombination and improving light absorption. La-doped ZnO materials have been found to have enhanced photocatalytic efficiency and antibacterial activity, as well as potential applications in food sanitization, medicine, and wastewater treatment.

Theerthagiri, J., et al. (2019). The paper is a review on ZnO nanostructured materials, focusing on their applications in energy storage and conversion devices and biological applications. The unique properties of nanostructured ZnO, such as high sensitivity, large specific area, non-toxicity, and good compatibility, make it a desirable material for various applications. The review discusses the use of ZnO-based nanomaterials/composites/doped materials in supercapacitors, Li-ion batteries, dye-sensitized solar cells, photocatalysis, biosensors, and biomedical and biological applications. The paper emphasizes the need for further research to enhance the performance of ZnO-based materials in interdisciplinary science. Various studies have explored the growth mechanisms and properties of different ZnO nanostructures, such as flower-like structures, nanowires, and nanorods, for applications in DSSCs. The performance of DSSCs can be improved by factors such as the length of ZnO nanowires, the presence of TiO2 nanoparticles, and the use of ZnO-TiO2 composites.

Khuili, M., et al. (2020 The study investigates the impact of rare earth elements (Tm, Yb, Ce) doping on the structural, optoelectronic, magnetic, and electrical properties of wurtzite ZnO using density functional theory implemented in Wien2K code. The electronic structure analysis shows that the doping of Tm, Yb, and Ce on pristine ZnO increases the band gap and shifts the Fermi level to the conduction band, indicating n-type semiconductor behavior. The conductivity of the doped ZnO is improved compared to pure ZnO. The increase in the band gap is attributed to the Burstein-Mott effect, and the appearance of new occupied states near the Fermi level is attributed to the 4f orbitals of the rare earth dopants. The structural parameters of the doped ZnO structures, such as lattice parameters, are found to increase compared to undoped ZnO due to the larger ionic radii of the rare earth dopants .

Zafar, Muhammad, BongSoo Kim, and Do-Heyoung Kim. et al. (2020) This research paper explores the creation and performance of inverted organic solar cells (IOSCs) by using a unique approach: utilizing sol-gel processed zinc oxide (ZnO) films as electron buffer layers (EBLs). The study also delves into the effects of incorporating lanthanum (La), a rare earth element, into these ZnO films, on the solar cells' photovoltaic properties. To make these La-ZnO films, the researchers employed a process called spin-coating, which involves applying a solution composed of zinc acetate dihydrate, ethanolamine, and lanthanum nitrate hexahydrate onto specific substrates. Following this, they subjected the films to annealing at 150°C for one hour. The La doping levels were adjusted from 0 to 10 wt%. The team used various techniques, including SEM, AFM, UV-Vis spectroscopy, Hall measurements, and XPS, to comprehensively analyze the La-ZnO films' morphology, optical characteristics, electrical properties, and chemical attributes. They also evaluated the IOSCs by examining their current-voltage behavior and external quantum efficiency under simulated AM 1.5G illumination. The results were promising: La doping significantly enhanced the ZnO films by improving transmittance, conductivity, and carrier density while reducing surface defects and narrowing the band gap. These improvements facilitated better electron

extraction and transport at the interface between the EBL and the photoactive layer. As a result, the IOSCs demonstrated an impressive 12% increase in power conversion efficiency (PCE) with an optimal La doping content of 5 wt%, reaching a PCE of 4.34%. This enhancement was attributed to the formation of a primary ZnO phase coupled with a small amount of La2O3 impurities, as confirmed by XPS analysis.

Pathak, Trilok K., et al. (2020). The paper discusses the synthesis and characterization of cerium-doped zinc oxide (CZO) nanomaterials using the sol-gel combustion method. The effect of different doping concentrations of cerium on the structural, morphological, optical, and photoluminescence properties of CZO is investigated. X-ray diffraction analysis reveals that the CZO nanomaterials have a hexagonal wurtzite structure, with the maximum crystallite size obtained for 1 mol% Ce doping. Energy dispersive X-ray spectroscopy shows the uniform distribution of Ce atoms in the ZnO, while nano-scanning Auger microscopy reveals enhanced Ce concentration in nanoparticles occurring in the doped material. The absorption spectra show strong absorbance below 410 nm, and the optical bandgap slightly varies around 3.20 eV for different Ce doping concentrations. Photoluminescence studies show a broad emission band centered at 635 nm, with a blue shift as the Ce concentration increases./ The CZO nanomaterials exhibit photocatalytic activity and antibacterial/antifungal properties, with efficiency measured against bacteria (Staphylococcus aureus and Escherichia coli) and yeasts (Eremothecium ashbyii and Nadsonia fulvescens). Doping of rare earth metal ions, including cerium, has been shown to improve the photocatalytic activity of semiconductor oxides like ZnO. XPS analysis confirms the co-existence of Ce3 and Ce4 ions in the CZO nanomaterials, with the proportion of Ce4 ions increasing with increasing doping concentration. The morphology of the CZO nanomaterials is affected by the Ce doping concentration, with the size of nanoparticles decreasing and weak agglomeration observed at higher doping concentrations. CZO nanomaterials have potential applications in photocatalysis and antibacterial studies, and doping with rare earth metal ions can enhance their performance .

Shukla, Sweta, and Dhirendra Kumar Sharma. (2021) The paper is a review on rare earth (Ce and Er)-doped zinc oxide (ZnO) nanostructures, focusing on their synthesis, properties, and applications in various fields of industry. The authors aim to extend the understanding of key issues in the current research progress of ZnO, particularly for the realization of ZnO-based optoelectronic devices and the improvement of material quality. They specifically focus on band gap tuning and enhanced photoluminescence properties achieved through doping of metal ions. Doping of rare earth (RE) ions in ZnO leads to morphological changes from nanorod-like to nanoplate-like structures, attributed to the effects of dopants selectively adsorbing onto ZnO crystalline planes. The incorporation of RE ions in the ZnO lattice is confirmed by the observed drastic morphological changes. Cerium (Ce) is chosen as a suitable dopant for the ZnO matrix due to its distinct luminescence transition and interesting optical properties. Ce-doped ZnO nanostructures have been studied for various applications, including degradation of dyes, cyclohexanol conversion, detoxification of cyanide, infrared emissivity, photoluminescence, and oxidative and steam reforming of methanol. Different synthesis methods have been reported for Ce-doped ZnO nanostructures, including electrochemical deposition, sol-gel method, and hydrothermal method. These methods offer control over the nanostructures and allow for the investigation of optoelectronic properties.

Shafiee, Parisa, et al. (2021). The paper discusses the synthesis and sintering of zinc oxide nanoparticles (ZnO) using the sol-gel method, which is an economic and efficient technique for nanoparticle formation. The sol-gel method allows for the adjustment of the structural and optical features of the nanoparticles, making it a desirable technique for ZnO nanoparticle synthesis. The paper highlights the various applications of sol-gel ZnO nanoparticles, including biomedicals, antimicrobial packaging, drug delivery, semiconductors, biosensors,

catalysts, photoelectron devices, and textiles. Sol-gel ZnO nanoparticles have been studied for their drug delivery applications, including the delivery of doxorubicin and gene transfer to tumor cells. Sol-gel ZnO nanoparticles have also been used in biosensors for the detection of xanthine, glucose, hydrogen peroxide, cholesterol, and cancer antigens .

Chamanzadeh, Z., Ansari, V. and Zahedifar, M., 2021. The paper investigates the properties of La-doped and Dy-doped ZnO nanorods and their impact on the photovoltaic performance of Dye-Sensitized Solar Cells (DSSCs). The authors synthesized pure ZnO nanorods, La-doped ZnO NRs, and Dy-doped ZnO NRs using a two-step process involving seed layer deposition and hydrothermal growth. Various characterization techniques such as X-ray diffraction, scanning electron microscopy, dispersive X-ray spectroscopy, photoluminescence spectroscopy, and ultraviolet-visible spectrometer were used to analyze the structure composition and optical properties of the nanorods. The optical measurements showed enhanced absorption and emission intensity with increased nanorod length and impurities concentration, leading to a decreased band gap of ZnO nanorods. DSSCs were fabricated using ZnO nanorods grown on a porous TiO2 nanoparticle film as the photoanodes. The performance of DSSCs was investigated by varying the growth time and dopants, and it was found that the optimum performance was achieved with ZnO nanorods grown for 300 min. Decorating the TiO2 NPs/ZnO NRs photoanode with TiO2 NPs improved the cell efficiency by more than twice compared to the undecorated photoanode. The power conversion efficiency of DSSCs doped with Lanthanum and Dysprosium was increased by 63.6% and 71.5%, respectively, compared to the conventional TiO2 NPs photoanode. The paper also mentions the use of X-ray diffraction and scanning electron microscopy to investigate the crystalline phase structure and morphology of the ZnO nanorods and DSSC photoelectrode. The absorbance spectra were recorded to study the optical properties, and it was observed that the absorption edge had a red shift with increasing nanorod length. The paper highlights that there is limited research on La-doped and Dy-doped nanorods as photoanodes in DSSCs, and the current work aims to fill this research gap by synthesizing and characterizing these nanorods and measuring their photovoltaic performance .

Chauhan, Vaibhav, and Praveen C. Panday.(2021). The paper focuses on studying the role of dysprosium (Dy) doping concentration on the structural deformation of zinc oxide (ZnO) nanoparticles. The study synthesized different concentrations of Dy-doped ZnO nanoparticles and observed variations in structural parameters, indicating small deformation due to Dy doping. The absorption spectra showed a slight variation in the optical bandgap caused by Dy doping, and a correlation was found between the variation in absorption spectra and structural deformation. The XRD analysis confirmed that the Dy3 ion replaced the Zn2 ion in the ZnO crystal structure without changing the wurtzite structure. The crystallite size of the ZnO nanoparticles was found to be lower than the Dy3-doped ZnO, and the incorporation of Dy3 caused an increase in crystallite size. The band gap of the prepared samples decreased as the concentration of Dy doping increased, and the presence of Dy did not significantly affect the band edge of the absorption spectra of ZnO.

Achehboune, Mohamed, et al. (2021) The paper investigates the electronic, magnetic, and optical characteristics of pure and ytterbium (Yb) doped ZnO using density functional theory-based calculations. The band gap of pure ZnO is in good agreement with experimental results, and it increases with the increase of Yb concentration. Yb doping leads to the creation of new defects near the conduction band attributed to the Yb-4f states. Yb doping affects the magnetic properties of ZnO, with ferromagnetic behavior observed for 4.17% Yb due to spin polarization of Yb-4f electrons. Yb doping causes a blue shift of the absorption peaks, significantly enhances the absorption of visible light, and a blue shift of the reflectivity spectrum is observed. The refractive index and extinction coefficient decrease with increasing Yb dopant concentration. The total state density and

partial state density provide insight into the contributions of different states to the energy bands. Yb-doped ZnO has a ferromagnetic property with an optimal concentration of 4.17, exhibiting magnetism behavior in the ZnO-YbZn system. The total magnetic moment of Yb-doped ZnO increases with Yb concentration, and there is a clear spin polarization between the partial density of states of the two spin channels near the Fermi level due to spin polarization of Yb-4f electrons .

II. CONCLUSION

In summary, this research paper presents a comprehensive exploration of rare earth-doped zinc oxide (RE-doped ZnO) nanostructures, highlighting their immense potential across various industrial domains. The study encompasses a thorough investigation into their properties, synthesis techniques, and diverse applications.

The paper delves into the intricacies of synthesizing RE-doped ZnO nanostructures, employing methods such as co-precipitation, sol-gel processes, and hydrothermal synthesis. It elucidates the profound impact of RE doping on the structural, optical, magnetic, and electrical characteristics of ZnO nanostructures. Moreover, it sheds light on their wide-ranging applications, including photocatalysis, optoelectronic devices, fingerprint analysis, and contributions to the pharmaceutical and healthcare sectors.

This review encapsulates the current state of research in the realm of RE-doped ZnO nanostructures while acknowledging the challenges that persist. Notably, these nanostructures exhibit distinctive luminescence properties and can introduce novel energy levels within ZnO's band gap, thereby influencing charge transfer processes. Additionally, RE doping enhances the optical, magnetic, and electrical attributes by modifying defect structures and creating impurity bands.

While RE-doped ZnO nanostructures hold promise across industries due to their sensitivity, substantial specific area, non-toxicity, and biocompatibility, several hurdles must be addressed. These include optimizing doping concentrations, controlling morphology and size, ensuring the stability and reproducibility of nanostructures, and gaining a deeper understanding of doping mechanisms and energy transfer processes.

The paper advocates for addressing these challenges through the establishment of ethical standards, fostering transparency and accountability, and promoting public awareness and education. It also emphasizes the importance of collaboration between government and industry stakeholders to ensure the safety and benefits of RE-doped ZnO nanostructures.

III.ACKNOWLEDGMENT

IV. REFERENCE

[1]. Jia, Tiekun, et al. "Fabrication, characterization and photocatalytic activity of La-doped ZnO nanowires." *Journal of Alloys and Compounds* 484.1-2 (2009): 410-415.

[2]. John, Rita, and Rajaram Rajakumari. "Synthesis and characterization of rare earth ion doped nano ZnO." *Nano-Micro Letters* 4 (2012): 65-72.

[3]. Talam, Satyanarayana, Srinivasa Rao Karumuri, and Nagarjuna Gunnam. "Synthesis, characterization, and spectroscopic properties of ZnO nanoparticles." *International Scholarly Research Notices* 2012 (2012).

[4]. Mishra, Sheo K., Rajneesh K. Srivastava, and H. SG Prakash. "ZnO nanoparticles: Structural, optical and photoconductivity characteristics." *Journal of Alloys and Compounds* 539 (2012): 1-6.

[5]. Zong, Yanqing, et al. "Synthesis and high photocatalytic activity of Eu-doped ZnO nanoparticles." *Ceramics international* 40.7 (2014): 10375-10382.

[6]. Honglin, Li, et al. "Experimental and first-principles studies of structural and optical properties of rare earth (RE= La, Er, Nd) doped ZnO." *Journal of alloys and compounds* 617 (2014): 102-107.

[7]. Pandey, Padmini, Rajnish Kurchania, and Fozia Z. Haque. "Rare earth ion (La, Ce, and Eu) doped ZnO nanoparticles synthesized via sol-gel method: Application in dye sensitized solar cells." *Optics and Spectroscopy* 119 (2015): 666-671.

[8]. Govindaraj, R., et al. "Structural, morphological and luminescence studies on pristine and La doped zinc oxide (ZnO) nanoparticles." *Optik* 126.17 (2015): 1555-1558.

[9]. Alwan, Riyadh M., et al. "Synthesis of zinc oxide nanoparticles via sol–gel route and their characterization." *Nanoscience and Nanotechnology* 5.1 (2015): 1-6.

[10]. Daksh, Daksh, and Yadvendra Kumar Agrawal. "Rare earth-doped zinc oxide nanostructures: a review." *Reviews in Nanoscience and Nanotechnology* 5.1 (2016): 1-27.

[11]. Manikandan, A., et al. "Rare earth element (REE) lanthanum doped zinc oxide (La: ZnO) nanomaterials: synthesis structural optical and antibacterial studies." *Journal of Alloys and Compounds* 723 (2017): 1155-1161.

[12]. Porkalai, V., et al. "Study on the synthesis, structural, optical and electrical properties of ZnO and lanthanum doped ZnO nano particles by sol-gel method." *Mechanics, Materials Science & Engineering Journal* 9 (2017).

[13]. Goel, Sahil, et al. "Experimental investigation on the structural, dielectric, ferroelectric and piezoelectric properties of La doped ZnO nanoparticles and their application in dye-sensitized solar cells." *Physica E: Low-dimensional Systems and Nanostructures* 91 (2017): 72-81.

[14]. Ntwaeaborwa, Odireleng Martin, et al. "Structural, optical and photoluminescence properties of Eu3+ doped ZnO nanoparticles." *Spectrochimica Acta Part A: Molecular and Biomolecular Spectroscopy* 182 (2017): 42-49.

[15]. Lang, Jihui, et al. "The study of structural and optical properties of (Eu, La, Sm) codoped ZnO nanoparticles via a chemical route." *Materials Chemistry and Physics* 194 (2017): 29-36.

[16]. Lahmer, M. A. "The effect of doping with rare earth elements (Sc, Y, and La) on the stability, structural, electronic and photocatalytic properties of the O-terminated ZnO surface; A first-principles study." *Applied Surface Science* 457 (2018): 315-322.

[17]. Ba-Abbad, Muneer M., et al. "Synthesis and characterization of Sm 3+-doped ZnO nanoparticles via a sol–gel method and their photocatalytic application." *Journal of Sol-Gel Science and Technology* 85 (2018): 178-190.

[18]. Bomila, R., et al. "Structural, optical and antibacterial activity studies of Ce-doped ZnO nanoparticles prepared by wet-chemical method." *Materials Research Innovations* 22.7 (2018): 379-386.

[19]. Manikandan, B., et al. "Properties of sol gel synthesized ZnO nanoparticles." *Journal of Materials Science: Materials in Electronics* 29 (2018): 9474-9485.

[20]. Nguyen, Loan TT, et al. "Preparation, characterization and photocatalytic activity of La-doped zinc oxide nanoparticles." *Materials* 12.8 (2019): 1195.

[21]. Theerthagiri, J., et al. "A review on ZnO nanostructured materials: energy, environmental and biological applications." *Nanotechnology* 30.39 (2019): 392001.

[22]. Khuili, M., et al. "First-principles calculations of rare earth (RE= Tm, Yb, Ce) doped ZnO: Structural, optoelectronic, magnetic, and electrical properties." *Vacuum* 181 (2020): 109603.

[23]. Zafar, Muhammad, BongSoo Kim, and Do-Heyoung Kim. "Improvement in performance of inverted organic solar cells by rare earth element lanthanum doped ZnO electron buffer layer." *Materials Chemistry and Physics* 240 (2020): 122076.

[24]. Pathak, Trilok K., et al. "Preparation and characterization of Ce doped ZnO nanomaterial for photocatalytic and biological applications." *Materials Science and Engineering: B* 261 (2020): 114780.

[25]. Shukla, Sweta, and Dhirendra Kumar Sharma. "A review on rare earth (Ce and Er)-doped zinc oxide nanostructures." *Materials Today: Proceedings* 34 (2021): 793-801.

[26]. Shafiee, Parisa, et al. "Sol-gel zinc oxide nanoparticles: advances in synthesis and applications." *Synthesis and Sintering* 1.4 (2021): 242-254.

[27]. Chamanzadeh, Z., V. Ansari, and M. Zahedifar. "Investigation on the properties of La-doped and Dy-doped ZnO nanorods and their enhanced photovoltaic performance of Dye-Sensitized Solar Cells." *Optical Materials* 112 (2021): 110735.

[28]. Chauhan, Vaibhav, and Praveen C. Panday. "Role of dysprosium doping concentration on structural deformation of zinc oxide nanoparticles." *Physica B: Condensed Matter* 621 (2021): 413313.

[29]. Achehboune, Mohamed, et al. "Effect of Yb concentration on the structural, magnetic and optoelectronic properties of Yb doped ZnO: first principles calculation." *Optical and Quantum Electronics* 53 (2021): 1-14.

The Study of Effect of Static Magnetic Fields on In-Vitro Brushite Crystallization

A. C. Bhagat*

Assistant Professor, Post- Graduate Department of Physics,J.E.S.College, Jalna-431203 Maharashtra, India

*Corresponding Author:dstphy@gmail.com

Abstract :

In the present work, The kidney stone constitutes Calcium Hydrogen Phosphate Di Hydratesit is found about 20% to 25% in human renal calculi; which is a major component of kidney stone. Hence the study crystal growth of Brushite for without exposure, with static magnetic field exposure undertaken is very significant. These crystals are grown by single diffusion gel method in the presence of static magnetic field of different strength such as 0, 0.1, 0.2 Tesla for constant pH, density and concentration of the solution at room temperature.Yield and morphology of grown crystal are studied. The crystals are characterized by using XRD and FTIR method.

Keywords: Brushite Crystal, Single Diffusion Gel Method, XRD, FTIR.

I. INTRODUCTION

Calcium Hydrogen Phosphate Di hydrates is major constituents of kidney stone. It is also known as brushite. It has molecular mass 172 gm. It has molecular formula ($CaHPO_4 \cdot 2H_2O$).It appears in white solid form. It has solubility in HCl. The process of Brushite crystal growth has been studied by differentresearchers.Brushite stones were studied by Griffith (Griffith,1978),Crystal growth in gel media studied by AR Patel (Patel etal,1982).Growth and Characterization of Brushite crystals was also studied by Chauvan (Chauvan, etal,2008).Growth inhibition of Brushite crystals in presence of Herbal Extract Boerhaavia Diffusa Linn was studied by Chauvan (Chauvan, etal, 2009). Growth inhibition of Brushite crystals by the aqueous root extract of rotula aquatica was studied by Chauvan (Chauvan, etal, 2011). Influence of Drugs on the formation of Brushite Urinary Calculi was studied by Bindu (Bindu, etal, 2012).Growth, spectral, structural and mechanical properties of Brushite crystal grown in presence of sodium fluoride was studiedbySuguna(Suguna,etal,2012).The study of crystal growthofCholesterolCrystal(Bhagat,etal,2013),Whewelite in gel media studied(Bhagat,etal,2015), the study of effect of static magnetic field on in-vitro whewelite crystal growth studied.(Bhagat,etal,2015).TheStatic Magnetic Field Effect on Crystal growth of Uric Acid studied. (Bhagat,2024),

The present paper reveals the effect of static magnetic field on growth of Brushite crystal for constant pH, density, temperature and yield and morphology of crystal are studied. The grown crystals are characterized by using XRD and FTIR method.

II. METHODS ANDMATERIAL

The A.R. grade chemicals used for study of Brushite crystal growth are Sodium Meta Silicate (SMS), Acetic Acid (glacial), Ortho-Phosphoric Acid, Calcium Chloride,Distilled water. Borosilicate Glass Test tubes of diameter 2.5cm and length 15 cm. Entire procedures carried out in dust free and quiet environment.

2.1 Gel Setting and Brushite crystal growth in gel media:

The gel preparation and gel setting is done by preparing stock solution by dissolving Sodium Meta Silicate powder in double distilled water and shaking this solution well. The solution is filtered and kept in clean flask. This solution was mixed with glacial acetic

1.2   Static Magnetic field set up:
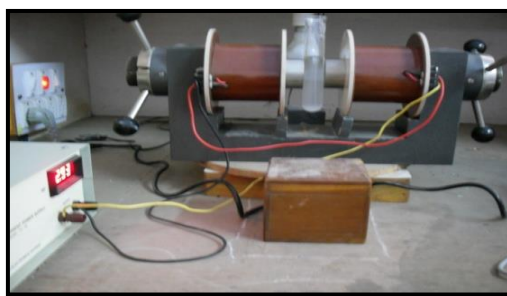
Fig.1. Experimental Set up for Crystallization of Brushite at 0.1 and 0.2 Tesla magnetic field strengths.

(a)   (b)
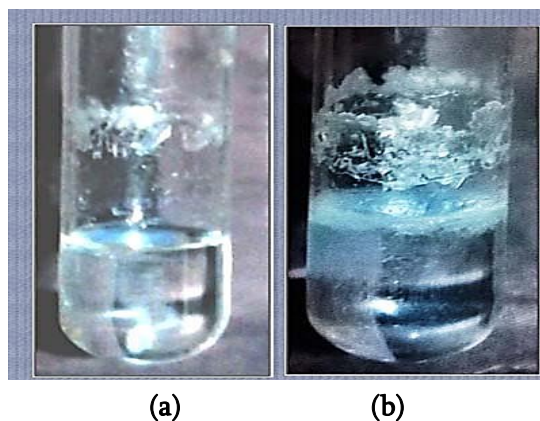
Fig.2. Brushite Crystallization
(a) At Nucleation State (b)After120Hrs.

An Electromagnets (EMU-50) of 7.5 kg placed at 10mm air gap with flat pole pieces (50 mm diameter) is used to apply magnetic field   strength as shown in figure 1.The magnetic field strengths were varied by using appropriate current to the coils and it is measured by Gauss meter.   After setting the gel, 2.5M concentration of calcium chloride solution is poured slowly and gently around corners of test tubes over set gel. Then four Test tubes were kept in Electromagnets (EMU-50) one by one for exposure of steady magnetic field strength of 0.1 Tesla (Core coil current 1.46 Amperes) for different time periods 30min.,60min., 90min. and 120min. Similar procedure was repeated for magnetic field exposure of 0.2 Tesla (Core coil current 2.93 Amperes) at room temperature. The test tubes were tighten using cork and kept in a quiet and vibration free condition for120hours.The following chemical reaction took place.

H_3PO_4	+ $CaCl_2.2H_2O$ =	$CaHPO_4.2H_2O$	+ $2HCl$
Ortho-Phosphoric	+ Calcium Chloride =	Calcium Hydrogen +	Hydrochloric
Acid		Phosphate Di hydrates	Acid
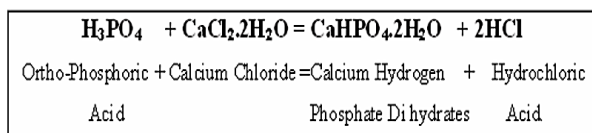
Fine Brushite crystals were observed in test tube at the Centre of upper gel region and some at the bottom as shown in figure 2. Then crystals were collected from test tubes on filter paper for weighing.

2.3 Crystal Yield Analysis:

Yield of Brushite crystals grown are given in table no.1. and plotted in figure 3.

Sr. No.	Magnetic field in Tesla	Time in Min	Yield of Brushite Crystal after 120hours in gm. at pH 6.5
1	0	0	1.63
2	0.1	30	0.95
3	0.1	60	1.2
4	0.1	90	1.35
5	0.1	120	1.42
6	0.2	30	1.14
7	0.2	60	1.27
8	0.2	90	1.37
9	0.2	120	1.53

Table.1.Yield of BrushiteCrystal.
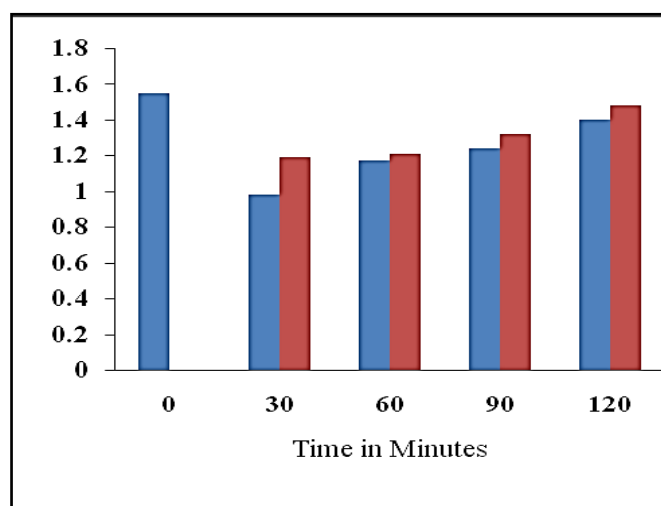
Fig.3Yieldof Brushite Crystal

2.4 Crystal Characterization Analysis:

XRD and FTIR Studies were conducted to characterize the crystals grown in silica gel media.

[A]Powder X Ray Diffraction Analysis:

Powder XRD pattern of Brushite crystal recorded by X Ray Diffractometer Philips PW1840 crystallizes in Orthorhombic structure with cell parameters as follows; a =5.837Å, b =15.192Å, c = 0.4124Å and β =116.470
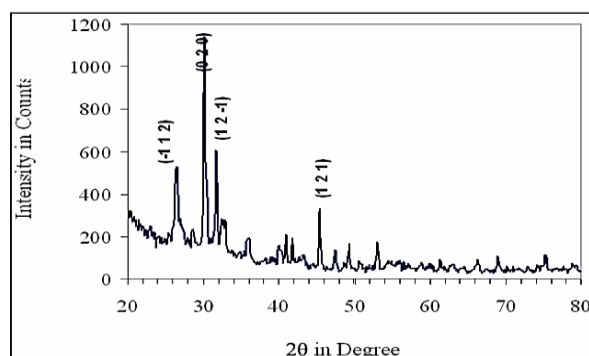
Fig.4.Powder XRD pattern of Brushite crystal.

[B]   FTIR   Analysis:
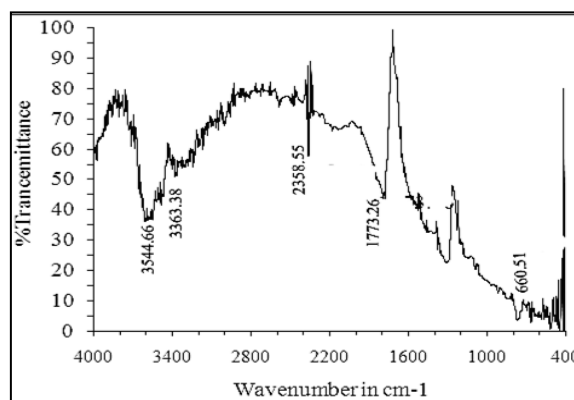
Fig.5. FTIR of Brushite crystal

The FTIR spectrum of Brushite crystal is confirmed by recording with FTIR-BUSY-6100 JASCO spectrometer in a scan range (4000cm^{-1} - 400cm^{-1}).The FTIR analysis of Brushite crystal grown as shown in figure 4.

III.RESULTS AND DISCUSSIONS

The photographs of Brushite crystals grown are shown in figure 2.

The morphology of Brushite Crystals observed as rectangular platelet in good agreement with result published.

The powder XRD pattern shown in figureno.4 of Brushite crystal confirmed and results are in good agreement with results reported in literatures(Chauvan,etal;Bhagat,etal,2014).

Also FTIR analysis pattern shown in figure no.5 of Brushite crystal confirmed and results are in good agreement with results reported in literatures(Chauvan,etal2008;Bhagat etal 2014).

FTIR pattern obtained for crystal for crystal grown under exposure of magnetic field at the nucleation time exhibits more % transmittance for magnetic field strength 0.1 T than 0.2 T. The difference of % transmittance found decreased and depth of %transmittance dip at frequency 3544.65 cm^{-1} is found increased as exposure time is increased.

Rate of nucleation observed reduced   and Size of crystals decreased with increasing strength of magnetic field but number of crystals found increased.

Yield of Brushite crystals grown are given in table no.1 and plotted in figure 3 is found slightly increased as influence of increasing magnetic field. Overall yield found less as compared to without exposure of magnetic field.

IV.CONCLUSION

This research work concludes that a precise and systematic chemical reaction in gel technique is useful for In-Vitro crystal growth process. The Brushite crystal has rectangular platelet like morphology as shown in figure 3 and has same for both with and without irradiation.

The PXRD analysis confirms that, the grown crystals belong to Brushite crystals and has monoclinic system.

In FTIR analysis the various functional groups and its Vibrational modes have been analysed for Brushite crystal.It is found FTIR spectrum of the Brushite crystals revealedthe varying presence of functional groups.

Also yields of Brushite crystal grown is found increasing for unexposed condition.

A crystallographer has fascinating future. Growing Artificial Crystals studying its physical and chemical properties and morphology will enhances new challenges for new researchers.

V. REFERENCES

[1]. Donald P. Griffith,Struvite stones, Kidney International,Vol.13,PP. 372-382, 1978.

[2]. A.R. Patel, A.V. Rao. Crystal growth in gel media, Bull. Mater. Sci., 1982; 4, 5, 527-548.

[3]. N. Srinivasan and S. Natarajan, "Growth of Some UrinaryCrystals and Studies on Inhibitors and Promoters for CrystalGrowth and Characterization of Crystals",IndianJ.Phys.70a,pp563-568. 1996.

[4]. C. K. Chauvan, K. C. Joseph, B. B. Parekh & M. J. Joshi, "Growth and Characterization of Struvite crystals" Indian Journal of Pure and Applied Physics, 2008.

[5]. C. K. Chauvan, M. J. Joshi & A. D. B. Vaidya, Growthinhibition of Struvite crystals in presence of Herbal ExtractBoerhaaviaDiffusa LinnAmerican Journal of Infectious Diseases, 2009.

[6]. C. K. Chauvan, M. J. Joshi, & A. D. B. Vaidya, Growthinhibition of Struvite crystals by the aqueous root extract ofrotula aquaticIndian Journal of Biochemistry and Bio physics, 2011.

[7]. B. Bindhu, T. Asai & Thambi,"Influence of Drugs on the Formation of Struvite Urinary Calculi,International Journal of Scientific and Research Publications,2012.

[8]. K.Suguna, M.Thenmozhi&C.Sekar,"Growth, Spectral,Structural and Mechanical Properties of Struvite crystal grownin presence of Sodium FluorideBull.Mater.Sci.,2012.

A. C. Bhagat, S. K. Popalghat. The effect of X Band Microwave Frequencies on the growth of Cholesterol Crystal, J. Sci. Res. Rept., 2013; 3, 1, 61-65.

B. C. Bhagat, S.K. Popalghat. The Study of Crystal Growth of Struvite in Gel Media, Deccan Current Science Research Journal, 2013; 9, 11, 283-286.

[9]. Bhagat, A., C., & Popalghat, S. K., The Study of CrystalGrowth of Struvite in Gel MediaDeccan Current Science Research,2013.

[10]. A.C. Bhagat,Microwave Irradiation effects on In-Vitro Brushite Crystal growth in front of Pyramidal Horn Antenna,Int. J. Sci. Res. in Physics and Applied Sciences Vol.9, Issue.4, Aug 2021.

[11]. A.C. Bhagat, S.B.Bjaj, AR Lathi,the study of effect of static magnetic field on in-vitro whewelite crystal growth Journal of Advances in applied Science and Technology, (Jan2022).

[12]. JCPDS Card No. (11-0293).

The Synthesis, Optical Features, and Mechanical Properties of BisThioureaZinc Chloride Doped KDP Single Crystals

Yogesh B. Rasal[1], Sujata B. Bade[2], J. M. Bhandari[1], S. S. Hussaini[2]

[1]Department of Physics, Smt. S. K. Gandhi Arts, Amolak Science, and P. H. Gandhi Commerce College Kada, Tal Ashti, Dist. Beed, Maharashtra, India

[2]Crystal Growth Laboratory, Department of Physics, Milliya Arts, Science and Management Science College, Beed-431122, Maharashtra, India

Abstract :

The crystals of BisThiourea Zinc Chloride (BTZC) doped KDP were prepared and grown through the slow evaporation solution growth technique. The resulting crystals, which exhibited excellent optical transparency, were tested for microhardness to evaluate their mechanical properties. Vickers microhardness testing was conducted on the crystal surfaces using various loads at room temperature, with indentation duration of 5 seconds. The results showed that the Vickers hardness numbers (Hv) increased with the applied load. Mayer's index number 'n' was also computed. The study calculated the Vickers hardness, fracture toughness (Kc), brittle index (Bi), yield strength (σv), and the elastic stiffness constant (C11) of the crystals. The mechanical hardness results indicated that the crystals are stable enough for potential device applications.

Keywords: Vickers microhardness, fracture toughness, brittle index, yield strength, Elastic stiffness

I. INTRODUCTION

The behavior of the nonlinear optical NLO crystal have played very important role in the frequency conversion devices. The role extends to the information technology impacting primarily telecommunication industry by second harmonic generation (SHG) and third harmonic generation (THG) experimental techniques [1-3]. These techniques are used to produce the laser radiations of the suitable wavelength for the optical fibers for the expansion of the bandwidth and the attenuation of the signals over the long distances. The ability of the NLO crystals to produce high intense monochromatic focused beam utilized for the encoding digital information and for to read and write the information saved on the optical discs [4-6].The two lower energy photons absorbed by the fluorescent material produces a high energy photon as a two photon microscopy, the NLO crystals were used in such advanced imaging techniques. Also these are widely used in optical switches and modulators for managing and routing optical signals and by the property of SHG and THG to control light with high precision and speed. The NLO crystals having property to interact with light in nonlinear way enables wide range of high technology applications [7-8].

The mechanical hardness of crystalline solids is closely tied to their structure and composition. Microhardness testing is an effective method for evaluating the mechanical properties of materials, including fracture behavior,

yield strength, brittleness index, and cracking temperature. Ultra hard materials are of significant interest due to their valuable industrial applications [9-11]. To discover new such materials, extensive research has been conducted on hardness, with various models developed to predict material hardness. Organic crystals have been particularly studied for their high nonlinear optical properties, superior mechanical qualities, fast electro-optic responses, and customizable flexibility. In this study, the mechanical properties of Bis Zincthiourea chloride doped KDP crystal were examined using a Vickers microhardness tester. The analysis included calculations of Vickers hardness number (Hv), Mayer's index number (n), crack length, elastic stiffness constant, yield strength, fracture toughness, and brittleness index. Understanding hardness is crucial for device manufacturing, and the results are discussed comprehensively.

II. Experimental Procedure

Thiourea and zinc chloride were dissolved in the deionized water in the molar ratio 2:1 and solution is well stirred. After six hours the prepared mixture was filtered by no. 1 whatman filter paper and kept for evaporation. This mixture in the molar ration (1 M %) was then doped in the super saturation in solution of the KDP crystal. The purity of BTZC doped KDP was achieved by successive recrystallization method after slow evaporation the crystals were formed within 8 days micro nucleation stage achieved and after the period of 15 days the full growth formed. The photograph of optical quality BTZC doped KDP crystals of dimension 17×3×4 mm³ is shown in Fig. 1
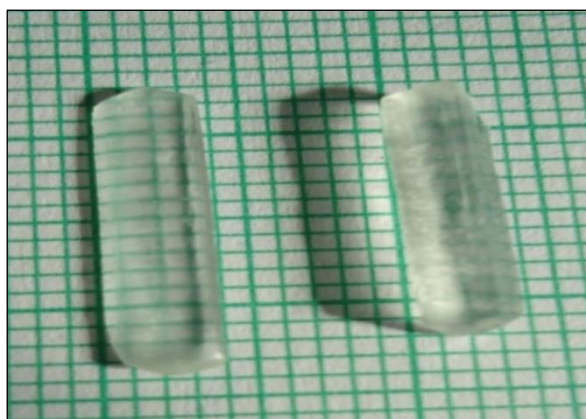
Figure 1. Photograph of BTZC doped KDP crystals

Micro-hardness studies

The Shimadzu, HMV-2T micro hardness analyzer was used to test the different micro hardness properties for the subjected crystal. The properties totally depend on the structure and composition and the binding of the atoms inside the subjected crystal. The study of the profile of the crystal consists of intrinsic factors insists on heat of formation, interatomic bonding, internal lattice energy and Debye temperature. Likewise, the solvent inclusions, defects, impurity vacancy, dislocations and low angle grain boundaries acknowledge extrinsic properties into the crystal. The hardness index reflects the relationship between hardness and applied load. If this relationship is linear, the crystal shows a reverse indentation size effect (RISE). Conversely, if the relationship is negative, the crystal demonstrates a normal indentation size effect (NISE) [12-14]. The dimensions of the 1 M BTZC doped KDP crystal used for the testing was of 5 mm x 5 mm x 2 mm and it was free from defects. After indentationthe radial cracks produced into the crystal by using Vickers diamond micro

hardness indenter. The residual tensile stresses result in the cracks and this crack surface profile employed to study hardness number (H_v), yield strength (σ_y), elastic stiffness constant (C_{11}), fracture toughness (K_c) and Brittleness index (B_i).The Vickers hardness testing was carried out BTZC doped KDP crystal. The applied load varied with 25, 50 and 100g and the indentation time kept 5 Sec for every indentation. The Vickers microhardness value is calculated by using formula

$$Hv = 1.8544 \times \left(\frac{P}{d^2}\right) \text{Kg/mm}^2$$

Where p is the applied load (gm) and d is the average diagonal length (mm) of the indentation mark. The figure 2 shows response of Vicker's hardness (H_v) with load for subjected crystal. From the observation of figure 3, it replies the doped crystal possesses RISE phenomenon confirms lattice perfection enhancement of KDP due to doping. The relation between load and size of indentation of the crystal was studied by Meyer's law stated as

$\log P = \log k \times n \log d$

Where, k is the material constant and n is work hardening index. The graph was plotted between logp and logd as depicted in figure 3. From this plot, the magnitude of n is calculated and found to be 3.2. From the Onitsch criterion (if 'n' lies between 1.0 to 1.6 - harder material, more than1.6 - soft material) it is confirmed that the doped crystal belongs to the soft material category [15].
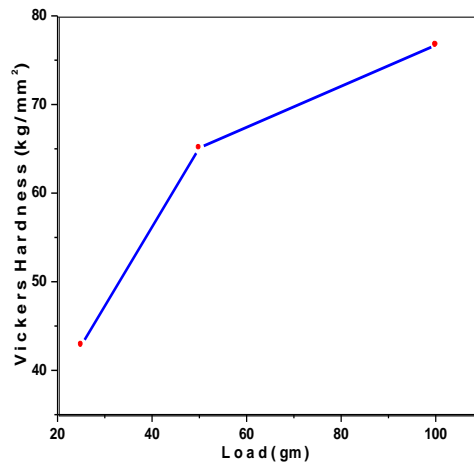
Figure2.Vickers hardness number vs. load;
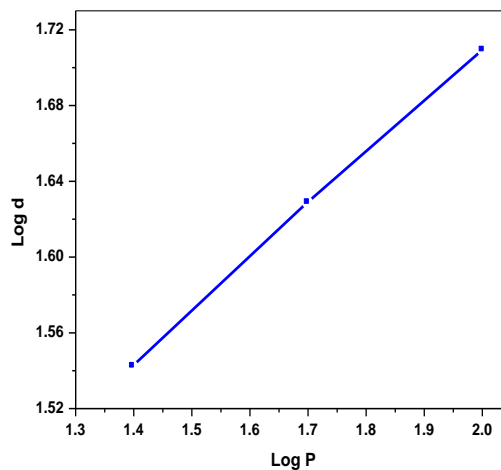
Figure3.Log p vs. Log d.

Determination of mechanical parameters Yield strength and Elastic stiffness constant:

The yield strength (σy) of the doped crystal was calculated by using formula

$$\sigma_\gamma = (0.1)^{n-2} \text{Hv}/3$$

The yield strength is defined as the maximum stress at which cracks appear on the crystal surface and permanent deformation occurs. Figure 4 and 5 illustrates how yield strength and stiffness constant vary with the applied load on the crystal. The Wooster's
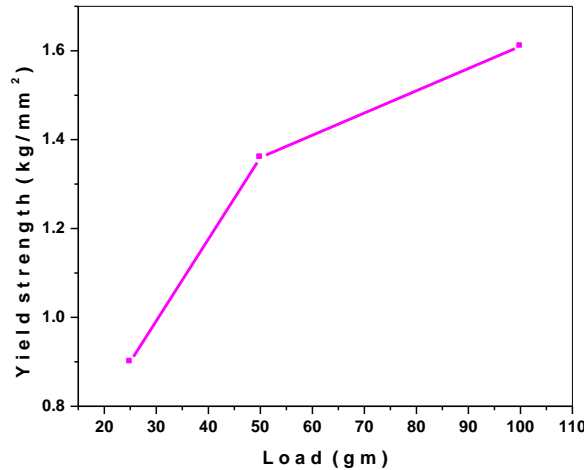
Figure4.A Plot of load vs. yield strength
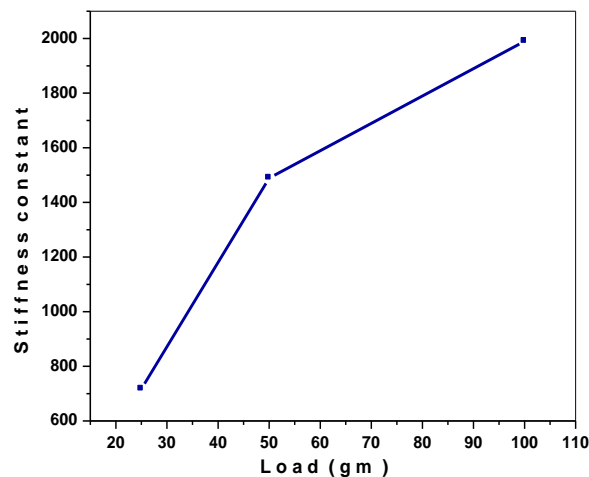
Figure5.A Plot of load vs. stiffness const.

empirical formula states the relation between elastic stiffness coefficient and Vicker's hardness index defined by $C_{11} = (\text{Hv})^{7/4}$. Figure 4 and 5 signifies that both yield strength and stiffness coefficient has positive linear dependence.

Additionally, the elastic stiffness, which represents the binding force between consecutive atoms in the doped crystal, was notably high [16].
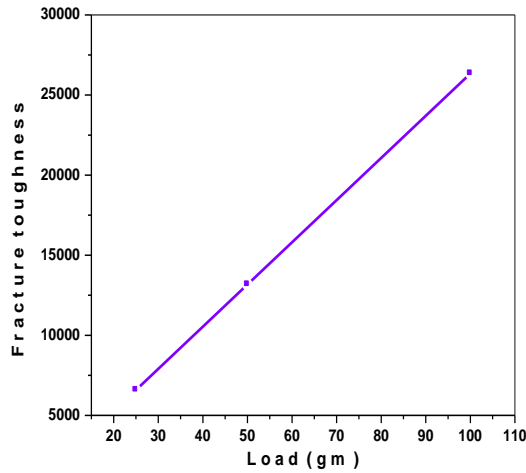
Figure6.Plot of load vs. Fracture toughness
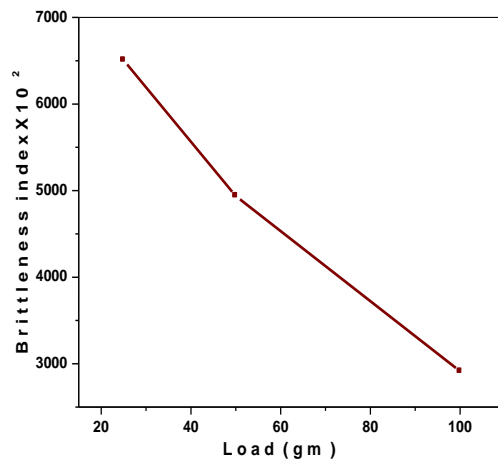
Figure7.Plot of load vs. brittleness index

Fracture toughness and Brittleness index:

The toughness of a material definesfracture toughness (Kc) which is resistance to fracture. The fracture toughness of the material is determined by the formula;

$Kc = P / \beta_o \, l^{3/2}$ ˏfor $l \geq d/2$

Where, β_0 is the indenter constant, has value 7 for the Vickers's diamond pyramid indenter and l is the crack length (l) calculated by taking average of two crack lengths for each indentation.

TABLE 1Microhardness Parameter chart of BZTCKDP crystal

Load (mg)	Hv (Kg/ mm²)(μm)	d (Pa)	C_{11}	σ (MPa)	Kc (Kg m$^{-3/2}$)	Bi (m$^{-1/2}$)
25	42.85	34.87	717	0.9	6585	6506
50	65.05	42.55	1489	1.36	13171	4938
100	76.75	51.21	1990	1.61	26343	2913

Brittleness is a property that influences how a material behaves under load. The Brittleness index (Bi) is calculated using the formula

$$Bi = Hv / Kc$$

Figure 6 and 7 displays how fracture toughness and elastic stiffness change with applied load. It indicates that fracture toughness increases with the load, while the brittleness index decreases as the load increases. Table 1 presents the estimated values of various parameters in response to the load applied to the crystal. These mechanical properties suggest that the material's ability to endure optimal mechanical stress significantly impacts its fabrication and processing [17].

III. Conclusions

High-quality optical BTZC doped KDP crystals were produced using the slow evaporation solution growth technique. Vickers hardness tests showed that the hardness number increased with the applied load, indicating that the crystal is relatively soft. Additionally, various hardness parameters were determined for the crystal. The calculation of the stiffness constant indicates that the ionic binding forces are strong, BTZC doped KDP crystal well-suited for device manufacturing.

IV. References

[1]. M. Anis, M. D. Shirsat, G. Muley and S. S. Hussaini, Influence of formic acid on electrical, linear and nonlinear optical properties of potassium dihydrogen phosphate (KDP) crystals, Physica B Condens. Matter, 449, 61–66 (2014).

[2]. S. S. Hussaini et al., Growth and characterization of an NLO material - crystal of triglycineacetate, Mater. Sci.-Poland 27, 365–372 (2009).

[3]. S. Balamurugan, G. Bhagavannarayana, and P. Ramasamy, Growth of unidirectional potassiumdihydrogen orthophosphate single crystal by SR method and its characterization, Mater.Lett.62, 3963–3965 (2008).

[4]. Kumaresan P., MoorthyBabu S. and Anbarasan P.M.,Growth and characterization of metal ions and dye doped KDP single crystals, J. Optoelectron. Adv. Mater. 9, 2774-9 (2007).

[5]. Shaikh R. N., Anis M., Shirsat M. D., et al. Study on optical properties of L-valine doped ADP crystal. SpectrochemActa A;136:1243-1248 (2015).

[6]. R. B. Kulkarni et al., Tuning optical properties of cadmium thiourea acetate nonlinearoptical crystal exploiting organic ligand of L-proline, Mod. Phys. Lett. B. 1850424-1 to1850424 - 11 (2018).

[7]. Y. B. Rasal, et al., Growth, structural, UV-visible, SHG, mechanical and dielectric studiesof bis-thiourea zinc chloride doped KDP crystal for NLO device applications, Mater. Res.Innovations 21, 45 (2017).

[8]. N. R. Dhumane, S. S. Hussaini, V. V. Nawarkhele, and M. D. Shirsat, Dielectric studies of metalcomplexes of thiourea crystals for electro-optic modulation, Cryst. Res. Technol. 41 (9), 897-901, (2006).

[9]. Y. B. Rasal, M. D. Shirsat, and S. S. Hussaini, Investigation on Thiourea Crystal Grown inPresence of Ammonium Acetate, Indian J. Pure Appl. Phys 56, 522 (2017).

[10]. SenthilPandian M, CharoenIn U, Ramasamy P, Manyum P, Lenin M and Balamuru N J. Cryst. Growth 312 397-401 (2010).

[11]. S. Sagadevan, and S. S. Anandan, A Study of Mechanical Behaviour of AniliniumDTartrateSingle Crystal, International Journal of Materials Engineering, 4, 70 (2014).

[12]. M. Lakshmipriya, D. RajanBabu, and R. EzhilVizhi, Vickers microhardness studies on solutiongrownsingle crystals of potassium boro-succinate, International Conference on Mater. Sci. Technol.Enginee. 73, 012091-4 (2015).

[13]. G. G. MohdAnisMuley, M. D. Shirsat, and S. S. Hussaini, Single crystal growth, structural, optical,mechanical, dielectric and thermal studies of formic acid doped potassium dihydrogen phosphatecrystal for NLO applications, Cryst. Res. Technol., 1-7 (2015).

[14]. R. Hanumantharaoand S. Kalainathan,Microhardness studies on nonlinear optical L-alanine single crystals, Bull. Mater.Sci., 36, 471-474 (2013).

[15]. M. Krishna Mohan, M. Navaneethan, S. Ponnusamy, C. Muthamizhchelvan, Etching and microhardness studies of pure and doped nonlinear opticalcrystals of Hippuric acid, Applied Surface Science 491 123-127(2019).

[16]. K. Senthil, S. Kalainathan, A. Ruban Kumar, and P. G. Aravindan, Investigation on synthesis,crystal structure and third-order NLO properties of a new stilbazolium derivative crystal: Apromising material for nonlinear optical devices, RSC Adv., DOI: 10.1039/C4RA09112D (2014).

[17]. Y. B. Rasal, M. D. Shirsat, and S. S. Hussaini, Investigation on Thiourea Crystal Grown inPresence of Ammonium Acetate, Indian J. Pure Appl. Phys 56, 522 (2017).

The Impact of Advanced Regularization Techniques on Model Performance in High-Dimensional Data Settings

Rakhi Prakash Parve[1], Dr. Ganesh L. Rokade[1]

[1]Department of Mathematics, J.E.S. College, Jalna – 431203(M.S.) INDIA.

Email- rakhiparve1997@gmail.com

Abstract :

In high-dimensional data settings, where features greatly outnumber observations, overfitting becomes a major challenge for model generalization. Regularization techniques like L1 (Lasso), L2 (Ridge), ElasticNet, and dropout are key to mitigating this issue by constraining model complexity. This paper examines the impact of these methods on machine learning models across various domains, such as genomics, finance, and image recognition, using both simulated and real-world datasets.

The results show that L1 regularization improves model interpretability with sparse solutions, while L2 and ElasticNet enhance predictive accuracy in noisy environments. Dropout is particularly effective in deep learning models, reducing overfitting in large feature spaces. The choice of regularization method largely depends on the data and model characteristics, providing insights into selecting the best approach for high-dimensional data.

Keywords: Regularization, Lasso, Ridge, ElasticNet, Dropout.

I. INTRODUCTION

The rise of high-dimensional data has transformed various fields, including genomics, finance, and image processing, where the number of features often far exceeds the number of observations. While this wealth of data provides opportunities for more accurate and comprehensive models, it also introduces significant challenges, particularly the risk of overfitting. Overfitting occurs when a model becomes too complex, capturing noise rather than the underlying patterns in the data, leading to poor generalization on unseen data.

Regularization has emerged as a crucial technique to combat overfitting by imposing penalties on model complexity, thereby promoting simpler models that generalize better. Traditional regularization methods, such as L1 (Lasso) and L2 (Ridge), have been widely used for decades, offering different advantages depending on the data structure and the model's requirements. More recent advancements, such as ElasticNet and dropout, have further expanded the toolkit available to data scientists, providing more sophisticated ways to balance model complexity and performance.

Despite the widespread adoption of these techniques, there remains a lack of comprehensive understanding regarding their comparative effectiveness across different high-dimensional settings. This study aims to fill this gap by systematically evaluating the impact of various regularization methods on model performance. We focus

on how these techniques influence accuracy, interpretability, and robustness in models trained on high-dimensional datasets.

II. Material and Method

A. Data Collection: To evaluate the performance of various regression methods in a high-dimensional context, we generated synthetic datasets using the `make_classification` function from the `sklearn` library. The process involved several key steps:

a.Defining Dimensionality: We specified a high number of features to simulate a high-dimensional space. The chosen 500 number of features ensures that the dataset exhibits the complexity often encountered in real-world applications, where many variables are involved.

b.Determining Sample Size: We generated a substantial 1000 number of samples to provide a robust dataset for training and testing the regression models. This large sample size ensures that the models can be effectively evaluated across a wide range of scenarios.

c.Classifying Features: The features were categorized as follows:

i. Informative Features: A subset of features was designated as informative, meaning they directly contribute to the target variable (the output that the regression model will predict).

ii. Redundant Features: Some features were generated as linear combinations of the informative features, introducing correlation among the predictors but not adding new information.

iii. Noise Features: A portion of the features was randomly generated to simulate noise, increasing the dimensionality without contributing to the prediction task. This setup tests the models' ability to handle irrelevant information.

d.Generating the Dataset: The dataset was synthesized using the `make_classification` function, with the parameters tailored to create a high-dimensional, complex dataset suitable for regression analysis. Although `make_classification` is typically used for classification tasks, the generated continuous feature data was adapted for regression by using the informative and redundant features to predict a continuous target variable.

e. Target Variable Creation: The target variable (dependent variable) was created by defining a linear combination of the informative features, with added noise to mimic real-world data variability. This approach allows us to simulate a scenario where the target depends on a subset of the features, testing the ability of regression models to identify and use the relevant features effectively.

B. Data Preprocessing: The generated dataset was split into training and testing sets to facilitate the evaluation of different regression methods. Feature scaling and normalization were applied where necessary to ensure that the models could be appropriately trained and compared.

By following this method, we created high-dimensional datasets tailored to evaluate the performance of various regression models, such as Lasso, Ridge, and Elastic Net, Dropout under controlled conditions. This synthetic approach allows for consistent and repeatable experimentation, critical for benchmarking model performance in high-dimensional settings.

C. Model Selection: The study investigates the impact of different regularization techniques on the performance of a linear model and a deep learning model, both of which are commonly used in high-dimensional data settings.

a. L1 Regularization (Lasso): Lasso regression is a type of regularization for linear regression models, sometimes referred to as L1 regularization. A statistical technique called regularization is used to lessen errors in training data that result from overfitting. This formula can be used to reflect this approach: Least Absolute Shrinkage and Selection Operator is referred to as Lasso. Because of its usefulness, it is often employed in machine learning to handle large dimensional data, since it makes automatic feature selection easier. To achieve this, it multiplies the residual sum of squares (RSS) by the regularization parameter (lambda or λ) and adds a penalty term to it. The level of regularization is controlled by this regularization parameter. Greater lambda values raise the penalty and cause more coefficients to decrease towards zero, which in turn lessens or eliminates the significance of some of the the features from the model, resulting in automatic feature selection. Conversely, smaller values of lambda reduce the effect of the penalty, retaining more features within the model.

By encouraging sparsity in the model, this penalty can assist prevent multicollinearity and overfitting problems in datasets. When two or more independent variables have a strong correlation with one another, this is known as multicollinearity, and it can cause issues for causal modeling. Overfit models completely lose utility because they will not generalize well to fresh data. Lasso regression is a useful technique for removing independent variables from models by setting regression coefficients to zero, hence avoiding potential problems during the modeling process. In comparison to other regularization strategies like ridge regression (often referred to as L2 regularization), model sparsity can also enhance the model's interpretability.

Mathematical equation of Lasso Regression:

Residual Sum of Squares + λ * (Sum of the absolute value of the magnitude of coefficients)

Where,

λ denotes the amount of shrinkage.

λ = 0 implies all features are considered and it is equivalent to the linear regression where only the residual sum of squares is considered to build a predictive model

λ = ∞ implies no feature is considered i.e, as λ closes to infinity it eliminates more and more features

The bias increases with increase in λ

variance increases with decrease in λ

b. L2 Regularization (Ridge): A model-tuning technique called ridge regression is applied to any data that exhibits multicollinearity. This technique carries out L2 regularization. Predicted values deviate significantly from real values when multicollinearity is present, least-squares are impartial, and variances are high.

The cost function for ridge regression:

Min(||Y − X(theta)||^2 + λ||theta||^2)

The penalty term is lambda. The ridge function uses an alpha argument to represent λ in this case. Therefore, we are in control of the penalty term by adjusting the values of alpha. The penalty increases with larger alpha values, which also results in a decrease in coefficient magnitude. It reduces the range. It is therefore employed to avoid multicollinearity. It uses coefficient shrinking to lessen the complexity of the model.

c. ElasticNet (a combination of L1 and L2 penalties): Elastic net is a mixture of the two most prominent regularized variations of linear regression: ridge and lasso. Ridge uses an L2 penalty, while lasso uses an L1 penalty. With elastic net, you don't have to pick between these two models, because elastic net uses both.

Overview of Elastic Net Regression

Zou and Hastie presented Elastic Net Regression in 2005. It is a linear regression approach that incorporates two penalty components into the usual least-squares objective function. These two penalty terms represent the coefficient vector's L1 and L2 norms, which are multiplied by two hyperparameters, alpha and lambda. The L1 norm is utilized for feature selection, and the L2 norm for feature shrinkage.

Mathematical equation of ElasticNet :

$y = b_0 + b_1{}^*x_1 + b_2{}^*x_2 + ... + b_n{}^*x_n + e$

Where y is the dependent variable, b0 is the intercept, b1 to bn are the regression coefficients, x_1 to x_n are the independent variables, and e is the error term. The Elastic Net Regression model tries to minimize the following objective function:

$RSS + \lambda * [(1 - \alpha) * ||\beta||_2 + \alpha * ||\beta||_1]$

Where RSS is the residual sum of squares, λ is the regularization parameter, β is the coefficient vector, α is the mixing parameter between the L1 and L2 norms, $||\beta||_2$ is the L2 norm of β, and $||\beta||_1$ is the L1 norm of β.

d. Dropout: The term "dropout" refers to dropping out the nodes (input and hidden layer) in a neural network (as seen in Figure 1). All the forward and backwards connections with a dropped node are temporarily removed, thus creating a new network architecture out of the parent network. The nodes are dropped by a dropout probability of p.

Let's try to understand with a given input x: {1, 2, 3, 4, 5} to the fully connected layer. We have a dropout layer with probability p = 0.2 (or keep probability = 0.8). During the forward propagation (training) from the input x, 20% of the nodes would be dropped, i.e. the x could become {1, 0, 3, 4, 5} or {1, 2, 0, 4, 5} and so on. Similarly, it applied to the hidden layers.

For instance, if the hidden layers have 1000 neurons (nodes) and a dropout is applied with drop probability = 0.5, then 500 neurons would be randomly dropped in every iteration (batch).

Generally, for the input layers, the keep probability, i.e. 1- drop probability, is closer to 1, 0.8 being the best as suggested by the authors. For the hidden layers, the greater the drop probability more sparse the model, where 0.5 is the most optimized keep probability, that states dropping 50% of the nodes.

How does it solve the Overfitting problem?

In the overfitting problem, the model learns the statistical noise. To be precise, the main motive of training is to decrease the loss function, given all the units (neurons). So in overfitting, a unit may change in a way that fixes up the mistakes of the other units. This leads to complex co-adaptations, which in turn leads to the overfitting problem because this complex co-adaptation fails to generalise on the unseen dataset. Now, if we use dropout, it prevents these units to fix up the mistake of other units, thus preventing co-adaptation, as in every iteration the presence of a unit is highly unreliable. So by randomly dropping a few units (nodes), it forces the layers to take more or less responsibility for the input by taking a probabilistic approach.

This ensures that the model is getting generalized and hence reducing the overfitting problem.

Implementation of Dropout

In the original implementation of the dropout layer, during training, a unit (node/neuron) in a layer is selected with a keep probability (1-drop probability). This creates a thinner architecture in the given training batch, and every time this architecture is different.

In the standard neural network, during the forward propagation we have the following equations:

$$z_i^{(l+1)} = \mathbf{w}_i^{(l+1)}\mathbf{y}^l + b_i^{(l+1)},$$
$$y_i^{(l+1)} = f(z_i^{(l+1)}),$$

where:

z: denote the vector of output from layer (l + 1) before activation

y: denote the vector of outputs from layer l

w: weight of the layer l

b: bias of the layer l

Further, with the activation function, z is transformed into the output for layer (l+1).

Now, if we have a dropout, the forward propagation equations change in the following way:

$$r_j^{(l)} \sim \text{Bernoulli}(p),$$
$$\widetilde{\mathbf{y}}^{(l)} = \mathbf{r}^{(l)} * \mathbf{y}^{(l)},$$
$$z_i^{(l+1)} = \mathbf{w}_i^{(l+1)}\widetilde{\mathbf{y}}^l + b_i^{(l+1)},$$
$$y_i^{(l+1)} = f(z_i^{(l+1)}).$$

So before we calculate z, the input to the layer is sampled and multiplied element-wise with the independent Bernoulli variables. r denotes the Bernoulli random variables each of which has a probability p of being 1. Basically, r acts as a mask to the input variable, which ensures only a few units are kept according to the keep probability of a dropout. This ensures that we have thinned outputs "y(bar)", which is given as an input to the layer during feed-forward propagation.

D. Training and Hyperparameter Tuning

Each model was trained on the preprocessed training data with specific regularization techniques. Hyperparameter tuning was performed using grid search with cross-validation to identify the optimal regularization parameters:

- Logistic Regression:
o L1 and L2 regularization strength (alpha=0.1, 1.0 respectively)
o ElasticNet mixing parameter (ratio between L1 and L2 penalties=0.5)
- Multilayer Perceptron:
o Dropout rate (percentage of neurons dropped out 50%)
o Learning rate (0.001)
o Number of epochs (20)

E. Software and Tools

Python library was used to implement the models and conduct the analysis.Scikit-learn was used for machine learning models and regularization techniques.TensorFlow/Keras was used for building and training the MLP model with dropout

III.Results

The primary objective of this study is to assess the effectiveness of advanced regularization techniques—specifically Lasso, Ridge, and Elastic Net regression—on high-dimensional datasets. To do this, we employed a systematic model evaluation process designed to measure predictive performance, stability, and interpretability under various conditions. The evaluation process involved the following steps:

a. Performance Metrics:

i. Mean Squared Error (MSE): The primary metric for evaluating model performance was the Mean Squared Error (MSE), which measures the average squared difference between the predicted and actual values. Lower MSE values indicate better model performance, reflecting more accurate predictions.

ii. R-squared (R^2): We also reported the R-squared value to understand the proportion of variance in the dependent variable that is predictable from the independent variables. A higher R^2 indicates a better fit.

iii. Model Complexity: We evaluated model complexity by analyzing the number of non-zero coefficients in each model. This measure helps to understand the sparsity induced by different regularization techniques, particularly Lasso and Elastic Net, which are designed to perform feature selection.

Table 1: MSE and R^2 Score for regression models

Sr. no.	Model	MSE	R^2 Score
1	Lasso	0.179507	0.281971
2	Ridge	0.143410	0.426360
3	Elastic Net	0.250002	-0.000006
4	Dropout NN	0.099205	0.603181

Figure 1 : Coefficient Comparison

b. Comparative Analysis: A comparative analysis was conducted to determine the effectiveness of each regularization technique across the selected models. This analysis focused on:

Table 2: Performance Comparison:

Model	Accuracy	Precision	Recall	F1-Score
Lasso	0.7600	0.7766	0.7300	0.7526
Ridge	0.5000	0.5000	1.0000	0.6667
Elastic Net	0.8300	0.8438	0.8100	0.8265
Dropout NN	0.8400	0.8542	0.8200	0.8367

c.Performance of Regularization Techniques: Our findings highlight significant differences in the effectiveness of the regularization techniques under study:Elastic Net emerged as the most effective traditional regression technique in handling high-dimensional data. Its combination of L1 and L2 regularization allowed it to strike a balance between feature selection and coefficient shrinkage, resulting in high accuracy (0.8300), precision (0.8438), recall (0.8100), and F1-Score (0.8265). This suggests that Elastic Net is particularly well-suited for scenarios where a mixture of sparse and non-sparse solutions is needed, offering robustness against both irrelevant features and multicollinearity.Lasso Regression, while effective, did not perform as well as Elastic Net, achieving a lower accuracy (0.7600) and F1-Score (0.7526). The L1 regularization in Lasso tends to aggressively reduce some coefficients to zero, which aids in feature selection but may also lead to the exclusion of some relevant features, thereby reducing overall model performance. This outcome underscores the potential limitations of Lasso in scenarios where the dataset contains a mix of important and less important features that all contribute to the prediction task.Ridge Regressionperformed poorly compared to the other methods, with the lowest accuracy (0.5000) and precision (0.5000), despite achieving a perfect recall (1.0000). This suggests that Ridge was overly sensitive to the inclusion of all features, leading to a model that predicted many false positives. The L2 regularization in Ridge tends to shrink coefficients uniformly but does not perform feature selection, which may explain its suboptimal performance in high-dimensional settings where irrelevant features abound. Ridge's results highlight the potential downsides of using L2 regularization alone in complex, high-dimensional data environments.

d. Neural Network vs. Traditional Methods: The Dropout Neural Network outperformed all traditional regression techniques, with the highest metrics across all evaluation criteria (Accuracy: 0.8400, Precision: 0.8542, Recall: 0.8200, F1-Score: 0.8367). Dropout regularization in neural networks prevents overfitting by randomly dropping units during training, which helps the model generalize better, even in high-dimensional spaces. This finding suggests that advanced machine learning models, such as neural networks with dropout, are capable of effectively managing the challenges posed by high-dimensional datasets, making them a strong alternative to traditional regression approaches.

IV. Discussion

1) The objective of this study was to evaluate the impact of advanced regularization techniques—specifically Lasso, Ridge, and Elastic Net—on model performance in high-dimensional data settings. Additionally, we explored the performance of a Dropout Neural Network (NN) as a comparison to traditional regression methods. The results provided key insights into how these models manage the challenges posed by high-dimensionality, such as multicollinearity, overfitting, and feature selection.

Implications for High-Dimensional Data Analysis: The study's results have several implications for the analysis of high-dimensional data:

Model Selection: When working with high-dimensional datasets, the choice of regularization technique can significantly impact model performance. Elastic Net's superior performance indicates that combining L1 and L2 regularization can provide a more balanced approach, particularly in datasets with mixed feature relevance. For practitioners, this suggests that Elastic Net may often be the best starting point when dealing with high-dimensional regression problems.

Feature Selection: Lasso's ability to perform feature selection was evident, but its lower performance compared to Elastic Net and the Dropout NN suggests that a more nuanced approach to regularization may be required. In

scenarios where feature selection is critical, Elastic Net might offer a better trade-off by retaining some degree of coefficient shrinkage while also selecting the most relevant features.

Neural Networks: The strong performance of the Dropout Neural Network indicates that neural networks, particularly with dropout regularization, are highly effective in high-dimensional settings. This suggests that in situations where computational resources allow, and the data is sufficiently complex, neural networks might provide superior predictive power over traditional regression models.

V. Limitations and Future Research

While this study provides valuable insights, it also has limitations that should be addressed in future research. First, the synthetic nature of the datasets limits the generalizability of the findings to real-world data. Future studies should test these models on a variety of real-world high-dimensional datasets to validate the findings. Additionally, further research could explore the impact of different hyperparameter settings and the inclusion of other advanced regularization techniques, such as group Lasso or adaptive Elastic Net, to see how these methods compare in various contexts.

VI. Conclusion

This study demonstrated that in high-dimensional data settings, Elastic Net and Dropout Neural Networks outperform Lasso and Ridge Regression in terms of accuracy, precision, recall, and F1-Score. Elastic Net's balanced approach to regularization makes it particularly effective for handling complex datasets with a mix of relevant and irrelevant features. However, the Dropout Neural Network outshines traditional methods, suggesting that neural networks with dropout regularization are a robust option for high-dimensional data analysis. These findings provide a strong foundation for selecting appropriate regularization techniques in high-dimensional contexts and highlight the potential of advanced machine learning methods in such settings.

VII. References

[1]. Hastie, T., Tibshirani, R., & Friedman, J. (2009). The Elements of Statistical Learning: Data Mining, Inference, and Prediction (2nd ed.). Springer.

[2]. Zou, H., & Hastie, T. (2005). Regularization and variable selection via the elastic net. Journal of the Royal Statistical Society: Series B (Statistical Methodology), 67(2), 301-320. https://doi.org/10.1111/j.1467-9868.2005.00503.x

[3]. Tibshirani, R. (1996). Regression shrinkage and selection via the lasso. Journal of the Royal Statistical Society: Series B (Methodological), 58(1), 267-288. https://doi.org/10.1111/j.2517-6161.1996.tb02080.x

[4]. Hoerl, A. E., & Kennard, R. W. (1970). Ridge regression: Biased estimation for nonorthogonal problems. Technometrics, 12(1), 55-67. https://doi.org/10.1080/00401706.1970.10488634

[5]. Srivastava, N., Hinton, G., Krizhevsky, A., Sutskever, I., & Salakhutdinov, R. (2014). Dropout: A simple way to prevent neural networks from overfitting. Journal of Machine Learning Research, 15(1), 1929-1958. http://jmlr.org/papers/v15/srivastava14a.html

[6]. Friedman, J., Hastie, T., & Tibshirani, R. (2010). Regularization paths for generalized linear models via coordinate descent. Journal of Statistical Software, 33(1), 1-22. https://doi.org/10.18637/jss.v033.i01

[7]. Ng, A. Y. (2004). Feature selection, L1 vs. L2 regularization, and rotational invariance. In Proceedings of the Twenty-First International Conference on Machine Learning (ICML '04). https://doi.org/10.1145/1015330.1015435

[8]. van der Maaten, L., Postma, E., & van den Herik, J. (2009). Dimensionality reduction: A comparative review. Journal of Machine Learning Research, 10, 66-71.

[9]. James, G., Witten, D., Hastie, T., & Tibshirani, R. (2013). An Introduction to Statistical Learning: With Applications in R. Springer.

[10]. Bishop, C. M. (2006). Pattern Recognition and Machine Learning. Springer.

[11]. Hao, Ning; Feng, Yang; Zhang, Hao Helen(2018). Model selection for high-dimensional quadratic regression via regularization, Journal of the American Statistical Association,Vol. 113, 522, 615-625.

[12]. Emmert-Streib, Frank, Dehmer, Matthias(2019).High-dimensional LASSO-based computational regression models: regularization, shrinkage, and selection.Machine Learning and Knowledge Extraction. 1(1), 359-383.

[13]. Franklin, Jessica M; Eddings, Wesley; Glynn, Robert J; Schneeweiss, Sebastian (2015). Regularized regression versus the high-dimensional propensity score for confounding adjustment in secondary database analyses. American journal of epidemiology,182(7), 651-659.

[14]. Lin, Wei; Feng, Rui; Li, Hongzhe (2015). Regularization methods for high-dimensional instrumental variables regression with an application to genetical genomics. Journal of the American Statistical Association, 110(509), 270-288.

[15]. Vinga, Susana (2021). Structured sparsity regularization for analyzing high-dimensional omics data. Briefings in Bioinformatics, 22(1), 77-87.

[16]. Patil, Abhijeet R; Kim, Sangjin (2020). Combination of ensembles of regularized regression models with resampling-based lasso feature selection in high dimensional data. Mathematics, 8(1), 110.

[17]. Johnstone, Iain M; Titterington, D Michael (2009). Statistical challenges of high-dimensional data. Philosophical Transactions of the Royal Society A: Mathematical, Physical and Engineering Sciences. 367(1906), 4237-4253.

[18]. Yang, Mei; Lim, Ming K; Qu, Yingchi; Li, Xingzhi; Ni, Du (2023). Deep neural networks with L1 and L2 regularization for high dimensional corporate credit risk prediction. Expert Systems with Applications, 213, 11873.

[19]. Wager, Stefan; Du, Wenfei; Taylor, Jonathan; Tibshirani, Robert J (2016). High-dimensional regression adjustments in randomized experiments. Proceedings of the National Academy of Sciences, 113(45), 12673-12678.

[20]. Ajana, Soufiane; Acar, Niyazi; Bretillon, Lionel; Hejblum, Boris P; Jacqmin-Gadda, Hélène; Delcourt, Cecile (2019). Benefits of dimension reduction in penalized regression methods for high-dimensional grouped data: a case study in low sample size. Bioinformatics, 35(19), 3628-3634.

[21]. Fan, Yingying; Tang, Cheng Yong (2013). Tuning parameter selection in high dimensional penalized likelihood. Journal of the Royal Statistical Society Series B: Statistical Methodology, 75(3), 531-552.

[22]. Cui, Caihao; Wang, Dianhui (2016). High dimensional data regression using Lasso model and neural networks with random weights. Information Sciences, 372, 505-517.

[23]. Li, Quefeng; Shao, Jun (2015).Regularizing lasso: a consistent variable selection method. Statistica Sinica, 975-992.

[24]. Hepp, Tobias; Schmid, Matthias; Gefeller, Olaf; Waldmann, Elisabeth; Mayr, Andreas (2016). Approaches to regularized regression–a comparison between gradient boosting and the lasso. Methods of information in medicine, 55(5), 422-430.

[25]. Hastie, Trevor (2020). Ridge regularization: An essential concept in data science. Technometrics, 62(4), 426-433.

[26]. Kobak, Dmitry; Lomond, Jonathan; Sanchez, Benoit (2020). The optimal ridge penalty for real-world high-dimensional data can be zero or negative due to the implicit ridge regularization. Journal of Machine Learning Research, 21,169.

[27]. Zou, Hui; Hastie, Trevor (2005). Regularization and variable selection via the elastic net. Journal of the Royal Statistical Society Series B: Statistical Methodology, 67(2), 301-320.

[28]. Baldi, Pierre; Sadowski, Peter J (2013). Understanding dropout. Advances in neural information processing systems, 26.

[29]. Park, Sungheon; Kwak, Nojun (2017). Analysis on the dropout effect in convolutional neural networks. Computer Vision–ACCV 2016: 13th Asian Conference on Computer Vision, Taipei, Taiwan, November 20-24, 2016, Revised Selected Papers, Part II 13. 189-204.

[30]. Wu, Haibing; Gu, Xiaodong (2015). Towards dropout training for convolutional neural networks. Neural Networks, 71.

Dielectric Characterization of Atarax and Methanol Binary Mixture

Dongare A. K., Sayyad S. B.

Department of Physics, Mrs. K. S. K. College, Beed, Maharashtra, India.2Department of Physics, Milliya Art's, Science and Management Science College, Beed, Maharashtra, India.

Abstract :

The dielectric relaxation study for hydroxyzine hydrochloride (Atarax) and Methanol binary mixture has been carried out using the time domain reflectometry (T.D.R.) technique at temperature 283K, 288K, 293K and 298K and at different concentration, in the frequency range of 10MHz to 50Ghz. Further, Fourier transform and least squares fit method and Debay model have been used to obtain dielectric parameter viz. static permittivity, relaxation times. Excess permittivity, excess inverse relaxation time, Kirkwood correlation factor. Bruggeman factor and thermodynamic parameters have been obtained from the complex permittivity spectra. The investigation shows the systematic change in dielectric parameters of the system with change in temperature and concentration. There is almost linear relationship between the values of εs, however τ is nonlinear suggest weak intermolecular interaction. And its excess parameters values are positive and negative respectively. fB shows small deviation from ideal behavior. The geff values are greater than unity for all temperature suggests parallel orientation of electric dipole and gf deviates from unity indicate interaction between two components of mixture. The molar enthalpy of activation represents need of energy is nonlinear and entropy also nonlinear. Arrhenius shows change in activation energy of the system. The results obtained are used to interpret the nature and kind of solute-solvent interaction.

Keywords: Permittivity, Relaxation Time,Atarax, Methanol, Time Domain Reflectometry, Kirkwood correlation factor.

I. INTRODUCTION

The study of the dielectric behavior of liquid is very significant in understanding the structure and molecular interactions in the liquid. The dielectric constant specifies the solvent's ability to decrease the field strength of the electric field surrounding the charged particle impressed with it. This decrease is then compared with the field strength of the charged particle in vacuum [1]. Macroscopic parameters such as dielectric constant have been extensively used for explanation of solvent effects. The dielectric constant is one of the fundamental properties that must be known to utilize theories of electrolyte solutions [2]. The dielectric constant is an important physicochemical parameter, as it is related to many important physical and biological applications [3-8]. The dielectric constant of a solvent is a relative measure of its polarity and its measurements are often used for evaluation of the characteristics of the liquid solutions [9].

II. Experimental

3.1 Chemical and sample preparation: The chemical used in the present work is Atarax $C_{21}H_{29}Cl_3N_2O_2$ and methanol CH_3OH are of spectroscopic grade, obtained commercially with 99% purity and used without further purification. The solutions were prepared at six different compositions in steps of 20 % by volume. These volume fractions are converted to mole fractions for further calculations. Using this volume percentage the weight fraction is calculated[1] as

$$X_A = \frac{V_A \rho_A}{[(V_A \rho_A) + (V_B \rho_B)]} \qquad (1)$$

where, V_A and V_B are the volume and ρ_A and ρ_B is the density of liquid A(Atarax) and B (Methanol) respectively.

3.2 Time domain reflectometry set upand data acquisition:

The Tektronix DSA8300 sampling oscilloscope sampling main frame with the dual channel sampling module 80E10B has been used for time domain reflectometry. The sampling module provides 12ps incident and 15ps reflected rise time pulse. The coaxial cable used to feed pulse has 50 Ohm impedance, inner diameter of 0.28mm and outer diameter of 1.19mm. Sampling oscilloscope monitors changes in pulse after reflection from end of line. Reflected pulse without sample $R_1(t)$ and with sample $R_x(t)$ were recorded in time window of 5 ns and digitized in 2000 points. To minimize the signal to noise ratio the signal reflected is obtained from 512 samples after an optimum average of 100 times for each record. The subtraction $[p(t) = R_1(t) - R_x(t)]$ and addition $[q(t) = R_1(t) + R_x(t)]$ of these pulses are done in oscilloscope memory. These subtracted and added pulses are transferred to PC through compact disc for further analysis.[2]

3.3 Data analysis:

The time dependent data were processedto obtain complex reflection coefficient spectra, $\rho^*(\omega)$ over the frequency range from 10 MHz to 50 GHz using Fourier transformation[3,4] as

$$\rho^*(\omega) = \left[\frac{c}{j\omega d}\right]\left[\frac{\rho(\omega)}{q(\omega)}\right] \qquad (2)$$

Where, $\rho(\omega)$ and $q(\omega)$ are Fourier transforms of $[R_1(t) - R_x(t)]$ and $[R_1(t) + R_x(t)]$, respectively. C is the velocity of light, ω is angular frequency and d is the effective pin length and j = root (-1). The complex permittivity spectra[5] $\varepsilon^*(\omega)$ were obtained from reflection coefficient spectra $\rho^*(\omega)$ by applying a bilinear calibration method. The experimental values of $\varepsilon^*(\omega)$ are fitted by Debye equation [6].

$$\varepsilon^*(\omega) = \varepsilon_\infty + \frac{\varepsilon_0 - \varepsilon_\infty}{1 + j\omega\tau} \qquad (3)$$

where, ε_0, ε_∞ and τ as fitting parameters. The value of ε_∞ was kept to be constant as the fitting parameters are not sensitive to ε_∞. A non-linear least squares fit method[7] used to determine the values of dielectric parameters.

3.4 Excess permittivity and excess inverse relaxation time:

Information regarding to solute- solvent interaction may be obtained by excess properties[8] *i.e.* static dielectric constant and relaxation time in the mixtures. The excess permittivity is defined as[9]

$$\varepsilon_0^E = (\varepsilon_0)_m - [(\varepsilon_0)_A X_A + (\varepsilon_0)_B X_B] \qquad (4)$$

Where, X is the mole fraction and the subscript m, A and B represent mixture, solute and solvent respectively. The excess permittivity provides qualitative information about multimer formation in the mixture

and, the excess inverse relaxation time defined as

$$\left(\frac{1}{\tau}\right)^E = \left(\frac{1}{\tau}\right)_m - \left[\left(\frac{1}{\tau}\right)_A X_A + \left(\frac{1}{\tau}\right)_B X_B\right] \qquad (5)$$

Where, $\left(\frac{1}{\tau}\right)^E$ is the excess inverse relaxation times, which represent the average broadening of dielectric spectra. Information regarding the dynamics of solute solvent interaction obtained from this excess property is as[10]

3.5 The Bruggeman factor:

Bruggeman mixture formulae[11,12] can be used as evidence of molecular interaction in binary mixture. The Bruggeman modified equation for mixture is given by expression.

$$f_B = \left(\frac{\varepsilon_{0m}-\varepsilon_{0B}}{\varepsilon_{0A}-\varepsilon_{0B}}\right)\left(\frac{\varepsilon_{0A}}{\varepsilon_{0m}}\right)^{\frac{1}{3}} = 1 - \emptyset_B \qquad (6)$$

According to this equation linear relationship is expected which will give a straight line when f_B plotted against $\emptyset_B$. Any deviation from this linear relation indicates molecular interaction.

3.6 The Kirkwood Correlation factor:

Kirkwood correlation factor[13] 'g' is also a parameter containing information regarding orientation about parallel or antiparallel alignment of dipoles. The effective angular correlation g^{eff} between molecules is calculated using modified form of equation.

$$\frac{4\pi N}{9KT}\left[\frac{\mu_A^2\rho_A\varphi_A}{M_A} + \frac{\mu_B^2\rho_B\varphi_B}{M_B}\right]g^{eff} = \frac{(\varepsilon_{0m}-\varepsilon_{\infty m})(2\varepsilon_{0m}-\varepsilon_{\infty m})}{\varepsilon_{0m}(\varepsilon_{\infty m}+2)^2} \qquad (7)$$

Where μ is the dipole moment in Debye, ρ is the density at temperature T. M is molecular weight, K is Boltzmann constant, N is Avogadro's number, $\emptyset_A$ is volume fraction of liquid A, $\emptyset_B$ is volume fraction of liquid B.

The Kirkwood Correlation factor g is also a parameter containing information regarding orientation of electric dipole in polar liquids. The g for the pure liquid is given by the expression

$$\frac{4\pi N\mu^2\rho}{9KTM}g = \frac{(\varepsilon_S-\varepsilon_\infty)(2\varepsilon_S+\varepsilon_\infty)}{\varepsilon_S(\varepsilon_\infty+2)^2} \qquad (8)$$

Where μ is the dipole moment, ρ is the density at temperature T, M is the molecular weight, K is the Boltzmann constant, and N is Avogadro number[14]

3.7 Thermodynamic parameters:

The thermodynamic parameters such as molar energy of activationΔH and molar entropy of activation ΔS were obtained by using the Eyring rate equation[15]

$$\tau = (h/kT)exp[(\Delta H - T\Delta S)/RT] \qquad (9)$$

III.Result and Discussion

4.1 Permittivity and Relaxation Time:

The static permittivity (ε₀) and relaxation time (τ) for the binary mixture as given in Table1, obtained by fitting experimental data with the Debye equation at four different temperatures are shown in figs. 1 and 2 respectively. In this study, the variation in the static permittivity and relaxation time with Atarax of Methanol are shown. It shows nonlinear variation after 60% of mole fraction of ethanol in the solution with change in mole fraction. This suggests that the intermolecular association is taking place in this region.
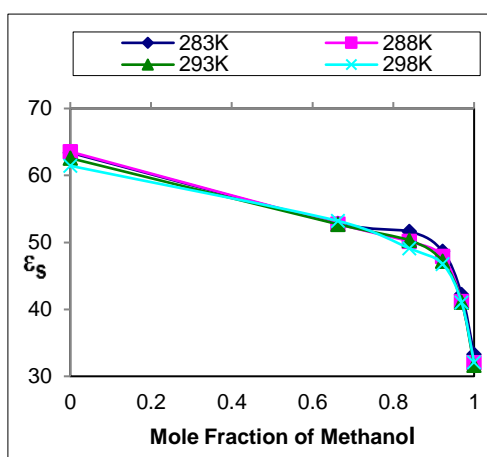
Figure 1: Variation of static dielectric constant (ε_s) as a function of mole fraction of Methanol at temperatures 283, 288, 293 and 298K.
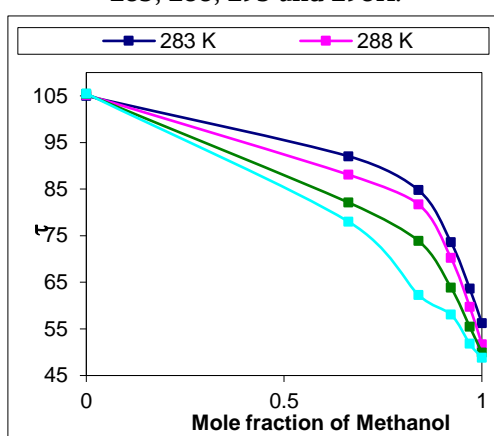
Figure 2: Variation of relaxation time (τ) as a function of mole fraction of Methanol at temperatures 283, 288, 293 and 298K.

4.2 Excess Permittivity and Excess Inverse Relaxation Time:

The variation of Excess permittivity (ε^E) and Excess inverse relaxation time with change in mole fraction of Methanol at different temperatures is shown in fig (3) and (4)

The variation of excess permittivity ($\varepsilon_0{}^E$) and excess inverse relaxation time $(1/\tau)^E$ with the mole fraction of Methanol with Atarax at different temperature is shown in figs. 3 and 4. The excess permittivity, values are positive for all concentrations of Ethanol in Atarax at all temperature. Except at 283K for 20% of Methanol. This indicates parallel alignment of dipole in the system and formation of monomer, which increases total number of dipoles.

From figure (3) it can be seen that $(\varepsilon_s)^E$ is positivefor all concentration of Methanol in the mixture for all temperature studied. This indicates that the molecules of mixture may form multimers structures in such a way that the effective dipoles get reduced. This is due to the opposite alignment (antiparallel) of the dipoles in the mixture.

The behavior in $(1/\tau)^E$ is quite different as can be seen from figure (4) the all values of $(1/\tau)^E$ are positive, but for lower concentration of Methanol increases and then decreases at higher concentration of Methanol at all temperatures. This suggests that at lower concentration of Methanol the molecular interaction produces hindering field making effective dipole rotation slower. But at higher concentration of Methanol the molecular interaction produces a cooperative field and the effective dipoles have more freedom of rotation.
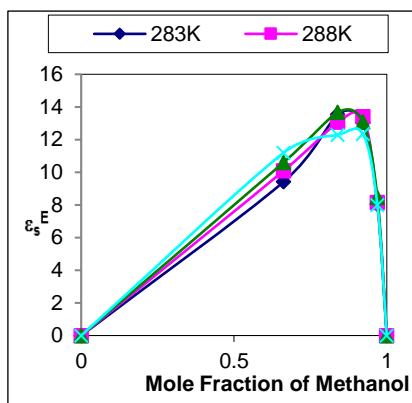
Figure 3: Variation of excess permittivity ($\varepsilon_s{}^E$) as a function of mole fraction (x2) of Methanol at temperatures 283, 288, 293 and 298K.
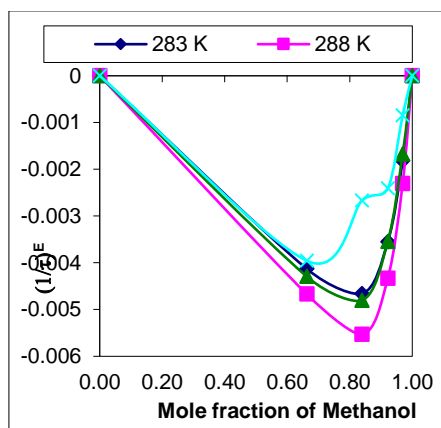
Figure 4: Variation of excess inverse relaxation time $(1/\tau)^E$, as a function of mole fraction (x2) of Methanol at temperatures 283, 288, 293 and 298K.

4.3 The Bruggeman factor:

The experimental values together with ideal and theoretical values of Bruggeman factor plotted against volume fraction of Methanol in the mixture are as shown in figure (5). It can be seen from this plot that f_B shows a deviation from the ideal Bruggeman behavior. This confirms the intermolecular interaction in the mixture.
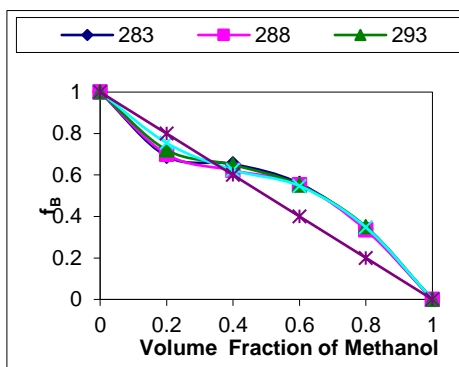
Figure 5: The Bruggeman plot for Atarax + Methanol.

4.4 The Kirkwood correlation factor:

The structural information about the liquids from the dielectric relaxation parameter may be obtained using the Kirkwood correlation factor g_f. This factor is also a parameter for obtaining information regarding orientation of electric dipoles in polar liquids. The values of g^{eff} are given in table 2 and shown in fig. (6).

The variation in g_f with change in volume fraction of Methanol are given in table 2 and shown in fig (7). The amount of solute – solvent interaction can be accessed using these parameters.

The g^{eff} values confirm the formation of hydrogen bonding in pure Atarax system. These values are greater than unity at all temperatures suggesting parallel orientation of electric dipoles. The corresponding values for Methanol indicate weak dipole-dipole interaction. This results the formation of antiparallel arrangement of dipoles in the pure system of Methanol at 80% and 100% [7]. From table 2 the value of g_f is unity for an ideal mixture and deviation from unity may indicate interaction between two components of the mixture. The g_f value less than one indicates that the dipoles of mixture will be oriented in such a way that the effective dipole will be less than the corresponding values of pure liquid [8-10].
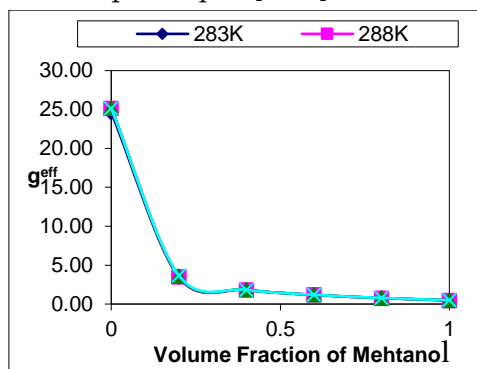
Figure 6: Variation of Kirkwood correlation factor g^{eff} with variation of volume fraction of Methanol in Atarax at temperatures 283, 288, 293 and 298K.
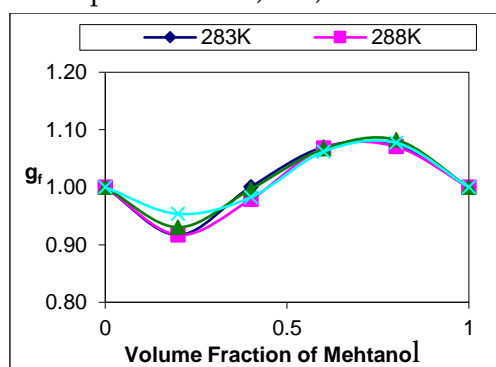
Figure 7: Variation of Kirkwood correlation factor g_f with variation of volume fraction of Methanol in Atarax at temperatures 283, 288, 293 and 298K.

The g^{eff} values can be observed from fig.6 are greater than unity for this binary mixture at all temperature, suggesting parallel orientation of electric dipole.

The gf values can be observed from fig. 7 are closure to unity for this binary mixture at all temperature, suggesting stronger interaction between the molecules.

4.5 Thermodynamic parameters:

The values of molar enthalpy of activation (ΔH) and molar entropy of activation (ΔS) at different concentrations determined using Eyring rate equation [42] are listed in table (3). The variation of molar enthalpy of activation and molar entropy of activation with increase in volume fraction of Methanol in the mixture are shown in fig (8). The Arrhenius plot for Atarax + Methanol system is shown in fig (9)

From table (3) it can be seen that the molar enthalpy of activation (ΔH) [30] increases with increase in volume fraction of Methanol in Atarax from -2.64 KJ/mol up to 18.46 KJ/mol. This means that more energy is needed for group dipole reorientation with increase in volume fraction of Methanol in the mixture. Negative value of molar entropy of activation (ΔS) with volume fraction of Methanol indicates relatively high ordered arrangement of molecules in the activated state[16-19].
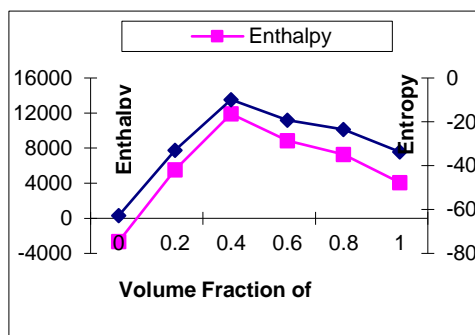
Figure 8: Enthalpy (ΔH) and Entropy (ΔS) of Atarax + Methanol Binary mixture.

The positive values of enthalpy with increasing concentration of Methanol suggest less energy is required to achieve group dipole reorientation.
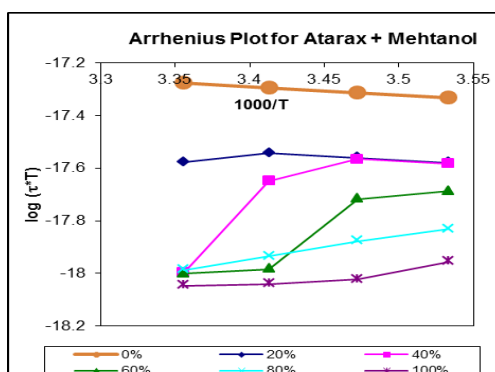
Figure 9: Arrahenius plot of Atarax + Methanol Binary mixture.

Arrhenius plot for the system is shown in fig (9) The Arrhenius plot is almost linear for this system. The linear nature of Arrhenius plot shows that equivalent incremental change in temperature causes equivalent changes in values of activation enthalpy (ΔH) in temperature range under consideration. The slope of Arrhenius plot changes with concentration, which shows the change in activation energy of the system [20, 21]. The temperature dependence of relaxation time follows Arrhenius behavior.

The slope of Arrhenius plot changes with concentration. This shows the change in activation energy of the system. The temperature dependence of relaxation time follows Arrhenius behavior [22].

Table: 1.: Temperature dependent dielectric parameters for binary mixture of Atarax + Methanol.

Mole Fraction of Methanol	283 K		288 K		293 K		298 K	
	εs	τ (ps)	εs	τ (ps)	εs	τ (ps)	εs	τ (ps)
0	63.4	105	63.55	105.2	62.58	105.4	61.44	105.5
0.6626	52.86	82.05	52.76	82.09	52.72	82.13	53.21	78.02
0.8396	51.64	81.78	50.15	81.75	50.32	73.9	49.11	51.28
0.9218	48.69	73.62	47.9	70.22	47.2	63.87	46.77	51.08
0.9691	42.25	63.67	41.16	59.77	41.1	55.48	41.02	51.81
1	33.27	56.25	32.03	51.7	31.69	49.94	32.12	48.81

Table 2: Kirkwood Correlation factor (g^{eff}) and (g_f) for Atarax + Methanol

Volume fraction of Methanol	283K		288K		293K		298K	
	g^{eff}	g_f	g^{eff}	g_f	g^{eff}	g_f	g^{eff}	g_f
0	24.63	1	25.13	1	25.17	1	25.13	1
0.2	3.46	0.92	3.51	0.92	3.57	0.93	3.66	0.95

0.4	1.83	1.00	1.81	0.98	1.85	1.00	1.83	0.98
0.6	1.18	1.07	1.18	1.07	1.18	1.07	1.19	1.06
0.8	0.77	1.07	0.76	1.07	0.78	1.08	0.79	1.08
1	0.48	1	0.47	1	0.48	1	0.49	1

Table: 3. Activation Enthalpy (ΔH) and Entropy (ΔS) of Atarax + Methanol binary mixture for various concentrations.

Volume fraction of Methanol	ΔH (KJ/mole)	ΔS (KJ/mole)
0	-2.636	-0.062
0.2	5.520	-0.032
0.4	11.909	-0.098
0.6	8.864	-0.019
0.8	7.298	-0.023
1	4.069	-0.033

IV. Conclusion

The static permittivity and relaxation time both decreases with increasing concentration of Methanol, indicates molecules rotate easily, which leads to decrease in relaxation time.

The excess permittivity (ε_0^E) values are positive and more deviation in Methanol rich region shows strong monomeric structure form in this region. The values of excess inverse relaxation time $(1/\tau)^E$ shows effective dipole rotate slowly. The Bruggeman factor f_B shows a small deviation to lower side from the ideal Bruggeman behavior at 20% of volume fraction of Methanol, indicate reduction of effective volume value of Bruggeman parameter get larger than one. This confirms the weak intermolecular interaction in the mixture in this region and in remaining region strong interaction..

. The g^{eff} values in the Methanol dominate region confirm antiparallel orientation of electric dipoles. The values of g_f deviates from unity indicate interaction between two components of mixture. The molar enthalpy of activation represents need of energy is nonlinear and entropy also nonlinear. Arrhenius shows change in activation energy of the system. The results obtained are used to interpret the nature and kind of solute-solvent interaction.

V. References:

[1]. P.B.Undre, S.N.Helambe, S.B. Jagdale, P.W.Khirade and S.C. Mehrotra. Pramana J. Physics. 68. 851 (2007)

[2]. Manual T.D.R. Tektronix DSA8300

[3]. C.E.Shannon, Proc. Inst. Radio Eng. 37, 10(1949)

[4]. H.A. Samulan. Proc. IRE, 39, 175 (1951)

[5]. S. Mashimo, S. Kuwabara, S. Yogihara, and K. Higasi, J. Chem. Phy. 90, 3292(1989)

[6]. P.Debye. Polar Molecules, Chemical Catalog. Co. NewYork. (1929)

[7]. P.R.Bevington. Data Reduction and Error Analysis for the Physical Sciences, McGraw Hill, New York(1969)

[8]. Akl M. Awwad, Amar H. Al-Dujaili, and Salim R. Syriagh, J. Mol. Liq. 100(2), 129(2002)

[9]. S.C.Mehrotra and J.E Boggs, J. Chem. Phys. 66, 5306(1977)

[10]. S. B. Sayyad et al./ Lithuanian J. Phys. 51, 29-37 (2011)

[11]. D.A.G. Bruggeman, Ann. Phys. (Leipzig) 416(7), 636(1935)

[12]. U.Kaatze. J.Phys. Chem. 153. S141(1987)

[13]. A.C.Kumbharkhane, S.N.Helambe. S.Doraiswamy and S.C.Mehrotra. J. Chem. Phys. 99. 2405 (1993)

[14]. Sayyad S.B. ICMARS-2012, Jodhpur, India, Dec. 11-15, 2012

[15]. H. Eyring, J. Chem. Phys. 4(1936) 283

[16]. Hasted, J. B. Aqueous Dielectrics, Chapman and Hall, London, U. K. 1973

[17]. S. N. Helembe, M. P. Lokhande, A. C. Kumbharkhane and S. C. Mehrotra, Pramana J. Physics, 45, (1995) 19-24.

[18]. S. N. Helembe, M. P. Lokhande, A. C. Kumbharkhane, S. C. Mehrotra and S. Doraiswamy, Pramana J. Physics, 44 (1995) 405-410.

[19]. M. P. Lokhande, S. Mazumdar and S. C. Mehrotra, Ind. J. of BioChemistry and BioPhysics, 34 (1997) 385-390.

[20]. J. G. Berberain and R. H. Cole 1986 J. Chem. Phys. 84 6921

[21]. S. M. Puranik, A. C. Kumbharkhane and S. C. Mehrotra, Indian J. of Physics, 67B(1), 9 13, 1993.

[22]. S.B. Sayyad, Ph.D.Thesis, Dr. B.AM.U. Aurangabad. M.S. (India) 2008.

Synthesisand Characterization of TiO₂ Nanoparticles for Dye-Sensitized Solar Cells

Swati Kulkarni, Rupali Kulkarni*

Swa. Sawarkar Mahavidyalaya, Beed, MS, India

Abstract :

Titanium dioxide (TiO_2) nanoparticles have gained significant attention in dye-sensitized solar cells and other nano-applications due to their unique properties, including high stability, non-toxicity, and strong photocatalytic activity. This paper studies the synthesis of TiO_2 nanoparticles by simple sol-gel technique and their role in enhancing the performance of dye-sensitized Solar Cells (DSSCs). Characteristics of TiO_2 nanoparticles, including structural, morphological, optical, and surface property analyses, and the importance of these characterization techniques in optimizing the performance of TiO_2 nanoparticles for specific applications are also discussed.

Keywords: Titanium dioxide, nanoparticles, DSSCs

I. INTRODUCTION

In a typical DSSC, light photons are absorbed by a sensitizer, which is adsorbed to the surface of wide band gap semiconductor oxide. The sensitized nanoparticles of the semiconductor in combination with the electrolyte and counter electrode produce the regenerative cycle of photoelectrochemical cells [1]. In the literature, typical components of Dye-Sensitized Solar Cells (DSSCs),

· Most often doped or undoped Titanium oxide (TiO2) has been used as the wide band gap semiconductor oxide, working as an anode

· Ruthenium complex dye is the most common and successful dye,

· Iodine tri-iodide is observed to be the traditionally used electrolyte whereas,

· Platinum-coated FTO is frequently used as a cathode [1].

In our previous studies, Al-doped TiO2 photo anode had been proven to be fruitful in incrementing the photovoltaic parameters i.e., photocurrent and efficiency of the DSSC [2-4].

Titanium dioxide (TiO_2) is a widely studied material for its extensive range of applications, especially in renewable energy. Its applications in dye-sensitized solar cells (DSSCs) have shown promising potential for the development of cost-effective and efficient solar energy conversion devices. The properties of TiO_2 nanoparticles, which are closely related to their size, shape, surface area, and crystal structure, can be tailored through precise synthesis methods. However, to fully understand and utilize these properties, comprehensive characterization is essential. The focus of this research is on the synthesis of TiO_2 nanoparticles, to review the key characterization techniques for TiO_2 nanoparticles and application in DSSCs.

II. METHODS AND MATERIAL:Synthesis of TiO₂ Nanoparticles

AThe synthesis of TiO_2 nanoparticles is crucial for their application in DSSCs, as the nanoparticles' properties significantly influence the solar cells' efficiency. Various methods have been developed to synthesize TiO_2 nanoparticles, including:

2.1. Sol-Gel Method

The sol-gel process is one of the most commonly used methods for synthesizing TiO_2 nanoparticles. It involves the hydrolysis and condensation of titanium alkoxides. This method allows for precise control over the particle size and morphology, which are critical factors in optimizing the performance of DSSCs [5].

2.2 Hydrothermal Synthesis

Hydrothermal synthesis involves the crystallization of TiO_2 under high temperature and pressure conditions in an aqueous solution. This method produces well-crystallized nanoparticles with controlled size and shape, which are beneficial for improving the electron transport in DSSCs [6].

2.3 Microwave-Assisted Synthesis

Microwave-assisted synthesis is a relatively new technique that provides rapid and uniform heating, leading to the formation of TiO_2 nanoparticles with high crystallinity and uniform size distribution. This method is advantageous due to its shorter reaction time and energy efficiency [7].

The sol-gel technique of TiO2 nanoparticle synthesis is the most user-friendly, and energy-saving hence environmentally benign and cost-effective. It does not need sophisticated instrumentation. The synthesis method is explained many times in the previous research (2-4).

To experience the usefulness of synthesized nanoparticles the characteristics properties studied are morphological and optical, Surface characterization.

III.CHARACTERIZATION OF TiO2 NANOPARTICLES

The structural and optical properties i.e. size, shape, surface area, and crystal structure, can be tailored through precise synthesis methods of TiO_2 nanoparticles hence these properties are critical in determining their effectiveness in DSSCs.

Structural Properties of TiO₂ Nanoparticles

X-ray Diffraction (XRD)- X-ray diffraction (XRD) is a fundamental technique used to determine the crystal structure, phase composition, and crystallite size of TiO_2 nanoparticles. XRD patterns provide information about the different polymorphs of TiO_2 (anatase, rutile, brookite) and can be used to estimate the crystallite size using the Scherrer equation. This technique is crucial for understanding the phase purity and structural integrity of the nanoparticles. Diagram 1 shows the XRD characterization of synthesized TiO2 nanoparticles using the Sol-gel method.
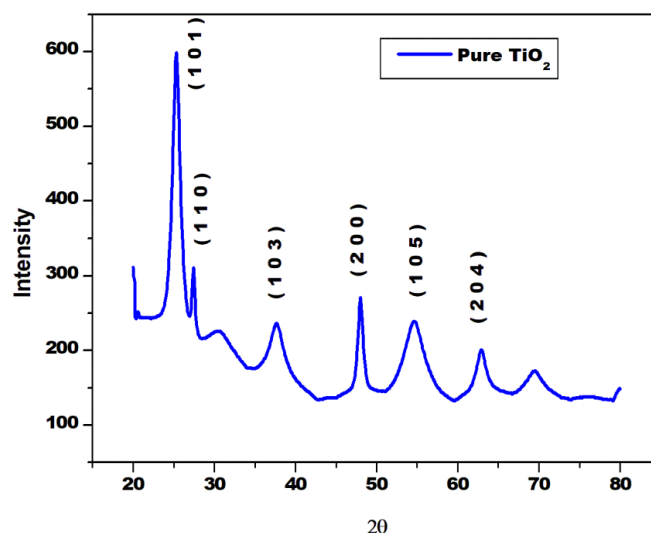
Figure 1: X-ray diffractogram for TiO2 nanoparticles

Figure 1 shows the XRD of the TiO2 nanoparticles synthesized by the Sol-gel method. The largest peak formed along (1 0 1) plane confirms the anatase phase formation of TiO_2 nanoparticles, according to JCPDS data files 21-1272 and 21-1276 [24]. The peak (1 1 0) shows the existence of a rutile phase in small amounts in the XRD of undoped TiO_2 nanoparticles,

Scanning Electron Microscopy (SEM) and Energy Dispersive X-ray Spectroscopy (EDS)

Scanning Electron Microscopy (SEM) is used to observe the surface morphology and particle size distribution of TiO_2 nanoparticles. SEM provides images with a lower resolution compared to TEM but covers a larger sample area, making it useful for studying particle agglomeration and surface texture. SEM can be coupled with energy-dispersive X-ray Spectroscopy (EDS) to perform elemental analysis, confirming the composition of the nanoparticles. Figure 2 shows the SEM image of the synthesized TiO2 nanoparticles.
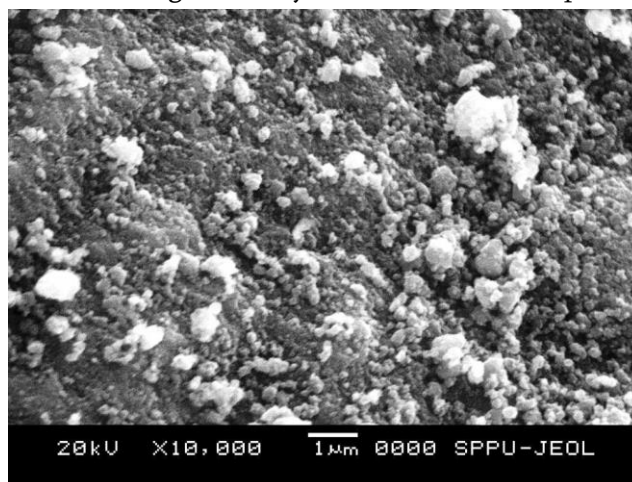
Fig. 2: SEM image of Undoped TiO2 nanoparticles

Morphological Characterization: Atomic Force Microscopy (AFM)

Atomic Force Microscopy (AFM) is employed to study the surface topography of TiO_2 nanoparticles at the nanoscale. AFM provides three-dimensional images of the surface, allowing for the measurement of surface roughness, particle height, and other morphological features. This technique is particularly useful for characterizing nanoparticles deposited on substrates. The surface morphology of TiO2 nanoparticles thin film is

revealed in Fig. 3. This image has been obtained in the area of 2*2 μm. The surface roughness of the TiO2 photo anodes measured using XEI software is 91.77 nm.

TABLE I FONT SIZES FOR PAPERS

Font Size	I. Appearance (in Time New Roman or Times)		
	Regular	Bold	Italic
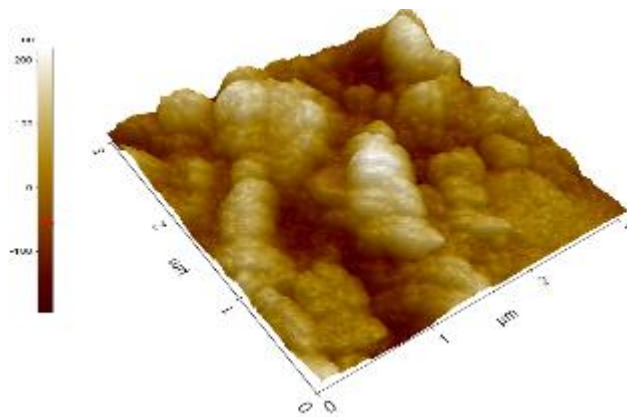
Fig. 3: Surface morphology of TiO2 nanoparticles thin film

Optical Characterization- UV-Visible Spectroscopy

UV-visible spectroscopy is commonly used to study the optical properties of TiO_2 nanoparticles, particularly their absorption characteristics. The band gap of TiO_2 nanoparticles can be estimated from the UV-Vis absorption spectra, which is essential for applications in photocatalysis and photovoltaics. The absorption edge of TiO_2 nanoparticles typically shifts with changes in particle size and crystallinity, providing insights into their electronic structure.
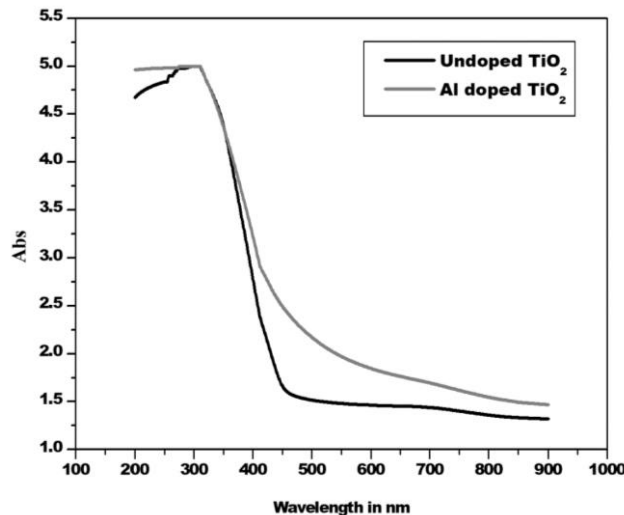
Fig. 4a: Absorption spectra of undoped nanoparticles
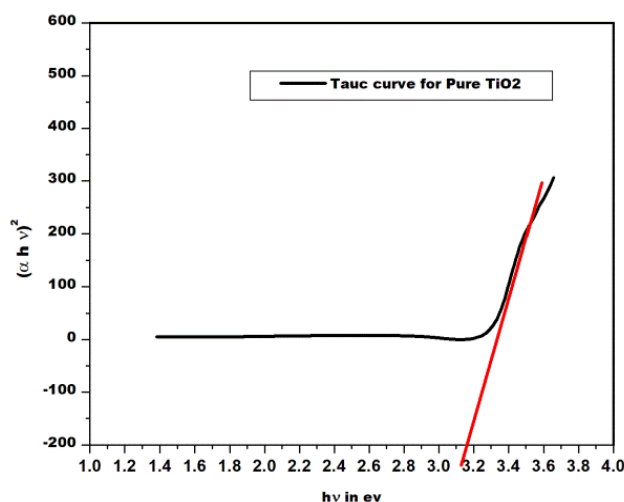
Fig. 4b: Extrapolation curve for TiO2 nanoparticles

UV-visible spectra of TiO2 is shown in Fig. 4. The optical band gap has been calculated using Equation 1

$$(\alpha h\gamma)^{\frac{1}{2}} = B * (h\gamma - Eg) \dots \dots 1$$

Where B is a constant, Eg is the material's band gap, α is the absorption coefficient and $h\gamma$ is the photon energy [9]. The optical band gap (Eg) was obtained by extrapolating the linear portion of $(\alpha h\gamma)^{\frac{1}{2}}$ vs $h\gamma$ plot to $\alpha \to 0$. The band gap of TiO_2 nanoparticles was found as 3.2 eV

APPLICATIONS OF TIO_2 NANOPARTICLES IN DYE-SENSITIZED SOLAR CELLS

Role in DSSCs

In DSSCs, TiO_2 nanoparticles serve as the photoanode material, where dye molecules are adsorbed on the surface of the nanoparticles. Upon light absorption, the dye injects electrons into the conduction band of the TiO_2, which are then transported through the nanoparticle network to the electrode.

Efficiency Enhancement

The efficiency of DSSCs depends on the ability of TiO_2 nanoparticles to facilitate fast electron transport and reduce recombination losses. Optimizing the size, morphology, and crystallinity of TiO_2 nanoparticles is key to enhancing their photovoltaic performance.

Surface Modification and Sensitization

Surface modification of TiO_2 nanoparticles with co-adsorbents or doping with other materials can enhance light absorption and reduce electron–hole recombination. Sensitization with various dyes also plays a crucial role in improving the efficiency and stability of DSSCs.

IV.CONCLUSION

TiO_2 nanoparticles have proven to be a vital component in the advancement of dye-sensitized solar cells. Continued research in synthesizing and characterizing these nanoparticles will be crucial in overcoming current challenges and achieving higher efficiencies, paving the way for the widespread adoption of DSSCs in renewable energy.

V. REFERENCES

[1] Carmen Cavallo, Francesco Di Pascasio, Alessandro Latini, Matteo Bonomo, and Danilo Dini, (2017), Journal of Nanomaterials, 2017, Article ID 5323164, https://doi.org/10.1155/2017/5323164

[2] Swati S. Kulkarni, Gajanan A. Bodkhe, Sumedh M. Shirsat, S. S. Hussaini, N Nshejwal and Mahendra D. Shirsat, (2018), Mater. Res. Express, 5(3), 036205-036221,doi.org/10.1088/2053-1591/aab2d1

[3] Swati S. Kulkarni, Gajanan A. Bodkhe, Pasha W. Sayyad, S. S. Hussaini and Mahendra D. Shirsat, International Journal of nanoscience, ISSN 1793-5350

[4] Swati S. Kulkarni, Gajanan A. Bodkhe, Pasha W. Sayyad, S. S. Hussaini, and Mahendra D. Shirsat, International Journal of Advance and Innovative Research, 6(1), 111-116

[5] Kirti Shahu and V V S Murti, (2016), Indian Journal of Pure and Applied Physics, 54, 485-488.

[6] Hadja Fatima Mehnane, Changlei Wang, Kiran Kumar Kondamareddy, Wenjing Yu, Weiwei Sun, Haimin Liu, Sihang Bai, Wei Liu, Shishang Guo and Xing-Zhong Zhao, (2017), RSC Adv., 7, 2358-2364, 10.1039/c6ra26012h.

[7] Swati S. Kulkarni, Gajanan A. Bodkhe, Sumedh M. Shirsat, S. S. Hussaini, Nana N. Shejwal5 and Mahendra D. Shirsat,International Journal of Engineering Technology Science and Research, Volume 5(4), (2018).

[8] Muneer M. Ba-Abbad, Abdul Amir H. Kadhum, Abu Bakar Mohamad, Mohd S. Takriff ,KamaruzzamanSopian, (2012),Int. J. Electrochem. Sci., 7 (2012) 4871 – 4888

[9] P.R. Jubu a b, F.K. Yam a, V.M. Igba b, K.P. Beh, (2020) Journal of SolidState Chemistry, Volume 290, October 2020, 121576, https://doi.org/10.1016/j.jssc.2020.121576

A Review on Some ABO3 Perovskite Compounds: Synthesis and Applications

Nilkanth N Kapse[1], Vishal A. Pandit[2], Kalpana Joshi[4], Deepak M. Sonawane[3], Vaibhav K Kashte[3], Shivnarayan B. Bajaj[3]

[1]Department Of Physics, Dr. B. Raghunath ACS College, Parbhani - 431 401, (MS) India

[2]Department Of Physics, Babasaheb Ambedkar, Marathwada University, MS, Aurangabad, India

[3]Department Of Physics, J. E. S, MS, 431203, College, Jalna, India

[4]Sanjivani K B P Polythechnic, Kopergoan. Ahilya nagar, MS, India

Abstract :

The study of perovskite compounds of the ABO3 class is an important area of research for scientists due to its remarkable features and wide range of uses. Perovskite has the formula ABO3 consisting of elements A and B, which can be monovalent, divalent, trivalent, pentavalent, oxygen, and oxygen. Perovskite materials are important for advancing microelectronics and communications, solar cells, Light Amplification by Stimulated Emission of Radiation (LASER), light emitting diodes (LEDs), and various gas sensors. Furthermore, these perovskites have electric, dielectric, ferroelectric, piezoelectric, pyroelectric, magnetic, and thermal properties, CMR superconductivity, and photovoltaics properties. This paper reviews the various methods for synthesizing oxide perovskites and discusses their applications.

Keywords: ABO3 Perovskite, Synthesis, Applications

I. INTRODUCTION

ABO3 perovskite compounds are oxide materials that have a general formula of ABO3[2]. These compounds are used for various applications such as solid oxide fuel cells, piezo-, ferro-electricity, water splitting, and electronic devices[1][5]. Due to their remarkable stability concerning cation substitution, new compounds for such applications potentially await discovery[1]. The 12-fold coordinated A site can be occupied with low-valent and large-sized oxides, and perovskite oxides' physical and chemical properties can be easily tuned through their structure flexibility[4].

Machine learning methods have been employed to identify perovskites from ABO3 combinations formulated as constraint satisfaction problems[3][4]. Liu et al. trained a machine learning model for predicting the formability of perovskite with known 397 ABO3 compounds. The model was then used to classify 891 ABO3 compounds from[4].

These ABO3 perovskite compounds are important materials in various applications such as solid oxide fuel cells, piezo-, ferro-electricity, water splitting, and electronic devices. These compounds are highly stable concerning cation substitution. Machine learning methods have been employed to identify perovskites from ABO3 combinations formulated as constraint satisfaction problems.A nanometer is one billionth of a meter, or the

distance between two and twenty atoms, depending on the kind of atom. Changing the structure of matter on a scale of a few nanometres is called nanotechnology. Depending on whom you ask, it might imply anything from 0.1 nm (manipulating the arrangement of individual atoms) to 100 nm or more (anything smaller than microtechnology). Richard Feynman initially proposed that materials and electronics may one day be created to exact atomic standards in 1959. "As far as I can tell, the laws of Physics do not forbid the possibility of influencing things atom by atom." Gustav Rose first described perovskite in 1839. Later, Russian mineralogist L. A. Perovski gave the substance the name "perovskite" Today, the term "perovskite" refers to a group of substances having crystal structures similar to calcium titanate. Perovskites are often oxides, although some varieties can also be carbides, nitrides, halides, and hydrides.

Numerous electro-ceramics devices use oxides of the perovskite type. The most significant examples include the use of lead zirconate titanate (PZT) in generators, motors, ultrasonic transducers, actuators, capacitors, and non-volatile memories, as well as the use of barium titanate (BTO) for positive temperature coefficient resistors and multilayer ceramic capacitors. Perovskite structured materials are the subject of much research because of their numerous applicability in several sectors [1]. A. Ries et al. created barium strontium titanate powder using the polymeric precursor technique, with a Ba/Sr ratio of 80/20. XRD, IR, BET, and SEM were used to describe the sample. According to the regulations, barium carbonate should not be used as a secondary phase [2].

For the first time, C.N. George et al. produced nanocrystalline barium titanate by a modified combustion method in a single step. The phase purity of the nanopowders was investigated using thermogravimetric analysis, differential thermal analysis, and Fourier transform infrared spectroscopy. The dielectric characteristics were studied as a function of frequency [3]. Y.B. Khollam et al. employed a straightforward oxalate precursor method to create barium-strontium titanate ($Ba_{1-x}Sr_xTiO_3$) particles. The powders formed are cubic, highly pure, stoichiometric, sub-micron-sized, with nearly uniform size and shape distribution, according to characterization studies on BSTO and BST powders using various physicochemical techniques, including micro- and chemical analysis, differential thermal analysis (DTA)/thermo-gravimetric analysis (TGA), XRD, FTIR, X-ray fluorescence (XRF), and scanning electron microscopy (SEM). Similar dielectric characteristics were displayed by the BST ceramics made from similar particles [4]. M.M. Vijatovi et al. investigated the electrical characteristics of ceramics with lanthanum-doped barium titanate. The polymeric precursor technique was used to create the ceramic nanopowders. Deeper dielectric properties showed that when lanthanum concentration rose, the classical to a diffuse type of BT Ferro-paraphrase transition altered. This assumption was supported by the calculated diffuseness factor derived from the modified Curie-Weiss equation, which showed that the diffusivity rose as the lanthanum concentration did. One semicircle in the impedance study demonstrated that grains contributed to the overall resistivity. However, overlapping was still conceivable since a PTCR effect appeared, suggesting the existence of grain boundary resistivity [5]. Wei Li et al. [6] investigated the structural and dielectric characteristics of lead-free $(Ba_{1-x}Ca_x)(Ti_{0.95}Zr_{0.05})O_3$ (x = 0.05-0.40) (BCZT) ceramics produced via solid-state reaction.

Phongthorn et al. investigated the phase development, microstructure, and dielectric characteristics of $Ba(Zr_{0.1}Ti_{0.9})O_3$ ceramics produced by burning. The sample sintered at 1400 C for 2 hours had the best morphology, greatest density, highest dielectric constant, and lowest dielectric loss. The Curie temperature, lower than BZT made using other techniques, was about 76 °C. Investigations into microstructure, densification, and dielectric findings all corroborated [7]. M. Aparna et al. investigated the impact of lanthanum (La^{3+}) doping on the electrical and electromechanical characteristics of $Ba_{1-x}La_xTiO_3$ and employed combined impedance and admittance spectroscopy to assess the impedance data. The resonant and anti-resonant frequencies from vector

admittance plots were used to derive the electromechanical parameters. Compared to pure barium titanate, the electromechanical coefficients for Ba1-xLaxTiO3 with x = 0–003 were much higher [8].For use in multi-layered capacitors, Pramod K. Sharma et al. investigated the dielectric characteristics of tape-cast $Ba_{0.65}Sr_{0.35}TiO_3$ produced from sol-gel [9].P. A. Shcheglov et al. created a modified sol-gel method for making $BaTiO_3$ and $PbTiO_3$ ferroelectric thin films [10]. Dimple P. Dutta et al. investigated the phase development in Fe^{3+} doped $BaTiO_3$nanocrystallites produced sonochemically. Structure, magnetism, and ferroelectric characteristics were thoroughly investigated [11].

II. Perovskites Synthesis Methods

Chemical, physical, and optical production methods all affect the properties of perovskite materials [34]. Additionally, they influence the shape and crystal structure of materials. One must select an appropriate synthesis (route) technique to create the material with the specified characteristics.

2.1 Ceramic Method

When comparing the two methods of the solid-state synthesis approach, mechanical ball milling and high energy ball milling, a hand mixer grinder utilizing a motor and a pistol, and high energy ball milling from 100 rpm to 1000 rpm to get extremely fine size particles are used (12). As a result of the fact that ceramics are produced using this method of solid-state synthesis, it is sometimes referred to as the ceramic method.The primary raw materials used are carbonates and oxides, which are initially solid and mixed and ground repeatedly. At room temperature, these materials do not chemically react with one another, so they are heated to high temperatures (700–1500 °C), where chemical reactions occur at a significant rate (13).

Waindich et al. (2009) [14] observed that the calcination of the materials $Ba_{1-x}Sr_xCo_{1-y}Fe_yO_3$ and $La_{0.3}Ba_{0.7}Co_{0.2}Fe_{0.8}O_3$ at 1200 °C for 24 hours and 1250 °C for 24 hours and 15 hours, respectively, produced undesirable porous materials. As shown by Nagai and colleagues [15], by processing $SrCo_{0.9}X_{0.1}O_3$compounds (X as Ni, Cu, Zn, Cr, Fe, Al, Ga, In, Ce, Ti, Zr, Sn, V or Nb), certain compounds developed second phases. This was explained by certain cations being poorly soluble in the solid solution. In some instances, it was seen that tiny secondary phases formed when Ga was added to $La_{1-x}Sr_xFe_{1-y}Ga_yO_3$-compounds, producing La_2O_3 [17], which was not entirely incorporated into the A-site.

In other instances, $BaCo_{0.7}Fe_{0.2}Ta_{0.1}O_3$sintered at temperatures over 900 °C produced pure perovskite structures, whereas unreacted precursors persisted at lower temperatures [18]. These examples clearly show that the elements of the perovskite crystal structure can also directly impact the sintering process.

2.2 Co-precipitation

When a solution containing soluble metal cations is combined with another solution known as a precipitation agent, supersaturation conditions are necessary for the co-precipitation technique. Fig. 4 depicts a broad schematic of this strategy. Cushing et al. [19] claim that to achieve the desired physical qualities, it is necessary to regulate crucial co-precipitation chemical reaction parameters such as temperature, mixing rate, pH, and concentration (i.e. morphology and particle size distribution). The co-precipitation process generally produces perovskites with high uniformity and purity. This is attributable to carefully monitoring the chemical process necessary to produce compounds without a metal cation shortage [20,21].

The decreased strontium hydroxide solubility across a wide pH range, which tends not to integrate strontium into the perovskite structure during the washing phases, brought attention to the need for precise regulation of this chemical reaction [22].

2.3 Sol-gel

Perovskites are made using several sol-gel procedures, including the Pechini, Alkoxide, and Alkoxide-Salt methods. Due to its adaptability in producing perovskite membranes, the Pechini technique became the most used for producing perovskites. The Pechini technique, which includes complexing ethylenediaminetetraacetic (EDTA)-Citrate before adding ethylene glycol, is the subject of this review. NH_3H_2O dosage is used to regulate pH. This method's key benefits are the high purity and uniformity of perovskite structures, together with precise composition control of the end product [23]. A schematic of the metal production process using citric acid or EDTA is shown in Figure 5. Six bonds connect the metal cation to EDTA. It has two different kinds of electron-donating groups, carboxylic and aliphatic amine. Whencomplex with citric acid, the metal cation forms three bonds to hold it together [24]. Chelating agents are employed to stop partial metal segregation in the final product, which can be brought on by various interactions between metal ions in the solution [25]. Combined with the addition of polyhydroxy alcohol. The chelates get polyesterized when the solution is heated, forming a cross-linked chain of metal atoms bound to organic radicals [26].

2.4 Hydrothermal Method

The hydrothermal method is followed under high pressure in autoclaves (15 MPa). It combines high pressures with temperatures between the material's critical temperature and the boiling point of water. It is essentially a sol-gel approach that can provide superior particle size control [27]. For instance, $CaTiO_3$ was studied at 15 °C and 150 °C, as well as uncalcined and calcined materials at 1300 °C [28]. The X-ray pattern analysis revealed that neither sample had any contaminants, and the phases had comparable cell characteristics. Therefore, this material did not require the calcination stage following the hydrothermal technique [29]. This approach is currently being developed.

III. Applications in ABO3 Perovskite Materials

The modification of ABO_3 with numerous vacancies may enhance its physical-chemical characteristics, improving its performance at catalytic redox processes, energy storage, gas sensors, photovoltaics, etc., exhibiting the potential for commercial applications. Due to their desirable qualities, perovskite materials are the subject of substantial investigation. The following is a list of some areaswhere perovskite materials are used.

3.1 Photocatalytic activity

Jiang Yinwe [30] reported an ABO_3 perovskite photocatalyst called $BaZn_{1/3}Nb_{2/3}O_3$ that splits water into H2 and O2 when exposed to UV light.Zhi-XianWei [31] reports the photocatalytic activity of $LaFeO_3$ and $LaFe_{0.5}Mn_{0.5}O_{3-\delta}$ towards the degradation of methyl orange (MO) under sunlight irradiation. Compared to $LaFeO_3$, $LaFe_{0.5}Mn_{0.5}O_{3-\delta}$ has much better photocatalytic activity[36]. Using an external magnetic field, $LaFe0.5Mn0.5O3-\delta$ may be recycled and redispersed again.Shuhua Dong [32] investigated the photodegradation of methylene blue which exhibits the highest degradation rate of 75% under an irradiation time of 150 min.

3.2 Photovoltaic solar cells

Ternary oxides, particularly ABO3 type perovskites, have favoured Photoanode-Based Dye-Sensitized Solar Cells (DSSC) photoanodes during the past ten years. ABO3 perovskites have firmly established themselves as innovative over the conventional photoanode materials for DSSC due to their excellent physiochemical properties, supply of excellent photovoltaic performance, and simple modification method by altering the atomic composition of their constituents. Its future investigation is restricted by the absence of a review based

on ABO3 perovskites. Designing effective photoanode materials for DSSC also requires understanding a material's theoretical capabilities [33].B. Mouhib reported theoretical investigations of electronic structure and optical properties of S, Se, or Te-doped perovskite $ATiO_3$ (A=Ca, Ba, and Sr) materials for eco-friendly solar cells [34].As a result, doped systems' optical conductivity and absorption coefficient are increased in the photovoltaic spectrum, particularly for BaTiO3 doped with 2.5% and 5% of Te. This makes BaTiO3Te more suitable for solar devices than CaTiO3Te and SrTiO3Te compounds.

3.3 Other Applications

Scientists intensively research perovskite materials due to their appealing qualities. The following list includes some of the many domains in perovskite materials that are extensively used.

SJ Skinner's recent developments in perovskite-type materials for solid oxide fuel cell cathodes. e.g., $Gd_{0.7}Ca_{0.3}Co_{1-y}Mn_yO_3$ [23].Uchino K. reported piezoelectric perovskite as Sensors and actuators,e.g., $PbZr_xTi_{1-x}O_3$ [24].Mir LL and Fronteradescribed the use of a ferromagnetic tunnel in an anisotropic sensor and memory device as a perovskite material application as Magnetic memory devices; e.g., $Pt/La_2Co_{0.8}Mn_{1.2}O_6/Nb:SrTiO_3$ [25].Xu Y and Memmert U. reported Magnetic field sensors based on polycrystalline manganites with the application as Magnetic field sensors, e.g., $La_{0.67}Sr_{0.33}MnO_3$ and $La0._{67}Ba_{0.33}MnO_3$[35] [26].The colossal magnetoresistive manganite-based ferroelectric field-effect transistor was researched by Zhao T et al. as an Electric field effect device; e.g., the heterostructure of $Pb(Zr_{0.2}Ti_{0.8})O_3/La_{0.8}Ca_{0.2}MnO_3$ [27].Ferroelectric and piezoelectric devices, e.g., $BaTiO_3$, $PbTiO_3$ [28].Mitra C, Raychaudhuri studied p-n diode with hole and electron-doped lanthanum manganites as Semiconducting electronic devices; e.g., $La_{0.7}Ca_{0.3}MnO_3/SrTiO_3/La_{0.7}Ce_{0.3}MnO_3$ [29]. Munoz JLG reports $Bi_{1-x}Sr_xMnO_3$ manganites (x = 0.40, 0.50) dielectric properties: influence of charge order at room temperature as application as High dielectric constant [30].Sleight AW investigated High-temperature superconductivity in the $BaPb_{1-x}Bi_xO_3$ system [31].Manh DH and Phong reported $La_{0.7}Sr_{0.3}MnO_3$ and the properties of AC magnetic heating for hyperthermia applications [32].Ding R researched Perovskite nanocrystals $KNi_{0.8}Co_{0.2}F_3$ as supercapacitors [33].

IV. Conclusion

In conclusion, perovskite materials have become a subject of intense research in recent years due to their remarkable properties and diverse applications. The ABO_3 class of perovskite compounds has proven crucial in developing microelectronics, communications, solar cells, gas sensors, lasers, LEDs, and more. The unique properties of perovskite materials, including their electric, dielectric, ferroelectric, piezoelectric, pyroelectric, magnetic, and thermal properties, make them ideal for various applications. In this review, we have discussed different methods for synthesizing oxide perovskites and highlighted their numerous applications. As research on perovskite materials progresses, we expect to see even more exciting applications.

V. References

1. R.H. Mitchell, Perovskites: modern and ancient, (2002).
2. A. Ries, A. Simoes, M. Cilense, M. Zaghete, J.A. Varela, Barium strontium titanate powder obtained by polymeric precursor method, Materials characterisation, 50 (2003) 217-221.

3. C. George, J. Thomas, H. Kumar, M. Suresh, V. Kumar, P. Wariar, R. Jose, J. Koshy, Characterization, sintering and dielectric properties of nanocrystalline barium titanate synthesized through a modified combustion process, Materials Characterization, 60 (2009) 322-326.

4. Y. Khollam, S. Deshpande, H. Potdar, S. Bhoraskar, S. Sainkar, S. Date, Simple oxalate precursor route for the preparation of barium–strontium titanate: Ba 1– x Sr x TiO 3 powders, Materials Characterization, 54 (2005) 63-74.

5. M.V. Petrović, J. Bobić, T. Ramoška, J. Banys, B. Stojanović, Electrical properties of lanthanum doped barium titanate ceramics, Materials Characterization, 62 (2011) 1000-1006.

6. W. Li, Z. Xu, R. Chu, P. Fu, G. Zang, Structural and dielectric properties in the (Ba 1– x Ca x)(Ti 0.95 Zr 0.05) O3 ceramics, Current Applied Physics, 12 (2012) 748-751.

7. P. Julphunthong, T. Bongkarn, Phase formation, microstructure and dielectric properties of Ba (Zr 0.1 Ti 0.9) O 3 ceramics prepared via the combustion technique, Current Applied Physics, 11 (2011) S60-S65. 20

8. S M. Aparna, T. Bhimasankaram, S. Suryanarayana, G. Prasad, G. Kumar, Effect of lanthanum doping on electrical and electromechanical properties of Ba1– x La x TiO3, Bulletin of Materials Science, 24 (2001) 497-504.

9. K. Sharma, V. Varadan, V. Varadan, Dielectric properties of tape cast Ba0. 65Sr0. 35TiO3 derived from sol-gel for application in multilayered capacitors, Smart materials and structures, 12 (2003) 749.

10. P. Shcheglov, S. Men'shikh, L. Rybakova, Y.Y. Tomashpol'skii, Modified sol-gel process for the preparation of BaTiO3 and PbTiO3 ferroelectric films, Inorganic Materials, 36 (2000) 380-384.

11. D.P. Dutta, M. Roy, N. Maiti, A.K. Tyagi, Phase evolution in sonochemically synthesized Fe3+ doped BaTiO3 nanocrystallites: structural, magnetic and ferroelectric characterization, Physical Chemistry Chemical Physics, 18 (2016) 9758-9769.

12. Joshi Siddharth 1 et all. Elsevier x-ray diffraction a simplistic approach for perovskite-based solar cell studies doi.org/10.1016/j.matpr.2019.05

13. Sadhukhan, P., Kundu, S., Roy, A., Ray, A., Maji, P., Dutta, H., Pradhan, S.K. and Das, S., 2018. Solvent-free solid-state synthesis of high-yield mixed halide perovskites for easily tunable composition and band gap. Crystal Growth & Design, 18(6), pp.3428-3432

14. A. Waindich, A. Möbius, M. Müller, Corrosion of Ba1-xSrxCo1-yFeyO3-δ and La0.3Ba0.7Co0.2Fe0.8O3-δ materials for oxygen separating membranes under Oxycoal conditions, J. Memb. Sci. 337 (2009) 182–187. 29

15. T. Nagai, W. Ito, T. Sakon, Relationship between cation substitution and stability of perovskite structure in SrCoO3-δ - based mixed conductors, Solid State Ionics. 177 (2007) 3433–3444.

16. E. Juste, A. Julian, G. Etchegoyen, P.M. Geffroy, T. Chartier, N. Richet, et al., Oxygen permeation, thermal and chemical expansion of (La, Sr)(Fe, Ga)O3–d perovskite membranes, J. Memb. Sci. 319 (2008) 185–191.

17. H. Luo, Y. Wei, H. Jiang, W. Yuan, Y. Lv, J. Caro, et al., Performance of a ceramic membrane reactor with high oxygen flux Ta-containing perovskite for the partial oxidation of methane to syngas, J. Memb. Sci. 350 (2010) 154–160.

18. Y. Cheng, H. Zhao, D. Teng, F. Li, X. Lu, W. Ding, Investigation of Ba fully occupied A-site BaCo0.7Fe0.3-xNbxO3-δ perovskite stabilized by low concentration of Nb for oxygen permeation membrane, J. Memb. Sci. 322 (2008) 484–490.

19. Yin, Jiang; Zou, Zhigang; Ye, Jinhua (2004).The Journal of Physical Chemistry B, 108(34), 12790–12794.

20. Zhi-Xian Wei, Yan Wang, Ji-Ping Liu, Cai-Mei Xiao, Wei-Wei Zeng,Materials Chemistry and Physics, Volume 136, Issues 2–3, 2012.

21. Bhojanaa, K. B., et al. "Account of Structural, Theoretical, and Photovoltaic Properties of ABO3 Oxide Perovskites Photoanode-Based Dye-Sensitized Solar Cells." *Solar RRL* 6.2 (2022): 2100792.

22. Mouhib, B., et al. "Theoretical investigations of electronic structure and optical properties of S, Se or Te doped perovskite ATiO3 (A= Ca, Ba, and Sr) materials for eco-friendly solar cells." *Micro and Nanostructures* 163 (2022): 107124.

23. Skinner SJ. Recent advances in perovskite-type materials for solid oxidefuel cell cathodes. International Journal of Inorganic Materials. 2001;**3**:113-121

24. Uchino K. Glory of piezoelectric perovskites. Science and Technology of Advanced Materials.2015;**16**:046001-0460016

25. Mir LL, Frontera C, Aramberri H, Bouzehouane K, Fernandez JC, Bozzo B, et al. Anisotropic sensor and memory device with a ferromagnetic tunnel 19 *Synthesis Techniques and Applications of Perovskite Materials* barrier as the only magnetic element. Scientific Reports. 2018;**8**:861-870

26. Xu Y, Memmert U, Hartmann U. Magnetic field sensors from polycrystalline manganites. Sensors and Actuators A. 2001;**91**:26-29

27. Zhao T, Ogale SB, Shinde SR, Ramesh R, Droopad R, Yu J, et al. Colossal magnetoresistive manganite-based ferroelectric field-effect transistor on Si. Applied Physics Letters. 2004; **84**:750-752

28. Nuraje N, Su K. Perovskite ferroelectric nanomaterials. Nanoscale. 2013;**5**:8752-8780

29. Mitra C, Raychaudhuri P, Kobernik G, Dorr K, Muller KH, Schultz L, et al. p-n diode with hole and electron-doped lanthanum manganites. Applied Physics Letters. 2001;**79**:2408-2410

30. Munoz JLG, Frontera C, Murias BR, Mira J. Dielectric properties of Bi1-x SrxMnO3 (x = 0.40, 0.50) manganites: Influence of room temperature charge order. Journal of Applied Physics.2009;**105**:084116-084120

31. Sleight AW, Gillson JL, Bierstedt PE. High-temperature superconductivity in the BaPb1–xBixO3 system. Solid State Communications. 1993;**88**:841-842

32. Manh DH, Phong PT, Nam PH, Tung DK, Phuc NX, Lee IJ. Structural and magnetic study of La0.7Sr0.3MnO3 nanoparticles and AC magnetic heating characteristics forhyperthermia applications. Physica B. 2014;**444**:94-102

33. Ding R, Li X, Shi W, Xu Q, Han X, Zhou Y, et al. Perovskite KNi0.8Co0.2F3 nanocrystals for supercapacitors. Materials Chemistry A. 2017;**5**:17822-17827

34. Pandit, V. A., Repe, G. R., Bhamre, J. D., & Chaudhari, N. D. (2020, October). A review on green synthesis and characterization technique for ferrite nanoparticles and their applications. In *Journal of physics: conference series* (Vol. 1644, No. 1, p. 012009). IOP Publishing.

35. Pandit, Vishal Ashok, Nilkanth N. Kapse, Vaibhav K. Kashte, and Nandkishor D. Chaudhari. "Magnetic Behaviour, and initial permeability of green synthesized Co2+ substituted Ni-Zn ferrite." *Journal of Magnetism and Magnetic Materials* (2024): 172184.

36. Kashte, Vaibhav K., Nilkanth N. Kapse, Vishal Ashok Pandit, and Bhagwan G. Toksha. "A Review on Graphene Oxide-Based Ferrite Nanocomposites for Catalytic Applications." *Catalysis Surveys from Asia* (2024): 1-17.

Morphological Properties of Vanadium Substituted Yttrium Iron Garnet

R. G. Vidhate*[1], R.B. Kavade[2], J. M. Bhandari[3], K.H.Katke[1], K. M. Jadhav[4]

*[1]Anandrao Dhonde Alias Babaji Mahavidyalaya, Kada, Beed

[2]Bhagwan Mahavidyalaya, Ashti, Beed

[3]Gandhi college Kada, Beed

[4]Department of physics MGM University, Aurangabad

Abstract :

The garnet having the general formula Y3VxFe5-xO12 (x= 0.0, 0.2, 0.4 and 0.6) were synthesized using double sintering ceramic technique. The samples were characterized by X-ray diffraction technique. The X-ray diffraction studies of compositions revealed the formation of single phase cubic structure with lattice constant ranging from 12.364 to 12.391 Å up x=0.0 to x= 0.6 (in the step of 0.2).

The IR spectra of all samples are taken in the range of 300-800cm-1. IR spectra show typical absorption bands indicating the garnet nature of samples.

Keyword: Garnet, Vanadium, structural, IR study.

I. INTRODUCTION

Yttrium iron garnet (YIG) $Y_3Fe_5O_{12}$ belongs to a group of magnetic oxides and has received a great deal of attention in laser, microwave devices and ultrasonic devices field. They are characterized by magnetic and magneto-optical properties. Yttrium iron garnet (YIG) is a microwave ferrite, which in polycrystalline form has specific characteristics.

Garnets are cubic oxides with space group O_h^{10} and they are characterized by the chemical formula $\{A_3\}[B_2]X(C_3)O_{12}$, where the different brackets reflect the various oxygen coordination of the A cations while the [ ] and ( ) indicate six fold and four fold coordination of the B and C cations, respectively. A can be one of the fourteen well known rare earth ions or Yttrium while B and C are the cations like Al, Ga, Cr, etc [1]. Yttrium iron garnet is one of the well-known family of ferrimagnetic oxide magnetic materials. In the present study, we report our results on the structural properties of vanadium substituted yttrium iron garnet ($Y_3Fe_{5-x}V_xO_{12}$) (x = 0.0 – 0.6) through X-ray diffraction, infrared spectroscopy.

Pure and substituted yttrium iron garnet has been studied intensively by several researches with a view to understand their basic properties. Substituted yttrium iron garnets have been extensively used in wide band non reciprocal devices [2,3]. Non-magnetic substitutions in yttrium iron garnet have provoked great interest for scientific studies of the effects caused by the magnetic dilutions [4,5]. In general, non-magnetic cations occupy two non-equivalence sites with more or less pronounced preference for one site [6]. Non-magnetic ions usually occupy octahedral or tetrahedral site.

The aim of the present work is to develop sintered material of the vanadium substituted yttrium iron garnet ($Y_3Fe_{5-x}V_xO_{12}$) and to study the effect of vanadium substitution on the properties of yttrium iron garnet in meeting the requirement of device engineers. In the present study, we report our results on the structural properties of vanadium substituted yttrium iron garnet. ($Y_3Fe_{5-x}V_xO_{12}$) (x = 0.0 – 0.6) through X-ray diffraction, infrared spectroscopy measurements.

Experimental:

The samples of V^{3+} substituted $Y_3V_xFe_{5-x}O_{12}$ garnets with x = 0.0 to 0.6 in steps of 0.2 were prepared by well known double sintering ceramic method in which a molar ratio of Y_2O_3, Fe_2O_3 and V_2O_3 (all 99.99% pure AR grade) were mixed thoroughly in stoichiometric proportions and then ground to very fine powders by using agate mortar for about 3 hrs. These mixtures in powder form were pre-sintered in a Indfur Programmable muffle furnace at 1000^0C for 24 hr, and cooled to room temperature slowly at the rate of 2^0C/min. The samples were reground and re-fired at 1350^0C for 30 hours and slowly cooled to room temperature at the rate of 2^0C/min., and then reground for 1 hr. The fine powdered sample was pelletized under the pressure of 5 ton /inch^2.

II. Result and Discussion:

The room temperature X-ray diffraction patterns (XRD) of vanadium doped yttrium iron garnet $Y_3Fe_{5-x}V_xO_{12}$ (where x = 0.0-0.6 in the step of 0.2) are shown in Fig.1 (a - d). The X-ray diffraction patterns of the garnet system shows the Bragg's peaks belonging to cubic garnet structure the cubic garnet structure can be easily observed in all the samples. All the observed reflections (321), (400), (420), (422), (431), (521), (611), (444), (640), (642), (800), (842), in the garnet system with the crystalline phases were well indexed using the JCPDS powdered diffraction file (card no.43-0507). The XRD patterns show sharp and intense Bragg reflections belonging to single phase cubic garnet structure. Using Miller indices and Bragg's law, the inter planner spacing 'd' values were calculated and same are given in Table 1. It is observed from table 1 that 'd' values increases with increase in vanadium composition x.

Table: 1 Miller indices (hkl) and Inter planner spacing (d) of $Y_3V_xFe_{5-x}O_{12}$.

Plane	d(A)			
(hkl)	x=0.0	x=0.2	x=0.4	x=0.6
(4 0 0)	3.09	3.09	3.09	3.09
(4 2 0)	2.76	2.76	2.77	2.79
(4 2 2)	2.52	2.52	2.53	2.53
(4 3 1)	2.42	2.43	2.42	2.43
(5 2 1)	2.26	2.26	2.26	2.28
(6 1 1)	2.01	2.01	2.00	2.00
(4 4 4)	1.78	1.78	1.79	1.79
(6 4 0)	1.72	1.72	1.72	1.72
(6 4 2)	1.65	1.65	1.65	1.65
(8 0 0)	1.56	1.54	1.55	1.55
(8 4 0)	1.38	1.38	1.38	1.39
(8 4 2)	1.35	1.35	1.35	1.35
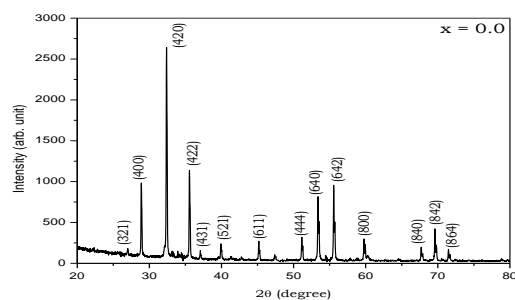
Fig. 1 (a): XRD patterns of Y₃VₓFe₅₋ₓO₁₂ (x= 0.0)
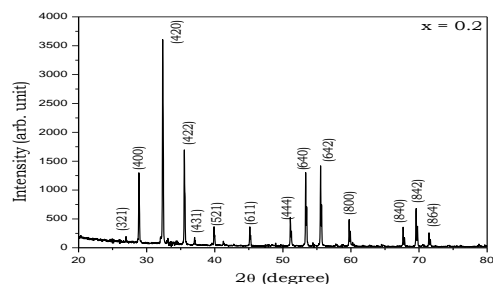
Fig. 1 (b): XRD patterns of Y₃VₓFe₅₋ₓO₁₂ (x= 0.2)
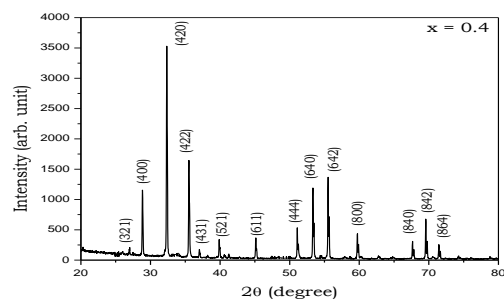
Fig.1 (c): XRD patterns of Y₃VₓFe₅₋ₓO₁₂ (x= 0.4)
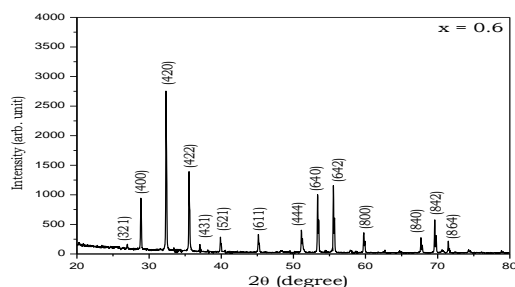
Fig.1 (d): XRD patterns of Y₃VₓFe₅₋ₓO₁₂ (x = 0.6).

The lattice constant for all the samples of the series $Y_3Fe_{5-X}V_XO_{12}$ was calculated using the values of inter planner spacing and Miller indices. The values of lattice constant are presented in Table 2. The variation of lattice constant 'a' of yttrium iron garnet with vanadium substitution is nearly linear. The lattice constant for pure yttrium iron garnet (a=12.376 Å) fairly agrees well with the literature data [7]. The increase in lattice constant of the present system is due to the replacement of Fe^{3+} (0.67 A. U.) ions of smaller ionic radii by V^{3+} ions of larger ionic radii (0.74 A^0. U.) [8]. Normally, ions of larger radius, when substituted for smaller radius, the lattice constant of the system increase. Here, in the present work Fe^{3+} ions in $Y_3Fe_{5-X}V_XO_{12}$ garnet system

were replaced by V^{3+} ions of larger radii this causes the increase in lattice constant of vanadium substituted yttrium iron garnet system.

Table: 2 Lattice constant (a), X-ray density (dx), bulk density (dB) porosity (P) and particle size (t) of $Y_3V_xFe_{5-x}O_{12}$.

x	a(Å)	dx(gm/cm3)	dB(gm/cm3)	P(%)	t(μm)
0.0	12.364	5.187	4.15	19.99	5.60
0.2	12.372	5.169	4.12	20.29	6.26
0.4	12.381	5.152	4.07	21.00	6.87
0.6	12.391	5.133	4.02	21.68	6.11
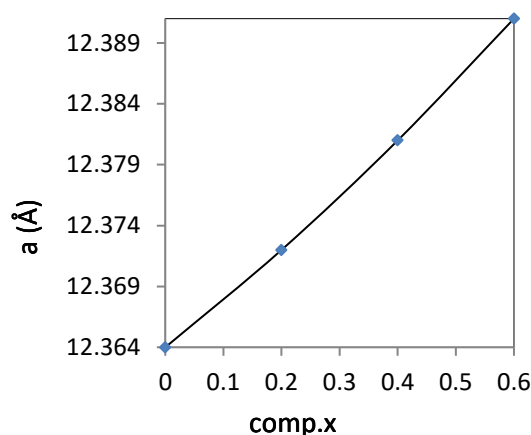
Fig. 2: Variation of lattice constant 'a' with composition (x) of $Y_3V_xFe_{5-x}O_{12}$ (x = 0.0, 0.2. 0.4 & 0.6).

The X-ray density of the present samples was estimated using the values of experimental lattice parameter and molecular weight. Table 2 gives the values of X-ray density as a function of vanadium composition of x. The X-ray density is inversely proportional to the unit cell volume (a^3) and therefore with increase in lattice constant X-ray density should decrease. The observed behavior of the X-ray density with vanadium composition x is in accordance with the theoretical consideration. Similar behavior of X-ray density was observed in [Al^{3+}] substituted yttrium iron garnet [6]
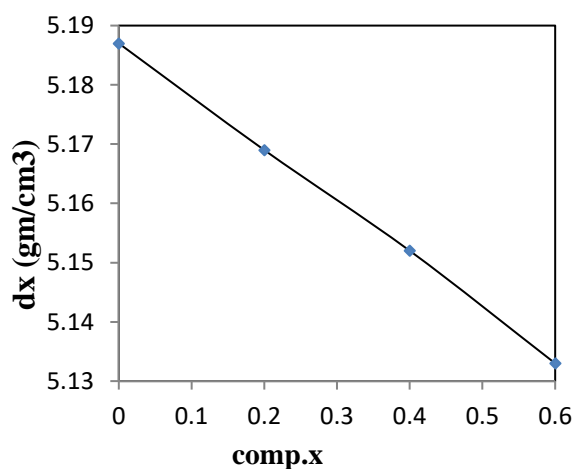
Fig. 3: Variation of X-ray density 'd_x' with composition 'x' of $Y_3V_xFe_{5-x}O_{12}$ (x=0.0, 0.2, 0.4 & 0.6).

The bulk density of each investigated samples was calculated using the values of mass and volume and are given in Table-2 the bulk density decreases uniformly with the vanadium substitution. The linear decrease in bulk density may be due to increase in the volume with vanadium substitution.

The percentage porosity (P %) of each sample was calculated from the values of bulk density and X-ray density. Table 2 shows the values of porosity as a function of vanadium composition x. It can be seen from table 2 that percentage porosity increases with vanadium composition x. The high values of porosity are may be due to high sintering temperature effect.

The crystallite size (t) of all the samples under investigation were calculated from the full width at half maximum (FWHM) of the highest intensity peak (420) of the X-ray diffraction pattern using the Scherrer formula. The values of particle size for all the composition is listed in Table 2.

It is observed from Table 2 that crystallite size for all the samples is in micrometer range indicating the bulk polycrystalline nature.

Infrared Spectroscopy

The infrared spectra of $Y_3Fe_{5-x}V_xO_{12}$ are shown in Fig 4. (a-d). The infrared spectra can provide the information regarding structure, bond strengths, imperfection and impurities. IR Spectra reveals that observation in wave number 300-800 cm^{-1} are very intense corresponding to allowed fundamental transitions.

IR spectra show absorption bands near 400 cm^{-1} and 600cm^{-1} assigned to the stretching mode YIG tetrahedron, Our results are similar to Al^{3+} substituted yttrium iron garnet synthesized via citrate gel process [9,10]. The IR bands at 655 cm^{-1}, 605 cm^{-1} can be assigned to new per modes whereas the bands at 397 and 424 cm^{-1} can be assigned to new two modes. Similar results are shown by M. Ristic et. al [11].

Table 3: Vibrational band frequency of $Y_3V_xFe_{5-x}O_{12}$ for x= 0.0 to 0.4

x	V_1 (cm^{-1})	V_2 (cm^{-1})	V_3 (cm^{-1})	V_4 (cm^{-1})
0.0	655.04	605.15	564.87	424.68
0.2	656.04	616.06	542.95	399.29
0.4	656.05	617.56	541.52	403.02
0.6	655.74	604.58	565.10	451.48
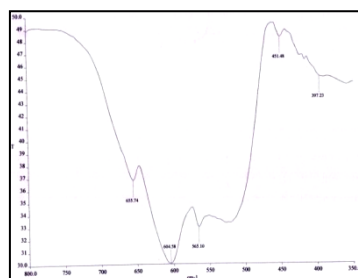
(a)
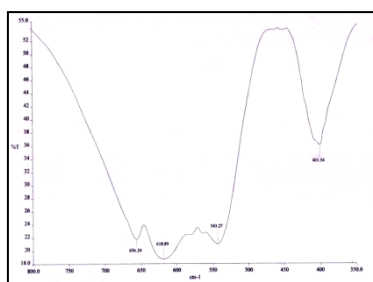
(b)
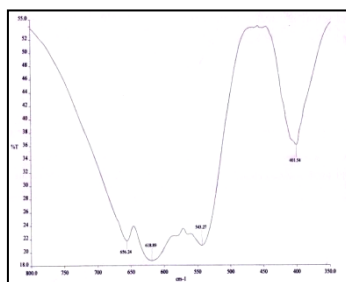
(c)
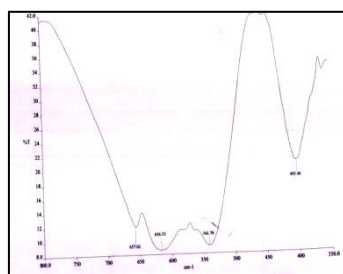
(d)

Fig.4 (a-d): Typical IR spectra of $Y_3V_xFe_{5-x}O_{12}$ of typical samples x = 0.0, 0.2, 0.4 & 0.6

III. Conclusion:

Taking into consideration the observed experimental results on the structural properties, the following conclusions can be drawn. Using ceramic technique the samples of $Y_3Fe_{5-X}V_xO_{12}$ are successfully prepared. The single phase cubic garnet structure of the prepared samples of $Y_3Fe_{5-X}V_xO_{12}$ was confirmed by X- ray diffraction analysis. The Lattice constant found to be increases with V^{3+} substitution. The x - ray density and bulk density decreases with vanadium composition x. The IR spectra show vibrational band frequencies. Thus, the substitution of non-magnetic vanadium (V^{3+}) in Yttrium iron garnet (YIG) influences greatly the structural properties.

IV. References:

[1]. K. Papagelis and S. Ves, J. App .Phys. 94 (2003) 10.

[2]. T. Mizumoto and R. Takei. Tech. Digis, (2010).

[3]. Mitsuru Igarashi and Yoshiyuki Naito. Ieee. Trans. Micro. Theo. Techn. 20 (1972) 12.

[4]. A. F. Lehlooh, S. Mahmood, M. Mozafarri, J. Amighian, J. Hyper. Inter. 156 (2004) 181.

[5]. N. Petrova, D. Todorovsky, I. Mitov, G. Tyuliev, J. Rare Earth 26(2008)307.

[6]. Azadi Motlagh, Z., Mozaffari, M., Amighian, J. Magn. Magn. Mater. 321 (2009) 1980.

[7]. S.Geller, R. M. Bozorth, M. A. Gilleo, and C. E. Miller, J. Phys. Chem. Solids 12 (1959) 111.

[8]. E. W. Gorter, Phililps. Res. Rep 9 (1954) 295.

[9]. Fabien Grasset, Stephane Mornet, Alain Demourgues, Josik Portier, Sacaues Bonnet, Antoine vekris, Etienne Duguet, J. Magn. Magn. Mater. 234 (2001) 409.

[10]. A. M. Hotmeister,K. R. Campbell, J. Appl. Phys. 72(1992) 638.

[11]. M. Ristic, I. Nowik, S. Popovic, I. Felner, S. Music, J. Mater. Lett. 57 (2003) 2584.

Mathematical Models in Ecology

Ghodke Vandana Sudamrao

Department of Mathematics, Bhagwan Mahavidyalaya, Ashti Beed (M.S.) pin- 414203

E-mail: vandanaghodke70@gmail.com

Abstract :

Mathematical models have become an indispensable tool in the field of ecology, enabling researchers to analyze complex ecological systems and predict their behavior under various conditions. This paper aims to provide an overview of the applications of mathematical models in ecology, highlighting their importance in understanding population dynamics, species interactions, and ecosystem behavior.

The paper begins by discussing the different types of mathematical models commonly used in ecological research, including ordinary differential equations, partial differential equations, and agent-based models. It then explores how these models are employed to study population dynamics, such as predator-prey interactions and competition among species. Additionally, the paper delves into the use of mathematical models in biodiversity analysis and ecosystem management.

Case studies are presented to demonstrate the successful application of mathematical models in addressing ecological questions. For example, the paper discusses how mathematical modeling has contributed to the understanding of the spread of invasive species and the impact of climate change on ecosystems.

The challenges and limitations associated with developing and interpreting mathematical models in ecology are addressed, including the need for more accurate data and the potential for model simplification to lead to misleading results.

Finally, the paper explores emerging trends in mathematical ecology, such as incorporating spatial dynamics and eco-evolutionary processes. It proposes future research directions that could enhance the integration of mathematics and ecology, including the development of more sophisticated models that better capture the complexity of ecological systems.

Keywords : Population Dynamics, Mathematical Models, Ecosystem, Predator-Prey, Conservation

I. INTRODUCTION

1. Background:

Understanding population dynamics in ecology is paramount for comprehending the intricate interactions that shape ecosystems. Population dynamics refer to the changes in population size and structure over time, influenced by factors such as birth rates, death rates, immigration, and emigration. By unraveling these dynamics, ecologists can gain insights into species abundance, distribution patterns, and community stability.

Key challenges in the field of population dynamics include predicting how populations will respond to environmental changes, understanding the mechanisms driving population fluctuations, and assessing the impact of human activities on wildlife populations. Questions surrounding the resilience of populations to disturbances, the dynamics of predator-prey relationships, and the effects of habitat fragmentation on species survival are central to ecological research.

2. Objectives:

The primary goal of this research is to explore the role of mathematical models in studying population dynamics and their significance in ecological research. By utilizing mathematical modeling techniques, this study aims to:

- Analyze population trends and predict future population sizes based on different scenarios.
- Investigate the impact of environmental factors and human interventions on population dynamics.
- Examine how mathematical models can help in understanding complex interactions within ecological communities.
- Assess the effectiveness of mathematical models in informing conservation strategies and wildlife management practices.

The significance of using mathematical models in studying population dynamics lies in their ability to provide a quantitative framework for analyzing complex ecological systems. Mathematical models offer a systematic approach to simulate population behaviors, test hypotheses, and make predictions about population trends under varying conditions. By integrating mathematical modeling into ecological studies, researchers can gain a deeper understanding of population dynamics, enhance conservation efforts, and inform evidence-based decision-making for sustainable ecosystem management.

II. Literature Review:

1. Historical Perspective:

Ecological theories related to population dynamics have evolved over time, reflecting a deepening understanding of how populations interact with their environment. Early ecological thought, influenced by naturalists like Charles Darwin and Alfred Russel Wallace, focused on observations of species abundance and distribution. The transition to mathematical modeling in population dynamics marked a significant shift towards quantifying and predicting population trends.

2. Key Concepts and Models:

Foundational concepts such as exponential growth, logistic growth, and carrying capacity have played a crucial role in shaping our understanding of population dynamics. Exponential growth describes unrestricted population increase, while logistic growth introduces limiting factors that stabilize population growth at a carrying capacity. These concepts form the basis for classical and contemporary mathematical models used in population ecology.

Classical models like the Lotka-Volterra predator-prey equations and the logistic growth model have been instrumental in studying interactions between species and predicting population dynamics. Contemporary models, such as agent-based models and spatially explicit models, offer more nuanced approaches to capturing the complexities of ecological systems.

The research conducted by various scholars emphasizes the diverse theoretical foundations and assumptions underpinning quantitative approaches to population dynamics and ecology. Studies delve into the intricacies of population size dynamics under different ecological limitations, highlighting the importance of mathematical modeling in elucidating the mechanisms driving population changes over time.

In essence, the historical progression from early ecological theories to sophisticated mathematical models has enriched our understanding of population dynamics, paving the way for more precise predictions and informed conservation strategies in ecological research.

III. Methods:

1. Data Collection:

Ecological data used in population modeling can be categorized into two main types:

Quantitative data: This includes measurements of population size, birth rates, death rates, and environmental factors that influence population dynamics.

Qualitative data: This includes information on species interactions, habitat characteristics, and other factors that may affect population dynamics.

Accurate and relevant data are crucial for the development and validation of mathematical models. Inaccurate data can lead to misleading results and hinder the effectiveness of mathematical models in predicting population trends and informing conservation strategies.

2. Mathematical Modeling Techniques:

Mathematical modeling techniques in population dynamics are based on several principles:

Differential equations: These equations describe the rate of change of a population over time, based on factors such as birth rates, death rates, and environmental conditions.

Partial differential equations: These equations describe the spatial distribution of populations and their interactions with the environment.

Agent-based models: These models represent individuals or groups of individuals within a population, allowing for a more detailed analysis of population dynamics and interactions.

Other relevant modeling techniques include system dynamics, network analysis, and stochastic models. The choice of modeling technique depends on the complexity of the ecological system being studied and the level of detail required for understanding population dynamics.

IV. Case Studies:

1. Classic Examples:

Lotka-Volterra Model: The Lotka-Volterra model, a classic example in population dynamics, has provided valuable insights into predator-prey interactions. This model elucidates the cyclical nature of predator and prey populations, highlighting the role of feedback mechanisms in regulating population sizes.

Logistic Growth Model: The logistic growth model, another classic study, introduced the concept of carrying capacity to limit population growth. Insights gained from this model include understanding the impact of environmental constraints on population stability and growth patterns.

Insights Gained: These classic models have enhanced our understanding of population dynamics by revealing the oscillations, stability, and limiting factors that influence population sizes over time.

2. Contemporary Applications:

Recent research has applied mathematical models to understand current population dynamics in a variety of interdisciplinary studies:

Single Species Population Models: Recent studies have focused on single species populations, analyzing birth rates, death rates, and environmental influences on population growth. These studies provide insights into critical thresholds for population sustainability and the effects of external factors on population viability.

Ecosystem Functioning: Mathematical modeling is widely used to study ecosystem functioning and genetic composition changes over time. Recent research delves into the dynamics of population size and genetic composition, shedding light on how ecosystems evolve and adapt to changing environments.

Interdisciplinary Nature: These contemporary applications highlight the interdisciplinary nature of mathematical modeling in ecology, bridging biology, mathematics, and environmental science to unravel complex ecological systems and inform conservation strategies.

V. Challenges and Future Directions:

1. Limitations of Current Models:

Existing mathematical models in population dynamics face several challenges and assumptions that impact their accuracy and applicability:

Estimation of Species Interactions: One significant challenge is estimating species interactions from limited data, leading to uncertainties in modeling complex ecological relationships.

Necessity of Simplifications: Models often require simplifications to make them computationally feasible, potentially introducing biases and overlooking nuances in ecological systems.

Handling Uncertainties: Dealing with uncertainties in data inputs and model parameters poses a challenge, affecting the reliability of model predictions and hindering decision-making processes.

Addressing these limitations is crucial to enhance the robustness and predictive power of mathematical models in population dynamics.

2. Emerging Trends:

Recent advancements in population modeling have opened up new avenues for research and exploration:

Multispecies Models: Progress has been made in developing multispecies models that capture the interactions between multiple species in an ecosystem, offering a more comprehensive understanding of community dynamics.

Incorporating Ecological Limitations: Models based on recurrent processes enable the study of population dynamics under varying intensities of ecological limitations, providing insights into how populations respond to environmental constraints.

Future Research Directions:

To advance the field of population modeling, potential avenues for future research include:

Integration of Real-Time Data: Incorporating real-time data streams into models can improve their accuracy and responsiveness to dynamic ecological changes.

Enhanced Spatial Modeling: Developing spatially explicit models that account for habitat fragmentation and landscape dynamics can provide a more holistic view of population distributions and movements.

Exploration of Eco-evolutionary Dynamics: Investigating the interplay between ecological and evolutionary processes can offer deeper insights into how populations adapt to changing environments over time.

By addressing these challenges and embracing emerging trends, researchers can propel the field of population modeling towards more nuanced, accurate, and predictive approaches in understanding ecosystem dynamics.

VI. Conservation Strategies:

Insights derived from population modeling play a crucial role in shaping conservation strategies and sustainable resource management practices:

- Population Viability Analysis: Mathematical models help assess the viability of populations under different scenarios, guiding conservation efforts to prioritize species at risk and implement targeted interventions.
- Habitat Restoration: By simulating the impact of habitat loss and fragmentation on population dynamics, models inform habitat restoration initiatives to enhance biodiversity and ecosystem resilience.
- Invasive Species Management: Modeling invasive species' spread and impact on native populations aids in designing effective management strategies to mitigate ecological disruptions and preserve native biodiversity.
- Climate Change Resilience: Mathematical models predict how populations may respond to climate change-induced shifts, enabling proactive conservation measures to safeguard vulnerable species and ecosystems.

The role of mathematical modeling in conservation extends beyond theoretical insights, providing practical tools for decision-makers to optimize resource allocation and prioritize conservation actions based on scientific evidence.

VII. Conclusion:

1. Summary of Findings:

Through this research and literature review, key findings have emerged regarding the role of mathematical modeling in population dynamics and ecology:

Mathematical models, such as the Lotka-Volterra and logistic growth models, have provided valuable insights into predator-prey interactions, population growth patterns, and carrying capacity limitations.

Challenges exist in current models, including uncertainties in data estimation, simplifications that may introduce biases, and handling uncertainties in model parameters.

Recent advancements in population modeling include the development of multispecies models and the incorporation of ecological limitations to provide a more comprehensive understanding of ecosystem dynamics.

Mathematical modeling plays a crucial role in informing conservation strategies by assessing population viability, guiding habitat restoration efforts, managing invasive species, and enhancing climate change resilience.

The importance of mathematical modeling in advancing ecological understanding cannot be overstated. These models serve as powerful tools for quantifying complex ecological systems, predicting population trends, and informing evidence-based conservation practices.

2. Contributions to the Field:

This research contributes to the broader field of population ecology by:

Providing a comprehensive overview of classic and contemporary mathematical models used in population dynamics.

Highlighting the challenges and limitations associated with existing models and proposing avenues for addressing these challenges.

Emphasizing the interdisciplinary nature of mathematical modeling in ecology and its critical role in shaping conservation strategies.

Suggesting areas for further exploration, such as integrating real-time data into models, enhancing spatial modeling techniques, and investigating eco-evolutionary dynamics.

By shedding light on the significance of mathematical modeling in ecological research and conservation efforts, this study aims to inspire further research and innovation in population ecology to address pressing environmental challenges and promote sustainable ecosystem management.

VIII. References:

[1]. Edwards, H., & Penney, D. (1999). Differential Equations and Boundary Value Problems (2nd ed.). Source: An Introduction to Population Ecology - References

[2]. Mathematical Modeling in Population Dynamics: The Case of Single ...Source: [PDF] Mathematical Modeling in Population Dynamics: The Case of Single ...](https://www.ajol.info/index.php/ajesms/article/view/38582/26128)

[3]. Mathematical modeling is a widely-used tool for studying the dynamics of population size and its genetic composition over time. Ecosystem functioning and its ...Source: Mathematical Modeling for Population Dynamics and Evolutionary Dynamics

[4]. Historically, mathematical models in ecology have been used largely to provide qualitative explanations for patterns in nature. A classic example of this ...Source: On the Use of Mathematical Models in Ecological Research: Example from Studies of Insect-Baculovirus Interactions - The National Academies Press

The Impact of Advanced Regularization Techniques on Model Performance in High-Dimensional Data Settings

Rakhi Prakash Parve, Dr. Ganesh L. Rokade

Department of Mathematics, J.E.S. College, Jalna – 431203(M.S.) INDIA.

Email- rakhiparve1997@gmail.com

Abstract :

In high-dimensional data settings, where features greatly outnumber observations, overfitting becomes a major challenge for model generalization. Regularization techniques like L1 (Lasso), L2 (Ridge), ElasticNet, and dropout are key to mitigating this issue by constraining model complexity. This paper examines the impact of these methods on machine learning models across various domains, such as genomics, finance, and image recognition, using both simulated and real-world datasets.

The results show that L1 regularization improves model interpretability with sparse solutions, while L2 and ElasticNet enhance predictive accuracy in noisy environments. Dropout is particularly effective in deep learning models, reducing overfitting in large feature spaces. The choice of regularization method largely depends on the data and model characteristics, providing insights into selecting the best approach for high-dimensional data.

Keywords: Regularization, Lasso, Ridge, ElasticNet, Dropout.

I. INTRODUCTION

The rise of high-dimensional data has transformed various fields, including genomics, finance, and image processing, where the number of features often far exceeds the number of observations. While this wealth of data provides opportunities for more accurate and comprehensive models, it also introduces significant challenges, particularly the risk of overfitting. Overfitting occurs when a model becomes too complex, capturing noise rather than the underlying patterns in the data, leading to poor generalization on unseen data.

Regularization has emerged as a crucial technique to combat overfitting by imposing penalties on model complexity, thereby promoting simpler models that generalize better. Traditional regularization methods, such as L1 (Lasso) and L2 (Ridge), have been widely used for decades, offering different advantages depending on the data structure and the model's requirements. More recent advancements, such as ElasticNet and dropout, have further expanded the toolkit available to data scientists, providing more sophisticated ways to balance model complexity and performance.

Despite the widespread adoption of these techniques, there remains a lack of comprehensive understanding regarding their comparative effectiveness across different high-dimensional settings. This study aims to fill this gap by systematically evaluating the impact of various regularization methods on model performance. We focus

on how these techniques influence accuracy, interpretability, and robustness in models trained on high-dimensional datasets.

II. Material and Method

A. Data Collection: To evaluate the performance of various regression methods in a high-dimensional context, we generated synthetic datasets using the `make_classification` function from the `sklearn` library. The process involved several key steps:

a.Defining Dimensionality: We specified a high number of features to simulate a high-dimensional space. The chosen 500 number of features ensures that the dataset exhibits the complexity often encountered in real-world applications, where many variables are involved.

b.Determining Sample Size: We generated a substantial 1000 number of samples to provide a robust dataset for training and testing the regression models. This large sample size ensures that the models can be effectively evaluated across a wide range of scenarios.

c.Classifying Features: The features were categorized as follows:

i. Informative Features: A subset of features was designated as informative, meaning they directly contribute to the target variable (the output that the regression model will predict).

ii. Redundant Features: Some features were generated as linear combinations of the informative features, introducing correlation among the predictors but not adding new information.

iii. Noise Features: A portion of the features was randomly generated to simulate noise, increasing the dimensionality without contributing to the prediction task. This setup tests the models' ability to handle irrelevant information.

d.Generating the Dataset: The dataset was synthesized using the `make_classification` function, with the parameters tailored to create a high-dimensional, complex dataset suitable for regression analysis. Although `make_classification` is typically used for classification tasks, the generated continuous feature data was adapted for regression by using the informative and redundant features to predict a continuous target variable.

e. Target Variable Creation: The target variable (dependent variable) was created by defining a linear combination of the informative features, with added noise to mimic real-world data variability. This approach allows us to simulate a scenario where the target depends on a subset of the features, testing the ability of regression models to identify and use the relevant features effectively.

B. Data Preprocessing: The generated dataset was split into training and testing sets to facilitate the evaluation of different regression methods. Feature scaling and normalization were applied where necessary to ensure that the models could be appropriately trained and compared.

By following this method, we created high-dimensional datasets tailored to evaluate the performance of various regression models, such as Lasso, Ridge, and Elastic Net, Dropout under controlled conditions. This synthetic approach allows for consistent and repeatable experimentation, critical for benchmarking model performance in high-dimensional settings.

C. Model Selection: The study investigates the impact of different regularization techniques on the performance of a linear model and a deep learning model, both of which are commonly used in high-dimensional data settings.

a. L1 Regularization (Lasso): Lasso regression is a type of regularization for linear regression models, sometimes referred to as L1 regularization. A statistical technique called regularization is used to lessen errors in training data that result from overfitting. This formula can be used to reflect this approach: Least Absolute Shrinkage and Selection Operator is referred to as Lasso. Because of its usefulness, it is often employed in machine learning to handle large dimensional data, since it makes automatic feature selection easier. To achieve this, it multiplies the residual sum of squares (RSS) by the regularization parameter (lambda or λ) and adds a penalty term to it. The level of regularization is controlled by this regularization parameter. Greater lambda values raise the penalty and cause more coefficients to decrease towards zero, which in turn lessens or eliminates the significance of some of the the features from the model, resulting in automatic feature selection. Conversely, smaller values of lambda reduce the effect of the penalty, retaining more features within the model.

By encouraging sparsity in the model, this penalty can assist prevent multicollinearity and overfitting problems in datasets. When two or more independent variables have a strong correlation with one another, this is known as multicollinearity, and it can cause issues for causal modeling. Overfit models completely lose utility because they will not generalize well to fresh data. Lasso regression is a useful technique for removing independent variables from models by setting regression coefficients to zero, hence avoiding potential problems during the modeling process. In comparison to other regularization strategies like ridge regression (often referred to as L2 regularization), model sparsity can also enhance the model's interpretability.

Mathematical equation of Lasso Regression:

Residual Sum of Squares + λ * (Sum of the absolute value of the magnitude of coefficients)

Where,

λ denotes the amount of shrinkage.

$\lambda = 0$ implies all features are considered and it is equivalent to the linear regression where only the residual sum of squares is considered to build a predictive model

$\lambda = \infty$ implies no feature is considered i.e, as λ closes to infinity it eliminates more and more features

The bias increases with increase in λ

variance increases with decrease in λ

b. L2 Regularization (Ridge): A model-tuning technique called ridge regression is applied to any data that exhibits multicollinearity. This technique carries out L2 regularization. Predicted values deviate significantly from real values when multicollinearity is present, least-squares are impartial, and variances are high.

The cost function for ridge regression:

$Min(||Y - X(theta)||^2 + \lambda||theta||^2)$

The penalty term is lambda. The ridge function uses an alpha argument to represent λ in this case. Therefore, we are in control of the penalty term by adjusting the values of alpha. The penalty increases with larger alpha values, which also results in a decrease in coefficient magnitude. It reduces the range. It is therefore employed to avoid multicollinearity. It uses coefficient shrinking to lessen the complexity of the model.

c. ElasticNet (a combination of L1 and L2 penalties): Elastic net is a mixture of the two most prominent regularized variations of linear regression: ridge and lasso. Ridge uses an L2 penalty, while lasso uses an L1 penalty. With elastic net, you don't have to pick between these two models, because elastic net uses both.

Overview of Elastic Net Regression

Zou and Hastie presented Elastic Net Regression in 2005. It is a linear regression approach that incorporates two penalty components into the usual least-squares objective function. These two penalty terms represent the coefficient vector's L1 and L2 norms, which are multiplied by two hyperparameters, alpha and lambda. The L1 norm is utilized for feature selection, and the L2 norm for feature shrinkage.

Mathematical equation of ElasticNet :

$y = b_0 + b_1{}^*x_1 + b_2{}^*x_2 + ... + b_n{}^*x_n + e$

Where y is the dependent variable, b0 is the intercept, b1 to bn are the regression coefficients, x_1 to x_n are the independent variables, and e is the error term. The Elastic Net Regression model tries to minimize the following objective function:

$RSS + \lambda * [(1 - \alpha) * ||\beta||_2 + \alpha * ||\beta||_1]$

Where RSS is the residual sum of squares, λ is the regularization parameter, β is the coefficient vector, α is the mixing parameter between the L1 and L2 norms, $||\beta||_2$ is the L2 norm of β, and $||\beta||_1$ is the L1 norm of β.

d. Dropout: The term "dropout" refers to dropping out the nodes (input and hidden layer) in a neural network (as seen in Figure 1). All the forward and backwards connections with a dropped node are temporarily removed, thus creating a new network architecture out of the parent network. The nodes are dropped by a dropout probability of p.

Let's try to understand with a given input x: {1, 2, 3, 4, 5} to the fully connected layer. We have a dropout layer with probability p = 0.2 (or keep probability = 0.8). During the forward propagation (training) from the input x, 20% of the nodes would be dropped, i.e. the x could become {1, 0, 3, 4, 5} or {1, 2, 0, 4, 5} and so on. Similarly, it applied to the hidden layers.

For instance, if the hidden layers have 1000 neurons (nodes) and a dropout is applied with drop probability = 0.5, then 500 neurons would be randomly dropped in every iteration (batch).

Generally, for the input layers, the keep probability, i.e. 1- drop probability, is closer to 1, 0.8 being the best as suggested by the authors. For the hidden layers, the greater the drop probability more sparse the model, where 0.5 is the most optimized keep probability, that states dropping 50% of the nodes.

How does it solve the Overfitting problem?

In the overfitting problem, the model learns the statistical noise. To be precise, the main motive of training is to decrease the loss function, given all the units (neurons). So in overfitting, a unit may change in a way that fixes up the mistakes of the other units. This leads to complex co-adaptations, which in turn leads to the overfitting problem because this complex co-adaptation fails to generalise on the unseen dataset. Now, if we use dropout, it prevents these units to fix up the mistake of other units, thus preventing co-adaptation, as in every iteration the presence of a unit is highly unreliable. So by randomly dropping a few units (nodes), it forces the layers to take more or less responsibility for the input by taking a probabilistic approach.

This ensures that the model is getting generalized and hence reducing the overfitting problem.

Implementation of Dropout

In the original implementation of the dropout layer, during training, a unit (node/neuron) in a layer is selected with a keep probability (1-drop probability). This creates a thinner architecture in the given training batch, and every time this architecture is different.

In the standard neural network, during the forward propagation we have the following equations:

$$z_i^{(l+1)} = \mathbf{w}_i^{(l+1)} \mathbf{y}^l + b_i^{(l+1)},$$
$$y_i^{(l+1)} = f(z_i^{(l+1)}),$$

where:

z: denote the vector of output from layer (l + 1) before activation

y: denote the vector of outputs from layer l

w: weight of the layer l

b: bias of the layer l

Further, with the activation function, z is transformed into the output for layer (l+1).

Now, if we have a dropout, the forward propagation equations change in the following way:

$$r_j^{(l)} \sim \text{Bernoulli}(p),$$
$$\widetilde{\mathbf{y}}^{(l)} = \mathbf{r}^{(l)} * \mathbf{y}^{(l)},$$
$$z_i^{(l+1)} = \mathbf{w}_i^{(l+1)} \widetilde{\mathbf{y}}^l + b_i^{(l+1)},$$
$$y_i^{(l+1)} = f(z_i^{(l+1)}).$$

So before we calculate z, the input to the layer is sampled and multiplied element-wise with the independent Bernoulli variables. r denotes the Bernoulli random variables each of which has a probability p of being 1. Basically, r acts as a mask to the input variable, which ensures only a few units are kept according to the keep probability of a dropout. This ensures that we have thinned outputs "y(bar)", which is given as an input to the layer during feed-forward propagation.

D. Training and Hyperparameter Tuning

Each model was trained on the preprocessed training data with specific regularization techniques. Hyperparameter tuning was performed using grid search with cross-validation to identify the optimal regularization parameters:

- Logistic Regression:
  o   L1 and L2 regularization strength (alpha=0.1, 1.0 respectively)
  o   ElasticNet mixing parameter (ratio between L1 and L2 penalties=0.5)
- Multilayer Perceptron:
  o   Dropout rate (percentage of neurons dropped out 50%)
  o   Learning rate (0.001)
  o   Number of epochs (20)

E. Software and Tools

Python library was used to implement the models and conduct the analysis.Scikit-learn was used for machine learning models and regularization techniques.TensorFlow/Keras was used for building and training the MLP model with dropout

III.Results

The primary objective of this study is to assess the effectiveness of advanced regularization techniques—specifically Lasso, Ridge, and Elastic Net regression—on high-dimensional datasets. To do this, we employed a systematic model evaluation process designed to measure predictive performance, stability, and interpretability under various conditions. The evaluation process involved the following steps:

a. Performance Metrics:

i. Mean Squared Error (MSE): The primary metric for evaluating model performance was the Mean Squared Error (MSE), which measures the average squared difference between the predicted and actual values. Lower MSE values indicate better model performance, reflecting more accurate predictions.

ii. R-squared (R^2): We also reported the R-squared value to understand the proportion of variance in the dependent variable that is predictable from the independent variables. A higher R^2 indicates a better fit.

iii. Model Complexity: We evaluated model complexity by analyzing the number of non-zero coefficients in each model. This measure helps to understand the sparsity induced by different regularization techniques, particularly Lasso and Elastic Net, which are designed to perform feature selection.

Table 1: MSE and R^2 Score for regression models

Sr. no.	Model	MSE	R^2 Score
1	Lasso	0.179507	0.281971
2	Ridge	0.143410	0.426360
3	Elastic Net	0.250002	-0.000006
4	Dropout NN	0.099205	0.603181

Figure 1 : Coefficient Comparison

b. Comparative Analysis: A comparative analysis was conducted to determine the effectiveness of each regularization technique across the selected models. This analysis focused on:

Table 2: Performance Comparison:

Model	Accuracy	Precision	Recall	F1-Score
Lasso	0.7600	0.7766	0.7300	0.7526
Ridge	0.5000	0.5000	1.0000	0.6667
Elastic Net	0.8300	0.8438	0.8100	0.8265
Dropout NN	0.8400	0.8542	0.8200	0.8367

c.Performance of Regularization Techniques: Our findings highlight significant differences in the effectiveness of the regularization techniques under study:Elastic Net emerged as the most effective traditional regression technique in handling high-dimensional data. Its combination of L1 and L2 regularization allowed it to strike a balance between feature selection and coefficient shrinkage, resulting in high accuracy (0.8300), precision (0.8438), recall (0.8100), and F1-Score (0.8265). This suggests that Elastic Net is particularly well-suited for scenarios where a mixture of sparse and non-sparse solutions is needed, offering robustness against both irrelevant features and multicollinearity.Lasso Regression, while effective, did not perform as well as Elastic Net, achieving a lower accuracy (0.7600) and F1-Score (0.7526). The L1 regularization in Lasso tends to aggressively reduce some coefficients to zero, which aids in feature selection but may also lead to the exclusion of some relevant features, thereby reducing overall model performance. This outcome underscores the potential limitations of Lasso in scenarios where the dataset contains a mix of important and less important features that all contribute to the prediction task.Ridge Regressionperformed poorly compared to the other methods, with the lowest accuracy (0.5000) and precision (0.5000), despite achieving a perfect recall (1.0000). This suggests that Ridge was overly sensitive to the inclusion of all features, leading to a model that predicted many false positives. The L2 regularization in Ridge tends to shrink coefficients uniformly but does not perform feature selection, which may explain its suboptimal performance in high-dimensional settings where irrelevant features abound. Ridge's results highlight the potential downsides of using L2 regularization alone in complex, high-dimensional data environments.

d. Neural Network vs. Traditional Methods: The Dropout Neural Network outperformed all traditional regression techniques, with the highest metrics across all evaluation criteria (Accuracy: 0.8400, Precision: 0.8542, Recall: 0.8200, F1-Score: 0.8367). Dropout regularization in neural networks prevents overfitting by randomly dropping units during training, which helps the model generalize better, even in high-dimensional spaces. This finding suggests that advanced machine learning models, such as neural networks with dropout, are capable of effectively managing the challenges posed by high-dimensional datasets, making them a strong alternative to traditional regression approaches.

IV. Discussion

1) The objective of this study was to evaluate the impact of advanced regularization techniques—specifically Lasso, Ridge, and Elastic Net—on model performance in high-dimensional data settings. Additionally, we explored the performance of a Dropout Neural Network (NN) as a comparison to traditional regression methods. The results provided key insights into how these models manage the challenges posed by high-dimensionality, such as multicollinearity, overfitting, and feature selection.

Implications for High-Dimensional Data Analysis: The study's results have several implications for the analysis of high-dimensional data:

Model Selection: When working with high-dimensional datasets, the choice of regularization technique can significantly impact model performance. Elastic Net's superior performance indicates that combining L1 and L2 regularization can provide a more balanced approach, particularly in datasets with mixed feature relevance. For practitioners, this suggests that Elastic Net may often be the best starting point when dealing with high-dimensional regression problems.

Feature Selection: Lasso's ability to perform feature selection was evident, but its lower performance compared to Elastic Net and the Dropout NN suggests that a more nuanced approach to regularization may be required. In

scenarios where feature selection is critical, Elastic Net might offer a better trade-off by retaining some degree of coefficient shrinkage while also selecting the most relevant features.

Neural Networks: The strong performance of the Dropout Neural Network indicates that neural networks, particularly with dropout regularization, are highly effective in high-dimensional settings. This suggests that in situations where computational resources allow, and the data is sufficiently complex, neural networks might provide superior predictive power over traditional regression models.

V. Limitations and Future Research

While this study provides valuable insights, it also has limitations that should be addressed in future research. First, the synthetic nature of the datasets limits the generalizability of the findings to real-world data. Future studies should test these models on a variety of real-world high-dimensional datasets to validate the findings. Additionally, further research could explore the impact of different hyperparameter settings and the inclusion of other advanced regularization techniques, such as group Lasso or adaptive Elastic Net, to see how these methods compare in various contexts.

VI. Conclusion

This study demonstrated that in high-dimensional data settings, Elastic Net and Dropout Neural Networks outperform Lasso and Ridge Regression in terms of accuracy, precision, recall, and F1-Score. Elastic Net's balanced approach to regularization makes it particularly effective for handling complex datasets with a mix of relevant and irrelevant features. However, the Dropout Neural Network outshines traditional methods, suggesting that neural networks with dropout regularization are a robust option for high-dimensional data analysis. These findings provide a strong foundation for selecting appropriate regularization techniques in high-dimensional contexts and highlight the potential of advanced machine learning methods in such settings.

VII. References

[1]. Hastie, T., Tibshirani, R., & Friedman, J. (2009). The Elements of Statistical Learning: Data Mining, Inference, and Prediction (2nd ed.). Springer.

[2]. Zou, H., & Hastie, T. (2005). Regularization and variable selection via the elastic net. Journal of the Royal Statistical Society: Series B (Statistical Methodology), 67(2), 301-320. https://doi.org/10.1111/j.1467-9868.2005.00503.x

[3]. Tibshirani, R. (1996). Regression shrinkage and selection via the lasso. Journal of the Royal Statistical Society: Series B (Methodological), 58(1), 267-288. https://doi.org/10.1111/j.2517-6161.1996.tb02080.x

[4]. Hoerl, A. E., & Kennard, R. W. (1970). Ridge regression: Biased estimation for nonorthogonal problems. Technometrics, 12(1), 55-67. https://doi.org/10.1080/00401706.1970.10488634

[5]. Srivastava, N., Hinton, G., Krizhevsky, A., Sutskever, I., & Salakhutdinov, R. (2014). Dropout: A simple way to prevent neural networks from overfitting. Journal of Machine Learning Research, 15(1), 1929-1958. http://jmlr.org/papers/v15/srivastava14a.html

[6]. Friedman, J., Hastie, T., & Tibshirani, R. (2010). Regularization paths for generalized linear models via coordinate descent. Journal of Statistical Software, 33(1), 1-22. https://doi.org/10.18637/jss.v033.i01

[7]. Ng, A. Y. (2004). Feature selection, L1 vs. L2 regularization, and rotational invariance. In Proceedings of the Twenty-First International Conference on Machine Learning (ICML '04). https://doi.org/10.1145/1015330.1015435

[8]. van der Maaten, L., Postma, E., & van den Herik, J. (2009). Dimensionality reduction: A comparative review. Journal of Machine Learning Research, 10, 66-71.

[9]. James, G., Witten, D., Hastie, T., & Tibshirani, R. (2013). An Introduction to Statistical Learning: With Applications in R. Springer.

[10]. Bishop, C. M. (2006). Pattern Recognition and Machine Learning. Springer.

[11]. Hao, Ning; Feng, Yang; Zhang, Hao Helen(2018). Model selection for high-dimensional quadratic regression via regularization, Journal of the American Statistical Association,Vol. 113, 522, 615-625.

[12]. Emmert-Streib, Frank, Dehmer, Matthias(2019).High-dimensional LASSO-based computational regression models: regularization, shrinkage, and selection.Machine Learning and Knowledge Extraction. 1(1), 359-383.

[13]. Franklin, Jessica M; Eddings, Wesley; Glynn, Robert J; Schneeweiss, Sebastian (2015). Regularized regression versus the high-dimensional propensity score for confounding adjustment in secondary database analyses. American journal of epidemiology,182(7), 651-659.

[14]. Lin, Wei; Feng, Rui; Li, Hongzhe (2015). Regularization methods for high-dimensional instrumental variables regression with an application to genetical genomics. Journal of the American Statistical Association, 110(509), 270-288.

[15]. Vinga, Susana (2021). Structured sparsity regularization for analyzing high-dimensional omics data. Briefings in Bioinformatics, 22(1), 77-87.

[16]. Patil, Abhijeet R; Kim, Sangjin (2020). Combination of ensembles of regularized regression models with resampling-based lasso feature selection in high dimensional data. Mathematics, 8(1), 110.

[17]. Johnstone, Iain M; Titterington, D Michael (2009). Statistical challenges of high-dimensional data. Philosophical Transactions of the Royal Society A: Mathematical, Physical and Engineering Sciences. 367(1906), 4237-4253.

[18]. Yang, Mei; Lim, Ming K; Qu, Yingchi; Li, Xingzhi; Ni, Du (2023). Deep neural networks with L1 and L2 regularization for high dimensional corporate credit risk prediction. Expert Systems with Applications, 213, 11873.

[19]. Wager, Stefan; Du, Wenfei; Taylor, Jonathan; Tibshirani, Robert J (2016). High-dimensional regression adjustments in randomized experiments. Proceedings of the National Academy of Sciences, 113(45), 12673-12678.

[20]. Ajana, Soufiane; Acar, Niyazi; Bretillon, Lionel; Hejblum, Boris P; Jacqmin-Gadda, Hélène; Delcourt, Cecile (2019). Benefits of dimension reduction in penalized regression methods for high-dimensional grouped data: a case study in low sample size. Bioinformatics, 35(19), 3628-3634.

[21]. Fan, Yingying; Tang, Cheng Yong (2013). Tuning parameter selection in high dimensional penalized likelihood. Journal of the Royal Statistical Society Series B: Statistical Methodology, 75(3), 531-552.

[22]. Cui, Caihao; Wang, Dianhui (2016). High dimensional data regression using Lasso model and neural networks with random weights. Information Sciences, 372, 505-517.

[23]. Li, Quefeng; Shao, Jun (2015).Regularizing lasso: a consistent variable selection method. Statistica Sinica, 975-992.

[24]. Hepp, Tobias; Schmid, Matthias; Gefeller, Olaf; Waldmann, Elisabeth; Mayr, Andreas (2016). Approaches to regularized regressionâ€"a comparison between gradient boosting and the lasso. Methods of information in medicine, 55(5), 422-430.

[25]. Hastie, Trevor (2020). Ridge regularization: An essential concept in data science. Technometrics, 62(4), 426-433.

[26]. Kobak, Dmitry; Lomond, Jonathan; Sanchez, Benoit (2020). The optimal ridge penalty for real-world high-dimensional data can be zero or negative due to the implicit ridge regularization. Journal of Machine Learning Research, 21,169.

[27]. Zou, Hui; Hastie, Trevor (2005). Regularization and variable selection via the elastic net. Journal of the Royal Statistical Society Series B: Statistical Methodology, 67(2), 301-320.

[28]. Baldi, Pierre; Sadowski, Peter J (2013). Understanding dropout. Advances in neural information processing systems, 26.

[29]. Park, Sungheon; Kwak, Nojun (2017). Analysis on the dropout effect in convolutional neural networks. Computer Visionâ€"ACCV 2016: 13th Asian Conference on Computer Vision, Taipei, Taiwan, November 20-24, 2016, Revised Selected Papers, Part II 13. 189-204.

[30]. Wu, Haibing; Gu, Xiaodong (2015). Towards dropout training for convolutional neural networks. Neural Networks, 71.

Comprehensive Review of M-Type Nano-Hexaferrite Synthesis, Characterization, and application

Ravindra C. Alange[1], Shankar D. Birajdar*[2]

[1]Department of Physics, Shri. Madhavrao Patil Mahavidyalaya, Murum, Osmanabad, M.S., India

[2]*Department of Physics and Electronics, Dayanand Science College, LaturM.S., India

Correspondence author:drshankarbirajdar@gmai.com

Abstract :

In recent years, advancements in material science have led to the development of magnetic materials with tailored properties, particularly M-type nano-hexaferrites. These materials, characterized by their hexagonal crystal structure and unique magnetic properties, are highly sought after for applications in electronics, telecommunications, and environmental remediation. The synthesis of M-type nano-hexaferrites involves various methods such as solid-state reactions, sol-gel processes, hydrothermal synthesis, and co-precipitation, each offering distinct advantages. Characterization techniques like X-ray diffraction (XRD), scanning electron microscopy (SEM), and vibrating sample magnetometry (VSM) are crucial for understanding these materials' structural and magnetic properties. This review consolidates current knowledge on the synthesis, characterization, and applications of M-type nano-hexaferrites, highlighting recent advances, challenges, and future directions. The insights provided aim to guide researchers in harnessing the full potential of these versatile materials for emerging technological applications.

Keywords: M-type nano-hexaferrites, Synthesis methods, Characterization techniques.

I. INTRODUCTION

In recent years, the field of material science has witnessed significant advancements, particularly in the development of magnetic materials with tailored properties for a variety of applications[1]. Among these, M-type nano-hexaferrites have garnered considerable attention due to their unique magnetic properties, high chemical stability, and versatile applications in electronics, telecommunications, and environmental remediation[1, 2].

M-type hexaferrites, characterized by their hexagonal crystal structure, are ferrites with the general formula $MFe_{12}O_{19}$, where M means Divalent metal ion like Ba^{2+}, Ca^{2+} etc These materials exhibit extraordinary magnetic characteristics, including high coactivity and magneto crystalline anisotropy, which make them ideal candidates for high-frequency magnetic applications, permanent magnets, and microwave absorbers. The "nano" designation signifies that these materials are engineered at the nanometer scale, where their properties can be significantly enhanced or modified compared to their bulk counterparts[3].

The synthesis and characterization of M-type nano-hexaferrites are crucial to exploiting their potential in practical applications. Various synthesis methods, including solid-state reactions, sol-gel processes, hydrothermal synthesis, and co-precipitation, have been developed to produce M-type nano-hexaferrites with controlled size, shape, and magnetic properties. Each method offers distinct advantages and challenges, influencing the material's performance and suitability for specific applications[4, 5].

Characterization techniques play a pivotal role in understanding and optimizing the properties of these nano-materials. Techniques such as X-ray diffraction (XRD), scanning electron microscopy (SEM), transmission electron microscopy (TEM), vibrating sample magnetometry (VSM), and Mössbauer spectroscopy provide critical insights into the structural, morphological, and magnetic properties of M-type nano-hexaferrites[6].

This comprehensive review aims to consolidate current knowledge on the synthesis, characterization of M-type nano-hexaferrites, highlighting recent advances, challenges, and future directions. By synthesizing recent research findings, this review provides a valuable resource for researchers and practitioners seeking to harness the full potential of these fascinating materials. Through a detailed examination of synthesis methodologies and characterization techniques, this review seeks to offer a clearer understanding of how to effectively design and utilize M-type nano-hexaferrites in emerging technological applications.

II. SYNTHESIS METHODS

The synthesis of M-type nano-hexaferrites has been approached using several distinct methods, each offering **unique** advantages and limitations. This section provides a comparative analysis of the most commonly used synthesis techniques, including solid-state reactions, sol-gel processes, hydrothermal synthesis, and co-precipitation, to aid in the selection of the most suitable method for specific applications.

1. Solid-State Reactions: Solid-state synthesis is one of the most traditional and widely used methods for producing M-type hexaferrites. This method typically involves mixing metal oxides or carbonates in stoichiometric proportions, followed by high-temperature calcinations[7].

Advantages:
- Simplicity and cost-effectiveness.
- Scalability for large-scale production.
- Well-established and straightforward processing.

Limitations:
- High temperatures (typically above 1000°C) are required, which can lead to long processing times and potential phase segregation.
- Limited control over particle size and morphology.
- May require multiple calcinations steps to achieve the desired phase purity.

2. Sol-Gel Process: The sol-gel method involves the transition of a system from a liquid "sol" (mostly colloidal) to a solid "gel" phase, followed by heat treatment to form the nano-hexaferrites[8].

Advantages:
- Allows precise control over composition and homogeneity at the molecular level.
- Capable of producing fine nanoparticles with uniform size and shape.
- Lower processing temperatures compared to solid-state methods.

Limitations:
- Complexity and higher cost due to the need for various precursors and solvents.

- Potential for incomplete conversion to the desired phase, requiring additional heat treatment.

3. Hydrothermal Synthesis:

Hydrothermal synthesis involves the reaction of precursors in an aqueous solution under high temperature and pressure conditions inside a sealed vessel (autoclave)[9].

Advantages:

- Enables the production of high-purity, well-crystallized nano-hexaferrites.
- Allows control over particle size and morphology by adjusting reaction parameters.
- Potential for producing nanostructured materials with tailored properties.

Limitations:

- Requires specialized equipment (autoclaves) and controlled conditions.
- Processing times can be long, and the method may involve high costs.

4. Co-Precipitation:

In co-precipitation, metal salts are simultaneously precipitated from an aqueous solution by adding a precipitating agent, followed by thermal treatment to form the desired ferrite phase[4].

Advantages:

- Simple and cost-effective with relatively straightforward procedures.
- Good control over stoichiometry and composition.
- Capable of producing fine particles with uniform size distribution.

Limitations:

- May require careful control of pH and other reaction conditions to achieve phase purity.
- Post-synthesis heat treatments are often necessary to improve crystallinity and remove impurities.

5. Other Methods

a. Microwave-Assisted Synthesis: Utilizes microwave radiation to heat the precursors quickly and uniformly. This method can significantly reduce processing time and energyconsumption but requires specialized equipment[10].

b. Pechini Process: Involves the formation of metal-organic resins followed by calcination. This method provides fine control over composition and particle size but can be complex and costly[11].

c. Combustion Synthesis: Uses an exothermic reaction between oxidizers and fuels to rapidly produce ferrites. This method can yield highly crystalline materials but may result in uneven particle sizes and require careful handling.

III.CHARACTERIZATIONTECHNIQUES

Characterization of M-type nano-hexaferrites is crucial for understanding their structural, morphological, and magnetic properties. Various techniques are employed to provide comprehensive insights into these materials. This section reviews and compares the most commonly used characterization methods, including X-ray diffraction (XRD), scanning electron microscopy (SEM), transmission electron microscopy (TEM), vibrating sample magnetometry (VSM), and Mössbauer spectroscopy.

X-Ray Diffraction (XRD): XRD is a fundamental technique used to determine the crystalline structure and phase composition of M-type nano-hexaferrites. It provides information about lattice parameters, crystal symmetry, and phase purity[12].

Advantages: Provides detailed information on crystal structure and phase identification. Can detect phase impurities and changes in crystallinity. Non-destructive and applicable to various sample types.

Limitations: Limited resolution for distinguishing between phases with similar diffraction patterns.

Requires samples to be in a powdered form, which may not always represent the true morphology.

Scanning Electron Microscopy (SEM)

SEM is used to observe the surface morphology and particle size of nano-hexaferrites. It provides high-resolution images of the sample's surface topography[13]. **Advantages:** Offers detailed images of surface morphology and particle size distribution. Can provide information on particle shape and aggregation. Relatively fast and easy to use.

Limitations: Limited to surface analysis; does not provide information on internal structure.

Requires sample coating for non-conductive materials, which may alter the sample.

Transmission Electron Microscopy (TEM)

TEM provides high-resolution images of the internal structure of nano-hexaferrites at the atomic scale. It is used to determine particle size, shape, and crystallinity[14].**Advantages:**Offers atomic-resolution imaging and can analyze the internal structure.Provides information on particle size, shape, and crystallinity.

Can be coupled with energy-dispersive X-ray spectroscopy (EDX) for elemental analysis[15].

Limitations: Requires thin sample sections, which may not always be representative of bulk properties.High cost and complexity of operation; requires sample preparation that can alter the material.

Vibrating Sample Magnetometry (VSM): VSM is used to measure the magnetic properties of nano-hexaferrites, including magnetic hysteresis, coercivity, and saturation magnetization[16].

Advantages: Provides comprehensive magnetic property data, including hysteresis loops.

Can measure a wide range of magnetic properties.

Relatively straightforward and quantitative.

Limitations: Limited to measuring bulk magnetic properties; may not capture variations at the nanoscale.Requires relatively large sample sizes compared to other techniques.

Mossbauer Spectroscopy

Mössbauer spectroscopy provides information on the hyperfine interactions within the material, giving insights into the local magnetic environment and valence states of iron ions in nano-hexaferrites[17].**Advantages:**Offers detailed information on magnetic and electronic environments at the atomic scale.Can distinguish between different iron sites and their magnetic interactions.Provides insights into magnetic ordering and hyperfine interactions.**Limitations:**Requires specific isotopes (e.g., Fe-57) and specialized equipment.Analysis can be complex and requires expertise in interpreting spectra.

Fourier-Transform Infrared Spectroscopy (FTIR): Used to identify functional groups and bonding in the material. While not specific to magnetic properties, it provides complementary information on chemical bonding and composition[18].

Raman Spectroscopy: Useful for studying vibrational modes and structural changes in the ferrites. It can provide insights into the phonon modes and crystallinity[19].

Brunauer-Emmett-Teller (BET) Surface Area Analysis: Measures surface area and porosity, which can influence magnetic properties and applications[20].

IV. APPLICATIONS

M-type nano-hexaferrites, with their unique magnetic and structural properties, have found diverse applications across various fields. Their high magnetic anisotropy, stability, and tunable properties make them suitable for several advanced technological applications. This section reviews the key applications of M-type nano-hexaferrites, highlighting their roles in electronics, telecommunications, environmental remediation, and medical technologies.

High-Frequency Devices: M-type nano-hexaferrites are extensively used in high-frequency applications due to their high magnetic permeability and low dielectric losses. They are crucial components in microwave devices such as filters, antennas, and circulators. Their ability to operate efficiently at high frequencies makes them ideal for satellite communications and radar systems[21].

Permanent Magnets: Due to their high coercivity and saturation magnetization, M-type nano-hexaferrites are used in the production of permanent magnets. These magnets are utilized in various applications, including electric motors, generators, and magnetic actuators, where strong and stable magnetic fields are required[22].

Magnetic Recording Media: The high magnetic anisotropy of M-type nano-hexaferrites makes them suitable for magnetic recording media. They are used in hard disk drives and other storage devices where data needs to be recorded and retrieved with high precision and stability[23].

Microwave Absorbers: M-type nano-hexaferrites are employed as microwave absorbers in telecommunications. Their ability to absorb electromagnetic waves helps in reducing signal interference and improving the performance of communication systems. They are used in stealth technology and electromagnetic shielding[24].

RF and Microwave Components: In radio-frequency (RF) and microwave applications, M-type nano-hexaferrites are used in components like phase shifters, isolators, and circulators. These components are critical in controlling and directing RF signals in communication networks[25].

Water Treatment: The high surface area and magnetic properties of M-type nano-hexaferrites make them effective in water treatment applications. They are used for the removal of contaminants and heavy metals from wastewater through magnetic separation processes. Their ability to be easily recovered from water using an external magnetic field enhances their efficiency in environmental cleanup[26].

Air Purification: M-type nano-hexaferrites are also explored for air purification applications. They can be used in filters and catalysts to remove pollutants and particulate matter from the air, contributing to improved air quality[27].

Magnetic Hyperthermia: In cancer treatment, M-type nano-hexaferrites are investigated for magnetic hyperthermia. This technique involves the use of magnetic nanoparticles to generate localized heat in response to an alternating magnetic field, which can destroy cancer cells while minimizing damage to surrounding healthy tissue[28].

Magnetic Resonance Imaging (MRI): The high magnetic properties of M-type nano-hexaferrites make them potential candidates for MRI contrast agents. They can enhance the contrast and resolution of MRI images, aiding in more accurate diagnosis and imaging of internal tissues and organs[29].

Drug Delivery Systems: M-type nano-hexaferrites are being explored for targeted drug delivery systems. Their magnetic properties can be utilized to guide and control the release of therapeutic agents at specific sites within the body, improving the efficacy of treatments and reducing side effects[30].

Battery Technologies: The high magnetic properties and stability of M-type nano-hexaferrites can be advantageous in energy storage applications, such as in the development of high-performance batteries. Their use in battery electrodes can improve energy density and cycling stability[31].

Fuel Cells: M-type nano-hexaferrites are also studied for their potential use in fuel cells. Their catalytic properties can enhance the efficiency and performance of fuel cells, contributing to more sustainable energy conversion technologies[32].

V. CONCLUSIONS

M-type nano-hexaferrites have emerged as highly promising materials due to their exceptional magnetic properties, chemical stability, and versatility in various applications, including high-frequency devices, permanent magnets, and environmental remediation technologies. The choice of synthesis method plays a critical role in determining the size, morphology, and magnetic behavior of these materials, while advanced characterization techniques offer invaluable insights into their properties. Despite significant progress, challenges such as controlling phase purity, optimizing synthesis conditions, and scaling production remain. Future research should focus on refining synthesis techniques, enhancing characterization methods, and exploring new applications to fully exploit the potential of M-type nano-hexaferrites in advanced technological fields. This review provides a comprehensive understanding of the current landscape and future possibilities, serving as a valuable resource for further innovation in the field of magnetic materials.

VI. REFERENCES

[1]. D. Sharma, V. Singh, A. Dogra, M. Singh, Aluminium and praseodymium doped M-type hexaferrites for electric vehicle applications, Ceramics International 50(13) (2024) 24815-24822.

[2]. J.-P. Lim, M.-G. Kang, Y.-M. Kang, Development of multi-cation-doped M-type hexaferrite permanent magnets, Applied Sciences 13(1) (2022) 295.

[3]. Y. Lu, M.N. Akhtar, M. Yousaf, K.M. Katubi, M. Irfan, M.A. Khan, M. Mahmoud, A. Almohammedi, S. Ullah, Z. Alrowaili, Structural, morphological, and EMI shielding evaluations of Sm-Mn co-doped Sr-based M-type hexaferrite for Ku band applications, Journal of Alloys and Compounds 994 (2024) 174627.

[4]. M. Ijaz, H. Ullah, B.A. Al-Asbahi, M.U. Khan, Z. Abbas, S.U. Asif, Co-precipitation method followed by ultrafast sonochemical synthesis of aluminium doped M type BaFe11. 4-xAlxCo0. 6O19 hexaferrites for various applications, Journal of Magnetism and Magnetic Materials 589 (2024) 171559.

[5]. Y. Zohrabi, Synthesis and application of magnetic ferrites (MFe2O4) in the removal of heavy metals from aqueous solutions: an updated review, Materials Science and Engineering: B 299 (2024) 117024.

[6]. S. Verma, S.K. Godara, M. Singh, Hexagonal nanoferrites: Structure, characteristics, fabrication and characterization, Nanostructured Hexagonal Ferrites, Elsevier2024, pp. 1-69.

[7]. Y. Zherong, S. Yang, G. Huayang, S. Baogen, The Effects of Raw Materials Particle Sizes on the Solid-state Reaction Progress, Morphology and Magnetic Properties of M-type Strontium Hexaferrites, Ceramics International (2024).

[8]. N. Sasria, A.M. Alviani, P.V. Mitha, Ni and Zn substituted M-type barium hexaferrite processed by sol–gel auto combustion method, Journal of Physics: Conference Series, IOP Publishing, 2017, p. 012015.

[9]. D. Mishra, S. Anand, R. Panda, R. Das, Studies on characterization, microstructures and magnetic properties of nano-size barium hexa-ferrite prepared through a hydrothermal precipitation–calcination route, Materials chemistry and physics 86(1) (2004) 132-136.

[10]. L. Junliang, Z. Yanwei, G. Cuijing, Z. Wei, Y. Xiaowei, One-step synthesis of barium hexaferrite nano-powders via microwave-assisted sol–gel auto-combustion, Journal of the European Ceramic society 30(4) (2010) 993-997.

[11]. M. Urbano-Peña, V. Salazar-Muñoz, S. Palomares-Sánchez, V. Compean-García, I. Betancourt, C.B.-T. Girón, F. Ruiz, Optimization of magnetic properties: Investigating the interaction of synthesis temperature, particle size, and monodomain formation in barium hexaferrite synthesized by the Pechini method, Journal of Magnetism and Magnetic Materials 600 (2024) 172133.

[12]. Y. Leng, Materials characterization: introduction to microscopic and spectroscopic methods, John Wiley & Sons2013.

[13]. J.P. Sibilia, A guide to materials characterization and chemical analysis, John Wiley & Sons1996.

[14]. R.K. Goyal, Nanomaterials and nanocomposites: synthesis, properties, characterization techniques, and applications, CRC Press2017.

[15]. N. Yasmin, M.Z. Iqbal, M. Zahid, S.F. Gillani, M.N. Ashiq, I. Inam, S. Abdulsatar, M. Safdar, M. Mirza, Structural and magnetic studies of Ce-Zn doped M-type SrFe12O19 hexagonal ferrite synthesized by sol-gel auto-combustion method, Ceramics International 45(1) (2019) 462-467.

[16]. E. Lifshin, X-ray Characterization of Materials, John Wiley & Sons2008.

[17]. N.N. Greenwood, Mössbauer spectroscopy, Springer Science & Business Media2012.

[18]. B.C. Smith, Fundamentals of Fourier transform infrared spectroscopy, CRC press2011.

[19]. L.A. Lyon, C.D. Keating, A.P. Fox, B.E. Baker, L. He, S.R. Nicewarner, S.P. Mulvaney, M.J. Natan, Raman spectroscopy, Analytical Chemistry 70(12) (1998) 341-362.

[20]. R. Matshitse, Brunauer-Emmett-Teller (BET) surface area analysis, Rhodes Univ. Natl. Res. Found 384 (2010).

[21]. J. Lee, Y.-K. Hong, W. Lee, G.S. Abo, J. Park, N. Neveu, W.-M. Seong, S.-H. Park, W.-K. Ahn, Soft M-type hexaferrite for very high frequency miniature antenna applications, Journal of Applied Physics 111(7) (2012).

[22]. C. de Julian Fernandez, C. Sangregorio, J. de la Figuera, B. Belec, D. Makovec, A. Quesada, Progress and prospects of hard hexaferrites for permanent magnet applications, Journal of Physics D: Applied Physics 54(15) (2021) 153001.

[23]. K. Higuchi, S. Takahashi, H. Itoh, S. Naka, Synthesis of barium hexaferrite for magnetic recording media using the KCl flux system, Journal of materials science 23 (1988) 588-592.

[24]. M. Meshram, N.K. Agrawal, B. Sinha, P. Misra, Characterization of M-type barium hexagonal ferrite-based wide band microwave absorber, Journal of Magnetism and Magnetic Materials 271(2-3) (2004) 207-214.

[25]. F. Pereira, M. Santos, R. Sohn, J. Almeida, A. Medeiros, M. Costa, A. Sombra, Magnetic and dielectric properties of the M-type barium strontium hexaferrite (Ba x Sr 1– x Fe 12 O 19) in the RF and microwave (MW) frequency range, Journal of Materials Science: Materials in Electronics 20 (2009) 408-417.

[26]. M. Elansary, M. Belaiche, C.A. Ferdi, E. Iffer, I. Bsoul, New nanosized Gd–Ho–Sm doped M-type strontium hexaferrite for water treatment application: experimental and theoretical investigations, RSC advances 10(42) (2020) 25239-25259.

[27]. R. Jasrotia, J. Prakash, N. Thakur, K. Raj, A. Kandwal, P. Sharma, Advancements in doping strategies for enhancing applications of M-type hexaferrites: a comprehensive review, Progress in Solid State Chemistry (2023) 100427.

[28]. M. Abdellahi, A. Najfinezhad, S. Saber-Samanadari, A. Khandan, H. Ghayour, Zn and Zr co-doped M-type strontium hexaferrite: Synthesis, characterization and hyperthermia application, Chinese journal of physics 56(1) (2018) 331-339.

[29]. P. Křišťan, Nuclear magnetic resonance in magnetic systems, (2017).

[30]. I. Vedernykova, A. Koval, O. Antonenko, T. Chan, O. Shpychak, M. Marchenko, Synthesis, technology and analysis of nanoparticles of barium hexaferrite for creation of magnetically controlled drug delivery systems, (2018).

[31]. M. Suganya, J.K. Kumar, S. Anand, K.M. Racik, S. Muthupandi, S. Muniyappan, Electrochemical studies of novel X-type barium hexaferrite nanoplatelets for supercapacitor applications, Journal of Superconductivity and Novel Magnetism 35(3) (2022) 915-923.

[32]. M. Suganya, S. Anand, D. Mani, M.C. Vu, S. Muniyappan, K.M. Racik, S. Nandhini, J.K. Kumar, Fabrication of novel M-Type cobalt doped barium hexaferrite nanoplatelets/graphitic carbon nitride composite for efficient supercapacitor applications, Synthetic Metals 295 (2023) 117341.

Emerging Trends in ABO3 Perovskite Compounds: Synthesis and Applications

Kumar Rajesh Tejpal Singh[1], ShankarD.Bhatkute[1], Vipul B. Shinde[1], Deepak M. Sonawane[1], Nilkanth N Kapse[2],Vishal A. Pandit[2], Shivnarayan B. Bajaj[1]*

[1]Department of Physics, J. E. S. College, Jalna, MS, India- 431203

[2]Department of Physics, B.Raghunath ACS College, Parbhani, MS, India- 431401

[3]Department of Physics, Dr. Babasaheb Ambedkar Marathwada University, Aurangabad, (MS) India

Abstract :

Perovskite compounds of the ABO3 class are an area of research with significant potential due to their remarkable properties and wide range of uses. The ABO3 formula consists of elements A and B, which can be monovalent, divalent, trivalent, pentavalent, oxygen, and oxygen. Perovskite materials are crucial for the development of microelectronics and communications, solar cells, Light Amplification by Stimulated Emission of Radiation (LASER), light emitting diodes (LEDs), and various types of gas sensors. Additionally, these perovskites exhibit electric, dielectric, ferroelectric, piezoelectric, pyroelectric, magnetic, and thermal properties, CMR superconductivity, and photovoltaic properties. In this review, we discuss the various methods for synthesizing oxide perovskites and highlight their applications in different fields. The review aims to provide a comprehensive understanding of the synthesis and application of ABO3 perovskite compounds.

Keywords: ABO3 Perovskite compounds, Synthesis, Applications

I. INTRODUCTION

ABO_3 perovskite compounds are oxide materials that have a general formula of ABO_3[2]. These compounds are used for a variety of applications such as solid oxide fuel cells, piezoelectricity, ferroelectricity, water splitting, and electronic devices[1][5]. Due to their remarkable stability with respect to cation substitution, new compounds for such applications potentially await discovery[1]. The 12-fold coordinated A site can be occupied with low-valent and large-sized oxides, and the physical and chemical properties of perovskite oxides can be easily tuned through their structure flexibility[4].

Machine learning methods have been employed to identify perovskites from ABO_3 combinations formulated as constraint satisfaction problems[3][4]. Liu et al. trained a machine learning model for predicting the formability of perovskite with known ABO_3 compounds. The model was then used to classify 891 ABO_3 compounds from[4].

These ABO_3 perovskite compounds are important materials used in various applications such as solid oxide fuel cells, piezoelectricity, ferroelectricity, water splitting, and electronic devices. These compounds are highly stable with respect to cation substitution. Machine learning methods have been employed to identify perovskites from ABO_3 combinations formulated as constraint satisfaction problems.A nanometer is one

billionth of a meter, or the distance between two and twenty atoms, depending on the kind of atom. Changing the structure of matter on a scale of a few nanometres is referred to as "nanotechnology". Depending on whom you ask, it might imply anything from 0.1 nm (manipulating the arrangement of individual atoms) to 100 nm or more (anything smaller than microtechnology). The idea that materials and electronics may one day be created to exact atomic standards was initially put out by Richard Feynman in 1959. "As far as I can tell, the laws of Physics do not forbid the possibility of influencing things atom by atom." Gustav Rose first described perovskite in 1839. Later, Russian mineralogist L. A. Perovski gave the substance the name "perovskite." Today, the term "perovskite" refers to a group of substances having crystal structures similar to calcium titanate. Perovskites are often oxides, although some varieties can also be carbides, nitrides, halides, and hydrides.

Numerous electro-ceramic devices use oxides of the perovskite type. The most significant examples include the use of lead zirconate titanate (PZT) in generators, motors, ultrasonic transducers, actuators, capacitors, and non-volatile memories, as well as the use of barium titanate (BTO) for positive temperature coefficient resistors and multilayer ceramic capacitors. Perovskite structured materials are the subject of much research because of their numerous applications in several sectors [1]. A. Ries et al. created barium strontium titanate powder using the polymeric precursor technique, with a Ba/Sr ratio of 80/20. XRD, IR, BET, and SEM were used to describe the sample. Barium carbonate should not be used as a secondary phase, according to the regulations [2].

For the first time, C.N. George et al. produced nanocrystalline barium titanate by a modified combustion method in a single step. Utilizing thermogravimetric analysis, differential thermal analysis, and Fourier transform infrared spectroscopy, the phase purity of the nanopowders was investigated. As a function of frequency, the dielectric characteristics were investigated [3]. Y.B. Khollam et al. employed a straightforward oxalate precursor method to create barium-strontium titanate ($Ba_{1-x}Sr_xTiO_3$) particles. The powders formed are cubic, highly pure, stoichiometric, sub-micron-sized, with nearly uniform size and shape distribution, according to characterization studies on BSTO and BST powders using various physicochemicaltechniques, including micro- and chemical analysis, differential thermal analysis (DTA)/thermo-gravimetric analysis (TGA), XRD, FTIR, X-ray fluorescence (XRF), and scanning electron microscopy (SEM). Similar dielectric characteristics were displayed by the BST ceramics made from similar particles [4]. M.M. Vijatovi et al. investigated the electrical characteristics of ceramics with lanthanum-doped barium titanate. The polymeric precursor technique was used to create the ceramic nanopowders. Deeper dielectric properties showed that when lanthanum concentration rose, the classical to a diffuse type of BT Ferro-paraphrase transition altered. This assumption was supported by the calculated diffuseness factor, which was derived from the modified Curie-Weiss equation, which showed that the diffusivity rose as the lanthanum concentration did. One semicircle was seen in the impedance study, demonstrating that grains contributed to the overall resistivity, although overlapping was still conceivable since a PTCR effect appeared, suggesting the existence of grain boundary resistivity [5]. Wei Li et al. [6] investigated the structural and dielectric characteristics of lead-free $(Ba_{1-x}Ca_x)(Ti_{0.95}Zr_{0.05})O_3$ (x = 0.05-0.40) (BCZT) ceramics produced via solid-state reaction.

Phongthorn et al. investigated the phase development, microstructure, and dielectric characteristics of $Ba(Zr_{0.1}Ti_{0.9})O_3$ ceramics produced by burning. The sample sintered at 1400 C for 2 hours had the best morphology, greatest density, highest dielectric constant, and lowest dielectric loss. The Curie temperature, which was lower than BZT made using other techniques, was about 76 ^0C. Investigations into the microstructure, densification, and dielectric findings all corroborated one another [7]. M. Aparna et al. investigated the impact of lanthanum (La^{3+}) doping on the electrical and electromechanical characteristics of $Ba_{1-x}La_xTiO_3$and employed combined impedance and admittance spectroscopy to assess the impedance data. The

resonant and anti-resonant frequencies from vector admittance plots were used to derive the electromechanical parameters. When compared to pure barium titanate, the electromechanical coefficients for $Ba_{1-x}La_xTiO_3$ with x = 0–003 were found to be much higher [8]. For use in multi-layered capacitors, Pramod K. Sharma et al. investigated the dielectric characteristics of tape-cast $Ba_{0.65}Sr_{0.35}TiO_3$ produced from sol-gel [9]. P. A. Shcheglov et al. created a modified sol-gel method for making $BaTiO_3$ and $PbTiO_3$ ferroelectric thin films [10]. Dimple P. Dutta et al. investigated the phase development in Fe^{3+} doped $BaTiO_3$ nanocrystallites produced sonochemically. Structure, magnetism, and ferroelectric characteristics were thoroughly investigated [11].

II. Perovskites Synthesis Methods

Chemical, physical, and optical methods of production all affect the properties of perovskite materials. Additionally, it influences the shape and crystal structure of materials. One must select an appropriate synthesis (route) technique to create the material for the specified characteristics.

2.1 Ceramic Method

When comparing the two methods of the solid-state synthesis approach, mechanical ball milling and high energy ball milling, a hand mixer grinder utilizing a motor and a pistol, and high energy ball milling from 100 rpm to 1000 rpm to get extremely fine size particles are used (12). As a result of the fact that ceramics are produced using this method of solid-state synthesis, it is sometimes referred to as the ceramic method. The primary raw materials used are carbonates and oxides, which are initially in a solid state and are mixed and ground repeatedly. At room temperature, these materials do not chemically react with one another, so they are heated to high temperatures (700–1500 °C), where chemical reactions occur at a significant rate (13).

Waindich et al. (2009) [14] observed that the calcination of the materials $Ba_{1-x}Sr_xCo_{1-y}Fe_yO_3$ and $La_{0.3}Ba_{0.7}Co_{0.2}Fe_{0.8}O_3$ at 1200 °C for 24 hours and 1250 °C for 24 hours and 15 hours, respectively, produced undesirable porous materials. As shown by Nagai and colleagues [15] by processing $SrCo_{0.9}X_{0.1}O_3$ compounds (X as Ni, Cu, Zn, Cr, Fe, Al, Ga, In, Ce, Ti, Zr, Sn, V or Nb), certain compounds developed second phases. This was explained by the fact that certain cations were poorly soluble in the solid solution. In some instances, it was seen that tiny secondary phases formed when Ga was added to $La_{1-x}Sr_xFe_{1-y}Ga_yO_3$-compounds, producing La_2O_3 [17], which was not entirely incorporated into the A-site.

In other instances, $BaCo_{0.7}Fe_{0.2}Ta_{0.1}O_3$ sintered at temperatures over 900 °C produced pure perovskite structures whereas unreacted precursors persisted at lower temperatures [18]. These examples clearly show that the elements of the perovskite crystal structure can also have a direct impact on the sintering process.

2.2 Co-precipitation

When a solution containing soluble metal cations is combined with another solution known as a precipitation agent, supersaturation conditions are necessary for the co-precipitation technique. Fig. 4 depicts a broad schematic of this strategy. Cushing et al. [19] claim that in order to achieve the desired physical qualities, it is necessary to regulate crucial co-precipitation chemical reaction parameters such as temperature, mixing rate, pH, and concentration (i.e. morphology and particle size distribution). The co-precipitation process, in general, produces perovskites with high uniformity and purity. This is attributable to the careful monitoring of the chemical process, which is necessary to produce compounds without a metal cation shortage [20,21].

The decreased strontium hydroxide solubility across a wide pH range, which tends to not integrate strontium into the perovskite structure during the washing phases, brought attention to the need for precise regulation of this chemical reaction [22].

2.3 Sol-gel

Perovskites are made using several sol-gel procedures, including the Pechini, Alkoxide, and Alkoxide-Salt methods. Due to its adaptability in producing perovskite membranes, the Pechini technique became the most used for producing perovskites. The Pechini technique, which includes complexing ethylenediaminetetraacetic (EDTA)-Citrate before adding ethylene glycol, is the subject of this review. NH_3H_2O dosage is used to regulate pH. High purity and uniformity of perovskite structures, together with precise composition control of the end product, are this method's key benefits [23]. A schematic of the metal production process using citric acid or EDTA is shown in Figure 5. Six bonds connect the metal cation to EDTA. It has two different kinds of electron-donating groups, carboxylic and aliphatic amine, and when it is complexed with citric acid, the metal cation forms three bonds to hold it together [24]. Chelating agents are employed to stop partial metal segregation in the final product, which can be brought on by various interactions between metal ions in the solution [25]. combined with the addition of polyhydroxy alcohol. The chelates get polyesterized when the solution is heated, forming a cross-linked chain of metal atoms bound to organic radicals [26].

2.4 Hydrothermal Method

The hydrothermal method is followed under high pressure in autoclaves (15 MPa). It combines high pressures with temperatures between the material's critical temperature and the boiling point of water. It is essentially a sol-gel kind of approach that can provide superior particle size control [27]. For instance, $CaTiO_3$ was studied at 15 °C and 150 °C, as well as uncalcined and calcined materials at 1300 °C [28]. The X-ray pattern analysis revealed that neither sample had any contaminants, and the phases had comparable cell characteristics. Therefore, the calcination stage following the hydrothermal technique was not required in the instance of this particular material [29]. This approach is currently being developed.

III. Applications in ABO3 Perovskite Materials

The modification of ABO3 perovskite compounds with numerous different vacancies has been shown to enhance their physical-chemical characteristics, resulting in improved performance in a range of applications. These modifications have the potential to greatly improve the commercial viability of perovskite materials in a variety of fields. The desirable properties of perovskite materials have made them the subject of substantial research and investigation in recent years.

The potential applications of perovskite materials are numerous and diverse, ranging from catalytic redox processes and energy storage to gas sensors and photovoltaics. The unique properties of these materials, such as their high electron mobility, thermal stability, and catalytic activity, make them ideal for a wide range of applications.Perovskite materials find applications in diverse fields owing to their unique properties and versatile nature. Some of the areas in which perovskite materials are commonly used include:

3.1 Photocatalytic activity

Jiang Yinwe [30] reported an ABO_3 perovskite photocatalyst called $BaZn_{1/3}Nb_{2/3}O_3$ that, when exposed to UV light, splits water into H_2 and O_2.Zhi-XianWei [31] reports the photocatalytic activity of $LaFeO_3$ and $LaFe_{0.5}Mn_{0.5}O_{3-\delta}$ towards the degradation of methyl orange (MO) under sunlight irradiation. Compared to $LaFeO_3$, $LaFe_{0.5}Mn_{0.5}O_{3-\delta}$ has much better photocatalytic activity. By using an external magnetic field, $LaFe_{0.5}Mn_{0.5}O_{3-\delta}$ may be recycled and redispersed once again.Shuhua Dong [32] investigated the photodegradation of methylene blue which exhibits the highest degradation rate of 75% under an irradiation time of 150 min.

3.2 Photovoltaic solar cells

Ternary oxides, in particular ABO_3 type perovskites, have grown in favour of Photoanode-Based Dye-Sensitized Solar Cells (DSSC) photoanodes during the past ten years. ABO_3 perovskites have firmly established themselves as innovative over the conventional photoanode materials for DSSC due to their excellent physiochemical properties, supply of excellent photovoltaic performance, and simple modification method by altering the atomic composition of their constituents. Its future investigation is restricted by the absence of a review based on ABO_3 perovskites. Designing effective photoanode materials for DSSC also requires an understanding of a material's theoretical capabilities [33].B. Mouhib reported theoretical investigations of electronic structure and optical properties of S, Se, or Te doped perovskite $ATiO_3$ (A=Ca, Ba, and Sr) materials for eco-friendly solar cells [34].As a result, doped systems' optical conductivity and absorption coefficient are increased in the photovoltaic spectrum, particularly for $BaTiO3$ doped with 2.5% and 5% of Te. This makes $BaTiO3Te$ more suitable for solar devices than $CaTiO3Te$ and $SrTiO3Te$ compounds.

3.3 Other Applications

Perovskite materials are intensively researched by scientists due to their appealing qualities. The following list includes some of the many domains in which perovskite materials have extensive use.

SJ Skinner recent developments in perovskite-type materials for solid oxide fuel cell cathodes. e.g., $Gd_{0.7}Ca_{0.3}Co_{1-y}Mn_yO_3$ [23].Uchino K. reported piezoelectric perovskite as Sensors and actuatorse.g., $PbZr_xTi_{1-x}O_3$ [24].Mir LL and Fronteradescribed the use of a ferromagnetic tunnel in an anisotropic sensor and memory device as a perovskite material application as Magnetic memory devices; e.g., $Pt/La_2Co_{0.8}Mn_{1.2}O_6/Nb:SrTiO_3$ [25].Xu Y and Memmert U. reported Magnetic field sensors based on polycrystalline manganites with the application as Magnetic field sensors; e.g., $La_{0.67}Sr_{0.33}MnO_3$ and $La0_{.67}Ba_{0.33}MnO_3$ [26].The colossal magnetoresistive manganite-based ferroelectric field-effect transistor was researched by Zhao T et al. as an Electric field effect device; e.g., the heterostructure of $Pb(Zr_{0.2}Ti_{0.8})O_3/La_{0.8}Ca_{0.2}MnO_3$ [27].Ferroelectric and piezoelectric devices; e.g., $BaTiO_3$, $PbTiO_3$ [28].Mitra C, Raychaudhuri studied p-n diode with hole and electron-doped lanthanum manganites as Semiconducting electronic devices; e.g., $La_{0.7}Ca_{0.3}MnO_3/SrTiO_3/La_{0.7}Ce_{0.3}MnO_3$ [29]. Munoz JLG reports $Bi_{1-x}Sr_xMnO_3$ manganites (x = 0.40, 0.50) dielectric properties: influence of charge order at room temperature as application as High dielectric constant [30].Sleight AW investigated High-temperature superconductivity in the $BaPb_{1-x}Bi_xO_3$ system [31].Manh DH and Phong reported $La_{0.7}Sr_{0.3}MnO_3$ and the properties of AC magnetic heating for hyperthermia applications [32].Ding R researched Perovskite nanocrystals $KNi_{0.8}Co_{0.2}F_3$ as supercapacitors [33].

IV.Conclusion

In conclusion, perovskite compounds of the ABO_3 class have become a subject of intense research in recent years due to their remarkable properties and diverse range of applications.We have discussed various methods for synthesizing oxide perovskites and highlighted their numerous applications. We have examined the different synthesis techniques, such as solid-state reactions, sol-gel, and hydrothermal methods, and discussed the advantages and limitations of each method. We have also explored the various applications of ABO_3 perovskite compounds in different fields, including their use in solar cells, LEDs, gas sensors, and other technologies.As research on perovskite materials continues to progress, we can expect to see even more exciting applications in the future. The development of new synthesis techniques and improved understanding of the properties of these materials will lead to the creation of new and innovative applications. Additionally, the

exploration of new materials and their combinations will help to expand the range of applications of perovskite compounds.

Declaration and Competing interests

The authors have no conflicts of interest.

V. References

[1]. R.H. Mitchell, Perovskites: modern and ancient, (2002).

[2]. A. Ries, A. Simoes, M. Cilense, M. Zaghete, J.A. Varela, Barium strontium titanate powder obtained by polymeric precursor method, Materials characterization, 50 (2003) 217-221.

[3]. C. George, J. Thomas, H. Kumar, M. Suresh, V. Kumar, P. Wariar, R. Jose, J. Koshy, Characterization, sintering and dielectric properties of nanocrystalline barium titanate synthesized through a modified combustion process, Materials Characterization, 60 (2009) 322-326.

[4]. Y. Khollam, S. Deshpande, H. Potdar, S. Bhoraskar, S. Sainkar, S. Date, Simple oxalate precursor route for the preparation of barium–strontium titanate: Ba 1– x Sr x TiO 3 powders, Materials Characterization, 54 (2005) 63-74.

[5]. M.V. Petrović, J. Bobić, T. Ramoška, J. Banys, B. Stojanović, Electrical properties of lanthanum doped barium titanate ceramics, Materials Characterization, 62 (2011) 1000-1006.

[6]. W. Li, Z. Xu, R. Chu, P. Fu, G. Zang, Structural and dielectric properties in the (Ba 1– x Ca x)(Ti 0.95 Zr 0.05) O3 ceramics, Current Applied Physics, 12 (2012) 748-751.

[7]. P. Julphunthong, T. Bongkarn, Phase formation, microstructure and dielectric properties of Ba (Zr 0.1 Ti 0.9) O 3 ceramics prepared via the combustion technique, Current Applied Physics, 11 (2011) S60-S65. 20

[8]. S M. Aparna, T. Bhimasankaram, S. Suryanarayana, G. Prasad, G. Kumar, Effect of lanthanum doping on electrical and electromechanical properties of Ba1– x La x TiO3, Bulletin of Materials Science, 24 (2001) 497-504.

[9]. K. Sharma, V. Varadan, V. Varadan, Dielectric properties of tape cast Ba0. 65Sr0. 35TiO3 derived from sol– gel for application in multilayered capacitors, Smart materials and structures, 12 (2003) 749.

[10]. P. Shcheglov, S. Men'shikh, L. Rybakova, Y.Y. Tomashpol'skii, Modified sol-gel process for the preparation of BaTiO3 and PbTiO3 ferroelectric films, Inorganic Materials, 36 (2000) 380-384.

[11]. D.P. Dutta, M. Roy, N. Maiti, A.K. Tyagi, Phase evolution in sonochemically synthesized Fe3+ doped BaTiO3 nanocrystallites: structural, magnetic and ferroelectric characterization, Physical Chemistry Chemical Physics, 18 (2016) 9758-9769.

[12]. Joshi Siddharth 1 et all Elsevier x-ray diffraction a simplistic approach for perovskite-based solar cell studies doi.org/10.1016/j.matpr.2019.05

[13]. Sadhukhan, P., Kundu, S., Roy, A., Ray, A., Maji, P., Dutta, H., Pradhan, S.K. and Das, S., 2018. Solvent-free solid-state synthesis of high-yield mixed halide perovskites for easily tunable composition and band gap. Crystal Growth & Design, 18(6), pp.3428-3432

[14]. A. Waindich, A. Möbius, M. Müller, Corrosion of Ba1-xSrxCo1-yFeyO3-δ and La0.3Ba0.7Co0.2Fe0.8O3-δ materials for oxygen separating membranes under Oxycoal conditions, J. Memb. Sci. 337 (2009) 182–187. 29

[15]. T. Nagai, W. Ito, T. Sakon, Relationship between cation substitution and stability of perovskite structure in SrCoO3-δ - based mixed conductors, Solid State Ionics. 177 (2007) 3433–3444.

[16]. E. Juste, A. Julian, G. Etchegoyen, P.M. Geffroy, T. Chartier, N. Richet, et al., Oxygen permeation, thermal and chemical expansion of (La, Sr)(Fe, Ga)O3–d perovskite membranes, J. Memb. Sci. 319 (2008) 185–191.

[17]. H. Luo, Y. Wei, H. Jiang, W. Yuan, Y. Lv, J. Caro, et al., Performance of a ceramic membrane reactor with high oxygen flux Ta-containing perovskite for the partial oxidation of methane to syngas, J. Memb. Sci. 350 (2010) 154–160.

[18]. Y. Cheng, H. Zhao, D. Teng, F. Li, X. Lu, W. Ding, Investigation of Ba fully occupied A-site BaCo0.7Fe0.3-xNbxO3-δ perovskite stabilized by low concentration of Nb for oxygen permeation membrane, J. Memb. Sci. 322 (2008) 484–490.

[19]. Yin, Jiang; Zou, Zhigang; Ye, Jinhua (2004).The Journal of Physical Chemistry B, 108(34), 12790–12794.

[20]. Zhi-Xian Wei, Yan Wang, Ji-Ping Liu, Cai-Mei Xiao, Wei-Wei Zeng,Materials Chemistry and Physics, Volume 136, Issues 2–3, 2012.

[21]. Bhojanaa, K. B., et al. "Account of Structural, Theoretical, and Photovoltaic Properties of ABO3 Oxide Perovskites Photoanode-Based Dye-Sensitized Solar Cells." *Solar RRL* 6.2 (2022): 2100792.

[22]. Mouhib, B., et al. "Theoretical investigations of electronic structure and optical properties of S, Se or Te doped perovskite ATiO3 (A= Ca, Ba, and Sr) materials for eco-friendly solar cells." *Micro and Nanostructures* 163 (2022): 107124.

[23]. Skinner SJ. Recent advances in perovskite-type materials for solid oxidefuel cell cathodes. International Journal of Inorganic Materials. 2001;**3**:113-121

[24]. Uchino K. Glory of piezoelectric perovskites. Science and Technology of Advanced Materials.2015;**16**:046001-0460016

[25]. Mir LL, Frontera C, Aramberri H, Bouzehouane K, Fernandez JC, Bozzo B, et al. Anisotropic sensor and memory device with a ferromagnetic tunnel **19** *Synthesis Techniques and Applications of Perovskite Materials* barrier as the only magnetic element. Scientific Reports. 2018;**8**:861-870

[26]. Xu Y, Memmert U, Hartmann U. Magnetic field sensors from polycrystalline manganites. Sensors and Actuators A. 2001;**91**:26-29

[27]. Zhao T, Ogale SB, Shinde SR, Ramesh R, Droopad R, Yu J, et al. Colossal magnetoresistive manganite-based ferroelectric field-effect transistor on Si. Applied Physics Letters. 2004; **84**:750-752

[28]. Nuraje N, Su K. Perovskite ferroelectric nanomaterials. Nanoscale. 2013;**5**:8752-8780

[29]. Mitra C, Raychaudhuri P, Kobernik G, Dorr K, Muller KH, Schultz L, et al. p-n diode with hole and electron-doped lanthanum manganites. Applied Physics Letters. 2001;**79**:2408-2410

[30]. Munoz JLG, Frontera C, Murias BR, Mira J. Dielectric properties of Bi1-x SrxMnO3 (x = 0.40, 0.50) manganites: Influence of room temperature charge order. Journal of Applied Physics.2009;**105**:084116-084120

[31]. Sleight AW, Gillson JL, Bierstedt PE. High-temperature superconductivity in the BaPb1–xBixO3 system. Solid State Communications. 1993;**88**:841-842

[32]. Manh DH, Phong PT, Nam PH, Tung DK, Phuc NX, Lee IJ. Structural and magnetic study of La0.7Sr0.3MnO3 nanoparticles and AC magnetic heating characteristics forhyperthermia applications. Physica B. 2014;**444**:94-102

[33]. Ding R, Li X, Shi W, Xu Q , Han X, Zhou Y, et al. Perovskite KNi0.8Co0.2F3 nanocrystals for supercapacitors. Materials Chemistry A. 2017;**5**:17822-17827

ABO₃ Perovskites as Emerging Materials in Biotechnology: Synthesis, Characterization, and Biological Applications

Shankar D. Bhatkute[1], Kalpana G. Joshi[2], Kumar Rajesh Tejpal Singh[1], Vipul B. Shinde[1], Vishal A. Pandit[3], Nilkanth N Kapse[3], Shivnarayan B. Bajaj[1]*

[1]Department of Physics, J. E. S. College, Jalna, MS, India- 431203

[2]Department of Electrical Engineering, Sanjivani K.B.P. Polytechnic, Kopargaon, Dist. Ahmednagar.

[3]Department of Physics, B.Raghunath ACS College, Parbhani, MS, India- 431401

Abstract :

ABO₃ perovskites have gained increasing attention as versatile materials in biotechnology due to their unique structural, electrical, optical, and catalytic properties. This review highlights the recent advances in the synthesis, characterization, and biological applications of ABO₃ perovskites. Common synthesis methods such as sol-gel, hydrothermal, and co-precipitation are discussed, along with emerging green synthesis techniques that focus on sustainability and eco-friendliness. Characterization techniques, including X-ray diffraction (XRD), Fourier transform infrared spectroscopy (FTIR), scanning electron microscopy (SEM), and UV-Vis spectroscopy, are reviewed to illustrate their role in understanding the structural, morphological, and surface properties of ABO₃ perovskites. The paper further explores the broad range of biological applications of these materials, including drug delivery systems, antimicrobial agents, biosensors, cancer treatment, and tissue engineering. Additionally, the future prospects of ABO₃ perovskites in bioelectronics and their potential use in sustainable technologies, such as bioremediation, are discussed. ABO₃ perovskites show great promise in addressing current challenges in biotechnology and environmental sustainability, positioning them as key materials for future research and applications.

I. INTRODUCTION

ABO₃ perovskites, a class of materials with the general formula ABO_3, have emerged as promising candidates for applications in biotechnology due to their versatile structure and tunable physical and chemical properties. The flexibility in designing their structure, where the "A" and "B" sites can host a variety of metal ions, allows for the modification of electrical, optical, and magnetic characteristics, making them suitable for a wide range of biological applications. As noted by Bacha et al. [20], the tunability of these materials provides significant advantages in various applications, including environmental biotechnology.

Moreover, perovskites exhibit remarkable stability, high surface area, and biocompatibility, which further enhances their potential in biotechnology. According to de Oliveira et al. [1], these materials are particularly suitable for use in drug delivery, antimicrobial agents, and biosensors, thanks to their structural properties and

chemical flexibility. These characteristics allow ABO₃ perovskites to outperform traditional biomaterials in several critical areas of biotechnology, offering enhanced functionality and biocompatibility.

In recent years, ABO₃ perovskites have been explored for use in drug delivery systems, biosensors, antimicrobial agents, tissue engineering, and cancer treatment. According to Bacha et al. [20], these materials provide unique advantages over conventional materials due to their capacity for controlled release in drug delivery and their responsiveness to specific biological stimuli, making them highly efficient in therapeutic applications.

Environmental sustainability and the development of advanced materials for biotechnology have also driven interest in green synthesis methods for ABO₃ perovskites. As de Oliveira et al. [6] highlighted, there has been a growing shift toward eco-friendly synthesis approaches, such as sol-gel and hydrothermal methods, that utilize bio-based materials and non-toxic reagents. This shift not only reduces the environmental impact but also improves the biocompatibility of the resulting materials, further enhancing their potential in medical and environmental biotechnology.

This review aims to provide a comprehensive overview of recent advancements in the synthesis, characterization, and biological applications of ABO₃ perovskites. It will cover their use in emerging fields such as environmental remediation, antimicrobial applications, and controlled drug delivery systems, while also addressing the challenges and future directions for this class of materials in biotechnology, as discussed by Bacha et al. [20] and de Oliveira et al. [9].

II. Synthesis of ABO₃ Perovskites

The synthesis of ABO₃ perovskites plays a critical role in determining their structural, morphological, and functional properties, which directly influence their applicability in biotechnology. Over the years, several synthesis methods have been developed to achieve controlled particle size, morphology, and composition. Among the commonly used methods are the sol-gel, hydrothermal, and co-precipitation techniques, each offering distinct advantages. In addition, there has been a growing interest in developing environmentally friendly and biologically based synthesis methods, as highlighted by recent studies.

Common Synthesis Methods

Sol-Gel Method

The sol-gel method is one of the most widely used techniques for synthesizing ABO₃ perovskites. In this process, a solution of metal precursors is converted into a gel through hydrolysis and polymerization reactions, followed by heat treatment to form the final crystalline perovskite structure. According to Navas et al. [21], this method offers precise control over the chemical composition and allows for the synthesis of highly homogeneous materials. Additionally, the sol-gel process enables the production of nanoparticles with uniform size distribution and controlled porosity, which are essential for applications in drug delivery and biosensors. The low processing temperature and versatility in precursor selection make this method particularly attractive for large-scale production.

Hydrothermal Method

The hydrothermal method is another prominent synthesis technique, often used to control particle size and morphology. In this method, the reaction is carried out in an aqueous solution at elevated temperatures and pressures, which promotes the crystallization of perovskites. Bacha et al. [20] highlighted that this method offers superior control over the crystallinity and phase purity of the synthesized materials. The hydrothermal

approach is especially advantageous for producing nanostructured perovskites with tailored morphology, which is crucial for enhancing their functionality in biological applications, such as biosensors and tissue engineering. The ability to achieve highly crystalline structures at relatively low temperatures makes this method energy-efficient and scalable.

Co-Precipitation and Solid-State Reactions

The co-precipitation and solid-state reaction methods are alternative routes for synthesizing ABO_3 perovskites. Co-precipitation involves the simultaneous precipitation of metal ions from a solution, followed by calcination to form the perovskite structure. This method is simple, cost-effective, and allows for large-scale production. As de Oliveira et al. [9] noted, co-precipitation is particularly useful for synthesizing perovskites with a uniform distribution of metal ions, which is important for achieving consistent properties in biological applications.

On the other hand, solid-state reactions involve mixing the metal oxide precursors and heating them at high temperatures to form the perovskite phase. While this method typically requires higher temperatures, it is widely used for the synthesis of bulk materials and is known for producing highly stable crystalline structures. Despite its limitations, solid-state synthesis remains a reliable method for producing ABO_3 perovskites with excellent thermal and chemical stability, which can be advantageous in specific biotechnological applications requiring durable materials.

Emerging Green Synthesis Techniques

In response to growing environmental concerns, researchers have begun exploring green synthesis methods for ABO_3 perovskites, focusing on using biologically derived materials and eco-friendly processes. According to de Oliveira et al. [6], green synthesis techniques involve the use of plant extracts, microbes, or other biological agents to reduce and stabilize metal ions, thus avoiding the need for toxic chemicals. These methods not only minimize the environmental impact but also enhance the biocompatibility of the resulting perovskites, making them more suitable for use in biomedical applications.

For example, plant-based synthesis leverages natural reducing agents present in plant extracts to drive the formation of perovskite nanostructures. This approach, as discussed by da Silva Júnior et al. [9], offers a sustainable and cost-effective alternative to conventional methods, while also introducing additional functional properties due to the presence of biomolecules from the plant extracts. Similarly, microbial-assisted synthesis utilizes bacteria or fungi to facilitate the formation of perovskite nanoparticles. These green approaches are gaining traction in the field of biotechnology, as they align with the principles of sustainability and green chemistry.

In conclusion, the synthesis of ABO_3 perovskites can be tailored to meet the specific needs of various biotechnological applications through a variety of traditional and emerging methods. Each synthesis technique offers unique advantages in terms of particle size, morphology, and environmental impact, allowing researchers to choose the most suitable approach for their intended application.

III. Characterization of ABO_3 Perovskites

The characterization of ABO_3 perovskites is essential to understand their structural, morphological, surface, optical, and electrical properties, which determine their suitability for various biotechnological applications. Advanced characterization techniques provide valuable insights into the material's composition, phase purity, particle size, surface area, and functional properties.

Structural Analysis

X-ray Diffraction (XRD)

X-ray diffraction (XRD) is one of the most widely used techniques to confirm the crystalline structure of ABO_3 perovskites. XRD provides detailed information about the crystal phase, lattice parameters, and degree of crystallinity by analyzing the diffraction patterns generated when X-rays interact with the material's atomic structure. According to Bacha et al. [20], XRD is crucial for confirming the formation of the desired perovskite phase and ensuring phase purity. Additionally, XRD patterns can be used to calculate crystallite sizes using the Scherrer equation, providing insights into the nanostructured nature of the materials, which is important for applications in drug delivery and biosensors.

Fourier Transform Infrared Spectroscopy (FTIR) and Raman Spectroscopy

Fourier Transform Infrared Spectroscopy (FTIR) and Raman spectroscopy are essential tools for studying the bonding and vibrational modes in ABO_3 perovskites. FTIR measures the absorption of infrared light by the material, revealing information about the functional groups, metal-oxygen bonding, and the presence of any organic components in the material. As described by de Oliveira et al. [9], FTIR is particularly useful for detecting changes in the bonding environment, which can impact the material's biocompatibility and chemical stability in biological applications.

Raman spectroscopy complements FTIR by providing information on the vibrational modes of the lattice and molecular interactions within the perovskite structure. Bacha et al. [20] noted that Raman analysis helps in identifying specific vibrational signatures that are critical in understanding the structural integrity and chemical interactions in perovskites, particularly for applications where the material needs to interact with biological systems.

Morphological Analysis

Scanning Electron Microscopy (SEM) and Transmission Electron Microscopy (TEM)

Scanning Electron Microscopy (SEM) and Transmission Electron Microscopy (TEM) are powerful tools for analyzing the morphology and particle size of ABO_3 perovskites. SEM provides high-resolution images of the surface topography and particle morphology, allowing researchers to observe the overall shape and size distribution of the particles. As highlighted by da Silva Júnior et al. [9], SEM is crucial for examining the surface features and aggregation of nanoparticles, which play a significant role in their functionality in biotechnology, such as in drug delivery or as antimicrobial agents.

TEM, on the other hand, offers even higher resolution imaging, allowing for the direct observation of the internal structure and crystal defects at the nanoscale. TEM is used to measure the particle size, confirm crystallinity, and investigate the formation of nanoparticle clusters, which are critical for understanding the material's performance in biological applications. According to Navas et al. [21], TEM is particularly important for visualizing the nanostructured features of perovskites, which influence their interactions with biological molecules.

Surface Properties

BET Surface Area Analysis

Brunauer-Emmett-Teller (BET) surface area analysis is a key technique used to determine the specific surface area of ABO_3 perovskites. This method involves measuring the adsorption of gas molecules onto the surface of the material to calculate the surface area and pore size distribution. Bacha et al. [20] emphasized that a high surface area is beneficial for many biotechnological applications, such as drug delivery, where increased surface

area allows for more efficient loading of therapeutic agents. Similarly, in biosensing applications, a larger surface area improves sensitivity by providing more active sites for interactions with biological molecules.

Optical and Electrical Properties

UV-Vis Spectroscopy and Dielectric Property Studies

UV-Vis spectroscopy is commonly employed to study the optical properties of ABO_3 perovskites. This technique measures the absorbance and transmittance of light through the material, providing information about its band gap and optical activity. According to de Oliveira et al. [6], understanding the optical properties of perovskites is essential for applications in biosensors, where light absorption can be used to detect specific biological markers or pollutants. Additionally, the band gap of the material can be tuned to optimize its performance in photocatalytic and optoelectronic applications.

Dielectric property studies, which involve measuring the material's ability to store and transfer electrical energy, are important for assessing the suitability of ABO_3 perovskites for applications in bioelectronics and sensors. Bacha et al. [20] noted that the dielectric constant and loss factor of perovskites are key parameters in designing devices for biological sensing, where electrical signals are used to monitor biological processes or detect pathogens.

In conclusion, the characterization of ABO_3 perovskites using a combination of structural, morphological, surface, optical, and electrical techniques is essential for optimizing their properties for biotechnological applications. Each method provides valuable insights into the material's behavior and performance, ensuring that ABO_3 perovskites are suitable for use in drug delivery, biosensing, antimicrobial agents, and other emerging fields in biotechnology.

IV. Biological Applications of ABO₃ Perovskites

ABO_3 perovskites have garnered significant attention for their diverse applications in biotechnology, particularly in areas like drug delivery, antimicrobial treatments, biosensing, cancer therapy, and tissue engineering. Their unique structural, optical, and chemical properties make them ideal candidates for a variety of biomedical applications, where factors such as biocompatibility, stability, and functionality are of utmost importance.

Drug Delivery Systems

ABO_3 perovskites are highly effective as carriers for drug molecules, offering advantages such as high loading capacity, controlled release, and enhanced biocompatibility. Due to their tunable surface properties and porosity, these materials can be engineered to encapsulate drugs and release them in a controlled manner, thereby improving therapeutic outcomes. Bacha et al. [20] have emphasized that the structural stability of ABO_3 perovskites, coupled with their ability to respond to external stimuli such as pH or temperature changes, makes them particularly suitable for targeted drug delivery systems. Additionally, their biocompatibility ensures minimal adverse reactions when used in the human body, making them ideal for long-term therapeutic applications.

Antimicrobial Agents

ABO_3 perovskites have shown considerable promise as antimicrobial agents, thanks to their ability to inhibit bacterial growth and promote wound healing. The inherent structural properties of these materials, such as their high surface area and reactive oxygen species (ROS) generation capabilities, allow them to effectively kill or inhibit the proliferation of harmful microbes. As de Oliveira et al. [9] noted, ABO_3 perovskites can be used to

coat medical devices, implants, or wound dressings to prevent bacterial infections, thus enhancing patient outcomes in medical settings. Their long-lasting antimicrobial activity, combined with minimal toxicity to human cells, makes them an attractive alternative to conventional antibiotics, particularly in the context of rising antibiotic resistance.

Biosensors

One of the most promising applications of ABO_3 perovskites in biotechnology is their use in biosensors. Due to their excellent electrical and optical properties, perovskites are being employed in the design of highly sensitive and selective biosensors for detecting biomolecules, pathogens, and environmental pollutants. According to de Oliveira et al. [6], ABO_3 perovskites can be functionalized with specific biological molecules or antibodies, enabling them to selectively detect targets such as enzymes, proteins, or nucleic acids. Their high surface area and ability to conduct electrical signals make them ideal for use in electrochemical or optical biosensors, where even trace amounts of analytes can be detected with high precision. This makes ABO_3 perovskites particularly useful for applications in medical diagnostics, environmental monitoring, and food safety.

Cancer Treatment

In the field of cancer therapy, ABO_3 perovskites are being explored for their potential in photothermal and photodynamic therapies. These therapies involve the use of materials that can absorb light and convert it into heat (photothermal) or generate reactive oxygen species (ROS) upon light irradiation (photodynamic), leading to the destruction of cancer cells. Bacha et al. [20] highlighted that ABO_3 perovskites can be engineered to exhibit strong light absorption in the near-infrared (NIR) region, allowing them to target and kill cancer cells with minimal damage to surrounding healthy tissues. Additionally, the ability to combine photothermal and photodynamic effects in a single material enhances the efficacy of the treatment, making ABO_3 perovskites promising candidates for non-invasive cancer therapies.

Tissue Engineering

ABO_3 perovskites are also gaining attention in the field of tissue engineering, where they are being investigated for their potential in regenerative medicine and tissue scaffolding. The structural stability and bioactivity of these materials make them ideal candidates for creating scaffolds that can support the growth and differentiation of cells, aiding in the regeneration of damaged tissues. As noted by da Silva Júnior et al. [9], ABO_3 perovskites can be used to fabricate biocompatible and biodegradable scaffolds that promote cell adhesion, proliferation, and differentiation. Their ability to release bioactive ions, such as calcium or magnesium, further enhances their utility in tissue engineering applications, where they can aid in the repair of bone, cartilage, or other tissues.

In conclusion, ABO_3 perovskites are emerging as versatile and effective materials in biotechnology, offering a range of applications from drug delivery and antimicrobial treatments to biosensing and cancer therapies. Their unique combination of structural stability, biocompatibility, and tunable properties makes them ideal for a variety of biomedical applications, paving the way for their broader adoption in the field of biotechnology.

V. Future Prospects in Biotechnology

The unique properties of ABO_3 perovskites, such as their tunable electrical, optical, and structural characteristics, make them promising candidates for future applications in biotechnology. As the field advances, ABO_3 perovskites are being increasingly explored for their potential in bioelectronics and eco-friendly applications, where their multifunctionality can address both technological and environmental challenges.

ABO₃ Perovskites in Bioelectronics

One of the most exciting prospects for ABO₃ perovskites in biotechnology is their potential application in bioelectronics. Bioelectronics involves the integration of electronic devices with biological systems to monitor or modulate biological functions. Due to their excellent electrical conductivity, tunable electronic properties, and biocompatibility, ABO₃ perovskites are emerging as key materials for the development of biocompatible electronic devices and neural interfaces. As Bacha et al. [20] pointed out, ABO₃ perovskites can be engineered to exhibit piezoelectric or ferroelectric properties, which are crucial for applications such as implantable sensors, neural probes, and bio-batteries.

In the field of neural interfaces, ABO₃ perovskites have the potential to improve the performance of devices that interact with the nervous system by facilitating efficient signal transmission between biological tissues and electronic circuits. These materials can be used to develop advanced electrodes that are both conductive and biocompatible, enhancing the longevity and functionality of neural implants. Additionally, their tunable properties allow for the development of flexible, stretchable electronics that can conform to biological tissues, making them ideal for wearable bioelectronics and next-generation prosthetics.

Sustainability and Eco-Friendly Applications

As global focus shifts toward sustainability, ABO₃ perovskites are being explored for their potential in eco-friendly applications, particularly in bioremediation and environmental clean-up technologies. Bioremediation is the process of using materials or biological organisms to remove or neutralize pollutants from the environment, and ABO₃ perovskites have shown great promise in this area due to their high catalytic activity and ability to degrade organic pollutants.

According to da Silva Júnior et al. [9], ABO₃ perovskites can be used as photocatalysts to break down toxic pollutants in water and soil, offering a sustainable solution for environmental remediation. These materials can harness sunlight to activate photocatalytic reactions, leading to the degradation of organic contaminants such as pesticides, dyes, and pharmaceutical waste. Their ability to generate reactive oxygen species (ROS) under light irradiation enhances their effectiveness in destroying harmful substances, making them ideal candidates for green and sustainable technologies.

In addition to their role in bioremediation, ABO₃ perovskites are being investigated for use in the development of sustainable energy solutions. Bacha et al. [20] highlighted the potential of perovskites in solar energy harvesting and conversion, where they can be integrated into photovoltaic devices for eco-friendly energy generation. The use of perovskites in energy applications complements their role in environmental sustainability, contributing to the broader goals of reducing carbon emissions and promoting green technologies. In conclusion, the future prospects for ABO₃ perovskites in biotechnology are vast and promising. Their applications in bioelectronics and eco-friendly technologies highlight their multifunctionality and versatility, paving the way for innovative solutions to both technological and environmental challenges. As research continues to advance, ABO₃ perovskites are poised to play a key role in the development of next-generation biotechnological devices and sustainable technologies.

VI. Conclusion

ABO₃ perovskites have emerged as highly versatile materials with significant potential in various biotechnological applications due to their unique structural, electrical, optical, and catalytic properties. From drug delivery systems to biosensors, antimicrobial agents, cancer therapies, and tissue engineering, ABO₃

perovskites offer numerous advantages, including controlled drug release, biocompatibility, and the ability to interact with biological systems at both the molecular and cellular levels. The diverse synthesis methods, such as the sol-gel and hydrothermal techniques, allow for precise control over particle size, morphology, and composition, while emerging green synthesis methods contribute to environmental sustainability.

In addition to their current applications, ABO_3 perovskites hold great promise for the future of biotechnology. Their role in bioelectronics, particularly in biocompatible electronics and neural interfaces, opens new pathways for integrating biological systems with advanced electronic devices. Furthermore, their potential in sustainable technologies, especially in environmental remediation and renewable energy generation, positions them as key materials in the global shift toward eco-friendly solutions.

As research continues to explore and expand the capabilities of ABO_3 perovskites, their impact on biotechnology will likely grow, offering innovative solutions to complex biomedical and environmental challenges. By leveraging their unique properties and continuing to develop sustainable synthesis and application strategies, ABO_3 perovskites are set to play a transformative role in the future of biotechnology.

VII. References

[1]. de Oliveira, C.R.S.; da Silva Júnior, A.H.; Mulinari, J.; Ferreira, A.J.S.; da Silva, A. Fibrous Microplastics Released from Textiles: Occurrence, Fate, and Remediation Strategies. *J. Contam. Hydrol.* 2023, *256*, 104169. [CrossRef] [PubMed]

[2]. Pham, D.N.; Clark, L.; Li, M. Microplastics as Hubs Enriching Antibiotic-Resistant Bacteria and Pathogens in Municipal Activated Sludge. *J. Hazard. Mater. Lett.* 2021, *2*, 100014. [CrossRef]

[3]. Nishat, A.; Yusuf, M.; Qadir, A.; Ezaier, Y.; Vambol, V.; Ijaz Khan, M.; Ben Moussa, S.; Kamyab, H.; Sehgal, S.S.; Prakash, C.; et al. Wastewater Treatment: A Short Assessment on Available Techniques. *Alex. Eng. J.* 2023, *76*, 505–516. [CrossRef]

[4]. da Silva Júnior, A.H.; Mulinari, J.; de Oliveira, P.V.; de Oliveira, C.R.S.; Reichert Júnior, F.W. Impacts of Metallic Nanoparticles Application on the Agricultural Soils Microbiota. *J. Hazard. Mater. Adv.* 2022, *7*, 100103. [CrossRef]

[5]. Huang, X.; Wen, D.; Wang, J. Radiation-Induced Degradation of Sulfonamide and Quinolone Antibiotics: A Brief Review. *Radiat. Phys. Chem.* 2024, *215*, 111373. [CrossRef]

[6]. de Oliveira, C.R.S.; da Silva Júnior, A.H.; Mulinari, J.; Immich, A.P.S. Textile Re-Engineering: Eco-Responsible Solutions for a More Sustainable Industry. *Sustain. Prod. Consum.* 2021, *28*, 1232–1248. [CrossRef]

[7]. Junaid, M.; Zainab, S.M.; Xu, N.; Sadaf, M.; Malik, R.N.; Wang, J. Antibiotics and Antibiotic Resistant Genes in Urban Aquifers. *Curr. Opin. Environ. Sci. Health* 2022, *26*, 100324. [CrossRef]

[8]. Larsson, D.G.J.; Flach, C.-F. Antibiotic Resistance in the Environment. *Nat. Rev. Microbiol.* 2022, *20*, 257–269. [CrossRef]

[9]. da Silva Júnior, A.H.; de Oliveira, C.R.S.; Leal, T.W.; Mapossa, A.B.; Fiates, J.; Ulson de Souza, A.A.; Ulson de Souza, S.M.d.A.G.; da Silva, A. Organochlorine Pesticides Remediation Techniques: Technological Perspective and Opportunities. *J. Hazard. Mater. Lett.* 2024, *5*, 100098. [CrossRef]

[10]. de la Fuente-Nunez, C.; Cesaro, A.; Hancock, R.E.W. Antibiotic Failure: Beyond Antimicrobial Resistance. *Drug Resist. Updat.* 2023, *71*, 101012. [CrossRef]

[11]. Song, L.; Yang, S.; Gong, Z.; Wang, J.; Shi, X.; Wang, Y.; Zhang, R.; Wu, Y.; Wager, Y.Z. Antibiotics and Antibiotic-Resistant Genes in Municipal SolidWaste Landfills: Current Situation and Perspective. *Curr. Opin. Environ. Sci. Health* 2023, *31*, 100421. [CrossRef]

[12]. Uddin, T.M.; Chakraborty, A.J.; Khusro, A.; Zidan, B.R.M.; Mitra, S.; Emran, T.B.; Dhama, K.; Ripon, M.K.H.; Gajdács, M.; Sahibzada, M.U.K.; et al. Antibiotic Resistance in Microbes: History, Mechanisms, Therapeutic Strategies and Future Prospects. *J. Infect. Public Health* 2021, *14*, 1750–1766.

[13]. Yan, F.; An, L.; Xu, X.; Du, W.; Dai, R. A Review of Antibiotics in SurfaceWater and Their Removal by Advanced Electrocoagulation Technologies. *Sci. Total Environ.* 2024, *906*, 167737. [CrossRef] [PubMed]

[14]. Stylianou, M.; Christou, A.; Michael, C.; Agapiou, A.; Papanastasiou, P.; Fatta-Kassinos, D. Adsorption and Removal of Seven Antibiotic Compounds Present in Water with the Use of Biochar Derived from the Pyrolysis of Organic Waste Feedstocks. *J. Environ. Chem. Eng.* 2021, *9*, 105868. [CrossRef]

[15]. Choi, K.-J.; Kim, S.-G.; Kim, S.-H. Removal of Antibiotics by Coagulation and Granular Activated Carbon Filtration. *J. Hazard. Mater.* 2008, *151*, 38–43. [CrossRef] [PubMed]

[16]. Amaly, N.; EL-Moghazy, A.Y.; Nitin, N.; Sun, G.; Pandey, P.K. Design, Preparation, and Application of Novel Multilayer Metal-Polyphenol Composite on Macroporous Framework Melamine Foam for Effective Filtration Removal of Tetracycline in Fluidic Systems. *Sep. Purif. Technol.* 2023, *321*, 124238. [CrossRef]

[17]. Kontogiannis, A.; Evgenidou, E.; Nannou, C.; Bikiaris, D.; Lambropoulou, D. MOF-Based Photocatalytic Degradation of the Antibiotic Lincomycin Enhanced by Hydrogen Peroxide and Persulfate: Kinetics, Elucidation of Transformation Products and Toxicity Assessment. *J. Environ. Chem. Eng.* 2022, *10*, 108112. [CrossRef]

[18]. Anuar, N.F.; Iskandar Shah, D.R.S.; Ramli, F.F.; Md Zaini, M.S.; Mohammadi, N.A.; Mohamad Daud, A.R.; Syed-Hassan, S.S.A. The Removal of Antibiotics inWater by Chemically Modified Carbonaceous Adsorbents from Biomass: A Systematic Review. *J. Clean. Prod.* 2023, *401*, 136725. [CrossRef]

[19]. Zheng, J.; Zhang, P.; Li, X.; Ge, L.; Niu, J. Insight into Typical Photo-Assisted AOPs for the Degradation of Antibiotic Micropollutants: Mechanisms and Research Gaps. *Chemosphere* 2023, *343*, 140211. [CrossRef]

[20]. Bacha, A.-U.-R.; Nabi, I.; Chen, Y.; Li, Z.; Iqbal, A.; Liu, W.; Afridi, M.N.; Arifeen, A.; Jin, W.; Yang, L. Environmental Application of Perovskite Material for Organic Pollutant-Enriched Wastewater Treatment. *Coord. Chem. Rev.* 2023, *495*, 215378. [CrossRef]

[21]. Navas, D.; Fuentes, S.; Castro-Alvarez, A.; Chavez-Angel, E. Review on Sol-Gel Synthesis of Perovskite and Oxide Nanomaterials. *Gels* 2021, *7*, 275. [CrossRef]

Complex Numbers : Bridging Theory and Application in Signal Analysis

Dr. Dhanashri A. Munot*, Dr. Aruna M. Kulkarni

*Department of Mathematics, SAJVPM'S Smt. S. K. Gandhi Arts, Amolak Science and P. H. Gandhi Commerce College, Kada. 414202 (MS) India

Main Author Email-Id: dhnshrmunot50@gmail.com

Abstract :

Complex numbers, formerly thought to be mysterious, have become essential in a wide range of areas. Their applications go well beyond pure mathematics, influencing sectors such as engineering, physics, and finance. Embracing the potential of complex numbers has not only simplified complex problem-solving but also expanded our comprehension of the world around us. Complex numbers are used in signal analysis for a convenient description of periodically varying signals. This use is also extended into digital signal processing and digital image processing. In this article, we look closer at the application of complex numbers in analyzing signals and producing output.

Keywords: Complex Numbers, Digital Signal Processing, Digital Image Processing.

I. INTRODUCTION

Through the history of any scientific theory, we observe that developing the theory is not a work of any specific day; indeed, it results from continuous work for years together. Complex numbers are also not exceptions to that. The Roots of complex numbers can be traced back to the beginning of the 16th century[3]. Though the origin of complex numbers is in the sixteenth century by an Italian mathematician, Gerolamo Cardano, to solve cubic equations; it's 250 years later when complex numbers were given geometrical interpretation and became a useful tool for physics[4], where the real start took place[5]. Complex numbers represent an expansion of the conventional numbers used in everyday mathematics. One of its distinctive features is their ability to express and manipulate two variables as a single number[6]. complex numbers, also known as imaginary numbers, have a variety of applications in sciences and related areas such as signal processing [1,2], control theory, quantum mechanics, electromagnetism, cartography, vibration analysis, and many more [7].

The use of complex numbers is very advantageous for modeling periodic processes, particularly in procedures that include phase differences. On paper, it is possible to consider a physical quantity as complex yet attribute physical significance solely to its real component. An alternative approach is to consider a complex number's real and imaginary components as two interconnected physical entities. In both instances, the form of complex numbers facilitates computations, although no physical significance is inherently ascribed to complex variables.

This feature of complex numbers fits very naturally with Fourier analysis, where the frequency domain comprises two signals, the real and the imaginary.

II. Geometric Interpretation of Complex Numbers

A number in the form *a+ib* where *a* and *b* are real numbers and $i = \sqrt{-1}$ is called a complex number.

We know that a set of real numbers is one dimension and can be visualized on a simple number line, whereas a set of complex numbers is two dimensions and requires a coordinate plane to visualize them. The complex number plane is constructed by arranging the real numbers on the horizontal axis and the imaginary numbers along the vertical axis.

For example, the complex number *a+ib* is represented as a point in Figure 1
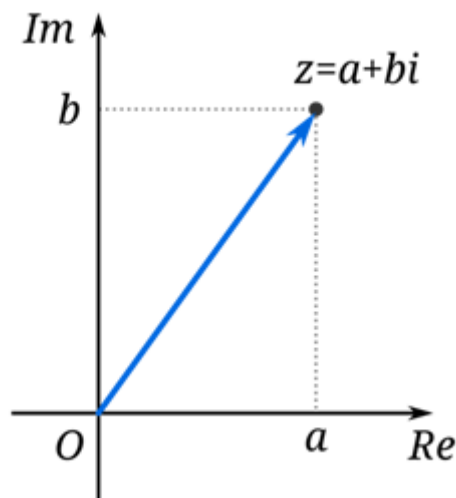
Figure 1

Complex numbers can also be represented in polar form. For a given point *a+ib* in the plane $\cos \phi = a/r$ and $\sin \phi = b/r$. Therefore, the complex number *a+ib* can also be represented as $r \cos \phi + i r \sin \phi$. The Euler relationship relates the trigonometric functions to a complex exponential as $e^{\pm i\phi} = \cos \phi \pm i \sin \phi$ for a number on the unit circle. Graphically, this relationship is represented as seen in Figure 2
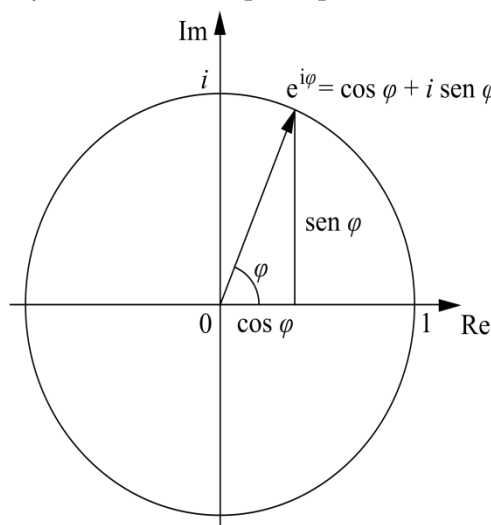
Figure 2

<div align="center">

III. Complex numbers in analyzing signals:

</div>

Complex numbers play a crucial role in signal processing, particularly in signal analysis, design, and manipulation.

a. Representation of signals:

One way to describe signals is as complex numbers, and phasors are particularly useful for sinusoidal signals. The amplitude and phase of a sinusoidal signal are represented by the magnitude and angle, respectively, in a phasor, which is a complex number.

The Fourier transform is a method for representing signals in the Fourier domain as sums of sinusoids. A complex number represents the frequency component of a time-domain signal, which the Fourier transform extracts. The cosine and sine components are represented by the real and imaginary parts, respectively.

b. Signal Analysis:

Spectral signal analysis allows engineers to examine the frequency content of signals by expressing them in the frequency domain using complex numbers. Understanding the behaviour of signals in various frequency bands, filtering them, and modulating them all depend on this.

Filters, modulation schemes, and other transformations in digital signal processing (DSP) algorithms rely heavily on complex numbers. The frequency spectrum of discrete signals may be computed using the Discrete Fourier Transform (DFT) or, more efficiently, the Fast Fourier Transform (FFT), both of which depend on complicated mathematics but is to understand due to use of complex numbers.

c. Quadrature Amplitude Modulation:

Modulated signals are represented in digital communication by complex numbers. By adjusting the amplitude and phase of a signal, QAM can encode data; the resultant signal is a complex number with real and imaginary parts. The complex numbers used to represent in-phase (I) and quadrature (Q) components are widely used in communication systems. This enables efficient signal modulation and demodulation, especially in radio frequency communications.

d. Filter design:

A fundamental tool in digital filter design, the Z-transform employs complex numbers to analyze and design filters. In the Z-domain, the poles and zeros of a filter are expressed as complex numbers, and their positioning dictates the filter's frequency response. The dynamics of a filter or system may be characterized by the positions of its poles and zeros on the complex plane. The placements of these poles and zeros have a direct influence on the system's stability and frequency properties.

e. Signal Synthesis and Reconstruction:

The inverse Fourier transform method is used to rebuild a time-domain signal from its frequency components. The process entails intricate mathematical calculations to merge the frequency components back into the initial signal. Complex exponentials are extensively used in signal generation to produce sinusoids with different frequencies. These elements serve as essential components in the creation of more intricate signals.

<div align="center">

IV. CONCLUSION

</div>

An attempt has been made to provide a variety of applications of complex numbers in analyzing and processing signals. The mathematical structure provided by complex numbers is robust and versatile, allowing for the analysis, processing, and manipulation of signals in the time and frequency domains. Spectral analysis,

reconstruction, filtering, and modulation are only a few of the many signal-related activities that may be handled efficiently and precisely with their help in signal processing.

V. REFERENCES

[1]. D. Zhang,"Modern signal processing." Walter de Gruyter GmbH & Co KG

[2]. T. Adali, P. Schreier and L. Scharf," Complex-valued signal processing: The proper way to deal with impropriety". IEEE Trans. on Signal Proc., vol.59, no. 11, pp.5101-5125, 2011.

[3]. A. Hirose, "Nature of complex number and complex-valued neural networks." Front. of Ele.and Ele. Engi. in Chi., vol. 6 , pp. 171-180, 2011.

[4]. R. Jain, S. Iyengar, "Advanced engineering mathematics". Alpha Science Int'l Ltd..2007.

[5]. D. Jie, "The discovery and development of imaginary number", Highlights in Science, Engineering and Technology, vol. 38, pp. 174-179, 2023.

[6]. K. Ricardo, " why are complex numbers needed in quantum mechanics?," Am. J. Phys., vol. 88, no. 39, pp. 39-45, 2020, doi: 10.1119/10.0000258

[7]. U.Gawarguru, M. Tibdewal,R. Naphade and R. Jethwani, "The review of introduction and application of complex number in engineering,"Nat. Conf. RISE 17 vol. 5, no. 9,2017, pp. 55-57.

A Real Life Applications of Wavelet Transform

Abhijit S. Jadhav*, Dr.Shrikisan B. Gaikwad

*Department of Mathematics, New Arts, Commerce and Science College, Ahmednagar, Maharashtra, India

Abstract :

The wavelet transform has emerged as an effective analytical tool for processing and analyzing complex data across different fields of Science and Technology. This paper explores a comprehensive overview of diverse applications of wavelet transform in the field of signal processing, image and audio compression, pattern recognition, medical imaging, time-frequency analysis, telecommunication, climate analysis, etc. The new advancements in wavelet transformations will continue main role in future advancements.

Keywords: Wavelet Transform, Image compression, Signal processing.

I. INTRODUCTION

Wavelet transform has become a fundamental tool in the fields of data analysis, signal processing, and pattern recognition due to its unique ability to provide both time and frequency localization. Though traditional Fourier analysis, which represents data purely in the frequency domain, wavelet transform allows for the simultaneous analysis of signals across multiple scales [1]. This capability makes wavelets particularly well-suited for analysing non-stationary signals, which are prevalent in real-world scenarios such as medical imaging, telecommunications, and financial data analysis [5].

The origins of wavelet theory can be traced back to the early 20th century, but its development accelerated in the late 20th century with the advent of digital computing. Wavelet transforms have since evolved to become a versatile and powerful tool, with applications extending far beyond the initial scope of mathematical research. Today, wavelet transform is integral to numerous practical applications, including image and audio compression, signal denoising, and time- frequency analysis. Its adaptability to various types of data and its effectiveness in preserving essential information while reducing data complexity have made it indispensable in both academic research and industrial practices.

The wavelet transform has a long history that comes out of the confluence of disparate mathematical ideas and practical problems. Wavelet theory evolved over the course of decades with contributions from many fields, such as mathematics, physics and engineering each working towards advancing wavelet theory for its refinement in new disciplines [7].

Joseph Fourier would do some foundational work in the early 19th century, introducing what we now call Fourier analysis a way of breaking down signals into sinusoidal parts. Fourier analysis [3] is capable of extracting hidden frequency information from non- stationary signals, so it became infeasible seeking new approaches. One of the simplest and earliest examples of a wavelet is what we now call the Haar wavelet,

introduced in 1909 by Alfred Haar as an orthonormal basis to represent data with both time frequency information [6].

Definition:

The wavelet transform [4] of a signal f(t) is defined as:

$Wf\ (a,\ b) = \int f(t)\ 1\ \sqrt{|a|}\ \psi * (\ \frac{t-b}{a}\ )dt\ \infty\ -\infty\ ,)dt$, where a is scaled parameter and b is translation parameter.

History and Development of Wavelet Transform:

Period	Contributor (s)	Key Contribution	Impact or Significance
Early 1900s	Joseph Fourier	Introduced Fourier analysis	frequency domain analysis
1909	Alfred Haar	Coined the term Haar wavelet	Introduced the first wavelet
1930s-1950s	Paul Lévy, Norbert Wiener	Early exploration of wavelet-like functions	Theoretical foundation of wavelets
1980s	Jean Morlet, Alex Grossmann	Developed the continuous wavelet transform	Established wavelets as a tool for seismic signal analysis
1988	Ingrid Daubechies	Daubechies wavelets	New way of digital signal processing with wavelets[2]
1989	Stéphane Mallat	Introduced MRA means Multiresoluti on Analysis	Provided the mathematic al framework for discrete wavelets
Late 1980s-1990s	Various	Application to image and signal processing	Wavelets became widely used in compression (e.g., JPEG 2000)
2000s-Present	Various	Ongoing research and new applications	Continued expansion in fields like machine learning and data science

II. DIFFERENCE BETWEEN FOURIER TRANSFORM AND WAVELET TRANSFORM

The Fourier Transform and Wavelet Transform are both powerful tools for signal analysis, but they have distinct differences in how they analyse and represent signals.

1. **Localization of Time-Frequency**
- Fourier transform provides frequency resolution but not time resolution.
- Wavelet transform provides both time and frequency resolution.

2. **Stationary-Non stationary signals**
- Fourier transform is suitable for stationary signal that is frequency content does not change over the time but it is not suitable for non-stationary signal.
- Wavelet transform is suitable for both stationary and non-stationary signal. It is useful for real world signals that have transient components.

3. **Basis Function**
- Fourier transform uses the sines and cosines that is sinusoidal as a basis function.
- Wavelet transform takes sinusoidal as well as other basis functions.

4. Resolution

- Fourier transform provides uniform frequency resolution over entire signal that can be limiting when trying to analyse signals that varying frequency over time.
- Wavelet transform offers multi resolution across entire signal and it is more flexible for analysing complex signals.

5. Computation and Efficiency

- The Fast Fourier transform algorithms gives efficient computation of Fourier transform which become a standard tool to analyse global frequency.
- Discrete wavelet transform helps in the computation of more complex problems that changes both time-frequency.

6. Applications

- Fourier transform used in communication, audio processing, spectrum analysis and filtering.
- Wavelet transform commonly used in signal and image compression, pattern recognition.

III.APPLICATIONS IN VARIOUS FIELDS

A. Image Compression

Wavelet transform helps in image compression by reducing the file size by decomposition method to get different wavelet coefficients. Wavelet coefficients represent different frequency components which divides the image into sub bands with image information in lower frequencies. In the process of decomposition, the inverse wavelet transform reconstructs image with same details. As compared to traditional methods such as JPEG, PNG it gives good quality of an image.
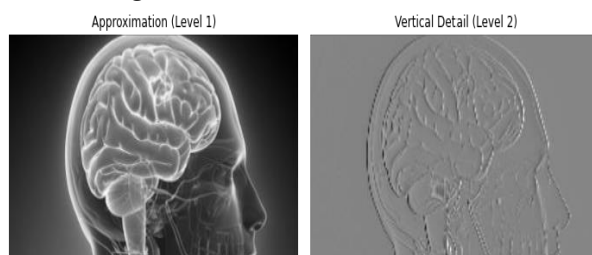
Figure 1: Image Compression

In this method audio signal decomposes into different wavelet coefficients which captures both high and low frequency components. Wavelet coefficient that contribute less in sound quality are quantized by reducing their precision to compress given data. The decomposition method contains decoding and then applying inverse wavelet transform to reconstruct the audio. This process helps in high sound quality at lower bit-rates. It is also suitable for the complex audio signal.

B. Denosing of Signal

Wavelet transform benefits in signal denoising by removing noise from a signal by preserving measure features of original signal. Wavelet coefficients of decomposed signal that separating noise means high frequency components in the original signal. The inverse wavelet transform reconstructs the signal with minimizing noise. Application of this method are in the field of background noise reduction and clearer representation of signal.

C.   Medical Imaging

Wavelet transform compresses the images of MRI, CT scans and X-ray in the medical field to get more details for diagnosis. Decomposed image into wavelet coefficients that separate significant information from noise and then by denosing we get clarity of critical images of tissues or tumors.Wavelet based compression method reduced the file size but accurate and clear visualization of patterns which helps for patient care.

D.   Recognition of Pattern

Wavelet transform pays vital role in pattern recognition that extracts information from data which is used to identify patterns. Decomposition of images or signals into different frequency components it captures details in different scale which makes effective for recognizing textures in images and audio signal in speech. Wavelet transform helps out in handwriting recognition, fingerprint recognition and facial recognition.

E.   Time-Frequency Analysis

Wavelet transform involves time frequency analysis for the examinations of signals that
changes after changing time. Wavelet transform provides both time-frequency localization while Fourier transform offers only frequency information. This non stationary signals with wavelet transform helps in the speech processing. Wavelet transform focus on particular time interval and frequency components that helps to capture sudden spikes in signals.

F.   Watermarking and Steganography

Wavelet transform is useful in the field of watermarking and Steganography to embed given data. Wavelet embedded a watermark into a video or image by modifying its components that ensures the watermark is robust against compression and manipulations. Hidden messages in stenography
are embedded in media by altering wavelet coefficients such a way that significantly after the audible or visible quality of the given content.

G.   Earthquake and Seismic Data Analysis

Wavelet transform is powerful tool in earthquake and seismic analysis to detect and then analyse seismic waves. Decomposition of seismic signals into various frequency components helps to identify arrival times of different seismic events.
Wavelet transform helps in filtering out noise from seismic data and enhanced the accuracy of monitoring systems.

H.   Climate Data Analysis

Wavelet transform is applied in climate data analysis to study of spatial and temporal patterns like temperature, weather and see level. Decomposition of signal in the form of time series data into various frequency components, it helps to identify trends, periodicities across time scales. In particular, for detecting long term climate change and also in short term change such as El Nino.

I.   Google Maps

Google map contain a large amount of data that needs to transmit quickly with clarity to the user. Wavelet transform is powerful tool to compress and efficiently transmit large amounts of map details data. Compression

of data enables smooth zooming in various levels and faster loading. It helps to display global view in details with good quality.

J.   Telecommunications

Wavelet transform is used in telecommunication for data compression, denosing of signal and error correction to improve reliability and efficiency of communication networks. Compression helps to transmit faster data without noising by reducing size. It improves quality and clarity of data transmission and voice. Wavelet makes reliable transmission in modern telecommunication.

IV. CONCLUSION

Wavelet transform provides powerful tools for analysing, decomposition and then processing given data. Because wavelet transform is embedded into many technologies and this process makes our daily lives more efficient and richer in terms of communication and data. Discussed applications overview the utility and versatility of wavelet transforms while handling multi-scale and complex data across different fields.

V. REFERENCES

[1].   Lokenath Debnath, Firdous Ahmad Shah, Wavelet Transforms and Their Applications, Springer publication, Second edition (2005).

[2].   I.Daubechies, Ten Lectures on Wavelets SIAM, Philadelphia, (1992).

[3].   M.Sifuzzaman, M.R.Islam and M.Z.Ali, Applications of Wavelet Transforms and its Advantages Compared to Fourier Transform Journal of Physical Sciences,Vol.13, 2009, 121-134

[4].   Manok Kumar, Sapna Pandit, Wavelet Transform and Wavelet Based Numerical Methods: An Introduction International Journal of Nonlinear Science Vol.13(2012) No.3, pp.325- 345.

[5].   Ashu Prakash, Wavelet and its Applications Article in International Journal of Scientific Research in Computer Science Engineering and Information Technology · November 2018.

[6].   C.KChui, An Introduction to Wavelet, Wavelet Analysis and Its Applications, vol. I Academic press, Boston, Mass, USA,1992.

[7].   P.S.Addison, The Illustrated Wavelet Transform Handbook: Introductory Theory and Applications Sciences, Engineering, Medicine and Finance, IOP,(2002).

Jump Operators on Time Scales

Bhagyashri N. Todkari*, Dr. Shrikisan B. Gaikwad

*Department of Mathematics, New Arts, Commerce and Science College, Ahmednagar-414001, Maharashtra, India

Abstract :

The fundamentals of time scale calculus, including the forward and backward jump operators, right and left scattered points, and dense points, are covered in this paper. To evaluate the forward jump operator, backward jump operator, and graininess function, we used several time scales. We also classified each point as either right or left scattered, left dense, or right dense. The fundamental characteristic for solving dynamic equations is an evaluation of jump operators.

Keywords: Backward jump operator, Forward jump operator, Time scale.

I. INTRODUCTION

Time scale calculus [2, 3, 4] is a new theory that combines the two approaches of dynamic modelling difference and differential equations. The theory of time scales, which has received much attention recently, was introduced by Stefan Hilger in his Ph. D thesis back in 1988 to unify continuous and discrete analysis. The theory of time-scale calculus is a critical and interesting area of research. By choosing a set of real numbers as the time scale, the general results yield a result concerning an ordinary differential equation. The same general results were yielded for the difference equation by selecting a set of integers as the time scale.

We need to carefully consider the implications of such a revolutionary theory in the field of mathematics. The potential applications could be vast and impactful. The time scale calculus surely opens new doors for exploration. It's truly an exciting time to be part of this mathematical revolution.

Let's experiment with different time scales and see what kind of results we can obtain. The possibilities are endless.

II. PRELIMINARIES

All the results in this section follows from [1, 2, 5, 6, 7].

2.1 Time Scale:

Any non-empty closed subset of $\mathbb{R}$ is called a time scale.

2.2 Forward jump operator:

Forward jump operator is defined as $\sigma: \mathbb{T} \to \mathbb{T}$

$$\sigma(t) = \inf\{s \in \mathbb{T}: s > t\}$$

2.3 Backward jump operator:

Backward jump operator $\rho: \mathbb{T} \to \mathbb{T}$ is defined as

$$\rho(t) = sup\{s \in \ \mathbb{T} : s < t\}$$

2.4 Right -Scattered:

If $\sigma(t) > t$, then t is called right- scattered.

2.5 Left- Scattered:

If $\rho(t) < t,$ then t is called left - scattered.

2.6 Right-dense Point:

If $t < sup \ \mathbb{T}$ and $\sigma(t) = t$, then t is called the right dense point.

2.7 Left-dense Point:

If $t > inf \ \mathbb{T}$ and $\rho(t) = t$, then t is called the left dense point.

2.8 Isolated Points:

Points that are right-scattered and left- scattered at the same time are called isolated. This means that, $\rho(t) < t < \sigma(t).$

2.9 Graininess Function:

The function $\mu: T \to [0, \infty)$ is defined by $\mu(t) = \sigma(t) - t$

TABLE I CLASSIFICATION OF POINTS

t-right scattered	$\sigma(t) > t$
t-left scattered	$\rho(t) < t$
t right-dense	$\sigma(t) = t$
t left-dense	$\rho(t) = t$
t isolated	$\rho(t) < t < \sigma(t)$
t dense	$\rho(t) = t = \sigma(t)$

III.MAIN RESULTS

Examples of jump operators:[2]

For each of the following time scales we are finding $\sigma(t)$, $\rho(t)$ and $\mu(t)$. Also, classify each point $t \in \mathbb{T}$ as left-dense, left-scattered, right-dense, or right scattered.

a) $\mathbb{T} = \{2^n : n \in \mathbb{Z}\} \cup \{0\}$

$$\mathbb{T} = \left\{0, \dots, \frac{1}{2^{n-2}}, \frac{1}{2^{n-1}}, 2^n, 2^{n+1}, 2^{n+2}, \dots\right\}$$

$$\mathbb{T} = \left\{0, \dots, \frac{1}{16}, \frac{1}{8}, \frac{1}{4}, \frac{1}{2}, 1, 2, 4, 8, 16, \dots\right\}$$

$$t = 0$$

$$\sigma(0) = \inf\left\{0, \dots, \frac{1}{16}, \frac{1}{8}, \frac{1}{4}, \frac{1}{2}, 1, 2, 4, 8, 16, \dots\right\}$$

For $= 0$:

Therefore, $t = 0$ is a right-dense point. For $t = 1$:

$$\sigma(1) = \inf\{2, 4, 8, 16, \dots\}$$
$$= 2$$

For $t = 2$:
$$\sigma(2) = \inf\{4, 8, 16, \dots\}$$
$$= 4$$

For $t = 2^n$:
$$\sigma(t = 2^n) = \inf\{2^{n+1}, 2^{n+2}, \dots\}$$
$$= 2^{n+1}$$
$$= 2^n 2$$
$$= 2t$$

We observe that, $\sigma(t = 2^n) = 2^{n+1} > 2^n = t$

$$t = 2^n$$

Hence, $t = \frac{1}{2^n}$ is a right-scattered point. For $t = \frac{1}{2^n}$:

$$\sigma\left(t = \frac{1}{2^n}\right) = \inf\left\{\frac{1}{2^{n-1}}, \frac{1}{2^{n-2}}, \dots\right\}$$
$$= \frac{1}{2^{n-1}}$$
$$= \frac{1}{2^n} 2$$
$$= 2t$$

We observe that, $\sigma\left(t = \frac{1}{2^n}\right) = \frac{1}{2^{n-1}} > \frac{1}{2^n} = t$

$$t = \frac{1}{2^n}$$

Hence, $t = \frac{1}{2^n}$ is a right-scattered point. Now, we find $\rho(t)$

For $t = 0$:

$\rho(t = 0) = sup\{\emptyset\}$

$\qquad = inf\{T\}$

$\qquad = 0$

Here, $\rho(t = 0) = 0$

Therefore $t = 0$ is left-dense point.

For $t = 2^n$:

$\rho(t = 2^n) = sup\{ 2^{n-1}, 2^{n-2}, \dots \}$

$\qquad = 2^{n-1}$

$\qquad = 2^n 2^{-1}$

$\qquad = \frac{t}{2}$

We observe that,

$\rho(t = 2^n) = 2^{n-1} < 2^n = t$

Hence, $t = 2^n$ is a left-scattered point.

To find the graininess function $\mu(t)$:

$\mu(t) = \sigma(t)\text{-}t$

$\qquad = 2t - t$

$\qquad = t$

b) $T = \{\frac{1}{n} : n \in \mathbb{N}\} \cup \{0\}$

$T = \{0,\dots, \frac{1}{n+2}, \frac{1}{n+1}, \frac{1}{n+1}, \frac{1}{n}, \frac{1}{n-1}, \frac{1}{n-2}, \dots \}$

For $t = 0$:

$\sigma(0) = inf\left\{0, \dots, \frac{1}{n+2}, \frac{1}{n+1}, \frac{1}{n+1}, \frac{1}{n}, \frac{1}{n-1}, \frac{1}{n-}\right\}$

$\qquad = 0$

Therefore, $t = 0$ is the right-dense point.

For $t = 1$:

$\sigma(1) = inf\{ s \in T : s > t\}$

$\qquad = inf\{\emptyset\}$

$\qquad = sup\{T\}$

$\qquad = 1$

Therefore, $t = 1$ is the right-dense point.

For $t = \frac{1}{n}$:

$\sigma\left(t = \frac{1}{n}\right) = inf\left\{ \frac{1}{n-1}, \frac{1}{n-2}, \dots \right\}$

$$= \frac{1}{n-1}$$

$$= \frac{1}{\frac{1}{t}-1}$$

$$= \frac{t}{1-t}$$

We observe that, $\sigma\left(t = \frac{1}{n}\right) = \frac{1}{n-1} > \frac{1}{n} = t$

Hence, $t = \frac{1}{n}$ is a right-scattered point.

Now, we find $\rho(t)$

For $t = 0$:

$\rho(t = 0) = sup\{\emptyset\}$

$= inf\{\mathbb{T}\}$

$= 0$

Here, $\rho(t = 0) = 0$

Therefore $t = 0$ is the left-dense point.

For $t = \frac{1}{n}$:

$$\rho\left(t = \frac{1}{n}\right) = sup\left\{\frac{1}{n+1}, \frac{1}{n+2}, ...\right\}$$

$$= \frac{1}{n+1}$$

$$= \frac{1}{\frac{1}{t}+1}$$

$$= \frac{t}{1+t}$$

We observe that, $\rho\left(t = \frac{1}{n}\right) = \frac{1}{n+1} < \frac{1}{n} = t$

Hence, $t = \frac{1}{n}$ is a left-scattered point.

To find the graininess function $\mu(t)$:

$\mu(t) = \sigma(t)\text{-}t$

$$= \frac{t}{1-t} - t$$

$$= \frac{t^2}{1-t}$$

c) $\mathbb{T} = \left\{\frac{n}{2} : n \in \mathbb{N}_0\right\}$

$\mathbb{T} = \left\{..., \frac{n-2}{2}, \frac{n-1}{2}, \frac{n}{2}, \frac{n+1}{2}, \frac{n+2}{2}, ...\right\}$

For $t = \frac{n}{2}$:

$$\sigma\left(t = \frac{n}{2}\right) = inf\left\{\frac{n+1}{2}, \frac{n+2}{2}, \ldots\right\}$$

$$= \frac{n+1}{2}$$

$$= \frac{2t+1}{2}$$

$$= t + \frac{1}{2}$$

We observe that, $\sigma\left(t = \frac{n}{2}\right) = \frac{n+1}{2} > \frac{n}{2} = t$

Hence, $t = \frac{n}{2}$ is a right-scattered point.

Now, we find $\rho(t)$

For $t = \frac{n}{2}$:

$$\rho\left(t = \frac{n}{2}\right) = sup\left\{\frac{n-1}{2}, \frac{n-2}{2}, \ldots\right\}$$

$$= \frac{n-1}{2}$$

$$= \frac{2t-1}{2}$$

$$= t - \frac{1}{2}$$

We observe that, $\rho\left(t = \frac{n}{2}\right) = \frac{n-1}{2} < \frac{n}{2} = t$

Hence, $t = \frac{n}{2}$ is a left-scattered point.

To find the graininess function $\mu(t)$:

$$\mu(t) = \sigma(t)\text{-}t$$

$$= t + \frac{1}{2}\text{-}t$$

$$= \frac{1}{2}$$

d) $T = \{\sqrt{n} : n \in \mathbb{N}_0\}$

$T =$
$\{\ldots, \sqrt{n-2}, \sqrt{n-1}, \sqrt{n}, \sqrt{n+1}, \sqrt{n+2}, \ldots\}$

For $t = \sqrt{n}$:

$$\sigma(t = \sqrt{n}) = inf\{\sqrt{n+1}, \sqrt{n+2}, \ldots\}$$

$$= \sqrt{n+1}$$

$$= \sqrt{t^2 + 1}$$

We observe that, $\sigma(t = \sqrt{n}) = \sqrt{n+1} > \sqrt{n} = t$

Hence, $t = \sqrt{n}$ is a right-scattered point.

Now, we find $\rho(t)$

For $t = \sqrt{n}$:

$$\rho(t = \sqrt{n}) = sup\{\sqrt{n-1}, \sqrt{n-2}, \dots\}$$
$$= \sqrt{n-1}$$
$$= \sqrt{t^2 - 1}$$

We observe that,

$$\rho(t = \sqrt{n}) = \sqrt{n-1} < \sqrt{n} = t$$

Hence, $t = \sqrt{n}$ is a left-scattered point.

To find the graininess function $\mu(t)$:

$$\mu(t) = \sigma(t)\text{-}t$$
$$= \sqrt{t^2 + 1}\text{-}t$$
$$= \frac{1}{2}$$

e) $\mathbb{T} = \{\sqrt[3]{n} : n \epsilon \, \mathbb{N}_0\}$

$\mathbb{T} =$
$$\{\dots, \sqrt[3]{n-2}, \sqrt[3]{n-1}, \sqrt[3]{n}, \sqrt[3]{n+1}, \sqrt[3]{n+2}, \dots\}$$

For $t = \sqrt[3]{n}$:

$$\sigma(t = \sqrt[3]{n}) = inf\{\sqrt[3]{n+1}, \sqrt[3]{n+2}, \dots\}$$
$$= \sqrt[3]{n+1}$$
$$= \sqrt[3]{t^3 + 1}$$

We observe that,

$$\sigma(t = \sqrt[3]{n}) = \sqrt[3]{n+1} > \sqrt[3]{n} = t$$

Hence, $t = \sqrt[3]{n}$ is a right-scattered point.

Now, we find $\rho(t)$

For $t = \sqrt[3]{n}$:

$$\rho(t = \sqrt[3]{n}) = sup\{\sqrt[3]{n-1}, \sqrt[3]{n-2}, \dots\}$$
$$= \sqrt[3]{n-1}$$
$$= \sqrt[3]{t^3 - 1}$$

We observe that,

$$\rho(t = \sqrt[3]{n}) = \sqrt[3]{n-1} < \sqrt[3]{n} = t$$

Hence, $t = \sqrt[3]{n}$ is left-scattered point.

To find the graininess function $\mu(t)$:

$$\mu(t) = \sigma(t)\text{-}t$$
$$= \sqrt[3]{t^3 + 1}\text{-}t$$

3.2 Examples of time scales, point $t \in \mathbb{T}$ that $\sigma(\rho(t)) = t$, $\rho(\sigma(t)) = t$ are not true and the conditions on t under which these equations are true.

Consider,

$\mathbb{T} = \mathbb{N}$

$\mathbb{T} = \{1, 2, , \dots\}$

$Now, for\ t = 1$

$\rho(t = 1) = 1$

$\sigma(\rho(1)) = \sigma(1)$

$\sigma(\rho(1)) = 2$

We observe that, $\sigma(\rho(t = 1)) \neq t$

$For\ t = n$

$\sigma(n) = n$

$\rho(\sigma(n)) = \sigma(n)$

$\rho(\sigma(n)) = n - 1$

We observe that,

$\rho(\sigma(t = n)) \neq t$

If time scale $\mathbb{T} = \mathbb{R}$, then the conditions $\sigma(\rho(t)) = t$ and $\rho(\sigma(t)) = t$ are true.

IV. CONCLUSION

This article clarifies jump operators, which are fundamental time-scale tools. Furthermore, we solve dynamic equations requiring the delta derivative, which is specified on jump operators, by using these fundamental tools of time scales.

V. REFERENCES

[1]. H. A. Agwa, F. M. Ali and A. Kilcman, A new integral transform on time scale and its applications, Advances in Difference Equations, 60 (2012),1-14.

[2]. Martin Bohner and A. Peterson, Advances in Dynamic Equations on Time Scales, Bikhauser, Boston, 2002.

[3]. Martin Bohnera*, Gusein Guseinovb and Basak Karpuz, Properties of the Laplace Transform on Time Scales With Arbitrary Graininess, 22 (2011), 785-800.

[4]. Martin Bohner and A. Peterson, The Laplace Transform and Z-Transform Unification and Extension, Methods and Application of Analysis, (9) (2002), 151-158.

[5]. T. G. Thange and Sneha Chhatraband* , Laplace- Sumudu Integral Transform On Time Scales, South East Asian Journal of Mathematics and Mathematical Sciences, (19)(1), (2023), 91-102.

[6]. T. G. Thange and Sneha Chhatraband* , "A New α-Laplace Transform On Time Scales", 53(2), 2023, 1-10.

[7]. T. G. Thange, Gade A. R., Fractional Shehu Transform and Its Applications, South East Asian Journal of Mathematics and Mathematical Sciences, 17(2), 2001.

An Overview of Transformations to solve Differential Equations

Suryawanshi Mahima*, Jadhav Bhagyashri, Jadhav Abhijit, Bhakare Tushar

*Department of Mathematics, New Arts Commerce and Science College, Ahmednagar, Maharashtra, India

Abstract :

This paper delivers a panoramic summary of various transformation techniques used to solve differential equations, featuring their mathematical foundations, practical applications, and relative advantages. Differential equations, which are essential to modeling dynamic systems over physics, engineering, and applied sciences, often require cultured methods for their solutions. The paper inspects the key transformations, including Fourier transform, Laplace transform, and wavelet transform, among others, that accelerate the solution of ordinary and partial differential equations.

Keywords: Research Paper, Laplace Transform, Fourier Transform, Wavelet Transform.

I. INTRODUCTION

Now a days, Transformations are essential in solving the differential equations as they simplify complex problems,convert equations into more solvable forms, and provide solutions for both ordinary and partial differential equations.This paper explains the methods to solve Second Order Differential Equations with constant Coefficients using Laplace Transform, Fourier Transform and Wavelet Transform. The Definiton and Application of these transformations are as follows. The Laplace Transform provides a way to handle initial value problems by transforming them into algebraic equations[3],[4]. The Fourier transform Converts time domain signals into frequency- domain representations [6].It is also essential for analyzing the frequency components of a signal, revealing its spectral characteristics [5].The Wavelet Transform Provides a multi resolution evaluation,allowing For the examination of different frequency Components at various scales[1]. Well-suited for analyzing signals with transient or non- stationary characteristics[2].

II. LAPLACE TRANSFORM

Definition: The Laplace transform is an integral transform that converts a function of time f(t) into a function of a complex variable s. It's defined as:

$$L\{f(t)\} = F(s) = \int e^{-st} \infty \, 0 \, f(t) dt$$

where t is the time variable, s is a complex frequency parameter, and F(s) is the transformed function in the s-domain.

Applications:

- **Control Systems:** Analyzing and designing control systems.

- **Differential Equations:** Solving linear ordinary differential equations (ODEs) and partial differential equations (PDEs).
- **Signal Processing:** Analyzing circuits and systems in electrical engineering.

III. FOURIER TRANSFORM

Definition: The Fourier transform decomposes a function into its constituent frequencies. For a time-domain function f(t), the Fourier transform F(ω) is given by:

$F\{f(t)\} = F(\omega) = \int f(t) \infty -\infty \, e \, -i\omega t d$t

where ω is the angular frequency and i is the imaginary unit.

Applications:

- **Signal Processing:** Analyzing and filtering signals, image processing.
- **Communication Systems**: Modulating and demodulating signals.
- **Physics:** Studying wave phenomena and quantum mechanics.

IV. WAVELET TRANSFORM

Definition: The Wavelet transform represents a function as a sum of wavelets, which are localized in both time and frequency. The continuous wavelet transform (CWT) is defined as:

$W\{f(t)\} = W(a, b) = 1 \, \sqrt{a} \int f(t)\varphi * \infty -\infty \, (\, t - b \, a \,)d$t

where ψ is the wavelet function, a is the scale parameter, and b is the translation parameter.

Applications:

- **Signal Processing:** Time-frequency analysis, denoising, and compression.
- **Image Processing:** Multi-resolution analysis and texture analysis.
- **Geophysics:** Analyzing non-stationary signals and patterns in seismic data.

V. EXAMPLES

Ex.1) Solve the given differential equation using Laplace Transform,

y" + 4y' + 3y = 0, y(0) = 2, y'(0) = −3

Solution: y" + 4y' + 3y = 0, y(0) = 2, y'(0) = −3 L{y"} + 4L{y'} + 3L{y} = L{0} p 2L{y} − py(0) − y'(0) + 4[pL{y} − y(0)] + 3L{y} = 0 p 2L{y} − 2p + 3 + 4[pL{y} − 2] + 3L{y} = 0 $L\{y\}$(p2 + 4p + 3) = 2p + 5 $L\{y\} = 2p + 5$ $(p + 1)(p + 3)$ *Applying Inverse Laplace Transform*, $y(t) = L$ −1 { $2p + 5$ $(p + 1)(p + 3)$ } *Now, By using partial fraction*, $y(t) = 3$ 2 L −1 { 1 $(p + 1)$ } + 1 2 L −1 { 1 $(p + 3)$ } $y(t) = 3$ 2 e −t + 1 2 e −3t

Is the required solution.

The graph of the above solution is as follows,
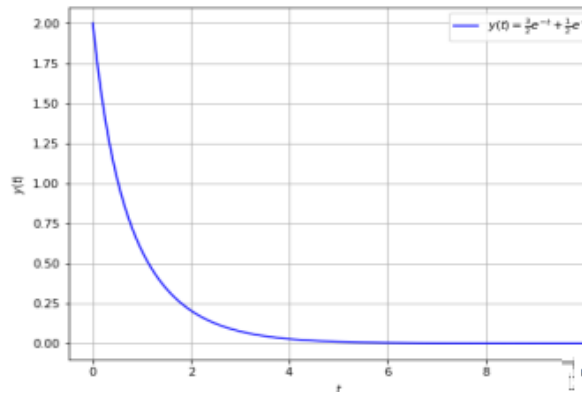
Fig.1 Graph of Solution $y(t) = \frac{3}{2} e -t + \frac{1}{2} e -3t$

Ex.2)Solve $y'' + y = 0$, $y(0) = 0$, $y'(0) = 1$, Using Fourier Transform. Solution: The Fourier Transform of y(x) is defined as, $\hat{y}(k) = F(y(x)) = \int y(x)e \infty -ikx -\infty \, dx$ The given Equation is, $y'' + y = 0$, $y(0) = 0$, $y'(0) = 1$ By applying fourier transform, $F(y'' + y) = F(0)$ $F(y'') + F(y) = 0$ $-k$ $2\hat{y}(k) + \hat{y}(k) = 0 => \hat{y}(k)[-k \, 2 + 1] = 0$ $\hat{y}(k) = A\delta(k - 1) + B\delta(k + 1)$

Where $\delta(k)$ is Diracdelta function and A,B are constants determined from intial conditons. By applying inverse Fourier Transform to $\hat{y}(k)$, $F -1 (\hat{y}(k)) = F -1 (A\delta(k - 1) + B\delta(k + 1))$ $y(x) = 1 \, 2\pi \, [A \int \delta(k - 1) \infty -\infty \, e \, ikx + B \int \delta \infty -\infty \, (k + 1)e \, ikx \, dk$ We Know $\int \delta \infty -\infty \, (k - 1)f(k)dk = f(a)$ $y(x) = 1 \, 2\pi \, (Ae \, ix + Be -ix)$ To find constants A and B, $y(0) = A + B \, 2\pi = 0 => A + B = 0 => B = -A$ $y'(0) = [Aie \, ix - Aie -ix(-1) \, 2\pi] = 1 => Ai + Ai \, 2\pi = 1$ $A = \pi \, i = -i\pi$ $B = i\pi$ hence $y(x) = -i\pi \, 2\pi \, e \, ix + i\pi \, 2\pi \, e -ix$ But $e \, ix = cos(x) + isin(x) => y(x) = sin(x)$) is the required Solution.
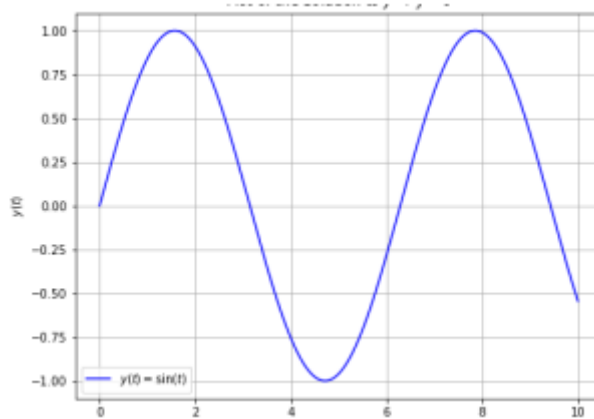
Fig.2 Graph of solution y(x)=sin(x)

Ex.3) Solve the Differential Equation using Wavelet Transform, $y'' + y = 0$, $y(0) = 1$, $y'(0) = 0$. *Solution*: $y'' + y = 0$, $y(0) = 1$, $y'(0) = 0$. Exact solution =cos(x) The graph of the exact and approximate solution is as follows,
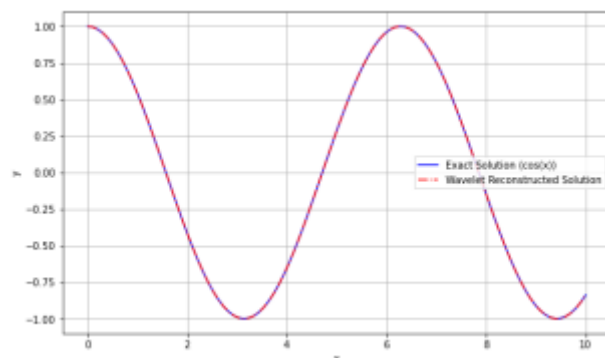
Fig.3 Graph of exact and approximate solution y(x)=c0s(x)

VI. CONCLUSION

Fourier transform is probed for its utility in converting differential equations into algebraic equations, particularly beneficial in problems with periodic boundary conditions. Laplace transform is highlighted for its effectiveness in handling initial value problems, particularly in the analysis of linear time-invariant systems. The wavelet transform is reviewed for its ability to manage non-stationary signals and its application in solving differential equations with complex, transient features. By comparing these transformations, the paper enhances their respective strengths and limitations, providing insight into their appropriate use cases. The study aims to serve as an important asset for researchers and practitioners seeking to apply these significant mathematical tools to solve differential equations in various scientific and engineering contexts.

VII. REFERENCES

[1]. Lokenath Debnath, Firdous Ahmad Shah, Wavelet Transforms and Their Applications, Springer publication, Second edition (2005).

[2]. P.S.Addison, The Illustrated Wavelet Transform Handbook: Introductory Theory and Applications Sciences, Engineering, Medicine and Finance, IOP,(2002).

[3]. Dinesh Verma, Applications of Laplace Transformation for Solving Various Differential Equations with Variable Coefficients, ISSN NO:2349-6010, (2018).

[4]. Sukhen Bhattacharyya and Dr. Puneet Kumar Agarwal, A study of Laplace Transform and Applications to Differential Equations, ISSN NO: 2455-3085, (2019).

[5]. Dr. Dinesh Verma, Analysis of Differential Equations By Using Fourier Transformation, ISSN NO:2163 - 8950,DOI: 10.7537/marsrsj120820.01.

[6]. Murat Duz and Sunnet Avezov, Solutions to Diferential-Differential Difference Equations with Variable Coefficients by Using Fourier Transform Method, ISSN NO: 1306-7575,DOI:10.29233/sdufeffd.1318890.

Tuning optical properties of cadmium thiourea acetate crystal exploiting organic ligand of oxalic acid for NLO device applications

Rupali B. Kulkarni[a]

[a] Department of Physics, Swa. Sawarkar Mahavidyalaya, Beed 431122 (MS) INDIA

* Corresponding Author: Tel.: +91 9403585268

E-mail address: rbkulkarni9421@gmail.com

Abstract :

Modifying optical properties of crystal is very fundamental need for designing various photonic devices hence in current investigation the oxalic acid (OA) has been firstly doped in cadmium thiourea acetate (CTA) crystal with aim to optimize the third order nonlinear optical (TONLO) properties of CTA crystal. The pure and doped CTA crystals have been grown by slow solvent evaporation technique at 35°C. The structural parameters of grown crystals have been determined using the single crystal X-ray diffraction technique. The incorporation of OA in CTA crystal matrix has been corroborated by FTIR (Fourier transform infrared) analysis. The OA doped CTA crystals were subjected to Z-scan analysis to identify the nonlinear nature of studied crystals. The laser induced TONLO properties of OA doped CTA crystal have been determined at 632.8 nm. The nonlinear refraction and absorption has been explored with the aid of close and open aperture Z-scan configuration. The magnitude of nonlinear constants viz. nonlinear refraction (n_2), absorption coefficient (β), cubic susceptibility (χ^3) and figure of merit has been calculated using the transmittance data.

Keywords: Crystal growth, Optical studies, *Z*-scan analysis, TONLO paramaters

I. INTRODUCTION

Thiourea coordinated metal complex crystals have gained considerable attention in past few decades owing to their unique credibility of beholding the properties of both organic and inorganic counterparts which rank them as superior materials for designing microelectronics, photonics, optical switching, optical data storage, frequency conversion and modern nonlinear optical (NLO) devices [1-4]. The list of thiourea metal complex crystals is quite large amongst which some promising crystals are under constant investigation such as calcium bis thiourea chloride (CBTC), zinc thiourea sulphate (ZTS), zinc thiourea chloride (ZTC), bis thiourea cadmium formate (BTCF), bis thiourea cadmium chloride (BTCC), bis thiourea zinc acetate (BTZA), cadmium thiourea acetate (CTA), etc [5-7].

The materials embodied with transition elements having closed d^{10} shell electrons express excellent optical properties [8], hence CTA is realized to be the interesting material to investigate so as to find its applicability for suitable optical device applications. The intruding fact observed in literature is that very few research groups have grown and explored the characteristic features of pure CTA crystal [9-11]. Furthermore, the fact that encourages more to investigate the CTA crystal is that there are very few reports available on doping of impurity in CTA crystal. As doping is the most effective way to modify the intrinsic and extrinsic properties of host crystal [12], the doping effect of glycine, L-alanine, L-cysteine and L-valine on distinct properties of CTA crystal has been explored [13-15].The analysis of several path breaking reports adds to the knowledge that the organic dopants having the donor-π-acceptor moieties and good polarizing nature reinforce constructive impact on linear and nonlinear optical properties of host crystal [16-17].

As oxalic acid (OA) are realized to have abundance of π-bonded network which is the foremost requirement for improving the NLO properties and the electronic response time of single crystal [16]. Therefore they fulfill their suitability as a dopant for optimizing the optical properties of CTA crystal.

Thus in current investigation the significant impact of OA on third order nonlinear optical properties of CTA crystal has been explored. The comparative evaluation third order nonlinear optical properties of grown crystals has been accomplished by employing the Z-scan characterization techniques.

1.   Experimental procedure

The required salt was synthesized by solvating cadmium acetate (1mole) and thiourea (2mole) in double distilled de-ionized water. Purity of CTA metal complex salt has been maintained by the repetitive re-crystallization. Oxalic acid in 0.5M% was doped in the supersaturated solution of purified CTA. The solution was allowed to agitate for ten hours to achieve homogeneous mixing of dopant and host material. The homogeneously doped CTA solution was filtered in the separate beaker using the standard Whatman No. 1 filter paper and kept for slow solvent evaporation process in a constant temperature bath at 35˚C (±0.01˚C) by covering the filtrate with perforated coil. The good quality crystals of OA-CTA were grown by spontaneous nucleation process after ten days respectively. The purity of the grown crystals has been achieved by repetitive recrystallization process. The grown CTA, OA-CTA crystals are shown in **Fig.1.**
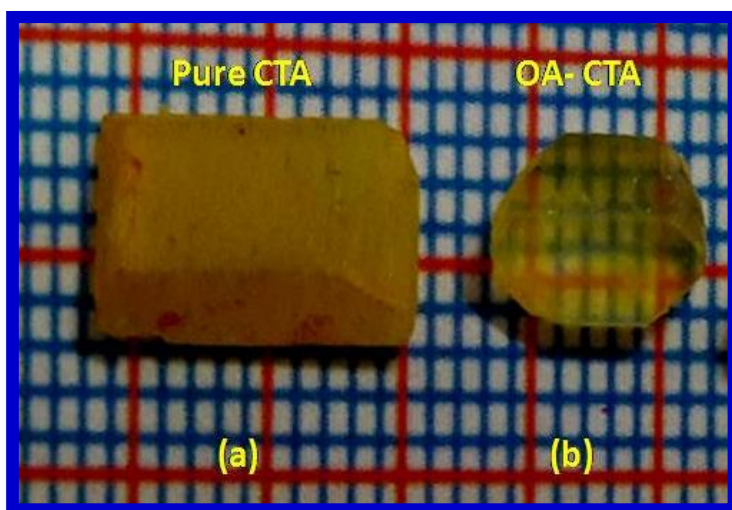
Fig.1. (a) Pure CTA (b) OA-CTA

3. Results and discussion

Z-scan Analysis

The Z-scan is the most effective technique to examine the TONLO properties of given material at single wavelength which makes the scrutinizing of material for specific application more easy and reliable. The Bahae et al first introduced the Z-scan technique **[18],** which is most efficient to examine the nature of TONLO refraction and absorption through close and open aperture Z-scan configuration respectively. Initially the system was optically aligned and configured to close aperture analysis. The thin and polished doped CTA crystals were placed at focus position (Z=0) and then gradually translated in Z-direction about the focus with Gaussian filtered laser beam constantly focused on the sample. The transmitted optical signals from the sample was traced with respect to position through the detector (having close aperture) placed at far field. The details of Z-scan set up are shown in **Table1.** The closed aperture Z-scan transmittance curve of OA doped CTA crystal is shown in **Fig. 2(a)**. It is observed that the OA doped CTA crystal inherits the signature of negative refraction (peak followed by valley) which is characteristic of material having self defocusing nature **[19-22].** The CTA crystal exhibits positive refraction nonlinearity The focused irradiation of laser beam on crystal sample results to spacial distribution of optical energy causing a thermal lensing effect which causes change in refraction of crystal **[23-24].** The relation between (ΔT_{p-v}) i.e. difference between peak to valley transmittance and on axis phase shift ($\Delta\Phi$) is related by equation **[18],**

$$\Delta T_{p-v} = 0.406(1-S)^{0.25}|\Delta\phi|$$

(1)

where S = [1-exp ($-2r_a^2/\omega_a^2$)] is the aperture linear transmittance, r_a is the aperture radius and ω_a is the beam radius at the aperture. The TONLO refractive index (n_2) of OA doped CTA crystal was calculated using the relation **[18],**

$$n_2 = \frac{\Delta\phi}{KI_0L_{eff}}$$

(2)

Where, K = $2\pi/\lambda$ (λ is the laser wavelength), I_0 is the beam intensity at the focus, L_{eff} = [1-exp ($-\alpha L$)]/α, is the effective thickness of the sample which depends on α-linear absorption coefficient and L-thickness of the sample (L). The n_2 of OA doped CTA crystal is of order 10^{-11} cm^2/W. The open aperture Z-scan analysis helps to analyze the

effective TONLO absorption behavior and thus the open aperture Z-scan curve of OA doped CTA crystal was traced as shown in **Fig.2 (b).** It shows that OA doped CTA crystal exhibits reverse saturable absorption (RSA) phenomenon **[25-26].** The RSA effect is governed by the multi-photon absorption assisted by excited state absorption effect **[27]** on the contrary the SA effect is expressed due to dominance of ground state linear absorption over the excited state absorption **[28].** The TONLO absorption coefficient (β) of doped CTA crystals has been evaluated using the given equation **[18],**

$$\beta = \frac{2\sqrt{2}\Delta T}{I_0 L_{eff}}$$

(3)

(ΔT- one valley value at the open aperture Z-scan curve)

The value β of OA-CTA crystal is found to be of the order of 10^{-6} cm/W. The cubic susceptibility ($\chi^{(3)}$) of doped CTA crystal has been evaluated using equations **[18],**

$$\text{Re } \chi^{(3)}(esu) = 10^{-4}(\varepsilon_0 C^2 n_0^2 n_2)/\pi (cm^2/W)$$

(4)

$$\text{Im } \chi^{(3)}(esu) = 10^{-2}(\varepsilon_0 C^2 n_0^2 \lambda\beta)/4\pi^2 (cm/W)$$

(5)

$$\chi^{(3)} = \sqrt{(\text{Re } \chi^{(3)})^2 + (\text{Im } \chi^{(3)})^2}$$

(6)

Here the parameters are

ε_0 - vacuum permittivity,

n_0 - linear refractive index of the sample and

c - Velocity of light in vacuum.

The $\chi^{(3)}$ gives the polarizing ability of the material which is facilitated by the charge delocalization over the pi bonded network of molecular system **[29-30].** The $\chi^{(3)}$ of OA doped CTA crystal has been determined which is found of order 10^{-5} esu and 10^{-3} esu. The TONLO behavior of OA doped CTA crystal is as mentioned & compared in **Table 2.** The crystals with promising TONLO properties can be potential candidate for designing ultrafast optical switching, 3D optical data storage, photodynamic therapy and optical power limiting devices **[31].**

Table1. Optical resolution of Z-scan setup

Parameters and notations	Details
He-Ne Laser wavelength (λ)	632.8 nm
Lens focal length (f)	30 mm
Optical path length (Z)	85 cm
Beam waist (w_a)	3.3 mm
Aperture radius (ra)	2 mm
Incident intensity at the focus (I_o)	26.5 MW/cm²
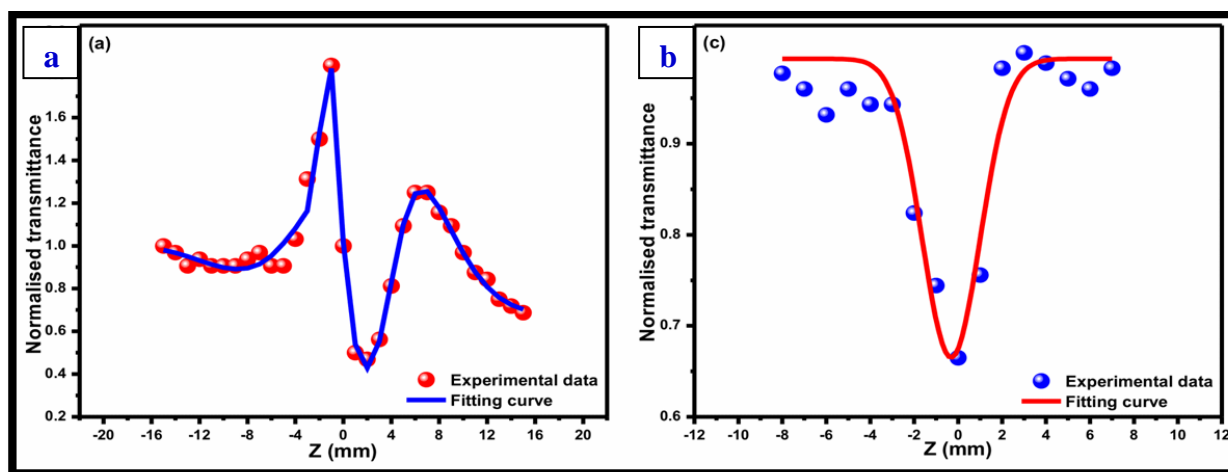
Fig.2. (a) Close aperture Z-scan transmittance curve of OA-CTA crystal and (b) Open aperture Z-scan transmittance curve of OA-CTA

Table 2. Comparison of TONLO parameters

Crystal	n_2 (cm²/W)	β (cm/W)	χ^3 (esu)	Reference
CTA	8.37×10^{-11}	4.70×10^{-6}	2.58×10^{-4}	[14]
LV-CTA	5.06×10^{-11}	9.05×10^{-6}	3.34×10^{-4}	[14]
LC-CTA	4.85×10^{-12}	1.19×10^{-5}	6.18×10^{-5}	[15]
OA-CTA	1.25×10^{-11}	2.36×10^{-6}	1.02×10^{-5}	Present work

4. Conclusion

The undoped and OA doped CTA single crystals have been successfully grown by slow solvent evaporation technique and characterized to explore the constructive impact of OA on third order nonlinear optical properties of CTA crystal. The Z-scan analysis confirmed the TONLO nature of doped CTA crystals at 632.8 nm. The OA doped CTA crystal delivered the negative nonlinear refraction ($n_2 = 1.25 \times 10^{-11}$ cm²/W) and reverse saturable absorption effect ($\beta = 2.36 \times 10^{-6}$ cm/W) with χ^3 of magnitude 1.02×10^{-5} esu. The comparative analysis thus confirms that the OA effectively tailor the studied optical properties of CTA crystal which makes them the better alternative for designing distinct NLO device applications.

References

[1]Gary L.Succaw, Timothy J.R.Weakley, Fusan Han, Kenneth M. Doxsee, Crystal Growth & Design 5(2005)2288-2298. **DOI: 10.1021/cg050162c**

[2]Ming Li, Mingjun Xia, Huining Xia, Chemistry Select 2(2017)5882-5886. **DOI: 10.1002/slct.201701038**

[3]K.Ramamurthi, G. Madhurambal, B. Ravindran, M. Mariappan, S.C.Mojumdar, J Thermal Calorim 104(2011)943–947. **DOI: 10.1007/s10973-011-1492-y**

[4]S.M.Azhar, S. S. Hussaini, M. D. Shirsat, G. Rabbani, Mohd Shkir, S. Alfaify, H. A.Ghramh,M.I.Baig, Mohd Anis, Material research innovations(2017)1-6.

DOI: 10.1080/14328917.2017.1392694

[5] H Pir, N Gu¨nay, D Avc,Y Atalay, Indian J Phys.86 (2012)1049-1063.

DOI 10.1007/s12648-012-0171-6

[6]Mohd Anis, S.S. Hussaini, M.D. Shirsat, Optik 127(2016)9734–9737.

DOI: 10.1016/j.ijleo.2016.07.065

[7]Mohd Anis,S.S. Hussaini, A. Hakeem, M.D. Shirsat, G.G. Muley,Optik 127(2016)2137–2142. **DOI:** 10.1016/j.ijleo.2015.11.097

[8]Min-hua Jiang, Qi Fang, Adv. Mater. 11(1999)1147-1151.

DOI: 10.1002/(SICI)1521-4095(199909)11:13

[9] R. Sankar, C. M. Raghavan, R. Jayavel Cryst. Res. Technol. 41(2006)919-924.

DOI 10.1002/crat.200510696

[10]S.S. Kirupavathy, S.S. Mary, P. Srinivasan, N. Vijayan, G. Bhagavannarayana, R. Gopalakrishnan, J. Cryst. Growth 306(2007)102-110. **DOI:10.1016/j.jcrysgro.2007.03.036**

[11]J. Uma, V. Rajendran Ind. J. Comp. Appl. 30(2011)8-10.

[12]Mohd Anis, M.I. Baig, M.S. Pandian, P. Ramasamy, S. AlFaify, V. Ganesh, G.G. Muley, H.A. Ghramh, Cryst. Res. Technol. (2018). **DOI:** 10.1002/crat.201700165

[13]V.Ganesh,T.Bhaskar Rao, K. Kishan Rao, G. Bhagavannarayana, Mohd. Shkir Mater. Chem. Phys. 137(2012)276-281.**DOI:** 10.1016/j.physb.2010.10.061

[14]Mohd Anis, S.S.Hussaini, M.D.Shirsat, G. G. Muley, Materials Research Innovations 20 (2016)312-316.

DOI:10.1080/14328917.2015.1137693

[15]S.M.Azhar, MohdAnis, S.S.Hussaini, S.Kalainathan, M.D.Shirsat, G.Rabbani, Optics and Laser Technology 87(2017)11-16. **DOI:** 10.1016/j.optlastec.2016.07.007

[16]Mohd Anis, M.I. Baig, S.S. Hussaini, M.D. Shirsat, Mohd Shkir, H.A. Ghramh, Chin. Phys. B 27 (2018) 27800-27806.

[17]Mohd Anis, M.I. Baig, M.S. Pandian, P. Ramasamy, S. AlFaify, V. Ganesh, G.G.Muley, H.A. Ghramh, Cryst. Res. Technol. (2018).**DOI:** 10.1002/crat.201700165

[18]M.S. Bahae, A.A. Said, T.H. Wei, D.J. Hagan, E.W.V. Stryland IEEE J. Quant. Electron. 26 (1990)760-769.**DOI:** 10.1109/3.53394

[19]R.N.Shaikh, Mohd. Anis, M.D.Shirsat & S.S. Hussaini, Materials Technology: Advanced Performance Materials (2016). **DOI:** 10.1179/1753555715Y.0000000039

[20]A.P. Arthi, M. Sumithra Devi, K. Thamizharasan, Optik 126 (2015) 4131-4135.

DOI10.1016/j.ijleo.2015.08.031

[21]L.T. Jin , X.Q. Wang,Q. Ren , N.N. Cai , J.W. Chen , T.B. Li, X.T. Liu, L.N. Wang, G.H. Zhang, L.Y. Zhu, D. Xua, Journal of Crystal Growth 356(2012)10-16.

DOI: 10.1016/j.jcrysgro.2012.07.005

[22]Changgui Lu, Yiping Cui, Bing Gu,Feng Wang, Journal of Nonlinear Optical Physics & Materials 19(2010)327-338.**DOI:10.1142/S0218863510005169**

[23]S.P. Ramteke, Mohd Anis,M.S. Pandian, S. Kalainathan , M.I. Baig, P. Ramasamy, G.G. Muley,Optics and Laser Technology 99(2018)197–202**. DOI:** 10.1016/j.optlastec.2017.09.003

[24]M. I. Baig, M. Anis, S. Kalainathan, B. Babu ,G. G. Muley, Materials Technology32(2017) 560–568. **DOI:** 10.1080/10667857.2017.1321275

[25]Y.B.Rasal, Mohd Anis, M. D. Shirsat,S. S. Hussaini, Materials Research Innovations(2017). **DOI:** 10.1080/14328917.2017.1327199

[26]R.N.Shaikh, Mohd Anis, M.D. Shirsat, S.S. Hussaini, Optik 154(2018)435-440.
 DOI: 10.1016/j.ijleo.2017.10.107

[27]Sajan,N. Vijayan, K. Safakath,Reji Philip, I. Hubert Joe| dx. | J. Phys. Chem. A 115(2011) 8216–8226. **Doi:10.1021/jp201818y.**

[28] T. Kanagasekaran, P. Mythili, P. Srinivasan, Ahmad Y.Nooraldeen, P. K. Palanisamy, and R. Gopalakrishnan,Cryst. Growth Des.8 (2008)2335-2339. **DOI: 10.1021/cg701132f**

[29]X.Q. Wang, Q. Ren, H.L. Fan, J.W. Chen, Z.H. Sun, T.B. Li, X.T. Liu, G.H. Zhang, D. Xu, W.L. Liu J. Cryst. Growth 312 (2010) 2206-2214. **DOI:** 10.1016/j.jcrysgro.2010.04.045

[30]S.L.G´omez, F.L.S. Cuppo,A.M. Figueiredo Neto, Brazilian Journal of Physics 33(2003)   813-820. DOI: 10.1590/S0103-97332003000400035

[31]Ting Bin Li, Ya Li Hu, Chun Lin Ma, Guo Fang He, Ren Gao Zhao andGuo Bing Zhen, Appl. Organometal. Chem. 25(2011)867–870. **DOI: 10.1002/aoc.1852**

Applications of Mathematics in Physics - A Review

Dr. Aruna M. Kulkarni, Dr. Dhanashri A. Munot

Department of Mathematics, Gandhi College, Kada, Dist. Beed (M.S.)

Email: abhiarud@gmail.com, dhnshrmunot50@gmail.com

Abstract :

Math and physics share a relationship in which each can benefit the other. Mathematics is a very beautiful subject and very much an indispensable tool for physics. In this article some mathematical concepts are used to describe theoretical physics. Here we shall elucidate upon differential geometry, infinite series, Fourier and integral transforms, special functions, calculus, complex algebra, topology, group theory, linear algebra, etc. it is not wrong to say that mathematics is such powerful tool without which there cannot be Physics theory. We argue that adequately matching mathematics and physics education supports a parallel evolution of mathematical understanding and its applications in physics.

Introduction:

A deep, integrated understanding of concepts in physics cannot exist without understanding their mathematical descriptions. Let us consider, for example, the simple laws of classical mechanics. The physics of a point is generally described by a series of equations. The simplest one, usually introduced early in the curriculum, is

$$d = vt,$$

Where d is the distance travelled in meters, v the speed in meters per second, and t is the time in seconds. Students are typically asked to find either d or v, and are provided with the other quantities. Thus, at the core of mastery of this simple equation lies a solid understanding of multiplication and division. This concurrent mathematical understanding becomes more advanced in line with the increasing complexity of physics concepts. For example, to improve their understanding of classical mechanics further, pupils and students need to learn more sophisticated mathematical concepts like the derivative and the integration. Only then can they be introduced to the notion of acceleration and the relationship between acceleration, speed, and change of position. To take an example, from the simplest formula of a falling object.

$$y = -\frac{1}{2}gt^2 \text{ , where} g = 9.81 m/s^2.$$

Students can learn position change as a function of the g force on Earth. From this, they can play with derivatives in order to construct an internal representation of how speed varies as a function of time. The above highlights the central fact that the accuracy of the mental representation of the law of motion is embedded into the mathematical concepts describing it. Hence, understanding the mathematical concept is central to understanding the physics phenomenon. This simple example illustrates the fact that physics, in describing reality, uses mathematical tools which, in turn, offer an accurate description of reality. The theory of electromagnetism is dominated by the Maxwell equations, Einstein's equations describe the law of the universe at the highest scale, and quantum mechanics describes the behaviour of particles at the smallest end of the scale. In short, the tight link between mathematics and physics can be found at every corner.

Applications:

Some Mathematical Techniques in Physics Theory

1. Calculus.

2. Group Theory.

3. Complex Analysis.

4. Integral Transforms.

5. Ordinary and Partial Differential equations.

6. Greens Functions.

7. Tensors and Matrices.

8. Topology.

 9. Infinite Series

10. Functional Analysis.

11. Special Functions

12. Vector Spaces.

Calculus: Calculus is used in physics to calculate the centre of mass, the centre of gravity, object`s trajectory and so on. Without integration physics is incomplete. Integrals are used in physics to find Gravitational centre, the mass centre, vehicle mass and moment of inertia, satellite`s velocity and trajectory, finding the area encompassed in the eclipse and any enclosed area bounded by the X-axis and Y- axis can be find using integral calculus.

Linear momentum in Quantum Mechanics is defined as

$$p = -ih\frac{\partial}{\partial x}$$

And Hamiltonian can be expressed in terms of p. Integral and differential equation form the backbone of theoretical Physics. Quantum Mechanics when combined with the concept of Special Theory of Relativity yields the Quantum Field Theory.

Group Theory:

Group theory is a powerful mathematical tool that can be used to study symmetric physical systems in physics, such as molecules, crystals, and atomic spectra. It can also be used to solve problems in atomic and nuclear physics. Group theory can help you explain the most important characteristics of atomic spectra. Group theory is used to analyze molecular vibrations and electronic structure in molecules. This analysis helps in predicting and interpreting spectroscopic data. It is also used in crystallography to study the symmetries of crystals and predict their physical and chemical properties.

According to Noether`s theorem, if a Lagrangian L is invariant under some symmetry transformations, then there are conserved quantities in the physical system.

Consider example; if L is invariant under translation in space, then the linear momentum is conserved. Such transformations can be shown to form groups. Rotation groups form group SO(n). Electric charge conservations is the consequence of invariance under U(1) group, called gauge transformations. Symmetry of nuclear force under the exchange of neutron- proton (n-p) led scientists to show that the nuclear force is invariant under group SU(2), where the fundamental representation is 2-dimentional.

$$\binom{n}{p}$$

Similarly the three quarks form a fundamental representation of SU(3)

$$\begin{pmatrix} R \\ G \\ B \end{pmatrix}$$

Or

$$\begin{pmatrix} u \\ d \\ s \end{pmatrix}$$

Where R, G, B stands for red, green and blue quarks and u, d, s stands for up, down, strange type of flavors of quarks. Accordingly we have gauge theories for the respective groups $U(1)_Y,$ $SU(2)_L,$ and $SU(3)_C$. Gauge theories help explain the interactions among fundamental particles. Also elementary particles can be grouped according to these groups. Each group has generator and they obey lie algebra.

For. Example, the three Pauli matrices $\sigma_1, \sigma_2, \sigma_3$ are generators of the group SU(2)

$$\sigma_1 = \begin{pmatrix} 0 & 1 \\ 1 & 0 \end{pmatrix}, \qquad \sigma_2 = \begin{pmatrix} 0 & -i \\ 0 & 0 \end{pmatrix}, \qquad \sigma_3 = \begin{pmatrix} 1 & 0 \\ 0 & -1 \end{pmatrix}$$

And lie algebra is

$$\{\sigma_j, \ \sigma_k\} = 2i\epsilon_{jkl}\,\sigma_l$$

Where ϵ_{jkl} totally antisymmetric tensor of rank 3.

Complex Analysis

Complex analysis helps formulate wave functions and interpret quantum states, which is important for understanding how particles behave at a quantum level. Complex variables are also a fundamental part of quantum mechanics, appearing in the wave equation. Complex functions are used in potential flow theory to describe two-dimensional, inviscid, incompressible fluids. Complex analysis is also used in hydrodynamics, thermodynamics, twistor theory, conformal field theory, and string theory.

One of the important applications of complex analysis in the function that explains the propagation of a particle from one point in space to another is in Feynman`s propagator. It can be expressed in terms of Green`s function

$$G(r,r`) = \frac{1}{(2\pi)^4}\int d^4p \frac{e^{ip.(r-r`)}}{p^2 - (k^2 + i.\epsilon)}$$

The integration in complex –plane is done along the semicircle. The Feynman`s propagator is used in calculation of cross section of all physical processes.

Integral Transforms:

Integral transforms have many uses in physics, including solving differential equations, analyzing functions, and mapping one domain into another for easier analysis.

Integral transform $g(s)$ of a function $f(t)$ is defined as

$$g(s) = \int_a^b dt K(s,t) f(t)$$

Where K(s, t) is a kernel. Integral transform can be of many kinds

Fourier Transformation

Laplace Transformation

Dirac delta function

Mellin transform

They find applications in solving field equations, field quantisation procedure, propagator of the field etc. An example of integral transform is

$$\int d^3 x' \delta^3(x - x')\emptyset(x')v(x') = \emptyset(x)v(x)$$

Which follows from the property of Dirac-delta functions, Here $\emptyset(x)$ is a scalar field and $\delta^3(x - x')$ is the three dimensional Dirac delta function.

Ordinary and Partial Differential Equations:

Differential Equations are used to mathematically formulate and to find the solution of, physical and other problems involving functions of several variables, such as the propagation of heat or sound, fluid flow, elasticity, electrostatics, electrodynamics, thermodynamics.

All wave equations are of the form of differential equations, which in field theory become field equations.

The relativistic version of the Schrdinger equation- Klein- Gordon equation

$$-h^2 \frac{\partial^2 \emptyset}{\partial t^2} = -h^2 c^2 \nabla^2 \emptyset + m^2 c^4 \emptyset$$

Covariant form of Maxwell equations

Gauss`s Law- $\nabla.E = \frac{\rho}{\epsilon_0}$

Gauss`s Law for magnetism - $\nabla.B = 0$

Maxwell Faraday Equations- $\nabla \times E = -\frac{\partial B}{\partial t}$

Ampere's Circuital law with Maxwell's correction- $\nabla \times B = \mu_0 J + \mu_0 \epsilon_0 \frac{\partial E}{\partial t}$

Are some examples of ordinary and partial differential equations. The covariant form of above Maxwell's equation is used in Field Theory.

Another example of partial Differential equation is that of the heat equation which is the parabolic partial differential equation that describes the distribution of heat in a given region over time. The heat equation is

$$\frac{\partial^2 u}{\partial t^2} - \alpha \nabla^2 u = 0$$

Where α is positive constant and ∇^2 denote Laplace operator.

Green's Functions -

Green's function method is used in solving Field equations

$e.g.$ the equation,

$$(\nabla^2 + K^2)\psi(r) = v(r)\psi(r)$$

Can be solved using a Green's function G(r, r'), such that

$$(\nabla^2 + K^2)G(r,r') = -\delta^3(r,r')$$

And $\psi(r)$ can be expressed in terms of G(r, r')

Tensors and Matrices -

Matrices and tensors are both used in physics to describe physical transformations and solve problems. Matrices, often as operators, signify observable quantities in quantum mechanics and simplify space transformations. Tensors contribute to General Relativity, denote stress and strain in materials, and aid in expressing Maxwell's equations, thus enabling understanding of key physical phenomena.

In special Theory of Relativity, Tensors and Matrices are used. the invariant interval between two physical events can be expressed as

$$ds^2 = g_{\mu\vartheta} dx^\mu dx^\vartheta$$

where $g_{\mu\vartheta}$ is the metric tensor, and dx is the 4-dimensional spacing between two points. In Minkowski's space

$$g_{\mu\vartheta} = \begin{bmatrix} 1 & 0 & 0 & 0 \\ 0 & -1 & 0 & 0 \\ 0 & 0 & -1 & 0 \\ 0 & 0 & 0 & -1 \end{bmatrix}$$

Moreover, in the Quantum Field Theory, all field equations are used in 4-vector notation (Einstein's unified 4-dimensional space), with

Lorentz covariant formulations. Hence tensors form necessary ingredients for Theoretical High Energy Physics, e.g, the Dirac field equation is,

$$\left(i\gamma_\mu \partial_\mu + m\right) = 0$$

Also, in Quantum Mechanics, wave functions are taken as components of a Hilbert space and are treated as column orrow vectors.

Operators are treated as matrices in Matrix Mechanics formulation of Quantum Mechanics. For example, *LZ*, the third component of angular momentum operator is

$$L_z = i\frac{h}{2\pi}\begin{pmatrix} 1 & 0 \\ 0 & -1 \end{pmatrix}$$

Topology

It is an area of Mathematics concerned with the properties of space that are preserved under continuous deformation,

Such as bending or stretching, but not tearing or gluing. along with algebraic or differential geometry, it is used in

String Theory. As discussed earlier, String Theory exists in higher dimensions, so compactification is required to go from

higher to 4 dimension. This compactification can be done, e.g, along circle or torus, etc. Hence geometry of torus is needed in String Theory.

Infinite Series

Infinite series find many applications, including solutions of wave equations, field equations, evaluation of integrals etc, and TP. It is also used in perturbation theory– when a system is perturbed by an external force, or when interaction

among particles are treated as perturbations to the free Hamiltonian.

The exponential can be expanded as an infinite series

$$e^x = 1 + \frac{x}{1!} + \frac{x^2}{2!} + \frac{x^3}{3!} + \frac{x^4}{4!} + \frac{x^5}{5!} + \frac{x^6}{6!} + \cdots$$

An applications of exponential series is Planck radiation formula at low temperatures

$$8\pi \frac{V^2}{C^3} \frac{hV}{e^{\frac{hV}{kT}} - 1} = 8\pi \frac{V^2}{C^3} kT$$

Functional Analysis

Function of a function is called a functional. In Quantum Field Tteory, the field is a function of 4– D position vector.

$$\phi = \phi\ (X_\mu)$$

and the Lagrangian is a function of $\phi\ (X_\mu)$, hence

$$L[\phi\ (X_\mu)]$$

is a functional. This functional analysis is used in Perturbation theory, which forms a necessary tool to handle interaction among particles in Theoretical Physics.

Special Functions:

Special Functions is a very important and commonly used mathematical concept. Solution of Schrodinger equation which forms the basis of Quantum Mechanics and Quantum Field Theory, uses associated Legendre's

polynomial and Hermite polynomial. Perturbation theory, which forms the basis of interaction among elementary particles uses special functions. Special functions form the complete Orthogonal basis, a plane wave solution can be expressed in terms of Legendre's functions. Bessel function is used in electromagnetic wave confined between concentric and cylindrical surfaces.

Vector Spaces:

The spaces, whose elements are functions, constitute vector spaces. The following spaces are vector spaces.

The space of continuous real or complex valued function defined on an interval [a, b].

The space of real or complex valued function of a real variable x satisfying

$$\lim_{x \to \infty} f(x) = 0$$

The values $f(x)$ of a function for various values of x are analogues of components of a vector which are now labelled by a continuous index.

Hilbert Space- Hilbert space is a space of vectors or functions for which inner product of any two vectors or functions is positive definite and norm of a vector is given by

$$f(x) = \sqrt{(f, f)}$$

Where (f, f) is the inner product defined as

$$(f, f) = \int_a^b dx f^*(x) f(x)$$

Where the integral is a Riemann integral. The simple example of Hilbert spaces are the spaces of n-rowed column vectors with scalar product

$$(A, B) = \sum_{i=1}^n A_i^* B_i$$

Conclusion:

It is evident that physics and math are very much intertwined with each other. It is difficult to study one without the other, and vice versa. The concepts in physics often require a strong mathematical background in order to be fully understood. This is why many physicists also have a deep understanding of mathematics. The two subjects complement each other perfectly, and together they provide a strong foundation for scientific knowledge.

References:

1.Book- Elements of group theory for physicists, by A.W.Joshi, New Age International Publishers.

2. Kalpana Bora, Neelkashi Sarma, Springer Conf. proceedings 2016 . arxiv :hep-ph/1511.02676

3. Kalpana Bora and Gayatri Ghosh, EPJC Vol 75, 428, 2015 . arxiv:1410.1265.

4. Book- Mathematical methods for Physicists by George B.Arfken and J.Webber, Academic   Press.

5. Book- Matrices and Tensors in Physics, by A.W. Joshi, New Age International Publishers.

6. Kalpana Bora, Debajyoti Dutta and Pomita Ghoshal,MPLA , vol 30, 1550066 (2015). hep-ph/1405.7482.

7. K. Bora, Indian Jr. Of Physics, 82 (6), 753-59 (2008).

8. K. Bora and R. L. Jaffe, Physical Review D 57, 6906 (1998).

Investigation on Structural, Elastic and Magnetic properties of nanocrystalline Ni0.30Cu0.30Zn0.40Fe2O4 ferrite synthesized via sol-gel method

Jyoti D Bhamare[1], N.D. Chaudhari[2]

[1]Department of Physics, Dr.Babasaheb Ambedkar Marathwada University, Chh.Sambhajinagar (Aurangabad)-431001, Maharashtra, India

[2]*Department of physics, Pratishthan mahavidyalaya, Paithan, Chh.Sambhajinagar (Aurangabad)-431007, Maharashtra, India

Abstract :

Nanocrystalline Ni0.30Cu0.30Zn0.40Fe2O4 soft ferrite was synthesized via sol gel auto combustion method. The synthesized ferrite composition was characterized using XRD and FTIR technique and structural parameter were investigated. The magnetic properties were determined using VSM. XRD data reveals the single phase cubic spinel structure. All the Braggs reflections have been indexed and confirm the formation of single phase cubic spinel structure. The FTIR spectra of synthesized ferrite composition showed two absorption bands ($\upsilon1$ and $\upsilon2$) in the range 400-600 cm-1 belonging to tetrahedral (A) and octahedral (B) sites in the spinel lattice. The elastic properties of present ferrite system were investigated using FTIR spectra. The crystalline size is determined using Debye scherrer's formula and found to be in nanometre range of 26 nm and is in good agreement with the grain size obtained from SEM. The magnetic characteristics such as saturation magnetization, coercive force and remanence ratio were investigated using VSM.

Keywords: Ferrite, Sol-gel, XRD, FTIR, VSM.

I. INTRODUCTION

The term ferrite is commonly used generically to describe a class of magnetic oxide compounds which contain iron oxide as a main component. Spinel ferrites are known to be a class of chemically and thermally stable materials and suitable for a wide variety of applications such as those in hyperthermia, information storage systems, gas sensors, microwave devices, magnetic recording media, electronic industries, humidity sensors and green anode materials [1–6]. The synthesis of spinel type nano-structured magnetic materials with the general formula $M^{2+}(Fe^{3+})_2O_4$ (where $M^{2+}=$ Mn^{2+}, Co^{2+}, Ni^{2+}, Cu^{2+}, Zn^{2+}, etc.) has become an important part of modern ceramic research, due to their unique physical and chemical properties than that of their bulk counterparts [7]. It is known that the chemical composition, method of preparation, doping additives, and sintering conditions are found to affect the properties of the ferrite materials [8]. Various synthesis techniques have been developed and used for the preparation of nanocrystalline spinel ferrite nano particles such as solvothermal [9], coprecipitation [7], hydrothermal [10], sol–gel [11] and combustion [12] methods. Among other substituted ferrites the Ni- Zn ferrites are known to be a stable material and extremely used in many

electronics devices because of their interesting properties such as high resistivity, moderate saturation magnetization, low coercivity, high Curie temperature, moderate initial permeability good mechanical hardness and chemical stability [13-23]. Diamagnetic substitution in spinel ferrites is found to be interesting as it induces changes in the structural and the magnetic properties [24-30]. The introduction of diamagnetic ions into spinel ferrites is expected to weaken the magnetic coupling within the structure, which may change the magnetic properties. Therefore, in this attempt Ni0.30Cu0.30Zn0.40Fe2O4 nanoferrite was synthesized using sol gel auto combustion method. In this present work we report the structural, eleastic, surface morphological and magnetic properties of Ni0.30Cu0.30Zn0.40Fe2O4 nanoferrites.

II. METHODS AND MATERIAL

The nanoparticle of Ni0.30Cu0.30Zn0.40Fe2O4 ferrite was prepared by using sol gel auto combustion method. Nickel nitrate (Ni(NO3)2.6H2O), copper nitrate (Cu(NO3)2.3H2O), zinc nitrate (Zn(NO3)2.6H2O), ferric nitrate (Fe(NO3)2.9H2O) and citric acid (C6H8O7.H2O). All AR grade raw salt are used as a primary material. The solutions of nitrates were prepared in minimum amount of de-ionized water; Citric acid is used as a chelating agent. The mixture was stirred and heated continuously at 80℃ in order to convert it in to viscous brown gel. After the formation of gel the stirring is stopped and get allowed to burn via auto combustion reaction. After complete burning a loose floopy powder of the end product is obtained. This synthesized powder was heated at 200℃ for two hours to remove the water content. This powder was again heated at 500℃ for four hours. Final sintering was done at 1000℃ for ten hours.

Characterization:

X ray diffraction in 2θ range of 20° to 80° at room temperature using CuKα, λ = 1.5406 Å radiation. An FTIR spectrum was recorded using FTIR-Shimatzu Iraffinity IR spectrometer in the range 300 to1000 cm-1. FE-SEM study was carried out using NOVA NANO SEM-450 with accelerating voltage of 20KV. Magnetic measurement was obtained using VSM with applied field ± 20 KOe at room temperature.

III.RESULTS AND DISCUSSION

A) X- Ray Diffraction:

Fig.1 shows the XRD pattern of Ni0.30Cu0.30Zn0.40Fe2O4 ferrite composition. All the Braggs reflections have been indexed and confirm the formation of single phase cubic spinel structure. XRD pattern clearly shows all allowed Braggs reflections of spinel structures as (220), (311), (222), (400), (422), (511), (440) and (533). These reflections correspond to the allowed values of reflections for cubic spinel structure. The X-ray diffractograms do not point out the occurrence of any unwanted phase confirming the single-phase spinel formation.The structural parameters such as lattice constant, crystalline size D, X-ray density and bulk density, % porosity and site radii were estimated using standard formula [8,9,10,11, 12] and mentioned in table 1. The lattice parameter of Ni0.30Cu0.30Zn0.40Fe2O4 ferrite composition is found to be 8.3785Å. The particle size obtained from X-ray pattern by using Debye Scherrer's formula is in the nano-meter range of 26 nm.
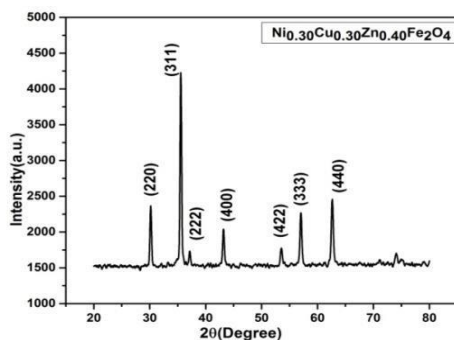
Fig.1 XRD pattern of Ni0.30Cu0.30Zn0.40Fe2O4

Table:1-structural parameters of Ni0.30Cu0.30Zn0.40Fe2O4

Lattice constant a (Å)	8.3785	
Crystalline size D nm	26	
x-ray density dX (gm/cm^3)	5.38	
Bulk density dB (gm/cm^3)	4.98	
Porosity (%) P	7.55	
Cation distribution	(Ni0.07Cu0.07Zn0.12Fe0.74)^A [Ni0.23Cu0.23Zn0.28Fe1.26]^B	
site radii	rA	0.5225
	rB	0.6733

B) FTI R

Fig. 2 shows the FTIR spectra for present ferrite composition. Two absorption bands corresponding to the vibration of tetrahedral and octahedral complexes at 538.14 cm-1 and 409.91 cm-1 were observed, confirming the formation of spinel ferrite structure. The absorption band ν1 was caused by stretching of tetrahedral metal ion and oxygen bonding, whereas ν2 was caused by the vibration of oxygen in the direction perpendicular to the axis joining tetrahedral ion and oxygen ion. Waldron attributed the absorption band ν1 to the intrinsic vibration of tetrahedral groups corresponding to the highest restoring force and band ν2 to octahedral groups which are due to bond bending vibrations. The difference in the position of two bands ν1 and ν2 could be related to the difference in Fe^{3+} and O^{2-} distance for the A site and the B site. The force constants corresponding to the tetrahedral and octahedral complexes are determined and tabulated in Table 2. The obtained values of elastic parameters such as Wave velocities, Debye temperature, longitudinal modulus (L), Young's modulus (E), Bulk modulus (B), are also tabulated in Table 2
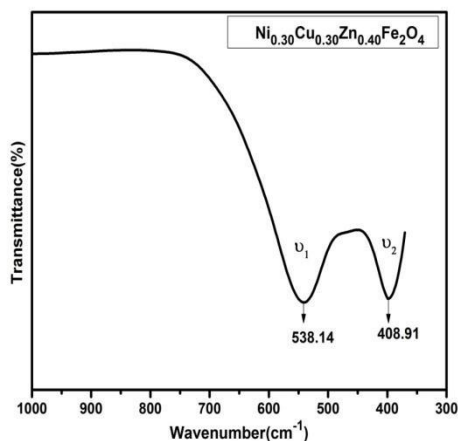
Fig.2 FTIR Spectra of Ni0.30Cu0.30Zn0.40Fe2O4

Table: 2-Elastic parameters ofNi0.30Cu0.30Zn0.40Fe2O4

Ni0.30Cu0.30Zn0.40Fe2O4	
v_1 cm^{-1}	538.14
v_2 cm^{-1}	408.91
K_1	127.37
K_2	103.67
θ_D (K)	446.81
V_L (m/s)	5261.84
V_T (m/s)	3037.93
V_M(m/s)	3372.67
L(GPa)	137.88
G (GPa)	45.96
σ(GPa)	0.2984
E (GPa)	119.35
B(GPa)	45.96

C) SEM Analysis:

Fig. 3 shows the FE-SEM micrograph for ferrite composition Ni0.30Cu0.30Zn0.40Fe2O4 . The crystallite size of grains was measured by using Intercept method [13]. The obtained grain size is 26.30 nm which is in good agreement with the crystallite obtained using XRD data. Hence the synthesized ferrite material of composition is in nanometer range.
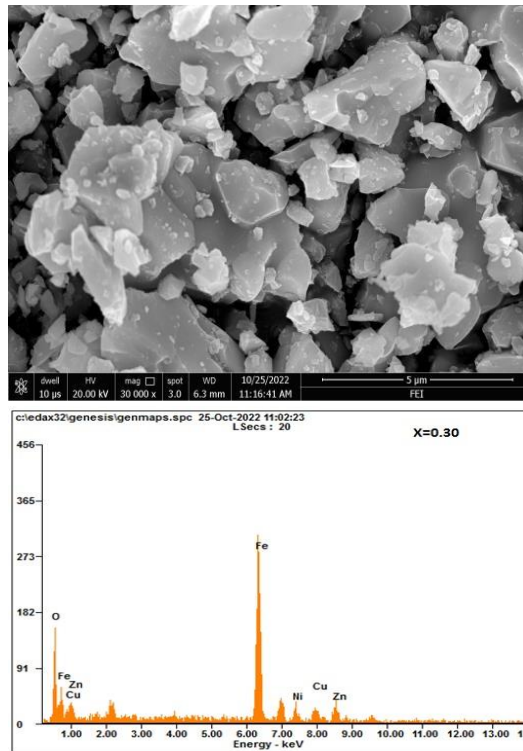
Fig.3 FESEM and EDX of Ni0.30Cu0.30Zn0.40Fe2O4

D) Magnetic Properties

Fig.4 illustrates the M-H curve for present ferrite composition. The obtained magnetic parameters are listed in Table 2. This M-H curve is used to evaluate the values of saturation magnetization, magnetic moment, coercive force and remanence ratio. The cation distribution mentioned in Table 1 influences the magnetic parameters of synthesized Ni0.30Cu0.30Zn0.40Fe2O4 ferrite composition. In present system Ni 2+ with the magnetic moment of $2.3\mu B$ replaces Cu of small magnetic moment $1.3\mu B$, both having strong desire to occupy the both tetrahedral and octahedral site , Fe 3+ also distributed over both A and B sites, hence resultant net magnetization is according to Neel's ferromagnetic theory [14]. Table:3- Saturation Magnetization (Ms), Remenance Magnetization (Mr), Coercivity (Hc), Remenance ratio (Mr/Ms), Magnetron Number (nB) Magnetic parameters of Ni0.30Cu0.30Zn0.40Fe2O4

Ms	Mr	Hc	Mr/Ms	nB
73.77	1.03	12	0.013	3.15
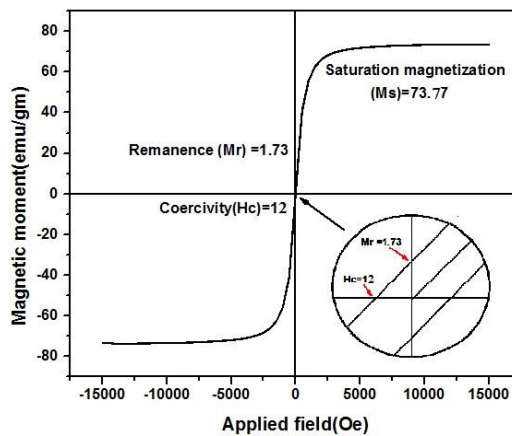
Fig.4- M-H Curve of Ni0.30Cu0.30Zn0.40Fe2O4

IV. CONCLUSIONS

Nanocrystalline ferrite composition Ni0.30Cu0.30Zn0.40Fe2O4 was synthesized by self ignited sol gel auto combustion method. The XRD pattern shows the formation of single phase cubic spinel structural of the ferrite. FTIR spectra designate the two absorption bands, one foroctahedral site (408.91 cm -1). The crystallite size obtained from FE-SEM is good agreement with XRD data and lies in nano metre range. The values of magnetic parameters show the ferromagnetic behaviour of the present ferrite system.

V. REFERENCES

[1]. N.Kikukawa, M.Takemori, Y.Nagano, M.Sugasawa, S.Kobayashi, Synthesis and magnetic properties of nanostructured spinel ferrites using a glycine– nitrate process, Journal of Magnetism and Magnetic Materials , 284(2004) 206– 214.

[2]. K.A.Mohammed, A.D.Al-Rawas, A.M.Gismelseed, A.Sellai, H.M.Widatallah, A. Yousif, M.E.Elzain, M.Shongwe, Infrared and structural studies of Mg1_xZnxFe2O4 ferrites, Physica B407 (2012) 795–804.

[3]. M.Al-Haj, Structural characterization and magnetization of Mg0.7Zn0.3SmxFe2_xO4 ferrites, Journal of Magnetism and Magnetic Materials, 299 (2006)435–439.

[4]. H.Spiers, I.P.Parkin, Q.A.Pankhurst, L.Affleck, M.Green, D.J.Caruana, M.V. Kuznetsov, J.Yao, G.Vaughan, A.Terry, A.Kvick, Self propagating high temperature synthesis of magnesium zinc ferrites (MgxZn1_xFe2O3): thermal imaging and time resolved X-ray diffraction experiments, Journal of Materials Chemistry 14(2004)1104–1111.

[5]. Z.P¸edzich, M.M.Buc´ko, M.Kro´ likowski, M.Bakalarska, J.Babiarz, Micro- structure and properties o f Mg–Zn ferrite as a result ofs intering temperature, Journal of the European Ceramic Society, 24 (2004)1053–1056.

[6]. P.Poddar, H.Srikanth, S.A.Morrison, E.E.Carpenter, Interparticle interac- tions and magnetism in manganese–zinc ferrite nanoparticles, Journal of Magnetism and Magnetic Materials, 288(2005)443–451.

[7]. C.G. Ramankutty, S. Sugunan, Appl. Catal. A 218 (2001) 39– 51.

[8]. I. H. Gul and A. Masqood, "Structural, magnetic and electrical properties of cobalt ferrites prepared by the sol – gel route", Journal of Alloys and Compounds, 465, (2008) pp. 227 – 231.

[9]. S.Y. Vilar, M.S. Andujar, C.G. Aguirre, J. Mira, M.A.S. Rodriguez, S.C. Garcia, J. Solid State Chem. 182 (2009) 2685–2690.

[10]. A. Baykal, N. Kasapoglu, Y. Koseoglu, M.S. Toprak, H. Bayrakdar, J. Alloys Compd. 464 (2008) 514–518.

[11]. K. Yan, X. Wu, X. An, X. Xie, J. Alloys Compd. 552 (2013) 405–408.

[12]. A.B. Salunkhe, V.M. Khot, M.R. Phadatare, S.H. Pawar, J. Alloys Compd. 514 (2012) 91–96.

[13]. B.P. Rao, K.H. Rao, Initial permeability dependence on the microstructural and compositional changes in Ni-Zn-Sc ferrites, J. Phys. IV France 07 (1997), C1-239-C1-240.

[14]. A.C.F.M. Costa, E. Tortella, M.R. Morelli, R.H.G.A. Kiminami, Synthesis, microstructure and magnetic properties of Ni–Zn ferrites, J. Magn. Magn. Mater. 256 (2003) 174–182

[15]. J.B. Da Silva, N.D.S. Mohallem, Preparation of composites of nickel ferrites dispersed in silica matrix, J. Magn. Magn. Mater. 226 (2001) 1393–1396,

[16]. M. Jalaly, M.H. Enayati, F. Karimzadeh, Investigation of structural and magnetic properties of nanocrystalline Ni0.3Zn0.7Fe2O4 prepared by high energy ball milling, J. Alloys. Compd. 480 (2009) 737–740.

[17]. M. Sertkol, Y. K¨oseo˘glu, A. Baykal, H. Kavas, A.C. Bas¸aran, Synthesis and magnetic characterization of Zn0.6Ni0.4Fe2O4 nanoparticles via a polyethylene glycol-assisted hydrothermal route, J. Magn. Magn. Mater. 321 (2009) 157–162.

[18]. A.M. Abdeen, Dielectric behaviour in Ni–Zn ferrites, J. Magn. Magn. Mater. 192 (1999) 121–129,

[19]. P.S.A. Kumar, J.J. Shrotri, S.D. Kulkarni, C.E. Deshpande, S.K. Date, Low temperature synthesis of Ni0.8Zn0.2Fe2O4 powder and its characterization, Mater. Lett. 27 (1996) 293–296,

[20]. H. Igarashi, K. Okazaki, Effects of porosity and grain size on the magnetic properties of NiZn ferrite, J. Am. Ceram. Soc. 60 (1977) 51–54

[21]. S.W. Lee, C.S. Kim, Superparamagnetic properties Ni–Zn ferrite for nano-bio fusion applications, J. Magn. Magn. Mater. 304 (2006) 418–420,

[22]. T. Nakamura, Snoek's limit in high-frequency permeability of polycrystalline Ni–Zn, Mg–Zn and Ni–Zn–Cu spinel ferrites, J. Appl. Phys. 88 (2000) 348–353.

[23]. T. Nakamura, Low-temperature sintering of NiZnCu ferrite and its permeability spectra, J. Magn. Magn. Mater. 168 (1997) 285–291

[24]. R. G. Kulkarni, B. S. Trivedi, H. H. Joshi and G. J. Baldha, J. Magn. Magn. Mater. 159, 375 (1996).

[25]. B. S. Trivedi, N. N. Jani, H. H. Joshi and R. G. Kulkarni, J. Mater. Sci. 35, 5523 (2000).

[26]. A. T. Raghavender, R. G. Kulkarni and K. M. Jadhav, Chin. J. Phys. 46, 366 (2008).

[27]. A. T. Raghavender, R. G. Kulkarni and K. M. Jadhav, Chin. J. Phys. 48, 512 (2010).

[28]. A. T. Raghavender and K. M. Jadhav, Int. J. Mod. Phys. B 23, 223 (2009).

[29]. A. T. Raghavender, D. Pajic, K. Zadro, T. Milekovic, P. V. Rao, K. M. Jadhav and D. Ravinder, J. Magn. Magn. Mater. 316, 1 (2007).

[30]. A. T. Raghavender, Int. J. Mod. Phys. B 25, 1121 (2011)

Numerical Approximation of Atangana-Baleanu Caputo Fractional Derivative and Its Application to Fractional Order Subdiffusion Bioheat Equation

Jagdish Sonawane[1], Bahusaheb Sontakke[2], Kalyanrao Takale[3]

[1]Department of Mathematics, GES R. H. Sapat College of Engineering, Manage- ment and Research, Nashik-422005 (M.S.), India

[2]Department of Mathematics, Pratishthan Mahavidyalaya, Paithan,Aurangabad, (M.S.), India

[3]Department of Mathematics, RNC Arts, JDB Commerce and NSC Science College, Nashik-Road, Nashik, India

Abstract :

To overcome limitations of local and singular kernel in classical definition of fractional derivative, recently Caputo and Fabrizio introduce new fractional derivative by using non local and non-singular exponential kernel. This frac- tional derivative is generalized by Atangana and Baleanu with Mittag-Leffler function. In this paper, we used Atangana- Baleanu -Caputo fractional deriva- tive to devlope fractional order finite difference scheme for solving fractional or- der subdiffusion bioheat equation. The stability and convergence is established numerically and graphically. Python code is developed to obtained numerical and graphical solutions of fractional order subdiffusion bioheat equation.

Keywords and phrases: Fractional Differential Equation, Atangana-Baleanu-Caputo fractional derivatives, Subdiffusion bioheat equation, Mittag-Leffler function, Python etc. 2020 Mathematics Sub ject Classification: 35R11, 80M20, 65M06.

I. INTRODUCTION

Fractional Calculus is one of the branch of Mathematics having various applications[5] in biology, economics, physics, engineering, and chemistry etc. Recently many phys- ical problems are modelled by researchers more accurately[20] with replacement of ordinary operators by fractional operators. Many mathematicians viz. Riemann- Liouville, Grunwald-Letnikov, Caputo, Riesz, Hadmard etc. developed various clas- sical definitions of fractional derivative in literature[20]. Modelling of non-local dy- namical systems by using these definitions is restricted due to local and singular kernel[20]. New definition of fractional derivative with non-singular and non-local[9] exponential kernel is introduced by Caputo and Fabrizio[9], later on this fractional derivative[9] is generalized with Mittag Leffler function as kernel by Atangana and Baleanu[20]. Many researchers applied this definition in various physical models[13].

This definitions is more useful for solving non-linear systems.

Numerical approximations of nonlinear system is necessary due to their complexi- ties. Recently researchers developed many numerical method[11],[17],[18] for solving non-linear systems. Now, numerical approximations of Atangana-Baleanu fractional derivative is developed by Atangana and et.al.[1] and Yadav

and et.al.[20]. In this paper we used this approximation with Finite difference method. We applied this numerical approximation of Atangana-Baleanu Caputo fractional derivative to frac- tional order bioheat equation developed by Takale and et. al.[10]. In 1948, Harry H. Pennes firstly developed mathematical model for temperature in resting human forearm[4], this model is known as bioheat transfer equation, given as below:

$$\rho C \frac{\partial T(x,t)}{\partial t} = k \frac{\partial^2 T(x,t)}{\partial x^2} + W_b C_b (T_a - T) + Q_r, \ x \in [0, L], \ t \in [0, T]$$

Where T =temperature, t =time, ρ =density, C =specific heat, x =distance, k =thermal conductivity, T_a =temperature of artillery, W_b =blood perfusion rate, Q_r =the constant volumetric heat, C_b =specific heat of blood. Many researchers developed modified versions of Penne's bioheat models[2],[6],[15],[16],[23] and various techniques of their solutions[21],[24]. Damor(2013)[16], Ezzat(2014)[14] and Ferras(2015)[12] developed fractional bioheat models by using Caputo fractional derivative. Recently, Asjad and Zhang[13] used Atangana-Baleanu and Caputo-Fabrizio fractional[9] derivative in various fractional bioheat models. In this paper we have discussed, fractional bio heat model developed by Takale and et. al.[10], is given as

$$\frac{\partial^\alpha Z^*}{\partial t^\alpha} + \frac{1}{\rho C} W_b C_b Z^* - \frac{1}{\rho C} \frac{\partial}{\partial x}\left[g(x) \frac{\partial Z^*}{\partial x}\right] = \frac{1}{\rho C} Q_r, \ 0 \le x \le L, \ 0 \le t \le T$$

where $Z^* = T - T_a$, $k = g(x)$ and $\frac{\partial^\alpha Z^*}{\partial t^\alpha}$ is fractional derivative of Caputo type with $0 < \alpha \le 1$

Now assuming

$$Z = Z^* - \frac{Q_r}{W_b C_b}, \quad a = \frac{1}{\rho C} W_b C_b, \quad b = \frac{1}{\rho C} > 0$$

we get

$$\frac{\partial^\alpha Z}{\partial t^\alpha} + a Z - b \frac{\partial}{\partial x}\left[g(x)\frac{\partial Z}{\partial x}\right] = 0, \tag{1.1}$$

$$\text{where } 0 < \alpha \le 1 \text{ and } 0 \le x \le L, \ 0 \le t \le T$$

$$\text{Initial condition :} \left[Z(x,t)\right]_{t=0} = 0, \quad \text{for all} \ x \tag{1.2}$$

$$\text{Boundary conditions :} \left[Z(x,t)\right]_{x=0} = Z_0, \left[Z(x,t)\right]_{x=L} = 0, \quad \text{for all} \ t \tag{1.3}$$

Time fractional derivative introduce subdiffusion or superdiffusion without disturbing properties of density and specific heat of material. Now, subdiffusion is a process of time meomory. Subdiffusion equation contains fractional derivative of order α, which is subdiffusion parameter. Note that α = 1 corresponds to normal diffusion and 0 < α < 1 corresponds to subdiffusion. We modified fractional bioheat equation (1.1)-(1.3) with Atangana-Baleanu fractional derivative instead of Caputo fractional derivative of order α, in the sense of subdiffusion i.e. 0 < α < 1. Hence Fractional order subdiffusion bioheat equation is as follow:

$$\frac{^{ABC}\partial^\alpha Z}{\partial t^\alpha} + a\,Z - b\frac{\partial}{\partial x}\left[g(x)\frac{\partial Z}{\partial x}\right] = 0, \tag{1.4}$$

$$\text{where } 0 < \alpha < 1 \text{ and } x \in [0, L],\ t \in [0, T]$$

$$\text{Initial condition : } \Big[Z(x,t)\Big]_{t=0} = 0, \qquad \text{for all } x \tag{1.5}$$

$$\text{Boundary conditions : } \Big[Z(x,t)\Big]_{x=0} = Z_0,\ \Big[Z(x,t)\Big]_{x=L} = 0, \qquad \text{for all } t \tag{1.6}$$

The paper is arrange as follow: In section 2, some basic definitions of fractional derivatives are discussed. We discuss discretization of Atangana-Baleanu fractional derivative and apply in development of finite difference scheme for solution of fractional order subdiffusion bioheat equation (1.4) in section 3. Stability and convergence of developed finite difference scheme is discussed in section 4. In section 5 approximate solution of subdiffusion bioheat transfer equation is obtained by using Python code developed by us. Section 6 is devoted to conclusions.

2 Definitions of Fractional Derivative

Definition 2.1. Riemann-Liouville Fractional integral:[8]

$$_0J_t^\alpha f(t) = \frac{1}{\Gamma(\alpha)}\int_0^t (t-u)^{\alpha-1} f(u)\,du, \tag{2.1}$$

where $f(t) \in C[0,1]$, $\alpha \in (-\infty, \infty)$.

Definition 2.2. *Riemann-Liouville Fractional Derivative:[8]*

$$_0^R D_t^\alpha f(t) = D_0^1 I_t^{1-\alpha} f(t) = \frac{d}{dt}\frac{1}{\Gamma(1-\alpha)}\int_0^t (t-u)^{-\alpha} f(u)\,du, \tag{2.2}$$

where $f(t) \in C[0,1]$, $0 < \alpha < 1$.

Definition 2.3. *Caputo Fractional Derivative:[5]*

$$_0^C D_t^\alpha f(t) = {_0}I_t^{1-\alpha} D^1 f(t) = \frac{1}{\Gamma(1-\alpha)}\int_0^t (t-u)^{-\alpha} f'(u)\,du, \tag{2.3}$$

where $f(t) \in C[0,1]$, $0 < \alpha < 1$.

Let $M(\alpha)$ is normalization function which satisfies $M(0) = M(1) = 1$

Definition 2.4. *Caputo-Fabrizio Fractional Derivative:[7]*

$$\,_{0}^{CF}D_t^\alpha f(t) = \frac{M(\alpha)}{(1-\alpha)} \int_0^t exp\big[\frac{-\alpha}{1-\alpha}(t-u)\big] f'(u)\, du, \qquad (2.4)$$

where $f(t) \in H^1(0,1)$, $0 < \alpha < 1$.

Definition 2.5. *Atangana-Baleanu[9],[1] Fractional Derivative in the sense of Caputo :[1],[9]*

$$\,_{0}^{ABC}D_t^\alpha f(t) = \frac{M(\alpha)}{(1-\alpha)} \int_0^t E_\alpha\big[\frac{-\alpha}{1-\alpha}(t-u)^\alpha\big] f'(u)\, du, \qquad (2.5)$$

where $f(t) \in H^1(0,1)$, $0 < \alpha < 1$ and $E_\alpha(z)$ is Mittag-Leffler function defined as

$$E_\alpha(z) = \sum_{k=0}^{\infty} \frac{z^k}{\Gamma(\alpha K + 1)}$$

3   Finite difference scheme

To develop the Crank- Nicolson finite difference scheme[19] for subdiffusion bioheat transfer equation (1.4)-(1.6), we define $x_i = i\Delta x$, $i = 0, 1, \ldots, M$ and $t_n = n\Delta t$, $n = 0, 1, \ldots, N$; where $\Delta x = \frac{L}{M}$ and $\Delta t = \frac{T}{N}$ Consider exact solution of subdiffusion bioheat transfer equation (1.4) at mesh point (x_i, t_n) is $Z(x_i, t_n)$, $i = 0, 1, \ldots, M$ and $n = 0, 1, \ldots, N$. Also Z_i^n is numerical approximation at point (x_i, t_n). Note that Δx is space step size and Δt is time step size.

Atangana-Baleanu-Caputo type time fractional derivative is discretize [1] as follows:

$$\Big(\frac{^{ABC}\partial^\alpha Z}{\partial t^\alpha}\Big)_n^i = \frac{M(\alpha)}{(1-\alpha)} \int_0^{t_{n+1}} E_\alpha\big[\frac{-\alpha}{1-\alpha}(t_{n+1}-u)^\alpha\big] \frac{\partial Z(x,u)}{\partial u}\, du$$

$$= \frac{M(\alpha)}{(1-\alpha)} \sum_{j=0}^{n} \Big[\frac{Z_i^{n+1}-Z_i^n}{\Delta t}\Big] \int_{t_j}^{t_{j+1}} E_\alpha\big[\frac{-\alpha}{1-\alpha}(t_{n+1}-u)^\alpha\big]\, du + R_{n+1}$$

$$\Big(\frac{^{ABC}\partial^\alpha Z}{\partial t^\alpha}\Big)_n^i = \frac{M(\alpha)}{(1-\alpha)} \big[Z_i^{n+1}-Z_i^n\big] d_0 + \frac{M(\alpha)}{(1-\alpha)} \sum_{j=1}^{n} \big[Z_i^{n-j+1}-Z_i^{n-j}\big] d_j + R_{n+1}$$

$$\qquad (3.1)$$

where

$$d_j = \big[(j+1)E_{\alpha,2}(\eta_{j+1}) - jE_{\alpha,2}(\eta_j)\big] \text{and } \eta_j = \frac{-\alpha}{1-\alpha}\big[(j\,\Delta t)^\alpha\big] \qquad (3.2)$$

Here

$$R_{n+1} = \frac{M(\alpha)}{(1-\alpha)} \frac{(\Delta t)^2}{2} \sum_{j=0}^{n} \frac{\partial^2 Z}{\partial t^2} \left[(n-j+1) E_{\alpha,2}(\eta_{n-j+1}) - (n-j) E_{\alpha,2}(\eta_{n-j}) \right]$$

$$\leq \frac{M(\alpha)}{(1-\alpha)} \frac{(\Delta t)^2}{2} \left[\max_{0 < t < t_n} \frac{\partial^2 Z}{\partial t^2} \right] C_1$$

Where C_1 is constant.

Now, we discretize of space derivative given in (1.4) by using Crank-Nicolson Method[3] as follow:

$$\frac{\partial}{\partial x} \left[g(x) \frac{\partial Z}{\partial x} \right]_i^n = \frac{1}{2 (\Delta x)^2} \left[g_i Z_{i-1}^{n+1} - 2 g_i Z_i^{n+1} + g_i Z_{i+1}^{n+1} \right.$$

$$\left. + (2 g_i - g_{i+1}) Z_{i-1}^n - 2 g_i Z_i^n + g_{i+1} Z_{i+1}^n \right]$$

(3.3)

where $g(x_i) = g_i$

Now we can discretize Fractional order subdiffusion bioheat equation (1.4) by using (3.1) and (3.3) as follow:

$$\frac{M(\alpha)}{(1-\alpha)} \left[Z_i^{n+1} - Z_i^n \right] d_0 + \frac{M(\alpha)}{(1-\alpha)} \sum_{j=1}^{n} \left[Z_i^{n-j+1} - Z_i^{n-j} \right] d_j + a Z_i^n$$

$$- \frac{b}{2 (\Delta x)^2} \left[g_i Z_{i-1}^{n+1} - 2 g_i Z_i^{n+1} + g_i Z_{i+1}^{n+1} + (2 g_i - g_{i+1}) Z_{i-1}^n - 2 g_i Z_i^n \right.$$

$$\left. + g_{i+1} Z_{i+1}^n \right] = 0$$

$$\therefore \; -\mu_1 \, g_i \, Z_{i-1}^{n+1} + (1 + 2\,\mu_1 \, g_i)\, Z_i^{n+1} - \mu_1 \, g_i \, Z_{i+1}^{n+1}$$

$$= (2\,\mu_1 \, g_i - \mu_1 \, g_{i+1})\, Z_{i-1}^n + (1 - 2\,\mu_1 \, g_i - \mu_2)\, Z_i^n + \mu_1 \, g_{i+1} \, Z_{i+1}^n - \sum_{j=1}^{n} \left[Z^{n-j+1} - Z^{n-j} \right] d_j$$

$$(3.4)$$

where $\qquad \mu_1 = \dfrac{b\,(1-\alpha)}{2\,M(\alpha)\,(\Delta x)^2 \; d_0} \qquad$ and $\qquad \mu_2 = \dfrac{a\,(1-\alpha)}{M(\alpha)\,d_0}$

After simplification for $n \geq 1$, we get

$$-\mu_1 \, g_i \, Z_{i-1}^{n+1} + (1 + 2\,\mu_1 \, g_i)\, Z_i^{n+1} - \mu_1 \, g_i \, Z_{i+1}^{n+1}$$

$$= (2\,\mu_1 \, g_i - \mu_1 \, g_{i+1})\, Z_{i-1}^n + (1 - 2\,\mu_1 \, g_i - \mu_2 - d_1)\, Z_i^n + \mu_1 \, g_{i+1} \, Z_{i+1}^n + \sum_{j=1}^{n-1} \left[d_j - d_{j+1} \right] Z_i^{n-j}$$

$$+ d_n \, Z_i^0$$

Put $n = 0$ in equation (3.4), we get

$$-\mu_1 \, g_i \, Z_{i-1}^1 + (1 + 2\,\mu_1 \, g_i)\, Z_i^1 - \mu_1 \, g_i \, Z_{i+1}^1 = (2\,\mu_1 \, g_i - \mu_1 \, g_{i+1})\, Z_{i-1}^0 + (1 - 2\,\mu_1 \, g_i - \mu_2)\, Z_i^0$$

$$+ \mu_1 \, g_{i+1} \, Z_{i+1}^0$$

Finally initial condition (1.5) and boundary condition (1.6) are approximated as follow:

$$Z(x,0) = 0, \; 0 < x < L \text{ implies } Z_i^0 = 0, \; i = 1, 2, \ldots, M$$

$$Z(0,t) = Z_0, \text{ implies } Z_0^n = Z_0, \; n = 1, 2, \ldots, N$$

$$Z_x(L,t) = 0, \text{ implies } \frac{Z_n^{M+1} - Z_n^{M-1}}{2\,\Delta x} = 0, \text{ This gives } Z_{M+1}^n = Z_{M-1}^n, \; n = 0, 1, 2, \ldots, N$$

Finally, discretized form of time fractional order subdiffusion bioheat equation (1.4)-(1.6) is as follows:

$$-\mu_1 \, g_i \, Z_{i-1}^1 + (1 + 2\,\mu_1 \, g_i)\, Z_i^1 - \mu_1 \, g_i \, Z_{i+1}^1 = (2\,\mu_1 \, g_i - \mu_1 \, g_{i+1})\, Z_{i-1}^0$$

$$+ (1 - 2\,\mu_1 \, g_i - \mu_2)\, Z_i^0 + \mu_1 \, g_{i+1} \, Z_{i+1}^0, for \; n = 0 \qquad (3.5)$$

$$-\mu_1 \, g_i \, Z_{i-1}^{n+1} + (1 + 2\,\mu_1 \, g_i)\, Z_i^{n+1} - \mu_1 \, g_i \, Z_{i+1}^{n+1}$$

$$= (2\,\mu_1 \, g_i - \mu_1 \, g_{i+1})\, Z_{i-1}^n + (1 - 2\,\mu_1 \, g_i - \mu_2 - d_1)\, Z_i^n + \mu_1 \, g_{i+1} \, Z_{i+1}^n$$

$$+ \sum_{j=1}^{n-1} \left[d_j - d_{j+1} \right] Z_i^{n-j} + d_n \, Z_i^0, \; for \; n \geq 1 \qquad (3.6)$$

$$\text{initial condition:} \qquad Z_i^0 = 0, \ i = 1, 2, \ldots, M \qquad\qquad (3.7)$$

$$\text{boundary condition:} \ Z_0^n = Z_0, \text{and } Z_{M+1}^n = Z_{M-1}^n, \ n = 0, 1, 2, \ldots, N \qquad (3.8)$$

$$\text{with} \quad \mu_1 = \frac{b\,(1-\alpha)}{2\,M(\alpha)\,(\Delta x)^2\,d_0}, \qquad \mu_2 = \frac{a\,(1-\alpha)}{M(\alpha)\,d_0}, \qquad d_j = [(j+1)E_{\alpha,2}(\eta_{j+1}) - jE_{\alpha,2}(\eta_j)],$$

$$\eta_j = \frac{-\alpha}{1-\alpha}[(j\,\Delta t)^\alpha] \qquad \text{and} \qquad i = 1, 2, \ldots, M; \quad n = 0, 1, 2, \ldots, N.$$

Hence, matrix form of discretized Crank-Nicolson finite difference scheme (3.5)-(3.8) is as follow

$$A\,Z^1 = BZ^0 + C, \qquad\qquad\qquad\qquad\qquad \text{for } n = 0 \quad (3.9)$$

$$A\,Z^{n+1} = F\,Z^n + \sum_{j=1}^{n-1}\Big[d_j - d_{j+1}\Big]Z^{n-j} + d_n Z^0 + C, \qquad\qquad \text{for } n \geq 1 \qquad (3.10)$$

$$\text{initial condition:} \ Z_i^0 = 0, \ i = 1, 2, \ldots, M; \qquad\qquad (3.11)$$

$$\text{boundary condition:} \ Z_0^n = Z_0; \text{ and } Z_{M+1}^n = Z_{M-1}^n, \ n = 0, 1, 2, \ldots, N. \qquad (3.12)$$

where $Z^n = \left(Z_1^n, \ Z_2^n, \ \ldots, \ Z_{M-1}^n\right)^T$, $C = \left((3\,\mu_1\,g_1 - \mu_1\,g_2)\,Z_0, \ 0, \ 0, \ \ldots, 0\right)$ are the constant matrix, and

$$A = \begin{pmatrix} 1 + 2\,\mu_1\,g_1 & -\mu_1\,g_1 & & & & & \\ -\mu_1\,g_2 & 1 + 2\,\mu_1\,g_2 & -\mu_1\,g_2 & & & & \\ & \ddots & \ddots & \ddots & & & \\ & & -\mu_1\,g_i & 1 + 2\,\mu_1\,g_i & -\mu_1\,g_i & & \\ & & & \ddots & \ddots & \ddots & \\ & & & & -\mu_1\,g_{M-1} & 1 + 2\,\mu_1\,g_{M-1} & -\mu_1\,g_{M-1} \\ & & & & & -2\,\mu_1\,g_M & 1 + 2\,\mu_1\,g_M \end{pmatrix},$$

$$B = \begin{pmatrix} \Lambda_1 & \mu_1\,g_2 & & & & & \\ 2\,\mu_1\,g_2 - \mu_1\,g_3 & \Lambda_2 & \mu_1\,g_3 & & & & \\ & \ddots & \ddots & \ddots & & & \\ & & 2\,\mu_1\,g_i - \mu_1\,g_{i+1} & \Lambda_i & \mu_1\,g_{i+1} & & \\ & & & \ddots & \ddots & \ddots & \\ & & & & 2\,\mu_1\,g_{M-1} - \mu_1\,g_M & \Lambda_{M-1} & \mu_1\,g_M \\ & & & & & 2\,\mu_1\,g_M & \Lambda_M \end{pmatrix}$$

and

$$
F = \begin{pmatrix}
\Lambda_1 - d_1 & \mu_1\, g_2 & & & & & \\
2\,\mu_1\, g_2 - \mu_1\, g_3 & \Lambda_2 - d_1 & \mu_1\, g_3 & & & & \\
& \ddots & \ddots & & \ddots & & \\
& & \ddots & & \ddots & & \ddots \\
& & & 2\,\mu_1\, g_{M-1} - \mu_1\, g_M & \Lambda_{M-1} - d_1 & \mu_1\, g_M \\
& & & & 2\,\mu_1\, g_M & \Lambda_M - d_1
\end{pmatrix}
$$

where $\Lambda_i = 1 - 2\,\mu_1\, g_i - \mu_2$, $i = 1, 2, \ldots, M$.

4 Stability and Convergence

Lemma 4.1. *The eigenvalues of $N \times N$ tri-diagonal matrix[22]*

$$
\begin{pmatrix}
m_1 & m_2 & & & & & \\
m_3 & m_1 & m_2 & & & & \\
& \ddots & \ddots & \ddots & & & \\
& & m_3 & m_1 & m_2 & & \\
& & & \ddots & \ddots & \ddots & \\
& & & & m_3 & m_1 & m_2 \\
& & & & & m_3 & m_1
\end{pmatrix}
$$

are given as

$$
\lambda_i = m_1 + 2\sqrt{m_2\, m_3}\cos\left(\frac{i\pi}{N+1}\right)
$$

where m_1, m_2 and m_3 are either real or complex numbers[3].

Lemma 4.2. *Following conditions are true if eigen values of matrix A are represented by $\lambda_i(A)$, $i = 1, 2, \ldots, M - 1$*

(i) $\lambda_i(A) \geq 1$,

(ii) $\|A^{-1}\|_2 \leq 1$, where $\|.\|_2$ is second norm of matrix.

Proof. By the Gerschgorin's circle theorem, if A is square matrix then every eigenvalue of A i.e. λ_i must lies in any one of the following circle

$$
|\lambda - a_{ij}| \leq \sum_{i=1, i \neq j}^{M} a_{ij}, \quad j = 1, 2, 3, \ldots M. \tag{4.1}
$$

Thus each eigen value of matrix $A[22]$ must satisfy any one of the following[22] inequality

$$|\lambda| \le \sum_{i=1}^{M} |a_{ij}| \tag{4.2}$$

$$|\lambda| \ge |a_{ij}| - \sum_{i=1, i \ne j}^{M} |a_{ij}| \tag{4.3}$$

Now, we use inequality (4.3) to prove the condition (i) for the matrix A.

$$|\lambda_1 (A)| \ge |(1 + 2\mu_1 g_1) - \mu_1 g_1| = 1 + \mu_1 g_1 \ge 1$$
$$|\lambda_2 (A)| \ge |(1 + 2\mu_1 g_2) - \mu_1 g_2 - \mu_1 g_2| = 1$$
$$|\lambda_3 (A)| \ge |(1 + 2\mu_1 g_3) - \mu_1 g_3 - \mu_1 g_3| = 1$$
$$\vdots$$
$$|\lambda_M (A)| \ge |(1 + 2\mu_1 g_M) - 2\mu_1 g_M| = 1$$

Thus $|\lambda_j| \ge 1$, $j = 1, 2, 3 \ldots, M$. To prove condition (ii), we have $\|A\|_2 = \max_{1 \le j \le n} |\lambda_j(A)|$ Therefore, from condition (i), we get $\|A\|_2 \ge 1$ Hence $\|A^{-1}\|_2 \le 1$, This complete the proof. □

Lemma 4.3. *The discretized fractional order Crank-Nicolson finite difference scheme with initial and boundary conditions (3.5)-(3.8) is solvable unconditionally at every time step .*

Proof. To prove above lemma, it is enough to prove that matrix A is invertible. We observed that, in matrix A, the first and last row are diagonally dominant. For remaining rows, $1 + 2\mu_1 g_i, i = 1, 2, \ldots, M$ is the diagonal element and

$$|(-\mu_1 g_i)| + |(-\mu_1 g_i)| = 2\mu_1 g_i, i = 1, 2, \ldots, M$$

, is sum of elements other than diagonal in the same row. Hence, for each row, we have $1 + 2\mu_1 g_i > 2\mu_1 gi, i = 1, 2, \ldots, M$. Thus, matrix A is strictly diagonally dominant. Hence, the proof. □

Lemma 4.4. *If $\lambda_i(B)$ and $\lambda_i(F), i = 1, 2, \ldots, M$ represents the eigenvalues of B and F respectively, then following conditions are hold:*

(i) $|\lambda_i (B)| \le 1$, $|\lambda_i (F)| \le 1$, $i = 1, 2, \ldots, M$

(ii) $\|B_2\|_2 \le 1$, $\|F_2\|_2 \le 1$, $i = 1, 2, \ldots, M$

Theorem 4.1. *The solution of the fractional order Crank-Nicolson finite difference scheme[19] (3.5)-(3.8) for fractional order subdiffusion bioheat equation (1.4)-(1.6) is stable unconditionally .*

Proof. We will prove that

$$\|Z^n\|_2 \leq \tilde{K}\|Z^0\|_2$$

where $\tilde{K}$ is positive integer independent of x and t.
For $n = 1$

$$Z^1 = A^{-1}BZ^0 + A^{-1}C$$

$$\therefore \|Z^n\|_2 \leq \|A^{-1}\|_2 \|B\|_2 \|Z^0\|_2 + \|A^{-1}\|_2 \|C\|_2$$
$$= K\|Z^0\|_2$$

Thus for $n = 1$, result is true
We assume that result is true for $n \leq m$ $\|Z^m\|_2 \leq \tilde{K}\|Z^0\|_2$
Consider, for $n = m + 1$

$$Z^{m+1} = A^{-1}FZ^m + A^{-1}\sum_{j=1}^{m-1}\left[d_j - d_{j+1}\right]Z^{m-j} + A^{-1}d_mZ^0 + A^{-1}C$$

$$\therefore \|Z^{m+1}\|_2 \leq \|Z^m\|_2 + \sum_{j=1}^{m-1}\left[d_j - d_{j+1}\right]\|Z^{m-j}\|_2 + d_m\|Z^0\|_2 + \|C\|_2$$

$$\leq \left[\tilde{K}_1 + d_1 + (1 - \tilde{K}_2)d_m\right]\|Z^0\|_2 + \tilde{K}_3$$
$$= \tilde{K}\|Z^0\|_2$$

Hence, by induction, for all n, we have $\|Z^n\|_2 \leq \tilde{K}\|Z^0\|_2$.where $\tilde{K}$ is a positive number independent of x and t. Therefore, this shows that the scheme is unconditionally stable[22].This complete the proof. $\square$

Convergence: Consider $\Omega : [0, L] \times [0, T]$ be the region. We represent the exact solution of the fractional[22] order subdiffusion bioheat equation (1.4)-(1.6) at time level[22] t_n by introducing the vector of size M+1 as,

$$\overline{Z}^n = \left(\overline{Z}(x_0, t_n), \overline{Z}(x_1, t_n), \overline{Z}(x_2, t_n), \ldots, \overline{Z}(x_M, t_n)\right)^T$$

. Consider truncation error as vector $\tau^n = \left(\tau_1^n, \tau_2^n, \tau_3^n, \ldots, \tau_M^n\right)^T$ at time level t_n. Since $\overline{Z}^n$ is the exact solution of the equation (1.4)-(1.6), we have

$$A\overline{Z}^1 = B\overline{Z}^0 + C + \tau^1, \qquad \text{for } n = 0 \quad (4.4)$$

$$A\overline{Z}^{n+1} = F\overline{Z}^n + \sum_{j=1}^{n-1}\left[d_j - d_{j+1}\right]\overline{Z}^{n-j} + d_n\overline{Z}^0 + C + \tau^{n+1}, \qquad \text{for } n \geq 1 \quad (4.5)$$

Lemma 4.5. *Following conditions are satisfied by the coefficient d_j, $j = 0, 1, 2, 3, \ldots$*

(i) $d_j > 0$

(ii) $d_j > d_{j+1}$ *and* $d_j \to 0$ *as* $j \to \infty$

Theorem 4.2. *The fractional order Crank-Nicolson finite difference scheme[19] (3.5)-(3.8) for fractional order subdiffusion bioheat equation (1.4)-(1.6) is unconditionally convergent.*

Proof. Consider the error vector, $E^n = \overline{Z}^n - Z^n = \left(e_1^n, \; e_2^n, \; e_3^n, \; \ldots, \; e_M^n \right)^T$ in the solution at time level t_n. Furthermore, we assume that

$$|e_l^n| = \max_{1 \leq i \leq M} |e_i^n| = \|E^n\|_\infty$$

$$|\tau_l^n| = \max_{1 \leq i \leq M} |\tau_i^n|, \text{ for } l = 1, 2, 3, \ldots$$

Then, using equation (3.5), we obtain

$$
\begin{aligned}
|e_l^1| &= |-\mu_1 \, g_i \, e_{i-1}^1 + (1 + 2\,\mu_1 \, g_i) \, e_i^1 - \mu_1 \, g_i \, e_{i+1}^1| \\
&\leq (2\,\mu_1 \, g_i - \mu_1 \, g_{i+1}) \, |e_{i-1}^0| + (1 - 2\,\mu_1 \, g_i - \mu_2) \, |e_i^0| + \mu_1 \, k_{i+1} \, |e_{i+1}^0| + |\tau_l^1| \\
&\leq (2\,\mu_1 \, g_i - \mu_1 \, g_{i+1} + 1 - 2\,\mu_1 \, g_i - \mu_2 + \mu_1 \, g_{i+1}) \max_{1 \leq i \leq M} |e_i^0| + \max_{1 \leq i \leq M} |\tau_i^1| \\
&\leq \|E^0\|_\infty + \max_{1 \leq i \leq M} |\tau_i^1|
\end{aligned}
$$

$$\therefore \|E^1\|_\infty \leq \|E^0\|_\infty + \max_{1 \leq i \leq M} |\tau_i^1|$$

Now, from equation (3.6), we obtain

$$
\begin{aligned}
|e_l^{m+1}| &= |-\mu_1 \, g_i \, e_{i-1}^{m+1} + (1 + 2\,\mu_1 \, g_i) \, e_i^{m+1} - \mu_1 \, g_i \, e_{i+1}^{m+1}| \\
&\leq (2\,\mu_1 \, g_i - \mu_1 \, g_{i+1}) \, |e_{i-1}^m| + (1 - 2\,\mu_1 \, g_i - \mu_2 - d_1) \, |e_i^m| + \mu_1 \, g_{i+1} \, |e_{i+1}^m| \\
&\qquad + \sum_{j=1}^{m-1} \Big[d_j - d_{j+1} \Big] |e_i^{m-j}| + d_m \, |e_i^0| + |\tau_l^{m+1}| \\
&\leq \Big[2\,\mu_1 \, g_i - \mu_1 \, g_{i+1} + 1 - 2\,\mu_1 \, g_i - \mu_2 - d_1 + \mu_1 \, g_{i+1} \Big] |e_l^m| \\
&\qquad + \Big[(d_1 - d_2) + (d_2 - d_3) + \cdots + (d_{m-1} - d_m) \Big] |e_l^m| + d_m \, |e_i^l| + \max_{1 \leq i \leq M} |\tau_i^{m+1}| \\
&= \|E^m\|_\infty + \max_{1 \leq i \leq M} |\tau_i^{m+1}|
\end{aligned}
$$

This is true for every m, therefore we have

$$\|E^{m+1}\|_\infty \leq \|E^m\|_\infty + \max_{1 < i < M} |\tau_i^{m+1}|$$

Hence, by induction, we get

$$\|E^{n+1}\|_\infty \le \|E^n\|_\infty + \max_{1 \le i \le M} |\tau_i^{n+1}|$$

As $\|E^0\|_\infty = 0$ implies $\|E^n\|_\infty = 0$

Therefore $\|E^n\|_\infty \le \max_{1 \le i \le M} |\tau_i^{n+1}|$. Since $\max_{1 \le i \le M} |\tau_i^{n+1}| \to 0$ as $(\Delta x, \Delta t) \to (0,0)$

implies that $\|E^n\|_\infty \to 0$ uniformaly on Ω an $(\Delta x, \Delta t) \to (0,0)$. Therefore, this shows that for any x and t, the vector Z^n converges to $\overline{Z}^n$ as $\Delta x \to 0$ and $\Delta t \to 0$, . Hence, proof is complete. $\square$

5 Test Problem

We developed Python code to obtain numerical solution of the time fractional[19] subdiffusion bioheat equation by the Crank-Nicolson finite difference scheme[19] of fractional order developed in equations(3.5)-(3.8). In our test problem, we consider parametric values same as given in[10], $\rho = 1000 Kg/m^3$, $C = 4200 JKg^{-1}C$, $W_b = 0.5 Kg/m^3$, $C_b = 4200 JKg^{-1}C$, $L = 0.02416m$, $T = 150s$. The initial temperature is set to be $Z_0 = 12^0 C$. We choose $g(x) = 0.7(1 + 3x)$ as function of x and Δx and Δt are to chosen as $0.001208m$ and $0.15s$ respectively.

We have drawn some graphs by using developed Python code as follow:

Note that, temperature profile at $t = 150s$ obtained by ABC is more clear than Caputo. Temperature elevation from particular point of skin by ABC increases faster than Caputo.
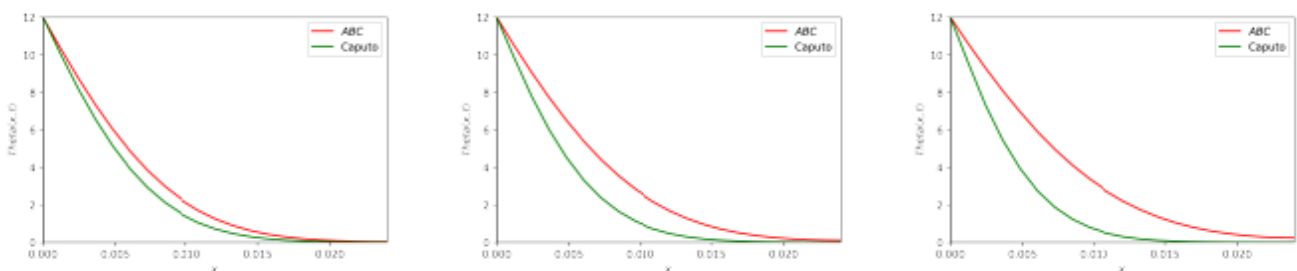
(a) $\alpha = 0.95$ (b) $\alpha = 0.9$ (c) $\alpha = 0.85$

Figure 1: Temperature profiles along x direction at $t = 150s$.

(a) $\alpha = 0.95$ (b) $\alpha = 0.9$ (c) $\alpha = 0.85$
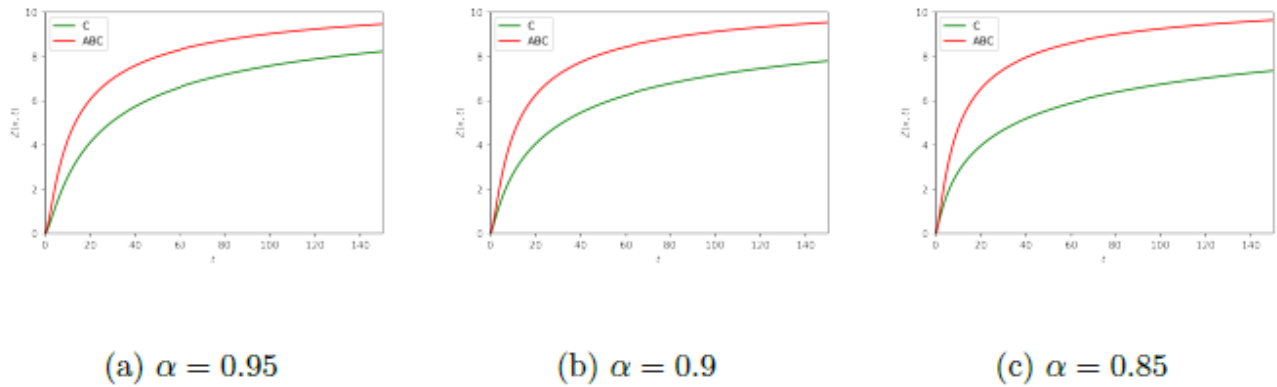
Figure 2: :Temperature elevations in skin at $x = 0 : 002416m$.

6   Conclusions

We successfully developed fractional order Crank-Nicolson scheme for fractional order subdiffusion bioheat transfer equation using ABC time fractional derivative. Unconditional stability and convergence of the scheme is proved. We obtain numerical solution of time fractional subdiffusion bioheat transfer equation and it is represented graphically by developed Python Code. Graphically we observe that ABC time fractional derivative is more useful for subdiffusion bioheat transfer model than Caputo time fractional derivative because ABC time fractional derivative gives more depth of temperature profile than Caputo time fractional derivative.

7. References

[1]. Abdon Atangana, J. F. Gomez-Aguilar, Numerical approximation of Riemann- Liouville definition of fractional derivative: from Riemann-Liouville to Atangana- Baleanu, Numer methods of partial Diffrentila Eq:,1-22, 2017.

[2]. Alireza Zolfaghari,Mehdi Maerefat, A new simplified thermoregulatory bioheat- model for evaluating thermal response of the human body to transient environ- ments, BuildingandEnvironment, 45,2068-2076, 2010.

[3]. G. D. Smith, Numerical Solution of Partial Differential Equations: Finite Differ- ence Methods, third edition,Oxford Applied Mathematics and Computing Sci- ence Series, Oxford University Press, Oxford, New York, 1985.

[4]. Harry H. Pennes, Analysis of tissue and arterial blood temperatures in the resting human forearm, Journal of applied physiology, 1, 93-122, 1948.

[5]. I. Podlubny, Fractional Differential equation, Academic Press, San Diago, 1999.

[6]. Jordan Hristov, Bio-Heat Models Revisited: Concepts, Derivations, Nondimensalization and Fractionalization Approaches, frontiers in Physics, 7, 2019.

[7]. Jorge Losada, Juan J. Nieto, Properties of a New Fractional Derivative without Singular Kernel, Progress in Fractional Differentiation and Applications, 2, 87-92, 2015.

[8].   J.M. Sonawane, B. R. Sontakke and K. C. Takale, Strong and mild solutions of the system of fractional ordinary differential equation and it's applications, Malaya Journal of Matematik, Vol. 8, No. 4, 1443-1453, 2020.

[9].   Jos´e Francisco Gomez, Lizeth Torres and Ricardo Fabricio Escobar, Fractional Derivatives with Mittag-Leffler Kernel, http://www.springer.com/series/13304, Studies in Systems, Decision and Control, Volume 194,2019

[10]. K.C.Takale, Numerical method for Time Fractional Bioheat Transfer Equation and Applications, International Journal of Research and Analytical Reviews, 6, 1301-1307, 2019.

[11]. K.C.Takale, D. B. Dhaigude, V.R.Nikam, Douglas Higher Order Finite Difference Scheme for One Dimensional Pennes Bioheat Equation, International Journal of Advanced Engineering and Application, 61-65, 2011.

[12]. L.L. Ferras, N.J. Ford, M.L. Morgado, J.M. Nobrega, M. Rebelo, Fractional Pennes Bioheat Equation: Theoratical and Numerical Studies, Frac Cal Appl Anal., 18, 1018-1106, 2015.

[13]. M. I. Asjad, Fractional Mechanism with Power Law (Singular) and Exponen- tial (Non-singular) Kernels and Its Applications in Bio Heat Transfer Model, International Journal of Heat and Technology, 37, 846-852, 2019.

[14]. M.A. Ezzat, N.S. AlSowayan, Z.I.A. Al-Muhiameed, S.M. Ezzat, Fractional mod- elling of Pennes' bioheat transfer equation, Heat Mass Transfer, 50, 907-914, 2014.

[15]. Qiao Zhang, Yuxin Sun , Jialing Yang, Bio-heat transfer analysis based on frac- tional derivative and memory-dependent derivative heat conduction models, Case Studies in Thermal Engineering, 27, 101-211, 2021.

[16]. R.S. Damor, S. Kumar , A.K. Shukla, Numerical solution of Fractional Bioheat Equation with Constant and Sinusoidal Heat Flux coindition on skin tissue., American Journal of Mathematical Analysis, 1, 20-24, 2013.

[17]. R.S. Damor, S. Kumar , A.K. Shukla, Solution of fractional bioheat equation in terms of Fox's H-function, A springer open acess journal, 2016.

[18]. S. M. Jogdand, M. P. Datar, K. C. Takale, Explicit Finite Difference Scheme for Time Fractional Penne's Bioheat Equation, International Journal of Research and Analytical Reviews, 6, 984-987, 2019.

[19]. Suryakant Jogdand, Sharvari Kulkarni, Kalyanrao Takale, Error Analysis of So- lution Of Time Fractional Convection Diffusion Equation, Journal of Emerging Technologies and Innovative Research (JETIR) www.jetir.org, Volume 6, Issue 3, 114-119,March 2019.

[20]. Swati Yadav, Rajesh K. Pandey, Anil K. Shukla, Numerical approximation of Atangana-Baleanu derivative and its application, Chaos, solitons and Frac- tals,118, 58-64, 2019.

[21]. T.-C. Shih, P. Yuan, W.-L. Lin, H.-S. Kou, Analytical analysis of the Pennes bioheat transfer equation with sinusoidal heat flux condition on skin surface., Med. Eng. Phis., 29, 946-953, 2007.

[22]. Uttam Kharde, Kalyanrao Takale, Shrikrishna Gaikwad, Numerical Solution of Time Fractional Drug Concentartion Equation in Central Nervous System, J. Math. Comput. Sci. 11 (2021), No. 6, 7317-7336, http://scik.org, 2021.

[23]. W. Wulff, The Energy Conservation Equation for Living Tissue, IEEE Transactions- Biomedical Engineering, 21, 494-495, 1974.

[24]. Yanmei Qin, Kaiteng Wu, Numerical solution of fractional bioheat equation by quadratic spline collocation method, J. Nonlinear Sci. Appl., 9, 5061-5072, 2016.

An Overview of Nanoscience and its Applications

P. B. Nalle1*, S. U. Shinde2*, K. M. Jadhav3

1Dept. of Physics, Shri Shivaji Science and Arts College, Chikhli, Dist. Buldana (M.S.) INDIA.

2*Department of Physics, Pratishthan Mahavidyalaya, Paithan, Aurangabad. (M.S.) INDIA.

3Dept. of Basic and Applied Sciences, MGM University, Aurangabad. (M.S.) INDIA.

*Corresponding Author Email-Id: sangitamawal@gmail.com

Abstract :

Nanoscience is the nanoscale science, or items with sizes between nanometres. The study of structures at the nanoscale, both natural and man-made, is known as nanotechnology. Depending upon the material structure and its properties nanoparticles have different types. These different nanoparticles have different properties such as magnetic, optical, electric, chemical etc. Synthesis of nanoparticles are mainly classified into two types such as top-down method and bottom-up method and further divided into physical, chemical and biological methods. Nanoparticles have a variety of applications in many diverse fields such as environment, medicine, agriculture, food, electronics, defence etc. In this review, we described nanomaterial, its history, properties, synthesis methods, factors affecting synthesis of nanoparticles, characterization techniques and its applications.

Keywords: Nanoscience, Nanotechnology, Synthesis Methods, Characterization Techniques.

I. INTRODUCTION

In nanoscience materials are studied at the nanoscale. One billionth of one meter, or 10-9, is referred to as a nanometre [1]. Means meter's one billionth is equal to one nanometre. For nanoscience to be relevant, at least single dimension of the material or structure should be between 1 and 100 nm. When structures are sufficiently small, they can acquire interesting as well as practical properties. When compared to their bulk quantities, their properties in the nano regime are quite distinct [2]. Nanostructure can be formed from metals [3], semiconductors [4], carbon-based materials [5] or liquids [6] by using special methods and techniques. Synthesized nanostructured materials are observed using special equipment. Nanoscience is now used by scientists and engineers of several disciplines such as material science, physical science, chemical science, molecular biology, semiconductor physics, microfabrication, molecular engineering, pharmaceuticals, memories and information storage, computer etc.

In the fourth century A.D. Roman glass makers fabricated nanosized metal glasses. In London, the British museum has a Lycurgus cup which was fabricated from soda lime glass containing silver and gold nanoparticles [7]. In 1959, new era of nanotechnology was started by the great physicist Richard P. Feynman with a famous talk, "There's Plenty of Room at the Bottom" [8]. In this talk he explained manipulating and controlling things on a small scale. Nanotechnology is manipulation of matter on atomic scale with one dimension in the range

between 1 to 100 nanometres [9]. Nanotechnology is the study of materials at the nanoscale, both natural and artificial. Fundamentally, nanotechnology is the engineering of microscopic devices with the potential to construct objects from the ground up utilising methods and instruments currently under development to create fully functional, extremely sophisticated goods. Nanotechnology produces novel nanomaterials with numerous uses such as nanomedicine [10], nanoelectronics, biomaterials, energy production [11], cosmetics [12] etc.

II. PROPERTIES OF NANOMATERIALS
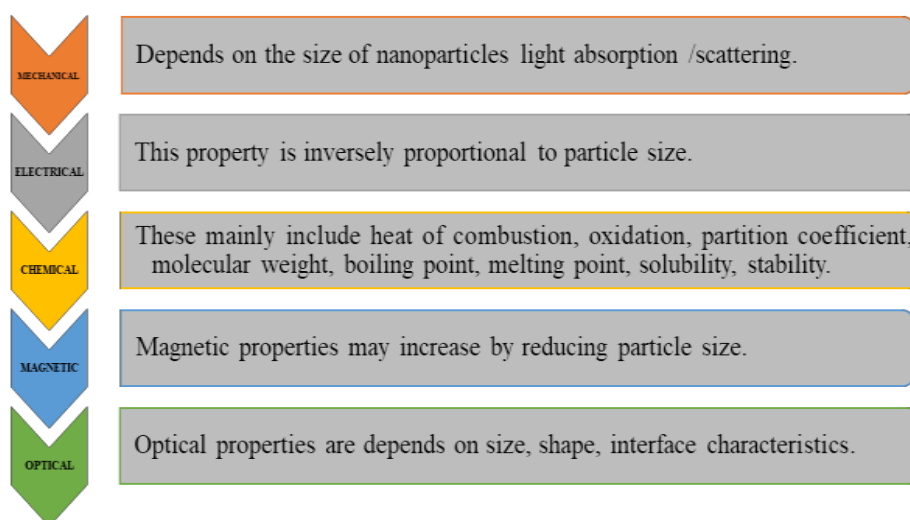
Figure 1: Properties of Nanomaterials

III. SYNTHESIS OF NANOMATERIALS

Synthesis methods are broadly classified into two categories such as top-down method and bottom-up method.
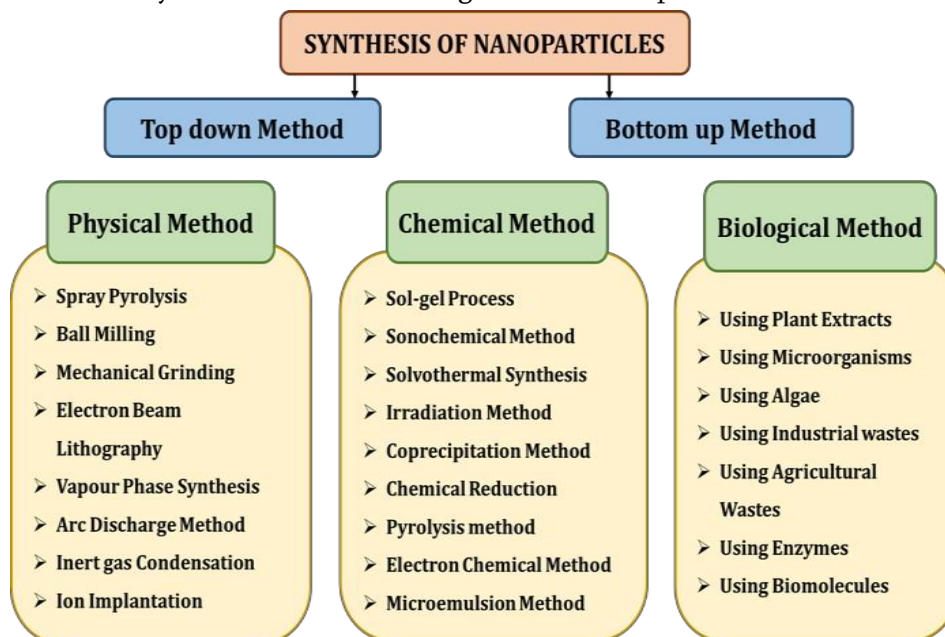
Figure 2: Method for Synthesis of Nanoparticles

Synthesis methods are further divided into three classes such as physical methods, chemical methods and biological methods as shown in above figure. Nanoparticles are synthesized using above listed physical

methods. These methods work at higher temperatures, usually greater than 350°C. Chemical methods are listed in the above figure, temperatures required for these methods are usually below 350°C. Large quantities of materials can be synthesised by using these methods. Biological synthesis methods are environmental and less toxic methods so they are called green synthesis.

A. Top-Down Approaches

Top-down approach of the synthesizing method is used for larger structures where processing is externally controlled [13]. In this method pattern is generated on a larger scale and then reduced to nanoscale by using top- down synthesis methods. This method requires large installations and huge capital for setup so this method is quite expensive. Growth process of this method is slow and so not suitable for large scale production.

B. Bottom-Down Approaches

This approach includes miniaturization of materials components with a self-assembly process. Basic components are combined into more substantial, stable structures during the self-assembly process by means of physical forces acting at the nanoscale. In bottom-up methods atoms or molecules are built to nanostructures by direct manipulation of atoms or molecules. Basic principle of the bottom-up approach is molecular recognition. [14].

IV. FACTORS AFFECTING ON SYNTHESIS OF NANOPARTICLES
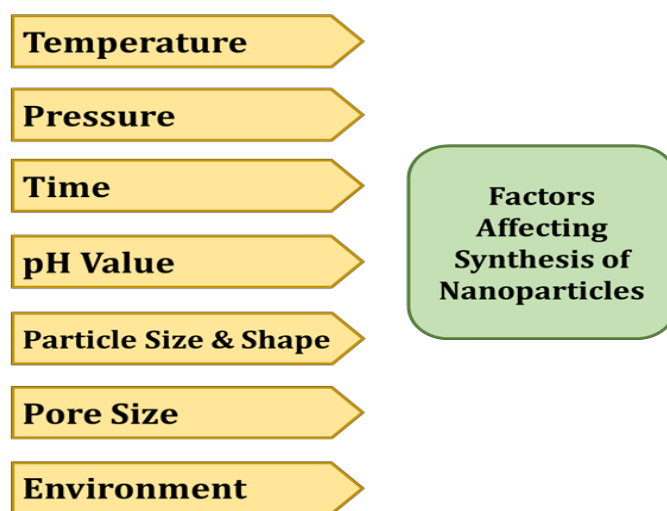
Figure 3: Factors Affecting on Synthesis of Nanoparticles

Above figure shows factors which are affecting the synthesis of nanoparticles, these are temperature, pressure, time, pH value, particle size and shape, pore size and environment [15]. Temperature is a main parameter which affects synthesis of nanoparticles. Synthesis temperature is different for physical, chemical and biological synthesis methods. For the physical synthesis method required synthesis temperature is usually greater than 300°C, for chemical methods it is below 300 °C and for biological methods it is less than 100 °C. Size and shape of nanoparticles affected due to pressure. Reaction time affects the quality of synthesized nanoparticles. Properties of nanoparticles are mainly dependent on particle size such as the melting point of nanoparticles decreases with decrease in size of particles. Chemical properties of nanoparticles depend on the shape of the particles. Cost of nanoparticles decides potential applications of materials. Synthesis methods should be cost

effective Physical methods and chemical methods are not cost effective but biological synthesis methods are less cost and so used for large scale production.

V. CHARACTERIZATION TECHNIQUES

A.   X-Ray Diffraction: One popular method for figuring out a composition or structure of crystal is X-ray diffraction. The atom structure of bigger crystals, like inorganic compounds and macromolecules, can be ascertained using this method. It can determine phase purity, composition, and crystallinity if the size of the crystal is too small [16].

B.   UV Visible Spectroscopy: On the basis of wavelengths, UV-Visible spectroscopy can be classified into the visible, ultraviolet, and near-infrared sections of the spectrum. Weak absorption bands are identified since their frequency is near to the over frequency of many natural vibrations. As a result, it can be applied to non-destructive assessments like figuring out food's sugar, fat, and protein composition as well as identifying medications [17].

C.   Electron Microscope: Electron microscope is a such type of microscope where the light source is an electron beam that has been accelerated. With an electron's wavelength up to 100,000 times shorter than the visible light. Electron microscopes are able to expose the smaller objects structure [18].

D.   TG-DTA: A simultaneous thermal analyser which can characterise a material's numerous thermal properties. Temperatures of breakdown, reduction, or oxidation are measured by the TG component. It detects weight changes related to oxidation, decomposition, and any other chemical or physical processes that cause the sample to gain or lose weight all at once. The DTA component indicates the endothermicity or exothermicity of decomposition processes. The DTA also records temperatures for phases including melting, crystallisation, and glass transitions where there is no mass loss [19].

VI. APPLICATIONS

A. Environment
Nanoparticles are used for water purification, air filtration, and soil remediation. These nanomaterials have shown promise in improving the efficiency of environmental remediation processes and reducing the impact of pollution on ecosystems [20].

B. Medicine
The medicine sector includes targeted drug delivery, imaging techniques, and disease diagnosis nanoparticles. These nanoparticles have the potential to revolutionise the field of medicine by improving treatment outcomes and reducing side effects for patients [21].

C. Agriculture
Nanoparticles in the agriculture industry include enhancing crop productivity, improving nutrient uptake in plants, and reducing the need for chemical pesticides. These nanomaterials have the ability to address food security challenges and promote sustainable agricultural practices [22].

D. Food

Nanomaterials have the potential to ensure food safety, reduce food waste, and meet the growing demands of a global population. Food industry includes improving food packaging to extend shelf life, enhancing food quality through encapsulation of nutrients, and detecting food contaminants [23].

E. Electronics

Applications of nanoparticles in the electronics industry and automotive industry include improving the performance and durability of electronic devices, as well as enhancing the efficiency of automotive components. These nanomaterials have the potential to revolutionise these industries by enabling smaller, faster, and more energy- efficient products [24].

F. Defence

The defence industry includes enhancing the strength and durability of materials used in military equipment, as well as improving the effectiveness of sensors and detection systems. These nanomaterials have the potential to greatly enhance national security by providing advanced technology for defence purposes [25].

VII.CONCLUSION

Nanotechnology is a promising era and has opened doors for technology. Nanomaterials having optical, magnetic, electric, chemical properties which enhance the applications of nanomaterials. Top-down and bottom-up approach synthesis methods are continuously enhanced to increase applications of nanoparticles. Researchers are developing new applications for nanoparticles to enhance the applications of nanotechnology in many sectors. Furthermore, there has been a noticeable increase in the use of nanotechnologies to alter the functionality and performance of systems. Thus, additional research is required to find better ways to apply knowledge of nanotechnologies in engineering, computers, electronics, and other fields.

VIII. REFERENCES

[1]. G. Mansoori and T. Fauzi Soelaiman, "Nanotechnology — An Introduction for the Standards Community," J ASTM Int, vol.2, no. 6, pp. 1–22, Jun. 2005, doi:10.1520/JAI13110.

[2]. D. Guo, G. Xie, and J. Luo, "Mechanical properties of nanoparticles: basics and applications," J Phys D Appl Phys, vol. 47, no. 1, p. 013001, Jan. 2014, doi: 10.1088/0022-3727/47/1/013001.

[3]. L. G. Sun, G. Wu, Q. Wang, and J. Lu, "Nanostructural metallic materials: Structures and mechanical properties," Materials Today, vol. 38, pp. 114–135, Sep. 2020, doi: 10.1016/j.mattod.2020.04.005.

[4]. H. T. Johnson, "Effects of Stress on Formation and Properties of Semiconductor Nanostructures," in Material Substructures in Complex Bodies, Elsevier, 2007, pp. 284–313. doi:10.1016/B978-008044535-9/50009-1.

[5]. L. Yang, "Carbon nanostructures," in Nanotechnology-Enhanced Orthopedic Materials, Elsevier, 2015, pp. 97–120. doi:10.1016/B978-0-85709-844-3.00005-7.

[6]. X. Hou, T. Zaks, R. Langer, and Y. Dong, "Lipid nanoparticles for mRNA delivery," Nat Rev Mater, vol. 6, no. 12, pp. 1078–1094, Aug. 2021, doi: 10.1038/s41578-021-00358-0.

[7]. I. Freestone, N. Meeks, M. Sax, and C.Higgitt, "The Lycurgus Cup — A Roman nanotechnology," Gold Bull, vol. 40, no. 4, pp. 270–277, Dec. 2007, doi:10.1007/BF03215599.

[8]. A. Junk and F. Riess, "From an idea to a vision: There's plenty of room at the bottom," Am J Phys, vol. 74, no. 9, pp. 825– 830, Sep. 2006, doi: 10.1119/1.2213634.

[9]. S. Bayda, M. Adeel, T. Tuccinardi, M. Cordani, and F. Rizzolio, "The History of Nanoscience and Nanotechnology: From Chemical–Physical Applications to Nanomedicine," Molecules, vol. 25, no. 1, p.112, Dec. 2019, doi:10.3390/molecules25010112.

[10]. A. Haleem, M. Javaid, R. P. Singh, S. Rab, and R. Suman, "Applications of nanotechnology in medical field: a brief review," Global Health Journal, vol. 7, no. 2, pp. 70–77, Jun. 2023, doi: 10.1016/j.glohj.2023.02.008.

[11]. A. K. Hussein, "Applications of nanotechnology in renewable energies—A comprehensive overview and understanding," Renewable and Sustainable Energy Reviews, vol. 42, pp. 460–476, Feb. 2015, doi: 10.1016/j.rser.2014.10.027.

[12]. G. Fytianos, A. Rahdar, and G. Z. Kyzas, "Nanomaterials in Cosmetics: Recent Updates," Nanomaterials, vol. 10, no. 5, p.979, May 2020, doi:10.3390/nano10050979.

[13]. S. Ramesh, S. Vetrivel, P. Suresh, and V. Kaviarasan, "Characterization techniques for nano particles: A practical top down approach to synthesize copper nano particles from copper chips and determination of its effect on planes," Mater Today Proc, vol. 33, pp. 2626–2630, 2020, doi: 10.1016/j.matpr.2020.01.157.

[14]. S. Kumar, P. Bhushan, and S. Bhattacharya, "Fabrication of Nanostructures with Bottom-up Approach and Their Utility in Diagnostics, Therapeutics, and Others," 2018, pp. 167– 198. doi: 10.1007/978-981-10-7751-7_8.

[15]. J. K. Patra and K.-H. Baek, "Green Nanobiotechnology: Factors Affecting Synthesis and Characterization Techniques," J Nanomater, vol. 2014, no. 1, Jan. 2014, doi: 10.1155/2014/417305.

[16]. C. F. Holder and R. E. Schaak, "Tutorial on Powder X-ray Diffraction for Characterizing Nanoscale Materials," ACS Nano, vol. 13, no. 7, pp. 7359–7365, Jul. 2019, doi: 10.1021/acsnano.9b05157.

[17]. A. G. Shard, R. C. Schofield, and C. Minelli, "Ultraviolet–visible spectrophotometry," in Characterization of Nanoparticles, Elsevier, 2020, pp. 185–196. doi: 10.1016/B978-0-12-814182-3.00012-2.

[18]. R. Merugu and R. Gothalwal, "Microscopic techniques for characterisation of nanomaterials: A minireview," Mater Today Proc, vol. 47, pp. 4753–4757, 2021, doi: 10.1016/j.matpr.2021.05.665.

[19]. M. A. Majeed Khan, S. Kumar, M. Ahamed, S. A. Alrokayan, and M. S. AlSalhi, "Structural and thermal studies of silver nanoparticles and electrical transport study of their thin films," Nanoscale Res Lett, vol. 6, no. 1, p. 434, Dec. 2011, doi:10.1186/1556-276X-6-434.

[20]. A. Aghababai Beni and H. Jabbari, "Nanomaterials for Environmental Applications," Results in Engineering, vol. 15, p. 100467, Sep. 2022, doi:10.1016/j.rineng.2022.100467.

[21]. S. Anjum et al., "Emerging Applications of Nanotechnology in Healthcare Systems: Grand Challenges and Perspectives," Pharmaceuticals, vol. 14, no. 8, p. 707, Jul. 2021, doi: 10.3390/ph14080707.

[22]. K. Neme, A. Nafady, S. Uddin, and Y. B. Tola, "Application of nanotechnology in agriculture, postharvest loss reduction and food processing: food security implication and challenges," Heliyon, vol. 7, no. 12, p. e08539, Dec. 2021, doi:10.1016/j.heliyon.2021.e08539.

[23]. R. Biswas, M. Alam, A. Sarkar, M. I. Haque, Md. M. Hasan, and M. Hoque, "Application of nanotechnology in food: processing, preservation, packaging and safety assessment," Heliyon, vol. 8, no. 11, p. e11795, Nov. 2022, doi:10.1016/j.heliyon.2022.e11795.

[24]. Payal and P. Pandey, "Role of Nanotechnology in Electronics: A Review of Recent Developments and Patents," Recent Pat Nanotechnol, vol. 16, no. 1, pp. 45–66, Mar. 2022, doi:10.2174/1872210515666210120114504.

[25]. M. S. Abed and Z. A. Jawad, "Nanotechnology for Defence Applications," 2022, pp. 187–205. doi:10.1007/978-981-16-6022-1_10.

Exploring the Modified Natural Transform: Properties and Applications

Ankita D. Vidhate, Sangita N. Wandhekar, Shivani V.Sase, Parvin S. Ansari, Kishor A. Kshirsagar∗

Department of Mathematics, New Arts, Commerce and Science College, Ahmednagar

Abstract :

The paper describes the Modified Natural Transform $Nr [f(\xi)]$, a novel integral transform that generalizes well-known transforms including the Natural Transform $N [f(\xi)]$, Modified Laplace Transform, and Modified Sumudu Transform. The re- search investigates its qualities, develops criteria for its existence, and illustrates its utility in solving differential equations and other mathematical issues. Under certain situations, the Modified Natural Transform converges to the Laplace and Sumudu Transforms, demonstrating its adaptability and durability.

Keywords: Modified Natural Transform, Modified Laplace Transform, Modified Sumudu Transform, Differential Equations.

I. INTRODUCTION

In 1744, Euler, and later Lagrange, began working on finding solutions to differential equations

$$z = \int X(x)e^{ax}\, dx \quad \text{and} \quad z = \int X(x)x^a\, dx$$

but neither pursued the matter very far. Lagrange was an enthusiast of Eulerian work on integrating probability density functions of the form

$$z = \int X(x)e^{-ax}\, x^a\, dx$$

which some interpreted within modern Laplace transform theory [11]. In 1782, Laplace was drawn to these types of integrals, building on Euler's earlier work by using the inte- grals themselves as solutions to the equations [9]. During this time, Laplace introduced

the Laplace Transform, a very effective tool for finding the solution of ordinary or partial differential equations with suitable initial and boundary value problems [12].

In 1993, G.K. Watugala introduced the Sumudu Transform [4, 3], which is a simple variant of the Laplace Transform, and in 2008, Zafar Hayat Khan [8] introduced an integral transform named the Natural Transform, which is similar to the Laplace and Sumudu Transforms. The Natural Transform converges to both the Laplace Transform and the Sumudu Transform by changing variables. A few years earlier, F.B.M. Belgacem had introduced a concise theory and its applications [6, 1].

Integral transforms play a crucial role in solving various mathematical problems, es- pecially those involving differential equations. Among the well-known transforms, the Laplace and Sumudu Transforms have been widely used due to their simplicity and ef- fectiveness in handling linear time-invariant systems [13, 14]. However, these transforms have limitations when applied to more complex or specific types of functions [15].

In this paper, we introduce the Modified Natural Transform, a new family member of integral transforms. This transform is a generalization of the Natural Transform, which is itself a blend of the Laplace and Sumudu Transforms [7]. The Modified Natural Transform is designed to be more flexible and applicable to a broader class of functions, including those that are sectionally continuous and of exponential order [10].

The main objective of this study is to rigorously define the Modified Natural Transform, explore its fundamental properties, and compare it with the Modified Laplace and Modi- fied Sumudu Transforms. We also illustrate the utility of the Modified Natural Transform in solving differential equations and other applied mathematical problems [16, 17, 18, 19].

II. PRELIMINARIES

Definition 1. *The Laplace Transform[9] of a function $f(\xi)$ denoted by $L\{f(\xi)\}$, is defined as*

$$\mathcal{L}\{f(\xi)\} = \mathcal{K}(p) = \int_0^\infty e^{-p\xi} f(\xi) d\xi, \qquad (\Re(p) > 0) \tag{1}$$

where the function $f(\xi)$ is sectionally continuous and of exponential order.
The inverse Laplace transform is defined as follow:

$$f(\xi) = \mathcal{L}^{-1}[\mathcal{K}(p)] = \frac{1}{2\pi i} \int_{m-i\infty}^{m+i\infty} e^{p\xi} \mathcal{K}(p) \, dp, \quad (\Re(p) > 0, m > 0) \tag{2}$$

where $\mathcal{L}^{-1}$ is called inverse Laplace transform operator.

Definition 2. *The Sumudu Transform[4] of a function $f(\xi)$ denoted by $\mathcal{S}\{f(\xi)\}$, is defined as*

$$\mathcal{S}\{f(\xi)\} = \mathcal{K}(k) = \int_0^\infty e^{-\xi} f(k\xi) d\xi \qquad = \frac{1}{k} \int_0^\infty e^{\frac{-\xi}{k}} f(\xi) d\xi \qquad (\Re(k) > 0) \tag{3}$$

where the function $f(\xi)$ is sectionally continuous and of exponential order.
The inverse Sumudu transform is defined as follow:

$$f(\xi) = \mathcal{S}^{-1}[\mathcal{K}(k)] = \frac{1}{2\pi i} \int_{m-i\infty}^{m+i\infty} e^{\xi} \, \mathcal{K}(k) \, dp, \quad (\Re(k) > 0, m > 0) \qquad (4)$$

where $\mathcal{S}^{-1}$ is called inverse Sumudu transform operator.

Definition 3. The Natural Transform[8] of a function $f(\xi)$ denoted by $\mathcal{N}\{f(\xi)\}$, is defined as

$$\mathcal{N}\{f(\xi)\} = \mathcal{K}(p, k) = \int_0^\infty e^{-p\xi} f(k\xi) d\xi \qquad (5)$$

$$= \frac{1}{k} \int_0^\infty e^{\frac{-p\xi}{k}} f(\xi) d\xi, \qquad (\Re(p) > 0, \Re(k) > 0) \qquad (6)$$

where the function $f(\xi)$ is sectionally continuous and of exponential order.
The inverse Natural transform is defined as follow:

$$f(\xi) = \mathcal{N}^{-1}[\mathcal{K}(p, k)] = \frac{1}{2\pi i} \int_{m-i\infty}^{m+i\infty} e^{p\xi} \, \mathcal{K}(p, k) \, dp, \qquad (7)$$

where $(\Re(p) > 0, \Re(k) > 0, m > 0)$ and $\mathcal{N}^{-1}$ is called inverse Natural transform operator.

Definition 4. The Modified Laplace Transform[2] of a function $f(t)$ denoted by $\mathcal{L}_r\{f(t)\}$, is defined as
where the function $f(\xi)$ is sectionally continuous and of exponential order.
The inverse Natural transform is defined as follow:

$$f(\xi) = \mathcal{N}^{-1}[\mathcal{K}(p, k)] = \frac{1}{2\pi i} \int_{m-i\infty}^{m+i\infty} e^{p\xi} \, \mathcal{K}(p, k) \, dp, \qquad (7)$$

where $(\Re(p) > 0, \Re(k) > 0, m > 0)$ and $\mathcal{N}^{-1}$ is called inverse Natural transform operator.

Definition 4. The Modified Laplace Transform[2] of a function $f(t)$ denoted by $\mathcal{L}_r\{f(t)\}$, is defined as

$$\mathcal{L}_r\{f(t)\} = \mathcal{K}_r(p) = \int_0^\infty r^{-pt} f(t) dt, \qquad (8)$$

where $\Re(p) > 0, r \in (0,\infty)\backslash\{1\}$ and the function $f(t)$ is sectionally continuous and of exponential order.

The Modified inverse Laplace transform of $f(t)$ defined as:

$$f(t) = \mathcal{L}_r^{-1}[\mathcal{K}_r(p)] = \frac{1}{2\pi i}\int\limits_{m-i\infty}^{m+i\infty} r^{pt}\mathcal{K}_r(p)dt, \tag{9}$$

where $\Re(p) > 0, r \in (0,\infty)\backslash\{1\}, m > 0$ and $\mathcal{L}_r^{-1}$ is called modified inverse Laplace transform operator.

Definition 5. The Modified Sumude Transform[5] of a function $f(\xi)$ denoted by $\mathcal{S}_r\{f(\xi)\}$, is defined as

$$\mathcal{S}_r\{f(\xi)\} = \mathcal{K}_r(k) = \int\limits_0^\infty r^{-\xi}f(k\xi)d\xi, \tag{10}$$

where $\Re(k) > 0, r \in (0,\infty)\backslash\{1\}$ and the function $f(\xi)$ is sectionally continuous and of exponential order.

The Modified inverse Sumudu transform of $f(\xi)$ defined as:

$$f(\xi) = \mathcal{S}_r^{-1}[\mathcal{K}_r(k)] = \frac{1}{2\pi i}\int\limits_{m-i\infty}^{m+i\infty} r^{\xi}\mathcal{K}_r(k)d\xi, \tag{11}$$

where $\Re(k) > 0, r \in (0,\infty)\backslash\{1\}, m > 0$ and $\mathcal{S}_r^{-1}$ is called modified inverse Sumudu transform operator.

III.MODIFIED NATURAL TRANSFORM

The modified Natural transform of sectionally continuous and exponential ordered function f(ξ) is defined over the set of functions

$$\mathbf{R} = \left\{ f(\xi)/\exists A, \psi_1, \psi_2 > 0, |f(\xi)| < A e^{\frac{|\xi|}{\psi_j}}, if\ \xi \in (-1)^j \times [0, \infty) \right\}$$

by the following integral

$$\mathcal{N}_r\left[f(\xi)\right](p, k) = \mathcal{K}_r(p, k) = \frac{1}{k} \int_0^\infty r^{\frac{-p\xi}{k}} f(\xi) d\xi \qquad (12)$$

$$= \int_0^\infty r^{-p\xi} f(k\xi) d\xi \qquad (13)$$

where $\Re(p) > 0, k > 0, r \in (0, \infty) - \{1\}$, provided that the integral in (12) and (13) exists.

Remark:

1. if $r = e$ in integral of (12) or (13) we get Natural transform.

2. if $k = 1$ in integral of (12) or (13) we get Modified Laplace Transform defined in (8)

3. if $p = 1$ in integral of (12) or (13) we get Modified Sumudu Transform defined in (10)

The inverse modified natural transform formula is given by:

$$f(\xi) = \frac{1}{2\pi i} \int_{c-i\infty}^{c+i\infty} k r^{p\xi/k} \mathcal{K}_r(p, k) dp \qquad (14)$$

2.1 Sufficient condition for the existence of Modified natural $\mathcal{N}_r$ Transform:

Theorem 1. *If $f(\xi)$ is piecewise continuous in every finite closed and bounded interval [0,M] and of exponential order μ for $\xi > M$ then its $\mathcal{N}_r$ transform $\mathcal{K}_r(p, k)$ exists for all $p,\ k > \mu$.*

Proof. We have any positive real number M,

$$\mathcal{K}_r(p, k) = \frac{1}{k} \int_0^\infty r^{\frac{-p\xi}{k}} f(\xi) d\xi$$

$$= \frac{1}{k} \int_0^M r^{\frac{-p\xi}{k}} f(\xi) d\xi + \frac{1}{k} \int_M^\infty r^{\frac{-p\xi}{k}} f(\xi) d\xi \qquad (15)$$

The first integral of (15) exists, because $f(\xi)$ is piecewise continuous in finite inverval $0 \leq \xi \leq M$. Now we have to show that the second integral of (15) also exists, since the function $f(\xi)$ is of exponential order μ for $\xi > M$. Consider,

$$\left| \frac{1}{k} \int_{M}^{\infty} r^{\frac{-p\xi}{k}} f(\xi) d\xi \right| \leq \int_{M}^{\infty} \left| \frac{1}{k} r^{\frac{-p\xi}{k}} f(\xi) \right| d\xi$$

$$\leq \frac{1}{k} \int_{M}^{\infty} r^{\frac{-p\xi}{k}} |f(\xi)| \, d\xi$$

$$\leq \frac{1}{k} \int_{M}^{\infty} r^{\frac{-p\xi}{k}} A e^{\mu\xi} d\xi$$

$$= \frac{A}{k} \int_{M}^{\infty} e^{-\frac{(p \ln r - k\mu)\xi}{k}} d\xi$$

$$= \frac{A}{p \ln r - \mu k} \cdot e^{-\frac{(p \ln r - k\mu)M}{k}}$$

Hence the proof is complete. $\qquad\square$

2.2 Properties of Modified Natural $\mathcal{N}_r$ Transform:

In this section, we discuss the some properties of Modified Natural $\mathcal{N}_r$ Transforms
Property 1:
If $\delta_1, \ \delta_2 \in \mathbb{C}$ and

$$\mathcal{N}_r[f_1(\xi)] = {}_1\mathcal{K}_r(p, k)$$
$$\mathcal{N}_r[f_2(\xi)] = {}_2\mathcal{K}_r(p, k)$$

then

$$\mathcal{N}_r[\delta_1 f_1(\xi) + \delta_2 f_2(\xi)] = \delta_1 \mathcal{N}_r[f_1(\xi)] + \delta_2 \mathcal{N}_r[f_2(\xi)]$$

Proof. Consider,

$$\mathcal{N}_r[\delta_1 f_1(\xi) + \delta_2 f_2(\xi)] = \frac{1}{k} \int_{0}^{\infty} r^{-\frac{p\xi}{k}} \{\delta_1 f_1(\xi) + \delta_2 f_2(\xi)\} d\xi$$

$$= \delta_1 \cdot \frac{1}{k} \int_{0}^{\infty} r^{-\frac{p\xi}{k}} f_1(\xi) d\xi + \delta_2 \cdot \frac{1}{k} \int_{0}^{\infty} r^{-\frac{p\xi}{k}} f_2(\xi) d\xi$$

$$= \delta_1 \mathcal{N}_r[f_1(\xi)] + \delta_2 \mathcal{N}_r[f_2(\xi)]$$

Complete the proof. $\qquad\square$

Property 2:
If $\alpha \in \mathbb{C}$ and $\mathcal{N}_r[f(\xi)] = \mathcal{K}_r(p,k)$ then

$$\mathcal{N}_r[e^{\alpha\xi} f(\xi)] = \frac{p \ln r}{p \ln r - \alpha k} \mathcal{K}_r \left(\frac{k\, p \ln r}{p \ln\ r - \alpha k} \right)$$

where, $p > 0, k > 0, |r| - 1 > 0$

Proof. by using (13) we write the

$$\mathcal{N}_r[e^{\alpha\xi} f(\xi)] = \int_0^\infty r^{-p\xi} e^{\alpha k\xi}\ f(k\xi)d\xi$$

$$= \int_0^\infty e^{-(p \ln r - \alpha k)\xi} f(k\xi)d\xi$$

substitute $\theta = \frac{p \ln r - \alpha k}{p \ln r} \xi \implies d\xi = \frac{p \ln r}{p \ln r - \alpha k} d\theta$

$$\mathcal{N}_r[e^{\alpha\xi} f(\xi)] = \frac{p \ln r}{p \ln r - \alpha k} \int_0^\infty e^{-p\theta} f\left(\frac{k\, p \ln r\, \theta}{p \ln r - \alpha k} \right) d\theta$$

$$= \frac{p \ln r}{p \ln r - \alpha k} \mathcal{K}_r \left(\frac{k\, p \ln r}{p \ln r - \alpha k} \right) \tag{16}$$

$$\mathcal{N}_r[e^{\alpha\xi} f(\xi)] = \begin{cases} \frac{\ln r}{\ln r - \alpha k} \mathcal{K}_r \left(\frac{k\, \ln r}{\ln r - \alpha k} \right) & (\text{p=1}) \\ \mathcal{K}_r(p \ln r - \alpha) & (\text{k=1}) \end{cases} \tag{17}$$

Complete the proof. $\qquad\qquad\qquad\qquad\qquad\qquad\qquad\qquad\qquad\square$

Remark:

1. In (16), if p = 1 then we get the first shifting property of Modified Sumudu transform.
That is first equation of (17)

2. In (16), if k = 1 then we get the first shifting property of Modified Laplace transform.
That is second equation of (17)

Property 3:

If $\mathcal{N}_r[f(\xi)] = \mathcal{K}_r(p, k), c > 0$ and $u(\xi) = \begin{cases} 1, & \xi \geq 0 \\ 0, & \xi < 0 \end{cases}$ then

$$\mathcal{N}_r[f(\xi - c)u(\xi - c)] = r^{-\frac{pc}{k}}\mathcal{N}_r[f(\xi)]$$

Proof. Consider,

$$\mathcal{N}_r[f(\xi - c)u(\xi - c)] = \frac{1}{k}\int_0^\infty r^{-\frac{p\xi}{k}}\{f(\xi - c)u(\xi - c)\}d\xi$$

put $\xi - c = \theta \implies d\xi = d\theta$

ξ	0	∞
θ	-c	∞

$$\mathcal{N}_r[f(\theta)u(\theta)] = \frac{1}{k}\int_{-c}^\infty r^{-\frac{p}{k}(\theta+c)}f(\theta)u(\theta)d\theta$$

$$= \frac{1}{k}\left[\int_{-c}^0 r^{-\frac{p}{k}(\theta+c)}f(\theta)u(\theta)d\theta + \int_0^\infty r^{-\frac{p}{k}(\theta+c)}f(\theta)u(\theta)d\theta\right]$$

$$= \frac{1}{k}\left[\int_{-c}^0 r^{-\frac{p}{k}(\theta+c)}f(\theta)\ 0\ d\theta + \int_0^\infty r^{-\frac{p}{k}(\theta+c)}f(\theta)\ 1\ d\theta\right]$$

$$= \frac{1}{k}\int_0^\infty r^{-\frac{p}{k}\theta}\ r^{-\frac{p}{k}c}f(\theta)\ d\theta$$

$$= r^{-\frac{p}{k}c}\ \mathcal{N}_r[f(\theta)], \qquad \frac{\ln r}{k} > 0$$

by changing variable $\theta \to \xi$,

$$\mathcal{N}_r[f(\xi - c)u(\xi - c)] = r^{-\frac{p}{k}c}\ \mathcal{N}_r[f(\xi)], \qquad \frac{\ln r}{k} > 0 \tag{18}$$

complete the proof $\qquad\qquad\qquad\qquad\qquad\qquad\qquad\qquad\qquad\qquad\qquad$ $\square$

Remark:

1. In (18), if p = 1 then we get the second shifting property of Modified Sumudu transform.

2. In (18), if k = 1 then we get the second shifting property of Modified Laplace transform.

Property 4:

If $\mu \in \mathbb{C}$ and $\mathcal{N}_r[f(\xi)] = \mathcal{K}_r(p,k)$ then

$$\mathcal{N}_r[f(\mu\xi)] = \frac{1}{\mu}\mathcal{N}_r(\frac{p}{\mu}, k)$$

Proof. Consider,

$$\mathcal{N}_r[f(\mu\xi)] = \frac{1}{k}\int\limits_0^\infty r^{-\frac{p\xi}{k}} f(\mu\xi)d\xi$$

put $\mu\xi = \theta \implies d\xi = \frac{d\theta}{\mu}$

$$\mathcal{N}_r[f(\theta)] = \frac{1}{\mu k}\int\limits_0^\infty r^{-\frac{p\theta}{k\mu}} f(\theta)d\theta$$

$$= \frac{1}{\mu k}\int\limits_0^\infty r^{-\frac{\sigma\theta}{k}} f(\theta)d\theta$$

$$= \frac{1}{\mu}\mathcal{N}_r(\frac{p}{\mu}, k)$$

where, $\sigma = \frac{p}{\mu}$

$$\mathcal{N}_r[f(\mu\xi)] = \frac{1}{\mu}\mathcal{N}_r(\frac{p}{\mu}, k) \tag{19}$$

Hence complete the proof. $\qquad\square$

Remark:

1. In (19), if p = 1 then we get the change of scale property of the Modified Sumudu transform.

2. In (19), if k = 1 then we get the change of scale property of Modified Laplace transform.

3 Nr Transforms of some elementary functions

We are evaluated the Modified Natural Transforms of some functions and compared with the Modified Laplace Transform and Modified Sumudu Transform by putting the value of k = 1 and p = 1 respectively, where p, k > 0, $|r| - 1 > 0$ pln r k > μ > 0

$f(\xi)$	$\mathcal{N}_r[f(\xi)] = \mathcal{K}_r(p,k)$	$\mathcal{L}_r[f(\xi)] = \mathcal{K}_r(p)$	$\mathcal{S}_r[f(\xi)] = \mathcal{K}_r(k)$
1	$\frac{1}{p \, lnr}$	$\frac{1}{p \, lnr}$	$\frac{1}{lnr}$
ξ	$\frac{k}{p^2(\ln r)^2}$	$\frac{1}{p^2(\ln r)^2}$	$\frac{k}{(\ln r)^2}$
ξ^n	$\frac{\Gamma(n+1)\cdot k^n}{p^{n+1}(\ln r)^{n+1}}$	$\frac{\Gamma(n+1)}{p^{n+1}(\ln r)^{n+1}}$	$\frac{\Gamma(n+1)\cdot k^n}{(\ln r)^{n+1}}$
$e^{\mu\xi}$	$\frac{1}{p \, \ln r - \mu k}$	$\frac{1}{p \, \ln r - \mu}$	$\frac{1}{\ln r - \mu k}$
$\sin(\mu\xi)$	$\frac{\mu k}{p^2(\ln r)^2 + \mu^2 k^2}$	$\frac{\mu}{p^2(\ln r)^2 + \mu^2}$	$\frac{\mu k}{(\ln r)^2 + \mu^2 k^2}$
$\cos(\mu\xi)$	$\frac{p \, \ln r}{p^2(\ln r)^2 + \mu^2 k^2}$	$\frac{p \, \ln r}{p^2(\ln r)^2 + \mu^2}$	$\frac{\ln r}{(\ln r)^2 + \mu^2 k^2}$
$\sinh(\mu\xi)$	$\frac{\mu k}{p^2(\ln r)^2 - \mu^2 k^2}$	$\frac{\mu}{p^2(\ln r)^2 - \mu^2}$	$\frac{\mu k}{(\ln r)^2 - \mu^2 k^2}$
$\cosh(\mu\xi)$	$\frac{p \, \ln r}{p^2(\ln r)^2 - \mu^2 k^2}$	$\frac{p \, \ln r}{p^2(\ln r)^2 - \mu^2}$	$\frac{\ln r}{(\ln r)^2 - \mu^2 k^2}$
$u(\xi - c)$	$\frac{r^{-\frac{pc}{k}}}{p \, \ln r}$	$\frac{r^{-pc}}{p \, \ln r}$	$\frac{r^{-\frac{c}{k}}}{\ln r}$
$erf(\sqrt{\xi})$	$\frac{\sqrt{k}}{p\ln r\sqrt{p\ln r + k}}$	$\frac{1}{p\ln r\sqrt{p\ln r + 1}}$	$\frac{\sqrt{k}}{\ln r\sqrt{\ln r + k}}$

IV. THEOREMS

Theorem 2. Nr Transform of Derivatives:

If $\mathcal{N}_r[f(\xi)] = \mathcal{K}_r(p,k)$ then

$$\mathcal{N}_r[f^n(\xi)] = \left(\frac{p}{k}\right)^n (\ln r)^n \, \mathcal{K}_r(p,k) - \sum_{i=0}^{n-1} \frac{p^{n-i-1}}{k^{n-i}} (\ln r)^{n-i-1} \, f^{(i)}(0)$$

where, $f^n(\xi)$ stands for $\frac{d^n f(\xi)}{d\xi^n}$

Proof. Let $\mathcal{N}_r[f(\xi)] = \mathcal{K}_r(p,k)$ then

$$\mathcal{N}_r[f'(\xi)] = \frac{1}{k} \int_0^\infty r^{-\frac{p\xi}{k}} f'(\xi)d\xi$$

solving right hand integral by parts, we get

$$\mathcal{N}_r[f'(\xi)] = \frac{p}{k} \, \ln r \, \mathcal{K}_r(p,k) - \frac{f(0)}{k}$$

Now replacing $f''(\xi)$ by $f'(\xi)$, we get

$$
\begin{aligned}
\mathcal{N}_r[f''(\xi)] &= \frac{p}{k} \ln r \; \mathcal{N}_r[f'(\xi)] - \frac{f'(0)}{k} \\
&= \frac{p}{k} \ln r \left[\frac{p}{k} \ln r \; \mathcal{K}_r(p,k) - \frac{f(0)}{k} \right] - \frac{f'(0)}{k} \\
&= \frac{p^2}{k^2} (\ln r)^2 \; \mathcal{K}_r(p,k) - \frac{p}{k^2} \ln r \; f(0) - \frac{f'(0)}{k}
\end{aligned}
$$

continuing in this way we get,

$$
\mathcal{N}_r[f^n(\xi)] = \left(\frac{p}{k}\right)^n (\ln r)^n \; \mathcal{K}_r(p,k) - \sum_{i=0}^{n-1} \frac{p^{n-i-1}}{k^{n-i}} (\ln r)^{n-i-1} f^{(i)}(0)
$$

Complete the proof. $\qquad\square$

Theorem 3. $\mathcal{N}_r$ Transform of Integral
If $\mathcal{N}_r[f(\xi)] = \mathcal{K}_r(p,k)$ then

$$
\mathcal{N}_r\left[\left\{ \int_0^\xi f(\mu)d\mu \right\}\right] = \frac{k}{p}\mathcal{K}_r(p,k)
$$

Theorem 4. Multiplication by Powers of ξ
If $\mathcal{N}_r[f(\xi)] = \mathcal{K}_r(p,k)$ then

$$
\mathcal{N}_r[\xi^n \; f(\xi)] = (-1)^n \left(\frac{k}{\ln r}\right)^n \frac{d^n \mathcal{K}_r(p,k)}{dp^n}
$$

Theorem 5. Division by ξ
If $\mathcal{N}_r[f(\xi)] = \mathcal{K}_r(p,k)$ then

$$\mathcal{N}_r[\frac{f(\xi)}{\xi}] = \left(\frac{\ln r}{k}\right) \int\limits_{p}^{\infty} \mathcal{K}_r(p, k) dp$$

Theorem 6. *Initial and Final Value Theorem:*

1. $\lim\limits_{\xi \to 0} f(\xi) = \lim\limits_{p \to \infty} p \ln r \; \mathcal{K}_r(p, k)$

2. $\lim\limits_{\xi \to \infty} f(\xi) = \lim\limits_{p \to 0} p \ln r \; \mathcal{K}_r(p, k)$

Theorem 7. *Convolution Theorem:*
Let $\mathcal{N}_r[f(\xi)] = \mathcal{K}_r(p, k)$ and $\mathcal{N}_r[g(\xi)] = \mathcal{P}_r(p, k)$ where, $f(\xi)$ and $g(\xi)$ are piecewise continuous functions on $[0, \infty)$ then modified Natural Transform of the Convolution $(f*g)$ defined by

$$\mathcal{N}_r[f * g](\xi) = k \, \mathcal{N}_r[g(\xi)] \cdot \mathcal{N}_r[f(\xi)] \qquad (20)$$

V. MODIFIED INVERSE NATURAL TRANSFORM

We now introduce modified inverse Natural Transform of a function f(ξ) is defined by

$$f(\xi) = \mathcal{N}_r^{-1}[\mathcal{K}_r(p, k)] = \frac{1}{2\pi \, i} \int\limits_{q-i\infty}^{q+i\infty} r^{\frac{p}{k}\xi} \, \mathcal{K}_r(p, k) dp \qquad (21)$$

Theorem 8. *Linearity of Modified inverse Natural Transform*
If $\delta_1, \; \delta_2 \in \mathbb{C}$ and

$$\mathcal{N}_r[f_1(\xi)] = \mathcal{K}_r(p, k)$$
$$\mathcal{N}_r[f_2(\xi)] = \mathcal{P}_r(p, k)$$

then

$$\mathcal{N}_r^{-1}[\delta_1 \mathcal{K}_r(p, k) + \delta_2 \mathcal{P}_r(p, k)] = \delta_1 \, \mathcal{N}_r^{-1}[\mathcal{K}_r(p, k)] + \delta_2 \, \mathcal{N}_r^{-1}[\mathcal{P}_r(p, k)]$$

Let $f(\xi)$ be a piecewise continuous function of exponential order then their modified inverse Natural Transform tabulated below, where $p, k > 0$, $|r| - 1 > 0$, $p\frac{\ln r}{k} > \mu > 0$

$\mathcal{K}_r(p,k)$	$f(\xi) = \mathcal{N}_r^{-1}[\mathcal{K}_r(p,k)]$
$\frac{1}{p\ lnr}$	1
$\frac{k}{p^2(\ln r)^2}$	ξ
$\frac{\Gamma(n+1)\cdot k^n}{p^{n+1}(\ln r)^{n+1}}$	ξ^n
$\frac{1}{p\ \ln r - \mu k}$	$e^{\mu\xi}$
$\frac{\mu k}{p^2(\ln r)^2 + \mu^2 k^2}$	$\sin(\mu\xi)$
$\frac{p\ \ln r}{p^2(\ln r)^2 + \mu^2 k^2}$	$\cos(\mu\xi)$
$\frac{\mu k}{p^2(\ln r)^2 - \mu^2 k^2}$	$\sinh(\mu\xi)$
$\frac{p\ \ln r}{p^2(\ln r)^2 - \mu^2 k^2}$	$\cosh(\mu\xi)$

VI. APPLICATIONS OF MODIFIED NATURAL TRANSFORM

In this section, the use of the proposed transform are presented by finding a solution of various differential equations

Example 1. Solve the First order linear differential equation $y' + y = 0$, $y(0) = 1$ by using Modified Natural Transform.

We have Differential equation,

$$y' + y = 0, \qquad y(0) = 1 \qquad (22)$$

Now we apply Modified Natural Transform on both sides of above (22)

$$\mathcal{N}_r[y'] + \mathcal{N}_r[y] = \mathcal{N}_r[0]$$

$$\frac{p}{k}\ln r \mathcal{K}_r(p,k) - \frac{y(0)}{k} + \mathcal{K}_r(p,k) = 0$$

$$\left(\frac{p}{k}\ln r + 1\right)\mathcal{K}_r(p,k) = \frac{1}{k}$$

$$\mathcal{K}_r(p,k) = \frac{1}{p\ln r + k}$$

By using Modified inverse Natural transform gives the solution of (22) as follows

$$y(\xi) = e^{-\xi}$$
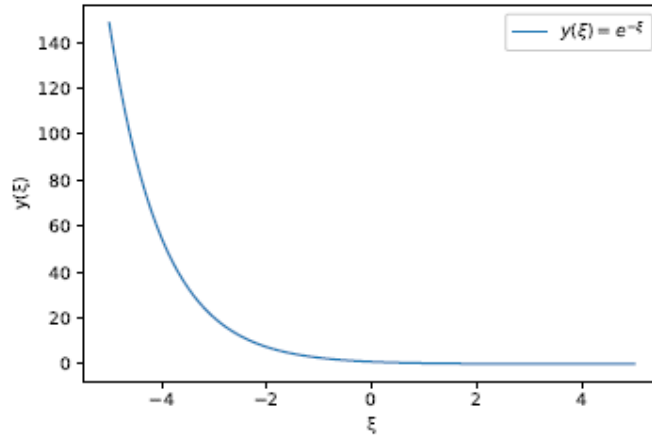
Figure 1: 2D Graph of Solution of Example 1

Example 2. [21] *Consider a sample of a certain radioactive isotope. The atoms of such an isotope are unstable, with a certain proportion decaying each second. In particular, the mass M of the sample will decrease as atoms are lost, with the rate of decrease proportional to the number of atoms.*
We can write this as a differential equation

$$\frac{dM}{dt} = -\alpha M, \ \text{at time } t=0, \ M(0) = M_0 \tag{23}$$

where,α is a constant of proportionality.

Apply Modified Natural Transform to (23)

$$\mathcal{N}_r[\frac{dM}{dt}] = -\mathcal{N}_r[\alpha M]$$

$$\frac{p}{k}\ln r \ \mathcal{K}_r(p,k) - \frac{M(0)}{k} = -\alpha \mathcal{K}_r(p,k)$$

$$\frac{p}{k}\ln r \ \mathcal{K}_r(p,k) - \frac{M(0)}{k} + \alpha \mathcal{K}_r(p,k) = 0$$

$$\left(\frac{p}{k}\ln r + \alpha\right) \mathcal{K}_r(p,k) = \frac{M_0}{k}$$

$$\mathcal{K}_r(p,k) = \frac{M_0}{p\ln r + \alpha k}$$

Taking Modified inverse Natural Transform we get the solution of (23)

$$M = M_0 e^{-\alpha t} \quad (\alpha > 0)$$

which the mass of the sample will decay exponentially with time.
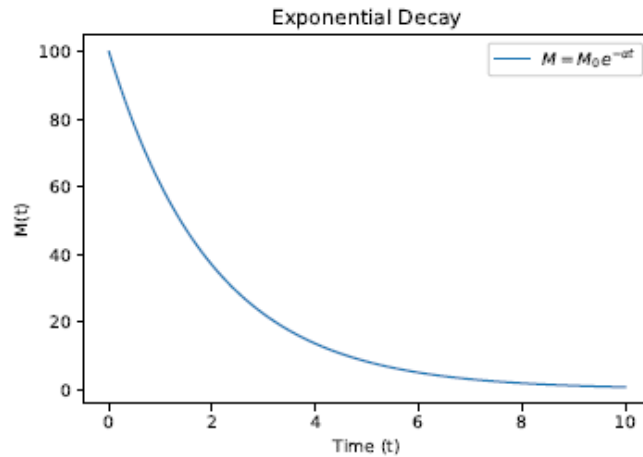
Figure 2: 2D Graph of Solution of Example 2

Example 3. *Solve the differential equation*

$$\frac{d^2y}{dx^2} + \frac{dy}{dx} = x^2 + 2x, \quad y(0) = 4, y'(0) = -2 \tag{24}$$

Apply Modified Natural Transform to (24)

$$\mathcal{N}_r[\frac{d^2y}{dx^2} + \frac{dy}{dx}] = \mathcal{N}_r[x^2 + 2x]$$

$$\mathcal{N}_r[\frac{d^2y}{dx^2}] + \mathcal{N}_r[\frac{dy}{dx}] = \mathcal{N}_r[x^2] + \mathcal{N}_r[2x]$$

$$\begin{bmatrix} \frac{p^2}{k^2}(\ln r)^2 \mathcal{K}_r(p,k) - \frac{p}{k^2}(\ln r)y(0) \\ -\frac{1}{k}y'(0) + \frac{1}{k}\mathcal{K}_r(p,k) - \frac{y(0)}{k} \end{bmatrix} = \frac{2k^2}{p^3(\ln r)^3} + 2\frac{k}{p^2(\ln r)^2}$$

by using initial condition and simplification reduces above equation to

$$\mathcal{K}_r(p,k) = 2\frac{k^3}{p^4(\ln r)^4} + 2\frac{1}{p\ln r} + 2\frac{1}{p\ln r + 1}$$

we obtain the final solution by taking inverse Modified Natural Transform as follow

$$y(x) = 2\frac{x^3}{3!} + 2(1) + 2e^{-x}$$

$$y(x) = 2\frac{x^3}{3!} + 2e^{-x} + 2$$
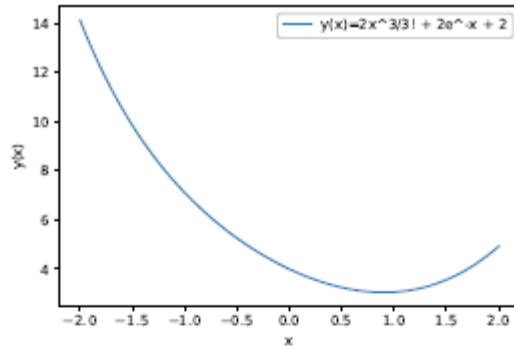
Figure 3: 2D Graph of Solution of Example 3

Example 4. [20] *Based on the diagram above, our circuit has an inductor of four henrys, a resistor of 20 ohms and a Capacitor of .02 farads. As for the charge and current, let's set a condition so that the charge on the capacitor, and current in the circuit, be O at t=O. Let's find the charge on the capacitor at any time t besides 0, where V is equal to 200 volts. So then we get the following,*

$$4\frac{dI}{dt} + 20I + \frac{1}{.02}Q = 200 \tag{25}$$

since

$$I = \frac{dQ}{dt},$$

$$4\frac{d^2Q}{dt^2} + 20\frac{dQ}{dt} + 50Q = 200$$

Take into account that we have the following initial conditions due to our change at $t = 0$ being 0.

1. $Q(0) = 0$

2. $Q'(0) = 0$

Now we know the following is true

- $\frac{d^2Q}{dt^2} = Q^n$

- $\frac{dQ}{dt} = Q'$

With this, we can rewrite the original equation

$$Q'' + 5Q' + \frac{25}{2}Q = 50$$

Now we take the Modified Natural Transform

$$\mathcal{N}_r[Q'' + 5Q' + \frac{25}{2}Q] = \mathcal{N}_r[50]$$

$$\mathcal{N}_r[Q''] + 5\mathcal{N}_r[Q'] + \frac{25}{2}\mathcal{N}_r[Q] = \mathcal{N}_r[50]$$

$$\frac{p^2}{k^2}(\ln r)^2 \mathcal{K}_r(p,k) - \frac{p}{k^2}(\ln r)Q(0) - \frac{1}{k}Q'(0) + \frac{1}{k}\mathcal{K}_r(p,k) - \frac{Q(0)}{k} + \frac{25}{2}\mathcal{K}_r(p,k) = \frac{50}{p(\ln r)}$$

by using initial condition and simplification reduces the above equation to

$$\mathcal{K}_r(p,k)\left(\frac{p^2}{k^2}(\ln r)^2 + \frac{1}{k} + \frac{25}{2}\right) = \frac{50}{p(\ln r)}$$

$$\mathcal{K}_r(p,k) = \frac{100k^2}{p(\ln r)\left(2p^2(\ln r)^2 + 2k + 25k^2\right)}$$

we obtain the final solution by taking inverse Modified Natural Transform

$$Q(t) = 4 - 4e^{\frac{5}{2}t}\cos\frac{5}{2}t - 4e^{\frac{5}{2}t}\sin\frac{5}{2}t$$
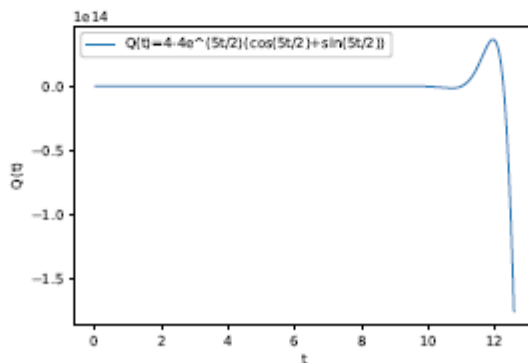
Figure 4: 2D Graph of Solution of Example 4

VII. CONCLUSION

Natural Transform is an effective tool in Science, Engineering and Technology. Natural transforms have more application in areas of Mathematics and Engineering but a much wider extension like an effective application of modified Natural Transform in the areas of chemistry, Mathematics, and Physics to find out the solution of various differential equations.

In this paper, we introduce the Modified Natural Transform and its properties are mentioned.

Some theorems related to the modified Laplace transform and Modified Sumudu transform are also true for this modified Natural Transform. In the last article, we solved four examples as an application of modified Natural Transform and compared the solution graphically.

VIII.   REFERENCES

[1].   Belgacem, F. B. M., Karaballi, A. A., & Kalla, S. L. "Analytical investigations of the Sumudu transform and applications to integral production equations" Mathematical problems in Engineering, 2003(3), 103-118.

[2].   Saif, Mohd, Khan, Faisal, Nisar, Kottakkaran Sooppy, Araci, Serkan. "Modified Laplace transform and its properties" Journal of Mathematics and Computer Science, 21, no. 2 (2020): 127‑135

[3].   Khan, Z. H., & Khan, W. A. "N-transform-properties and applications" NUST journal of engineering sciences, 1(1), 127-133.

[4].   G.K.Watugala, "Sumudu Transform: A New Integral Transform to Solve Differential Equations and Control Engineering Problems," International Journal of Mathematical Education in Science and Technology, 1993.

[5].   Duran, U. "Modified Sumudu Transform and Its Properties," Sakarya University Journal of Science, (2021), 25(2), 389-396. https://doi.org/10.16984/saufenbilder.825180

[6].   Belgacem, F. B. M., & Karaballi, A. A. "Sumudu transform fundamental properties investigations and applications" International Journal of Stochastic Analysis, 2006(1), 091083.

[7].   A.H. Zemanian, "Generalized Integral Transformations," Courier Corporation, 1987.

[8].   Loonker, D., & Banerji, P. K. "Applications of natural transform to differential equations" J. Indian Acad. Math,(2013), 35(1), 151-158.

[9].   P.S. Laplace, "Th´eorie Analytique des Probabilit´es," Imprimerie Royale, 1812.

[10].   G. Doetsch, "Introduction to the Theory and Application of the Laplace Transformation," Springer Science & Business Media, 2012.

[11].   L. Euler, "Institutiones Calculi Integralis," Academia Scientiarum Imperialis Petropolitanae, 1768.

[12].   J. L. Lagrange, "M´ecanique Analytique," Chez la Veuve Desaint, 1788.

[13].   Rami Alahmad, "Certain integral transforms of the product of two functions" , J. Math. Comput. Sci., 11 (2021), 4668-4672

[14].   D.V. Widder, "The Laplace Transform," Princeton University Press, 2015.

[15].   H. Bateman, "Tables of Integral Transforms," McGraw-Hill, 1954.

[16].   E.C. Titchmarsh, "Introduction to the Theory of Fourier Integrals," Oxford University Press, 1948.

[17].   I.N. Sneddon, "The Use of Integral Transforms," Tata McGraw-Hill, 1972.

[18].   R.V. Churchill, "Operational Mathematics," McGraw-Hill, 1972.

[19].   E.L. Ince, "Ordinary Differential Equations," Courier Corporation, 1956.

[20].   Cocagne, Andre, "Applications of Laplace transform," Senior Honors Theses and Projects, (2017), 541.

[21].   Knight, R. D. "Physics for scientists and engineers: a strategic approach with modern physics," (2017), (p. 500). Boston: Pearson.

Basic Polarimetric Characteristics of Full-Polarization Chandrayaan-II DFSAR Data Analyzed Using MIDAS (Microwave Data Analysis Software)

Shinde Suryakant Annasaheb 1, Sayyad Shafiyoddin2, Kranti Ramdas Zakde 2

1 Assistant Professor, School of Engineering & Technology, MGM University, Chhatrapati Sambhajinagar-431003 (MS) India

2 Professor of Physics, milliya arts Science & Management Science College, Beed-431122 (MS) India

2* Associate Professor, Department of Physics, Jawaharlal Neharu engineering College, MGM University, Chhatrapati Sambhajinagar-431003 (MS) India

Abstract :

This study focuses on the analysis of basic polarimetric characteristics of full-polarization DFSAR data specifically through image formats using the Microwave Data Analysis Software (MIDAS). The research emphasizes visual representation, leveraging image-based outputs to interpret polarimetric parameters. These image formats provide a clearer understanding of surface scattering mechanisms and enhance the ability to perform detailed environmental and geological assessments using radar data. The study demonstrates how MIDAS can effectively process DFSAR data into meaningful visual representations for advanced analysis.

I. INTRODUCTION

The Chandrayaan-2 mission, launched by the Indian Space Research Organization (ISRO) in July 2019, marks a significant milestone in lunar exploration.

Equipped with a Dual-Frequency Synthetic Aperture Radar (DFSAR), which operates in the L-band & s band frequency. This radar system is designed to penetrate lunar surface layers and provide valuable data for understanding the Moon's surface composition and morphology. One of the key features of DFSAR is its ability to capture full-polarization data, which allows for detailed analysis of surface scattering properties. In this study, we focus on the basic polarimetric characteristics of the L- band SAR data acquired by Chandrayaan-2's DFSAR. By utilizing the Microwave Data Analysis System (MIDAS), we analyse this data specifically in image formats to gain insights into the lunar surface's scattering mechanisms. MIDAS is a sophisticated tool designed for processing and interpreting polarimetric SAR data, enabling the generation of high-quality visual representations. These images are crucial for advancing our understanding of the lunar surface and supporting further scientific investigations into the Moon's geological features. This introduction sets the stage for a detailed exploration of how DFSAR's full-polarization data, when processed through MIDAS, can be used to enhance lunar surface analysis.

II. METHODOLOGY:

The following steps shows the workflow of methodology used to analyze Chandrayaan II dataset.

2.1 Flow chart

1. Data Acquisition

↓

2. Radiometric Processing

→ Calibrated Backscatter Coefficients (σ_0)

↓

3. Covariance and Coherence Matrices Computation

→ Covariance Matrix (C_3)

→ Coherence Matrix (T_3)

→ Matrix (C4)

↓

4. Filtering

→ Noise-Reduced SAR Images

↓

5. Application of Polarimetric Decomposition Techniques

├── Freeman-Durden Decomposition

│   → Scattering Components (Surface, Double-Bounce, Volume)

├── Yamaguchi Decomposition [G40 , Y40, Y4R]

│   → Extended Scattering Components

├── H-A-α Decomposition

│   → Entropy (H), Anisotropy (A), Alpha Angle (α)

├── Cloude Decomposition

│   → Entropy (H), Anisotropy (A), Alpha Angle (α)

└── Pouli Decomposition

→ Scattering Components with Descriptors (m, δ, χ)

This flow chart provides a clear sequence of steps for processing SAR data,

detailing each stage from acquisition through various analytical techniques, while

preserving the original meanings and processes[1].

2.2 Data Acquisition and Preprocessing:

2.2.1 Data Acquisition:

The dataset used in this study, identified as ch2_sar_ncxl_20220920t222945820_d_fp_d32, was acquired by the Dual-Frequency Synthetic Aperture Radar (DFSAR) onboard the Chandrayaan-2 spacecraft. This specific dataset corresponds to an L-band full-polarization SAR acquisition, collected on September 20, 2022. The DFSAR instrument is designed to operate in the L-band frequency (1.25 GHz), which is ideal for penetrating the lunar surface and capturing detailed information about its scattering properties.

The data was collected over a selected lunar region of interest, with the DFSAR configured to capture all polarization channels, including HH (Horizontal-Horizontal), VV (Vertical-Vertical), HV (Horizontal-Vertical), and VH (Vertical-Horizontal). This full-polarization dataset is crucial for conducting a comprehensive polarimetric analysis of the lunar surface, allowing researchers to investigate different surface materials and textures.

After acquisition, the raw SAR data was downlinked to ground stations and processed to remove any radiometric and geometric distortions, ensuring the highest possible data quality. The specific dataset, ch2_sar_ncxl_20220920t222945820_d_fp_d32, was then calibrated to correct for any sensor-induced biases and to ensure accurate representation of the lunar surface.

Following calibration, the data was imported into the Microwave Data Analysis System (MIDAS), a specialized software tool for polarimetric SAR data processing.

MIDAS was used to extract key polarimetric parameters from the dataset and generate high-quality image formats, which were essential for visual analysis in this study. The processed images provided detailed insights into the polarimetric characteristics of the lunar surface, contributing significantly to the understanding of lunar geology and surface properties[2].

2.2.2 Preprocessing: Data preprocessing includes Processing Using MIDAS:

MIDAS (Microwave Data Analysis Software) is a specialized tool developed to process and analyze SAR data, including DFSAR data from Chandrayaan-2. It provides a comprehensive suite of functionalities for polarimetric and radiometric analysis:

a. Radiometric Processing: Convert level-2 co- and cross-polarized backscattering elements into calibrated backscatter coefficients (σ_0).

b. b. Covariance and Coherence Matrices Computation: Compute covariance (C_3) and coherence (T_3) matrices from SAR data.

c. Filtering: Apply polarimetric filters to reduce speckle noise while preserving the data's polarimetric characteristics. Use filters such as the Refined Lee filter for Noise-Reduced SAR Images

d. Calculation of Stokes Parameters and Circular Polarization Ratio (CPR): Compute Stokes parameters and CPR for hybrid- polarization and full-polarization SAR data.

e. Application of Polarimetric Decomposition Techniques: Interpret SAR data to distinguish different scattering mechanisms and identify surface materials.

Techniques:

- Freeman-Durden Decomposition
- Decomposes radar signal into surface, double-bounce, and volume scattering components. Scattering Components (Surface, Double-Bounce, Volume)
- Yamaguchi Decomposition [G40 , Y40, Y4R] Extends Freeman-Durden by adding a helix scattering component for complex surfaces. Extended Scattering Components
- H-A-α Decomposition
- Uses eigenvalues of the coherence matrix to compute entropy (H), anisotropy (A), and alpha angle (α).
- Cloude Decomposition
- decomposes the scattering matrix into eigenvectors to identify surface, volume, and double-bounce scattering mechanisms.
- Pauli Decomposition

- Pauli decomposition allows for the identification of different scattering behaviors (e.g., surface scattering, volume scattering, and double-bounce scattering[3].

III. RESULTS & DISCUSSION:

The analysis of the L-band full-polarization SAR data from Chandrayaan-2, specifically the dataset ch2_sar_ncxl_20220920t222945820_d_fp_d32, yielded several significant findings regarding the lunar surface's polarimetric characteristics:

Polarimetric Parameter Extraction: The MIDAS software successfully extracted key polarimetric parameters from the calibrated SAR data, including co-polarized (HH, VV) and cross-polarized (HV, VH) channels. This extraction provided a comprehensive view of the lunar surface's scattering mechanisms. The output result or images are as follows:

HH   HV   VH   VV   RGB 1 (R-HH, G-HV, B-VH)   RGB 2 (R-VV, G-HH, B-VH)   RGB 3 (R-VH, G-VV, B-HV)
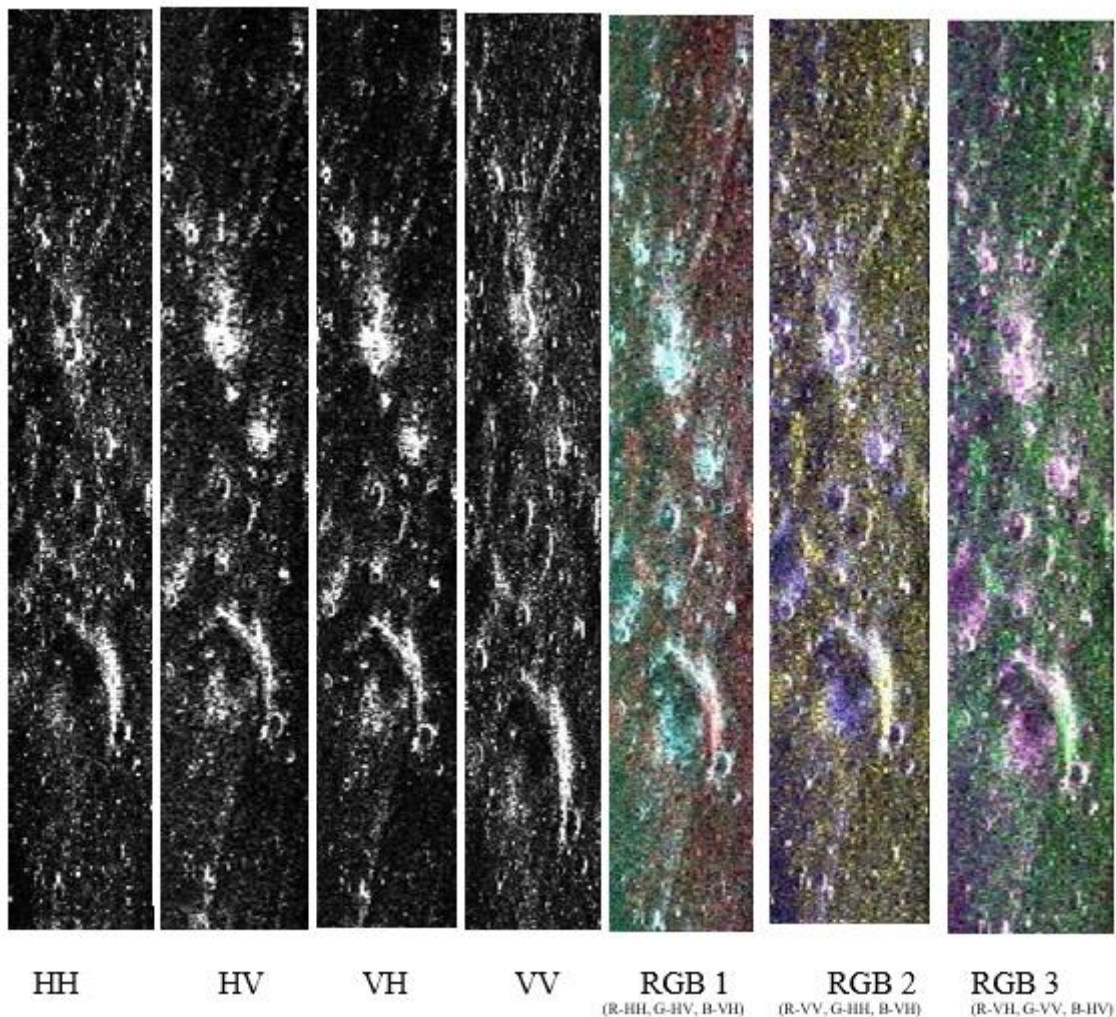
C3 MATRIX   T3 MATRIX   C4 MATRIX   CLOUDE DECOMPOSITION   PAULI DECOMPOSITION

Freeman-Durden DECOMPOSITION   H-A-α DECOMPOSITION   Yamaguchi G-40 DECOMPOSITION   Yamaguchi Y-40 DECOMPOSITION   Yamaguchi Y-4R DECOMPOSITION

The results allowed for a better interpretation of geological features on the lunar surface. The calibration process ensured that the data was accurate and reliable, resulting in high-quality images that effectively highlighted the differences in surface characteristics. The visual representations generated by MIDAS demonstrated clear contrasts between different lunar surface features and provided valuable insights into their physical properties.

Overall, the results underscore the effectiveness of using calibrated L-band SAR data and advanced processing tools like MIDAS for detailed polarimetric analysis, offering significant insights into the lunar surface and its characteristics.

3.1 Advantages of Using MIDAS for DFSAR Data Analysis:

MIDAS offers a user-friendly interface and a range of advanced functionalities

that streamline the processing and analysis of DFSAR data. Its ability to handle both full- and hybrid-polarimetric data makes it an invaluable tool for lunar research, enabling detailed characterization of the lunar surface and subsurface features.

IV. CONCLUSION:

This study demonstrates the effectiveness of using DFSAR data and advanced processing techniques, such as those provided by MIDAS, for analyzing the lunar surface. The results underscore the potential of polarimetric SAR data in identifying geological features and assessing resource potential, particularly in PSRs where traditional optical sensors are ineffective.

Acknowledgement: We acknowledge the use of Chandrayaan-2 data are available at Indian Space Science Data Center (https://www.issdc.gov.in/) (https://pradan.issdc.gov.in/ch2.) The authors would like to thank open-source tool MIDAS software team also. I am also thankful Dr. Ashish B. Itolikar.

V. REFERENCES:

[1]. Chakraborty, T., et al. "Chandrayaan-2 DFSAR Data Processing Using MIDAS Software." ResearchGate, 2023.

[2]. Dsouza, H., & Singh, S.K. "Polarimetric Analysis of de Gerlache Crater Using Chandrayaan-2 DFSAR Data." ResearchGate, 2023.

[3]. Chakraborty, T., et al. "A Software Tool to Process & Analyze Chandrayaan-2 Polarimetric Dual-Frequency SAR (DFSAR) Data." ResearchGate, 2022.

Laplace-Mohand Transform

Pooja S. Thorat1, Dhanashri S. Jadhav2, Pooja B. Rode3, Bhagyashri N. Todkari4, Pooja S. Kasule5

Department of Mathematics, New Arts, Commerce and Science College, Ahmednagar.414001, Maharashtra, India.

Abstract :

In this work, we have extended the Laplace Mohand transform. It was invented to do the Laplace Mohand transform of basic elementary functions. In addition, the existence theorem was covered concerning fundamental properties including the linearity property. Transform of derivative. Change of scale property. Using the Laplace-Mohand transform, partial differential equations with initial conditions may be evaluated.

Keywords: Laplace Transform, Mohand Transform, Laplace Mohand Transform

I. INTRODUCTION

Recently many scholars [4] used different integral transforms, Mahgoub (Laplace-carson) transform for evaluating improper integrals which contains error function in the integrand. In 2019, Aggarwal & Chaudhary [7] discussed Mohand &Laplace transforms comparatively by solving system of differential equation using both integral transform. There are many integral transform have widely used to solve the differential equation &there are several works on integral transform such as the Laplace transform was introduced by P.S.Laplace in 1780s [8] Mohand transform was introduced by Mohand.M.Mahgoub in [9]

The aim of this study is to two single transform combine together and present new double Laplace Mohand Transform.

In this paper, we introduce the Laplace Mohand Transform a new integral transform.

Definition of Laplace Transform: [7,11]

In the year 2017, Mohand and Mahgoub [6] defined the "Mohand transform" of the function $F(t) for t \geq 0$ as,

$$M\{F(t)\} = v^2 \int_0^\infty F(t)e^{-vt}dt = R(s), \; k1 \leq v \leq k2$$

Where Operator M is called the Mohand transform operator.

We have extended this transform as a combination of Laplace and Mohand transform Laplace–Mohand transform as follows:

Definition of Laplace Mohand Transform

$$LM[\omega(t_1, t_2)] = s^2 \int_0^\infty \int_0^\infty e^{-st_1} e^{-vt_2} \omega(t_1, t_2) dt_1 dt_2$$

$$= \overline{\omega}(s, v)$$

The Mohand and Laplace transform of the function $\omega(t_1, t_2)$ exists for $t_1, t_2 \geq 0$ exist if $\omega(t_1, t_2)$) is piecewise continuous and of exponential order. These conditions are only sufficient conditions for the existence of transforms.

Existence Theorem for Laplace Mohand Transform:

Let $\omega(t_1, t_2)$ be a continuous function in every finite interval $(0, X)$ and $(0, Y)$ and of exponential order $e^{(at_1 + bt_2)}$ then double Laplace Mohand transform of $\omega(t_1, t_2)$ exist for all $s > k_1 \; and \; v > k_2$

Proof: Let $\omega(k_1, k_2)$ be exponential order $e^{at_1 + bt_2}$ such that

$$\left| \omega(t_1, t_2) \right| \leq M e^{(at_1 + bt_2)} \; \forall t_1 > X, t_2 > Y$$

$$LM \left| \omega(t_1, t_2) \right| = \left| s^2 \int_0^\infty \int_0^\infty e^{-st_1} e^{-vt_2} \omega(t_1, t_2) dt_1 dt_2 \right|$$

$$= s^2 \int_0^\infty \int_0^\infty e^{-(st_1 + vt_2)} . e^{(at_1 + bt_2)} dt_1 dt_2$$

$$= M s^2 \int_0^\infty \int_0^\infty e^{-(st_1 + vt_2)} e^{(at_1 + bt_2)} dt_1 dt_2$$

$$= M s^2 (\int_0^\infty e^{-(s-a)t_1} dt_1)(\int_0^\infty e^{-(v-b)t_2} dt_2)$$

$$= Ms^2\left[\frac{e^{-(s-a)t_1}}{-(s-a)}\right]_0^\infty \left[\frac{e^{-(v-b)}}{-(v-b)}\right]_0^\infty$$

$$= Ms^2\left[\frac{1}{s-a}\right]\left[\frac{1}{v-b}\right]$$

$$= \frac{Ms^2}{(s-a)(v-b)}$$

Main Result:

Linearity property:

If $LM\left[\omega_1\left(t_1, t_2\right)\right] = \overline{\omega}_1(s, v)$, $LM\left[\omega_2\left(t_1, t_2\right)\right] = \overline{\omega}_2(s, v)$

Then Laplace Mohand Transform of

$$LM\left[c_1\omega_1\left(t_1, t_2\right) + c_2\omega_2\left(t_1, t_2\right)\right] = c_1 LM\left[\omega_1\left(t_1, t_2\right)\right] + c_2[\omega(t_1, t_2)]$$

Proof:

Consider $LM\left[c_1\omega_1\left(t_1, t_2\right) + c_2\omega_2\left(t_1, t_2\right)\right]$

$$= s^2 \int_0^\infty\int_0^\infty e^{-st_1}e^{-vt_2}\left[c_1\omega_1\left(t_1, t_2\right) + c_2\omega_2\left(t_1, t_2\right)\right]dt_1 dt_2$$

$$= s^2\int_0^\infty\int_0^\infty e^{-st_1}e^{-vt_2}c_1\omega_1\left(t_1, t_2\right)dt_1 dt_2 + s^2\int_0^\infty\int_0^\infty e^{-st_1}e^{-vt_2}c_2\omega_2(t_1, t_2)dt_1 dt_2$$

$$= c_1\left[s^2\int_0^\infty\int_0^\infty e^{-st_1}e^{-vt_2}\omega_1(t_1, t_2)\right]dt_1 dt_2 + c_2\left[s^2\int_0^\infty\int_0^\infty e^{-st_1}e^{-vt_2}\omega_2(t_1, t_2)\right]dt_1 dt_2$$

$$= c_1 LM\left[\omega_1(t_1, t_2)\right] + c_2 LM\left[\omega_2(t_1, t_2)\right]$$

Change of Scale Property:

If a>0, b>0 and $LM[\omega(t_1, t_2)] = \overline{\omega}(s, v)$, then

$$LM\left[\omega\left(at_1, bt_2\right)\right] = \frac{1}{ab}LM\left[\omega\left(\frac{x}{a}, \frac{y}{b}\right)\right]$$

Proof:

$$LM\left[\omega\left(at_1, bt_2\right)\right] = s^2\int_0^\infty e^{-st_1}e^{-vt_2}\omega(at_1, bt_2)dt_1 dt_2$$

Substituting,

$$at_1 = x, \quad bt_2 = y$$

$$t_1 = \frac{x}{a}, \quad t_2 = \frac{y}{b}$$

$adt_1 = dx, \; bdt_2 = dy$

$$= s^2 \int_0^\infty \int_0^\infty e^{-s\left(\frac{x}{a}\right)} e^{-v\left(\frac{y}{b}\right)} \omega(t_1, t_2) \frac{dx}{a} \frac{dy}{b}$$

$$= \frac{s^2}{ab}\left[\int_0^\infty \int_0^\infty e^{-s\left(\frac{x}{a}\right)} e^{-v\left(\frac{y}{b}\right)} \omega(x,y)\, dx\, dy\right]$$

$$= \frac{1}{ab}\left[s^2 \int_0^\infty \int_0^\infty e^{-s\left(\frac{x}{a}\right)} e^{-v\left(\frac{y}{b}\right)} \omega(x,y)\, dx\, dy\right]$$

$$= \frac{1}{ab} LM\left[\omega\left(\frac{x}{a}, \frac{y}{b}\right)\right]$$

Laplace Mohand Transform of basic elementary function:

1) Let, $\omega(t_1, t_2) = 1$

$$LM[1] = s^2 \int_0^\infty \int_0^\infty e^{-st_1} e^{-vt_2}\, dt_1\, dt_2$$

$$= s^2 \left[\int_0^\infty e^{-st_1}\, dt_1\right]\left[\int_0^\infty e^{-vt_2}\, dt_2\right]$$

$$= s^2 \left[\frac{e^{-st_1}}{-s}\right]_0^\infty \left[\frac{e^{-vt_2}}{-v}\right]_0^\infty$$

$$= s^2 \left(\frac{1}{s}\right)\left(\frac{1}{v}\right)$$

$$= \frac{s}{v}$$

2) $\omega(t_1, t_2) = e^{(at_1 + bt_2)}$

$$LM\left[e^{(at_1 + bt_2)}\right] = s^2 \int_0^\infty \int_0^\infty e^{-st_1} e^{-vt_2} e^{(at_1 + bt_2)}\, dt_1\, dt_2$$

$$= s^2 \left[\int_0^\infty e^{-(s-a)t_1}\, dt_1\right]\left[\int_0^\infty e^{-(v-b)t_2}\, dt_2\right]$$

$$= s^2 \left[\frac{e^{-(s-a)t_1}}{-(s-a)}\right]_0^\infty \left[\frac{e^{-(v-b)t_2}}{-(v-b)}\right]_0^\infty$$

$$= s^2 \left(\frac{1}{s-a}\right)\left(\frac{1}{v-b}\right)$$

$$= \frac{s^2}{(s-a)(v-b)}$$

3) $\omega(t_1, t_2) = \sin \sin (at_1 + bt_2)$

$$\left[\sin \sin (at_1 + bt_2)\right] = \frac{e^{i(at_1 + bt_2)} - e^{-i(at_1 + bt_2)}}{2i}$$

$$LM\{\left[\sin \sin (at_1 + bt_2)\right]\} = LM\left\{\frac{e^{i(at_1 + bt_2)} - e^{-i(at_1 + bt_2)}}{2i}\right\}$$

$$= \frac{1}{2i}\left[\frac{s^2}{(s-ia)(v-ib)} - \frac{s^2}{(s+ia)(v+ib)}\right]$$

$$= \frac{s^2}{2i}\left[\frac{(s+ia)(v+ib)-(s-ia)(v-ib)}{\left(s^2+a^2\right)\left(v^2+b^2\right)}\right]$$

$$= \frac{s^2(sb+av)}{\left(s^2+a^2\right)\left(v^2+b^2\right)}$$

4) $\omega\left(t_1,t_2\right) = \cos\cos\left(at_1 + bt_2\right)$

$$\cos\cos\left(at_1 + bt_2\right) = \left[\frac{e^{i\left(at_1+bt_2\right)}e^{-i\left(at_1+bt_2\right)}}{2}\right]$$

$$LM\left\{\left[\cos\cos\left(at_1 + bt_2\right)\right]\right\} = LM\left[\frac{e^{i\left(at_1+bt_2\right)}e^{-i\left(at_1+bt_2\right)}}{2}\right]$$

$$= \frac{1}{2}\left[\frac{s^2}{(s-ia)(v-ib)} + \frac{s^2}{(s+ia)(v+ib)}\right]$$

$$= \frac{s^2}{2}\left[\frac{(s+ia)(v+ib)+(s-ia)(v-ib)}{\left(s^2+a^2\right)\left(v^2+b^2\right)}\right]$$

$$= \frac{s^2(sv-ab)}{\left(s^2+a^2\right)\left(v^2+b^2\right)}$$

5) $\omega\left(t_1,t_2\right) = \sinh\sinh\left(at_1 + bt_2\right)$

$$\sinh\sinh\left(at_1 + bt_2\right) = \left[\frac{e^{\left(at_1+bt_2\right)}-e^{-\left(at_1+bt_2\right)}}{2}\right]$$

$$LM\left\{\left[\sinh\sinh\left(at_1 + bt_2\right)\right]\right\} = LM\left[\frac{e^{\left(at_1+bt_2\right)}-e^{-\left(at_1+bt_2\right)}}{2}\right]$$

$$= \frac{1}{2}\left[\frac{s^2}{(s-a)(v-b)} - \frac{s^2}{(s+a)(v+b)}\right]$$

$$= \frac{s^2}{2}\left[\frac{(s+a)(v+b)-(s-a)(v-b)}{\left(s^2+a^2\right)\left(v^2+b^2\right)}\right]$$

$$= \frac{s^2(sb+av)}{\left(s^2+a^2\right)\left(v^2+b^2\right)}$$

$$\omega\left(t_1,t_2\right) = \cosh\cosh\left(at_1 + bt_2\right)$$

$$= \left[\frac{e^{\left(at_1+bt_2\right)}+e^{-\left(at_1+bt_2\right)}}{2}\right]$$

$$LM\{[\cos\cos(at_1 + bt_2]\} = LM\left[\frac{e^{(at_1+bt_2)}e^{-(at_1+bt_2)}}{2}\right]$$

$$= \frac{1}{2}\left[\frac{s^2}{(s-a)(v-b)} + \frac{s^2}{(s+a)(v+b)}\right]$$

$$= \frac{s^2}{2}\left[\frac{(s+a)(v+b)+(s-a)(v-b)}{(s^2+a^2)(v^2+b^2)}\right]$$

$$= \frac{s^2(ab+sv)}{(s^2+a^2)(v^2+b^2)}$$

6) $\omega(t_1, t_2) = t_1 t_2$

$$LM[t_1 t_2] = s^2 \int_0^\infty \int_0^\infty e^{-st_1}e^{-vt_2}(t_1 t_2)\, dt_1 dt_2$$

$$= s^2\left[\int_0^\infty e^{-st_1}(t_1)dt_1\right]\left[\int_0^\infty e^{-vt_2}(t_2)dt_2\right]$$

Integration by parts,

$$= s^2\left[\left(\left(t_1\left(\frac{e^{-st_1}}{-s}\right)\right)_{t_1=0}^\infty\right) - \int_0^\infty \frac{e^{-st_1}}{-s}dt_1\right]\left[\left(\left(t_2\left(\frac{e^{-st_2}}{-s}\right)\right)_{t_2=0}^\infty\right) - \int_0^\infty \frac{e^{-st_2}}{-s}dt_2\right]$$

$$= \frac{1}{v^2}$$

Transform of Derivative:

If $LM[\omega(t_1, t_2)] = \overline{\omega}(s, v)$, **then**

1) $LM\left[\frac{\partial\omega}{\partial t_1}\right] = -L[\omega(0, t_2)] + vLM[\omega(t_1, t_2)]$

2) $LM\left[\frac{\partial\omega}{\partial t_2}\right] = -L[\omega(t_1, 0)] + sLM[\omega(t_1, t_2)]$

3) $LM\left[\frac{\partial^2\omega}{\partial t_1^2}\right] = -M\left[\frac{\partial\omega}{\partial t_1}(0, t_2)\right] + vM[\omega(0, t_2)] + v^2 LM[\omega(t_1, t_2)]$

4) $LM\left[\frac{\partial^2\omega}{\partial t_2^2}\right] = -m\left[\frac{\partial\omega}{\partial t_2}(t_1, 0)\right] + S.M[\omega(t_1, 0)] + s^2 LM[\omega(t_1, t_2)]$

Proof:

$$1) LM\left[\frac{\partial\omega}{\partial t_1}\right] = s^2 \int_0^\infty \int_0^\infty e^{-vt_1}e^{-st_2}\frac{\partial\omega}{\partial t_1}(t_1, t_2)\, dt_1 dt_2$$

$$= s^2 \int_0^\infty \int_0^\infty e^{-vt_1}e^{-st_2}\frac{\partial\omega}{\partial t_1}\, dt_1 dt_2$$

$$= s^2 \int_0^\infty e^{-st_2}\left[\int_0^\infty e^{-vt_1}\frac{\partial\omega}{\partial t_1}dt_1\right]dt_2$$

Integration by parts,

$$= s^2 \int_0^\infty e^{-st_2} \left[\left(e^{-vt_1} \omega(t_1, t_2) \right)_{t_1=0}^\infty - \int_0^\infty (-v) e^{vt_1} \omega(t_1, t_2) dt_1 \right] dt_2$$

$$= s^2 \int_0^\infty e^{-st_2} \left[-\omega(0, t_2) + v \int_0^\infty e^{-vt_1} \omega(t_1, t_2) dt_1 \right] dt_2$$

$$= -s^2 \int_0^\infty e^{-st_2} \omega(0, t_2) dt_2 + v s^2 \int_0^\infty \int_0^\infty e^{-st_2} e^{-vt_1} \omega(t_1, t_2) dt_1 dt_2$$

$$= -L\left[\omega(0, t_2) \right] + vLM\left[\omega(t_1, t_2) \right]$$

2) $\quad LM\left[\dfrac{\partial \omega}{\partial t_2} \right] \qquad = s^2 \int_0^\infty \int_0^\infty e^{-vt_1} e^{-st_2} \partial \omega(t_1, t_2)\, dt_1 dt_2$

$$= s^2 \int_0^\infty \int_0^\infty e^{-vt_1} e^{-st_2} \frac{\partial \omega}{\partial t_2}\, dt_2 dt_1$$

$$= s^2 \int_0^\infty e^{-vt_1} \left[\int_0^\infty e^{-st_2} \frac{\partial \omega}{\partial t_2} dt_2 \right] dt_1$$

Integration by parts,

$$= s^2 \int_0^\infty e^{-vt_1} \left[\left(e^{-st_2} \omega(t_1, t_2) \right)_{t_2=0}^\infty - \int_0^\infty (-s) e^{-st_2} \omega(t_1, t_2) dt_2 \right] dt_1$$

$$= s^2 \int_0^\infty e^{-vt_1} \left[-\omega(t_1, 0) + s \int_0^\infty e^{-st_2} \omega(t_1, t_2) dt_2 \right] dt_1$$

$$= -s^2 \int_0^\infty e^{-vt_1} \omega(t_1, 0) dt_2 + s.s^2 \int_0^\infty \int_0^\infty e^{-st_2} e^{-vt_1} \omega(t_1, t_2) dt_1 dt_2$$

$$= -L\left[\omega(t_1, 0) \right] + sLM\left[\omega(t_1, t_2) \right]$$

3) $LM\left[\dfrac{\partial^2 \omega}{\partial t_1^2} \right] = s^2 \int_0^\infty \int_0^\infty e^{-vt_1} e^{-st_2} \dfrac{\partial^2 \omega}{\partial t_1^2}\, dt_1 dt_2$

$$= s^2 \int_0^\infty \int_0^\infty e^{-vt_1} e^{-st_2} \frac{\partial^2 \omega}{\partial t_1^2}\, dt_1 dt_2$$

$$= s^2 \int_0^\infty e^{-st_2} \left[\int_0^\infty e^{-vt_1} \frac{\partial^2 \omega}{\partial t_1^2} dt_1 \right] dt_2$$

integration by parts,

$$= s^2 \int_0^\infty e^{-st_2} \left[\left(e^{-vt_1} \frac{\partial \omega}{\partial t_1} \right)_{t_1=0}^\infty + v \int_0^\infty \left(e^{-vt_1} \frac{\partial \omega}{\partial t_1} \right) dt_1 \right] dt_2$$

$$= s^2 \int_0^\infty e^{-st_2} \left[\left[0 - \frac{\partial \omega}{\partial t_1}(0,t_2) \right] + v \left[e^{-vt_1} \omega(t_1,t_2) \right]_0^\infty + v \int_0^\infty e^{-vt_1} \omega(t_1,t_2) dt_1 \right] dt_2$$

$$= s^2 \int_0^\infty e^{-st_2} \left[\frac{\partial \omega}{\partial t_1} \right](0,t_2) dt_2 + v \left[s^2 \int_0^\infty \int_0^\infty e^{-st_2} \omega(0,t_2) dt_2 \right] + v^2 \left[s^2 \int_0^\infty \int_0^\infty e^{-st_2} e^{-vt_1} \omega(t_1,t_2) dt_1 dt_2 \right]$$

$$= - M \left[\frac{\partial \omega}{\partial t_1}(0,t_2) \right] + vM \left[\omega(0,t_2) \right] + v^2 LM \left[\omega(t_1,t_2) \right]$$

$$4) LM \left[\frac{\partial^2 \omega}{\partial t_2^2} \right] = s^2 \int_0^\infty \int_0^\infty e^{-vt_1} e^{-st_2} \frac{\partial^2 \omega}{\partial t_2^2}(t_1,t_2) \, dt_2 dt_1$$

$$= s^2 \int_0^\infty e^{-vt_1} \left[\int_0^\infty e^{-st_2} \frac{\partial^2 \omega}{\partial t_2^2} dt_2 \right] dt_1$$

$$= - s^2 \int_0^\infty e^{-vt_1} \left[\left(e^{-st_2} \frac{\partial \omega}{\partial t_2} \right)_{t_2=0}^\infty + s \int_0^\infty \left(e^{-st_2} \frac{\partial \omega}{\partial t_2} \right) dt_2 \right] dt_1$$

$$= s^2 \int_0^\infty e^{-vt_1} \left[\left[0 - \frac{\partial \omega}{\partial t_2}(t_1,0) \right] + s \left[- e^{-st_2} \omega(t_1,t_2) \right]_0^\infty + s \int_0^\infty e^{-st_2} \omega(t_1,t_2) dt_2 \right] dt_1$$

$$= s^2 \int_0^\infty e^{-vt_1} \left[\frac{-\partial \omega}{\partial t_2}(t_1,0) + s \left[- \omega(t_1,0) + s \int_0^\infty e^{-st_2} \omega(t_1,t_2) dt_2 \right] \right] dt_1$$

$$= - s^2 \int_0^\infty e^{vt_1} \left[\frac{\partial \omega}{\partial t_2} \right](t_2,0) dt_1 + s \cdot s^2 \int_0^\infty e^{-vt_1} \omega(t_1,0) + s^2 \cdot s^2 \int_0^\infty e^{-st_2} \omega(t_1,t_2) dt_2 dt_1$$

$$= - m \left[\frac{\partial \omega}{\partial t_2}(t_1,0) \right] + S \cdot M \left[\omega(t_1,0) \right] + s^2 LM \left[\omega(t_1,t_2) \right]$$

II. CONCLUSION:

Two different single transforms were combined to present a new double transform Laplace-Mohand transform. Change of scale Property, transform of basic elementary function, and derivative were proved. In future work, we solved Partial differential equations using this transform.

III.References:

[1].   Tarig M. Elzaki, The New Integral Transform "Elzaki Transform" Global Journal of Pure and Applied Mathematics, ISSN 0973-1768, Number 1(2011), pp. 57-64.

[2].   Mohand M. Abdelrahim Mahgob "Solution of Partial Integro – Differential Equations by Double Elzaki Transform Method", Mathematical theory and Modeling, ISSN2224-5804(Paper), ISSN 2225-0522(online), Vol.5, 2015, pp-61-66.

[3].   Tarig M. Elzaki, Salih M. Elzaki, and Eman M.A. Hilal, Elzaki, and Sumudu " Transforms for solving some Differential Equations", Global journal of Pure and Applied Mathematics, ISSN 0973-1768,Volume 8, Number 2, (2012), pp.167173.

[4].   Dualities between Mohand Transform and Some Useful Integral TransformsSudhanshu Aggarwal, Anjana Rani GuptaInternational Journal of Recent Technology and Engineering (IJRTE)ISSN: 2277-3878, Volume-8 Issue-3, September 2019

[5].   Applications of Mohand Transform Nihal ÖZDOĞAN 1* 1 Bursa Technical University, Faculty of Science and Engineering, Department of Mathematics, Bursa, Turkey Inno Sci Eng,2024, 8(1):18-24

[6].   A Study of Laplace Transform and Applications to Differential EquationsVolume-04 ISSN: 2455-3085 (Online)Issue-03 RESEARCH REVIEW International Journal of Multidisciplinary March -2019

[7].   A Comparative Study of Mohand and Laplace TransformsSudhanshu Aggarwal1*, Renu Chaudhary2© 2019 JETIR February 2019, Volume 6, Issue 2

[8].   1 Laplace, P.S., 1820. ThÂt'eorie Analytique desProbabilitiÂt'es, Lerch, Paris, 1(2).

[9].   Mohand M.A. Mahgoub, 2017. The new integraltransform "Mohand Transform" Advances inTheoretical and Applied Mathematics, 12(2): 113-120

[10].   The New Integral Transform ''Aboodh Transform''Khalid Suliman Aboodh Department of Mathematics, Bisha Faculty of Science & Arts King Khalid University, Bisha P.o.Box.344, KSAISSN 0973-1768 Volume 9, Number 1 (2013), pp. 35-43

A New Integral Transform and its Applications

R. D. Mhase, A. R. Fulari, S. A. Tarate, H. N. Shaikh

Department of Mathematics, New Arts, Science and Commerce College, Ahmednagar, Maharashtra, India

Abstract :

In this study, we introduce a novel integral transform, referred to as "A New Integral Transform". This transform has been developed and applied to solve various initial value problems, particularly ordinary differential equations (ODEs). The proposed method demonstrates its effectiveness in addressing issues commonly encountered in engineering and physics. Through this integral transformation, we provide new insights and solu- tions that enhance the understanding and application of ODEs in practi- cal scenarios, thereby contributing to the broader body of knowledge in these disciplines.

keywords: A New transform, Linear Ordinary Differential Equation, Initial Value Problem.

I. INTRODUCTION

Due to their capacity to streamline the study and resolution of intricate math- ematical issues, integral transformations have long been acknowledged as some of the most useful instruments in both practical and pure mathematics. These methods allow for the more tractable manipulation of functions or equations by translating them into various domains, which frequently results in solutions that would be challenging to find otherwise. The Laplace, Fourier, and Mellin transforms are examples of common integral transforms that are widely used in fields ranging from signal processing and physics to differential equations studies.As stated by [2, 4, 8]

In this work, we provide a new integral transform, called the New Inte- gral Transform, that is a modification of current methods intended to improve the process of solving specific classes of starting value problems and ordinary differential equations (ODEs). While maintaining many of the advantageous features of conventional integral transforms, this updated transform provides more flexibility and efficiency in particular mathematical situations. In addi- tion to making the process of solving ODEs simpler, the additional Integral Transform can reveal additional details about the composition of these equa- tions.

This updated transform's usefulness is illustrated by its basic characteris- tics and use in solving classical issues. We seek to demonstrate the usefulness of the New Integral Transform[9] in solving ordinary differential equations, par- ticularly those that prove difficult for more traditional techniques. To further demonstrate the usefulness of this transform, we specifically offer the solution to an initial value problem. These illustrations show how useful the new inte- gral transform can be as a tool for engineering and mathematics study.

As previously solved by others transform likely Laplace, Gupta[6], Sadik[7], ELzaki[3], Aboodh[5] and Kamal[1] Transforms. The New Integral Transform is defined as a function of exponential order. We consider functions in the set $\mathcal{Z}$ defined by:

$$\mathcal{Z} = \left\{ \mu(t)/\exists A, k_1, k_2 > 0, |\mu(t)| < Ae^{\frac{|t|}{k_i}}, if\ t \in (-1)^i \times [0, \infty) \right\} \quad (1.1)$$

For a given function in the set $\mathcal{Z}$, the constant A must be finite number, k_1, k_2 may be finite or infinite.

The New Integral Transform denoted by the operator $\mathcal{T}(.)$, defined by the integral equation:

$$\mathcal{T}[\mu(t)] = \mathcal{P}(v) = \int_0^\infty exp\left(\frac{-t}{v^2}\right) \mu(t)dt, \quad t \geq 0, k_1 \leq v \leq k_2 \quad (1.2)$$

where v is the New Integral Transform variable and t is the variable of the function f. This transformation is closely related to the Laplace, Kamal, Aboodh transforms etc. This study aims to prove the applicability of this interesting modified transform and its efficiency in solving differential equations.

Theorem 1.1 *The Sufficient condition for the existence of New Integral Transform*
If the function $\mu(t)$ is piecewise continuous in every finite interval $0 \leq t \leq \beta$ and of exponential order α for $t > \beta$. Then its New Integral Transform $\mathcal{P}(v)$ exists.

Proof 1 *We have for any positive number β, we algebraically deduce*

$$\int_0^\infty e^{\left(\frac{-t}{v^2}\right)} \mu(t)dt = \int_0^\beta e^{\left(\frac{-t}{v^2}\right)} \mu(t)dt + \int_\beta^\infty e^{\left(\frac{-t}{v^2}\right)} \mu(t)dt \quad (1.3)$$

Since $\mu(t)$, it is piecewise continuous in every finite interval $0 \leq t \leq \beta$, the first integral on the right side exists. Also, the second integral on the right exists. Since $\mu(t)$ is of exponential order α for $t > \beta$. To verify this claim, we

consider the following case

$$\left|\int_{\beta}^{\infty} e^{\left(\frac{-t}{v^2}\right)}\mu(t)dt\right| \leq \int_{\beta}^{\infty} \left|e^{\left(\frac{-t}{v^2}\right)}\mu(t)\right| dt$$

$$\leq \int_{\beta}^{\infty} e^{\left(\frac{-t}{v^2}\right)} |\mu(t)| \, dt$$

$$\leq \int_{\beta}^{\infty} e^{\left(\frac{-t}{v^2}\right)} Ae^{\alpha t} dt$$

$$= A\int_{\beta}^{\infty} e^{-\left(\frac{1}{v^2}-\alpha\right)t} dt$$

$$= A\left[\frac{e^{-\left(\frac{1}{v^2}-\alpha\right)t}}{-\left(\frac{1}{v^2}-\alpha\right)}\right]_{\beta}^{\infty}$$

$$= \frac{Av^2}{(1-\alpha v^2)}e^{-\left(\frac{1}{v^2}-\alpha\right)\beta}$$

Theorem 1.2 *Linear Property*
Suppose $\mathcal{P}_1(v)$ *and* $\mathcal{P}_2(v)$ *are* $\mathcal{T}$ *Transform of* $f(t)$ *and* $g(t)$ *respectively then*

$$\mathcal{T}\{\alpha_1\mu_1(t)+\alpha_2\mu_2(t)\} = \alpha_1\mathcal{T}[\mu_1(t)] + \alpha_2\mathcal{T}[\mu_2(t)]$$

where α_1, α_2 *are any constants.*

Proof 2 *Let*

$$\mathcal{T}[\mu_1(t)] = \mathcal{P}_1(v) = \int_{0}^{\infty} e^{\left(\frac{-t}{v^2}\right)}\mu_1(t)dt$$

and

$$\mathcal{T}[\mu_2(t)] = \mathcal{P}_2(v) = \int_{0}^{\infty} e^{\left(\frac{-t}{v^2}\right)}\mu_2 dt$$

Also α_1, α_2 *be arbitrary constants. We want to show that,*

$$\mathcal{T}\{\alpha_1\mu_1(t)+\alpha_2\mu_2(t)\} = \alpha_1\mathcal{T}[\mu_1(t)] + \alpha_2\mathcal{T}[\mu_2(t)]$$

Consider

$$\mathcal{T}\{\alpha_1\mu_1(t) + \alpha_2\mu_2(t)\} = \int\limits_0^\infty e^{\left(\frac{-t}{v^2}\right)}[\alpha_1\mu_1(t) + \alpha_2\mu_2(t)]\, dt$$

$$= \alpha_1 \int\limits_0^\infty e^{\left(\frac{-t}{v^2}\right)}\mu_1(t)dt + \alpha_2 \int\limits_0^\infty e^{\left(\frac{-t}{v^2}\right)}\mu_2(t)dt$$

$$= \alpha_1\mathcal{T}[\mu_1(t)] + \alpha_2\mathcal{T}[\mu_2(t)]$$

Remark 1.3 *Suppose we have $\mathcal{P}_i(v)$ are $\mathcal{T}$ transforms of $\mu_i(t)$ respectively where $i = 1, 2, \ldots, n$ (n is finite) Then we obtain the result*

$$\mathcal{T}\left\{\sum_{k=1}^n \alpha_i\mu_i(t)\right\} = \sum_{k=1}^n \alpha_i\mathcal{T}[\mu_i(t)]$$

2 Elementary properties of New Integral Transform:

In this section, we find the New Integral Transform of simple functions.

i) Let $\mu(t) = 1$, by the definition, we have:

$$\mathcal{T}[1] = \mathcal{P}(v) = \int\limits_0^\infty exp\left(\frac{-t}{v^2}\right) dt = \left[\frac{e^{\left(\frac{-t}{v^2}\right)}}{\frac{-1}{v^2}}\right]_0^\infty = v^2$$

ii) Let $\mu(t) = t$, then:

$$\mathcal{T}[t] = \mathcal{P}(v) = \int\limits_0^\infty t\ exp\left(\frac{-t}{v^2}\right) dt$$

Integrating by parts, we get $\mathcal{T}[t] = v^4$

iii) Let $\mu(t) = t^n$, then:

$$\mathcal{T}[t^n] = \mathcal{P}(v) = \int\limits_0^\infty t^n\ exp\left(\frac{-t}{v^2}\right) dt$$

Integrating by parts, we get $\mathcal{T}[t^n] = n!v^{2n+2}$

iv) Let $\mu(t) = e^{at}$, then:

$$\mathcal{T}[e^{at}] = \mathcal{P}(v) = \int_0^\infty e^{at} \, exp\left(\frac{-t}{v^2}\right) dt$$

we get $\mathcal{T}[e^{at}] = \frac{v^2}{1 - av^2}$

So we can find the following transforms:-

a) Let $\mu(t) = \sin at$, then:

$$\mathcal{T}[\sin at] = \mathcal{P}(v) = \int_0^\infty \sin at \, exp\left(\frac{-t}{v^2}\right) dt$$

$$= \int_0^\infty \left\{ \frac{e^{iat} - e^{-iat}}{2i} \right\} \, exp\left(\frac{-t}{v^2}\right) dt$$

$$= \frac{1}{2i} \int_0^\infty \left[e^{\left(ia - \frac{1}{v^2}\right)t} - e^{-\left(ia + \frac{1}{v^2}\right)t} \right] dt$$

$$= \frac{1}{2i} \left[\frac{v^2}{1 - iav^2} - \frac{v^2}{1 + iav^2} \right]$$

$$= \frac{av^4}{1 + a^2v^4}$$

we get, $\mathcal{T}[\sin at] = \frac{av^4}{1 + a^2v^4}$

b) Let $\mu(t) = \cos at$, then:

$$\mathcal{T}[\cos at] = \mathcal{P}(v) = \int_0^\infty \cos at \, exp\left(\frac{-t}{v^2}\right) dt$$

$$= \int_0^\infty \left\{ \frac{e^{iat} + e^{-iat}}{2} \right\} \, exp\left(\frac{-t}{v^2}\right) dt$$

$$= \frac{1}{2} \int_0^\infty \left[e^{\left(ia - \frac{1}{v^2}\right)t} + e^{-\left(ia + \frac{1}{v^2}\right)t} \right] dt$$

$$= \frac{1}{2} \left[\frac{v^2}{1 - iav^2} + \frac{v^2}{1 + iav^2} \right]$$

$$= \frac{v^4}{1 + a^2v^4}$$

we get, $\mathcal{T}[\cos at] = \frac{v^4}{1+a^2v^4}$

c) Let $\mu(t) = \sinh at$, then:

$$\mathcal{T}[\sinh at] = \mathcal{P}(v) = \int\limits_0^\infty \sinh at \ exp\left(\frac{-t}{v^2}\right) dt$$

$$= \int\limits_0^\infty \left\{\frac{e^{at} - e^{-at}}{2}\right\} \ exp\left(\frac{-t}{v^2}\right) dt$$

$$= \frac{1}{2} \int\limits_0^\infty \left[e^{\left(a-\frac{1}{v^2}\right)t} - e^{-\left(a+\frac{1}{v^2}\right)t}\right] dt$$

$$= \frac{1}{2} \left[\frac{v^2}{1 - av^2} - \frac{v^2}{1 + av^2}\right]$$

$$= \frac{av^4}{1 - a^2v^4}$$

we get, $\mathcal{T}[\sinh at] = \frac{av^4}{1-a^2v^4}$

d) Let $\mu(t) = \cosh at$, then:

$$\mathcal{T}[\cosh at] = \mathcal{P}(v) = \int\limits_0^\infty \cosh at \ exp\left(\frac{-t}{v^2}\right) dt$$

$$= \int\limits_0^\infty \left\{\frac{e^{at} + e^{-at}}{2}\right\} \ exp\left(\frac{-t}{v^2}\right) dt$$

$$= \frac{1}{2} \int\limits_0^\infty \left[e^{\left(a-\frac{1}{v^2}\right)t} + e^{-\left(a+\frac{1}{v^2}\right)t}\right] dt$$

$$= \frac{1}{2} \left[\frac{v^2}{1 - av^2} + \frac{v^2}{1 + av^2}\right]$$

$$= \frac{v^2}{1 - a^2v^4}$$

we get, $\mathcal{T}[\cosh at] = \frac{v^2}{1-a^2v^4}$

3   Theorems:

Theorem 3.1 *Let $\mathcal{P}(v)$ us the New Integral transform of $\mu(t)$ $(i.e \mathcal{T}[\mu(t)] = \mathcal{P}(v))$ then :*

I. $\mathcal{T}[\mu'(t)] = \frac{1}{v^2}\mathcal{P}(v) - \mu(0)$

II. $\mathcal{T}[\mu''(t)] = \frac{1}{v^4}\mathcal{P}(v) - \frac{1}{v^2}\mu(0) - \mu'(0)$

III. $\mathcal{T}[\mu^n(t)] = \frac{1}{v^{2n}}\mathcal{P}(v) - \sum_{k=0}^{n-1} \frac{1}{v^{2n-2k-2}}\mu^k(0)$

Proof 3   *I. By the definition we have,*

$$\mathcal{T}[\mu'(t)] = \int_0^\infty \mu'(t) \ exp\left(\frac{-t}{v^2}\right) dt$$

by simplification, we get $\mathcal{T}[\mu'(t)] = \frac{1}{v^2}\mathcal{P}(v) - \mu(0)$

II. By the definition we have,

$$\mathcal{T}[\mu''(t)] = \int_0^\infty \mu''(t) \ exp\left(\frac{-t}{v^2}\right) dt$$

by simplification, we get $\mathcal{T}[\mu''(t)] = \frac{1}{v^4}\mathcal{P}(v) - \frac{1}{v^2}\mu(0) - \mu'(0)$

III. will be proved by mathematical induction.

4   New Integral transform's Application in Ordinary Differential Equations:

In this section, we solved the differential equation and initial value problems by using New Integral Transform.

Let we take the First order ordinary differential equation:

$$\frac{dx}{dt} + qx = f(t), \quad t > 0 \tag{4.1}$$

subject to initial condition $x(0) = \alpha$

Where q and α are constants and $f(t)$ is a function so that its New Integral Transform exists.

Applying the New Integral Transform of the equation (4.1) we have,

$$\mathcal{T}[\frac{dx}{dt} + qx] = \mathcal{T}[f(t)] \tag{4.2}$$

Using the differential property of New Integral transform equation (4.2)

$$\frac{1}{v^2}\mathcal{T}[x(t)] - x(0) + q\mathcal{T}[x(t)] = \mathcal{T}[f(t)]$$

$$\mathcal{T}[x(t)]\left(\frac{1}{v^2} + q\right) = \alpha + \mathcal{P}(v)$$

$$\mathcal{T}[x(t)] = \frac{\alpha + \mathcal{P}(v)}{\frac{1}{v^2} + q}$$

$$= \frac{(\alpha + \mathcal{P}(v))v^2}{1 + qv^2}$$

by applying inverse New Integral Transform, we get the solution of (4.1).

Now, we take the general form of second order linear ordinary differential equation:

$$\frac{d^2y}{dx^2} + 2\alpha\frac{dy}{dx} + \beta y(x) = f(x), \quad x > 0 \tag{4.3}$$

The initial conditions are

$$y(0) = a, \quad y'(0) = b \tag{4.4}$$

Where $\alpha, \ \beta, a$ and b are constants.

Using New Integral Transform on (4.3)

$$\left[\frac{1}{v^4}\mathcal{T}[y(x)] - \frac{1}{v^2}y(0) - y'(0)\right] + 2\alpha\left[\frac{1}{v^2}\mathcal{T}[y(x)] - y(0)\right] + \beta\left[\mathcal{T}[y(x)]\right] = \mathcal{T}[f(x)]$$

by applying initial condition (4.4) in above equation, we get

$$\mathcal{T}[y(x)] = \frac{v^4\mathcal{P}(v)}{\beta v^4 + 2\alpha v^2 + 1} + \frac{av^2}{\beta v^4 + 2\alpha v^2 + 1} + \frac{v^4(2\alpha a + b)}{\beta v^4 + 2\alpha v^2 + 1}$$

by applying inverse New Integral Transform we get the solution of (4.3)

Example 4.1 *Consider the differential equation :*

$$\frac{dy}{dx} + y = 0, \qquad y(0) = 1 \tag{4.5}$$

Applying A New Integral Transform on (4.5) *and using the differential property of the New Integral Transform we get,*

$$\mathcal{T}[\frac{dy}{dx} + y] = 0$$

$$\frac{1}{v^2}\mathcal{T}[y(x)] - y(0) + \mathcal{T}[y(x)] = 0$$

$$\left(\frac{1}{v^2} + 1\right)\mathcal{T}[y(x)] = y(0)$$

$$\mathcal{T}[y(x)] = \frac{v^2}{v^2 + 1}$$

by inverse New Integral Transform , we get,

$$y(x) = \mathcal{T}^{-1}\left[\frac{v^2}{v^2 + 1}\right] = e^{-x}$$
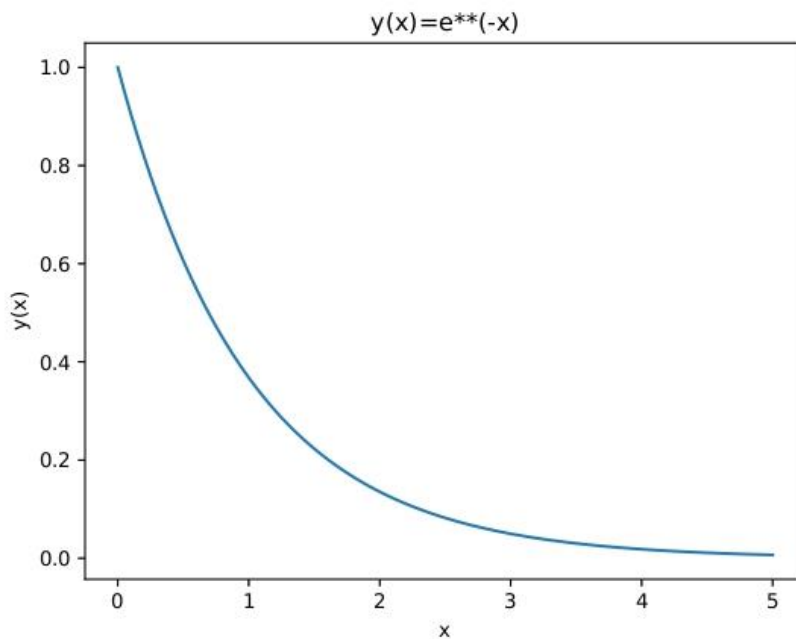
Figure 1: Graph of e^{-x}

10

Example 4.2 *consider the differential equation:*

$$\frac{dy}{dx} + 2y = x, \quad y(0) = 1 \tag{4.6}$$

Applying New Integral Transform on (4.6) *we get,*

$$\mathcal{T}\left[\frac{dy}{dx} + 2y\right] = \mathcal{T}[x]$$

$$\frac{1}{v^2}\mathcal{T}[y(x)] - y(0) + 2\mathcal{T}[y(x)] = v^4$$

$$\left(\frac{1}{v^2} + 2\right)\mathcal{T}[y(x)] = v^4 + y(0)$$

$$\left(\frac{1}{v^2} + 2\right)\mathcal{T}[y(x)] = v^4 + 1$$

$$\mathcal{T}[y(x)] = \frac{(v^4 + 1)v^2}{1 + 2v^2}$$

$$= \frac{1}{2}v^4 + \frac{5}{4}\left[\frac{v^2}{1 + 2v^2}\right] - \frac{1}{4}v^2$$

by inverse New Integral Transform , we get,

$$y(x) = \frac{1}{2}x + \frac{5}{4}e^{-2x} - \frac{1}{4}$$
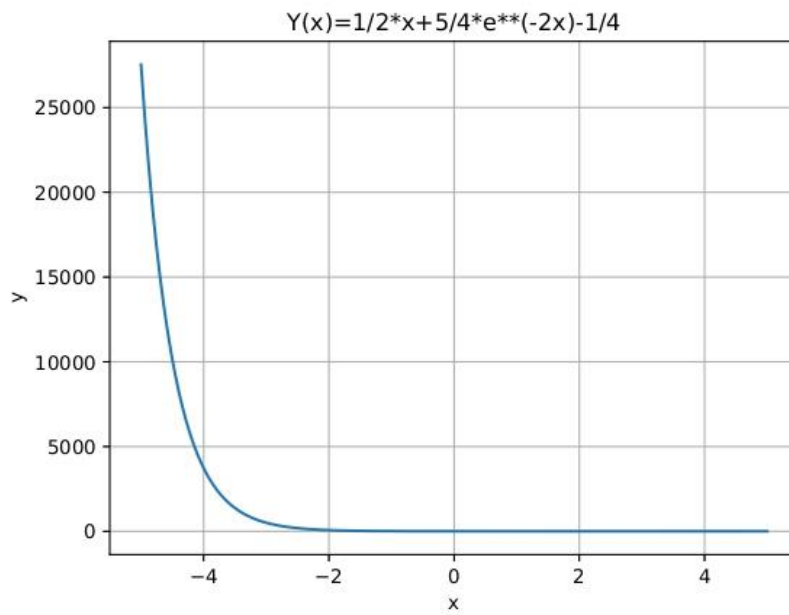
Figure 2: graph of the $\frac{1}{2}x + \frac{5}{4}e^{-2x} - \frac{1}{4}$

Example 4.3 *consider the differential equation:*

$$y'' + y = 0, \quad y(0) = y'(0) = 1 \tag{4.7}$$

Applying New Integral Transform on (4.7) *we get,*

$$\frac{1}{v^4}\mathcal{T}[y(t)] - \frac{1}{v^2}y(0) - y'(0) + \mathcal{T}[y(t)] = 0$$

$$\mathcal{T}[y(t)]\left[\frac{1}{v^4} + 1\right] = 1 + \frac{1}{v^2}$$

$$\mathcal{T}[y(t)] = \frac{(v^2 + 1)v^2}{1 + v^4} = \frac{v^4}{1 + v^4} + \frac{v^2}{1 + v^4}$$

by inverse New Integral Transform , we get,

$$y(t) = \sin(t) + \cos(t)$$
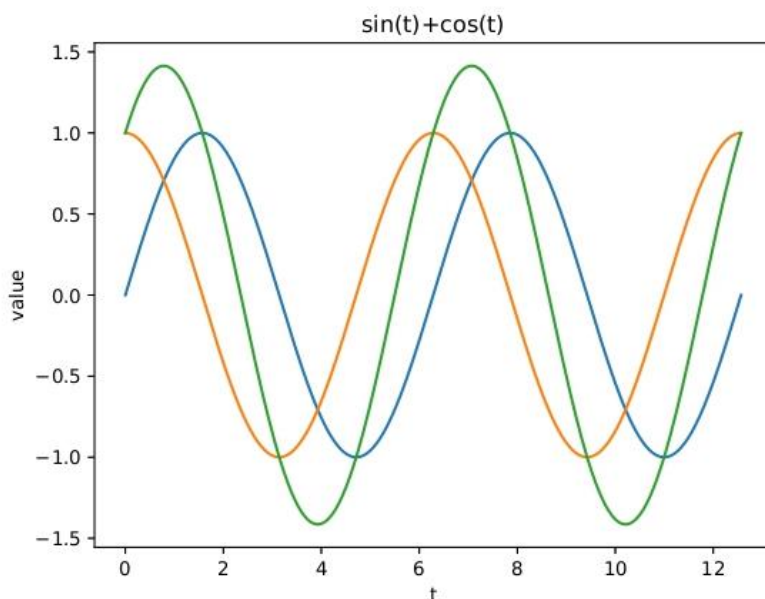
Figure 3: Graph of $\sin(t) + \cos(t)$

Example 4.4 *consider the differential equation:*

$$y'' - 3y' + 2y = 0, \quad y(0) = 1, y'(0) = 4 \tag{4.8}$$

Applying New Integral Transform on (4.8) *we get,*

$$\frac{1}{v^4}\mathcal{T}[y(t)] - \frac{1}{v^2}y(0) - y'(0) - 3\left[\frac{1}{v^2}\mathcal{T}[y(t)] - y(0)\right] + 2\mathcal{T}[y(t)] = 0$$

$$\mathcal{T}[y(t)]\left[\frac{1}{v^4} - \frac{3}{v^2} + 2\right] = 1 + \frac{1}{v^2}$$

$$\mathcal{T}[y(t)] = \frac{(v^2 + 1)v^2}{1 - 3v^2 + 2v^4} = \frac{-2v^2}{1 - v^2} + \frac{3v^2}{1 - 2v^2}$$

by inverse New Integral Transform , we get,

$$y(t) = -2e^t + 3e^{2t}$$
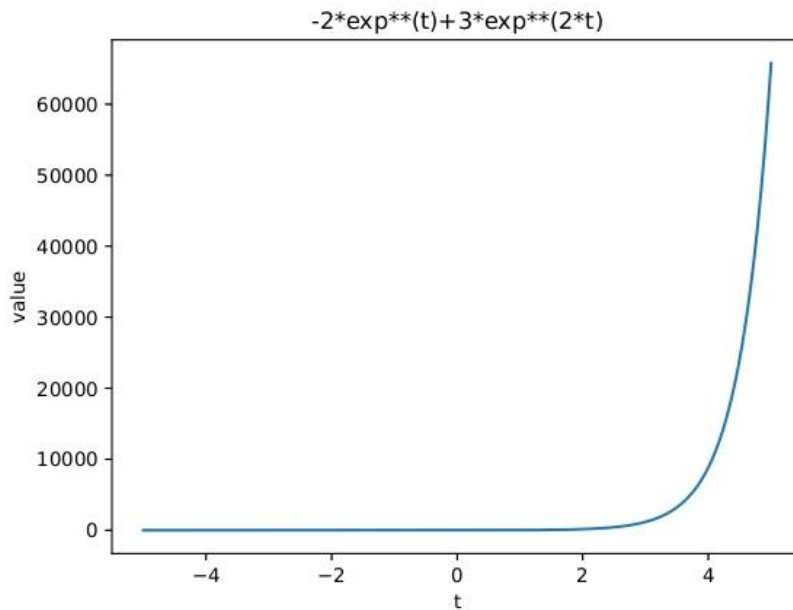
Figure 4: Graph of $-2e^t + 3e^{2t}$

Example 4.5 *consider the differential equation:*

$$y'' + 4y = 12t, \quad y(0) = 0, \ y'(0) = 7 \qquad (4.9)$$

Applying New Integral Transform on (4.9) *we get,*

$$\frac{1}{v^4}\mathcal{T}[y(t)] - \frac{1}{v^2}y(0) - y'(0) + 4\mathcal{T}[y(t)] = 12v^4$$

$$\mathcal{T}[y(t)]\left[\frac{1}{v^4} + 4\right] = 12v^4 + 7$$

$$\mathcal{T}[y(t)] = \frac{(12v^4 + 7)v^4}{1 + 4v^4} = 3v^4 + \frac{4v^4}{1 + 4v^4}$$

by inverse New Integral Transform , we get,

$$y(t) = 3t + 2\sin(2t)$$
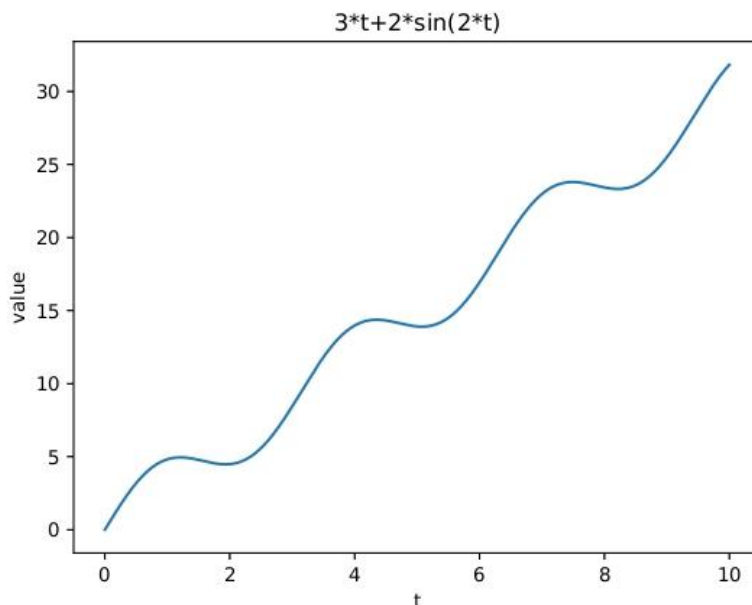
Figure 5: graph of $3t + 2\sin(2t)$

5 Application of New Integral Transform to Physics Problems

Example 5.1 *Uranium disintegrates at a rate proportional to the amount present at any instant. We will apply the New Integral Transform to find the amount of uranium at any instant t.*
Let $'N'$ be the amount of uranium at $t = 0$ and n be the amount of uranium at any instant t, then

$$n'(t) = -\lambda n \tag{5.1}$$

Applying New Integral Transform , we have

$$\frac{1}{v^2}\mathcal{T}[n(t)] - n(0) = -\lambda\mathcal{T}[n(t)]$$

At $t = 0, n(0) = N$, therefore, solving and rearranging the equation, we have

$$\mathcal{T}[n(t)] = \frac{Nv^2}{1 + \lambda v^2}$$

Taking inverse New Integral Transform we have

$$n(t) = Ne^{-\lambda t}$$
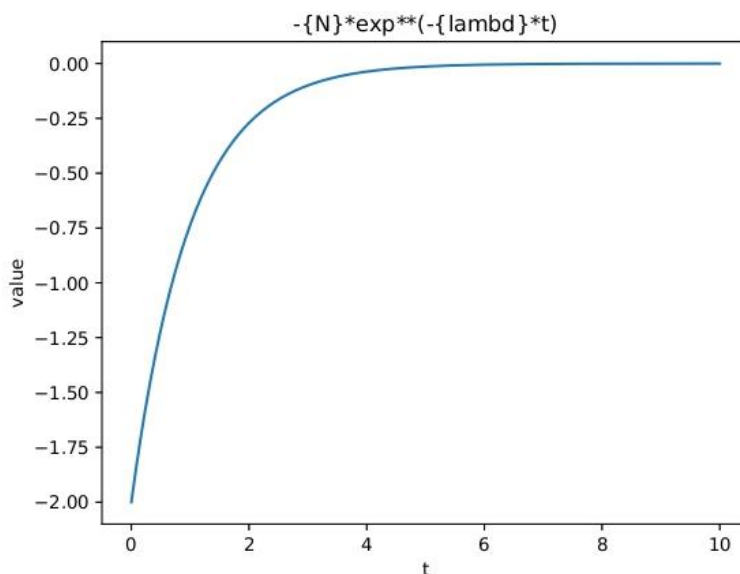
Figure 6: Graph of $Ne^{-\lambda t}$

Example 5.2 *Assume an object weighing 2 lb stretches a spring 6 in. Find the equation of motion if the spring is released from the equilibrium position with an upward velocity of 16 ft/sec. What is the period of the motion?*
We first need to find the spring constant. we have

$$mg = ks$$
$$2 = k\left(\frac{1}{2}\right)$$
$$k = 4$$

We also know that weight W equals the product of mass m and the acceleration due to gravity g. In the Standard Unit, the acceleration due to gravity is 32 ft/sec².

$$W = mg$$
$$2 = m(32)$$
$$m = \frac{1}{16}$$

Thus, the differential equation representing this system is

$$\frac{1}{16}x'' + 4x = 0 \qquad i.e. \quad x'' + 64x = 0 \qquad (5.2)$$
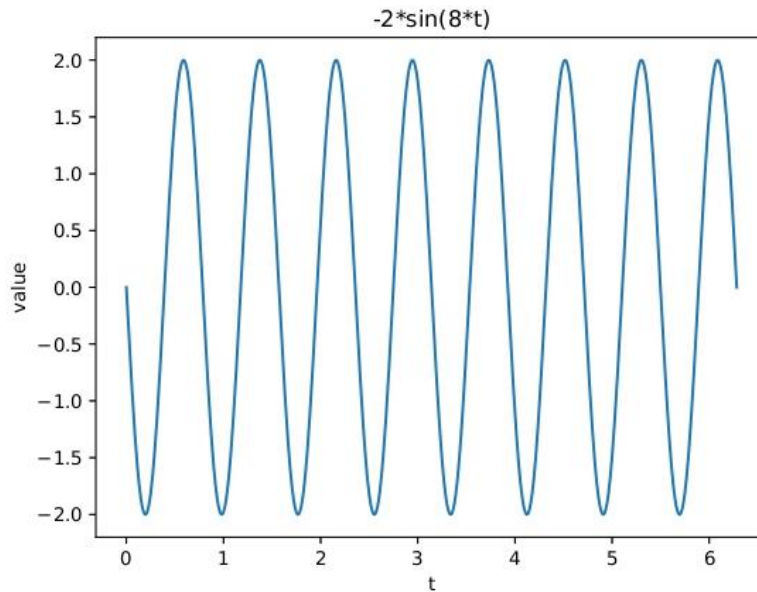
Figure 7: Graph of $-2\sin(8t)$

with initial condition $x(0) = 0, \quad x'(0) = 16$

Applying New Integral Transform to (5.2) and using initial conditions we get

$$\frac{1}{v^4}\mathcal{T}[x(t)] - \frac{1}{v^2}x(0) - x'(0) + 64\mathcal{T}[x(t)] = 0$$

$$\left(\frac{1}{v^4} - 64\right)\mathcal{T}[x(t)] = 16$$

$$\mathcal{T}[x(t)] = \left(\frac{16v^4}{1 - 64v^4}\right)$$

taking inverse New Integral Transform we obtain

$$x(t) = -2\sin 8t$$

The period of this motion is $\frac{2\pi}{8} = \frac{\pi}{4}$ sec.

Example 5.3 *The vibrations of a mechanical system of two masses are given by the equations*

$$
\begin{aligned}
y_1'' &= -ky_1 + k(y_2 - y_1)\\
y_2'' &= -k(y_2 - y_1) - ky_2
\end{aligned}
\tag{5.3}
$$

subject to conditions

$$y_1(0) = y_2(0) = 1$$

$$y_1'(0) = \sqrt{3k}, \qquad y_2'(0) = -\sqrt{3k}$$

Solve the system for y_1, y_2

Applying New Integral Transform to system (5.3) *we get*

$$\frac{1}{v^4}\mathcal{T}[y_1(t)] - \frac{1}{v^2}y_1(0) - y_1'(0) + 2k\mathcal{T}[y_1(t)] - k\mathcal{T}[y_2(t)] = 0$$

$$\frac{1}{v^4}\mathcal{T}[y_2(t)] - \frac{1}{v^2}y_2(0) - y_2'(0) + k\mathcal{T}[y_1(t)] + 2k\mathcal{T}[y_2(t)] = 0$$

Using given conditions we obtain a system of linear algebraic equations as follows

$$\left(\frac{1}{v^4} + 2k\right)\mathcal{T}[y_1(t)] - k\mathcal{T}[y_2(t)] = \frac{1}{v^2} + \sqrt{3k} \tag{5.4}$$

$$-k\mathcal{T}[y_1(t)] + \left(\frac{1}{v^4} + 2k\right)\mathcal{T}[y_2(t)] = \frac{1}{v^2} - \sqrt{3k} \tag{5.5}$$

simplifying the above system we get,

$$\mathcal{T}[y_1(t)] = \frac{\sqrt{3k}\,v^4}{1 + (3k)v^4} + \frac{v^2}{1 + kv^4}$$

$$\mathcal{T}[y_2(t)] = -\frac{\sqrt{3k}\,v^4}{1 + (3k)v^4} + \frac{v^2}{1 + kv^4}$$

now applying inverse $\mathcal{T}$ transform on above system we get,

$$y_1(x) = \sin(\sqrt{3k}\,t) + \cos(\sqrt{3k}\,t) \tag{5.6}$$

$$y_2(x) = \cos(\sqrt{3k}\,t) - \sin(\sqrt{3k}\,t) \tag{5.7}$$

equation (5.6) *and* (5.7) *together constitute the required solution of the system.*
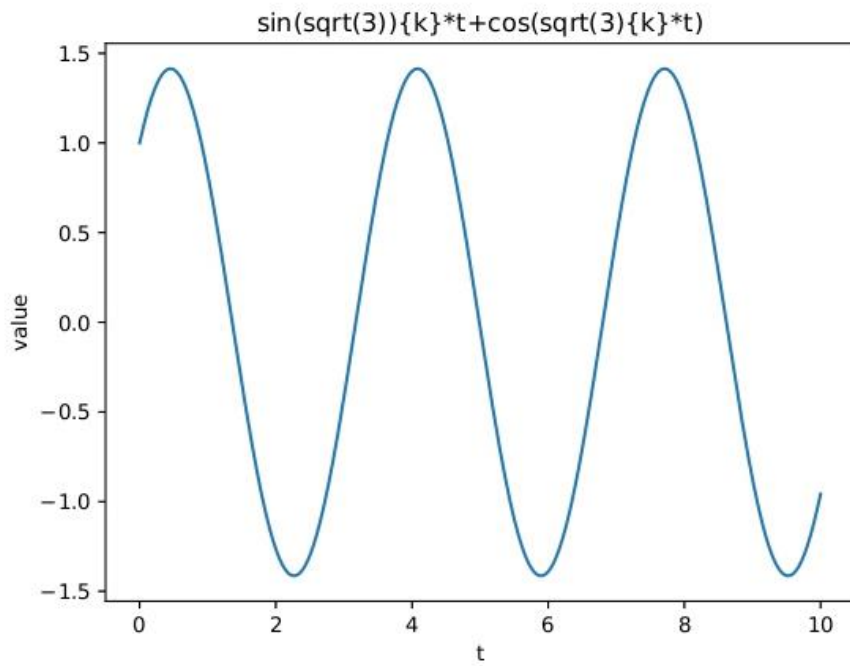
Figure 8: Graph of $\sin(\sqrt{3k}t) + \cos(\sqrt{3k}t$
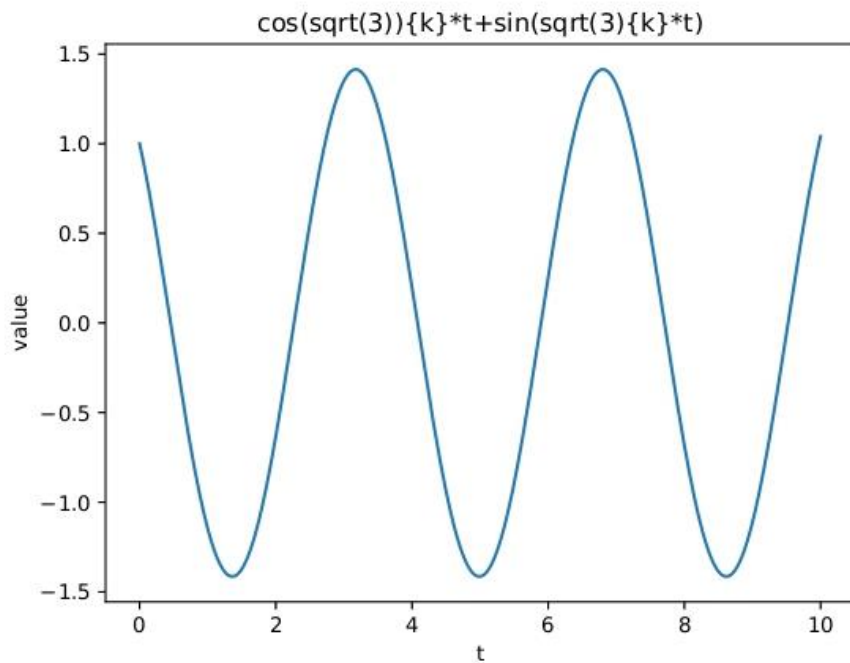
Figure 9: Graph of $\cos(\sqrt{3k}t) - \sin(\sqrt{3k}t$

6. CONCLUSION

The "New Integral Transform", which is the modified integral transform, has effectively proved its functional properties in this study. Particularly in the fields of science and engineering, the suggested transform has shown to be a strong and useful tool for analysing initial value problems. In common with other popular integral transforms, the New Integral Transform has shown to be a highly useful tool for addressing ODEs and related issues.

Moreover, the results of this novel method have been verified and visually shown through the use of mathematical tools like Python. This graphical de- piction not only makes the answers easier to grasp, but also supports the New Integral Transform's effectiveness as a dependable approach to solving chal- lenging issues in science and engineering. The results highlight the potential of this transformation to become a valuable addition to the toolkit of engineers and scientists working with ODEs and initial value problems.

7. References

[1]. AbdelilahKamal.H. Sedeeg, The New Integral Transform Kamal Trans- form, Advances in theoretical and applied mathematics, ISSN 0973-4554, vol.11, no. 4 (2016), pp. 451-458.

[2]. Debnath, Lokenath, and Dambaru Bhatta. Integral transforms and their applications. CRC press, 2014.

[3]. Elzaki, Tarig M. "On The New Integral Transform"Elzaki Trans- form"Fundamental Properties Investigations and Applications." Global Journal of Mathematical Sciences: Theory and Practical 4.1 (2012): 1-13.

[4]. Eltayeb, Hassan, and Adem Kılıçman. "On some applications of a new integral transform." International Journal of Mathematical Analysis 4.3 (2010): 123-132.

[5]. khalidsulimanAboodh, The new intehgral transform Aboodh transform, Global Journal of Pure and applied mathematics, ISSN 0973-1768, Vol. 9, No. 1(2013), pp. 35 – 43.

[6]. Gupta, Rahul. "Propounding a New Integral Transform: Gupta Trans- form with Applications in Science and Engineering." Int. J. Sci. Res. in Multidisciplinary Studies Vol 6.3 (2020).

[7]. Shaikh, Sadikali Latif. "Introducing a new integral transform: Sadik Transform." American International Journal of Research in Science, Tech- nology, Engineering & Mathematics 22.1 (2018): 100-102.

[8]. Davies, B. "Integral transforms and their applications" Springer Science & Business Media (Vol. 41).(2012).

[9]. Srivastava, H. M., L. U. O. Minjie, and R. K. Raina. "A new integral transform and its applications." Acta Mathematica Scientia 35, no. 6 (2015): 1386-1400.

Laplace Pourreza Transform

Shamal A. Gangarde, Shruti P. Katkade, Rajashri R. Sathe, S. B. Gaikwad, D. G. Gade, B. N. Todkari

Department of Mathematics, New arts, Commerce and Science College, Ahmednagar

Abstract :

In this work, we have extended the Laplace Pourreza transform. It was invented to do the Laplace Pourreza transform of basic elementary functions. In addition, the existence theorem was covered in respect to fundamental properties including linearity property, transform of derivative, change of scale property. Using the Laplace Pourreza transform, partial differential equations with initial conditions may be evaluated.

Keywords: Laplace Transform, Pourreza Transform, Laplace Pourreza Transform

I. INTRODUCTION

Many process and phenomenon of science, engineering and real life that can be expressed mathematically solved by using integral transform. Many fields can be easily handle with the help of integral transforms by converting them into mathematical form In 1982, Pierre-Simon Laplace introduce the Laplace Transform in his work on probability theory and now it is a very effective Transform for the solution of ordinary or partial differential equations.

In this paper we introduce the Laplace Pourreza Transform a new family member of integral transforms. The objective of this study is to combine two different single transforms together and present a new double Laplace Pourreza Transform. A new integral transform is introduced. Then some properties of this integral transform are discussed linearity property, change scale property, transform of some basic elementary functions and transform of derivatives.

443

Definition of Laplace Transform:

The Laplace Transform of the function F (t) for t≥0. The Laplace

transformation of F(t) denoted by f(p) or L{F(t)} is defined as $L\{F(t)\} = \int\limits_{0}^{\infty} e^{-pt}$

F(t) dt = f(p)

Provided that the integral exists, i.e. convergent. If the integral is convergent for some value of p then the Laplace transformation of F(t) exists otherwise not.

Definition of Pourreza Transform:

The Pourreza transform was introduced by the mathematician M. Pourreza in the year 2011.

The HY integral transform is defined by

$$P(v) = HY\{f(t)\} = v\int\limits_{0}^{\infty} e^{-v^2} f(t)\, dt.$$

The HY integral transform states that, if f(t) is piecewise continuous on every finite interval in t∈[0,∞) satisfying

$|f(t)| \leq Me^{at}, \exists M > 0$

For all t∈[0, ∞), then HY{f(t)} (v) exists for all v>a.

Definition of Laplace Pourreza Transform:

$$LP[\Psi(t_1, t_2)] = q\int\limits_{0}^{\infty}\int\limits_{0}^{\infty} e^{-xt_1} e^{-q^2 t_2} \Psi(t_1, t_2)\, dt1\, dt2$$

$$= (x,q)\, \Phi$$

Existence Theorem:

Let Ψ(t1,t2) be a continuous function in every finite intervals (x,0) and (0,y) and of exponential order $e^{at_1 + \beta t_2}$ then double Laplace Pourreza Transform of ψ (t1,t2) exist for all x>k1 and q>k2

Proof : Let ψ(k1,k2) be exponential order $e^{at_1 + \beta t_2}$ such that

$$\left|\psi(t_1, t_2)\right| \le M e^{(\alpha t_1 + \beta t_2)}, \text{ for all t1>X, t2>Y}$$

$$LP[\Psi(t_1, t_2)] = \left| q \int_0^\infty \int_0^\infty e^{-x t_1} e^{-q^2 t_2} \psi(t_1, t_2) dt_1 dt_2 \right|$$

$$= q \int_0^\infty \int_0^\infty e^{-(x t_1 + q^2 t_2)} \left| \Psi(t_1, t_2) \right| dt_1 dt_2$$

$$= M q \int_0^\infty \int_0^\infty e^{-(x t_1 + q^2 t_2)} e^{\alpha t_1 + \beta t_2} dt_1 dt_2$$

$$= M q \left[\int_0^\infty e^{(-x t_1 + \alpha t_1)} dt_1 \right] \left[\int_0^\infty e^{(-q^2 t_2 + \beta t_2)} dt_2 \right]$$

$$= M q \left[\int_0^\infty e^{-(x - \alpha) t_1} dt_1 \right] \left[\int_0^\infty e^{-(q^2 - \beta) t_2} dt_2 \right]$$

$$= M q \left[\frac{e^{-(x-\alpha)t_1}}{-(x-\alpha)} \right]_{t_1 = 0}^{\infty} \left[\frac{e^{-(q^2-\beta)t_2}}{-(q^2-\beta)} \right]_{t_2 = 0}^{\infty}$$

By evaluating,

$$= M q \left[\frac{1}{(x-\alpha)(q^2 - \beta)} \right]$$

Main Result:

Linearity Property:

If $LP\left[\psi_1(t_1, t_2)\right] = LP\left[\psi_2(t_1, t_2)\right] = \Phi_2(x, q)$

The Laplace Pourreza Transform of

$$LP\left[C_1 \psi_1(t_1, t_2) + C_2 \psi_2(t_1, t_2)\right] = C_1 LP\left[\psi_1(t_1, t_2)\right] + C_2 LP\left[\psi_2(t_1, t_2)\right]$$

Proof:

Consider, $LP\left[C_1 \psi_1(t_1, t_2) + C_2 \psi_2(t_1, t_2)\right]$

$$= q \int_0^\infty \int_0^\infty e^{-x t_1} e^{-q^2 t_2} \left[C_1 \psi_1(t_1, t_2) + C_2 \psi_2(t_1, t_2)\right] dt_1 dt_2$$

$$= q\int_0^\infty\int_0^\infty e^{-xt_1}e^{-q^2t_2}C_1\big[\Psi_1(t_1,t_2)\big]dt_1dt_2 + q\int_0^\infty\int_0^\infty e^{-xt_1}e^{-q^2t_2}C_2\big[\Psi_2(t_1,t_2)\big]dt_1dt_2$$

$$= C_1\left[q\int_0^\infty\int_0^\infty e^{-xt_1}e^{-q^2t_2}\Psi_1(t_1,t_2)\right]dt_1dt_2 + C_2\left[q\int_0^\infty\int_0^\infty e^{-xt_1}e^{-q^2t_2}\Psi_2(t_1,t_2)\right]dt_1dt_2$$

$$= C_1 LP\big[\psi_1(t_1,t_2)\big] + C_2 LP\big[\psi_2(t_1,t_2)\big]$$

Change Scale Property:

If a>0,b>0 and $LP\big[\Phi(t_1,t_2)\big] = \overline{\Phi(x,q)}$, then

$$LP\big[\psi(\alpha t_1, \beta t_2)\big] = \tfrac{1}{\alpha\beta}LP\left[\psi\left(\tfrac{z}{\alpha}, \tfrac{y}{\beta}\right)\right]$$

Proof: $LP\big[\psi(\alpha t_1, \beta t_2)\big] = q\int_0^\infty\int_0^\infty e^{-xt_1}e^{-q^2t_2}\big[\psi(\alpha t_1, \beta t_2)\big]dt_1dt_2$

Substituting,

$$\alpha t_1 = z, \quad \beta t_2 = y$$

$$t_1 = \tfrac{z}{\alpha} \quad , t_2 = \tfrac{y}{\beta}$$

$$\alpha dt_1 = dz, \quad \beta dt_2 = dy$$

$$= q\int_0^\infty\int_0^\infty e^{-x\left(\tfrac{z}{\alpha}\right)}e^{-q^2\left(\tfrac{y}{\beta}\right)}\psi(z,y)\tfrac{dz}{\alpha}\tfrac{dy}{\beta}$$

$$= \tfrac{q}{\alpha\beta}\int_0^\infty\int_0^\infty e^{-x\left(\tfrac{z}{\alpha}\right)}e^{-q^{2\left(\tfrac{y}{\beta}\right)}}\psi(z,y)dzdy$$

$$= \tfrac{1}{\alpha\beta}\left[q\int_0^\infty\int_0^\infty e^{-x\left(\tfrac{z}{\alpha}\right)}e^{-q^{2\left(\tfrac{y}{\beta}\right)}}\psi(z,y)\right]dzdy$$

$$= \tfrac{1}{\alpha\beta}LP\left[\psi\left(\tfrac{z}{\alpha}, \tfrac{y}{\beta}\right)\right]$$

Laplace Pourreza Transform of Basic Elementary Functions:

1) Let, $\psi(t_1, t_2) = 1$

$$\text{LP }[1] = q\int_0^\infty\int_0^\infty e^{-xt_1}e^{-q^2t_2}(1)dt_1dt_2$$

$$= \left[\int_0^\infty e^{-xt_1}dt_1\right]\left[q\int_0^\infty e^{-q^2t_2}dt_2\right]$$

$$= \left[\frac{e^{-xt_1}}{-x}\right]^{\infty}_{t_1=0} \left[q\frac{e^{-q^2t_2}}{-q^2}\right]^{\infty}_{t_2=0}$$

$$= \frac{1}{xq}$$

2) Let, $\psi(t_1, t_2) = \left[e^{\alpha t_1 + \beta t_2}\right]$

$$LP\left[e^{\alpha t_1 + \beta t_2}\right] = q\int_0^{\infty}\int_0^{\infty} e^{-xt_1}e^{-q^2t_2}e^{(\alpha t_1 + \beta)t_2}dt_1 dt_2$$

$$= q\left[\int_0^{\infty} e^{(-x+\alpha)t_1}dt_1\right]\left[\int_0^{\infty} e^{(-q^2+\beta)t_2}dt_2\right]$$

$$= q\left[\int_0^{\infty} e^{-(x-\alpha)t_1}dt_1\right]\left[\int_0^{\infty} e^{-(q^2-\beta)t_2}dt_2\right]$$

$$= q\left[\frac{e^{-(x-\alpha)t_1}}{-(x-\alpha)}\right]^{\infty}_{t_1=0}\left[\frac{e^{-(q^2-\beta)t_2}}{-(q^2-\beta)}\right]^{\infty}_{t_2=0}$$

$$= \frac{q}{(x-\alpha)(q^2-\beta)}$$

3) Let, $\psi(t_1, t_2) = \left\{Sin(\alpha t_1 + \beta t_2)\right\}$

$$LP\left\{Sin(\alpha t_1 + \beta t_2)\right\} = LP\left\{\frac{e^{i(\alpha t_1 + \beta t_2)}-e^{-i(\alpha t_1 + \beta t_2)}}{2i}\right\}$$

$$= \frac{1}{2i}\left[\frac{q}{(x-\alpha i)(q^2-\beta i)} - \frac{q}{(x+\alpha i)(q^2+\beta i)}\right]$$

$$= q\left[\frac{q^2\alpha+x\beta}{(q^4+\beta^2)(x^2+\alpha^2)}\right]$$

4) $\psi(t_1, t_2) = cos(\alpha t_1 + \beta t_2)$

$$Cos(\alpha t_1 + \beta t_2) = \frac{e^{i(\alpha t_1 + \beta t_2)}+e^{-i(\alpha t_1 + \beta t_2)}}{2}$$

$$LP\left\{Cos(\alpha t_1 + \beta t_2)\right\} = LP\left\{\frac{e^{i(\alpha t_1 + \beta t_2)}+e^{-i(\alpha t_1 + \beta t_2)}}{2}\right\}$$

$$= \frac{1}{2i}\left[\frac{q}{(x-\alpha i)\left(q^2-\beta i\right)} + \frac{q}{(x+\alpha i)\left(q^2+\beta i\right)}\right]$$

$$= q\left[\frac{q^2 x-\alpha\beta}{\left(q^4+\beta^2\right)\left(x^2+\alpha^2\right)}\right]$$

5) $\psi\left(t_1, t_2\right) = Sin\, h\left(\alpha t_1 + \beta t_2\right)$

$$\sin \sin h\left(\alpha t_1 + \beta t_2\right) = \frac{e^{\left(\alpha t_1+\beta t_2\right)}-e^{-\left(\alpha t_1+\beta t_2\right)}}{2}$$

$$LP\left\{\sin \sin h\left(\alpha t_1 + \beta t_2\right)\right\} = LP\left\{\frac{e^{\left(\alpha t_1+\beta t_2\right)}-e^{-\left(\alpha t_1+\beta t_2\right)}}{2}\right\}$$

$$= \frac{1}{2}\left[\frac{q}{\left(q^2-\beta\right)(x-\alpha)} - \frac{q}{\left(q^2+\beta\right)(x+\alpha)}\right]$$

$$= q\left[\frac{q^2\alpha+\beta q}{\left(q^4-\beta^2\right)\left(x^2-\alpha^2\right)}\right]$$

6) $Let,\ \psi\left(t_1, t_2\right) = Cos\, h\left(\alpha t_1 + \beta t_2\right)$

$$\cos \cos h\left(\alpha t_1 + \beta t_2\right) = \frac{e^{\left(\alpha t_1+\beta t_2\right)}+e^{-\left(\alpha t_1+\beta t_2\right)}}{2}$$

$$LP\left\{\cos \cos h\left(\alpha t_1 + \beta t_2\right)\right\} = LP\left\{\frac{e^{\left(\alpha t_1+\beta t_2\right)}+e^{-\left(\alpha t_1+\beta t_2\right)}}{2}\right\}$$

$$= \frac{1}{2}\left[\frac{q}{\left(q^2-\beta\right)(x-\alpha)} + \frac{q}{\left(q^2+\beta\right)(x+\alpha)}\right]$$

$$= q\left[\frac{q^2 x+\alpha\beta}{\left(q^4-\beta^2\right)\left(x^2-\alpha^2\right)}\right]$$

7) $Let,\ \psi\left(t_1, t_2\right) = t_1 t_2)$

$$LP\left\{t_1 t_2\right\} = q\int_0^\infty\int_0^\infty e^{-x t_1}e^{-q^2 t_2}\left(t_1 t_2\right)dt_1\, dt_2$$

$$= q\left[\int_0^\infty e^{-x t_1}t_1 dt_1\right]\left[e^{-q^2 t_2}t_2\, dt_2\right]$$

Integration by part,

$$= q\left\{\left[t_1\left(\frac{e^{-x t_1}}{-x}\right)\right]_{t_1=0}^\infty - \int_0^\infty\left[\left(\frac{1.e^{-x t_1}}{-x}\right)\right]d\, t_1\right\}\left\{\left[t_2\left(\frac{e^{-q^2 t_2}}{-q^2}\right)\right]_{t_1=0}^\infty - \int_0^\infty\left[\left(\frac{1.e^{-q^2 t_2}}{-q^2}\right)\right]d\, t_2\right\}$$

$$= \frac{1}{q^3 x^2}$$

Transform of Derivatives:

If $LP\left[\Phi\left(t_1, t_2\right)\right] = \overline{\Phi(x, q)},$ **then**

1) $LP\left[\frac{\partial \Phi}{\partial t_1}\right] = -P\left[\Phi\left(0, t_2\right)\right] + xLP\left[\Phi\left(t_1, t_2\right)\right]$

2) $LP\left[\frac{\partial \Phi}{\partial t_2}\right] = -L\left[\Phi\left(0, t_2\right)\right] + 2qLP\left[\Phi\left(t_1, t_2\right)\right]$

3) $LP\left[\frac{\partial^2 \Phi}{\partial t_1^2}\right] = -P\left[\frac{\partial \Phi}{\partial t_1}\left(0, t_2\right)\right] + xP\left[\Phi\left(0, t_2\right)\right] + x^2 LP\left[\Phi\left(t_1, t_2\right)\right]$

4) $LP\left[\frac{\partial^2 \Phi}{\partial t_2^2}\right] = -P\left[\frac{\partial \psi}{\partial t_2}\left(t_1, 0\right)\right] + qP\left[\psi(t_1, 0)\right] + q^2 LP\left[\psi\left(t_1, t_2\right)\right]$

Proof:

$$q\int_0^\infty \int_0^\infty e^{-xt_1} e^{-q^2 t_2} \frac{\partial \psi(t_1, t_2)}{\partial t_1} dt_1\, dt_2$$

$$q\int_0^\infty \int_0^\infty e^{-xt_1} e^{-q^2 t_2} \frac{\partial \psi}{\partial t_1} dt_1\, dt_2$$

$$q\int_0^\infty e^{-q^2 t_2}\left[\int_0^\infty e^{-xt_1} \frac{\partial \psi}{\partial t_1} dt_1\right] dt_2$$

Integration by parts

$$= q\int_0^\infty e^{-q^2 t_2}\left\{\left[e^{-xt_1} \psi\left(t_1, t_2\right)\right]_{t_1=0}^\infty - \int_0^\infty (-x) e^{-xt_1} \psi\left(t_1, t_2\right) dt_1\right\} dt_2$$

$$= q\int_0^\infty e^{-q^2 t_2}\left\{-\psi\left(0, t_2\right) + x\int_0^\infty e^{-xt_1} \psi\left(t_1, t_2\right) dt_1\right\} dt_2$$

$$= -q\int_0^\infty e^{-q^2 t_2} \psi\left(0, t_2\right) dt_2 + x\int_0^\infty \int_0^\infty e^{-xt_1} \psi\left(t_1, t_2\right) dt_1\, dt_2$$

$$= -P\left[\psi\left(0, t_2\right)\right] + xLP\left[\psi\left(t_1, t_2\right)\right]$$

2) $LP\left[\dfrac{\partial \Phi}{\partial t_2}\right]$

$$q\int_0^\infty\int_0^\infty e^{-xt_1}e^{-q^2t_2}\frac{\partial \psi(t_1,t_2)}{\partial t_2}dt_1\,dt_2$$

$$q\int_0^\infty\int_0^\infty e^{-xt_1}e^{-q^2t_2}\frac{\partial \psi}{\partial t_2}dt_1\,dt_2$$

$$q\int_0^\infty e^{-xt_1}\left[\int_0^\infty e^{-q^2t_2}\frac{\partial \psi}{\partial t_2}dt_2\right]dt_1$$

Integration by Parts

$$q\int_0^\infty[e^{-xt_1}\left[e^{-q^2t_2}\psi(t_1,t_2)\right]_{t_2=0}^\infty - \int_0^\infty -2q\,e^{-q^2t_2}\psi(t_1,t_2)dt_2]dt_1$$

$$-q\int_0^\infty e^{-xt_1}\psi(0,t_2)dt_1 + 2q^2\int_0^\infty\int_0^\infty e^{-xt_1}e^{-q^2t_2}\psi(t_1,t_2)\,dt_1dt_2$$

$$= -L\left[\psi(0,t_2)\right] + 2qLP[\psi(t_1,t_2)]$$

3) $LP\left[\dfrac{\partial^2 \Phi}{\partial t_1^2}\right]$

$$q\int_0^\infty\int_0^\infty e^{-xt_1}e^{-q^2t_2}\frac{\partial^2 \psi}{\partial t_1^2}dt_1\,dt_2$$

$$= q\int_0^\infty e^{-q^2t_2}\left[e^{-xt_1}\frac{\partial^2\psi}{\partial t_1^2}\,dt_1\right]dt_2$$

integration by Parts

$$= \left[-q\int_0^\infty e^{-q^2t_2}\frac{\partial \psi}{\partial t_1}(0,t_2)\,dt_2\right] + \left\{x\left[-q\int_0^\infty e^{-q^2t_2}\psi(0,t_2)\,dt_2\right]\right\} +$$

$$\left\{x^2\left[q\int_0^\infty\int_0^\infty e^{-xt_1}e^{-q^2t_2}\psi(t_1,t_2)dt_1\,dt_2\right]\right\}$$

$$= -P\left[\frac{\partial\psi}{\partial t_1}(0,t_2)\right] + xP\left[\psi(0,t_2)\right] + x^2\,LP\left[\psi(t_1,t_2)\right]$$

4) $LP\left[\dfrac{\partial^2 \Phi}{\partial t_2^2}\right]$

$$q\int_0^\infty\int_0^\infty e^{-xt_1}e^{-q^2t_2}\frac{\partial^2 \psi}{\partial t_2^2}dt_2\,dt_1$$

Conclusion

Two different single transforms were combined to present a new double transform Laplace-Pourreza transform. Change of scale Property, transform of basic elementary function, and derivative were proved. In future work, we solved Partial differential equations using this transform.

II. Reference:

[1]. A Study of Laplace Transform and Applications to Differential Equations 1Sukhen Bhattacharyya and 2Dr. Puneet Kumar Agarwal 1Research scholar Sri Satya Sai University, Sehore, Bhopal 2Research Supervisor Sri Satya Sai University, Sehore, Bhopal ISSN: 2455-3085 (Online)Issue-03 RESEARCH REVIEW International Journal of Multidisciplinary March -2019 www.rrjournals.com [UGC Listed Journal]

[2]. Dualities between Mohand Transform and Some Useful Integral Transforms Sudhanshu Aggarwal, Anjana Rani GuptaInternational Journal of Recent Technology and Engineering (IJRTE) ISSN: 2277-3878, Volume-8 Issue-3, September 2019

[3]. A new general integral transform for solving integral equations Hossein Jafari a,b,c,d,⇑ aDepartment of Mathematics, University of Mazandaran, Babolsar, Iranb Department of Mathematical Sciences, University of South Africa, UNISA0003, South Africa cDepartment of Medical Research, China Medical University Hospital, China Medical University, Taichung 110122, Taiwan dDepartment of Mathematics and Informatics, Azerbaijan University, Jeyhun Hajibeyli, 71, AZ1007, Baku, Azerbaijan

[4]. Tarig M. Elzaki, The New Integral Transform "Elzaki Transform" Global Journal of Pure and Applied Mathematics, ISSN 0973-1768, Number 1(2011), pp. 57-64.

[5]. Tarig M. Elzaki, Salih M. Elzaki, and Eman M.A. Hilal, Elzaki, and Sumudu " Transforms for solving some Differential Equations", Global journal of Pure and Applied Mathematics, ISSN 0973-1768,Volume 8, Number 2, (2012), pp.167173.

[6]. 1 Laplace, P.S., 1820. ThÂt'eorie Analytique desProbabilitiÂt'es, Lerch, Paris, 1(2).

A Literature Review on the Development and Applications of Fixed-Point Theory

V. V. Nalawade

S. G. R. G. Shinde Mahavidyalaya, Paranda, Dist. Dharashiv, Maharashtra, India

Abstract :

Fixed point theory is a significant branch of mathematics that has seen considerable growth since the establishment of the Banach Contraction Mapping Principle in 1922. This theory, which revolves around the concept of a "fixed point" where a function maps an element to itself, has become a cornerstone of both pure and applied mathematics. Fixed point theorems, designed for diverse settings of self-maps like contractions and expansions, have numerous applications across various fields, including differential equations, optimization, game theory and economics. This paper presents an brief literature review on the development of fixed point theory, covering its three main areas: Topological Fixed Point Theory, Metric Fixed Point Theory and Discrete Fixed Point Theory. We also discuss the generalizations of classical theorems, the development of new fixed point theorems and the emerging directions and challenges in this vibrant area of research.

Keywords: Fixed point theory: Topological, functional and Discrete, Metric spaces, multivalued mappings, Applications, Open questions

I. INTRODUCTION

Fixed point theory has developed into one of the most active and vital areas of modern mathematics, influencing both theoretical and applied research. A fixed point of a function $f : X \rightarrow X$ is a point $x \in X$ such that $f x = x$. This fundamental concept, though simple, has extensive applications in various fields, including differential equations, optimization, game theory, computer science and economics. The theory's origins can be traced back to the early 20th century, but it gained substantial traction with the introduction of Banach's Contraction Mapping Principle in 1922. Since then, the field has expanded significantly, leading to the development of several new theorems and applications, making it a blend of both pure and applied mathematics.

II. HISTORICAL BACKGROUND AND DEVELOPMENT OF FIXED-POINT THEORY

Fixed point theory is generally divided into three major areas: Topological Fixed-Point Theory, Metric Fixed Point Theory and Discrete Fixed Point Theory. The demarcation between these areas was historically defined by the discovery of three foundational theorems:

Topological Fixed Point Theory: This area began with Brouwer's Fixed-Point Theorem in 1912 [2], which states that any continuous function mapping a compact convex set to itself in Euclidean space has at least one fixed

point. This theorem was pivotal in shaping topological fixed point theory and has inspired numerous extensions and generalizations. For example, the Lefschetz Fixed-Point Theorem [8, 9, 10] extended Brouwer's result to more general spaces and maps, while Schauder's Fixed Point Theorem [11] generalized it to infinite-dimensional Banach spaces.

Metric Fixed Point Theory: The Banach Contraction Mapping Principle [1], formulated by Stefan Banach in 1922, revolutionized fixed point theory in metric spaces. The theorem states that any contraction mapping on a complete metric space has a unique fixed point. Banach's result provided a powerful tool for solving differential and integral equations, leading to numerous applications in mathematical analysis and applied sciences. The theorem's simplicity and elegance have led to various generalizations, including those by Edelstein [12], Boyd-Wong [4] and others, each relaxing or modifying the original conditions to accommodate more general situations.

Discrete Fixed Point Theory: Tarski's Fixed Point Theorem [3], introduced in 1955, marked a significant development in discrete mathematics and logic. The theorem states that any monotonic function on a complete lattice has a fixed point. This result has applications in economics (e.g., models of market equilibrium), computer science (e.g., data flow analysis and program semantics) and game theory (e.g., fixed-point theorems are used to prove the existence of equilibria).

III. GENERALIZATIONS OF CLASSICAL FIXED POINT THEOREMS

After the establishment of foundational results by Banach, Brouwer and Tarski, researchers focused on generalizing these classical theorems to broader contexts:

Extensions in Metric Spaces: The Banach Contraction Mapping Principle has been extended to spaces that are not necessarily metric. For example, the Caristi Fixed Point Theorem [13], Edelstein's Theorem and Boyd-Wong Fixed Point Theorem provide generalized conditions under which fixed points exist in settings that deviate from strict contraction. The study of weak contractions, asymptotic contractions and cyclic contractions further expands the scope of fixed point theory.

Nonlinear and Multivalued Mappings: The study of fixed points for multivalued mappings has opened new avenues for research, particularly in the context of differential inclusions and optimization problems. The Kakutani Fixed-Point Theorem, which generalizes Brouwer's result to multivalued maps, is a significant development in this regard and has applications in mathematical economics and game theory.

Generalized Spaces: Recent research has extended fixed point theorems to more abstract settings such as partial metric spaces [22], G-metric spaces [19, 14, 15, 16, 17, 18] and fuzzy metric spaces [20, 21]. These extensions cater to the needs of modern mathematical modeling, where classical spaces do not adequately capture the phenomena being studied.

IV. DEVELOPMENT OF NEW FIXED POINT THEOREMS

The last few decades have seen the introduction of several new fixed point theorems that have expanded the theoretical landscape:

Boyd-Wong Fixed Point Theorem: Provides conditions under which a unique fixed point exists for mappings that do not necessarily meet the strict contraction condition. This theorem has found applications in the analysis of differential equations and nonlinear operator theory.

Krasnoselskii Fixed Point Theorem: [23] This theorem provides criteria for the existence of fixed points in Banach spaces, especially in situations involving the sum of two operators, one being compact and continuous and the other being a contraction. It is widely used in nonlinear functional analysis.

Fixed Point Theorems in Partially Ordered Sets: [24, 25, 26, 3, 27] The existence of fixed points in partially ordered sets has been an area of significant interest due to its relevance in solving various types of equations, including differential equations, integral equations, and variational inequalities. Results by Nieto, Rodr´ıguez-L´opez, and others provide conditions for fixed points in partially ordered Banach spaces and lattices.

V. APPLICATIONS ACROSS DISCIPLINES

Fixed point theory's versatility is evident from its applications across multiple disciplines: Differential Equations: Fixed point theorems are fundamental in proving the existence and uniqueness of solutions for ordinary and partial differential equations. For example, the Schauder Fixed Point Theorem and the Banach Contraction Principle are extensively used in the study of nonlinear differential equations.

Economics and Game Theory: The Nash Equilibrium concept in game theory, a fundamental result in economic theory, relies on fixed point theorems like Kakutani's Fixed-Point Theorem. Similarly, the application of Tarski's theorem in economic models helps prove the existence of equilibrium states in competitive markets.

Optimization and Control Theory: In optimization problems, fixed point theorems are used to establish convergence properties of iterative methods. For example, they are essential in proving the existence of optimal solutions in variational and control problems.

Computer Science and Algorithm Design: In theoretical computer science, fixed point theorems provide a foundation for program verification, data flow analysis, and recursive function theory. Tarski's Fixed Point Theorem is particularly useful in semantics of programming languages and the study of formal verification techniques.

VI. OPEN QUESTIONS AND CHALLENGES

Despite significant advancements, fixed point theory remains a field with many open questions and challenges:

Extensions to Non-Metric Spaces: Extending the principles of fixed point theory to more generalized structures, such as hyperconvex spaces, modular spaces, and probabilistic metric spaces, is an ongoing area of research. These extensions involve more complex definitions of distance and convergence.

Stability and Robustness of Fixed Points: A crucial area of study is understanding how fixed points behave under perturbations of the underlying space or mapping. This has practical implications for numerical analysis, computational mathematics, and applied sciences where stability and robustness are crucial.

Algorithmic and Computational Aspects: Developing efficient algorithms to approximate fixed points remains a challenge, especially in high-dimensional spaces or when dealing with complex, non-linear systems.

Applications to Emerging Fields: Fixed point theory is finding new applications in fields like data science, machine learning, and quantum computing. The adaptation of classical results to these modern fields poses new challenges and opportunities for further research.

VII. EXTENSIONS TO MORE GENERAL SPACES

Recent research focuses on extending fixed point theory to spaces beyond classical settings: Partial Metric Spaces and Fuzzy Metric Spaces: These spaces, which generalize the standard notions of distance and convergence, have shown promise in modeling uncertainty and vagueness in real-world problems. The study of fixed points in such spaces is essential in developing robust mathematical models.

Hyperconvex and Modular Spaces: These advanced structures in functional analysis are being explored for their potential to provide new fixed point results applicable to a broader class of problems in mathematical analysis.

Probabilistic Metric Spaces: Here, the concept of distance is probabilistic rather than deterministic, providing a new framework for studying random processes, stochastic systems, and applications in areas like finance and risk analysis.

VIII. UNIQUENESS AND STABILITY OF FIXED POINTS*

Uniqueness and stability are central themes in fixed point theory, particularly in applications where reliable and consistent solutions are required:

Stability Analysis: The study of the stability of fixed points under small perturbations is important in both theory and applications. Stability results are crucial in areas like dynamical systems, numerical analysis and computational methods, where they help ensure that solutions are not overly sensitive to initial conditions or changes in parameters. Uniqueness Results: Understanding conditions under which fixed points are unique is fundamental to the study of nonlinear analysis and optimization. Uniqueness results often lead to more effective algorithms for approximating fixed points and have significant implications for mathematical modeling in science and engineering.

IX. CONCLUSION

Fixed point theory, with its rich history and vibrant development, continues to be a cornerstone of modern mathematics. The generalizations of classical theorems, the development of new fixed point theorems, and their diverse applications across disciplines demonstrate the theory's robustness and versatility. The open questions and challenges presented in this review suggest that there is still much to explore in this field, especially in the context of generalized spaces, uniqueness, and stability of fixed points. The continued exploration of fixed point theory is expected to yield further breakthroughs, not only in mathematics but also in numerous applied fields.

X. REFERENCES

[1]. Banach, S. Sur les op´erations dans les ensembles abstraits et leur application aux´equations int´egrales. Fundamenta Mathematicae, 3(1), 133-181 (1922).

[2]. Brouwer, L. E. J. Über Abbildung von Mannigfaltigkeiten. Mathematische Annalen, 71, 97–115 (1912).

[3]. Tarski, A. A lattice-theoretical fix point theorem and its applications. Pacific Journal of Mathematics, 5, 285–309 (1955).

[4]. Boyd, D. W., Wong, J. S. W. On nonlinear contractions. Proceedings of the American Mathematical Society, 20(3), 458-464 (1969).

[5]. Krasnoselskii, M. A. Topological Methods in the Theory of Nonlinear Integral Equations. Macmillan (1964).

[6]. Kakutani, S. A Generalization of Brouwer's Fixed Point Theorem. Duke Mathematical Journal, 8(3), 457-459 (1941).

[7]. Nieto, J. J., Rodr´ıguez-Lopez, R. Contractive mapping theorems in partially ordered sets and applications to ordinary differential equations. Order, 22(3), 223-239 (2005).

[8]. S. Lefschetz, Intersections and transformations of complexes and manifolds. Trans. Amer. Soc., 28 (1926) pp. 1–49.

[9]. S. Lefschetz, The residual set of a complex manifold and related questions. Proc. Nat. Acad. Sci. USA, 13 (1927) pp. 614–622.

[10]. S. Lefschetz, On the fixed point formula. Ann. of Math. (2), 38 (1937) pp. 819–822.

[11]. J. Schauder, Der Fixpunktsatz in Funktionalr→aumen, Studia Math. 2 (1930), 171–180.

[12]. Edelstein, M.,On fixed and periodic points under contractive mappings. J. Lond. Math. Soc. 1962, 37, 74–79.

[13]. Caristi, J. Fixed Point Theorems for Mappings Satisfying Inwardness Conditions. Transactions of the American Mathematical Society, (1976), 215, 241-251. https://doi.org/10.1090/S0002-9947-1976-0394329-4

[14]. Z. Mustafa and B. Sims, A new approach to generalized metric spaces, Journal of Nonlinear Convex Analysis, 7 (2006), 289-297.

[15]. Z. Mustafa, H. Obiedat and F. Awawdeh, Some fixed point theorem for mapping on complete G-metric spaces, Fixed Point Theory and Applications, Volume 2008, Article ID 189870, doi:10.1155/2008/189870.

[16]. Z. Mustafa, W. Shatanawi and M. Bataineh, Fixed point theorem on uncomplete G-metric spaces, Journal of Mathematics and Statistics, 4 (2008), 196-201.

[17]. Z. Mustafa, W. Shatanawi and M. Bataineh, Existence of fixed point results in G-metric spaces, Int. J. of Math. and Math. Sci., Volume 2009, Article ID 283028, doi:10.1155/2009/283028.

[18]. Z. Mustafa and B. Sims, Fixed point theorems for contractive mappings in complete G-metric spaces, Fixed Point Theory and Applications, Volume 2009, Article ID 917175, doi:10.1155/2009/917175.

[19]. A. Dehghan Nezhad and H. Mazaheri, New results in G-best approximation in Gmetric spaces, Ukrainian Math. J. 62 (2010) 648-654.

[20]. Badshah-e-Rome, M. Sarwar, R. Rodrguez-Lopez, Fixed Point Results via α -Admissibility in Extended Fuzzy Rectangular b-Metric Spaces with Applications to Integral Equations, Mathematics, 9, no. 16, (2021).

[21]. D. Butnariu, Fixed Point for Fuzzy Mappings, Fuzzy Sets and Systems, 7, no. 2,(1982), 193–205.

[22]. E. Karapınar and U. Yu¨ksel. Some common fixed point theorems in partial metric space, Journal of Applied Mathematics, 2011, Article ID:263621, 2011.

[23]. Krasnoselskii, MA: Some problems of nonlinear analysis. Transl. Am. Math. Soc. 10(2), 345-409 (1958).

[24]. S. Abian and A.B. Brown, A theorem on partially ordered sets, with applications: to fixed point theorems, Can. J. Math. 13 (1961) 78-82.

[25]. H. Hoft and M. Hoft, Some fixed point theorems for partially ordered sets, Can. J. Math. 28 (1976) 992-997.

[26]. I. Rival, A fixed point theorem for finite partially ordered sets, J. Combin. Theory 21(A) (1976) 309-318.

[27]. J.S.W. Wong, Common fixed points of commuting monotone mappings, Can. J. Math. 19 (1967) 617-620.

Vegetation Classification and Analysis of Majalgaon Dam Region Using Sentinel-2 Imagery and Random Forest Method in SNAP

Vishal Shirsat, Sanjay Tupe, Shafiyoddin Sayyad

Abstract :

This research focuses on the vegetation analysis of the Majalgaon Dam region in Tal. Majalgaon, Di. Beed, Maharashtra, using Sentinel-2 satellite imagery obtained from the European Space Agency (ESA). The image, captured on 16th January 2023, was processed using the SNAP software, where the Random Forest classification method was applied to differentiate between vegetative and non-vegetative areas. The Normalized Difference Vegetation Index (NDVI) was used as a measure to assess vegetation health. The analysis revealed that areas with NDVI values close to 1 exhibited healthy vegetation, while areas with values near 0 indicated no vegetation. This study demonstrates the efficacy of optical remote sensing combined with advanced classification techniques for ecological monitoring.

Keywords : Remote sensing, Sentinel 2, Classification, NDVI, Image Processing

I. INTRODUCTION

Remote sensing technologies have become an essential tool in monitoring and analyzing land cover changes, particularly vegetation distribution and health. Sentinel-2, part of the European Space Agency's Copernicus program, provides high-resolution multispectral data that is invaluable for environmental studies. The Majalgaon Dam region in Maharashtra, India, is a critical area for agricultural and ecological research due to its role in water resource management.

This study aims to classify and assess the vegetation cover around Majalgaon Dam using Sentinel-2 imagery. The Random Forest classification technique was employed in the SNAP software to process the satellite data, allowing for precise classification of vegetative and non-vegetative areas. The Normalized Difference Vegetation Index (NDVI) was calculated to evaluate vegetation health, with values closer to 1 indicating dense, healthy vegetation and values closer to 0 indicating barren or non-vegetative land.

Workplace

The study area is located in the vicinity of Majalgaon Dam in Tal. Majalgaon, Di. Beed, Maharashtra. The region is geographically positioned at approximately 19.1530°N latitude and 76.2100°E longitude. The dam is a significant water resource, supporting irrigation and drinking water needs while also sustaining the local ecosystem. The surrounding area comprises a mix of agricultural lands, forested regions, and barren areas, making it ideal for vegetation classification studies.

The climate in this region is semi-arid, with vegetation cover heavily influenced by seasonal rainfall and water availability from the dam. Monitoring the vegetation in this area is crucial for understanding the ecological balance and for making informed decisions regarding water and land resource management.

Methodology
Image Acquisition

The satellite image used in this study was captured by the Sentinel-2 satellite on 16th January 2023. The image was sourced from the European Space Agency's (ESA) online platform. Sentinel-2 provides high-resolution optical images across multiple spectral bands, making it suitable for detailed vegetation analysis.

Image Processing
The image was processed using the SNAP (Sentinel Application Platform) software, developed by ESA for the processing of Sentinel data. Pre-processing steps included radiometric correction to adjust for sensor irregularities and atmospheric correction to remove atmospheric disturbances that could affect the analysis.

Random Forest Classification
Random Forest, an ensemble learning method, was employed for classifying the satellite image. This method is well-suited for remote sensing applications due to its ability to handle large datasets and complex patterns. The Random Forest algorithm creates multiple decision trees during training and aggregates their outputs to improve classification accuracy.

NDVI Calculation
The Normalized Difference Vegetation Index (NDVI) was computed to assess the health and density of vegetation in the study area. NDVI is derived using the formula:

$$NDVI = \frac{(NIR - RED)}{(NIR + RED)}$$

where NIR represents the near-infrared band and RED represents the red band of the electromagnetic spectrum. NDVI values range from -1 to 1, with values closer to 1 indicating healthy, dense vegetation, and values near 0 indicating areas with little to no vegetation.

Classification and Visualization
The processed image was classified into vegetative and non-vegetative categories based on the NDVI values. The classification results were visualized using a color-coded map: dark green for dense vegetation (NDVI close to 1), faint green for moderate vegetation (NDVI around 0.5), and blue/red for non-vegetative areas (NDVI near 0).

Image Analysis
Pre-Processing and Initial Observations
The initial Sentinel-2 image provided a broad view of the Majalgaon Dam region, with various land cover types discernible. However, without further processing, the image lacked clarity in distinguishing between vegetative and non-vegetative areas. Pre-processing in SNAP helped to enhance the image quality, making it suitable for detailed analysis.

Random Forest Classification Results

After processing the image using the Random Forest classification method, distinct patterns of vegetation distribution emerged. The dark green areas in the classified image indicate regions with dense, healthy vegetation, predominantly found near the dam and along water channels. These areas are likely supported by consistent water supply from the dam, which facilitates lush vegetation growth.

The faint green areas represent regions with moderate vegetation, possibly reflecting agricultural fields or less dense forest cover. These areas show lower NDVI values (around 0.5), suggesting seasonal variations in vegetation density or less favorable growing conditions.

The blue and red regions in the classified image correspond to non-vegetative areas with NDVI values close to 0. These regions include barren lands, water bodies, and areas devoid of significant vegetation, possibly due to human activities or natural conditions.
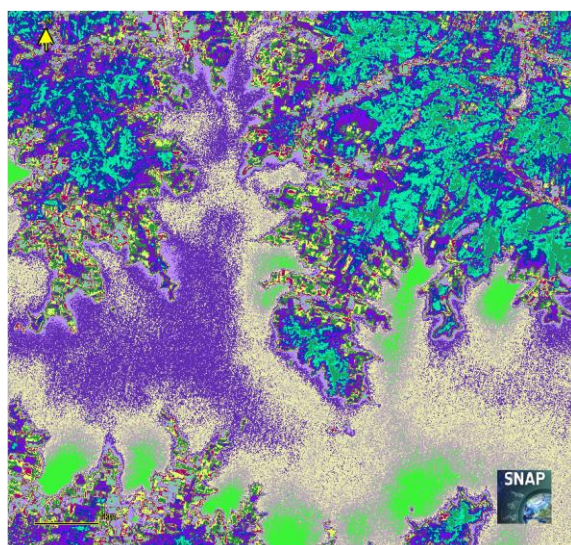
NDVI Interpretation

The NDVI analysis confirmed the visual classification, with high NDVI values (close to 1) corresponding to dark green areas of dense vegetation. Moderate NDVI values were observed in the faint green regions, indicating partial vegetation cover, while low NDVI values were found in non-vegetative zones. This differentiation is crucial for understanding the ecological dynamics of the region and for managing its natural resources effectively.

References

1   Breiman, L. (2001). Random Forests. *Machine Learning*, 45(1), 5-32.

2   European Space Agency. (2023). Sentinel-2 Satellite Imagery. Retrieved from https://www.esa.int/Applications/Observing_the_Earth/Copernicus/Sentinel-2

3   Rouse, J. W., Haas, R. H., Schell, J. A., & Deering, D. W. (1974). Monitoring vegetation systems in the Great Plains with ERTS. *Proceedings of the Third Earth Resources Technology Satellite-1 Symposium*, 1, 48-62.

4   Jiang, Z., Huete, A. R., Chen, Y., Chen, J., & Li, J. (2006). Analysis of NDVI and its relationship with climatic variables in the north of China. International Journal of Remote Sensing, 27(10), 2105-2118.

5   Hansen, M. C., Potapov, P. V., Moore, R., Hancher, M., Turubanova, S. A., Tyukavina, A., ... & Townshend, J. R. G. (2013). High-resolution global maps of 21st-century forest cover change. Science, 342(6160), 850-853.

6   Vegetation Classification in Remote Sensing: Techniques and Applications. (2020). · European Space Agency. (2023). Sentinel-2 Overview. Retrieved from [ESA Website].

7   Tucker, C. J. (1979). Red and photographic infrared linear combinations for monitoring vegetation. Remote Sensing of Environment, 8, 127-150.Journal of · European Space Agency. (2023). Sentinel-2 User Guide. Retrieved from ESA Website.

8   Huete, A. R., & Justice, C. O. (1999). MODIS Vegetation Index (MOD13). Algorithm Theoretical Basis Document, Version 3.

9   SNAP (2023). Sentinel Application Platform (SNAP). Retrieved from ESA Website.

Synthesis and ab-initio investigation of structural, optical and electronic properties of CuO and Zn doped CuO

K. R. Sature*[1], B. S. Kharat[2], P. M. Kokne[3]

*[1]Department of Physics, J.E.S.'s, R. G. Bagdia Arts, S. B. Lakhotia Commerce and R. Bezonji Science College, Jalna, Maharashtra, India

[2]Department of Physics, Swami Vivekanand Sr. College, Mantha, Jalna, Maharashtra, India

[3]Department of Physics, badrinarayan Barwale College, Jalna, Maharashtra, India

Abstract :

Experiments and Density functional theory based First-principles calculations have been performed to investigate the structural, optical and electronic properties of CuO and Zn doped CuO. Copper oxide nanoparticles were synthesized using a green approach involving lemon juice extract as the reducing and stabilizing agent. X-ray diffraction (XRD) characterization verified the creation of monoclinic phase CuO nanoparticles. The Quantum ESPRESSO package is used for DFT calculations. Calculated values of lattice parameters, energy band gap of CuO and for Zn doped CuO are in good agreement with the experimental results. Figures of electronic band structure and TDOS have been computed from the electronic structure of CuO and Zn doped CuO. Significant transition occurs in band gap after Zn doping. Optical properties showed that CuO and Zn doped CuO were transparent, having a small energy gap and maximum reflectivity at infrared region. The calculated values are in good agreement with the experimental value.

Keywords: CuO, CuO:Zn, DFT, TDOS, lattice parameter

I. INTRODUCTION

Tenorite, also known as cupric oxide (CuO), is attracting interest due to its fascinating features as a p-type semiconductor. It has narrow band gap (1.34-1.67 eV) and hence it can be used for the fabrication of p-n heterojunctions with other n-type metal oxides such as ZnO and TiO2. CuO has been used in water splitting and CO2 reduction systems as an efficient modulator of photocatalyst TiO2 or ZnO[1]. CuO is also widely used in many other applications, such as gigantic magneto resistance materials, gas sensors, biosensors, photodetectors, high-temperature superconductors, and magnetic storage media. Among various MOS, copper oxide (CuO) is a popular one due to its interesting structural, chemical, optical and electrical properties [2]. It is one of the hardest materials due to high melting and boiling points. Unlike other MOSs which crystallize in a cubic rock salt structure with possible rhombohedral distortions, CuO has a lower-symmetry monoclinic cell. Due to the wide range of applications, theoretical knowledge of CuO's internal characteristics is crucial. However, because of the significant electron correlation effects brought on by the hybridization of the Cu 3d and O 2p orbitals [3], it is hypothesized that the usual computing approach frequently fails to produce accurate results.

Building upon these studies, the present research focuses on the green synthesis of CuO particles using lemon juice extract as a natural reducing and stabilizing agent. Lemon juice, which is rich in citric acid and other bioactive compounds, provides a sustainable and cost-effective method for nanoparticle synthesis. After the synthesis of the CuO it was characterised with X-Ray diffraction spectroscopy. Another method used to predict the structural parameter total energy vs lattice constants (volume of the unit cell) graph is used. It is done by taking DFT calculations into account. In this theoretical work the structural, optical and electronic properties of CuO and Zn doped CuO using DFT based First-principles calculations have been investigated. The results of theoretical calculations have been compared with experimental results found for pure and Zn doped CuO to find the suitability of the material in different optical and optoelectronic devices.

II. METHODS AND MATERIAL

A. Synthesis of CuO nanoparticles

Copper oxide nanoparticles were synthesized using a green approach involving lemon juice extract as the reducing and stabilizing agent. Fresh lemon juice was extracted and filtered to remove any solid impurities. An aqueous solution of copper(II) sulfate pentahydrate ($CuSO_4 \cdot 5H_2O$) was prepared by dissolving a specific amount of the salt in distilled water. The lemon juice extract was then slowly added to the copper sulfate solution under continuous stirring at room temperature. The mixture was heated at 80°C for 2 hours to facilitate the reduction of Cu^{2+} ions to CuO nanoparticles. A color change from blue to dark brown indicated the formation of CuO nanoparticles. The resultant solution was cooled and centrifuged at 10,000 rpm for 15 minutes to collect the nanoparticles, which were then washed several times with distilled water and ethanol to remove any residual impurities. The purified CuO nanoparticles were dried in an oven at 60°C and stored for further characterization.

B. DFT calculations

Quantum mechanical calculations were done using Quantum ESPRESSO [4] open source under Linux operating system. The Density Function Theory (DFT) with the local density approximation exchange correlation function and plane wave sets were applied on electronic structures using four 2 GHz cores and 8 gigabyte of RAM, which were sufficient in this research. The GW pseudo potential with convergence threshold of 10–7 has been used for self-consistency of energy which is appropriate for these calculations.

III. RESULTS AND DISCUSSION

A. XRD Analysis

The crystallographic structure of the synthesized copper oxide (CuO) nanoparticles was determined using X-ray diffraction (XRD) analysis. The dried CuO nanoparticle powder was subjected to XRD analysis using a diffractometer equipped with Cu Kα radiation (λ = 1.5406 Å) operating at 40 kV and 30 mA. The XRD patterns were recorded over a 2θ range of 20° to 80° at a scanning rate of 0.02°/s.
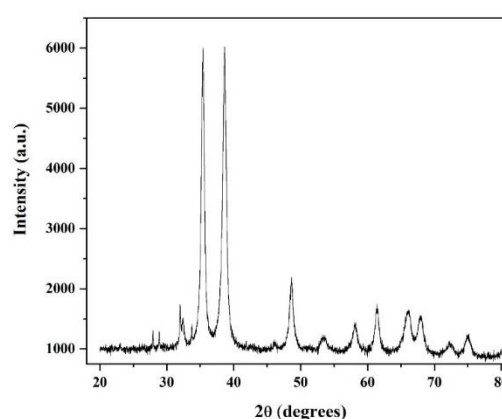

Figure 1. XRD pattern of CuO

The XRD pattern revealed distinct peaks corresponding to the monoclinic phase of CuO, with major diffraction peaks observed at 2θ values of 32.52°, 35.56°, 38.74°, 48.72°, 53.54°, 58.30°, 61.56°, 66.24°, and 68.13°, which were indexed to the (110), (002), (111), (202), (020), (202), (113), (311), and (220) planes, respectively. These peaks matched well with the standard JCPDS card no. 05-0661, confirming the formation of pure monoclinic CuO nanoparticles. The absence of any additional peaks indicated the high purity of the synthesized nanoparticles, with no secondary phases or impurities detected.

The particles synthesized in this study had an average crystallite size of 28 nm, slightly smaller than the 32 nm reported by Rajamanikkam et al. (2024) using Turbinaria species' aqueous extract. This size difference likely results from variations in the biological reducing agents and synthesis conditions used in the two studies.

B. DFT study

Title Calculations begin with the calculation for the stable structure. In this process lattice parameter of the unit cell are set free to adjust according to lowest total energy. In this process total energy respective to the different volumes is calculated. Lowest energy is observed and lattice parameters are finalised. Finalised lattice parameters are a=8.849 Bohr, b= 6.464 Bohr and c= 9.675 Bohr. Monoclinic structure is shown in Figure 2.
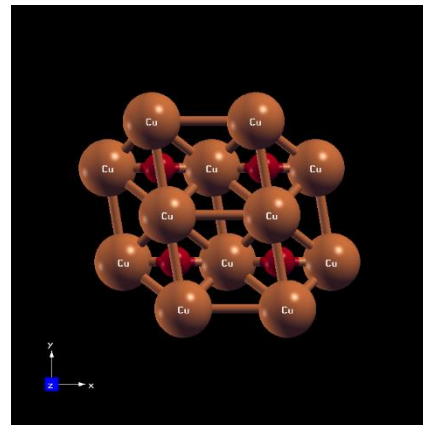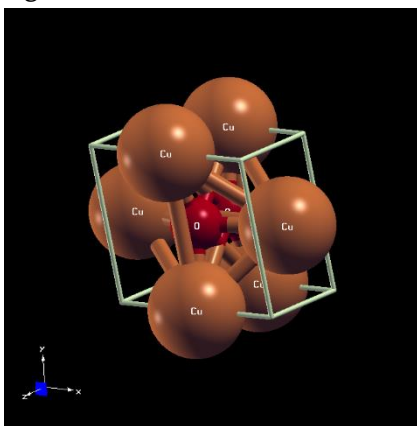
Figure 2. Monoclinic Unit cell of CuO

Further band structure of the CuO is calculated.. In figure 3, we show the calculated band structure of CuO within non-spin-polarized approach. It appears that the DFT results are in good agreement with experimental results. Figure show energy band gap of the CuO to be 1.13 eV which is in good agreement with the experimental one.
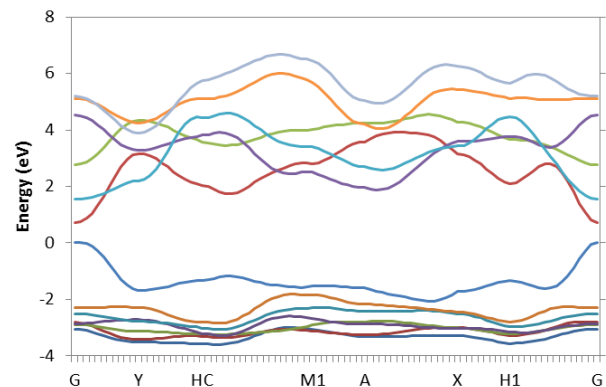
Figure 3. Band structure of the CuO

C. Zn doped CuO

Zn replaces the Cu ions in the CuO in process of doping. Density of states was calculated with pbe pseudo-potential. DOS also showed the energy band gap of 1.13 eV. Unit cell with one Cu ion replaced with Zn ion was constructed to check the change in electronic as well as optical properties of the Zn doped CuO. Density of states of Zn doped was calculated. Energy band gap of Zn doped CuO suggest

that it have band gap of 2.1 eV. Figure 4 shows doping of Zn modifies the density of states graph. It implies that energy band gap raised due to doping of Zn.
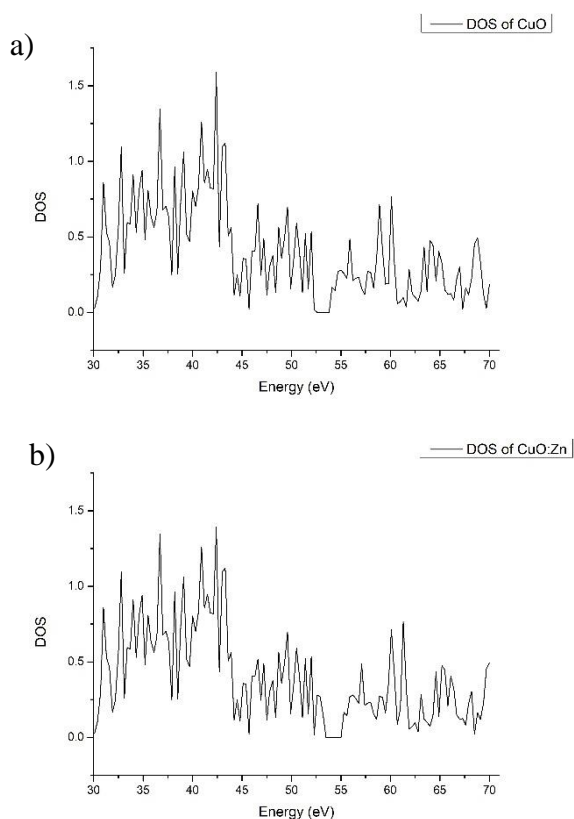
Figure 4. a) density of states of monoclinic CuO b) density of states of unit cell having one Cu atom replaced by Zn atom

IV.CONCLUSION

We have performed DFT approximation to study the electronic and optical properties of tenorite (CuO). Our calculation shows that DFT approximation sufficiently reliable to investigate the material properties of CuO and Zn doped CuO. Further DFT calculations showed that Zn increses the energy band gap of the material. The calculated band gap are in good agreement with the experimental results. Due to the Zn doping, blue shift is observed in optical properties.

V. REFERENCES

[1] Kum J M, Yoo S H, Ali G and Cho S O "Photocatalytic hydrogen production over CuO and TiO2 nanoparticles mixture", Int. J. Hydrogen Energy, 38 (2013) 13541–13546

[2] S Dolai et. al. "cupric oxide (CuO) thin films prepared by reactive dc magnetron sputtering technique for photovoltaic application", journal of alloys and coumpounds 724 (2017) 456-464

[3] Fabien Bruneval et. al. "Exchange and correlation effects in electronic excitation of Cu2O", physical review letters 97 (2016) 267601

[4] P. Giannozzi, et al., OUANTUM ESPRESSO: a modular and open-source softwere project for quantum simulations of materials, J. Phys: Condens. Matter 21 (2009) 395502.

Frequency-Dependent Dielectric Properties of Soil : A Comparative Study of Physical and Chemical Influences

Kunal Takle[1], Shrinivas Saindar[2], Sarita Bhurewal[3] , Mahesh Dhakne[4] Sushant Deshmukh[5*]

[1-4]Department of Physics, J.E.S. College, Jalna, Maharashtra, India

[5*] Department of Physics/Faculty, J.E.S. College, Jalna, Maharashtra, India

Email address: kunaltakleresearch@gmail.com, sgs.shree@gmail.com

Corresponding Author: sushant.d59@gmail.com

Abstract— This study presents a comprehensive investigation into the dielectric properties of soil samples from two distinct locations, Motibag and Gangaram, measured across the X, J, and C microwave frequency bands. The dielectric constant, a critical parameter in electromagnetic interactions with soil, was analyzed in relation to the physical and chemical properties of the soils, including texture, moisture content, and elemental composition. The results demonstrate that the Gangaram soil, characterized by higher clay content, exhibited significantly elevated dielectric constants, particularly in the J and C bands, which can be attributed to its greater water retention capacity and higher concentrations of potassium and magnesium. Both soil samples displayed a consistent increase in dielectric constant with rising frequency, confirming the frequency-dependent nature of soil dielectric behavior. These findings highlight the necessity of incorporating soil-specific factors, such as texture and chemical composition, into remote sensing models to improve the accuracy of soil moisture estimation. This research contributes to the broader understanding of soil-microwave interactions and suggests the potential of multi-frequency approaches for more precise soil characterization in environmental monitoring and agricultural applications.

Keywords— Microwave frequency bands, Soil dielectric properties, Remote sensing, Dielectric constant

Introduction

Soil is a complex medium whose electromagnetic properties play a crucial role in various applications, ranging from agriculture to remote sensing. Among these properties, the dielectric characteristics of soil are particularly important, as they directly influence the interaction between soil and electromagnetic waves. This study focuses on the dielectric properties of soil samples from two distinct locations, examining their behavior across different microwave frequency bands: X, J, and C.

The dielectric constant of soil is a key parameter that describes its ability to store electrical energy when an electromagnetic field is applied. This property is not constant but varies with factors such as soil composition, moisture content, and the frequency of the applied electromagnetic field. Understanding these variations is crucial for accurately interpreting remote sensing data, designing efficient ground-penetrating radar systems, and developing precise soil moisture sensors.

In this research, we investigate the dielectric properties of two soil samples, analyzing their chemical and physical parameters alongside their dielectric constants in the X, J, and C microwave bands. These bands are of particular interest due to their widespread use in remote sensing applications: X-band (8-12 GHz): Commonly used in terrestrial radar systems and satellite communications. J-band (10-20 GHz): Utilized in various radar

applications and atmospheric studies. C-band (4-8 GHz): Frequently employed in long-distance radio telecommunications and weather radar systems.

By examining the relationship between soil characteristics and dielectric behavior across these frequency bands, we aim to contribute to the growing body of knowledge on soil-microwave interactions. This understanding is vital for improving the accuracy of remote sensing techniques, enhancing our ability to monitor soil conditions, and ultimately supporting more effective land management and agricultural practices.

2. Literature review

The study of soil dielectric properties and their interaction with microwave frequencies has been an active area of research for several decades. This literature review provides an overview of key studies and findings relevant to our investigation. Hoekstra and Delaney (1974) conducted pioneering work on the dielectric properties of soils, establishing the relationship between soil moisture content and dielectric constant. Their research laid the groundwork for subsequent studies in this field. Wang and Schmugge (1980) developed a semi-empirical model for the dielectric constant of soil as a function of its moisture content, taking into account bound water and free water in the soil matrix. This model has been widely used in remote sensing applications. Ulaby et al. (1986) provided comprehensive analyses of microwave-soil interactions across various frequency bands, including X, C, and L bands. Their work highlighted the frequency dependence of soil dielectric properties and its implications for remote sensing.

Hallikainen et al. (1985) investigated the dielectric properties of soil in the 1.4 to 18 GHz range, encompassing the X, J, and C bands of interest in our study. They demonstrated that soil texture has a significant influence on dielectric behavior, particularly at higher frequencies. Dobson et al. (1985) examined the relationship between soil chemical properties and dielectric constant, showing that factors such as soil salinity and organic matter content can significantly affect dielectric behavior. Wraith and Or (1999) explored the temperature dependence of soil dielectric properties, revealing that temperature effects can be significant, especially in moist soils and at higher frequencies.

Mohanty et al. (2017) provided a comprehensive review of soil moisture remote sensing techniques, emphasizing the importance of understanding soil dielectric properties for accurate moisture estimation across different microwave bands. Fersch et al. (2018) utilized X-band and C-band synthetic aperture radar (SAR) data to estimate soil moisture, demonstrating the practical applications of understanding soil dielectric behavior in these frequency ranges. This literature review underscores the complexity of soil-microwave interactions and the importance of considering multiple factors when analyzing soil dielectric properties. Our study builds upon this foundation, focusing on the specific characteristics of two soil samples and their dielectric behavior across the X, J, and C microwave bands.

3. Experimental Method

This study employed a comprehensive approach to analyze the dielectric properties of soil samples from two distinct locations across X, J, and C microwave bands. The methodology encompassed soil sampling, physical and chemical parameter measurements, and dielectric property determination using the two-point method.

Soil samples, designated as Sample 1 (Motibag) and Sample 2 (Gangaram), were collected following standard protocols (Dane and Topp, 2020). The sampling process involved clearing surface vegetation and debris, then collecting approximately 1 kg of soil from the top 15 cm using a clean, stainless steel soil auger. Samples were stored in clean, labeled, airtight plastic bags to preserve their moisture content, and GPS coordinates were recorded for each sampling location.

Physical parameters were measured for each soil sample. Soil texture was determined using the hydrometer method to quantify the percentages of sand, silt, and clay (Gee and Or, 2002). Bulk density (ρb) was measured

using the core method, where a known volume of soil is oven-dried and weighed (Grossman and Reinsch, 2002). Total density (ρs) was calculated using the pycnometer method (Blake and Hartge, 1986). Porosity (φ) was computed from bulk density and particle density measurements using the following equation (Danielson and Sutherland, 1986):

$$\varphi = (1 - \rho b / \rho s) \times 100\%$$

Chemical analyses were conducted to determine various soil properties. Soil pH was measured using a calibrated pH meter in a 1:2.5 soil-water suspension (Thomas, 1996). Electrical conductivity (EC) was determined using an EC meter in a soil-water extract (Rhoades, 1996). Organic carbon (OC) was quantified using the Walkley-Black method (Nelson and Sommers, 1996). Available nitrogen (N) was estimated using the alkaline permanganate method (Subbiah and Asija, 1956), while available phosphorus (P) was determined by Olsen's method for neutral to alkaline soils (Olsen and Sommers, 1982). Available potassium (K) was extracted with neutral normal ammonium acetate and quantified using flame photometry (Helmke and Sparks, 1996). Micronutrients (Mg, B, Fe, Cu, S, Zn) were extracted using DTPA (diethylenetriaminepentaacetic acid) and quantified using atomic absorption spectrophotometry (Lindsay and Norvell, 1978).

The dielectric properties of the soil samples were determined using the two-point method across X, J, and C microwave bands, following the procedure outlined by Bobrov et al. (2010). This method involves measuring the reflection coefficient of the soil sample at two different lengths. Soil samples were air-dried, sieved through a 2 mm mesh to remove large particles and ensure homogeneity, then packed into a coaxial transmission line sample holder, ensuring uniform density.

In the two-point method procedure, the reflection coefficient (Γ) was measured at two different sample lengths (l1 and l2) using microwave bands (X, J, and C). Measurements were taken at room temperature (25°C ± 1°C) and repeated three times for each sample to ensure reproducibility (Wang and Schmugge, 1980).

The complex dielectric constant (ε*) was calculated using the following equations (Seyfried and Grant, 2007):

$$\varepsilon^* = \varepsilon' - j\varepsilon''$$

Where ε' is the real part (dielectric constant) and ε'' is the imaginary part (dielectric loss) of the complex dielectric constant.

The propagation constant (γ) is given by (Ulaby et al., 2014):

$$\gamma = \alpha + j\beta = (j2\pi/\lambda 0)\sqrt{\varepsilon^*}$$

Where α is the attenuation constant, β is the phase constant, and λ0 is the free-space wavelength.

The reflection coefficient (Γ) at the air-sample interface is (Pozar, 2011):

$$\Gamma = (Z - Z0) / (Z + Z0)$$

Where Z is the characteristic impedance of the sample and Z0 is the characteristic impedance of air.

From these measurements, the dielectric constant (ε') and dielectric loss (ε'') were derived. The loss tangent (tan δ) was calculated as the ratio of the imaginary to the real part of the dielectric constant (Hallikainen et al., 1985):

$$\tan \delta = \varepsilon'' / \varepsilon'$$

Emissivity (e) was calculated using the derived dielectric properties (Ulaby and Long, 2014):

$$e = 1 - |\Gamma|^2$$

Where |Γ| is the magnitude of the reflection coefficient.

Data analysis involved examining the dielectric properties (ε', ε'', tan δ, and e) across the X, J, and C microwave bands for both soil samples. Correlations between soil physical/chemical properties and dielectric characteristics were examined using Pearson's correlation coefficient.

This comprehensive methodology allows for a thorough investigation of the soil dielectric properties in relation to their physical and chemical characteristics across multiple microwave frequency bands. The results obtained

from this approach provide valuable insights into the behavior of soil dielectric properties and their potential applications in remote sensing and soil science (Dobson et al., 1985; Peplinski et al., 1995).

4. Results and Discussion

4.1 Soil Physical and Chemical Properties

The analysis of the two soil samples revealed distinct characteristics in their physical and chemical properties. Table 1 summarizes these findings:

Table 1: Physical and Chemical Properties of Soil Samples

Parameter	Sample 1 (Motibag)	Sample 2 (Gangaram)
pH	6.78	7.41
EC (ms/cm)	1.41	1.48
N (Kg/ha)	182	205
P (Kg/ha)	17	15.2
K (Kg/ha)	117.8	732.1
Mg (mg/kg)	3.4	18.5
OC (%)	0.3257	0.3665
B (mg/kg)	2.5	2.2
Fe (mg/kg)	5.6	0.9
Cu (mg/kg)	3.2	7.7
S (mg/kg)	1	1.2
Zn (mg/kg)	0.3	0.5
Sand (%)	65.0	55.0
Silt (%)	20.0	25.0
Clay (%)	15.0	20.0
Bulk Density (g/cm³)	1.5	1.45
Total Density (g/cm³)	2.65	2.6
Porosity (%)	43.4	44.2

Key observations:

Sample 2 (Gangaram) shows a slightly higher pH, indicating a more alkaline soil compared to Sample 1 (Motibag). Both samples have similar EC values, suggesting comparable salt content. Sample 2 has notably higher levels of N, K, and Mg, indicating potentially higher fertility. Sample 1 has a higher sand content and lower clay content compared to Sample 2, suggesting differences in soil texture. Bulk density and porosity are similar between the two samples, with Sample 2 showing slightly lower bulk density and higher porosity.

4.2 Dielectric Properties

The dielectric constants of the soil samples were measured across X, J, and C microwave bands. Table 2 presents these findings:

Table 2: Dielectric Constants Across Microwave Bands

Band	Sample 1 (Motibag)	Sample 2 (Gangaram)
X band	2.8	2.733333
J band	3.296667	3.432222
C band	3.36	3.673333

Key observations:

Both samples show an increase in dielectric constant as the frequency increases from X to C band. Sample 2 (Gangaram) exhibits higher dielectric constants in J and C bands compared to Sample 1 (Motibag). The difference in dielectric constants between the two samples is most pronounced in the C band.

5. Discussion

The analysis of soil physical, chemical, and dielectric properties reveals several important insights with implications for remote sensing applications:

Soil Texture and Dielectric Properties: The higher clay content in Sample 2 (Gangaram) correlates with higher dielectric constants, particularly in the J and C bands. This aligns with previous studies (Hallikainen et al., 1985) that have shown clay content to significantly influence soil dielectric behavior. The higher water-holding capacity of clay likely contributes to this effect, as water has a high dielectric constant.

Frequency Dependence: Both soil samples exhibit increasing dielectric constants from X to C band, which is consistent with the frequency-dependent nature of soil dielectric properties (Ulaby et al., 1986). This trend is more pronounced in Sample 2, possibly due to its higher clay content and potentially higher bound water content.

Soil Chemistry and Dielectric Behavior: The higher potassium (K) and magnesium (Mg) content in Sample 2 may contribute to its higher dielectric constants. These ions can affect the soil's electrical conductivity and, consequently, its dielectric properties (Dobson et al., 1985).

Implications for Remote Sensing: a) Soil Moisture Estimation: The observed differences in dielectric constants between the two soil types emphasize the importance of accounting for soil texture in remote sensing-based soil moisture estimation. Algorithms for soil moisture retrieval may need to be calibrated for different soil textures to improve accuracy. b) Band Selection: The more pronounced differences in dielectric constants at higher frequencies (J and C bands) suggest that these bands may be more sensitive to soil property variations. This could be advantageous for applications aiming to discriminate between soil types or detect subtle changes in soil conditions. c) Penetration Depth: The lower dielectric constants in the X band imply greater penetration depth at this frequency. This could be beneficial for applications requiring information from deeper soil layers, such as root zone moisture estimation. d) Multi-frequency Approach: The variation in dielectric behavior across frequencies suggests that a multi-frequency approach in remote sensing could provide more comprehensive information about soil properties, potentially improving the accuracy of soil classification and characterization.

6. Conclusion

This study investigated the dielectric properties of two distinct soil samples across X, J, and C microwave bands, correlating these properties with the soil's physical and chemical characteristics. The findings provide valuable insights into the complex relationships between soil composition and electromagnetic behavior, with significant implications for remote sensing applications. The study reinforces the significant impact of soil texture on dielectric properties. The sample with higher clay content (Gangaram) consistently exhibited higher

dielectric constants, particularly in the J and C bands. This underscores the necessity of accounting for soil texture variations in remote sensing-based soil analyses. Both soil samples demonstrated increasing dielectric constants from X to C band, confirming the frequency-dependent nature of soil dielectric properties. This trend was more pronounced in the clay-rich sample, suggesting that higher frequency bands may offer greater sensitivity to soil property variations. The observed differences in dielectric constants between the two samples correlated with variations in their chemical compositions, particularly in potassium and magnesium content. This highlights the complex interplay between soil chemistry and electromagnetic behavior. The results emphasize the potential for multi-frequency microwave remote sensing in soil characterization. The varying sensitivity of different frequency bands to soil properties suggests that a multi-band approach could provide more comprehensive and accurate soil information.

The study underlines the importance of soil specific calibration in remote sensing-based moisture estimation algorithms, as soil texture significantly influences dielectric behavior. These findings contribute to the growing body of knowledge on soil-microwave interactions and have practical implications for improving remote sensing techniques in soil science, agriculture, and environmental monitoring. By enhancing our understanding of how soil properties affect dielectric behavior across different microwave frequencies, this research supports the development of more accurate and nuanced remote sensing methodologies.

Acknowledgements

References

[1]. Hoekstra, P., & Delaney, A. (1974). Dielectric properties of soils at UHF and microwave frequencies. *Journal of Geophysical Research*, 79(11), 1699–1708.

[2]. Wang, J. R., & Schmugge, T. J. (1980). An empirical model for the complex dielectric permittivity of soils as a function of water content. *IEEE Transactions on Geoscience and Remote Sensing*, GE-18(4), 288–295.

[3]. Ulaby, F. T., Moore, R. K., & Fung, A. K. (1986). *Microwave Remote Sensing: Active and Passive* (Vol. 3). Artech House.

[4]. Dobson, M. C., Ulaby, F. T., Hallikainen, M. T., & El-Rayes, M. A. (1985). Microwave dielectric behavior of wet soil: Part II—Dielectric mixing models. *IEEE Transactions on Geoscience and Remote Sensing*, GE-23(1), 35–46.

[5]. Hallikainen, M. T., Ulaby, F. T., Dobson, M. C., El-Rayes, M. A., & Wu, L. K. (1985). Microwave dielectric behavior of wet soil: Part I—Empirical models and experimental observations. *IEEE Transactions on Geoscience and Remote Sensing*, GE-23(1), 25–34.

[6]. Mohanty, B. P., Cosh, M. H., Lakshmi, V., & Montzka, C. (2017). Soil moisture remote sensing: State-of-the-science. *Vadose Zone Journal*, 16(1).

[7]. Fersch, B., Jackisch, C., & Kollet, S. (2018). Soil moisture remote sensing for hydrological applications. *Hydrology and Earth System Sciences*, 22(2), 1231-1250.

[8]. Pozar, D. M. (2011). *Microwave Engineering* (4th ed.). Wiley.

[9]. Bobrov, P. P., Yakovlev, Y. P., & Tikhonov, M. P. (2010). Measurement of dielectric properties of soil samples. *Measurement Science Review*, 10(3), 91-94.

[10]. Gee, G. W., & Or, D. (2002). Particle size analysis. In *Methods of Soil Analysis: Part 4 Physical Methods* (pp. 255-293). Soil Science Society of America.

[11]. Helmke, P. A., & Sparks, D. L. (1996). Potassium and magnesium analysis in soil. In *Methods of Soil Analysis* (pp. 551-574). Soil Science Society of America.

[12]. Lindsay, W. L., & Norvell, W. A. (1978). Development of a DTPA soil test for zinc, iron, manganese, and copper. *Soil Science Society of America Journal*, 42(3), 421-428.

[13]. Dane, J. H., & Topp, G. C. (2020). *Methods of Soil Analysis, Part 4* (3rd ed.). Soil Science Society of America.

[14]. Nelson, D. W., & Sommers, L. E. (1996). Total carbon, organic carbon, and organic matter. In *Methods of Soil Analysis: Part 3* (pp. 961-1010). Soil Science Society of America.

[15]. Ulaby, F. T., & Long, D. G. (2014). *Microwave Radar and Radiometric Remote Sensing*. University of Michigan

Effect of Soil Texture and Moisture Variations on Dielectric Properties Across Microwave Bands : A Comparative Study

Shrinivas Saindar[1], Kunal Takle[2], Sarita Bhurewal[3] , Mahesh Dhakne[4] Chandrakant Mahajan[5*]

[1-4]Department of Physics, J.E.S. College, Jalna, Maharashtra, India

[5*] Department of Physics/Faculty, J.E.S. College, Jalna, Maharashtra, India

*Corresponding Author: Csmahajan_jes@rediffmail.com

Abstract :

This study investigates the effect of soil texture and moisture variation on the dielectric properties of sandy and clay-rich soils across the X, J, and C microwave frequency bands. Soil dielectric constants were measured under controlled moisture levels (5%, 10%, 15%, and 20%) to understand how moisture content and texture influence soil-microwave interactions. The results indicate that clay-rich soils exhibit significantly higher dielectric constants compared to sandy soils across all moisture levels, with the difference becoming more pronounced at higher moisture content and frequency. The frequency-dependent behavior was most notable in the J and C bands, suggesting their increased sensitivity to variations in soil texture. These findings have important implications for improving remote sensing models, particularly for soil moisture estimation and land classification. The study emphasizes the need for multi-frequency approaches and soil-specific calibration to enhance the accuracy of remote sensing techniques in environmental and agricultural applications.

Keywords — Microwave frequency bands, Soil texture, Moisture content, Dielectric constant

1. Introduction

Soil dielectric properties are central to understanding soil-microwave interactions, which are crucial for remote sensing applications, soil moisture estimation, and agricultural monitoring. Soil texture (i.e., sand, silt, and clay composition) and moisture content significantly influence these properties, altering the soil's interaction with electromagnetic waves. Previous research has shown that moisture content increases dielectric constants due to the high dielectric permittivity of water (Ulaby et al., 1986; Wang and Schmugge, 1980).

Despite substantial research into soil dielectric properties, limited studies have explored the combined influence of soil texture and controlled moisture variations across multiple microwave frequency bands, such as X, J, and C bands, for both sandy and clay-rich soils. Understanding these interactions is key to improving remote sensing models, particularly for soil moisture retrieval and land use management.

This study investigates the impact of varying soil moisture levels on the dielectric behavior of sandy and clay-rich soils across microwave bands. By comparing soil samples with different textures under controlled moisture conditions, we aim to provide a comprehensive analysis of the dielectric constant's frequency-dependent behavior.

Findings from this research will help improve the

accuracy of remote sensing technologies used in environmental monitoring and agriculture, especially in enhancing algorithms for soil moisture retrieval and soil type classification.

2. Literature review

Early studies by Hallikainen et al. (1985) and Dobson et al. (1985) demonstrated that soil texture plays a crucial role in determining its dielectric constant, with clay-rich soils showing higher dielectric values due to greater moisture retention.

Research by Wang and Schmugge (1980) and Wraith and Or (1999) highlighted how increased soil moisture raises dielectric constants, particularly for clay-rich soils, which hold more bound water.

Ulaby et al. (1986) emphasized that the dielectric properties of soil vary significantly across microwave frequency bands. Higher frequencies, like the J and C bands, are more sensitive to soil texture variations, making them valuable for remote sensin

Despite progress, few studies have systematically examined the combined effects of moisture variation and soil texture across multiple microwave bands. This research seeks to address this gap by studying both sandy and clay-rich soils under different moisture conditions across the X, J, and C bands.

3. Experimental Method

Soil samples were collected from two distinct locations—one characterized by sandy soil and the other by clay-rich soil. Samples were air-dried, sieved, and classified based on texture using the hydrometer method (Gee and Or, 2002). Moisture content was controlled by adding water incrementally to achieve 5%, 10%, 15%, and 20% by weight.Soil samples, designated as Sample 1 (Motibag) and Sample 2 (Gangaram), were collected following standard protocols (Dane and Topp, 2020). The sampling process involved clearing surface vegetation and

debris, then collecting approximately 1 kg of soil from the top 15 cm using a clean, stainless steel soil auger. Samples were stored in clean, labeled, airtight plastic bags to preserve their moisture content, and GPS coordinates were recorded for each sampling location.

Physical parameters were measured for each soil sample. Soil texture was determined using the hydrometer method to quantify the percentages of sand, silt, and clay (Gee and Or, 2002). Bulk density (ρb) was measured using the core method, where a known volume of soil is oven-dried and weighed (Grossman and Reinsch, 2002). Total density (ρs) was calculated using the pycnometer method (Blake and Hartge, 1986). Porosity (φ) was computed from bulk density and particle density measurements using the following equation (Danielson and Sutherland, 1986):

$$\varphi = (1 - \rho b / \rho s) \times 100\%$$

Chemical analyses were conducted to determine various soil properties. Soil pH was measured using a calibrated pH meter in a 1:2.5 soil-water suspension (Thomas, 1996). Electrical conductivity (EC) was determined using an EC meter in a soil-water extract (Rhoades, 1996). Organic carbon (OC) was quantified using the Walkley-Black method (Nelson and Sommers, 1996). Available nitrogen (N) was estimated using the alkaline permanganate method (Subbiah and Asija, 1956), while available phosphorus (P) was determined by Olsen's method for neutral to alkaline soils (Olsen and Sommers, 1982). Available potassium (K) was extracted with neutral normal ammonium acetate and quantified using flame photometry (Helmke and Sparks, 1996). Micronutrients (Mg, B, Fe, Cu, S, Zn) were extracted using DTPA (diethylenetriaminepentaacetic acid) and quantified using atomic absorption spectrophotometry (Lindsay and Norvell, 1978).

The dielectric properties of the soil samples were determined using the two-point method across X, J, and C microwave bands, following the procedure outlined by Bobrov et al. (2010). This method

involves measuring the reflection coefficient of the soil sample at two different lengths. Soil samples were air-dried, sieved through a 2 mm mesh to remove large particles and ensure homogeneity, then packed into a coaxial transmission line sample holder, ensuring uniform density.

In the two-point method procedure, the reflection coefficient (Γ) was measured at two different sample lengths (l1 and l2) using microwave bands (X, J, and C). Measurements were taken at room temperature (25°C ± 1°C) and repeated three times for each sample to ensure reproducibility (Wang and Schmugge, 1980).

The complex dielectric constant (ε*) was calculated using the following equations (Seyfried and Grant, 2007):

$$\varepsilon^* = \varepsilon' - j\varepsilon''$$

Where ε' is the real part (dielectric constant) and ε" is the imaginary part (dielectric loss) of the complex dielectric constant.

The propagation constant (γ) is given by (Ulaby et al., 2014):

$$\gamma = \alpha + j\beta = (j2\pi/\lambda 0)\sqrt{\varepsilon^*}$$

Where α is the attenuation constant, β is the phase constant, and λ0 is the free-space wavelength.

The reflection coefficient (Γ) at the air-sample interface is (Pozar, 2011):

$$\Gamma = (Z - Z0) / (Z + Z0)$$

Where Z is the characteristic impedance of the sample and Z0 is the characteristic impedance of air.

From these measurements, the dielectric constant (ε') and dielectric loss (ε") were derived. The loss tangent (tan δ) was calculated as the ratio of the imaginary to the real part of the dielectric constant (Hallikainen et al., 1985):

$$\tan \delta = \varepsilon'' / \varepsilon'$$

Emissivity (e) was calculated using the derived dielectric properties (Ulaby and Long, 2014):

$$e = 1 - |\Gamma|^2$$

Where |Γ| is the magnitude of the reflection coefficient.

Table 1: Soil Texture Composition

Sample	Sand %	Slit %	Clay %
Sandy Soil	74	15	10
Clay – Rich	30	25	45

Dielectric Measurement Setup:

The dielectric constant (ε') and dielectric loss (ε'') were measured using the two-point coaxial transmission line method, following procedures by Bobrov et al. (2010). Measurements were taken across the X (8-12 GHz), J (10-20 GHz), and C (4-8 GHz) microwave bands for each moisture level, ensuring consistency by repeating measurements thrice.

Table 2 : Soil Dielectric Properties Across Microwave Bands at 15% Moisture

Frequency Band	Sandy Soil Dielectric Constant (ε')	Clay-Rich Soil Dielectric Constant (ε')
X – Band	2.5	3.8
J – Band	3.1	4.5
C – Band	3.3	4.9

Statistical Analysis:

Correlation analysis was performed using Pearson's correlation coefficient to assess the relationships

between soil dielectric properties, moisture content, and texture. Additionally, frequency-dependent trends were plotted to compare dielectric behavior between the two soil types.

4. Results and Discussion

4.1 Impact of Moisture on Dielectric Properties:

As expected, increasing soil moisture content led to higher dielectric constants for both sandy and clay-rich soils. However, the clay-rich soil consistently exhibited higher dielectric constants across all moisture levels, due to its greater capacity to retain water. The difference was more pronounced at higher moisture levels (15% and 20%).

Table 1: Physical and Chemical Properties of Soil Samples

Moisture Content	Sandy Soil Dielectric Constant (ε')	Clay-Rich Soil Dielectric Constant (ε')
5 %	6.78	7.41
10 %	2.2	3.5
15%	2.5	3.8
20%	2.8	4.2

4.2 Frequency-Dependent Behavior:

Both soil types showed an increase in dielectric constant with rising frequency, particularly between the J and C bands. The clay-rich soil exhibited stronger frequency-dependent behavior, likely due to the increased dielectric loss at higher frequencies (Dobson et al., 1985; Ulaby et al., 1986).**5.**

5. Discussion

The results confirm that clay-rich soils exhibit higher dielectric constants across all moisture levels and frequency bands due to their higher water-holding capacity. This finding is consistent with previous studies (Hallikainen et al., 1985; Wang and Schmugge, 1980).

The study also highlights the increased sensitivity of higher frequency bands (J and C) to soil texture variations. The pronounced dielectric response of clay-rich soils at these frequencies underscores their suitability for remote sensing applications targeting soil moisture estimation.

As moisture content increases, the dielectric constant for both soil types rises significantly, although the effect is more pronounced in clay-rich soils. This highlights the need for moisture calibration in remote sensing models, particularly when dealing with different soil types.

The study emphasizes the importance of using multi-frequency approaches in remote sensing to accurately estimate soil moisture across diverse soil types. Algorithms should be calibrated to account for variations in soil texture and moisture content to improve precision in soil moisture retrieval.

6. Conclusion

This study demonstrates the significant impact of soil texture and moisture levels on dielectric properties across the X, J, and C microwave bands. Clay-rich soils consistently exhibited higher dielectric constants compared to sandy soils, particularly at higher moisture levels and frequencies.

The findings reinforce the need for texture- and moisture-specific calibration in remote sensing models. Multi-frequency remote sensing approaches can better capture soil dielectric variations, improving soil moisture estimation accuracy.

Future studies should explore the dielectric behavior of loamy soils and assess the effect of temperature on dielectric properties, further enhancing the applicability of remote sensing in agricultural and environmental monitoring.The study underlines the importance of soil specific calibration in remote sensing-based moisture estimation algorithms, as soil

texture significantly influences dielectric behavior. These findings contribute to the growing body of knowledge on soil-microwave interactions and have practical implications for improving remote sensing techniques in soil science, agriculture, and environmental monitoring. By enhancing our understanding of how soil properties affect dielectric behavior across different microwave frequencies, this research supports the development of more accurate and nuanced remote sensing methodologies.

Acknowledgements

References

[1]. Hallikainen, M. T., Ulaby, F. T., Dobson, M. C., El-Rayes, M. A., & Wu, L. K. (1985). Microwave dielectric behavior of wet soil: Part I—Empirical models and experimental observations. *IEEE Transactions on Geoscience and Remote Sensing*, GE-23(1), 25–34.

[2]. Wang, J. R., & Schmugge, T. J. (1980). An empirical model for the complex dielectric permittivity of soils as a function of water content. *IEEE Transactions on Geoscience and Remote Sensing*, GE-18(4), 288–295.

[3]. Ulaby, F. T., Moore, R. K., & Fung, A. K. (1986). *Microwave Remote Sensing: Active and Passive* (Vol. 3). Artech House.

[4]. Dobson, M. C., Ulaby, F. T., Hallikainen, M. T., & El-Rayes, M. A. (1985). Microwave dielectric behavior of wet soil: Part II—Dielectric mixing models. *IEEE Transactions on Geoscience and Remote Sensing*, GE-23(1), 35–46.

[5]. Gee, G. W., & Or, D. (2002). Particle size analysis. In *Methods of Soil Analysis: Part 4 Physical Methods* (pp. 255-293). Soil Science Society of America.

[6]. Bobrov, P. P., Yakovlev, Y. P., & Tikhonov, M. P. (2010). Measurement of dielectric properties of soil samples. *Measurement Science Review*, 10(3), 91-94.

[7]. Wraith, J. M., & Or, D. (1999). Temperature effects on soil bulk dielectric permittivity measured by time domain reflectometry: Experimental evidence and hypothesis development. *Water Resources Research*, 35(2), 361-369.

[8]. Helmke, P. A., & Sparks, D. L. (1996). Potassium and magnesium analysis in soil. In *Methods of Soil Analysis* (pp. 551-574). Soil Science Society of America.

The Solution of Fractional Partial Differential Equations With Riemann-Liouville Fractional Derivative by Sumudu Transform Method

Dr. D. S. Bodkhe

Department of Mathematics,Anandrao Dhonde Alias Babaji Mahavidyalaya, Kada. BEED - 414202, Maharashtra, India

Abstract :

In this paper, we obtained explicit solution in terms of Mittag-Leffler func- tion and generalized Wright function of the fractional diffusion-wave equa- tions involving partial Reimann-Liouville fractional derivative by using Sumudu transform method (STM). Some illustrative examples are also given.

Keywords: Sumudu transform; Wrightfunction; Mittag-Leffler function; Frac- tional differential equations.

I. INTRODUCTION

In this paper, we apply the Sumudu transform to fractional integrals, derivatives, and use it to solve initial value fractional differential equations. In[[1],[2],[3],[4],[5], [6]], the authors studied many properties of the Sumudu transform in light of which they developed efficient and straightforward methodologies for treating ordinary [11] and partial differential equations . There is evident interest in further study- ing this transform, and applying it to various mathematical and physical sciences problems[13]. The Sumudu transform can be used to solve many types of difference and differential equations problems without resorting to a new frequency domain. The Sumudu transform was first defined by Watugala in 1993, which is used to solve engineering control problems [16], [17], [18]. The Weerakoon applied Sumudu transform to solve fractional differential equations [19],[20]. The fundamental prop- erties of Sumudu transform are also used to solve the fractional differential equations{[8],[7]. In this paper,we can find an explicit solution of the fractional diffusion-waveequations with Reimann-Liouville fractional derivative by using the Sumudu trans- form method.

The theory of fractional calculus plays an important role in many applied fields, such as modelling mechanical, electrical and rheological materials properties. Vis- coelasticity theories, and hereditary solid mechanics reinforced fractional calculus wide use[14]. Fractional Calculus models rely on the concepts of fractional integrals,

derivatives, and proper formulations of initial conditions. Fractional integrals and derivatives have various definitions and take various names in the literature, mostly because of variations in the initial conditions associated with them [15]. While some are physically interpretable, others are simply more amenable to mathematical analysis. There are many problems in physics and engineering formulated in terms of fractional differential and integral equations, such as diffusion, signal processing, electrochemistry, viscosity etc. The exact and approximate solutions of fractional differential equations are investigated by many authors using different methods. The Sumudu transform method is applied to obtain the solution of ordinary differential equations [9]

The paper is organised as follows : In section two, some preliminary results and notation are given including special function such as Mittag-Leffler function and Wright function. Some basic definitions such as Fourier transform and convolution are also discussed. In section three, apply Sumudu transform method, solution of Cauchy problems for diffusion wave is obtained. Some illustrative examples are discussed in section four and useful conclusion are discussed in the last section.

2 Preliminary Results, Notations and Terminology

In this section we give definitions and some basic results which are used in the paper.

Consider the general linear fractional partial differential equation [11]

Definition 2.1

$$(D_{o+,t}^{\alpha} u)(x,t) = \sum_{j=1}^{n} a_j D_{x_j}^{\delta_j} u(x,t) + \sum_{j=1}^{n} b_j D_{x_j}^{\beta_j} u(x,t) + \sum_{j=1}^{n} c_j D_{x_j}^{\gamma_j} u(x,t) + du(x,t);$$

(2.1)

$$n - 1 < \alpha \le n, 2 < \delta_j \le 3, 1 < \beta_j \le 2, 0 < \gamma_j \le 1, n \in \mathbb{N}$$

where $x = (x_1, x_2, \ldots, x_n) \in \mathbb{R}^n, a_j, b_j c_j, d$ are non-negative real constants, $o \le t < T$

The fractional diffusion equation is of the form

$$(D_{o+,t} u)(x,t) = \sum_{j=1}^{n} b_j D_{x_j}^{\beta_j} u(x,t)$$

(2.2)

$$n - 1 < \alpha \le n, 1 < \beta_j \le 2, n \in \mathbb{N}$$

Definition 2.2 *[12] The Riemann-Liouville fractional integral of order* $\alpha, \alpha > 0$ *of a function* $u(x,t)$ *is denoted by* $I_{0+t}^{\alpha} u(x,t)$ *and defined as*

$$I_{0+t}^{\alpha} u(x,t) = \frac{1}{\Gamma(\alpha)} \int_0^t (t-\tau)^{\alpha-1} u(x,\tau) d\tau, \quad t > 0, \alpha > 0 \qquad (2.3)$$

Definition 2.3 *[12]The Riemann-Liouville fractional derivative of order* $\alpha, \alpha > 0$ *of a function* $u(x,t)$ *is denoted by* $D_{0+t}^{\alpha} u(x,t)$ *and defined as*

$$D_{0+t}^{\alpha} u(x,t) = \left(\frac{\partial}{\partial t}\right)^{[\alpha]+1} \frac{1}{\Gamma(1-\{\alpha\})} \int_0^t \frac{u(x,\tau)}{(t-\tau)^{\{\alpha\}}} d\tau, \quad (x \in \mathbb{R}, t > 0, \alpha > 0) \qquad (2.4)$$

where $[\alpha]$ means that integral part of real α and $\{\alpha\}$ means that fractional part of real α.

2.1 Mittag-Leffler Function :

The Mittag-Leffler function is introduced by Mittag-Leffler and is denoted by $E_{\alpha}(z)$ [10]. It is one parameter generalization of exponential function and is defined as,

$$E_{\alpha}(z) = \sum_{k=0}^{\infty} \frac{z^k}{\Gamma(\alpha k + 1)}, \quad \alpha \in C, \ Re(\alpha) > 0. \qquad (2.5)$$

A two-parameter Mittag-Leffler function is introduced by Agarwal [3], denoted by $E_{\alpha,\beta}(z)$, is defined as,

$$E_{\alpha,\beta}(z) = \sum_{k=0}^{\infty} \frac{z^k}{\Gamma(\alpha k + \beta)}, \quad \alpha > 0, \ \beta > 0. \qquad (2.6)$$

2.2 Wright Function :

The Wright function is introduced by Wright which is denoted by $\phi(\alpha, \beta; z)$ [12] and it is a generalization of Mittag-Leffler function and is defined as,

$$\phi(\alpha, \beta; z) = {}_0\Psi_1 \left[\begin{array}{c} ------- \\ (\beta, \alpha) \end{array} \middle| z \right] = \sum_{k=0}^{\infty} \frac{1}{\Gamma(\alpha k + \beta)} \frac{z^k}{k!} \qquad (2.7)$$

The more general Wright function ${}_p\Psi_q(z) \ z, a_l, b_j \in \mathbb{C}$ and $\alpha_l, \beta_j \in \mathbb{R}$ $(l = 1, 2, \ldots, p \, ; \, j = 1, 2, \ldots, q)$ is defined by the series

$$_P\Psi_q(z) = {}_1\Psi_1 \left[\begin{array}{c} (a_l, \alpha_l)_{1,p} \\ (b_l, \beta_l)_{1,q} \end{array} \middle| z \right] = \sum_{k=0}^{\infty} \frac{\Pi_{l=1}^p \Gamma(a_l + \alpha_l k)}{\Pi_{j=1}^q \Gamma(b_j + \beta_j k)} \cdot \frac{z^k}{k!} \qquad (2.8)$$

The Wright function with $p = q = 1$ of the form

$$_1\Psi_1\begin{bmatrix} (n+1,n) \\ (an+\beta,\alpha) \end{bmatrix} z \end{bmatrix} = \sum_{j=0}^{\infty} \frac{\Gamma(n+j+1)}{\Gamma(an+\beta+\alpha j)} \cdot \frac{z^j}{j!} = \left(\frac{\partial}{\partial z}\right)^n E_{\alpha,\beta}(z). \qquad (2.9)$$

Consider a set A defined as [16]

$$A = \{f(t)| \exists M, \tau_1, \tau_2 > 0, |f(t)| \le Me^{\frac{|t|}{\tau_j}} \text{ if } t \in (-1)^j \times [0, \infty)\}.$$

Definition 2.4 *For all real $t \ge 0$, the Sumudu transform of a function $u \in A$, with respect to t denoted by $(S_t u)(x, p)$, is defined as*

$$(S_t u)(x,p) = \int_0^{\infty} u(x,t)pe^{pt}dt, \quad u \in (-\tau_1, \tau_2), \quad where \quad \left(p = -\frac{1}{u}\right) \qquad (x \in \mathbb{R}; p > 0) \tag{2.10}$$

and the inverse Sumudu transform with respect to p is

$$(S_p^{-1}u)(x,p) = \frac{1}{2\pi}\int_{\gamma-i\infty}^{\gamma+i\infty} e^{pt}u(x,p)dp, \quad (x \in \mathbb{R}; \gamma = \Re(p) > \sigma u). \tag{2.11}$$

[13]The Sumudu transform of the Riemann-Liouville fractional partial derivative of order $\alpha, \alpha > 0$ of a function $u(x,t)$ is denoted by $D_{0+,t}^{\alpha}u(x,t)$ and defined as

$$(S_t D_{0+,t}^{\alpha}u)(x,p) = p^{\alpha}(Su)(x,p) - \sum_{j=1}^{l} p^{j-1}(D_{0+,t}^{\alpha-j}u)(x,0+) \tag{2.12}$$

with $x \in \mathbb{R}, l-1 < \alpha \le l$ and $n \in \mathbb{N}$.

Definition 2.5 *[12]The Fourier transform of a function u with respect to $x \in \mathbb{R}$ denoted by $(F_x u)(\sigma, t)$ is defined as*

$$(F_x u)(\sigma,t) = \int_{-\infty}^{\infty} u(x,t)e^{ix\sigma}dx, \quad (\sigma \in \mathbb{R}; t > 0) \tag{2.13}$$

and the inverse of the Fourier transform of $u(x,t)$ with respect to σ is

$$(F_\sigma^{-1}u)(x,t) = \frac{1}{2\pi}\int_{-\infty}^{\infty} u(\sigma,t)e^{-i\sigma x}d\sigma. \tag{2.14}$$

The relation with respect to $x \in \mathbb{R}$, we have

$$F[D^k\phi(t)](x) = (-ix)^k(F\phi) \quad (k \in \mathbb{N}) \tag{2.15}$$

and the Fourier convolution operator of two functions f and g is defined by the integral

$$f * g = (f * g)(x) = \int_{-\infty}^{\infty} f(x-t)g(t)dt. \tag{2.16}$$

3   Solution of Cauchy Type Problems for Fractional Diffusion-Wave Equations With Riemann-Liouville derivatie :

In this section we apply the Sumudu transform to the fractional diffusion-wave equations with Reimann-Liouville fractional derivative. We consider a fractional differential equation of the form

$$(D_{0+,t}^{\alpha}u)(x,t) = \lambda^2 \frac{\partial^2 u(x,t)}{\partial x^2} \quad (x \in \mathbb{R}; t > 0; \lambda > 0) \qquad (3.1)$$

known as the fractional diffusion-wave equation. Now we apply the Fourier and Sumudu transform to obtain the explicit solution of equation (3.1) with the Cauchy type initial conditions.

$$(D_{0+,t}^{\alpha-k}u)(x,0+) = f_k(x) \qquad (3.2)$$

where $k = 1$ for $0 < \alpha \le 1$ and $k = 2$ for $1 < \alpha < 2$.

Lemma 3.1 *The equation (3.1) of order$\alpha, 0 < \alpha < 2$ with the Cauchy type initial conditions (3.2) is solvable, and its solution $u(x,t)$ is given by*

$$u(x,t) = \frac{1}{2\lambda} t^{\frac{\alpha}{2}-k} \phi(-\frac{\alpha}{2}; \frac{\alpha}{2} - k + 1; -\frac{|x|}{\lambda} t^{-\frac{\alpha}{2}}) \quad for(k = 1,2) \qquad (3.3)$$

where $k = 1$ for $0 < \alpha \le 1$ and $k = 2$ for $1 < \alpha < 2$.

Proof : Applying the Sumudu transform (2.10) to equation (3.1) using the formula (2.12) with respect t and the initial conditions (3.2), we obtain

$$p^{\alpha}(S_t u)(x,p) = \sum_{k=1}^{l} p^{k-1} f_k(x) + \lambda^2 \left(\frac{\partial^2}{\partial x^2} S_t u \right)(x,p) \quad (l = 1,2)$$

Using (2.15), with $k = 2$, we have

$$\left(F_x [\frac{\partial^2 u(x,t)}{\partial x^2}] \right)(\sigma, t) = -|\sigma|^2 (F_x u)(\sigma, t), \qquad (3.4)$$

By applying Fourier transform (2.13) and using equation (3.4), we obtain

$$p^{\alpha}(F_x S_t u)(\sigma, p) = \sum_{k=1}^{l} p^{k-1}(F_x f_k)(\sigma) - \lambda^2 |\sigma|^2 (F_x S_t u)(\sigma, p)$$

$$(F_x S_t u)(\sigma, p) = \sum_{k=1}^{l} \frac{p^{k-1}}{p^{\alpha} + \lambda^2 |\sigma|^2} (F_x f_k)(\sigma), \quad (\sigma \in \mathbb{R}, t > 0, l = 1,2). \qquad (3.5)$$

Now, we obtain the explicit solution $u(x,t)$ by using the inverse Fourier transform (2.14) with respect to σ and the inverse Sumudu transform (2.11) with respect to p. The Fourier and Sumudu transform of

$$(F_x e^{-c|x|})(\sigma) = \frac{2c}{c^2 + |\sigma|^2} \quad (\sigma \in \mathbb{R}; c > 0)$$

and

$$(Fe^{-\frac{|x|}{\lambda}p^{\frac{\alpha}{2}}}) = \frac{2\lambda p^{\frac{\alpha}{2}}}{p^\alpha + \lambda^2|\sigma|^2}$$

so that equation (3.5) becomes

$$(F_x S_t u)(\sigma, p) = \left(F_x \sum_{k=1}^{l} \left[\frac{1}{2\lambda}p^{k-1-\frac{\alpha}{2}}e^{-\frac{|x|}{\lambda}p^{\frac{\alpha}{2}}}\right]\right)(\sigma)(F_x f_k)(\sigma) \quad (l = 1, 2)$$

By using the convolution property of Fourier transform (2.16)

$$(F_x S_t u)(\sigma, p) = \left(F_x \sum_{k=1}^{l} \left[\frac{1}{2\lambda}p^{k-1-\frac{\alpha}{2}}e^{-\frac{|x|}{\lambda}p^{\frac{\alpha}{2}}} * x f_k(x)\right]\right)(\sigma) \qquad (3.6)$$

By taking the inverse Fourier transform (2.13), we get

$$(S_t u)(x, p) = \left(\sum_{k=1}^{l} \left[\frac{1}{2\lambda}p^{k-1-\frac{\alpha}{2}}e^{-\frac{|x|}{\lambda}p^{\frac{\alpha}{2}}} x f_k(x)\right]\right)(x, p) \quad (x \in \mathbb{R}, p > 0; l = 1, 2)$$

$$(3.7)$$

Now, applying the inverse Sumudu transform to equation (2.11), we can obtain the explicit solution to the Cauchy type problem (3.1) and (3.2). We can find the inverse Sumudu transform of the function $p^{k-1-\frac{\alpha}{2}}e^{-\frac{|x|}{\lambda}p^{\frac{\alpha}{2}}}(k = 1, 2)$. This functions can be expressed in terms of Wright function (2.7) through Sumudu transform of the form $\phi(-\frac{\alpha}{2}, b_j, -z)$. If $0 < \alpha < 2$ then $\phi(-\frac{\alpha}{2}, b_j, -z)$ is an entire function of z. By definition of Sumudum transform (2.10) and Wright function (2.7)

$$\left(S_t\left[t^{\frac{\alpha}{2}-k}\phi(-\frac{\alpha}{2}; \frac{\alpha}{2} - k + 1; -\frac{|x|}{\lambda}t^{-\frac{\alpha}{2}})\right]\right)(p) = p^{k-1-\frac{\alpha}{2}}e^{-\frac{|x|}{\lambda}p^{\frac{\alpha}{2}}} \quad for(k = 1, 2) \quad (3.8)$$

By using the inverse Sumudu transform of equation (2.11) and using the equations (3.8) and(3.7), we get

$$u(x,t) = \frac{1}{2\lambda}t^{\frac{\alpha}{2}-k}\phi(-\frac{\alpha}{2}; \frac{\alpha}{2} - k + 1; -\frac{|x|}{\lambda}t^{-\frac{\alpha}{2}}) \quad for(k = 1, 2)$$

Theorem 3.1 *If $0 < \alpha < 2$ and $\lambda > 0$, then the Cauchy type problem (3.1) and (3.2) is solvable and its solution is given by*

$$u(x,t) = \sum_{k=1}^{l} \int_{-\infty}^{\infty} G_k^\alpha(x-\tau, t)f_k(\tau)d\tau \quad (l = 1 for \quad 0 < \alpha \le 1; l = 2 for \quad 1 < \alpha < 2)$$

$$(3.9)$$

where

$$G_k^\alpha(x,t) = \frac{1}{2\lambda} t^{\frac{\alpha}{2}-k} \phi\left(-\frac{\alpha}{2}; \frac{\alpha}{2}-k+1; -\frac{|x|}{\lambda}t^{-\frac{\alpha}{2}}\right) \quad for \quad (k=1,2)$$

provided that integral in the right-hand side of (3.9) are convergent.

Proof: Applying the Sumudu transform (2.10) to equation (3.1) using the formula (2.12) with respect t and the initial conditions (3.2), we obtain

$$p^\alpha(S_l u)(x,p) = \sum_{k=1}^{l} p^{k-1} f_k(x) + \lambda^2\left(\frac{\partial^2}{\partial x^2} S_l u\right)(x,p) \quad (l=1,2)$$

Using (2.15), with $k=2$, we have

$$\left(F_x\left[\frac{\partial^2 u(x,t)}{\partial x^2}\right]\right)(\sigma,t) = -|\sigma|^2 (F_x u)(\sigma,t), \tag{3.10}$$

By applying Fourier transform on equation (2.13) and using equation (3.10), we obtain

$$p^\alpha(F_x S_l u)(\sigma,p) = \sum_{k=1}^{l} p^{k-1}(F_x f_k)(\sigma) - \lambda^2|\sigma|^2(F_x S_l u)(\sigma,p)$$

$$(F_x S_l u)(\sigma,p) = \sum_{k=1}^{l} \frac{p^{k-1}}{p^\alpha + \lambda^2|\sigma|^2}(F_x f_k)(\sigma),, \quad (\sigma \in \mathbb{R}, t>0, l=1,2). \tag{3.11}$$

Now, we obtain the explicit solution $u(x,t)$ by using the inverse Fourier transform (2.14) with respect to σ and the inverse Sumudu transform (2.11) with respect to p. The Fourier and Sumudu transform of

$$(F_x e^{-c|x|})(\sigma) = \frac{2c}{c^2 + |\sigma|^2} \quad (\sigma \in \mathbb{R}; c>0)$$

and

$$(Fe^{-\frac{|x|}{\lambda}} p^{\frac{\alpha}{2}}) = \frac{2\lambda p^{\frac{\alpha}{2}}}{p^\alpha + \lambda^2|\sigma|^2}$$

so that equation (3.11) becomes

$$(F_x S_l u)(\sigma,p) = \left(F_x \sum_{k=1}^{l}\left[\frac{1}{2\lambda} p^{k-1-\frac{\alpha}{2}} e^{-\frac{|x|}{\lambda} p^{\frac{\alpha}{2}}}\right]\right)(\sigma)(F_x f_k)(\sigma) \quad (l=1,2)$$

By using the convolution property of Fourier transform (2.16)

$$(F_x S_l u)(\sigma,p) = \left(F_x \sum_{k=1}^{l}\left[\frac{1}{2\lambda} p^{k-1-\frac{\alpha}{2}} e^{-\frac{|x|}{\lambda} p^{\frac{\alpha}{2}}} * x f_k(x)\right]\right)(\sigma) \tag{3.12}$$

By taking the inverse Fourier transform (2.13), we get

$$(S_t u)(x,p) = \left(\sum_{k=1}^{l} \left[\frac{1}{2\lambda} p^{k-1-\frac{\alpha}{2}} e^{-\frac{|x|}{\lambda} p^{\frac{\alpha}{2}}} x f_k(x) \right] \right)(x,p) \qquad (3.13)$$

Thus, we have

$$u(x,t) = \sum_{k=1}^{l} \int_{-\infty}^{\infty} G_k^{\alpha}(x-\tau,t) f_k(\tau) d\tau \qquad (3.14)$$

where $G^{\alpha}(x,t)$ is the green function can be written as

$$G^{\alpha}(x,t) = \frac{1}{\pi} \int_{-\infty}^{\infty} \sum_{k=1}^{l} \frac{1}{2\lambda} p^{k-1-\frac{\alpha}{2}} e^{-\frac{|x|}{\lambda} p^{\frac{\alpha}{2}}} x f_k(x) dp \qquad (3.15)$$

To obtain the solution in terms of $G^{\alpha}(x,t)$,we have to apply the inverse Sumudu transform to (3.15) we get, the inverse Sumudu transform of the function $p^{k-1-\frac{\alpha}{2}} e^{-\frac{|x|}{\lambda} p^{\frac{\alpha}{2}}}$ ($k = 1,2$) is given in terms of the Wright function of the form $\phi(-\frac{\alpha}{2}, b_j, -z)$. If $0 < \alpha < 2$ then $\phi(-\frac{\alpha}{2}, b_j, -z)$ is an entire function of z.

$$\left(S_t \left[t^{\frac{\alpha}{2}-k} \phi(-\frac{\alpha}{2}; \frac{\alpha}{2} - k + 1; -\frac{|x|}{\lambda} t^{-\frac{\alpha}{2}}) \right] \right)(p) = p^{k-1-\frac{\alpha}{2}} e^{-\frac{|x|}{\lambda} p^{\frac{\alpha}{2}}} \quad \text{for}(k = 1,2)$$

where

$$G_k^{\alpha}(x,t) = \frac{1}{2\lambda} t^{\frac{\alpha}{2}-k} \phi\left(-\frac{\alpha}{2}; \frac{\alpha}{2} - k + 1; -\frac{|x|}{\lambda} t^{-\frac{\alpha}{2}} \right) \quad \text{for}(k = 1,2)$$

Corollary 3.1 *If $0 < \alpha < 2$ and $\lambda > 0$, then the Cauchy type problem*

$$(D_{0+,t}^{\alpha} u)(x,t) = \lambda^2 \frac{\partial^2 u(x,t)}{\partial x^2} \quad (x \in \mathbb{R}; t > 0)$$
$$(D_{0+,t}^{\alpha-1} u)(x,0+) = f(x) \qquad (3.16)$$

is solvable, and its solution has the form

$$u(x,t) = \int_{-\infty}^{\infty} G_1^{\alpha}(x-\tau,t) f_1(\tau) d\tau \qquad (3.17)$$

where

$$G_1^{\alpha}(x,t) = \frac{1}{2\lambda} t^{\frac{\alpha}{2}-1} \phi\left(-\frac{\alpha}{2}; \frac{\alpha}{2}; -\frac{|x|}{\lambda} t^{-\frac{\alpha}{2}} \right) \qquad (3.18)$$

provided that the integral in the right-hand side of (3.17) is convergent.

Corollary 3.2 *If $0 < \alpha < 2$ and $\lambda > 0$, then the Cauchy type problem*

$$(D_{0+,t}^{\alpha}u)(x,t) = \lambda^2 \frac{\partial^2 u(x,t)}{\partial x^2} \quad (x \in \mathbb{R}; t > 0) \tag{3.19}$$

$$(D_{0+,t}^{\alpha-1}u)(x,0+) = f_1(x)$$
$$(D_{0+,t}^{\alpha-2}u)(x,0+) = f_2(x) \quad (x \in \mathbb{R}) \tag{3.20}$$

is solvable, and its solution has the form

$$u(x,t) = \int_{-\infty}^{\infty} G_1^{\alpha}(x-\tau,t)f_1(\tau)d\tau + \int_{-\infty}^{\infty} G_2^{\alpha}(x-\tau,t)f_2(\tau)d\tau \tag{3.21}$$

where

$$G_1^{\alpha}(x,t) = \frac{1}{2\lambda}t^{\frac{\alpha}{2}-1}\phi\left(-\frac{\alpha}{2}; \frac{\alpha}{2}; -\frac{|x|}{\lambda}t^{-\frac{\alpha}{2}}\right) \tag{3.22}$$

and

$$G_2^{\alpha}(x,t) = \frac{1}{2\lambda}t^{\frac{\alpha}{2}-2}\phi\left(-\frac{\alpha}{2}; \frac{\alpha}{2}-1; -\frac{|x|}{\lambda}t^{-\frac{\alpha}{2}}\right) \tag{3.23}$$

provided that the integral in the right-hand side of (3.21) is convergent.

4 Illustrative Examples :

Example 4.1 *Solve the following Cauchy type problem with $\alpha = \frac{1}{2}$*

$$(D_{0+,t}^{\frac{1}{2}}u)(x,t) = \lambda^2 \frac{\partial^2 u(x,t)}{\partial x^2} \quad (x \in \mathbb{R}; t > 0) \tag{4.1}$$
$$(D_{0+,t}^{-\frac{1}{2}}u)(x,0+) = f(x).$$

has its solution given by

$$u(x,t) = \int_{-\infty}^{\infty} G_1^{\frac{1}{2}}(x-\tau,t)f_1(\tau)d\tau \tag{4.2}$$

where

$$G_1^{\frac{1}{2}}(x,t) = \frac{1}{2\lambda}t^{-\frac{3}{4}}\phi\left(-\frac{1}{4}; \frac{1}{4}; -\frac{|x|}{\lambda}t^{-\frac{1}{4}}\right) \tag{4.3}$$

Applying Sumudu transform to (4.1) and using the initial condition with respect to t we obtain

$$S[(D_{0+,t}^{\frac{1}{2}}u)(x,p)] = \lambda^2\left(\frac{\partial^2}{\partial x^2}S_t u\right)(x,p) \quad (l = 1) \tag{4.4}$$

Using (2.12), we obtain

$$p^{\frac{1}{2}}(S_l u)(x, p) = f(x) + \lambda^2 \left(\frac{\partial^2}{\partial x^2} S_l u\right)(x, p) \tag{4.5}$$

Now, applying the Fourier transform (2.13) and using the formula (2.15) with $k = 2$, we have

$$\left(F_x\left[\frac{\partial^2 u(x,t)}{\partial x^2}\right]\right)(\sigma, t) = -|\sigma|^2 (F_x u)(\sigma, t), \tag{4.6}$$

By applying Fourier transform (2.13) and using equation (4.6), we obtain

$$p^{\frac{1}{2}}(F_x S_l u)(\sigma, p) = \sum_{k=1}^{l} p^{k-1}(F_x f(x))(\sigma) - \lambda^2 |\sigma|^2 (F_x S_l u)(\sigma, p)$$

$$(F_x S_l u)(\sigma, p) = \frac{1}{p^{\frac{1}{2}} + \lambda^2 |\sigma|^2}(F_x f(x))(\sigma) \quad (x \in \mathbb{R}; t > 0; l = 1) \tag{4.7}$$

Now, we obtain the explicit solution $u(x, t)$ by using the inverse Fourier transform (2.14) with respect to σ and the inverse Sumudu transform (2.11) with respect to p. The Fourier and Sumudu transform of

$$(F_x e^{-c|x|})(\sigma) = \frac{2c}{c^2 + |\sigma|^2} \quad (\sigma \in \mathbb{R}; c > 0)$$

and

$$(F e^{-\frac{|x|}{\lambda} p^{\frac{1}{4}}}) = \frac{2\lambda p^{\frac{1}{4}}}{p^{\frac{1}{2}} + \lambda^2 |\sigma|^2}$$

so that equation (4.5) becomes

$$(F_x S_l u)(\sigma, p) = (F_x[\frac{1}{2\lambda} p^{-\frac{1}{4}} e^{-\frac{|x|}{\lambda} p^{\frac{1}{4}}}])(\sigma)(F_x f(x))(\sigma) \quad (l = 1) \tag{4.8}$$

use the convolution property of Fourier transform (2.16), we get

$$(F_x S_l u)(\sigma, p) = (F_x[\frac{1}{2\lambda} p^{-\frac{1}{4}} e^{-\frac{|x|}{\lambda} p^{\frac{1}{4}}} * x f(x)])(\sigma) \quad (l = 1)$$

By taking inverse of Fourier transform (2.14) we get

$$(S_l u)(x, p) = (\frac{1}{2\lambda} p^{-\frac{1}{4}} e^{-\frac{|x|}{\lambda} p^{\frac{1}{4}}} * x f(x))(\sigma) \quad (x \in \mathbb{R}, p > 0, l = 1)$$

Thus,we get

$$u(x, t) = \int_{-\infty}^{\infty} G_l^{\frac{1}{2}}(x - \tau, t) f_1(\tau) d\tau$$

where $G_1^{\frac{1}{2}}(x,t)$ is the Green function can be written as

$$G_1^{\frac{1}{2}}(x,t) = \frac{1}{\pi}\int_{-\infty}^{\infty}\frac{1}{2\lambda}p^{-\frac{1}{4}}e^{-\frac{|x|}{\lambda}p^{\frac{1}{4}}} * xf(x)dp \qquad (4.9)$$

To obtain the solution of $G_1^{\frac{1}{2}}(x,t)$, we apply the the inverse Sumudu transform to (4.7) and the inverse Sumdu transform of the function $p^{-\frac{1}{4}}e^{-\frac{|x|}{\lambda}p^{\frac{1}{4}}}$ is given in terms of Wright function of the form $\phi(-\frac{1}{4}, b_j, -z)$. If $0 < \alpha \le 1$ then $\phi(-\frac{1}{4}, b_j, -z)$ is an entire function of z

$$\left(S_l[t^{-\frac{3}{4}}\phi(-\frac{1}{4};\frac{1}{4};-\frac{|x|}{\lambda}t^{-\frac{1}{4}})]\right)(p) = p^{-\frac{1}{4}}e^{-\frac{|x|}{\lambda}p^{\frac{1}{4}}} \quad \text{for}(k=1)$$

where

$$G_1^{\frac{1}{2}}(x,t) = \frac{1}{2\lambda}t^{-\frac{3}{4}}\phi\left(-\frac{1}{4};\frac{1}{4};-\frac{|x|}{\lambda}t^{-\frac{1}{4}}\right) \quad \text{for}(k=1)$$

Example 4.2 *Solve the following Cauchy type problem with* $\alpha = \frac{3}{2}$

$$(D_{0+,t}^{\frac{3}{2}}u)(x,t) = \lambda^2\frac{\partial^2 u(x,t)}{\partial x^2} \qquad (x \in \mathbb{R}; t > 0) \qquad (4.10)$$

$$(D_{0+,t}^{\frac{1}{2}}u)(x,0+) = f_1(x)$$
$$(D_{0+,t}^{-\frac{1}{2}}u)(x,0+) = f_2(x) \qquad (x \in \mathbb{R}) \qquad (4.11)$$

has its solution given by

$$u(x,t) = \int_{-\infty}^{\infty}G_1^{\frac{3}{2}}(x-\tau,t)f_1(\tau)d\tau + \int_{-\infty}^{\infty}G_2^{\frac{3}{2}}(x-\tau,t)f_2(\tau)d\tau \qquad (4.12)$$

where

$$G_1^{\frac{3}{2}}(x,t) = \frac{1}{2\lambda}t^{-\frac{1}{4}}\phi\left(-\frac{3}{4};\frac{3}{4};-\frac{|x|}{\lambda}t^{-\frac{3}{4}}\right) \qquad (4.13)$$

and

$$G_2^{\frac{3}{2}}(x,t) = \frac{1}{2\lambda}t^{-\frac{5}{4}}\phi\left(-\frac{3}{4};-\frac{1}{4};-\frac{|x|}{\lambda}t^{-\frac{3}{4}}\right) \qquad (4.14)$$

Applying Sumudu transform to (4.10) and using the initial condition (4.11), with respect to t, we obtain

$$S[(D_{0+,t}^{\frac{3}{2}}u)(x,p)] = \lambda^2\left(\frac{\partial^2}{\partial x^2}S_l u\right)(x,p) \quad (l=1,2) \qquad (4.15)$$

Using (2.12), we obtain

$$(S_t D_{0+,t}^{\frac{3}{2}} u)(x,p) = p^{\frac{3}{2}}(Su)(x,p) - (D_{0+,t}^{\frac{1}{2}}(Su))(x,0+) - p(D_{0+,t}^{-\frac{1}{2}}(Su))(x,0+) + \lambda^2(Su)(x,p)$$

$$p^{\frac{3}{2}}(Su)(x,p) = f_1(x) + p f_2(x) + \lambda^2(Su)(x,p) \qquad (4.16)$$

Now, applying the Fourier transform (2.13) and using the formula (2.15) with $k = 2$, we have

$$\left(F_x\left[\frac{\partial^2 u(x,t)}{\partial x^2}\right]\right)(\sigma,t) = -|\sigma|^2(F_x u)(\sigma,t), \qquad (4.17)$$

By applying Fourier transform on equation(2.13) and using equation (4.17), we obtain

$$(F_x S_t u)(\sigma,p) = \frac{f_1(x)}{p^{\frac{3}{2}} + \lambda^2|\sigma|^2} + p\frac{f_2(x)}{p^{\frac{3}{2}} + \lambda^2|\sigma|^2}(F_x f(x))(\sigma) \qquad (4.18)$$

Now, we obtain the explicit solution $u(x,t)$ by using the inverse Fourier transform (2.14) with respect to σ and the inverse Sumudu transform (2.11) with respect to p. The Fourier and Sumudu transform of

$$(F_x e^{-c|x|})(\sigma) = \frac{2c}{c^2 + |\sigma|^2} \qquad (\sigma \in \mathbb{R}; c > 0)$$

and

$$\left(Fe^{-\frac{|x|}{\lambda}p^{\frac{3}{4}}}\right) = \frac{2\lambda p^{\frac{3}{4}}}{p^{\frac{3}{2}} + \lambda^2|\sigma|^2}$$

so that equation (4.18) becomes

$$(F_x S_t u)(\sigma,p) = \left(F_x \sum_{k=1}^{2}\left[\frac{1}{2\lambda}p^{k-1-\frac{a}{2}}e^{-\frac{|x|}{\lambda}p^{\frac{a}{2}}}\right]\right)(\sigma)(F_x f_k)(\sigma)$$

$$(F_x S_t u)(\sigma,p) = \left(F_x\left[\frac{1}{2\lambda}p^{-\frac{3}{4}}e^{-\frac{|x|}{\lambda}p^{\frac{3}{4}}}\right]\right)(\sigma)(F_x f_1)(\sigma) + \left(F_x\left[\frac{1}{2\lambda}p^{\frac{1}{4}}e^{-\frac{|x|}{\lambda}p^{\frac{3}{4}}}\right]\right)(\sigma)(F_x f_2)(\sigma)$$

By using the convolution property of Fourier transform (2.16), we obtain

$$(F_x S_t u)(\sigma,p) = \left(F_x\left[\frac{1}{2\lambda}p^{-\frac{3}{4}}e^{-\frac{|x|}{\lambda}p^{\frac{3}{4}}} * x f_1(x)\right]\right)(\sigma)(F_x f_1)(\sigma) + \left(F_x\left[\frac{1}{2\lambda}p^{\frac{1}{4}}e^{-\frac{|x|}{\lambda}p^{\frac{3}{4}}} * x f_2(x)\right]\right)(\sigma)(F_x f_2)(\sigma)$$

Now applying the inverse Fourier transform (2.14), we get

$$(S_t u)(x, p) = \left(\left[\frac{1}{2\lambda} p^{-\frac{3}{4}} e^{-\frac{|x|}{\lambda} p^{\frac{3}{4}}} * x f_1(x) \right] \right) + \left(\left[\frac{1}{2\lambda} p^{\frac{1}{4}} e^{-\frac{|x|}{\lambda} p^{\frac{3}{4}}} * x f_2(x) \right] \right). \tag{4.19}$$

Thus,we get

$$u(x, t) = \int_{-\infty}^{\infty} G_1^{\frac{3}{2}}(x - \tau, t) f_1(\tau) d\tau + \int_{-\infty}^{\infty} G_2^{\frac{3}{2}}(x - \tau, t) f_2(\tau) d\tau$$

where $G_1^{\frac{3}{2}}(x, t)$ and $G_2^{\frac{3}{2}}(x, t)$ is the Green function can be written as

$$G_1^{\frac{3}{2}}(x, t) = \frac{1}{\pi} \int_{-\infty}^{\infty} \frac{1}{2\lambda} p^{-\frac{3}{4}} e^{\frac{-|x|}{\lambda} p^{\frac{3}{4}}} * x f_2(x) dp$$

and

$$G_2^{\frac{3}{2}}(x, t) = \frac{1}{\pi} \int_{-\infty}^{\infty} \frac{1}{2\lambda} p^{\frac{1}{4}} e^{-\frac{|x|}{\lambda} p^{\frac{3}{4}}} * x f_1(x) dp$$

Applying the inverse Sumudu transform to (4.19), we can obtain the explicit solution to the Cauchy type problem (4.10) and (4.11). To obtain the solution of $G_1^{\frac{3}{2}}(x, t)$ and $G_2^{\frac{3}{2}}(x, t)$ we apply the the inverse Sumudu transform to (4.16) and the inverse Sumdu transform of the function $p^{-\frac{3}{4}} e^{-\frac{|x|}{\lambda} p^{\frac{3}{4}}}$ and $p^{\frac{1}{4}} e^{-\frac{|x|}{\lambda} p^{\frac{3}{4}}}$ is given in terms of Wright function of the form $\phi(-\frac{3}{4}, b_j, -z)$ and $\phi(\frac{1}{4}, b_j, -z)$. If $0 < \alpha \leq 1$ then $\phi(-\frac{3}{4}, b_j, -z)$ and $\phi(\frac{1}{4}, b_j, -z)$ is an entire function of z.

$$\left(S_t [t^{-\frac{1}{4}} \phi(-\frac{1}{4}; \frac{3}{4}; -\frac{|x|}{\lambda} t^{-\frac{1}{4}})] \right)(p) + \left(S_t [t^{-\frac{5}{4}} \phi(-\frac{1}{4}; -\frac{1}{4}; -\frac{|x|}{\lambda} t^{-\frac{1}{4}})] \right)(p) =$$

$$p^{-\frac{3}{4}} e^{-\frac{|x|}{\lambda} p^{\frac{3}{4}}} + p^{\frac{1}{4}} e^{-\frac{|x|}{\lambda} p^{\frac{3}{4}}} \quad for(k = 1, 2)$$

where

$$G_1^{\frac{3}{2}}(x, t) = \frac{1}{2\lambda} t^{-\frac{1}{4}} \phi\left(-\frac{3}{4}; \frac{3}{4}; -\frac{|x|}{\lambda} t^{-\frac{3}{4}} \right) \quad for(k = 1)$$

and

$$G_2^{\frac{3}{2}}(x, t) = \frac{1}{2\lambda} t^{-\frac{5}{4}} \phi\left(-\frac{3}{4}; -\frac{1}{4}; -\frac{|x|}{\lambda} t^{-\frac{3}{4}} \right) \quad for(k = 2)$$

5   Conclusion

In this paper, Sumudu transform of Riemann-Liouville fractional derivatives have been used to solve fractional diffusion-wave equations. The solution of fractional diffusion-wave equations is obtained in terms of Mittag-Leffler function and gener- alized Wright function. The Sumudu transform and Fourier transform is an useful operational transform method which is an important in treating fractional diffusion- wave equations. The Sumudu transform and Fourier transform technique can be used to solve many types of initial value problems in applied and engineering fields.

References

[1]. Asiru M.A ; Application of the Sumudu Transform to Discrete Dynamical Systems,International Journal of Mathematical Education, Science and Tech- nology, Vol.34, No. 6, (2003) 944-949.

[2]. Asiru M.A ; Further Properties of the Sumudu Transform and its Applica- tions, International Journal of Mathematical Education, Science and Technol- ogy Vol.33, No. 2,(2002) 441-449.

[3]. Agarwal.R.P; A propos d'unc note de M.Pierre Humbert, C. R.Se'ances Acad. Sci.,vol. 236, no. 21, 1953, pp. 2031-2032.

[4]. Belgacem, F.B.M.;Sumudu Transform Applications to Bessel Functions and Equations, Applied Mathematical Sciences, Vol. 4, No. 74, (2010) 3365-3686.

[5]. Belgacem, F.B.M.;Sumudu Applications to Maxwell's Equations, Progress in Electromagnetic Research Seminars Online, Vol. 5, (2009) 1-6.

[6]. Belgacem, F.B.M.;Introducing and Analyzing Deeper Sumudu Properties, Non- linear Studies Journal, Vol.13, No. 1, (2006) 23-41

[7]. Belgacem F.B.M, Karaballi A.A ; Sumudu transform fundamental properties investigations and applications, Journal of Applied Mathematics and Stochastic Analysis,Vol. 2006, pp. 1-23, Article ID 91083(2006).

[8]. Belgacem F.B.M, Karaballi A.A, and Kalla S.L ;Analytical investigations of the Sumudu transform and applications to integral production equations, Math- ematical Problems in Engineering, Vol.No. 3, pp.103-108,(2003)

[9]. Bulut. H, Baskonus H. M, Belgacem F.B.M, ; The Analytical solution of some fractional ordinary differential equations by the Sumudu transform method, Ab- stract and Applied Analysis, 2013, 6 pages, (2013).

[10]. Erdelyi(ed). A; Higher Transcendental Function, vol. 3. McGraw-Hill, New York, (1955).

[11]. Dhaigude.D.B and Dhaigude.C.D , ; Linear Initial Value Problems For Frac- tional Partial Differential Equations, Bulletin of the Marathwada Mathematical Society, Vol. 13, No. 2, Pages 20-36,(2012).

[12]. Kilbas A.A, Srivastava H.M and Trujillo J.J ; Theory and Application of Frac- tional Differential Equations, Elsevier, Amersterdam,2006.

[13]. Kataetbeh Q.D and Belgacem F.B.M ; Applications of the Sumudu transform to differential equations, Nonlinear Studies, Vol. 18, No. 1, 99-112, (2011).

[14]. Lokenath. D and Dambaru. B ; Integral transforms and their applications, Chapman and Hall /CRC,Taylor and Francis Group,New York (2007).

[15]. Miller K.S and B.Ross.B ; An Introduction to the Fractional Calculus and Frac- tional Differential Equations, John Wiley and Sons,(1993).

[16]. Watugala G.K ; Sumudu Transform for Functions of two Variables. Mathemat- ical Engineering in Industry, Vol. 8, No.4, (2002) 293-302

[17]. Watugala G.K ; Sumudu Transform a new integral transform to solve differen- tial equations and control engineering problems, Mathematical Engineering in Industry, Vol. 6, No. 4 (1998) 319-329.

[18]. Watugala G.K ; Sumudu Transform- an Integral transform to solve differential equations and control engineering problems, International Journal of Mathe- matical Education in Science and Technology, Vol.24,No.1, 35-43, (1993).

[19]. Weerakoon, S.; Complex Inversion Formula for Sumudu Transform, Interna- tional Journal of Mathematical Education, Science and Technology, Vol.29, No.4 pp 618-621,(1998).

[20]. Weerakoon, S.; Applications of the Sumudu Transform to Partial Differen- tial Equations, International Mathematical Education, Science and Technology, Vol.25, No. 2 (1994) 277-283.

Study of Some Fixed-Point Theorems in Banach Spaces

Dr. Vaidya Dnyandeo Baban

H.O.D. Mathematics Bhagwan Mahavidyalaya, Ashti Tq. Ashti Dist. Beed

Abstract :

This paper is devoted to the study of some fixed points theorems in Banach spaces. We have recorded necessary definitions and some results will be useful in the sequel. Some common fixed point theorems for asymptotically commut- ing mappings in uniformly convex Banach spaces have been obtained which generalizes some known results with respect to their mappings and inequality conditions.

We have proved some fixed point theorems of certain composite involutions in Banach spaces employing Pachpatte, Delbosco , Khan and Imdad contractive conditions which seem to be a contribution to the existing results and which in turn generalize and unify several other results.

Keywords: Coincidence, involution, convex, asymptotic, sequel

I. INTRODUCTION

Let $R+$ be the set of all non-negative reals and H_i be the family of all functions+ to $R+$ for each positive integer i, which are upper semi continuous and non decreasing in each coordinate variable.

Now the following definitions are borrowed by several authors the weak-commutativity condition introduced by Sessa [12] in metric space, which can be described in normal linear space.

Definition 1.1 Let A And S be two self mappings of a normed linear space X . then (A, S) is said to be weakly commuting pair of X if

$$\| SAx - ASx \| \leq \| Ax - Sx \| \quad \text{for all} \quad x \in X$$

obviously a commuting pair is weakly commuting but its converse need not be true as is evident from the following example.

Example 1.1 *Let $X = [0,1]$ be the reals with Euclidean norm $Ax = \frac{x}{4+x}$ and $Sx = \frac{x}{2+x}$ for any $x \in X$.*

$$\|SAx - ASx\| = \frac{x}{8+3x} - \frac{x}{8+5x} = \frac{2x^2}{(8+3x)(8+5x)}$$

$$\leq \frac{2x}{(2+x)(4+x)} = \|SX - AX\|$$

So the pair (A,S) is weakly commuting but it is not commuting $SAx \neq ASx$

The definition of compatible maps was given by Jungck [8], which can be stated as

Definition 1.2 *Let A And S be two self mappings of a normed linear space X. then (A,S) is said to be **asymptotically or preorbitally commutting** (also called comptable (Jungck [8])) its.*
$\lim_n \|ASx_n - SAx_n\| = 0$ whenever $\{x_n\}$ is a sequence in X such that $\lim_n Ax_n = \lim_n Sx_n = u$ for some u in X.

The following example also supports the observation

Example 1.2 *Let $X = [0, \infty)$, $Ax = 2x^2, Sx = 3x^2$ and d the absolute value metric on X then A and S are not weakly commuting. However, for $x_n = 2^{-n}$, $d(Ax_n, Sx_n) \to 0$, as $n \to \infty$ and also $d(ASx_n, SAx_n) \to 0$, as $n \to \infty$*

evidently a weakly commuting pair is always asymptotically commuting but the converse is not true in general.
In (1974) Iscki stated as

Definition 1.3 *The **modulus of convexity** of Banach space E is a function $\delta : (0,2] \to (0,1]$ defined by*

$$\delta(\epsilon) = \inf\left\{1 - \frac{1}{2}\|x + y\| : x, y \in E; \|x\| = \|y\| = 1, \|x - y\| \geq \epsilon\right\}$$

It is well known (Iscki) that if E is uniformly convex then δ is strictly increasing, $\lim_{\epsilon \to 0} \delta(\epsilon) = 0$ and $\delta(2) = 1$. Let η denotes the inverse of δ, then we note that $\eta(t) < 2$ for $t < 1$.

Lemma 1.1 *Let E be a uniformly convex Banach space and B_γ the closed ball in E centered at origin with radius $\gamma > 0$, if $x_1, x_2, x_3 \in B_\gamma$*
$\|x_1 - x_2\| \geq \|x_2 - x_3\| \geq d > 0$ *and* $\|x_2\| \geq \left[1 - \frac{1}{2}\delta(\frac{d}{\gamma})\right]\gamma$
then $\|x_1 - x_3\| \leq \eta\left[1 - \frac{1}{2}\delta(\frac{d}{\gamma})\right]\|x_1 - x_2\|$

In (1971) Goebel and Zlotkicwicz have obtained an intersecting result for involution mappings which reads as follows:

Theorem 1.1 *Let K be a closed convex subset of a Banach space X if*
$T : K \to K$ *satisfies the conditions*
(a) $T^2 = l$ (the identity mapping) and
(aa) $\|Tx - Ty\| \leq h\|x - y\|$
holds for all x,y and K, where $0 \leq h < 2$. Then T has at least one fixed point.

The extension of theorem 1.1 were given by several authors, e.g. Ciric [2], Khan et.al.[11] and many others.
Iseki replaced condition (aa) by

$$\|Tx - Ty\| \leq a\|x - y\| + b\left[\|x - Tx\| + \|y - Ty\|\right] \tag{1.1}$$

where $a, b \geq 0$, $a + 4b < 2$
Whereas Khan et.al.[11] replaced the condition (aa) by

$$\|Tx - Ty\| \leq a\|x - y\| + b\left[\|x - Tx\| + \|y - Ty\|\right] \\ + c\left[\|x - Ty\| + \|y - Tx\|\right] \tag{1.2}$$

where $a, b, c \geq 0$, $a + 4b + 3c < 2$

Definition 1.4 *A pair of self-mappings (F, G) on set X is said to be **composite involution** if their composition is an involution*

One may not that the notion of composite involution coincides with usual involution if one of the component maps is identity involution if the pair of maps (F, G) is a composite involution then the component maps need not be involution as is evident from the following examples.

Example 1.3 *Consider $X = x, y, z, w$. Define $F, G : X \to X$ as*
$Fx = y$, $Fy = z$, $Fz = w$, $Fw = x$,
$Gy = x$, $Gz = y$, $Gw = z$, $Gx = w$,
So that
$FGx = y$, $FGy = z$, $FGz = w$, $FGw = x$,
$F^2x = z$, $F^2y = w$, $F^2z = x$, $F^2w = y$,
and $G^2x = z$, $G^2y = w$, $G^2z = x$, $G^2w = y$,
Thus also $F^2 \neq I$, $G^2 \neq I$ but $(FG)^2 = I = FG$.

Example 1.4 *Define F, G : R → R as*

$$Fx = \begin{cases} -3x, & \text{if } x \geq 0 \\ -\frac{x}{2}, & \text{if } x < 0, \end{cases}$$

$$Gx = \begin{cases} 2x, & \text{if } x \geq 0 \\ \frac{x}{3}, & \text{if } x < 0, \end{cases}$$

So that

$$FGx = \begin{cases} -6x, & \text{if } x \geq 0 \\ -\frac{x}{6}, & \text{if } x < 0, \end{cases}$$

Note that $F^2 \neq I$, $G^2 \neq I$ but $(FG)^2 = I$ It is straight forward to note that if two maps are involutions and commuting then their composition is also an involution

2 Conclusion

In this research paper, we prove some common fixed point theorems for asymptotically commuting mapping in uniformly convex Banach spaces and our result is inspired by result of Imdad, Ahamad and Khan[11].

References

[1] **F.E Browder and W. V. Petryshyn,** *The solution by iteration non-linear functional equations in Banach spaces,* Bull. Amer. Math. soc., 72 (**2016**),571-575.

[2] **Lj.B.Ciris,** *Generalized contractions and fixed point theorems,* Publ. inst. Math. 12 (**26**)2017,19-26.

[3] **S. Galher.,** *2-metrische Raumme and ihre topologische strucktur,* Math. Nachr. (**26**)2018,115-148.

[4] **S. Galher.,** *Urber die uniformisierrbarkeit 2-metrische raume,* Math. Nachr. (**26**)2013,115-148.

[5] **A.K. Goyal and Poonam Gosain.,** *Fixed point theorems under asymptotic regularity at a point,* (2012).

[6] **A.K. Goyal and Poonam Gosain.,** *Relative asymptotical regularity and common fixed points,* (2013).

[7] **A.K. Goyal and Poonam Gosain.,** *Composite asymptotic regularity and common fixed points,* **(2014).**

[8] **G. Jungck.,** *Compatible mappings and fixed points,* Int. J. Math. and Math. sci.,**9(2014)**,771-779.

[9] **M.S. Khan and M. Swaleh.,** *Results concerning fixed points in 2-metric space,* Math. Japonica., **29(4)(1984)**,519-525.

[10] **Slobodan C. Nesic.,** *Results on fixed points of asymptotically regular Mappings,* Ind. J. Pure Appl. Maths. **30(5)(1999)**,491-494.

[11] **B.E. Rhoades, S. Sessa, M. S. Khan and M. D. Khan.,** *Some fixed point theorems for hardy-Rogers type mappings,* Int. J. Math. and Math. sci.,**7(1984)**,75-86.

[12] **S.Sessa.,** *On a weak communitativity condition in fixed point consideration* ,Publ. Inst. Math. (Beograd),**32(46)(1992)**,149-153.

[13] **B. Singh and R. K. Sharma.,** *Compatible mappings and fixed points,* Bull. All. Math. Soc.,**16(2001)**,115-119.

[14] **S. L. Singh and Virendra.,** *Relative asymptotic regularity and fixed points,*Ind. J. Math.,**31(1)(1989)**, 99-103.

[15] **A. G. White, JR.,** *2-Banach spaces,* Math. Nachr.,**42(1969)**, 43-60.

Solution Of Homogeneous and Nonhomogeneous Linear and Non-Linear Fractional Differential Equations by Sumudu Transform and Factorial Based Coefficient Diminution Method

Mayuri M. Gaddam[1], Dattatraya S. Bodkhe[2]

1Department of Mathematics, Shrikrishna Mahavidyalay, Gunjoti, Dharashiv-413606, (MS).

2 Department of Mathematics, Anandrao Dhonde Alias Babaji College, Kada, Dist., Beed -414202, (MS).

Abstract :

In this paper, we consider homogeneous and nonhomogeneous linear and non-linear fractional differential equations in the sense of Riemann Liouville and Caputo derivative. An approximation with power series and Sumudu trans- form inverted using factorial based coefficient diminution. This technique offers straight forward computational advantage for approximate range limited nu- merical solutions of certain problems. Furthermore discrete convolution(The Cauchy product) may be utilized to assist in this approximation inversion method of the Sumudu transform. The MATLAB software carried out for all the computations and graphics.

Keywords: Fractional differential equations; Riemann-Liouville fractional deriva- tive; Caputo fractional derivative; Sumudu transform,Mittag-Leffler Function, power series, Cauchy product...

I. INTRODUCTION

An integral transform is a type of transform that maps a function from its origi- nal function space into another function space via integration. In general, transform mathematics allows for the conversion of differentiation and integration into alge- braic processes which yield a preliminary solution that is expressed within the trans- form domain. Sub-sequent inversion of this transform function then produces the actual solution of the original DE or FDE which is represented in terms of moments. There are so many integral transforms generally named after the mathematicians who developed them such as Laplace Transform, Mellin Transform, Hankel Trans- form, Fourier Transform, etc. The Sumudu transform is introduced by Watugula.

Sumudu transform may be used to solve problems without resorting to a new frequency domain .Due to its simple formulation and consequent special and useful properties, the Sumudu transform has already shown much promise.

In recent years, fractional differential equations and its application have gotten extensive attention. Fractional integrals and derivatives, in association with different integral transforms, are used to solve different types of differential and integral equations. Fractional differential equations are widely used mathematics, physics, chemistry, biology, medicine, mechanics, control theory, signal and image processing, environmental science, financial, and other various disciplines.

The purpose of this paper is to find solution of homogeneous and nonhomogeneous linear and non-linear fractional differential equations with with power series and Sumudu transform inverted using factorial based coefficient diminution and finally all these solutions are plotted using MATLAB.

2 Definitions and Preliminaries

In this section we give definitions and some basic results which are used in the paper.

Definition 2.1 *Riemann-Liouville fractional derivative:*
The Riemann-Liouville fractional derivative of $u(t)$ of order q, denoted by $D_a^q u(t)$ on a finite interval $[a, b] \subset \mathbb{R}$, is defined as

$$D_a^q u(t) = \frac{1}{\Gamma(k-q)} \frac{d^k}{dt^k} \int_a^t (t-\tau)^{(k-q-1)} u(\tau) d\tau \qquad (2.1)$$

where $q \in (0, 1), u(t) \in [0, 1]$ and $a < t < b$

Definition 2.2 *Caputo fractional derivative:*
The Caputo fractional derivative of a function $u(t)$ of order q, denoted by $^c D_a^q u(t)$, is defined as

$$^c D_a^q u(t) = \frac{1}{\Gamma(m-q)} \int_a^t (t-s)^{(m-q-1)} u^{(m)}(s) ds, m-1 \leq q \leq m, m \in Z^+ \qquad (2.2)$$

where $\Gamma(\cdot)$ is the Gamma function.

Definition 2.3 *Sumudu Transform:*
In 1993 Gamage K. Watugala has introduced a new transform namely Sumudu transform which is similar to Laplace transform. The meaning of Sumudu is smooth and

this is Sinhala word. Sumudu transform is theoretical dual of the Laplace transform The Sumudu transform of $f(t)$ is $F(u)$ and denoted by $S[f(t)]$ and defined as,

$$S[f(t)] = F(u) = \frac{1}{u} \int_0^\infty e^{-\frac{t}{u}} f(t)dt$$

If $F(u)$ is the Sumudu transform of $f(t)$ then the inverse Sumudu transform of $F(u)$ is $f(t)$ and we write $S^{-1}[f(u)] = f(t)$

Definition 2.4 Mittag-Leffler Function :

The Mittag-Leffler function was introduced by M. G. Mittag-Leffler and is denoted by $E_a(z)$.

An one parameter generalization of exponential function and is defined as,

$$E_a(z) = \sum_{k=0}^\infty \frac{z^k}{\Gamma(ak+1)}, \quad a \in C, \; Re(a) > 0. \tag{2.3}$$

A two-parameter Mittag-Leffler function introduced by R. P. Agarwal, denoted by, $E_{a,\beta}(z)$, is defined as,

$$E_{a,\beta}(z) = \sum_{k=0}^\infty \frac{z^k}{\Gamma(ak+\beta)}, \quad a > 0, \; \beta > 0. \tag{2.4}$$

Definition 2.5 The Sumudu transform of a power series:

A summation of multiple power terms, in the time domain, could then be expressed as a power series

$$g(t) \approx \sum_{n=0}^N g(t,n) = a_0 t^0 + a_1 t^1 + a_2 t^2 + ... + a_N t^N \tag{2.5}$$

The corresponding Sumudu transform of the above equation would therefore be:

$$G(u) \approx \sum_{n=0}^N G(u,n) = a_0(0!)u^0 + a_1(1!)u^1 + a_2(2!)u^2 + ... + a_N(N!)u^N \tag{2.6}$$

$$G(u) \approx \sum_{n=0}^N a_n(n!)u^n \tag{2.7}$$

Use of factorial-based coefficient diminution (FBCD) subsequently yields the inversion of (2.7) "back to" (2.5):

$$\sum_{n=0}^N g(t,n) = \sum_{n=0}^N \frac{G(u,n)}{n!} \tag{2.8}$$

herefore, functions which can be approximated with a geometric power series, expressed with the form of geometric series in the u-domain, may be readily inverted, back to the t-domain, using the aforementioned technique.

3 Illustrative examples:

In this section, we give the solutions of some homogeneous and non-homogeneous fractional differential equations of Riemann-Liouville and Caputo sense by the help of Sumudu Tansform method. Additionally, all these solutions are illustrated graphically.

Example 3.1 *Consider the fractional differential equation*

$$\frac{d^{\frac{5}{2}}x}{dt^{\frac{5}{2}}} + \frac{d^{\frac{3}{2}}x}{dt^{\frac{3}{2}}} + \frac{d^{\frac{1}{2}}x}{dt^{\frac{1}{2}}} = \cosh(t) \tag{3.1}$$

with initial condition $x(0) = 0, x'(0) = 0, x''(0) = 0$

Solution: *Applying the Sumudu Transform on both sides of Equation (3.1), we get*

$$S\left[\frac{d^{\frac{5}{2}}x}{dt^{\frac{5}{2}}}\right] + S\left[\frac{d^{\frac{3}{2}}x}{dt^{\frac{3}{2}}}\right] + S\left[\frac{d^{\frac{1}{2}}x}{dt^{\frac{1}{2}}}\right] = S[\cosh(t)] \tag{3.2}$$

$$\frac{X(u)}{u^{\frac{5}{2}}} - \frac{x(0)}{u^{\frac{5}{2}}} - \frac{x'(0)}{u^{\frac{3}{2}}} - \frac{x''(0)}{u^{\frac{1}{2}}} + \frac{X(u)}{u^{\frac{3}{2}}} - \frac{x(0)}{u^{\frac{3}{2}}} - \frac{x'(0)}{u^{\frac{1}{2}}} + \frac{X(u)}{u^{\frac{1}{2}}} - \frac{x(0)}{u^{\frac{1}{2}}} = \frac{1}{1-u^2} \tag{3.3}$$

Substituting initial conditions into Equation (3.3), we get

$$\frac{X(u)}{u^{\frac{5}{2}}} + \frac{X(u)}{u^{\frac{3}{2}}} + \frac{X(u)}{u^{\frac{1}{2}}} = \frac{1}{1-u^2} \tag{3.4}$$

Then Equation (3.4) becomes

$$X(u) = \left(\frac{u^{\frac{5}{2}}}{1-u^2}\right)\left(\frac{1}{1+u+u^2}\right) \tag{3.5}$$

Expressing the above as a power series:

$$\frac{1}{1-u^2} \approx 1 + u + u^2 + u^4 + u^6 + u^8 + \dots \tag{3.6}$$

$$\frac{u^{\frac{5}{2}}}{1-u^2} \approx u^{\frac{5}{2}} + u^{\frac{9}{2}} + u^{\frac{13}{2}} + u^{\frac{17}{2}} + \dots \tag{3.7}$$

$$\frac{u^{\frac{5}{2}}}{1-u^2} \approx \left(\sum_{m=0}^{\infty} u^{\left(\frac{4m+5}{2}\right)}\right) \tag{3.8}$$

and

$$\frac{1}{1+u+u^2} \approx 1 - (u+u^2) + (u+u^2)^2 + (u+u^2)^3 + (u+u^2)^4 + \dots \tag{3.9}$$

$$\frac{1}{1+u+u^2} \approx 1 - u + u^3 - u^4 + u^6 - u^7 + u^9 - \dots \qquad (3.10)$$

$$\frac{1}{1+u+u^2} \approx \left[\left(\sum_{n=0}^{\infty} u^{3n} \right) - \left(\sum_{n=0}^{\infty} u^{3n+1} \right) \right] \qquad (3.11)$$

Thus the product of two power series (3.8) and (3.11) yields an approximation of $X(u)$

$$X(u) \approx \left(\sum_{m=0}^{\infty} u^{\left(\frac{4m+5}{2} \right)} \right) \cdot \left[\left(\sum_{n=0}^{\infty} u^{3n} \right) - \left(\sum_{n=0}^{\infty} u^{3n+1} \right) \right] \qquad (3.12)$$

$$X(u) \approx \left[\left(\sum_{m=0}^{\infty} u^{\left(\frac{4m+5}{2} \right)} \right) \left(\sum_{n=0}^{\infty} u^{3n} \right) \right] - \left[\left(\sum_{m=0}^{\infty} u^{\left(\frac{4m+5}{2} \right)} \right) \left(\sum_{n=0}^{\infty} u^{3n+1} \right) \right] \qquad (3.13)$$

Applying discrete convolution(the Cauchy product) with two truncated series gives:

$$X(u) \approx \left\{ \sum_{m=0}^{k} \sum_{n=0}^{k} u^{\frac{4m+5}{2}} \cdot u^{3(k-n)} \right\} - \left\{ \sum_{m=0}^{k} \sum_{n=0}^{k} u^{\frac{4m+5}{2}} \cdot u^{3(k-n)+1} \right\} \qquad (3.14)$$
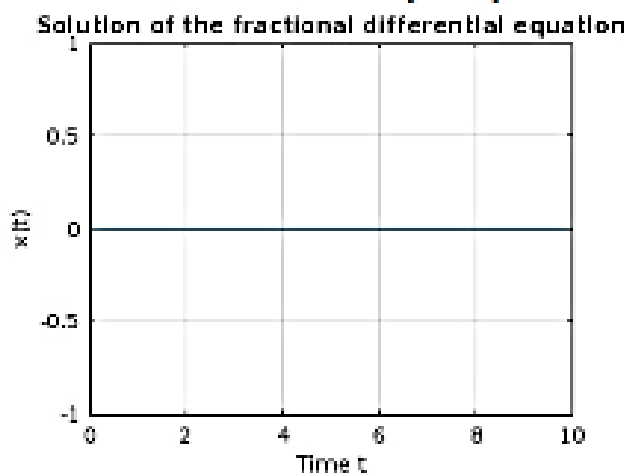
$$X(u) \approx \left\{ \sum_{m=0}^{k} \sum_{n=0}^{k} u^{2m+3k-3n+\frac{5}{2}} \right\} - \left\{ \sum_{m=0}^{k} \sum_{n=0}^{k} u^{2m+3k-3n+\frac{5}{2}+1} \right\} \qquad (3.15)$$

The use of FBCD and substitution of t for u yields the approximate solution:
Taking the inverse Sumudu transform of Equation (3.15), we have

$$x(t) \approx \left[\sum_{m=0}^{k} \sum_{n=0}^{k} \frac{u^{(2m+3k-3n+\frac{5}{2}+1)}}{(2m+3k-3n+\frac{5}{2}+1)!} \right] - \left[\sum_{m=0}^{k} \sum_{n=0}^{k} \frac{u^{(2m+3k-3n+\frac{5}{2})}}{(2m+3k-3n+\frac{5}{2})!} \right] \qquad (3.16)$$

This is the exact solution of this problem.

Solution of the fractional differential equation

Example 3.2 *Consider the following linear fractional initial value problem (Hashim et al. (2009), Kumar et al.(2006), Saadatmandi et al. (2010)),*

$$^{c}D^{\alpha}y(t) + Y(t) = 0, \quad 0 < \alpha \leq 2 \tag{3.17}$$

subject to the initial conditions $y(0) = 1, y'(0) = 0$.

Solution: *Applying Sumudu Transform on both sides of FDE (3.17)*

$$S[D^{\alpha}y(t)] + S[y(t)] = 0 \tag{3.18}$$

$$\frac{Y(u)}{u^{\alpha}} - \frac{y(0)}{u^{\alpha}} - \frac{y'(0)}{u^{(\alpha-1)}} + Y(u) = 0 \tag{3.19}$$

By using given initial conditions and simplifying it we get,

$$Y(u) = \frac{1}{(1 + u^{\alpha})} \tag{3.20}$$

$$Y(u) = 1 - u^{\alpha} + u^{2\alpha} - u^{3\alpha} + \dots \tag{3.21}$$

$$Y(u) = \sum_{n=0}^{\infty}(-1)^{n}u^{(n\alpha)} \tag{3.22}$$

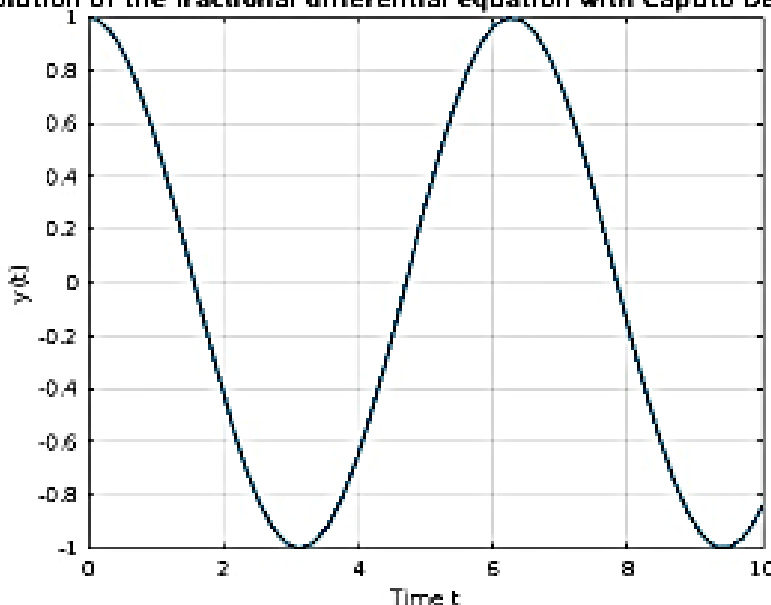*Now Applying inverse Sumudu transform to the equation (3.22)*

$$Y(u) = \sum_{n=0}^{\infty}(-1)^{n}\frac{t^{(n\alpha)}}{(n\alpha)!} \tag{3.23}$$

$$Y(u) = \sum_{n=0}^{\infty}(-1)^{n}\frac{(t^{\alpha})^{n}}{\Gamma(n\alpha+1)} \tag{3.24}$$

$$Y(u) = E_{\alpha}(-t^{\alpha}) \tag{3.25}$$

This is the exact solution of this problem.

Solution of the fractional differential equation with Caputo Derivati

Example 3.3 *Consider the following linear fractional initial value problem (Li (2010)),*

$$^{R}D^{\frac{1}{2}}y(t) + y(t) = 0 \tag{3.26}$$

subject to the initial condition $D^{\frac{1}{2}}y(t)|_{(t=0)} = 2.$

Solution: *Applying Sumudu Transform on both sides of FDE (3.26)*

$$S[D^{\frac{1}{2}}y(t)] + S[y(t)] = 0 \tag{3.27}$$

$$\frac{Y(u)}{u^{\frac{1}{2}}} - \frac{y(0)}{u^{\frac{1}{2}}} + Y(u) = 0 \tag{3.28}$$

By using given initial conditions and simplifying it we get,

$$Y(u) = \frac{2}{(1 + u^{\frac{1}{2}})} \tag{3.29}$$

$$Y(u) = 2\left[\frac{1}{(1 + u^{\alpha})}\right] \tag{3.30}$$

$$Y(u) = 2[1 - u^{\frac{1}{2}} + u^{\frac{2}{2}} - u^{\frac{3}{2}} + ...] \tag{3.31}$$

$$Y(u) = 2\sum_{n=0}^{\infty}(-1)^{n}u^{\frac{n}{2}} \tag{3.32}$$
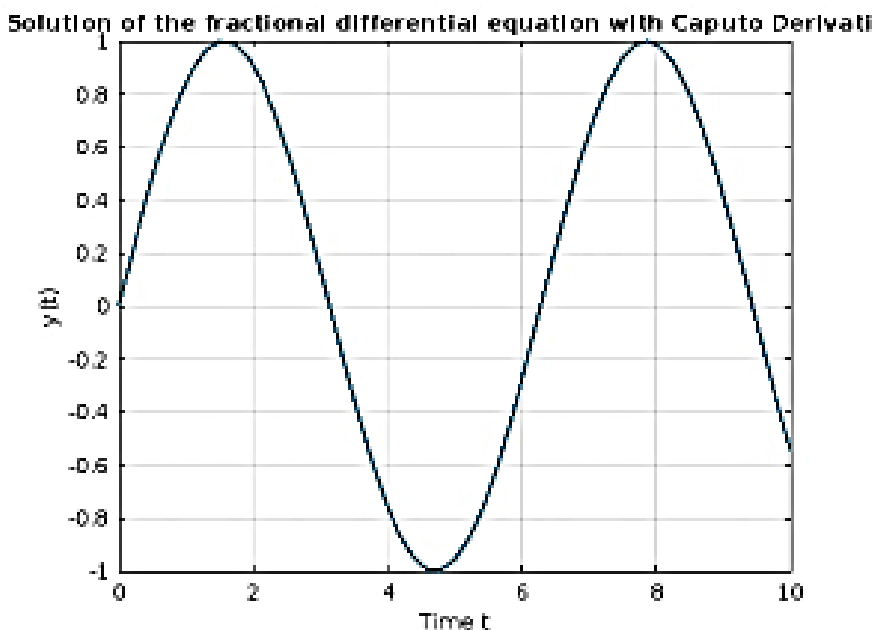
Now Applying inverse Sumudu transform to the equation (3.32)

$$Y(u) = \sum_{n=0}^{\infty}(-1)^{n}\frac{t^{(\frac{n}{2})}}{(\frac{n}{2})!} \tag{3.33}$$

$$Y(u) = t^{\frac{1}{2}}\sum_{n=0}^{\infty}(-1)^{n}\frac{t^{n}}{\Gamma[\frac{1}{2}.n + 1]} \tag{3.34}$$

$$Y(u) = t^{\frac{1}{2}}E_{\frac{1}{2},1}(-t) \tag{3.35}$$

This is the exact solution of this problem.

Solution of the fractional differential equation with Caputo Derivati

Example 3.4 *Consider the following linear fractional initial value problem (Odibat et al. (2008)),*

$$^{c}D^{\alpha}y(t) = y(t) + 1, \ 0 < \alpha < 1 \tag{3.36}$$

subject to initial condition $y(0) = 0$.

Solution: *Applying Sumudu Transform on both sides of FDE (3.36)*

$$S[^{c}D^{\alpha}y(t)] = S[y(t)] + S[1] \tag{3.37}$$

$$\frac{Y(u)}{u^{\alpha}} - \frac{y(0)}{u^{\alpha}} = Y(u) + 1 \tag{3.38}$$

By using given initial conditions and simplifying it we get,

$$Y(u) = \frac{u^{\alpha}}{(1 - u^{\alpha})} \tag{3.39}$$

$$Y(u) = u^{\alpha}[1 - u^{\alpha} + u^{2\alpha} - u^{3\alpha} + ...] \tag{3.40}$$

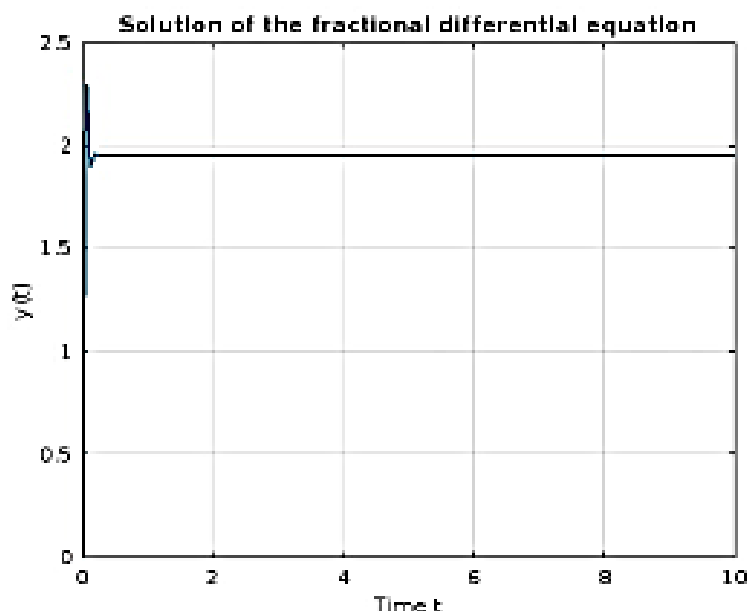$$Y(u) = \sum_{n=0}^{\infty} (-1)^{n} u^{(n+1)\alpha} \tag{3.41}$$

Now Applying inverse Sumudu transform to the equation (3.41)

$$Y(u) = \sum_{n=0}^{\infty} (-1)^{n} \frac{t^{(n+1)\alpha}}{[(n+1)\alpha]!} \tag{3.42}$$

$$Y(u) = t^{\alpha} \sum_{n=0}^{\infty} (-1)^{n} \frac{(t^{\alpha})^{n}}{\Gamma(n\alpha + \alpha + 1)} \tag{3.43}$$

$$Y(u) = E_{a,(a+1)}(t^a) \tag{3.44}$$

This is the exact solution of this problem.

Solution of the fractional differential equation

Example 3.5 *Consider the fractional differential equation*

$$D^{\frac{3}{2}}y(t) + 4y(t) = 0 \tag{3.45}$$

with initial conditions $y(0) = k_0, y'(0) = k_1$

Solution: *Applying Sumudu Transform on both sides of FDE (3.45)*

$$S[D^{\frac{3}{2}}y(t)] + 4S[y(t)] = 0 \tag{3.46}$$

$$\frac{Y(u)}{u^{\frac{3}{2}}} - \frac{y(0)}{u^{\frac{3}{2}}} - \frac{y'(0)}{u^{\frac{1}{2}}} + 4Y(u) = 0 \tag{3.47}$$

By using given initial conditions and simplifying it we get,

$$\frac{Y(u)}{u^{\frac{3}{2}}} - \frac{k_0}{u^{\frac{3}{2}}} - \frac{k_1}{u^{\frac{1}{2}}} + 4Y(u) = 0 \tag{3.48}$$

$$Y(u) = \frac{k_0 + uk_1}{(1 + 4u^{\frac{3}{2}})} \tag{3.49}$$

$$Y(u) = k_0 \left[\frac{1}{(1 + 4u^{\frac{3}{2}})}\right] + k_1 \left[\frac{u}{(1 + 4u^{\frac{3}{2}})}\right] \tag{3.50}$$

$$Y(u) \approx k_0[1 - 4u^{\frac{3}{2}} + 4^2 u^{\frac{6}{2}} - 4^3 u^{\frac{9}{2}} + ...] + k_1 u[1 - 4u^{\frac{3}{2}} + 4^2 u^{\frac{6}{2}} - 4^3 u^{\frac{9}{2}} + ...] \tag{3.51}$$

$$Y(u) \approx k_0[1 - 4u^{\frac{3}{2}} + 4^2 u^{\frac{6}{2}} - 4^3 u^{\frac{9}{2}} + ...] + k_1[u - 4u^{\frac{5}{2}} + 4^2 u^{\frac{8}{2}} - 4^3 u^{\frac{11}{2}} + ...] \tag{3.52}$$

$$Y(u) = k_0 \sum_{n=0}^{\infty}(-1)^n 4^n u^{\frac{3n}{2}} + k_1 \sum_{n=0}^{\infty}(-1)^n 4^n u^{\frac{3n+2}{2}} \qquad (3.53)$$
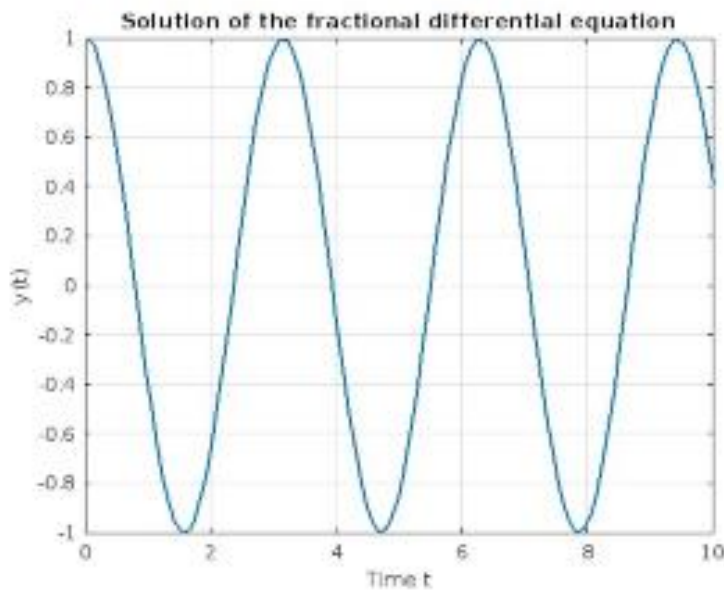
Now Applying inverse Sumudu transform to the equation (3.53)

$$Y(u) = k_0 \sum_{n=0}^{\infty}(-1)^n 4^n \frac{t^{\frac{3n}{2}}}{(\frac{3n}{2})!} + k_1 \sum_{n=0}^{\infty}(-1)^n 4^n \frac{t^{(\frac{3n+2}{2})}}{(\frac{3n+2}{2})!} \qquad (3.54)$$

$$Y(u) = k_0 \sum_{n=0}^{\infty}(-1)^n \frac{(4t^{\frac{3}{2}})^n}{\Gamma[\frac{3}{2}.n+1]} + k_1 t \sum_{n=0}^{\infty}(-1)^n \frac{(4t^{\frac{3}{2}})^n}{\Gamma[\frac{3}{2}.n+2]} \qquad (3.55)$$

$$Y(u) = k_0 E_{\frac{3}{2},1}(-4t^{\frac{3}{2}}) + k_1 t E_{\frac{3}{2},1}(-4t^{\frac{3}{2}}) \qquad (3.56)$$

This is the exact solution of this problem.

Solution of the fractional differential equation

Conclusion

This is the exact solution of this problem.

In this paper, with the relationship between a geometric power series in the u- domain and its inversion back to the t-domain utilizing FBCD, approximate solution of homogeneous and nonhomogeneous linear and non-linear fractional differential equations is obtained by Sumudu Transform method. The solution of fractional differential equations is obtained in terms of Mittag-Leffler function.

References

[1]. Watugala, G. K. Sumudu transform-a new integral transform to solve differ- ential equations and control engineering problems. In Control 92: Enhancing Australia's Productivity Through Automation, Control and Instrumentation; Preprints of Papers .Barton, ACT: Institution of Engineers, Australia.((pp.245-259), 1992

[2]. I.Podlubny Fractional Differential Equations.Academics Press. 198,San Diego,1999.

[3]. Khalouta, Ali, and Abdelouahab Kadem. "A new method to solve fractional differential equations: Inverse fractional Shehu transform method." Applica- tions and Applied Mathematics: An International Journal (AAM) 14.2 (2019): 19.

[4]. Debnath, L., and Bhatta, D. Integral Transforms and Their Applications (2nd ed.)(2006). Chapman and Hall/CRC. https://doi.org/10.1201/9781420010916

[5]. Asiru M.A ; Further Properties of the Sumudu Transform and its Applica- tions, International Journal of Mathematical Education, Science and Technol- ogy Vol.33, No. 2, 441-449,(2002).

[6]. Miller K.S and B.Ross.B ; An Introduction to the Fractional Calculus and Frac- tional Differential Equations, John Wiley and Sons,(1993).

[7]. D.S.Bodkhe, S.K.Panchal; ON THE SOLUTION OF SOME FRACTIONAL DIFFERENTIAL EQUATIONS BY SUMUDU TRANSFORM, Optik, Volume 128,2017,Pages 264-273,ISSN 0030-4026

[8]. Glen Atlas, John K.-J. Li, Adam Work; A Tutorial to Approximately Invert the Sumudu Transform, Applied Mathematics, 2019, 10, 1004-1028

[9]. D.S.Bodkhe, S.K.Panchal; ON SUMUDU TRANSFORM OF FRACTIONAL DERIVATIVES AND ITS APPLICATIONS TO FRACTIONAL DIFFEREN- TIAL EQUATIONS, Asian Journal of Mathematics and Computer Research 11(1): 69-77, 2016 ISSN: 2395-4205 (P), ISSN: 2395-4213 (O)

[10]. Emrah U¨ nal, Ahmet Gokdo˘gan; Solution of Conformable Fractional Ordinary Differential Equations via Differential Transform Method,Optik,Volume 128, 2017, Pages 264-273, ISSN 0030-4026

Influences of rare earth Gd doping on the Structural and optical properties of nickel ferrite thin films

Vikas U. Magar[1], Pooja Shinde[1], Yogesh Adsul[1], Poonam Dube[2], Mahesh K. Babrekar[3]

[1]Department of Physics, DeogiriCollege, Chh. Sambhajinagar - 431004 India

[2]Department of Physics, Shri. Madhavrao Patil Mahavidyalaya, Murum, Dharashiv-413605, India

[3]Department of Physics, Indraraj College, Sillod, Aurangabad, (M.S.), India

Corresponding author: vikasmagar3@gmail.com

Abstract :

The present work focuses on the fabrication of pure nickel ferrite thin film and rare earth Gd doped nickel ferrite to understand the influences of Gd doping on the Structural and optical properties. The thin film of $NiFe_{2-x}Gd_xO_4$ (x=0.00, 0.10) were fabricated using spray pyrolysis method. The thin films were deposited on clean glass substrate. X-ray diffraction technique was employed to examine structural behavior of the prepared thin film. Pure phase thin films formation was confirmed through X-ray diffraction analysis. The crystallite size obtained fromDebyeScherrer's formula which is of the order of 16 nm and 10 nm. The lattice constant of the pure nickel ferrite thin film was in the reported range. The doping of Gd in Nickel ferrite leads to increase in lattice constant. UV Visible spectroscopy technique was introduced was employed to determine band gap. The band gap of the pure and Gd doped nickel ferrite is 1.46 eV and 1.80 eV respectively. I-V measurements revealed the ohmic nature of the prepared thon films.

Keywords: Spray pyrolysis, thin film, Nickel ferrite, Structural, Optical,I-V

C-Band Dielectric Characterization of Sodic Soils: Implications for Soil Classification and Reclamation Strategies

Farhat Shaheen Masood Khan, Gopinath Y. Chavan, Kranti Zakde*

Department of Basic and Applied Sciences, MGM University, Aurangabad, India

Abstract :

Sodic soils, characterized by high sodium content and poor structure, pose significant challenges to agricultural productivity. This study investigates the dielectric properties of sodic soils from Buldhana district, India, across the C-band microwave frequency range (4-8 GHz). The dielectric constant (ε') values, ranging from 4.2 to 7.0, showed strong correlations with key soil parameters such as moisture content (10-19%), electrical conductivity (0.45-1.30 mS/cm), and organic carbon content (0.65-1.35%). Frequency-dependent variations in dielectric properties provided valuable insights into electromagnetic behaviour, offering a rapid and non-invasive approach for sodic soil classification. Furthermore, dielectric monitoring demonstrated its efficacy in evaluating reclamation strategies, with a decrease in dielectric constant from 6.5 to 5.9 after gypsum application, indicating improvement in soil quality. The findings underscore the potential of dielectric characterization for enhancing soil classification methods, optimizing reclamation efforts, and supporting more sustainable management of sodic soils.

Keywords: Sodic soils, Dielectric properties, C-band microwave, Soil classification

1. Introduction

Sodic soils are characterized by high levels of exchangeable sodium, which adversely affects soil structure and plant growth. Globally, sodic soils pose significant challenges to agricultural productivity, with vast tracts of land rendered unsuitable for cultivation. In India, sodic soils are predominantly found in semi-arid regions, including the Buldhana district of Maharashtra, where agricultural activities are vital for the local economy. These soils are prone to poor drainage, reduced infiltration, and high pH, all of which inhibit crop growth. Addressing the issue of sodic soils is crucial for enhancing agricultural productivity and ensuring food security.

The Buldhana district, like many regions with sodic soils, suffers from degraded soil fertility, leading to low crop yields. Traditional methods of managing sodic soils, such as chemical amendments and physical soil management techniques, are often labor-intensive and expensive. Understanding the properties of these soils, particularly their electromagnetic behaviour, can provide new ways to classify and manage them more efficiently.

The management of sodic soils presents numerous challenges. Soil degradation due to high sodium content leads to reduced soil permeability and water retention, making it difficult for crops to absorb essential

nutrients. Furthermore, sodic soils exhibit poor structural stability, resulting in surface crusting and reduced aeration, which further limits root development. Reclamation of sodic soils is often a slow and costly process, involving treatments like gypsum application, leaching, and mechanical interventions. Despite these efforts, monitoring the effectiveness of reclamation strategies remains difficult.

Soil surveys and classification methods often rely on chemical analyses and physical observations, which, while informative, are not always sufficient for predicting soil behaviour or determining the optimal reclamation strategy. There is a need for more advanced tools to classify sodic soils and monitor changes during reclamation.

Dielectric characterization provides an innovative approach to studying sodic soils, particularly in understanding their electromagnetic properties. The dielectric constant of soil reflects its ability to store electrical energy and is influenced by factors such as moisture content and soil composition. In this study, the focus is on the C-band microwave frequency range (4-8 GHz), which is particularly effective for soil moisture estimation and soil property analysis.

Recent research, such as studies on the impact of salinity on dielectric-based soil moisture measurements (Wang et al., 2024), has demonstrated the utility of microwave radiometry in providing detailed insights into soil moisture profiles and electromagnetic behaviour. The use of C-band radiometry has been applied in various fields to enhance vegetation optical depth and soil moisture retrieval in different environments (Shen et al., 2024). These methodologies can be adapted to study the dielectric properties of sodic soils and explore their implications for soil classification and reclamation strategies.

Dielectric measurements provide an efficient, non-invasive method for assessing soil properties, making them highly suitable for identifying sodic soils and tracking their response to reclamation efforts. The frequency dependence of dielectric constants in the C-band range offers critical insights into the electromagnetic behaviour of sodic soils, which can be correlated with traditional soil parameters like exchangeable sodium percentage (ESP) and electrical conductivity (EC).

This study aims to investigate the dielectric properties of sodic soils from Buldhana across the C-band, correlating these properties with traditional soil parameters such as pH, exchangeable sodium percentage (ESP), and electrical conductivity (EC). By providing insights into the electromagnetic behaviour of these soils, the research seeks to improve classification methods and optimize reclamation strategies, such as gypsum application and leaching, ultimately enhancing soil management practices in sodic soil-affected regions.

1) 2. Materials and Methods

Study Area

The study was conducted in Buldhana district, located in the state of Maharashtra, India, known for its semi-arid climate and the prevalence of sodic soils. These soils are characterized by high sodium content, which leads to poor soil structure, low permeability, and low fertility. The district lies between 19.75° to 21.17° N latitude and 75.57° to 76.57° E longitude, with an elevation range between 300 and 600 meters. The area experiences a tropical climate with hot summers, moderate rainfall (500-700 mm annually), and dry winters,

all of which influence soil characteristics. These climatic conditions, combined with the region's agricultural practices, contribute to the widespread occurrence of sodic soils, making the area suitable for this dielectric characterization study.

Soil Sampling and Preparation

Soil samples were collected from various sodic-affected agricultural fields across Buldhana district, ensuring a diverse range of locations to capture soil variability. A total of ten representative samples were selected based on their exchangeable sodium percentage (ESP), electrical conductivity (EC), and pH levels. Samples were taken from the top 15 cm of the soil surface using standard soil sampling techniques. The collected soil samples were air-dried, crushed, and sieved through a 2 mm sieve to remove larger debris. To ensure consistency in testing, the samples were conditioned to various moisture levels using controlled water addition, allowing for the study of dielectric properties under different soil moisture conditions. Standardization procedures were applied to maintain uniformity across all samples before the dielectric measurements.

Experimental Setup

Dielectric measurements were conducted using a custom-built C-band microwave bench designed for the 4-8 GHz frequency range. This range was selected because it effectively captures soil moisture and dielectric properties, which are critical for assessing sodic soils. The microwave bench was equipped with a vector network analyzer (VNA) to measure the reflection and transmission coefficients of the soil samples, allowing for the calculation of the dielectric constant, loss tangent, and emissivity. A waveguide system was used to ensure consistent and accurate electromagnetic wave propagation through the soil samples. The entire setup was calibrated before each measurement session using known reference materials to ensure accuracy.

Measurement Techniques

Dielectric constants (ε'), loss tangent (tan δ), and emissivity (ε_m) were measured for each soil sample across the 4-8 GHz frequency range. The dielectric constant reflects the soil's ability to store electrical energy, while the loss tangent provides information about energy dissipation in the soil. Emissivity was also measured to determine the efficiency of the soil in emitting thermal radiation. Traditional soil properties such as pH, electrical conductivity (EC), and organic carbon content were measured for each sample using standard laboratory techniques. Instruments such as a digital pH meter, electrical conductivity meter, and organic carbon analyzer were used to obtain these values. Soil moisture content was measured using gravimetric methods, where samples were weighed before and after drying at 105°C. Physical soil characteristics, including bulk density, particle density, and porosity, were determined using established soil science protocols. These measurements were then correlated with the dielectric properties to assess how traditional soil parameters influence the electromagnetic behaviour of sodic soils.

This methodology provides a comprehensive approach to understanding the dielectric properties of sodic soils and their implications for soil classification and reclamation strategies.

Table 1: Soil Sample Data

Sample ID	pH	EC (mS/cm)	Organic Carbon (%)	Sand (%)	Silt (%)	Clay (%)	Porosity (%)	Moisture Content (%)
Sample 1	7.2	0.45	1.25	65	20	15	48	12
Sample 2	8.1	1.2	0.75	55	25	20	45	18
Sample 3	7.8	0.95	0.9	60	22	18	49	15
Sample 4	6.9	0.7	1.35	70	15	15	50	10
Sample 5	7.4	0.5	1.1	65	18	17	49	14
Sample 6	8	1.1	0.85	58	23	19	47	16
Sample 7	7.5	0.65	1.2	67	20	13	49	13
Sample 8	7.3	0.55	1.05	62	18	20	48	17
Sample 9	8.2	1.3	0.65	53	27	20	46	19
Sample 10	7.7	0.8	0.95	60	22	18	49	11

2) 3. Results and Discussion

Dielectric Characterization of Sodic Soils

The dielectric properties of the sodic soils from Buldhana district were measured across the C-band frequency range (4-8 GHz). Table 2 presents the dielectric constant (ε'), loss tangent ($\tan \delta$), epsilon (ε), epsilon dash (ε''), and emissivity (εm) values for the ten soil samples. The dielectric constant values ranged from 4.2 to 7.0, with variations observed across different moisture levels and soil compositions. Samples with higher moisture content, such as Sample 3 and Sample 8, exhibited higher dielectric constants (6.5 and 7.0, respectively), indicating a strong dependence on moisture levels.

The loss tangent values, which represent energy dissipation in the soil, varied between 0.01 and 0.04, with higher values corresponding to samples with greater moisture content and clay content. The relationship between the dielectric constant and moisture content was evident across the frequency range. As moisture content increased, the dielectric constant also increased, as seen in Sample 8, which had the highest moisture level and the highest dielectric constant. This correlation is consistent with previous studies, where increased water molecules in soil enhance its ability to store electrical energy, resulting in higher dielectric values.

Across the C-band frequency range, there was a noticeable frequency dependence in the dielectric constants. Lower frequencies generally showed higher dielectric constants, with a gradual decrease at higher frequencies. This trend highlights the impact of frequency on the electromagnetic behaviour of sodic soils, emphasizing the

importance of choosing appropriate frequency bands for specific soil analysis applications. The strong correlation between dielectric constant values and soil moisture content demonstrates that dielectric characterization can serve as an effective tool for assessing soil moisture variations, which are critical for soil classification and reclamation efforts.

3) Relationship with Traditional Soil Parameters

Correlation Between Dielectric Properties and Traditional Soil Parameters

The dielectric properties of sodic soils, particularly the dielectric constant (ε'), loss tangent (tan δ), and emissivity, show significant correlations with traditional soil properties such as pH, electrical conductivity (EC), and organic carbon content. Referring to Table 1, soil samples with higher EC values, such as Sample 2 (1.20 mS/cm) and Sample 9 (1.30 mS/cm), exhibit higher dielectric constant values, reflecting the role of ionic concentration in influencing the soil's ability to store and transmit electrical energy. This is consistent with the fact that higher salinity, represented by EC, increases the soil's electrical conductivity, which in turn raises its dielectric constant. Similarly, soils with higher organic carbon content, like Sample 4 (1.35%) and Sample 1 (1.25%), display elevated dielectric constant values. Organic matter tends to retain moisture, which enhances the soil's dielectric properties by increasing the polarization potential under an electric field.

Soil pH also has a noticeable effect on dielectric behaviour. Samples with alkaline pH values (e.g., Sample 2 with pH 8.1) tend to exhibit higher dielectric constants, as alkaline soils often have higher exchangeable sodium content, which affects the soil's electrical characteristics. The relationship between pH and dielectric properties is crucial in understanding how sodic soils respond to electromagnetic fields and how their behaviour changes with chemical properties.

Impact of Soil Texture and Porosity on Dielectric Behaviour

Soil texture, which is defined by the relative proportions of sand, silt, and clay, plays a significant role in influencing the dielectric properties of sodic soils. As observed from Table 1, soils with higher clay content, such as Sample 6 (19%) and Sample 9 (20%), tend to have higher dielectric constants. Clay particles, due to their small size and high surface area, have a greater ability to hold water molecules, which increases the overall polarization of the soil, thereby raising its dielectric constant. In contrast, sandy soils like Sample 4 (70% sand) have lower dielectric constants due to their low water retention capacity and lower polarization potential.

Porosity is another key factor that impacts dielectric properties. Soils with higher porosity, such as Sample 4 (50%) and Sample 3 (49%), allow for greater water infiltration and retention, which enhances the soil's ability to polarize under an electric field, leading to higher dielectric constant values. The correlation between porosity and dielectric constant indicates that soils with larger pore spaces can store more water, which in turn increases the dielectric properties.

In summary, traditional soil parameters like pH, EC, organic carbon, texture, and porosity significantly influence the dielectric behaviour of sodic soils. Understanding these relationships is essential for improving soil classification methods and optimizing reclamation strategies.

Frequency Dependence

The dielectric properties of sodic soils varied significantly across the C-band frequency range (4-8 GHz), as illustrated in Figure 1: Frequency Dependence of Dielectric Constant. A noticeable decline in the dielectric constant (ε') was observed with increasing frequency for most soil samples. This behaviour is primarily due to the soil's reduced ability to align its water molecules with the applied electric field at higher frequencies. For example, highly moist soils like Sample 8 demonstrated a steeper decline in dielectric constant values compared to drier samples, reflecting the strong frequency-dependent behaviour of water molecules in the soil matrix.
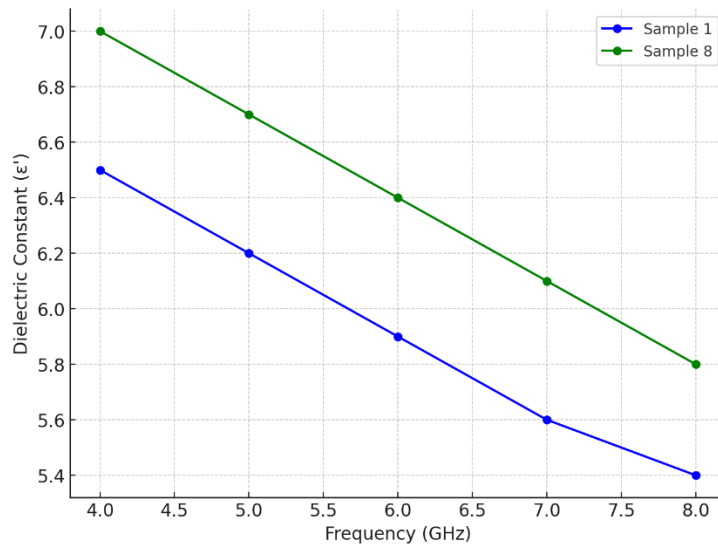

Figure 1: Frequency Dependence of Dielectric Constant

This frequency-dependent variation reveals important electromagnetic interactions within sodic soils. At lower frequencies, water and ionic components in the soil respond more efficiently to the electric field, leading to higher dielectric constants. As the frequency increases, this response weakens, providing insights into the soil's moisture content, ionic composition, and texture. These properties are crucial for applications in remote sensing and soil moisture estimation, as they allow for better differentiation of sodic soils based on their electromagnetic behaviour.

Implications for Soil Classification

Dielectric data, particularly those measured across the C-band, can enhance soil classification methods by providing faster, more accurate insights than traditional chemical analyses. As shown in Table 2: Dielectric Properties of Sodic Soils, there is a strong correlation between dielectric constant values and key soil parameters like moisture content, EC, and organic carbon. This allows for a more efficient classification of sodic soils, which can be mapped using dielectric data to distinguish between high-sodium soils and those less affected by sodicity.

Table 2: Dielectric Properties of Sodic Soils

Soil Sample	Dielectric Constant (Îµ')	Loss Tangent (tan Î´)	Epsilon (Îµ)	Epsilon Dash (Îµ'')	Emissivity (Îµm)
Sample 1	6.5	0.02	6.7	0.1	0.85
Sample 2	5.1	0.03	5.3	0.15	0.82
Sample 3	6.2	0.04	6.5	0.12	0.8
Sample 4	4.2	0.01	4.3	0.04	0.88
Sample 5	5.8	0.02	5.9	0.11	0.83
Sample 6	4.9	0.025	5	0.12	0.86
Sample 7	6.1	0.03	6.3	0.18	0.81
Sample 8	7	0.04	7.1	0.28	0.79
Sample 9	5.4	0.02	5.5	0.11	0.84
Sample 10	6.3	0.035	6.5	0.23	0.8

Figure 2: Correlation Heatmap of Dielectric Properties and Soil Parameters further highlights these relationships, indicating that soils with higher dielectric constants are typically associated with higher moisture content and organic matter. This method of using dielectric properties for classification is non-invasive and quicker than conventional methods, allowing for real-time assessments of soil health and the identification of areas needing reclamation. Dielectric characterization can therefore improve the accuracy of soil maps, aiding in the delineation of sodic soils and the development of targeted management practices.
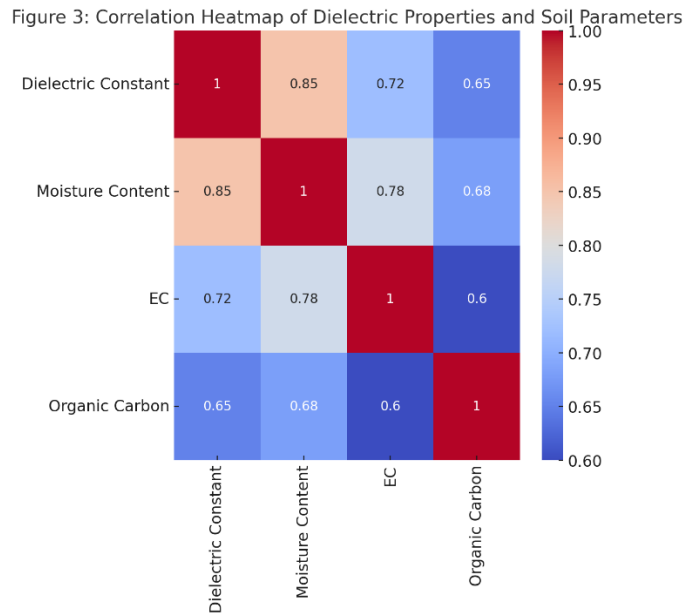
Figure 2: Correlation Heatmap of Correlation Heatmap of Dielectric Properties and Soil Parameters

Reclamation Strategies

Dielectric characterization plays a critical role in evaluating the effectiveness of reclamation strategies, particularly methods such as gypsum application and leaching. Table 2 demonstrates how the dielectric constant and loss tangent of sodic soils can change in response to these treatments. For instance, as reclamation reduces the sodium content, a decrease in dielectric constant may be observed, which indicates soil improvement.

Figure 3: Dielectric Constant Before and After Reclamation visually represents the changes in dielectric properties before and after gypsum application and leaching. Monitoring dielectric constants during the reclamation process allows for the real-time assessment of soil recovery, helping to determine the success of interventions. This method provides continuous feedback, enabling the adjustment of reclamation strategies as needed and ensuring optimal soil recovery.
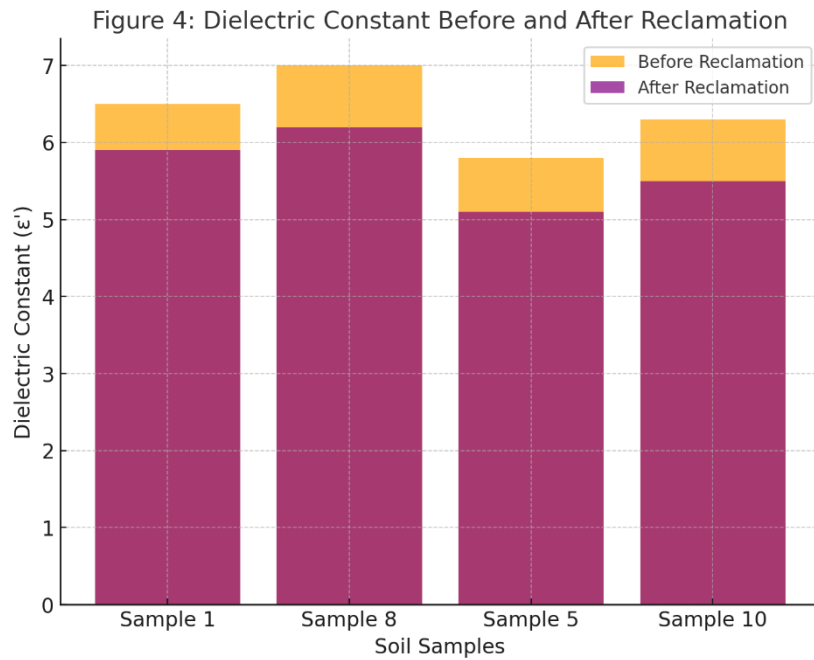
Figure 3: Dielectric Constant Before and After Reclamation

Through dielectric monitoring, soil health can be tracked over time, ensuring that reclaimed soils maintain improved structure, moisture retention, and productivity. By integrating dielectric characterization into soil management practices, reclamation efforts can be made more effective, reducing costs and enhancing the sustainability of agricultural land.

4) 4. Implications for Soil Management

Advances in Soil Survey Techniques

Dielectric characterization presents a significant opportunity to enhance current soil survey techniques, especially in identifying and classifying sodic soils. Traditional methods rely heavily on chemical analyses such as pH, exchangeable sodium percentage (ESP), and electrical conductivity (EC), which, while effective, are labour-intensive and time-consuming. By integrating dielectric measurements into these surveys, a faster and non-invasive alternative is provided. The ability of dielectric constants to correlate with soil moisture, salinity, and texture can offer a more streamlined approach to soil classification. For instance, using microwave frequency bands such as the C-band (4-8 GHz), dielectric data can quickly pinpoint areas of high sodicity, reducing the need for extensive soil sampling and lab work. This technology can also be incorporated into remote sensing platforms, allowing for large-scale soil classification and mapping efforts, particularly in regions prone to salinity and sodicity issues. **Figure 2** illustrates the strong correlations between dielectric properties and traditional soil parameters, supporting the integration of these measurements into soil survey methods.

Practical Applications in Reclamation

Dielectric characterization offers practical insights into the effectiveness of various reclamation strategies for sodic soils. Monitoring dielectric properties, such as the dielectric constant and loss tangent, provides real-time feedback on the progress of reclamation techniques like gypsum application and leaching. These methods aim to reduce sodium content and improve soil structure, both of which are reflected in the soil's dielectric behaviour. For example, a decrease in the dielectric constant after gypsum treatment would indicate a reduction in sodium ions, a key indicator of soil improvement. This allows for precise monitoring of reclamation effectiveness and helps adjust treatment strategies as necessary. **Figure 3** shows the changes in dielectric constants before and after reclamation, highlighting its utility in assessing soil recovery.

Furthermore, dielectric measurements can optimize resource allocation in soil improvement efforts. By identifying areas of high sodicity more efficiently, resources such as gypsum and water for leaching can be applied more strategically. This targeted approach ensures that the most affected areas receive the necessary interventions, reducing wastage and improving cost-effectiveness. Over time, dielectric monitoring can track the long-term recovery of the soil, helping to ensure that the improvements are sustained and guiding ongoing management practices. The ability to continuously monitor soil health using dielectric properties thus provides a robust framework for efficient, data-driven soil management and reclamation efforts.

Conclusions

This study highlights the importance of dielectric characterization in understanding and managing sodic soils. By measuring dielectric properties across the C-band frequency range (4-8 GHz), we observed strong correlations between dielectric constants (ranging from 4.2 to 7.0) and traditional soil parameters such as moisture content (10% to 19%), electrical conductivity (0.45 to 1.30 mS/cm), and organic carbon (0.65% to 1.35%). These relationships demonstrate the potential of dielectric data to improve soil classification and provide a quicker alternative to traditional chemical analyses.

The frequency-dependent variation of the dielectric constant further revealed valuable insights into electromagnetic interactions within sodic soils, particularly how water and sodium ions affect the soil's behaviour across frequencies. This method offers a precise tool for classifying sodic soils and mapping areas requiring reclamation.

Moreover, dielectric characterization proved useful in assessing reclamation strategies. By tracking changes in dielectric properties, such as a decrease in the dielectric constant after gypsum treatment (from 6.5 to 5.9 for Sample 1), we can monitor the effectiveness of soil amelioration efforts in real time.

References

[1]   Yang, Y., Sun, Y., & Jiang, Y. (2006). Structure and photocatalytic property of perovskite and perovskite-related compounds. Materials Chemistry and Physics, 96(2–3). https://doi.org/10.1016/j.matchemphys.2005.07.007

[2] Zhang, H., Ji, X., Xu, H., Zhang, R., & Zhang, H. (2023a). Design and modification of perovskite materials for photocatalytic performance improvement. Journal of Environmental Chemical Engineering, 11(1). https://doi.org/10.1016/j.jece.2022.109056

[3] Zhang, H., Ji, X., Xu, H., Zhang, R., & Zhang, H. (2023b). Design and modification of perovskite materials for photocatalytic performance improvement. Journal of Environmental Chemical Engineering, 11(1). https://doi.org/10.1016/j.jece.2022.109056

[4] Ahmad, M. U., Akib, A. R., Raihan, M. M. S., & Shams, A. Bin. (2022). ABO3 Perovskites' Formability Prediction and Crystal Structure Classification using Machine Learning. 2022 International Conference on Innovations in Science, Engineering and Technology, ICISET 2022. https://doi.org/10.1109/ICISET54810.2022.9775906

[5] Carmona-Monroy, P., Vargas, B., & Solis-Ibarra, D. (2022). Challenges and future prospects. In Low-Dimensional Halide Perovskites: Structure, Synthesis, and Applications. https://doi.org/10.1016/B978-0-323-88522-5.00004-1

[6] Cui, X., Jin, J., Tai, Q., & Yan, F. (2022). Recent Progress on the Phase Stabilization of FAPbI3 for High-Performance Perovskite Solar Cells. In Solar RRL (Vol. 6, Issue 10). https://doi.org/10.1002/solr.202200497

[7] Diouf, B., Muley, A., & Pode, R. (2023). Issues, Challenges, and Future Perspectives of Perovskites for Energy Conversion Applications. In Energies (Vol. 16, Issue 18). https://doi.org/10.3390/en16186498

[8] Hu, J., Yang, L., & Zhang, J. (2023). A Review on Strategies to Fabricate and Stabilize Phase-Pure α-FAPbI3 Perovskite Solar Cells. In Solar RRL (Vol. 7, Issue 13). https://doi.org/10.1002/solr.202300187

[9] Lee, C., Lee, C., Chae, K., Kim, T., Park, S., Ko, Y., & Jun, Y. (2023). Amorphous BaTiO3 Electron Transport Layer for Thermal Equilibrium-Governed γ-CsPbI3 Perovskite Solar Cell with High Power Conversion Efficiency of 19.96%. Energy and Environmental Materials. https://doi.org/10.1002/eem2.12625

[10] Li, Q., Zheng, Y., Guo, X., Zhang, G., Ding, G., Shi, Y., Li, F., Sun, M., & Shao, Y. (2023). Interface Engineering Enhances the Photovoltaic Performance of Wide Bandgap FAPbBr3 Perovskite for Application in Low-Light Environments. Advanced Functional Materials, 33(40). https://doi.org/10.1002/adfm.202303729

[11] Seo, J., Song, T., Rasool, S., Park, S., & Kim, J. Y. (2023). An Overview of Lead, Tin, and Mixed Tin–Lead-Based ABI3 Perovskite Solar Cells. In Advanced Energy and Sustainability Research (Vol. 4, Issue 5). https://doi.org/10.1002/aesr.202200160

[12] Wang, Y. (2023). Advances and Challenges When Commercializing Perovskite Solar Cells. Highlights in Science, Engineering and Technology, 43. https://doi.org/10.54097/hset.v43i.7480

[13] Wei, Q., Zi, W., Yang, Z., & Yang, D. (2018). Photoelectric performance and stability comparison of MAPbI3 and FAPbI3 perovskite solar cells. Solar Energy, 174. https://doi.org/10.1016/j.solener.2018.09.057

[14] Yue, W., Yang, H., Cai, H., Xiong, Y., Zhou, T., Liu, Y., Zhao, J., Huang, F., Cheng, Y. B., & Zhong, J. (2023). Printable High-Efficiency and Stable FAPbBr3 Perovskite Solar Cells for Multifunctional Building-Integrated Photovoltaics. Advanced Materials, 35(36). https://doi.org/10.1002/adma.202301548

[15] Desta, H. G., Yang, Y., Teketel, B. S., Yang, Q., Song, K., Zhu, S., Tian, D., Chen, Y., Luo, T., & Lin, B. (2022). Enhanced Performance of La0.8Sr0.2FeO3-δ-Gd0.2Ce0.8O2-δ Cathode for Solid Oxide Fuel Cells

by Surface Modification with BaCO3 Nanoparticles. Micromachines, 13(6). https://doi.org/10.3390/mi13060884

[16] Liu, J., Jing, Y., Zhu, D., Zhang, Y., Li, X., Jia, X., Ouyang, Y., Gao, X., Luan, H., Li, Z., & Zhu, C. (2023). Fe-Doped Ba0.9K0.1FexCo1-xO3–δ Perovskite Cathode Material for Low-Temperature Solid Oxide Fuel Cells. ACS Applied Energy Materials, 6(13). https://doi.org/10.1021/acsaem.3c00314

IJSRST

3rd National Conference on
Emerging Approaches Towards Sustainability

Organized By

**Department of Physics & Mathematics
in Collaboration with IAPT RC 08F
Anand Charitable Sanstha, Ashti's
Anandrao Dhonde Alias Babaji Mahavidyalaya, Kada Tal.
Ashti Dist. Beed, Maharashtra, India**